"STATIC AND DYNAMIC BRITTLE FRACTURE"

by Anas H. Yaghi, B.Eng

Thesis submitted to the University of Nottingham
for the degree of Doctor of Philosophy

June 1993

CONTENTS

ABSTRACT

The project examined the static and dynamic fracture mechanics of brittle materials. Destructive testing was performed on brittle, elastic, isotropic and homogeneous epoxy resin specimens made of Araldite CT-200 with Hardener HT-907.

Three types of specimen were investigated, namely the three point bend (3PB) beam, the compact mixed-mode (CMM) specimen and the pressure tube. The 3PB and CMM specimens contained both narrow notches and real cracks. The pressure tubes included semi-circular notches. The real cracks were obtained by controlled fatiguing.

The research involved the evaluation of the static mode-I and mode-II real and apparent critical stress intensity factors. The fracture surfaces and the phenomenon of crack branching were studied. The dynamic mode-I stress intensity factor was obtained at the inception of crack instability and also at branching.

The concept of the existence of a unique relationship between the dynamic stress intensity factor and the instantaneous crack velocity was addressed.

The possibility of modelling cracks in structural components by using cast shim notches in epoxy resin was discussed. The modelling of the static behaviour was proposed to be accurate and relatively easy. The dynamic behaviour would be approximately modelled; therefore suggestions on how to improve the dynamic modelling of propagating cracks were recommended, paying particular attention to the branching process and the instantaneous crack velocity.

In addition to the experimental work, finite element analysis was conducted for the 3PB and CMM specimens containing narrow notches. It was shown that the specific geometry and loading conditions were unimportant and that the loading was conveniently characterised by the stress intensity factors for an equivalent crack. A method was devised which provided a relatively cheap and efficient means of determining stress concentration factors for what might appear to be complex geometries and loading conditions.

ACKNOWLEDGEMENTS

I am sincerely thankful to many people, nevertheless I will limit the following acknowledgements to those who have been directly involved in my PhD project and the writing of my thesis.

My first and foremost acknowledgement is to my father, mother and family without whose love guidance and wisdom this achievement in my education would not have reached fruition. My father was the one who continuously emphasized that my future success would be based upon a sound education.

My supervisor, Tom Hyde, was consistently helpful and his ability to perceive the relevant elements in what at times seemed a morass of detail was greatly appreciated.

Two persons who were special to me were Annie Cresham and Bashar Barghouti. Their effort towards the final part of my work was highly valued.

The person whose technical skill was vital to my research was Tony Higgins. The other technical staff who were kindly involved in my project were Bernard

Mynett, Ray Pickard and Mike Sloman.

My final thanks will go to all my colleagues at the University of Nottingham, who created a pleasant and friendly environment.

NOMENCLATURE

A_1 : Location point defined in Figs. 7.9 & 8.7.

A_2 : Location point defined in Figs. 7.9 & 8.7.

A_3 : Location point defined in Figs. 7.9 & 8.7.

a : Length of straight notch or crack, or radius of semi-circular notch.

a_C : Critical value of a at which crack propagation starts.

a_{cen} : Crack length at the centre of the crack front.

a_{end} : Crack length at either end of the crack front.

a_{mid} : Crack length at the midway point between the centre and either end of the crack front.

å (≡v) : Velocity of crack propagation.

B : Specimen thickness.

B_s : Specific value of B defined in Fig. 2.16.

B_0 : A value of B defined in Fig. 2.16.

C : Compliance of a plate which is defined in equation (2.9).

C_1 : A constant defined in equation (1.1).

C_2 : Dimensionless factor defined in equation (2.3).

C_3 : Empirical material constant defined in equation (2.34).

CMM : Compact mixed-mode.

c_1 : Velocity of dilatational waves defined in equations (2.36 & 2.37) for an infinite elastic solid.

c_2 : Velocity of distortional waves defined in equation (2.38) for an infinite elastic solid.

d : Internal diameter of pressure tubes.

ds : Element of ark length along Γ.

E : Modulus of elasticity (Young's modulus).

E_{kin} : Kinetic energy of the material at the crack tip which is represented in Fig. 2.18.

F : Compressive force acting on the 3PB specimen as shown in Figs. 5.8, 5.15, 7.1 & I.1.

F_C : Critical value of F (at failure).

G : Energy release rate (crack extension force) defined in section 2.3.

G_C : Critical value of G.

G_I : G in mode-I loading conditions.

G_{IC} : G_C in mode-I loading conditions.

G_{II} : G in mode-II loading conditions.

G_{III} : G in mode-III loading conditions.

H : Work preformed by external force on a plate containing a crack which is defined in section 2.3.

I : Second moment of area of beam.

i : Suffix substituting for x, y or z.

J : J-integral defined in equation (2.15).

j : Suffix substituting for x, y or z.

K : Stress intensity factor.

K_C : Fracture toughness, or critical stress intensity factor.

K_D : Dynamic stress intensity factor.

K_I : Mode-I stress intensity factor (usually for plane strain conditions).

K_{IC} : Plane strain fracture toughness, or critical mode-I stress intensity factor.

K_{ID} : Plane strain dynamic fracture toughness or dynamic mode-I stress intensity factor.

K_{II} : Mode-II stress intensity factor.

K_{IIC} : Critical mode-II stress intensity factor.

K_{III} : Mode-III stress intensity factor.

K_{max} : Maximum value of K.

K_{min} : Minimum value of K.

K_1 : Mode-I stress intensity factor.

K_{1C} : Fracture toughness, or critical mode-I stress intensity factor.

K^{APP} : Apparent stress intensity factor.

K_C^{APP} : Apparent critical stress intensity factor.

K_I^{APP} : Apparent mode-I stress intensity factor.

K_{IC}^{APP} : Apparent critical mode-I stress intensity factor.

K_I^0 : Mode-I stress intensity factor for $\alpha = 0°$.

K_I^{90} : Mode-I stress intensity factor for $\alpha = 90°$.

K_{II}^0 : Mode-II stress intensity factor for $\alpha = 0°$.

K_{II}^{90} : Mode-II stress intensity factor for $\alpha = 90°$.

L : Specimen loading span (shown in Figs. 5.8, 5.15 and 7.1).

M : Dimension shown in Figs. 5.2, 5.11 and 5.13.

m : Empirical material constant defined in equation (2.34).

N : Dimension shown in Figs. 5.2, 5.11 and 5.13.

N_{cyc} : Number of fatigue cycles.

N_* : Number of unbroken electrically-conductive grid lines.

n : Magnitude of $\bar{n}$.

$\bar{n}$: Normal unit vector defined in Fig. 2.8.

P : Tensile force acting on specimen as shown in Figs. 2.7, 6.1, 6.5, 6.6 and 8.2.

P_c : Critical value of P (at fracture).

p : Hydraulic internal pressure in tubes.

Q : Energy needed for crack formation which is defined in section 2.3.

R : Crack resistance (crack resistance force) defined in equation (2.7) and shown in Fig. 2.18.

R_{cyc} : Fatigue cycle ratio defined in equation (2.35)

R_1 : Electric resistance shown in Figs. 9.5 and 9.6.

R_2 : Electric resistance shown in Figs. 9.5 and 9.6.

R_* : Electric resistance per grid line shown in Fig. 9.5.

r : Radial position relative to notch or crack tip as shown in Figs. 2.5, 7.3 and 8.1.

r_p : Irwin's plastic-zone size (shown in Figs. 2.9 & 2.10).

s : Half the width of notch or crack (occasionally the width is referred to as the thickness) - it is assumed to be zero for a crack.

T : Magnitude of $\bar{T}$.

$\bar{T}$: Traction vector defined according to the outward normal along Γ.

t : Thickness of pressure-tubes side-walls.

U : Elastic energy contained in a plate with a crack, which is defined in section 2.3.

$\bar{u}$: The displacement vector (in the x-direction).

V : Displacement of load-application point as shown in Fig. 2.7.

V_i : Input voltage shown in Fig. 9.5.

V_o : Output voltage shown in Fig. 9.5.

v ($\equiv \dot{a}$) : Velocity of crack propagation.

v_{avg} : Average value of v.

v_s : Velocity of sound waves in a material.

W : Specimen width.

x : Cartesian coordinate.

Y : Dimensionless geometry factor.

y : Cartesian coordinate.

z : Cartesian coordinate.

α : Loading angle shown in Figs. 6.1, 6.5, 6.6 and 8.2.

β : Rigidity modulus (shear modulus of elasticity).

Γ : Contour for the J-integral defined in Fig. 2.8.

γ : Angle of crack-initiation for the semi-circular notches which is defined in Fig. 9.14.

ΔK : The change in K as defined in equation (2.33).

ΔK_{th} : The threshold value of K below which fatigue crack growth does not occur (shown in Fig. 2.17).

δ : Mass density (specific density).

ε : Strain.

ζ : Dugdale plastic-zone size (shown in Fig. 2.11).

η : Notch shape factor defined in sections 7.2.2 and 8.2.2.

θ : Angular position relative to notch or crack tip as shown in Figs. 2.5, 7.3 and 8.1.

κ : Bulk modulus.

Λ : Strain-energy density as defined in equation (2.16).

λ : Lamé's constant.

μ : Displacement in x-direction.

ν : Displacement in y-direction.

ξ : Gradient of straight-line-graph of F versus deflection of beam in appendix I (F and beam are shown in Fig. I.1).

$\rho(\equiv\varrho)$: Notch corner radius.

σ : Stress.

σ_{max} : Maximum stress at a point.

σ_{nom} : Nominal stress.

σ_{rem} : Remote tensile stress perpendicular to crack.

σ_u : Ultimate tensile stress.

σ_Y : Tensile yield stress.

σ_θ : Hoop stress.

σ_1 : Principal stress where $\sigma_1>\sigma_2>\sigma_3$.

σ_2 : Principal stress where $\sigma_1>\sigma_2>\sigma_3$.

σ_3 : Principal stress where $\sigma_1>\sigma_2>\sigma_3$.

$\hat{\sigma}$: Peak stress.

τ	:	Shear stress.
υ	:	Poisson's ratio.
ψ	:	Angular position in notch radius as shown in Figs. 7.3(b), 7.9 and 8.7.
ψ_{peak}	:	Angular position of peak stress.
ω	:	Displacement in z-direction.
$\varrho(\equiv\rho)$	:	Notch corner radius.
$f(\theta)$	:	Known function of θ.
3PB	:	Three point bend.

CHAPTER ONE

INTRODUCTION: HISTORY REVIEW

Early this century engineers were becoming increasingly aware of the failure of structures due to crack propagation. Recently, Anderson [1] and Broek [2] described many accidents which occurred in the last two hundred years. Poor design and the lack of knowledge in fatigue and fracture science were the main contributors. A few of their examples follow.

In 1830 about seven hundred people had gathered on Montrose suspension bridge when one of its main chains gave way, causing considerable loss of life. Between 1860 and 1870 railway accidents in Britain killed about two hundred people per year. In 1866 the government received a complaint stating that some fifty to sixty boilers exploded annually in the United Kingdom causing the loss of many lives and the destruction of property. During the Second World War, 2500 Liberty ships were built in which welding was involved; 145 ships broke in two and almost 700 experienced serious failure.

The need to improve the predictability of fracture, in order to prevent catastrophic structural failures was becoming more imperative. The science of

mechanics of fracture is very recent. Engineers and scientists at the beginning of this century started developing this field. In 1913, Inglis [3] provided a stress solution for a flat plate under uniform tension with an elliptical hole which could be degenerated into a crack. Griffith [4] made use of that in 1920. He also referred to the work done by Love [5] when he performed his potential and strain energy analysis on "a flat homogenous isotropic plate of uniform thickness, containing a straight crack which passes normally through it, the plate being subjected to stresses applied in its plane at its outer edge". Griffith found an expression for the total energy (potential and strain energy) of the cracked plate, and mathematically stated that the crack would propagate when the energy released due to crack extension was equal to the energy required to produce the new surfaces of the crack. Griffith also derived an expression which could be simplified to the following equation.

$$\sigma_{rem}\sqrt{a} = C_1 \qquad (1.1)$$

where, σ_{rem} is the remote tensile stress perpendicular to the crack, a is the crack length, and C_1 is a constant.

In 1939, Westergaard [6] published his famous paper in which he considered the case of a stressed cracked cylinder. He derived an expression which showed that the stress tended to infinity at the crack tip. The expression was in the complex form, which was developed and relied upon by many later authors.

In 1946, Sneddon [7] considered two examples of a crack, firstly the Griffith crack, in the two-dimensional case, which was described here earlier, and secondly a

circular crack in the three-dimensional model. Sneddon's calculations were based on a solution of the elastic equations given by Westergaard. Sneddon was the first to produce expressions for the stresses in the vicinity of the crack tip.

In 1957, Irwin [8], using the Westergaard method, developed expressions for the stresses in the vicinity of a crack tip, which included the stress intensity factor in the opening mode of loading. Irwin referred to the work of other authors such as Sneddon [7] and Orowan [9]. He wrote another paper in 1958 [10] stating expressions for the stresses and displacements at a crack tip including the stress intensity factor in the three different loading modes. These equations were extracted by Paris and Sih and written in their well-presented paper in 1964 [11], and later used by the like of Knott (1973) [12], Broek (1974) [2] and Parker (1981) [13]. Paris and Sih provided a concise historical background for the general development of the science of fracture mechanics. A good historical review was also presented by Weiss and Yukawa [14]. They started by referring to authors like Griffith and Irwin, and went on to give their own interpretation of fracture toughness, commenting on the issue of the plastic zone at the crack front. Fuchs and Stephens wrote a book which was published in 1980 [15]; in the first chapter of their book they presented a historical overview about the science of fatigue and fracture mechanics. They explained how Griffith became the "father" of fracture mechanics, and how Irwin introduced the stress intensity factor.

The dynamic side of fracture mechanics was firstly looked upon by Mott [16], in 1948, who studied the Griffith crack and produced an expression for its propagation velocity, by analytical kinetic energy considerations. He stated "..., the analysis

suggests that the velocity of propagation, under uniform stress, of a crack in a material that is not ductile, will tend towards a value of the order of the velocity of sound in the material and which is independent of the stress applied or of the atomic cohesive forces across the cleavage plane".

Elizabeth Yoffe was one of the pioneers in the dynamic fracture mechanics field. Her famous paper [17] was published in 1951. She was the first scientist to develop an equation describing the stresses in the vicinity of a propagating crack tip. She has shown that, if a crack propagates in a direction normal to the maximum tensile stress, there is a critical velocity of about 0.6 c_2 at which the crack tends to become curved, where c_2 is the velocity of propagation of shear waves in the material. At a lower velocity the crack extends in a straight line. As the speed increases the crack may form branches. At even higher velocities there is a certain preferred direction for the propagation of branches which is at approximately 60 degrees to the direction of the original crack.

Yoffe used the stress solution provided by Inglis [3] for a static stress field in the case of a straight narrow crack. She also used the solution of the stress field given by Westergaard [6] which she thought was presented in a more convenient form. She referred to Love's work [5] in her elastic-waves application.

In her analysis, Yoffe simplified her model by assuming a Griffith crack propagating at one tip and healing at the other, thus maintaining a constant crack length. She explained by saying, "This is justified by the fact that the stress

distribution close to one end of the crack is not influenced by its distance from the other end".

In 1954, Roberts and Wells [18] obtained an expression for the velocity of crack propagation for a Griffith crack. They based their analysis on the solution given by Mott [16]. Having studied some experimental results, their conclusion was that the terminal crack velocity is governed by the supply of kinetic energy to the crack field. They also stated that, "The influence of stress waves appears to be to limit the volume of material to which kinetic energy must be supplied rather than to modify the stress distribution from the static values about the crack".

Craggs [19], in 1960, developed expressions for the stresses in the vicinity of a dynamic crack tip. He made use of the Griffith theory [4] to analyze a semi-infinite crack in an infinite medium which was extended by finite forces. He thought his method had two advantages over that of Yoffe [17]: his solution might be obtained by much more elementary methods; and an estimate of the force required to extend the crack could be included.

Craggs concluded that the force required to maintain a steady rate of crack extension would be smaller for a higher rate of extension. The same conclusion was arrived at by McClintock and Sukhatme in their paper published in 1960 [20]. They used the solution given by Bilby and Bullough [21] for the stress field in the vicinity of a travelling crack under shear forces. By analogy, they obtained a solution for the tensile-forces case for the same crack studied by Craggs [19]. Their result was in

agreement with that of Yoffe [17] when they found that branching of a travelling crack would start at a critical velocity of about 0.6 times that of the shear wave velocity. In their analysis they compared two different fracture criteria: the Griffith energy criterion and that of local average shear strain. As far as McClintock's and Sukhatme's results were concerned, both criteria yielded similar results.

In 1962, Baker [22] obtained a solution for the stresses in the vicinity of a crack tip for the case in which a semi-infinite crack suddenly appeared and grew at constant velocity in a stretched elastic body. He commented on Yoffe's result for a critical crack velocity and indicated a slight disagreement according to the conclusion he extracted from Williams' paper [23], which is that in the vicinity of the crack tip the hoop stress is not the largest principal stress.

In 1964, Cotterell [24] did some work on the dynamic elastic-wave equations. In his paper, he gave an explanation for the effect of the crack velocity on the surface roughness of the fracture surfaces. He associated the increase in surface roughness with the increase in fracture toughness for steel. Also, he explained the surface roughness generally by referring to the theory that at high crack velocity, the principal stresses ahead of the crack tip would not be at right angles to the direction of propagation.

In his paper in 1972, Nilsson [25] considered a strip of a linearly elastic, homogenous and isotropic material having finite width and thickness and infinite length. The strip contained a through-the-thickness crack of semi-infinite length

running along the length of the strip with a constant velocity. The effects of finite boundaries were incorporated. He described the problems that he treated to be highly idealized, but might still serve as good approximations of real situations in experiments carried out in order to study crack propagation.

He derived an expression for the stress intensity factor, and showed that it would decrease with an increase in the crack velocity in a non-linear manner, until it reached zero when the crack velocity was equal to the Rayleigh velocity (surface wave velocity).

Nilsson compared his solution with the solution obtained by Willis [26] and that obtained by Sih and Chen [27]. Willis found that for infinite sheets, the stress intensity factor is independent of the crack velocity. Sih and Chen treated a problem similar to the one treated by Nilsson, but in the tearing mode; they obtained a similar result to Nilsson. Thus Nilsson concluded that the independence of the stress intensity factor, in the opening mode, of the propagation velocity was a feature that arose in the idealization of a real problem to an infinite sheet problem.

Many other authors have written about the dynamic side of crack propagation. Freund in his paper published in 1973 [28], and Hartranft and Sih in their paper published in 1974 [29], described the effect of stress waves on crack propagation. Achenbach published a paper in 1974 [30] which treated the problem of crack branching. Also, in 1974, Atkinson [31] looked upon the problem of fracture, paying particular attention to a crack running along the interface between two different elastic

media. In 1974, Broek [2] gave an elementary account of the general behaviour of a dynamic crack in his well-known book which was revised and reprinted in 1978, 1982 and 1986.

CHAPTER TWO

THEORETICAL BACKGROUND

2.1. Ductile Tearing and Brittle Fracture

In general, engineering components can break in two different manners, or in a combination of the two. The first is called ductile tearing or ductile fracture and is associated with ductile materials. The other is called cleavage or brittle fracture and is associated with brittle materials. Fracture occurs due to overloading a component. It is very important to be able to predict the critical forces below which safety would be maintained.

Toughness is the term used to describe the ability of a material to deform plastically and to absorb energy before and during rupture [2]. If the material is not tough, or in other words when its fracture toughness, K_C, is small, then the material is described to be brittle. When the material is tough, or has a high fracture toughness, the material is ductile. Fig. 2.1 describes the relationship between the Charpy impact energy and temperature for steel, which clarifies the relationship between toughness and the energy absorption when fracture occurs; the material in consideration is steel, showing transition from the brittle state at low temperature to

the ductile state at high temperature.

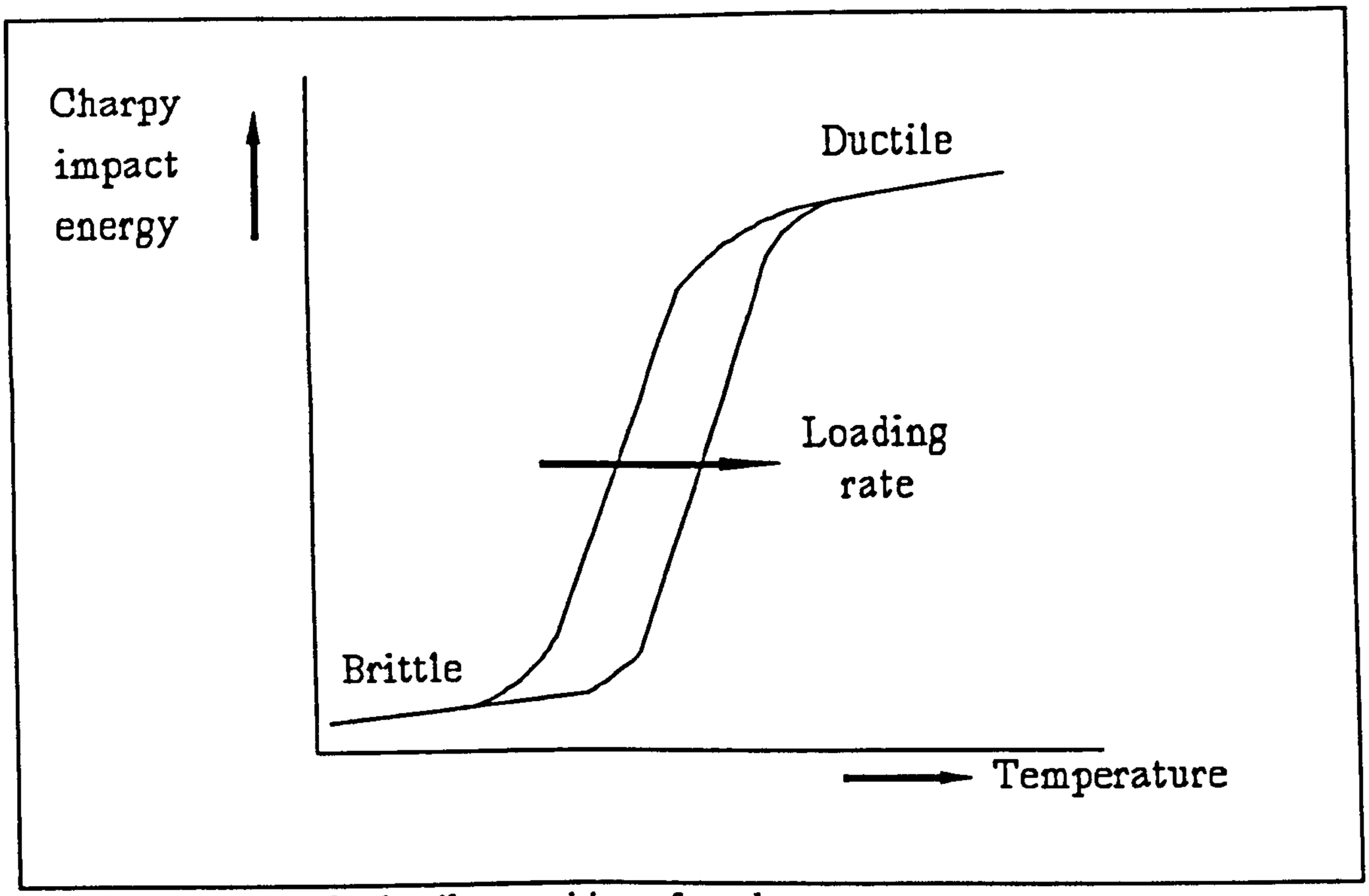

Fig. 2.1. Brittle-ductile transition of steel.

The shape of a broken component can give a good indication of how tough the material is. This is another aspect of component failure. There are three types of fracture: a point, a flat, and a cup and cone fracture [13].

When a ductile component is overloaded in uniaxial tension, it can deform by necking until the reduction in its cross-sectional area is almost 100%; then, final fracture will occur at a point. Slipping occurs on the planes of maximum shear stress - Fig. 2.2(a). When the component is brittle it will fail with hardly any plastic deformation. The fracture surfaces will be flat and perpendicular to the axis of the component; cleavage fracture occurs on the planes of maximum tensile stress - Fig. 2.2(b). The most common type of fracture is the cup and cone fracture. It is

associated with a material which is neither extremely brittle nor extremely ductile. A component under uniaxial overloading will start off by slipping on the maximum shear stress planes, followed by cleavage fracture on the maximum tensile stress planes when the cross-sectional area is not sufficiently large to withstand the tensile stress - Fig. 2.2(c).

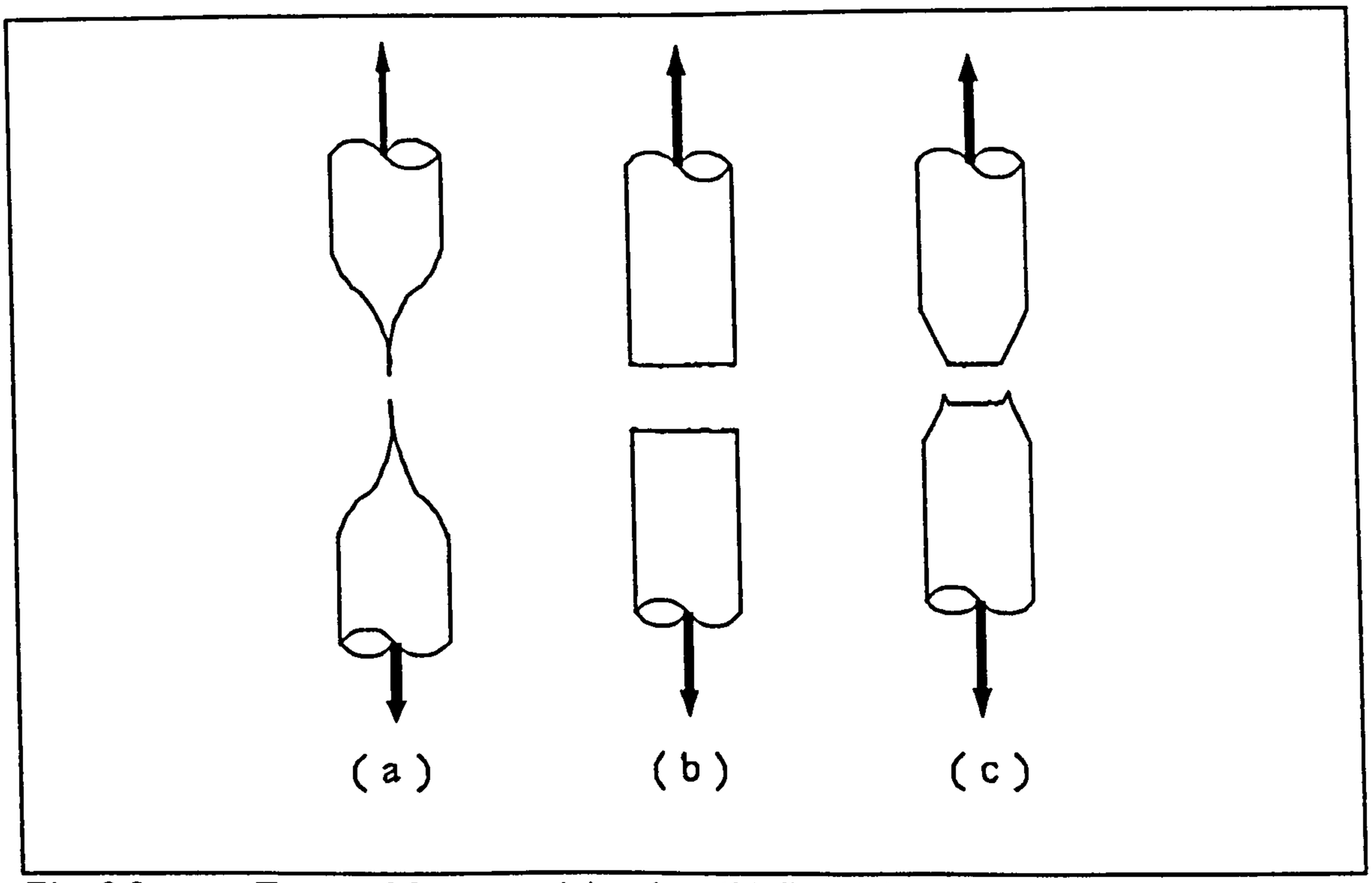

Fig. 2.2. Types of fracture: (a) point; (b) flat; (c) cup and cone.

Fig. 2.3 describes the relationship of fracture toughness and the three types of fracture. The fracture toughness, K_c, is also called the critical stress intensity factor. On the brittle side the fracture toughness is called the critical stress intensity factor in mode-I loading, K_{IC}, which will be considered in detail in other sections of the thesis.

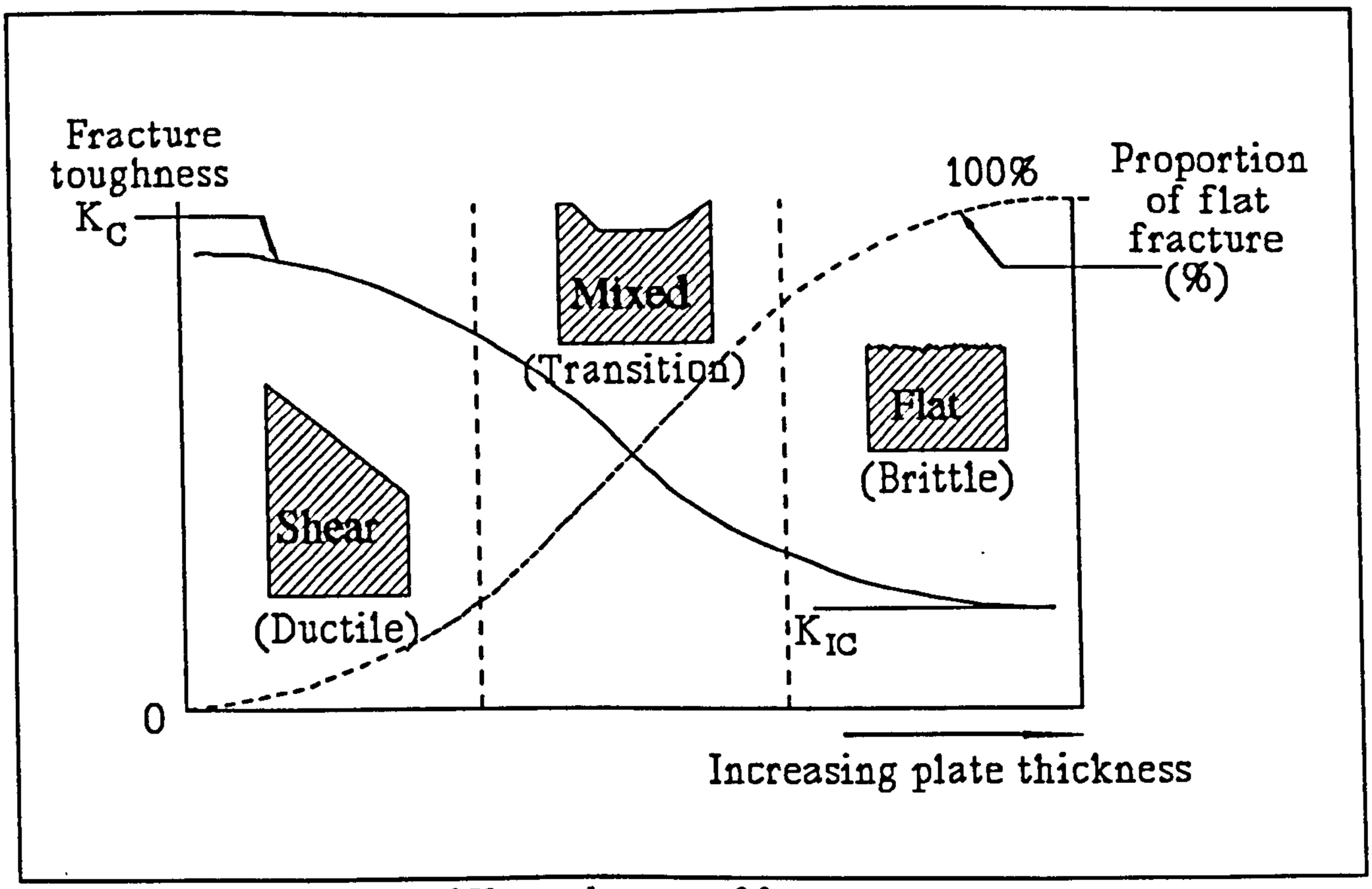

Fig. 2.3. The effect of K_C on the type of fracture.

2.2. A Crack in a Structure

The presence of cracks in a structure, no matter how small, may have some significance on the strength of the structure. As the structure is loaded, the cracks will be stimulated to grow, and when they reach a critical size they may dictate whether the structure will fail.

A crack in a structure will give rise to a stress concentration at the crack tip. Similarly a notch in a component will give rise to a stress concentration at the notch tip. The stress at the notch tip can be calculated using a parameter called the stress concentration factor, which has been tabulated in numerous publications [e.g. 32, 33, 34, 35 and 36]. The stress concentration factor is the stress at the notch tip divided

by the nominal stress.

The stress concentration factor increases with an increase in the sharpness of the notch tip. A real crack has an infinitesimally small thickness, and therefore the stress concentration factor approaches infinity at the crack tip.

The theoretical infinitely-large stresses at the crack tips introduce complexity to the task of stress analysis. Plasticity at the crack tip re-evaluates and redistributes stresses, preventing them from reaching infinity; in fact, they can never exceed the ultimate tensile stress. Thus, the insufficiency of the stress concentration factor in such problems is disadvantageous. The need for another parameter which describes the field stresses in the vicinity of the crack tip prevails. This parameter is called the stress intensity factor. The stress intensity factor defines the magnitude of the elastic stress field in the vicinity of a crack tip.

Depending on the loading conditions, a crack can deform in three different ways, shown in Fig. 2.4: the opening mode (mode-I), the sliding or shear mode (mode-II), and the tearing mode (mode-III).

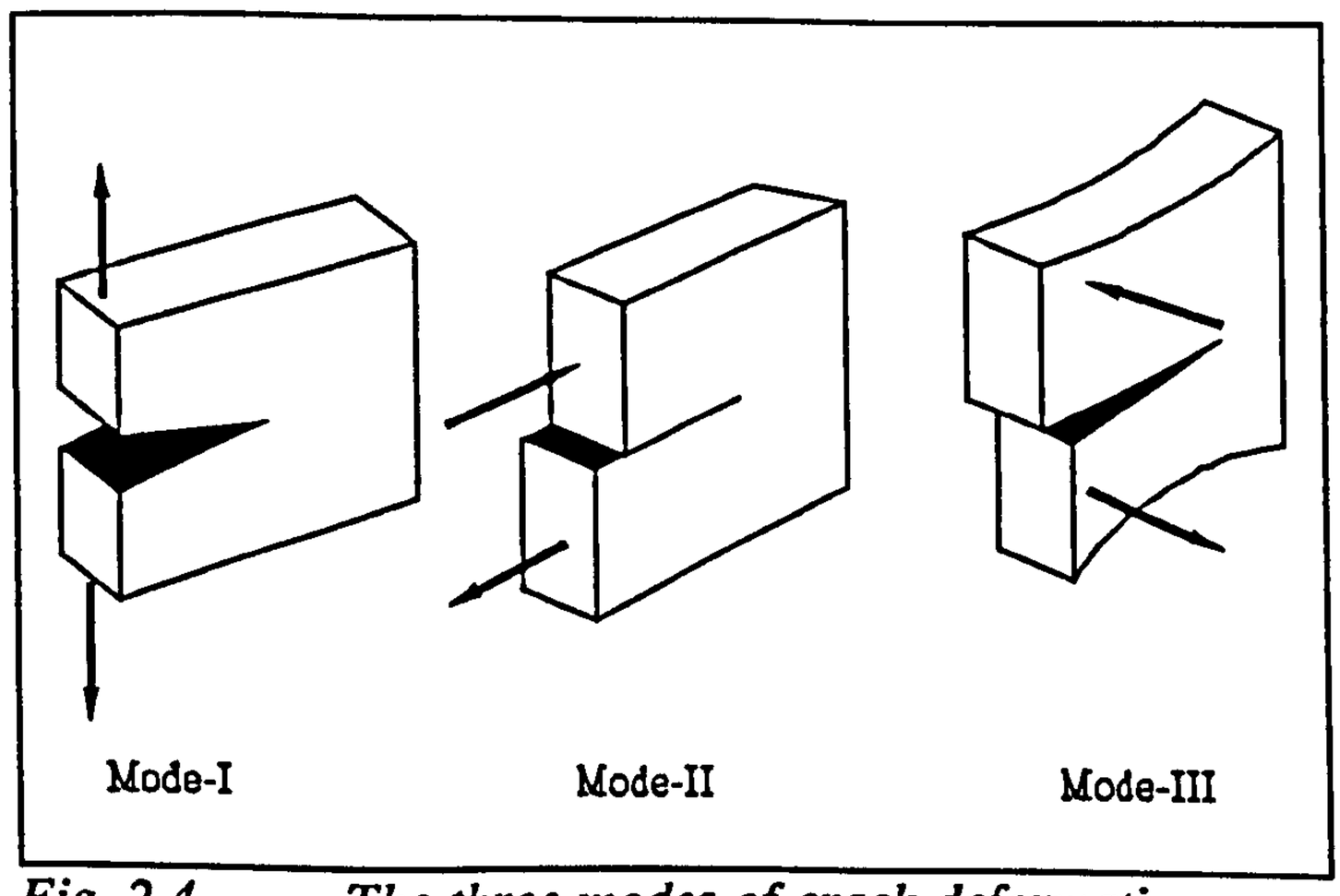

Fig. 2.4. The three modes of crack deformation.

In the opening mode, the displacement of the crack surfaces are perpendicular to the plane of the crack. In the sliding mode, the displacements of the crack surfaces are in the plane of the crack and perpendicular to the leading edge of the crack (the crack front). In the tearing mode the crack surface displacements are in the plane of the crack and parallel to the crack front [2]. The three modes are called the crack deformation modes or the loading modes.

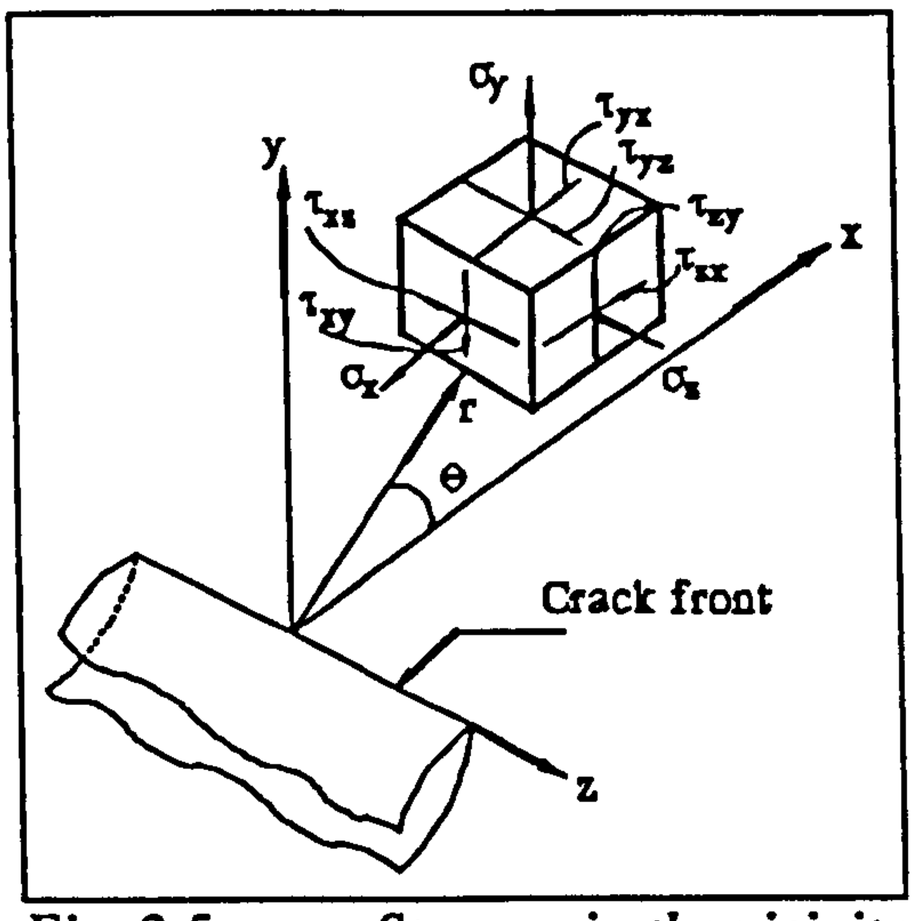

Fig. 2.5. Stresses in the vicinity of a crack tip.

There is a stress intensity factor, K, for each of the three modes. For modes I, II and III the stress intensity factor is called K_I, K_{II} and K_{III} respectively.

The conventions concerning the stresses in the vicinity of the crack tip are shown in Fig. 2.5.

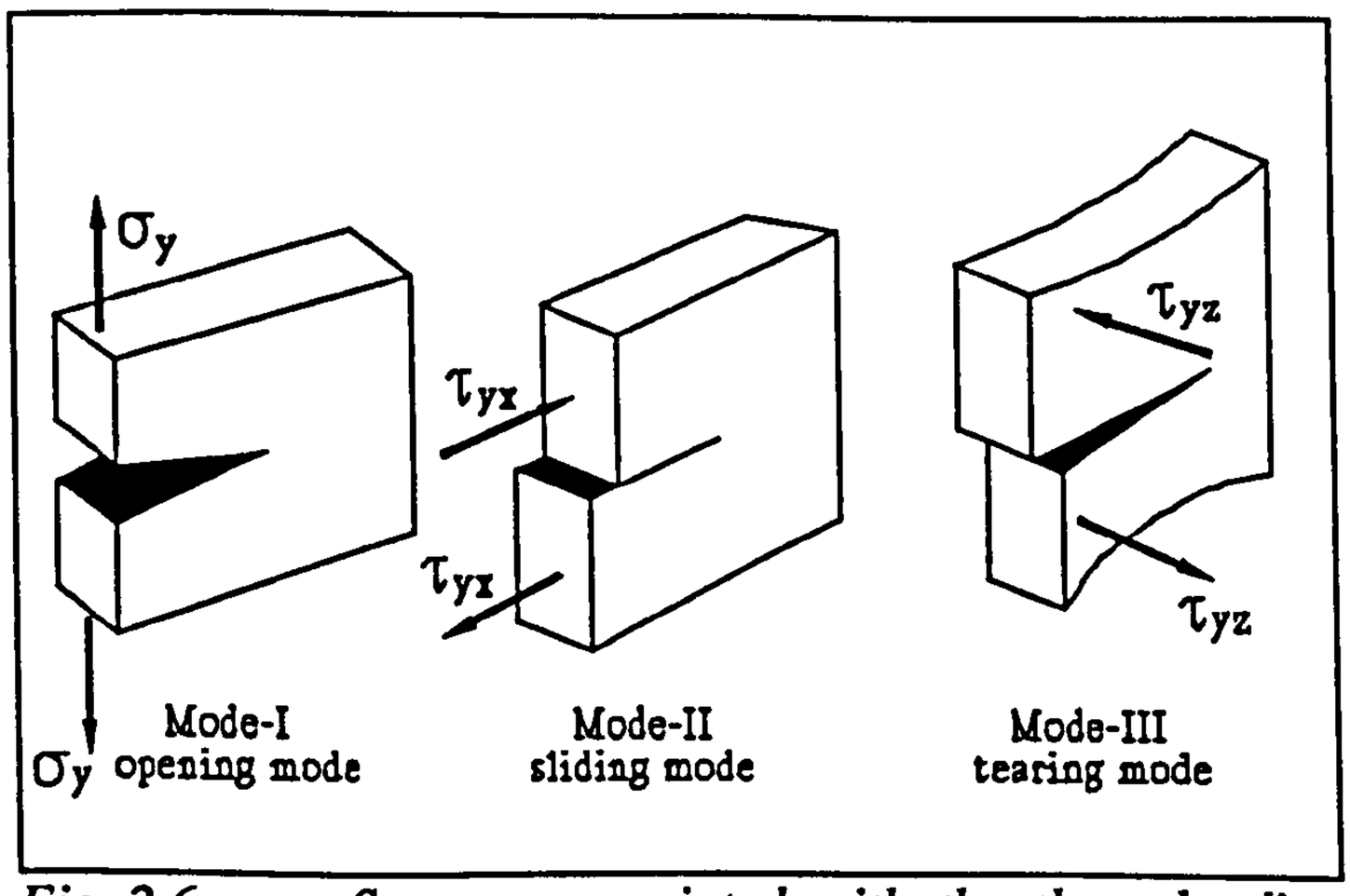

Fig. 2.6. Stresses associated with the three loading modes.

In order to give the mathematical definitions of the stress intensity factors for the three modes, Fig. 2.6 shows the relevant stresses.

Mathematically, the pure stress intensity factors are defined in equations (2.1) [37].

$$K_I = \lim_{r \to 0} \{ \sqrt{2\pi r}\ \sigma_y (r,0) \} \qquad \textbf{(2.1.a)}$$

$$K_{II} = \lim_{r \to 0} \{ \sqrt{2\pi r}\ \tau_{yx} (r,0) \} \qquad \textbf{(2.1.b)}$$

$$K_{III} = \lim_{r \to 0} \{ \sqrt{2\pi r}\ \tau_{yz} (r,0) \} \qquad \textbf{(2.1.c)}$$

The stresses in the vicinity of a crack tip are usually expressed in the form

$$\sigma_i (r,\theta) = \frac{K}{\sqrt{2\pi r}} f_i(\theta) + \textit{non-singular terms} \qquad \textbf{(2.2.a)}$$

$$\tau_{ij} (r,\theta) = \frac{K}{\sqrt{2\pi r}} f_{ij}(\theta) + \textit{non-singular terms} \qquad \textbf{(2.2.b)}$$

where σ_i, τ_{ij}, r and θ are defined in Fig. 2.5 (i and j being any of x, y and z), and $f_i(\theta)$ and $f_{ij}(\theta)$ are known functions of θ. Both σ_i and τ_{ij} are occasionally expressed in the form σ_{ij}. K can be K_I, K_{II} or K_{III} according to the mode of loading. The "other terms" contain higher orders of r, and hence can be ignored if the point (r,θ) is sufficiently close to the crack tip. Equations (2.2) are called the linear elastic solution for the stress field in the vicinity of the crack tip. They predict infinite stresses when $r = 0$. This is not realistic since plastic deformation prevents stresses from reaching an

infinite value. If the region of plastic flow is small compared to the region over which the "other terms" can be ignored, "it may be assumed that the behaviour of the crack is determined by the elastic stress intensity factor. This assumption forms the basis of linear elastic fracture mechanics" [37].

Griffith [4] established the energy criterion for fracture mechanics on which many later authors based their work. In addition, Griffith was the first to present an expression for the stress intensity factor which could be written in the form

$$K = C_2 \, \sigma_{rem} \sqrt{a} \qquad (2.3)$$

where σ_{rem} is the remote tensile stress, a is the length of the crack and C_2 is a dimensionless factor which depends on the geometry of the plate in question or any other component.

2.3. Energy Considerations

Griffith [4] stated that a crack would propagate if the energy released by the system upon crack growth was sufficient to provide the energy required to break the atomic bonds and produce the new surfaces of the crack.

Broek [2] referred to Griffith [4 & 38] and presented the following equations.

Consider a crack of length 2a in the centre of a plate (the crack having two tips), or a crack of length a at the side of a plate (the crack having one tip). In both

cases, for the crack to grow by da,

$$\frac{d}{da}(H-U) = \frac{dQ}{da} \tag{2.4}$$

where U is the elastic energy contained in the plate, H is the work performed by the external force, and Q is the energy needed for crack formation, all of which are per unit thickness of the plate. The energy release rate, sometimes called the crack extension force, is denoted by G.

$$G = \frac{d}{da}(H-U) \tag{2.5}$$

At fracture, G reaches its critical value which is denoted by G_C. Corresponding to the three different modes of loading, there are G_I, G_{II} and G_{III}. The total energy release rate in combined mode cracking is obtained by adding the energies from the different modes - equation (2.6).

$$G = G_I + G_{II} + G_{III} \tag{2.6}$$

The crack resistance, sometimes called the crack resistance force, is denoted by R.

$$R = \frac{dQ}{da} \tag{2.7}$$

It is reasonable to assume that the force required to break the molecular bonds to produce a crack is constant for a material. In the case of plane strain where there

is very little plasticity at the crack tip, most of the work done to produce the new surfaces of the crack is lost in the breakage of the molecular bonds. Therefore, it is assumed that the crack resistance, R, is constant for a plane strain brittle fracture situation in the static stage. In the dynamic stage, after the crack actually starts running with a high velocity, complications associated with the dynamic effects occur, such as the existence of stress waves. In the static stage, the constant value of R leads to a constant value of the critical energy release rate, G_c, for a particular material (see Fig. 2.18).

In ductile tearing, plasticity at the crack tip occurs, and a large portion of the work done to produce the fracture surfaces is lost in the plastic deformation of the material. Here, G cannot be determined from the linear elastic stress field; also, R is not constant any more.

Broek [2] showed that for a cracked plate of thickness B under load P, as shown in Fig. 2.7,

$$G = \frac{P^2}{2B}\left(\frac{\partial C}{\partial a}\right) \tag{2.8}$$

where a is the crack length and C is the compliance of the plate. As long as there is no crack growth, C is defined by

$$V = C\,P \tag{2.9}$$

where V is the displacement of the load-application points, as shown in Fig. 2.7. From equation (2.9) it is seen that the compliance is the reciprocal of the stiffness.

By considering the Griffith crack [4], which is a through-the-thickness crack of length 2a in a plate under tensile stress, σ, along its length, having an infinite length and width and finite thickness, the crack being perpendicular to the length of the plate,

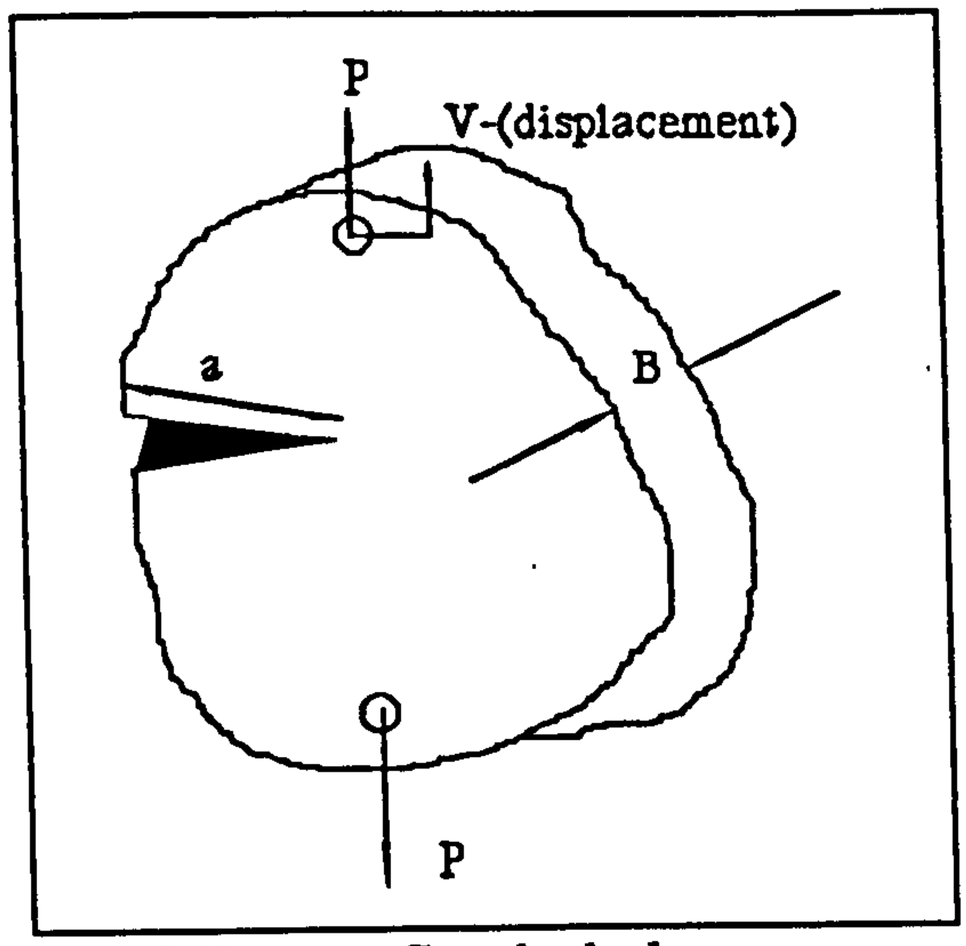

Fig. 2.7. Cracked plate.

Broek [2] showed that for plane stress

$$G_I = \frac{\pi\sigma^2 a}{E} \tag{2.10}$$

and for plane strain

$$G_I = (1-\upsilon^2)\frac{\pi\sigma^2 a}{E} \tag{2.11}$$

where E is Young's modulus and υ is Poisson's ratio. Also, for plane stress

$$G = \frac{K^2}{E} \tag{2.12}$$

and for plane strain

$$G_I = (1-\upsilon^2)\frac{K_I^2}{E} \tag{2.13.a}$$

$$G_{II} = (1-\upsilon^2)\frac{K_{II}^2}{E} \tag{2.13.b}$$

$$G_{III} = (1+\upsilon)\frac{K_{III}^2}{E} \tag{2.13.c}$$

and

$$G = G_I+G_{II}+G_{III} = \frac{1-\upsilon^2}{E}(K_I^2+K_{II}^2+\frac{K_{III}^2}{1-\upsilon}) \qquad (2.14)$$

When there is a considerable amount of plasticity at the crack tip, G cannot be determined from the linear elastic stress field. Therefore, another parameter is introduced for energy considerations. The J-integral is equivalent to the energy release rate.

Rice [39] defined the J-integral and proved that it is path independent. He considered a homogeneous body of linear or non-linear (i.e, with significant plasticity occurring) material free of body forces and subjected to a two-dimensional deformation field so that all stresses, σ_{ij}, and strains, ε_{ij}, depended only on two Cartesian coordinates x and y, which contained a notch or a crack as shown in Fig. 2.8.

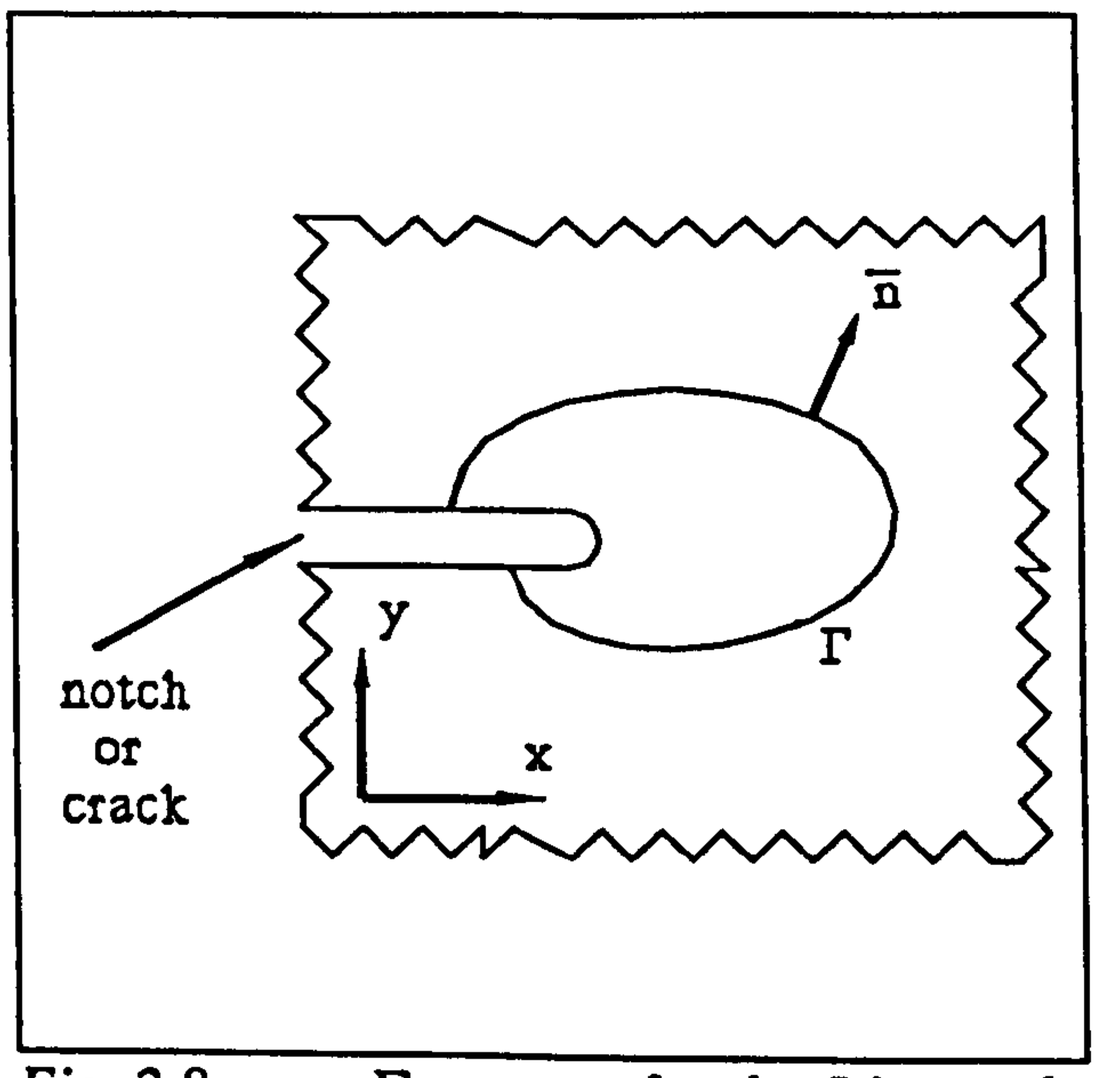

Fig. 2.8. Γ *contour for the J-integral.*

The J-integral is defined as

$$J = \int_{\Gamma}(\Lambda\, dy - \bar{T}.\frac{\partial \bar{u}}{\partial x}ds) \qquad (2.15)$$

where the strain-energy density, Λ, is defined by

$$\Lambda = \Lambda(x,y) = \Lambda(\varepsilon) = \int_0^{\varepsilon} \sigma_{ij}\, d\varepsilon_{ij} \qquad (2.16)$$

Γ is a curve surrounding the notch tip, starting from the lower flat notch surface and moving anticlockwise to the upper flat notch surface, $\bar{u}$ is the displacement vector, ds is an element of arc length along Γ, and T is the traction vector defined according to the outward normal along Γ by the equation

$$T_i = \sigma_{ij}\, n_j \qquad (2.17)$$

When the material is linear elastic and there is no significant plasticity at the crack tip,

$$J = G \qquad (2.18)$$

Generally, the J-integral is evaluated from the load-displacement diagrams.

2.4. Crack Tip Stress and Displacement Equations

When a brittle, homogeneous, isotropic material, which contains a crack, is stressed, the stresses and displacements of the elements of the material at the crack tip can be found using a set of equations firstly derived by Irwin [8 & 10] and re-stated by many later authors such as Parker [13].

The equations predict that at zero distance from the crack tip, the values of the stresses approach infinity. This is called stress singularity at the crack tip. In reality the stresses are prevented from approaching infinity by the plastic deformation which occurs at the crack tip. This plasticity is small when the material behaves in a brittle manner.

Referring to Fig. 2.5, the stresses and displacements are given by equations (2.19, 2.20 and 2.21). β is the shear modulus of elasticity. μ, ν and ω are the displacements in the x, y and z directions respectively. Other terms with r having a higher order than that in the first term (i.e., non-singular terms) have been neglected since r is considered to be very small compared to the crack length. The larger the value of r, the less accurate the equations become.

Mode-I (plane strain):

$$\sigma_x = \frac{K_I}{\sqrt{2\pi r}}\cos(\frac{\theta}{2})[1-\sin(\frac{\theta}{2})\sin(\frac{3\theta}{2})] \qquad (2.19.a)$$

$$\sigma_y = \frac{K_I}{\sqrt{2\pi r}}\cos(\frac{\theta}{2})[1+\sin(\frac{\theta}{2})\sin(\frac{3\theta}{2})] \qquad (2.19.b)$$

$$\tau_{xy} = \frac{K_I}{\sqrt{2\pi r}}\sin(\frac{\theta}{2})\cos(\frac{\theta}{2})\cos(\frac{3\theta}{2}) \qquad (2.19.c)$$

$$\sigma_z = \upsilon(\sigma_x+\sigma_y) \qquad (2.19.d)$$

$$\tau_{xz} = \tau_{yz} = 0 \qquad (2.19.e)$$

$$\mu = \frac{K_I}{\beta}\sqrt{\frac{r}{2\pi}}\cos(\frac{\theta}{2})[1-2\upsilon+\sin^2(\frac{\theta}{2})] \qquad (2.19.f)$$

$$\nu = \frac{K_I}{\beta}\sqrt{\frac{r}{2\pi}}\sin(\frac{\theta}{2})[2-2\upsilon-\cos^2(\frac{\theta}{2})] \qquad (2.19.g)$$

$$\omega = 0 \qquad (2.19.h)$$

Mode-II (plane strain):

$$\sigma_x = -\frac{K_{II}}{\sqrt{2\pi r}}\sin(\frac{\theta}{2})[2+\cos(\frac{\theta}{2})\cos(\frac{3\theta}{2})] \qquad (2.20.a)$$

$$\sigma_y = \frac{K_{II}}{\sqrt{2\pi r}}\sin(\frac{\theta}{2})\cos(\frac{\theta}{2})\cos(\frac{3\theta}{2}) \qquad (2.20.b)$$

$$\tau_{xy} = \frac{K_{II}}{\sqrt{2\pi r}}\cos(\frac{\theta}{2})[1-\sin(\frac{\theta}{2})\sin(\frac{3\theta}{2})] \qquad (2.20.c)$$

$$\sigma_z = \upsilon(\sigma_x+\sigma_y) \qquad (2.20.d)$$

$$\tau_{xz} = \tau_{yz} = 0 \qquad (2.20.e)$$

$$\mu = \frac{K_{II}}{\beta}\sqrt{\frac{r}{2\pi}}\sin(\frac{\theta}{2})[2-2\upsilon+\cos^2(\frac{\theta}{2})] \qquad (2.20.f)$$

$$\nu = \frac{K_{II}}{\beta}\sqrt{\frac{r}{2\pi}}\cos(\frac{\theta}{2})[-1+2\upsilon+\sin^2(\frac{\theta}{2})] \qquad (2.20.g)$$

$$\omega = 0 \tag{2.20.h}$$

To convert equations (2.19 & 2.20) to apply for plane stress, σ_z is set to zero, and υ is replaced by $\upsilon/(1+\upsilon)$.

Mode-III:

$$\tau_{xz} = -\frac{K_{III}}{\sqrt{2\pi r}}\sin(\frac{\theta}{2}) \tag{2.21.a}$$

$$\tau_{yz} = \frac{K_{III}}{\sqrt{2\pi r}}\cos(\frac{\theta}{2}) \tag{2.21.b}$$

$$\sigma_x = \sigma_y = \sigma_z = \tau_{xy} = 0 \tag{2.21.c}$$

$$\omega = \frac{k_{III}}{\beta}\sqrt{\frac{2r}{\pi}}\sin(\frac{\theta}{2}) \tag{2.21.d}$$

$$\mu = \nu = 0 \tag{2.21.e}$$

2.5. Crack Tip Plasticity

2.5.1. Yield Criteria

It was discussed previously that plasticity at a crack tip prevents singularity from occurring. Considering the stresses in the vicinity of a crack tip, the stresses will increase with a decrease in the distance from the crack tip. At some point from the crack tip, the stresses will reach the yield stress of the material and plastic

deformation will commence. This is the simplest method of deciding the inception of yielding.

More realistically, one of the two following yield criteria should be consulted for the start of yielding. If σ_1, σ_2 and σ_3 are the principal stresses ($\sigma_1 > \sigma_2 > \sigma_3$) and σ_Y is the uniaxial yield stress, then Tresca's criterion predicts yielding when,

$$|\sigma_1 - \sigma_3| = \sigma_Y \tag{2.22}$$

and Von Mises' criterion predicts yielding when,

$$(\sigma_1-\sigma_2)^2 + (\sigma_2-\sigma_3)^2 + (\sigma_3-\sigma_1)^2 = 2\sigma_Y^2 \tag{2.23}$$

2.5.2. Irwin's Plastic Zone Model

Broek [2] and Parker [13] explained how Irwin [10] derived and expression for the plastic zone size. He assumed a circular plastic zone of size r_p. The redistribution of the stresses due to the presence of the plastic zone was accounted for, and the final stress field was found, as shown in Fig. 2.9.

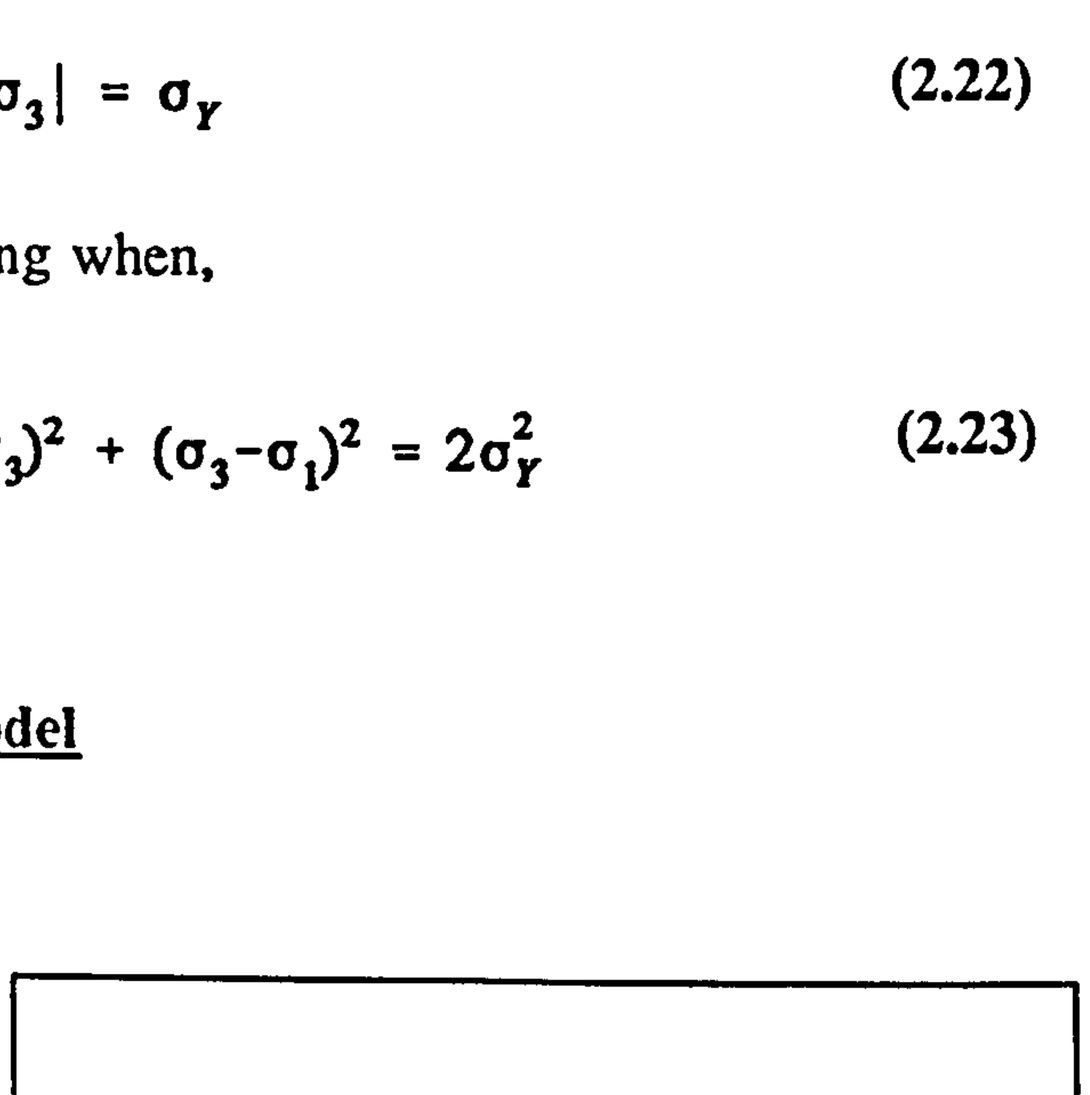

Fig. 2.9. Stresses of the plastic zone.

Irwin [10] argued that the crack behaved as if it had a length ($a + r_p/2$), as shown in Fig. 2.10 with the dashed line.

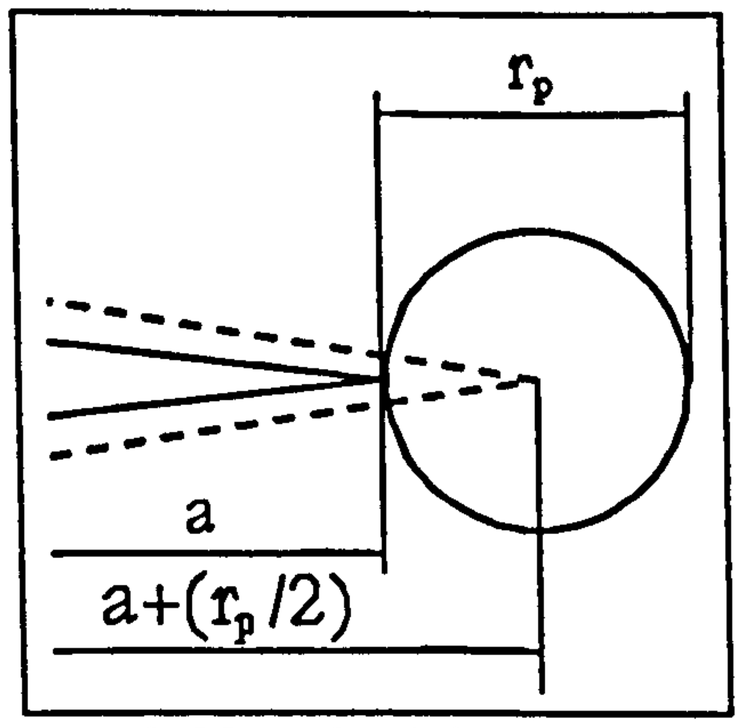

Fig. 2.10. Irwin's corrected crack size.

Irwin's plastic zone size is given by,

$$r_p = \frac{1}{\pi}\left(\frac{K}{\sigma_Y}\right)^2 \qquad \textit{plane stress} \quad (2.24)$$

$$r_p = \frac{1}{3\pi}\left(\frac{K}{\sigma_Y}\right)^2 \qquad \textit{plane strain} \quad (2.25)$$

2.5.3. Dugdale Plastic Zone Model

Broek [2] and Parker [13] presented the model proposed by Dugdale [40]. He assumed that the effective crack would extend right through the plastic zone which is of size ζ, as shown in Fig. 2.11, but in fact the length ζ on either end of the actual crack, 2a, tend to close the crack by withstanding the yield stress, σ_Y.

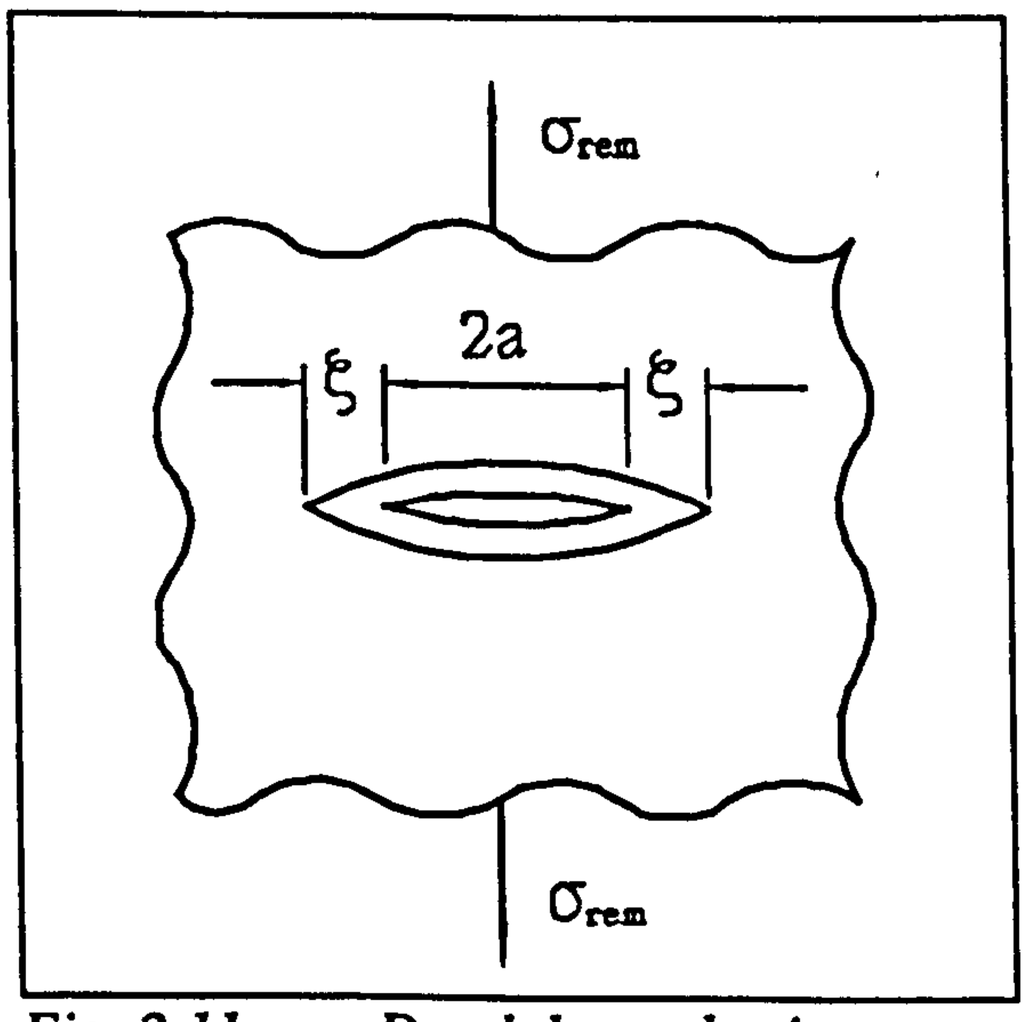

Fig. 2.11. Dugdale plastic zone model.

Dugdale derived the expression

$$\frac{a}{a+\zeta} = \cos\frac{\pi\sigma_{rem}}{2\sigma_Y} \qquad \textit{plane stress} \tag{2.26}$$

For low remote stress values, the higher order terms in the series development of the cosine in equation (2.26) can be neglected, giving

$$\zeta = \frac{\pi}{8}\left(\frac{K}{\sigma_Y}\right)^2 \tag{2.27}$$

which compares well with Irwin's expression - equation (2.24).

2.5.4. Plastic Zone Shapes

The Irwin and Dugdale plastic zone models assumed an oversimplified yield criterion and circular plastic zone shape. For a more accurate analysis, either the Tresca's or the Von Mises' Criterion is used, together with the stress equations given in section 2.4.

Broek [2] and Parker [13] provided equations (2.28, 2.29, 2.30, 2.31.a and 2.31.b) for the plastic zone size and Figs. 2.12 & 2.13 for the plastic zone shapes.

Using Von Mises' criterion,

$$r_p(\theta) = \frac{K^2}{4\pi\sigma_Y^2}\left[\frac{3}{2}\sin^2\theta + (1-2\upsilon)^2(1+\cos\theta)\right] \qquad \textit{plane strain} \tag{2.28}$$

and

$$r_p(\theta) = \frac{K^2}{4\pi\sigma_Y^2}[1+\frac{3}{2}\sin^2\theta+\cos\theta] \quad \textit{plane stress} \tag{2.29}$$

Assuming Tresca's criterion,

$$r_p(\theta) = \frac{K^2}{2\pi\sigma_Y^2}\{\cos(\frac{\theta}{2})[1+\sin(\frac{\theta}{2})]\}^2 \quad \textit{plane stress} \tag{2.30}$$

and for plane strain,

$$r_p(\theta) = \frac{K^2}{2\pi\sigma_Y^2}\cos^2(\frac{\theta}{2})[1-2\upsilon+\sin(\frac{\theta}{2})]^2 \tag{2.31.a}$$

or

$$r_p(\theta) = \frac{K^2}{2\pi\sigma_Y^2}\cos^2(\frac{\theta}{2}) \tag{2.31.b}$$

whichever is the greater.

Here, the redistribution of the stress due to the presence of the plastic zone has not been accounted for, otherwise the analysis would become too complicated.

The shapes of the plastic zones are shown in Figs. 2.12 and 2.13 for the three loading modes.

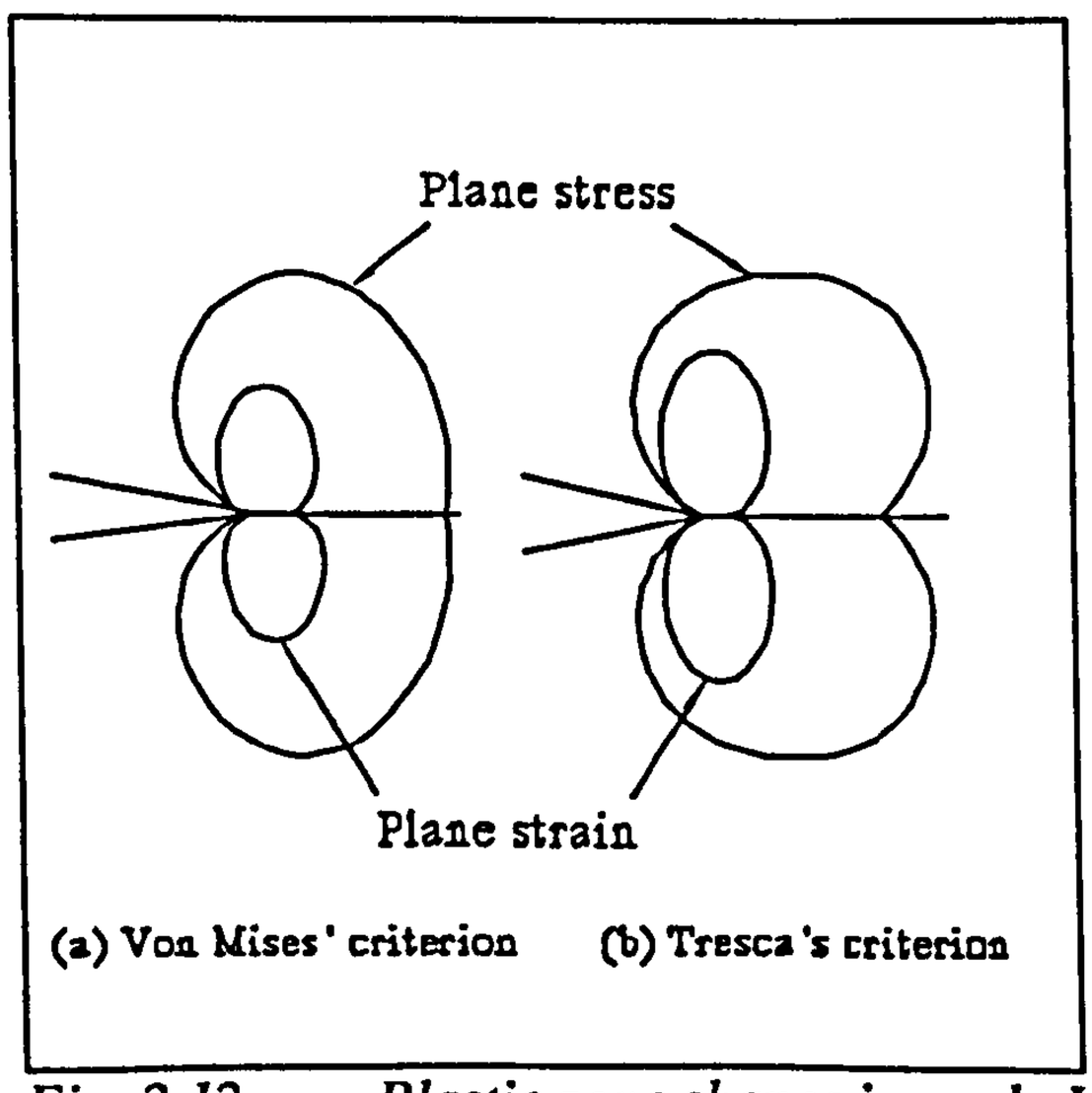

Fig. 2.12. Plastic zone shapes in mode-I loading conditions.

The shapes shown in Fig. 2.13 are based on Von Mises' yield criterion.

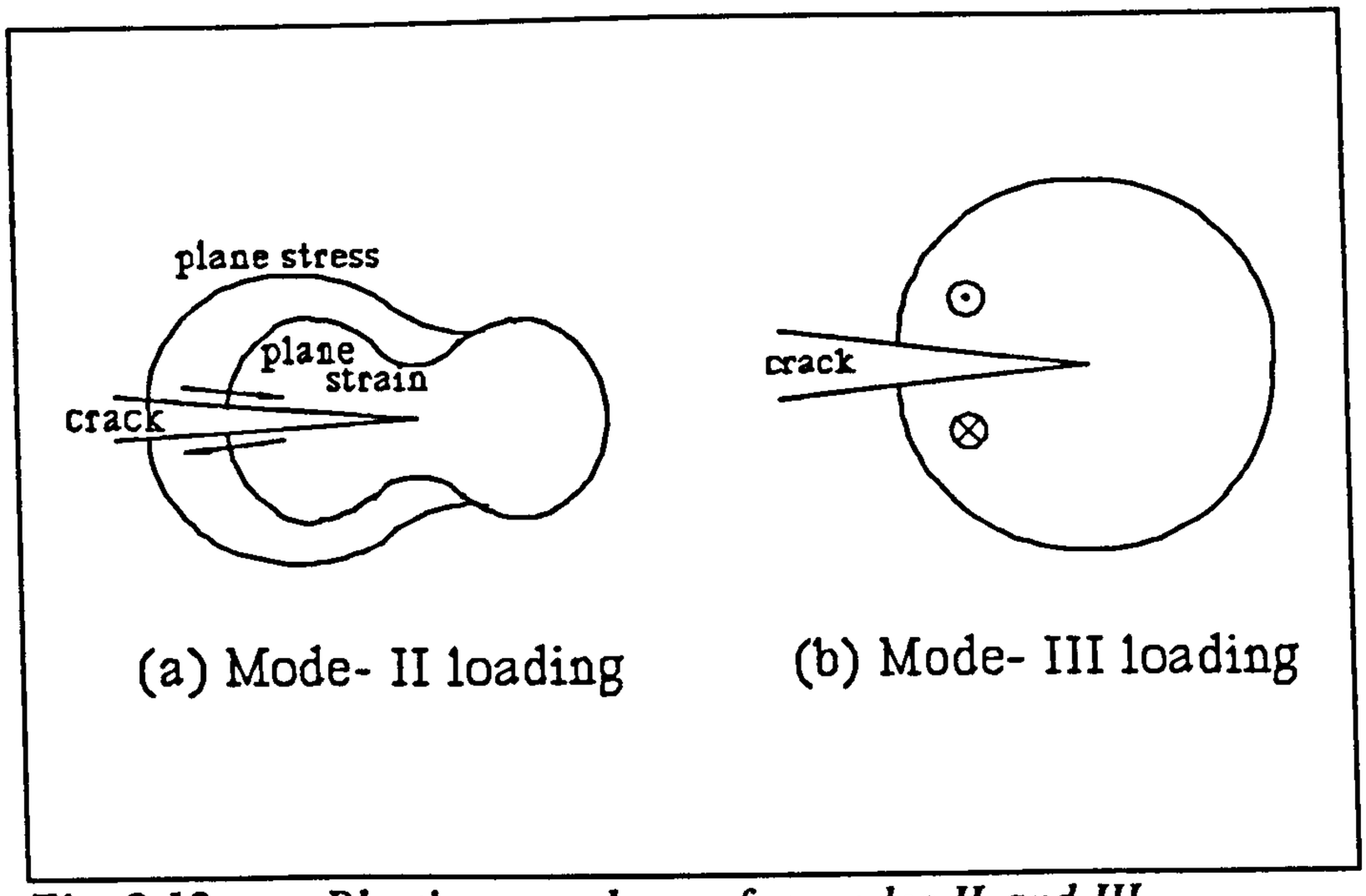

Fig. 2.13. Plastic zone shapes for modes II and III.

2.5.5. Plane Stress and Plane Strain

Looking at Fig. 2.14, the conditions are described to be plane stress conditions if $\sigma_z = 0$. If $\sigma_z = \upsilon(\sigma_x + \sigma_y)$, where υ is Poisson's ratio, then plane strain conditions prevail.

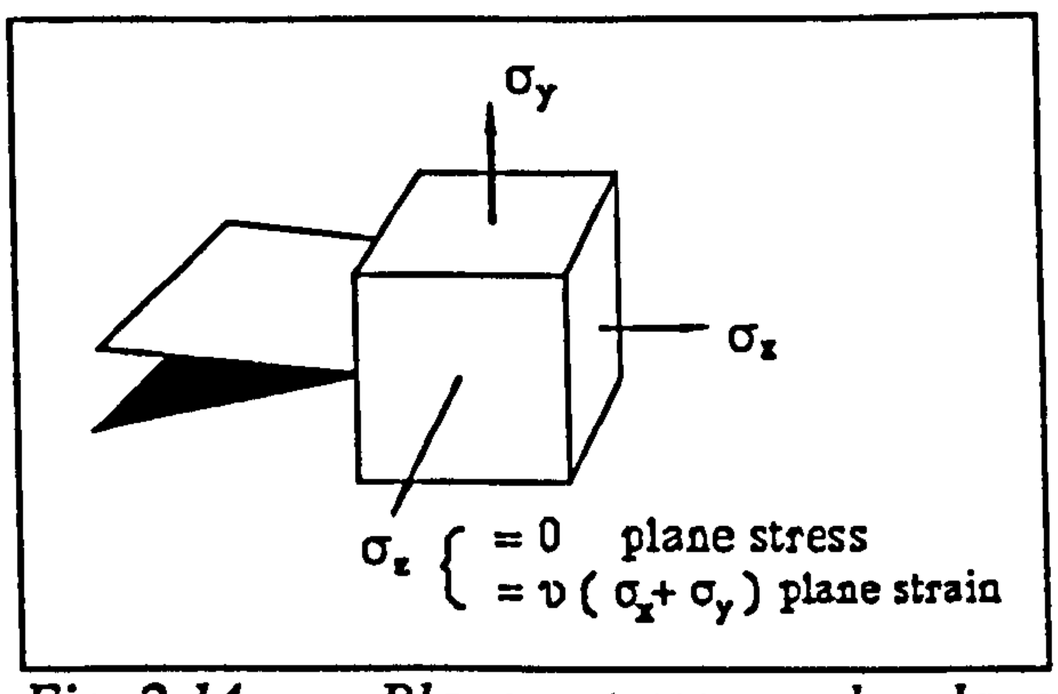

Fig. 2.14. Plane stress and plane strain conditions.

For a brittle material, where plane strain conditions occur inside a thick specimen, σ_z at the surface of the specimen must be zero, and therefore the surface has plane stress conditions. A transitional region exists between the surface and the inside of the specimen where a transformation from plane stress to plane strain conditions takes place. The shape of the resulting plastic zone is shown in Fig. 2.15.

Apparently the thickness of a specimen is important in deciding whether plane strain or plane stress conditions dominate. When the ratio of r_p divided by the thickness is appreciably smaller than unity, plane strain prevails. As the ratio approaches unity, plane stress becomes more prominent.

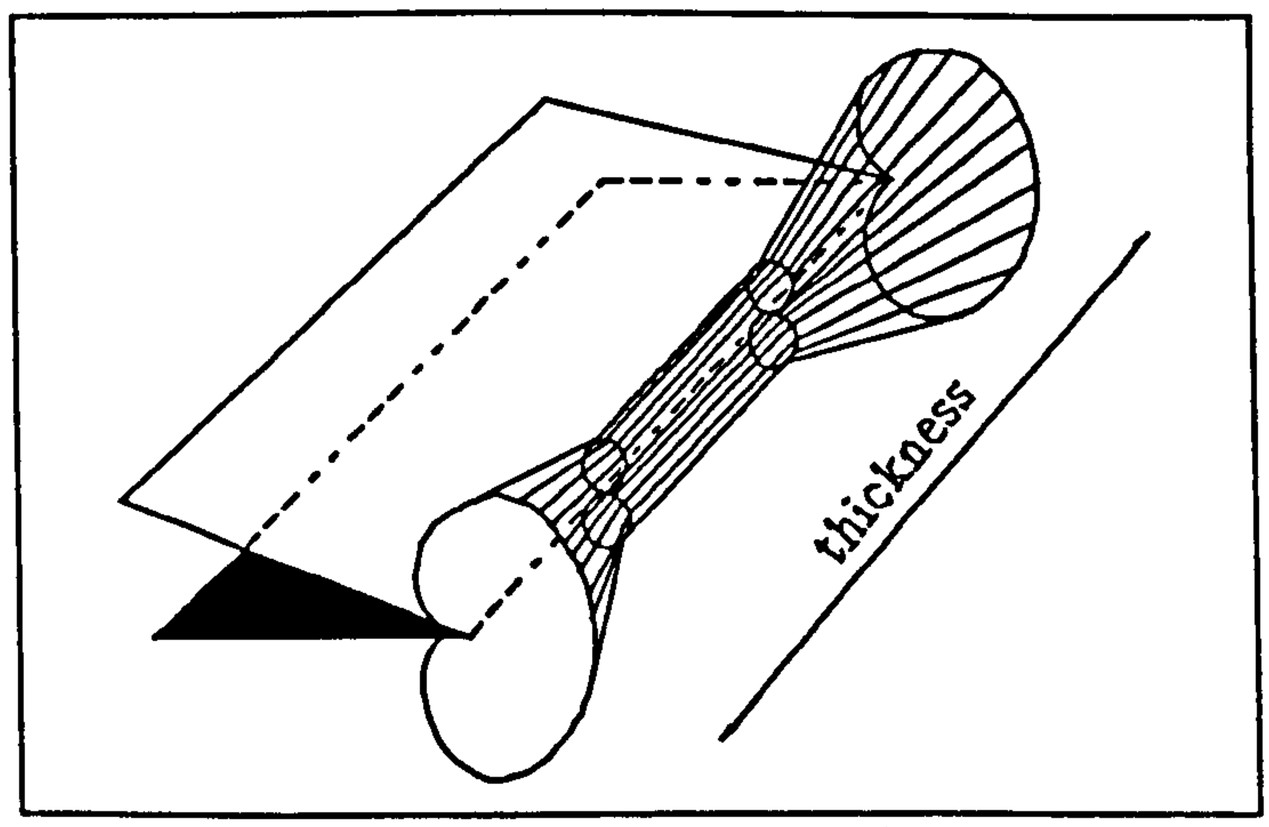

Fig. 2.15. Three-dimensional plastic zone.

The plastic zone is proportional to $(K/\sigma_Y)^2$, where σ_Y is the yield stress. Therefore, for plane strain fracture toughness tests, thicker plates are required for materials with higher K and lower σ_Y. It has been found that for plane strain conditions

$$B \geq 2.5(K_{IC}/\sigma_Y)^2 \tag{2.32}$$

where B is the thickness of a specimen [2].

Fig. 2.16 shows that when B is larger than a specific value, B_s, plane strain prevails and K_{IC} has a constant value. At thickness B_0, the

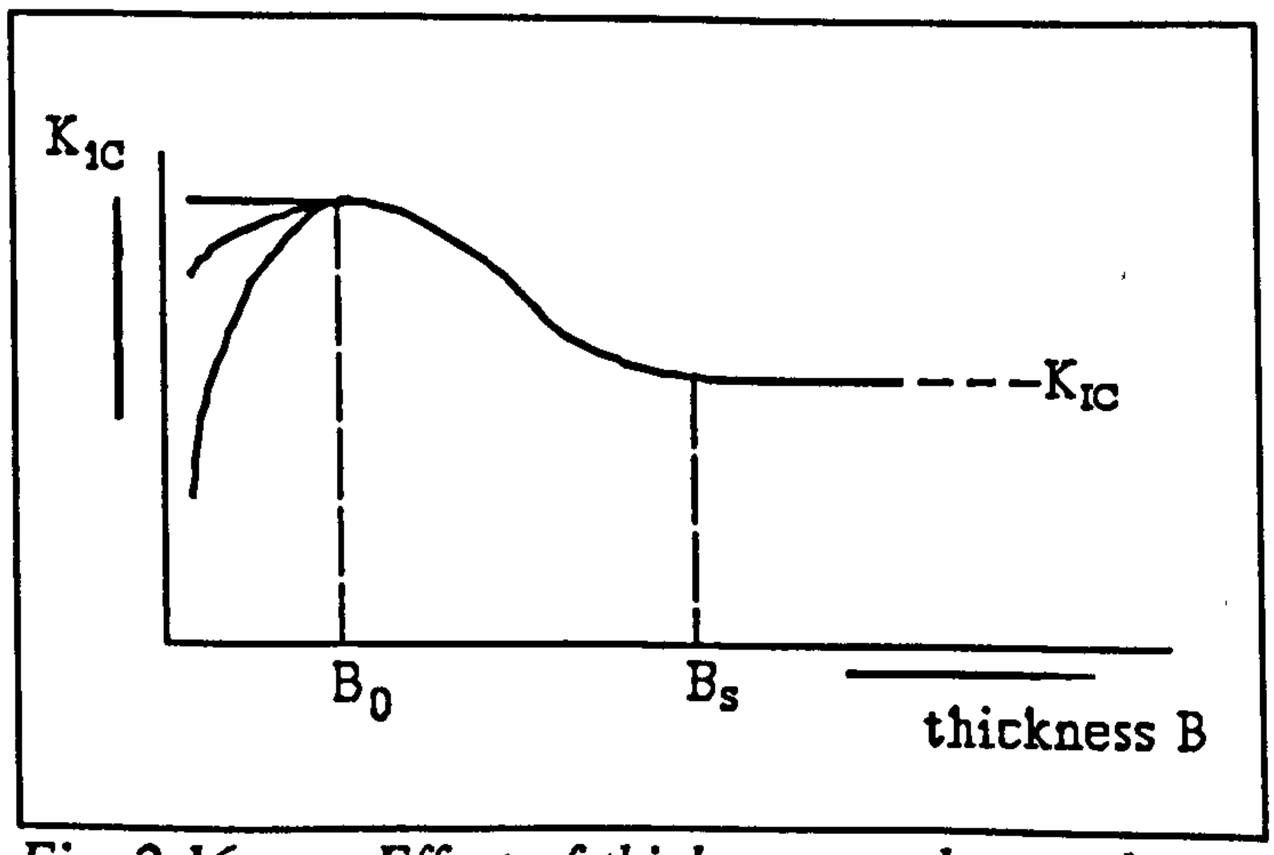

Fig. 2.16. Effect of thickness on the toughness.

toughness of the specimen, K_{1C}, reaches its highest value. It is usually assumed that the real plane stress fracture toughness corresponds to the value B_0. When B is smaller than B_0, there is uncertainty in the value of K_{1C}.

2.5.6. Effect of Temperature

For most materials, within their practical range of use, K_{IC} increases with temperature. On the other hand the yield stress, σ_Y, tends to decrease with an increase in temperature. Therefore $(K_{IC}/\sigma_Y)^2$ increases with temperature and so does the required thickness of the material for plane strain conditions to prevail.

2.6. Fatigue Crack Growth

Bearing in mind that the mechanism of fatigue crack growth depends on the plasticity at the crack tip, it can be said that reproducing and controlling fatigue is easier in ductile materials than in brittle ones.

It has been found that the rate of fatigue, da/dN_{cyc}, is a function of ΔK, where

$$\Delta K = K_{max} - K_{min} \tag{2.33}$$

K_{max} and K_{min} are the stress intensity factors corresponding to the maximum and minimum stresses respectively, a is the crack length and N_{cyc} is the number of cycles. The stresses acquire their minimum and maximum values as the load is increased from the minimum to the maximum value in half a cycle.

Broek [2] and Parker [13] state Paris' law which is empirical:

$$\frac{da}{dN_{cyc}} = C_3(\Delta K)^m \tag{2.34}$$

where C_3 and m are experimentally determined material constants.

In Fig. 2.17 $\log(da/dN_{cyc})$ is plotted against $\log(\Delta K)$, where three regions are identified.

The threshold value of ΔK, ΔK_{th}, occurs in region 1. Below this value, crack propagation does not occur. Region 2 is a linear region where Paris' law is obeyed. In region 3, rapid crack growth occurs due to the presence of relatively large plastic zones when K_{max} approaches K_{IC}.

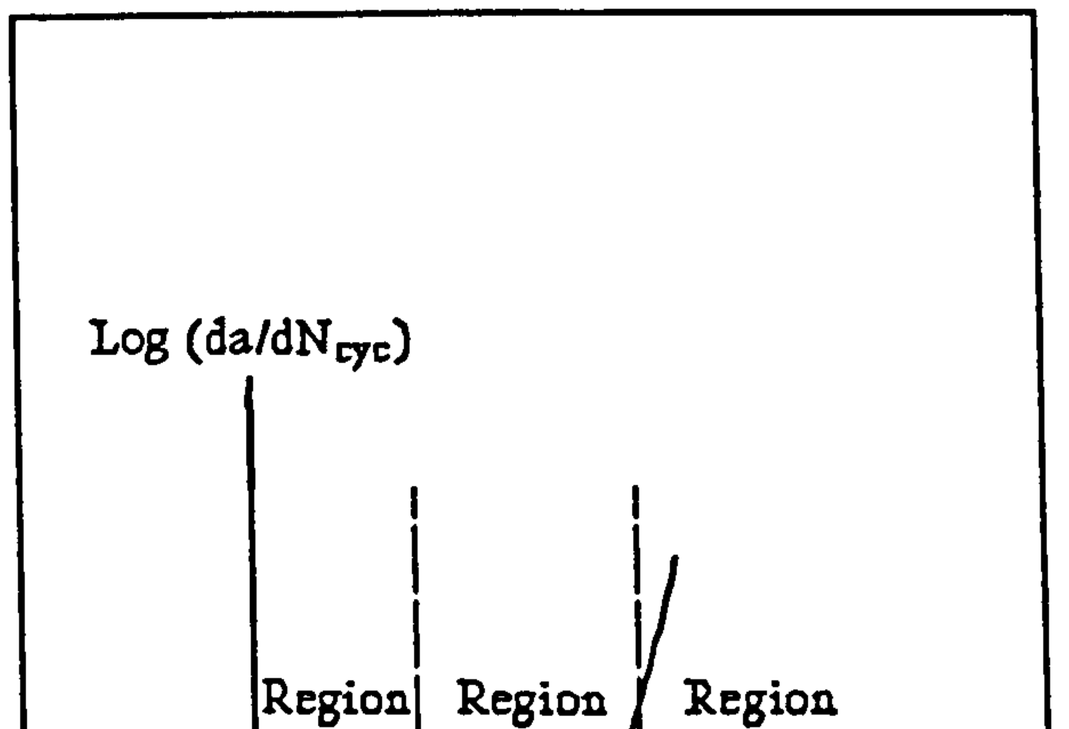

Fig. 2.17. Schematic representation of fatigue crack propagation rate.

The cycle ratio, R_{cyc}, is defined as

$$R_{cyc} = \frac{K_{min}}{K_{max}} \tag{2.35}$$

The effect of varying R_{cyc} is generally somewhat limited for steel, but

aluminum alloys may be sensitive to the value of R_{cyc} [13]. For most materials, the constant C_3 in Paris' law and the value of ΔK_{th} depend on the R_{cyc}-value.

2.7. Dynamics of Propagating Cracks

The dynamic analysis of a propagating crack is much more complex than the static analysis of a stationary crack. The reasons behind the complexity of the dynamic behaviour are outlined in the following paragraph.

A crack propagates at such a high velocity that it becomes impossible for a solution of the stress field in the vicinity of the crack tip to be obtained using equilibrium equations. Instead, equations of motion which include time dependent parameters are used to predict the stress field. These equations are mathematically complex. In addition, the kinetic energy of the material elements at the crack tip plays an important role in deciding whether a crack branches or whether it arrests. An important phenomenon is the stress waves travelling in the material. The stress waves are introduced at the commencement of crack propagation. They reflect at boundaries and travel back to meet the crack front and superimpose on its stress field.

In this section a basic account of the dynamics of propagating cracks will be presented.

2.7.1. Different Waves in a Material

In addition to electromagnetic waves, only one type of wave can exist in liquids. Liquids can transmit tensile and compressive stresses but not shear stresses. Therefore they can only transmit dilatational waves which are sound waves. On the other hand, solids can transmit shear stresses in addition to tensile and compressive ones. Therefore solids can transmit distortional as well as dilatational waves. Both types are called plane waves. In addition, solids with boundaries can transmit surface waves which are called Rayleigh waves. The following is a description of all the stress waves which can exist in a solid.

(i) Plane Waves

Two types of waves can exist in a solid regardless of whether the solid has boundaries. When the solid transmits tensile and compressive stresses the motion of its particles is in the direction of wave motion, and the produced waves are dilatational. When the solid transmits shear stresses the motion of particles is transverse to the direction of propagation; the resulting waves are distortional.

Dilatational waves are also called irrotational, primary, longitudinal, push and pressure waves, while distortional waves can be termed rotational, secondary, shear, shake and equi-voluminal waves [41].

When a solid is deformed, both types of waves are normally produced. When a wave of either type impinges on a boundary and reflects, waves of both types are generated.

The velocity of dilatational waves in an infinite elastic solid is given by

$$c_1 = \sqrt{[\kappa+(4\beta/3)]/\delta} \tag{2.36}$$

where κ is the bulk modulus, β is the rigidity or shear modulus and δ is the specific density. Also,

$$c_1 = \sqrt{(\lambda+2\beta)/\delta} \tag{2.37}$$

where λ is Lamé's constant.

The distortional wave velocity in an infinite elastic solid is given by

$$c_2 = \sqrt{\beta/\delta} \tag{2.38}$$

(ii) Surface Waves

Surface waves occur where there is a bounding surface. In the absence of boundaries they cannot exist. They were first investigated by Lord Rayleigh in 1887, who showed that they decayed exponentially with depth and that their velocity of propagation was smaller than body wave (plane wave) velocities [41 & 42].

Rayleigh waves are elastic waves which can only spread in two dimensions (on the surface) and consequently they decay more slowly with distance than elastic body waves. They consist of two wave components: one vibrating in the same direction as the Rayleigh wave propagation, and the other vibrating perpendicular to both the direction of wave propagation and the surface of the solid.

The velocity of the Rayleigh waves is called the Rayleigh velocity. It is typically about 90% of the shear wave velocity [2].

2.7.2. Limiting Crack Velocity

Broek [2] in his book presents a basic concept to account for the instability of a crack and the development of kinetic energy.

It is explained that crack instability occurs when the elastic energy release rate remains larger than the crack resistance R [2]. The energy available which converts into kinetic energy is (G - R), governing the velocity at which the crack propagates. Broek makes the following simplifying assumptions in presenting the concept diagrammatically (Fig. 2.18):

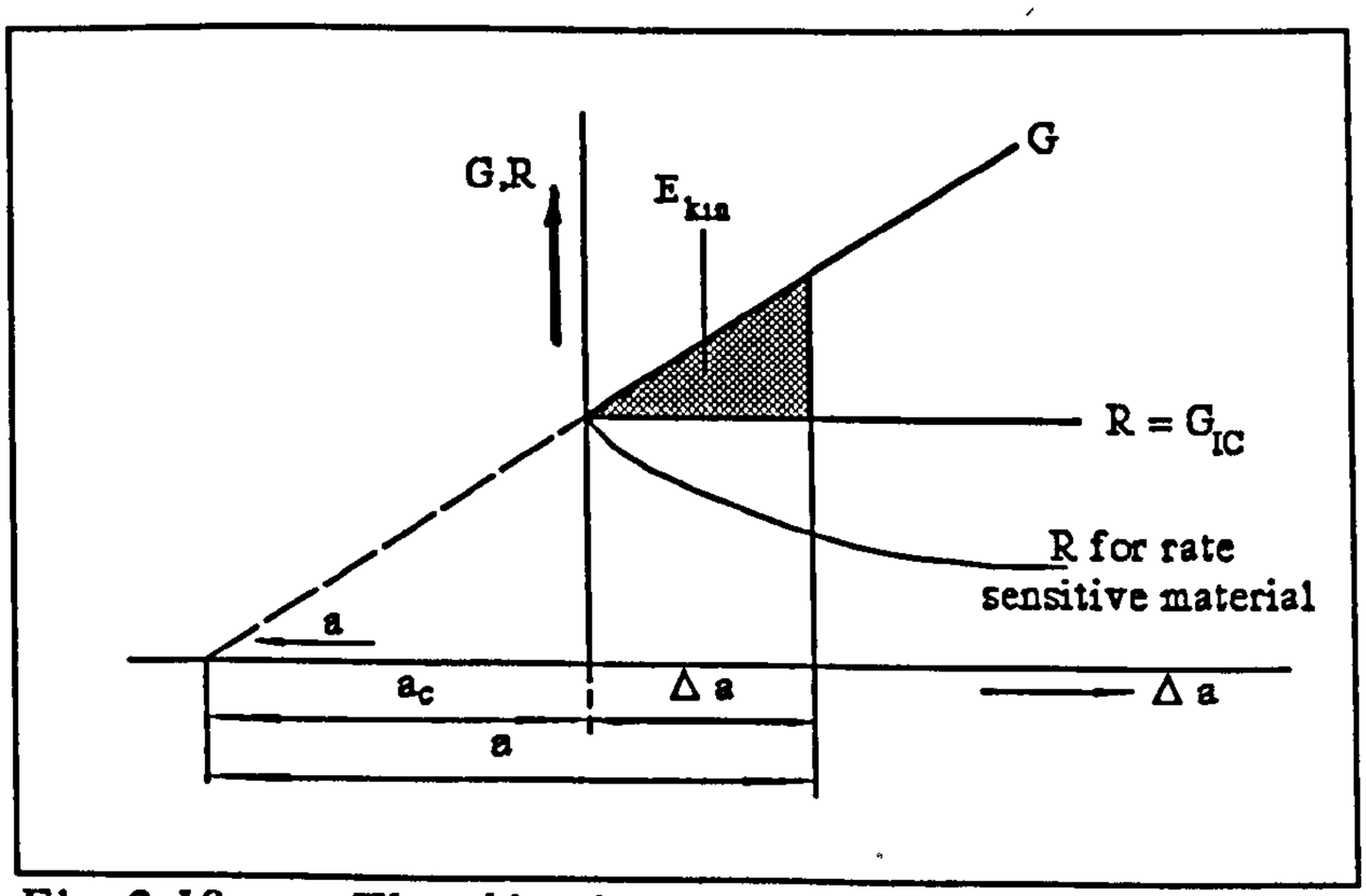

Fig. 2.18. The kinetic energy available for crack propagation.

(i) Crack propagation takes place under a constant stress.

(ii) The elastic energy release rate does not depend upon crack speed.

(iii) The crack growth resistance, R, is constant.

The shaded area in the diagram represents the kinetic energy of the material, E_{kin}, at the crack tip.

The simultaneous crack length is a and the critical crack length at which instability occurs is a_c. Δa is the increase in crack length.

For plane strain, the crack growth resistance, R, is approximately constant. But in plane stress it is usually a rising function. However, some materials are strain rate sensitive; the higher the strain rate, the more brittle they become and the less energy is dissipated due to plastic deformation, which explains the decreasing value of R for rate sensitive materials - Fig. 2.18.

Roberts and Wells [18] derived an expression for the velocity of crack propagation for a Griffith crack. They based their analysis on the solution obtained by Mott [16]. They found that the terminal (maximum possible) velocity was given by

$$d = 0.38 \sqrt{\frac{E}{\delta}} \sqrt{1-\frac{a_c}{a}} \qquad \textit{for plane stress} \tag{2.39}$$

$$d = 0.38 \sqrt{\frac{E}{(1-\upsilon^2)\delta}} \sqrt{1-\frac{a_c}{a}} \qquad \textit{for plane strain} \tag{2.40}$$

where E is Young's modulus, δ is the specific density, $2a_c$ is the critical crack length at which the crack starts to propagate and 2a is the instantaneous crack length. They assumed that the crack propagated at velocity $\dot{a}$ ($\equiv$ v) at each end.

In order to compare their theoretical solution to some experimental results they provided the data shown in Table 2.1, in which v is the velocity of crack propagation and v_s is the velocity of sound in the material ($=\sqrt{(E/\delta)}$) which is equal to the velocity of longitudinal waves, c_1, in an elastic solid with boundaries. It is interesting to note at this stage that many authors non-dimensionalize the velocity of crack propagation by dividing it by $\sqrt{(E/\delta)}$, and they refer to $\sqrt{(E/\delta)}$ as being either the velocity of sound or the velocity of longitudinal waves in the material. In fact, the velocity of longitudinal waves in an elastic solid is equal to $\sqrt{(E/\delta)}$ only when it has boundaries.

Investigator	Material	Type	v_s(m/s)	v(m/s)	v/v_s	Date
Schardin & Struth [43]	Glass	-	5180	1420 to 1570	0.27 to 0.30	1938
	Fused quartz	-	5180	2190	0.42	1938
Greenfield & Hudson [44]	Steel	Edge	5030	1030	0.20	1947
Edgerton & Barstow [45]	Glass	Internal and edge	5490	1520	0.28	1941
Ferguson & Smith [46]	Cellulose acetate	Internal	1130	300	0.27	1950
		Internal	1130	420	0.37	1950
Kennedy [47]	Steel	Edge	5030	1370	0.27	1945
Boodberg & collaborators [48]	Steel	Internal	5030	1400	0.28	1948
		Internal	5030	2010	0.40	1948
Robertson [49]	Steel	Edge	5030	1830	0.36	1953

Table 2.1. Brittle fracture velocity measurements [18]. The values of v_s and v are accurate to the nearest 10 integers. Only Edgerton and Barstow [45] measured v_s for their material; conventional values were given for the remainder [18].

2.7.3. The Dynamic Stress Intensity Factor

The dynamic stress intensity factor, unlike its static equivalent, is dependent upon the velocity of crack propagation. Attempts have been made to derive an analytical expression in order to quantify it. But in every case, many simplifying assumptions have been adopted. Some publications contain useful graphs of how the ratio of dynamic to static stress intensity factor varies with the increase in propagation velocity [e.g. 25 & 50]. Broek [2] gives a general description of the problem; particular reference has been made to other authors such as Yoffe [17], Broberg [51], Nilsson [25], Freund [28] and Baker [22].

2.7.4. Crack Branching and Arrest

An analysis of the phenomena of crack branching and arrest has been presented by Broek [2]. The analysis is characterised by their complexity in such a way that an attempt to explain them with basic mathematics will most certainly be of a qualitative nature. It is argued that when the speed of the crack is sufficiently high, the rate of energy release at fracture is adequate to cause branching. Moreover, the direction of the maximum tensile stress is no longer perpendicular to the direction of propagation.

The rate of release of strain energy is essential for the production of the new fracture surfaces. Once the kinetic energy and the strain energy released are smaller than the energy required to break the bondage between the material molecules, the crack arrests.

2.8. The Texture of Fracture Surfaces

Andrews [52] has presented a description of the different types of surface markings of cracked surfaces together with an explanation of their causes. In this section, the relevant characteristics of the surface texture are outlined.

2.8.1. Conic Markings [52]

Conic markings are illustrated in Fig. 2.19. They are caused by the

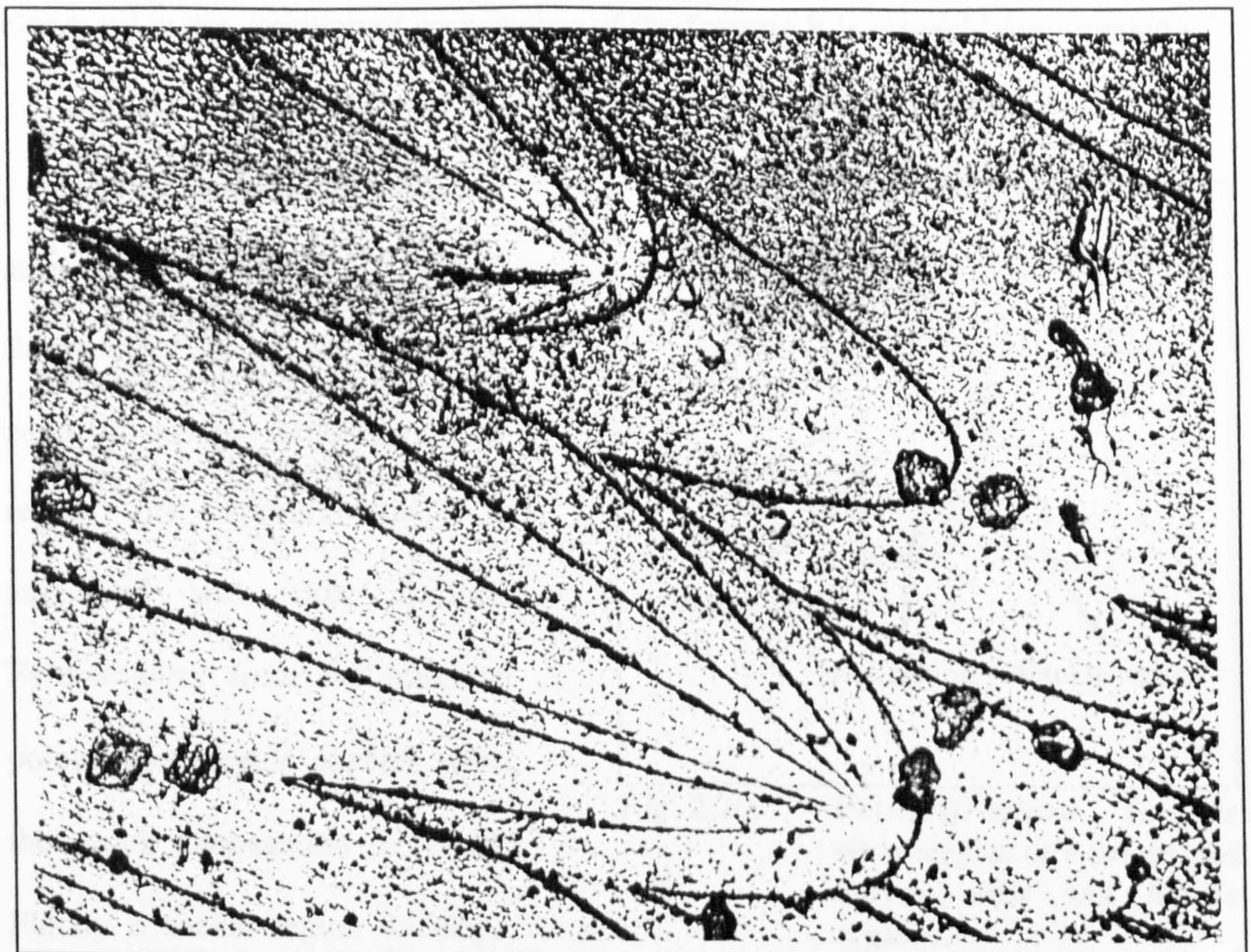

Fig. 2.19. Conic markings in a fast-fracture surface of PMMA (Polymethylmethacrylate). Magnification 180 [52].

inhomogeneities in the material. When the stress concentrations at the

inhomogeneities superimpose on the stresses of the crack tip, they cause the fracture stress of the material to be exceeded in a number of dispersed regions in front of the crack tip and to its sides.

2.8.2. Surface Roughness [52]

This consists of three regions. The mirror region is the one with the least roughness. It reflects light specularly. The mist region is a matt surface and the area with the most roughness is the hackle region. The latter can be seen where fracture has propagated on different levels over small areas of the surface. When it is elongated in the direction of propagation of the fracture it is termed "river markings".

The three regions can be seen in all kinds of solids. Surrounding the point at which crack propagation initiates, a mirror region first appears which is associated with slow fracture. Further away from the initiation point a mist region appears when the crack propagation is faster. Finally a hackle region develops.

The three regions are demonstrated in Fig. 2.20.

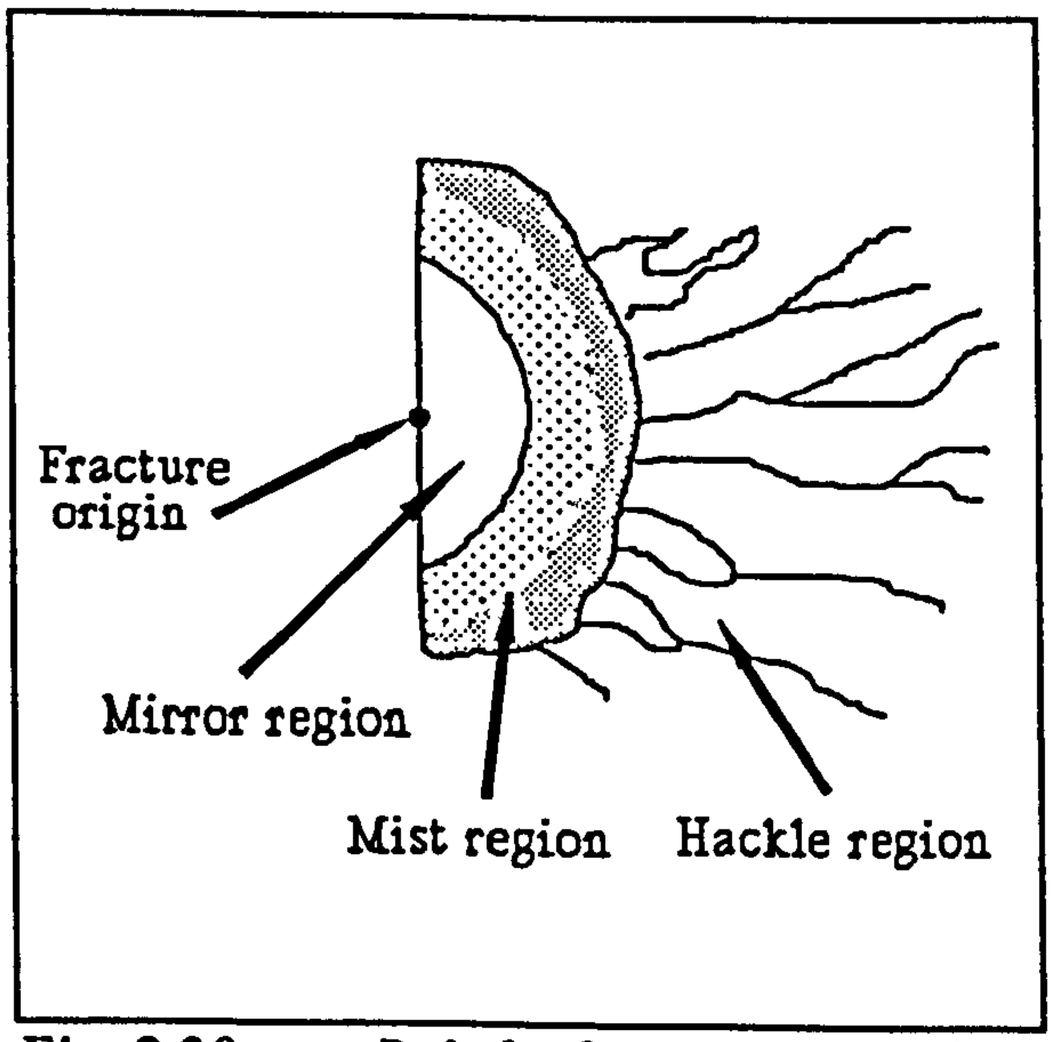

Fig. 2.20. Brittle-fracture surface showing fracture origin and mirror, mist and hackle regions.

The increase in roughness can be explained in terms of the energy available. The further the crack travels the more energy is released, and thus the excess energy is absorbed by the multiplanar fracture and the repeated forking.

2.8.3. Fracture Markings Caused by the Behaviour of the Fracture Front

(i) Wallner Lines [52]

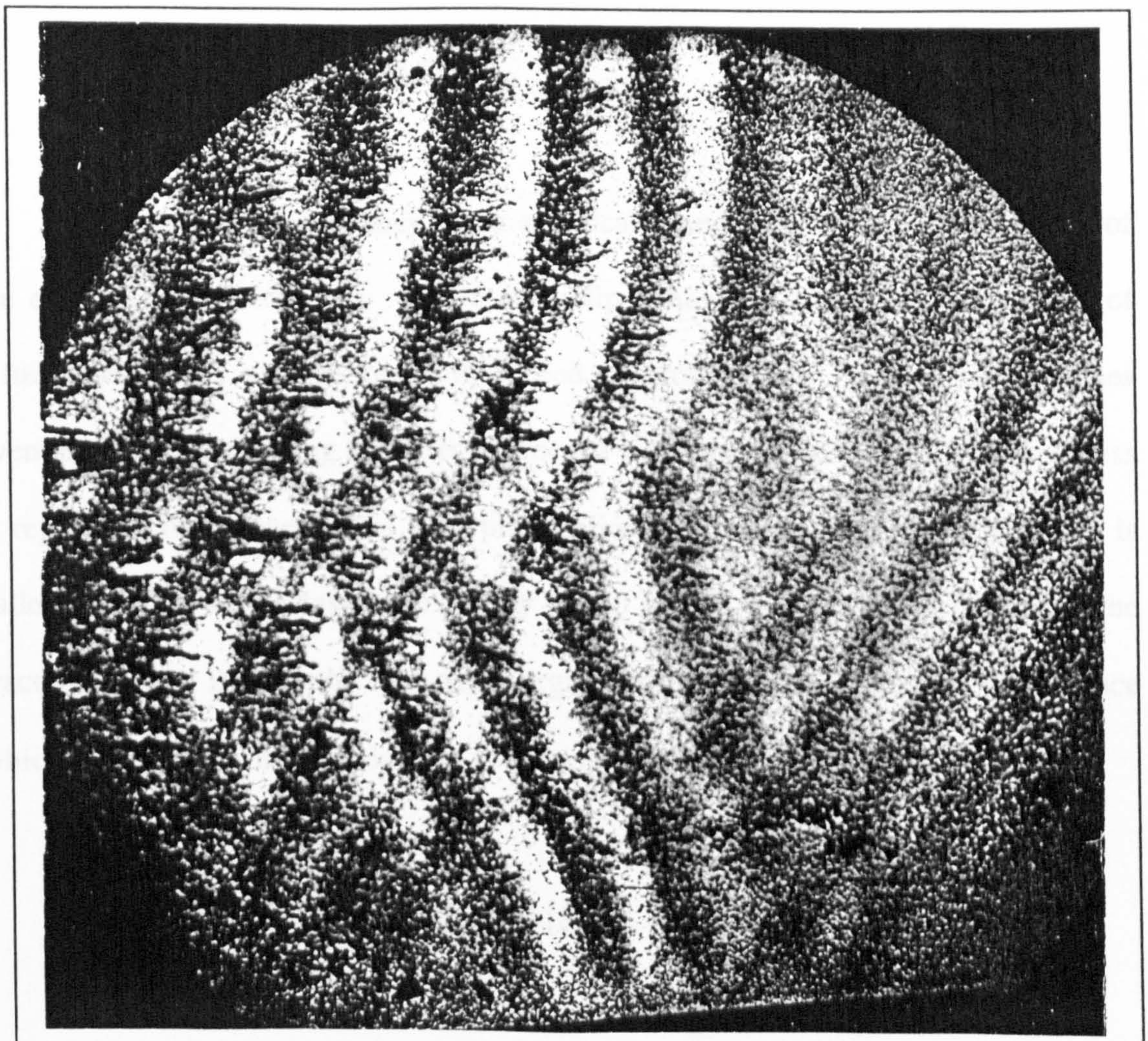

Fig. 2.21. Wallner lines produced by low-temperature brittle fracture in a carbon filled rubber. Magnification 110 [52].

Wallner lines are caused by the reflection of stress waves on the boundaries and their superposition on the crack front, which distort the stresses at the front causing it to deviate. The stress waves are periodical, and so are the Wallner lines, as can be seen in Fig. 2.21.

In glass, Wallner lines take the form of smooth undulations. In polymers, they take the form of periodic variations in surface roughness, because polymers are less homogeneous than glass.

(ii) Stick-Slip Behaviour [52]

A propagating crack may reach a critical speed leading to the bifurcation of the crack into two branches. In the stick-slip behaviour of cracks, the process of bifurcation causes a reduction in the speed of propagation. One of the branches eventually arrests allowing the other to proceed with an increasing speed. The process is repeatedly reproduced. The slow propagation stage of any set of two branches is called stick, while the fast stage of any single branch is called slip, for which the fracture surface is smooth. The stick region has roughness in the fracture surface which is the cause of the reduction in propagation speed in that region.

(iii) Local Plastic Deformation [52]

The plasticity at the tip of a propagating crack can allow the crack to deposit a region of plastically deformed material forming a layer on each fracture surface.

The refractive index is slightly different for these layers and the undeformed material underneath. This might explain the colours seen in the fracture surfaces of PMMA, although there is a disagreement regarding this issue.

CHAPTER THREE

LITERATURE REVIEW

The historic background and the basic theories for the field of fracture mechanics are the subject of the previous chapters. The more recent work and discoveries are presented here independently.

In recent years, the science of fracture mechanics has expanded to include a number of new and sophisticated techniques such as the involvement of thermoelastic infra-red emissions [53] in the determination of stress intensity factors and crack tip velocities (only in the case of very slow velocities of metal fatigue). Many of the problems inherent in fracture mechanics have been approached both theoretically and experimentally. The literature for this field of science is presented in two sections. Static fracture concerns themes which may lead to crack propagation. Dynamic fracture deals with more complex issues which arise from the actual propagation of cracks.

3.1. Static Fracture

Cartwright and Rooke [54] described many useful methods of evaluating stress

intensity factors in a concise form. The theoretical methods included the analytical, the boundary collocation, the conformal mapping, the stress concentrations, the Green's functions, the integral transforms and dislocation models, the force-displacement matching, the alternating methods, and the finite element techniques. The experimental methods included the compliance, the photoelasticity, the fatigue crack growth rate, and the interferometry and Holography techniques. Advice on the suitability of some methods was also given. Moreover, the issue of accuracy was discussed for some techniques.

The plane-strain, mode-I critical stress intensity factor, K_{IC}, of Araldite CT-200 was evaluated by Evans and Barr [55]. Two different methods were used: photoelasticity and the quasistatic energy method. The first involved the two-dimensional photoelastic strain distribution around the crack tip. The second measured the total energy introduced into a test specimen during crack propagation. The energy divided by the change in crack area during crack propagation gave the fracture toughness value which was defined as the work required to create unit crack area. The energy technique gave an average value for K_{IC} of 20.0 $N/mm^{3/2}$, while the average value obtained by photoelasticity was 21.6 $N/mm^{3/2}$. It was concluded that the value of K_{IC} would be affected by temperature, strain rate and creep.

Hollmann and Hahn [56] performed brittle fracture tests on compact tension specimens. Two materials were used: a ductile and a brittle epoxy. Practical difficulties were encountered in precracking the specimens by the fatiguing technique. They concluded that K_{IC} decreased with an increase in either the loading rate or the

yield stress.

The difficulty of introducing a real crack in a specimen was also identified by Breslauer, Voloshin and Manson [57]. They investigated two methods of introducing a crack in compact tension specimens, namely the cyclic fatiguing and the impact blow at the notch tip using a very sharp blade. A comparison between machined and cast specimens was conducted. It was found that crack initiation was difficult to control in machined specimens. Either there was no initiation, or there was initiation followed by fast propagation to the final fracture of the specimen. The crack initiation in a cast specimen was much easier. Only a few specimens fractured catastrophically while initiating a crack. The reason behind the difference in behaviour between both types of specimen was explained by the residual stresses concentrated at the notch tip of the cast specimens which were not present in the machined specimens. The casting process introduced residual tensile stresses at the notch tip, which were instrumental during crack initiation. They affected a relatively small area, and thus did not disturb the subsequent crack propagation.

S. Harada, Endo, Y. Harada and Murakami [58] destructively tested a number of epoxy resin specimens, containing a single narrow notch each, in order to determine the apparent critical stress intensity factor in mode-I loading conditions, K_{IC}^{APP}. The epoxy resin was prepared by mixing the solutions of Araldite CY-230 and hardener HY-956 in the ratio of 5:1 (weight). The narrow notches were introduced during the casting process using a fin with a thickness of 0.02mm. The average value of K_{IC}^{APP} was found to be 50.3 $N/mm^{3/2}$.

The effect of the plastic deformation zone on notched specimens was considered by Narisawa, Murayama and Ogawa [59]. The brittle fracture of round-notched epoxy resin bars subjected to plane strain bending was studied at varying strain rates. The growth of the internal crack was so rapid that it was impossible to control the applied moment to observe it. A decrease in the bending rate caused a slight decrease in the fracture moment and an increase in the plastic zone size of each sample. The experimentation revealed that the internal crack initiated at the plastic-elastic boundary when the plastic deformation zone at the notch tip reached a certain size. Moreover, fracture occurred when the stress level ahead of the plastic zone was raised by a plastic constraint to an ideal fracture stress.

Maccagno and Knott aimed their investigation at the angle of propagation in brittle fracture [60]. Their experimentation was performed on PMMA at room temperature. A thorough investigation of the three hypotheses predicting the angle of crack propagation in mixed-mode (I and II) loading conditions, which included the work of many other researchers, was presented. The maximum tangential tensile stress criterion gave the best agreement with the experimental results. The maximum elastic energy release rate and the minimum strain energy density criteria gave less accurate predictions of the angle of crack propagation. The paper also presented a description of the process of crazing which preceded fracture.

The brittle fracture experimentation performed by Erdogan and Sih [61] showed that, under pure mode-II loading conditions, cracks grew in the direction approximately 70 degrees from the plane of the crack. The direction of maximum

tangential tensile stress was 70.5 degrees. They concluded that a brittle crack under combined tension and shear would grow in the direction perpendicular to the largest tensile stress at the crack tip. They also plotted K_{II} against K_I for a comprehensive range of mixed-mode (I and II) loading conditions.

3.2. Dynamic Fracture

Dynamic fracture involves parameters and phenomena such as the dynamic stress intensity factor, crack propagation velocity, branching, angle of kinking and branching, crack arrest and stress waves. They may all have inter-related relationships.

Lo [62] investigated the phenomenon of branching in a two dimensional infinite plate containing a finite crack in the plane perpendicular to the uniaxial stress. For an asymmetrical (single) branched crack, the angle of initiation was generally assumed to be the angle that gave the greatest energy release. The stress intensity factors, K_I and K_{II}, were analytically obtained for asymmetrically, symmetrically and doubly symmetrically branched cracks. The results agreed with some publications and disagreed with others.

The parameters affecting the dynamic stress intensity factor were considered by Takahashi and Arakawa [63]. Their experiments were performed on single-edge-cracked, pin-loading, tensile specimens of PMMA (Acrylite S-001) and epoxy (room-temperature hardened Araldite D) at room temperature. The caustics method in

combination with high-speed photography demonstrated the velocity effect on the dynamic stress intensity factor of fast cracks. The results showed that the dynamic stress intensity factor depended not only on the crack velocity but also on crack acceleration. The accelerating crack had a smaller value of stress intensity factor than that of the decelerating crack at the same velocity.

A parameter which is closely related to the dynamic stress intensity factor is the velocity of crack propagation. During the experimentation of Glover, Johnson and Radon [64] on five different polymers it was found that the velocity of crack propagation depended on temperature more than testing speed, specimen geometry or static stress intensity factor, K_{IC}. They concluded that the velocity of propagation was probably a property of the material closely related to the elastic modulus. Their distance-time graphs had a point of inflection indicative of a slowing down of the crack followed by a final increase in speed near the end of the crack path.

The effect of the propagation velocity on the branching phenomenon has been discussed by many researchers. Ramulu, Kobayashi and Kang [65] have criticised the critical crack velocity criterion by saying that although the prebranching distortion of the crack tip stress field at a critical crack velocity is the most popular held cause of dynamic crack branching, experimentally the crack velocities never reach the high velocity predicted by this criterion. Knauss [66] has gone a step further by saying that although branching is only observed at high crack speeds, there is increasing evidence that the velocity aspects are an adjunct to the branching phenomenon rather than the driving factor.

The phenomenon of branching has been studied both experimentally and theoretically by numerous researchers. The ability to predict when and how branching occurs is highly desirable. Therefore, the quantifying of the dynamic stress intensity factor at the inception of branching and also the evaluation of the angle of branching have been attempted by many authors.

Kobayashi and Mall [67] conducted photoelastic and caustics experimentation on Homalite-100 and compared their results to those published elsewhere. The ratio of the dynamic fracture toughness to the static fracture toughness, K_{ID}/K_{IC}, was plotted against the ratio of the crack velocity to the dilatational-wave velocity, v/c_1. The propagation of the crack was stable until v/c_1 was about 0.2. Then, there was an unsuccessful attempt of branching at K_{ID}/K_{IC} of about 3 and a successful branching process at K_{ID}/K_{IC} of about 4. The ratio K_{ID}/K_{IC} was approximately 1 when v/c_1 lay between 0 and 0.15.

Ramulu, Kobayashi and Kang [65] obtained a value of 5 for the ratio K_{ID}/K_{IC} at the onset of branching. They compared it with a value of 4 given by other authors. They also showed that the crack branching angles were very similar for each specimen configuration.

The characteristics of the angle of branching, were described by Knauss [66]: "A persistently recurring question for analytical modelling purposes is whether branched cracks form smoothly from the main crack by turning through a deflection angle with high curvature or whether the branches emanate with a well defined angle

from the main crack; in post mortem examination both seem to occur; but the possibility exists that observed definite angles have been formed as *flash backs* to the main crack".

Research on brittle polymers performed by Dempsey and Burgers [68] confirmed that a branch subtended an angle with the original crack plane ranging between ±10 degrees and ±45 degrees.

Tests conducted by Knauss and Ravi-Chandar [69] on Homalite-100 with the aid of direct high-speed photography showed that at sufficiently high crack tip stresses associated with branching, the microfractures which were generated away from the main crack axis grew and turned smoothly away from the main crack. Experimental results indicated that the crack tip stress state was altered when stress waves reflecting from the specimen boundaries returned to the crack tip. This resulted in a change of crack speed and even caused branching in cases of high-intensity stress waves.

Ramulu and Kobayashi [70 & 71] employed the maximum tangential tensile stress principle to produce two theoretical criteria for the prediction of the angle of kinking and that of branching in brittle fracture. The analytical prediction was confirmed by experimental results obtained for Homalite-100 and Polycarbonate specimens. The dynamic crack curving criterion which involved the remote stress component in addition to the singular stresses, predicted the actual crack kinking angles in fracturing photoelastic specimens. The dynamic crack branching criterion was the same as the curving criterion with the addition of a requirement involving a

critical value of the dynamic stress intensity factor. It was used in successfully predicting the crack branching angle in a bursting metal pipe.

The phenomenon of crack arrest is another feature of dynamic fracture. Extensive research on brittle and ductile materials performed by Kobayashi [72] brought him to the conclusion that there was an apparent existence of a minimum dynamic stress intensity factor below which the crack ceased to propagate. The dynamic arrest stress intensity factor is another name for the minimum stress intensity factor which is always less than or equal to the static fracture toughness [72].

Popelar and Gehlen [73] developed a method of analysis for rapid fracture and crack arrest in wedge-loaded rectangular fracture specimens by using energy-derived difference equations. They also conducted experiments on Araldite B wedge-loaded double-cantilever-beam fracture specimens. There was good agreement between the analytical and experimental results with regard to the length of crack growth, the crack-tip-time history, and the variation of both the stress intensity factor and crack speed with crack length during propagation.

Researchers have strived to substantiate different relationships between the various parameters of fracture mechanics. One such relationship is that between the dynamic stress intensity factor, K_{ID}, and the velocity of crack propagation, v.

Knauss [66] suggests that there are supporters for the idea that the crack velocity is a unique function of the instantaneous stress intensity factor and that there

are others who have consistently questioned the generality of such a relationship. The small differences between the K_{ID} versus v relationships, detected by Knauss [66] when testing different types of specimen of the same material, cast some doubt on the uniqueness of such a relationship for a given material.

Kobayashi and Mall [74] presented many plots of the dynamic fracture toughness, K_{ID}, against crack velocity, v, for different materials and specimen types. In their paper, they confirmed the likelihood of the existence of a unique K_{ID} versus v relationship.

Dally, Fourney and Irwin [75] performed photoelastic experimentation on the propagation of cracks in Homalite-100 over a period of ten years. In addition, they produced a review of the experimental results obtained by many other investigators establishing the relationship between the dynamic stress intensity factor, K_{ID}, and the crack velocity, v. The errors introduced during the determination of K_{ID} and v due to practical difficulties and theoretical assumptions were investigated and quantified. The scatter in the K_{ID} versus v plots could not be justified beyond doubt by the experimental or analytical errors. Therefore, they concluded that the method of controlling the crack tip velocity through the uniqueness of the K_{ID} versus v relationship was in question.

Kobayashi [72] declares that the relationship between K_{ID} and v in polymers and steel can be treated as a unique material property within a generous engineering tolerance. He proceeds further by proposing that model testing can be used to predict

the dynamic fracture response of a prototype structural component provided the normalized K_{ID}/K_{IC} versus v/c_1 relations of the model and prototype materials coincide and that scaled geometries are used. This suggestion is still in need of verification.

CHAPTER FOUR

RESEARCH PURPOSE

AND

MATERIAL PREPARATION AND PROPERTIES

A few examples of catastrophic accidents have been described in chapter 1. The need to understand and anticipate secular misfortunes has also been outlined. This lays the foundation for the importance of mechanics of fracture and the ability to predict failure to avoid its undesirable outcome.

4.1. Research Purpose

The benefits of studying mechanics of fracture and its ramifications are self-evident. Brittle fracture is one field in the fracture world which has beleaguered scientists and engineers, prompting them to search for means of anticipating such kind of failure. The modelling of cracks in engineering components is a way of predicting fracture behaviour. Therefore, the effort for this project has been directed towards understanding the process of modelling cracks in brittle materials.

Considering a component with a crack of known shape and size, a model of

that component can be cast using a convenient plastic material with the introduction of a narrow notch having the same shape and size of the real crack by using a metal shim. Although the thickness of the notch can never reach the infinitesimally small value associated with that of the crack, nonetheless this can be accounted for. Knowing how the crack and the notch behave in relation to one another, the fracture of the real component can be predicted by observing the behaviour of the model, bearing in mind that $K_c/\sigma_{nom}\sqrt{a}$ must have the same value for both the component and the model, where K_c is the critical stress intensity factor, σ_{nom} is the nominal stress and a is the length of either the crack or the notch. Thus, the need for a detailed study of notches in relation to real cracks has arisen. It is important to note that whenever K_c is considered for a notch, the apparent value is the one in consideration, and naturally it is denoted by the suffix "APP". The difficulty and sometimes impossibility of introducing a real crack of a specific shape and size into a cast model and the relative ease of including a narrow notch promoted the idea of using narrow notches in the modelling of cracks.

The research for this project was channelled into two main categories: static and dynamic fracture. The static study covered pure mode-I, pure mode-II and mixed-mode loading conditions. It was directed towards understanding and predicting the initiation of fracture for real cracks and narrow notches in different specimens. The dynamic study aimed at understanding and explaining the phenomena of crack propagation and branching paying particular attention to the speed of propagation.

The above topics were investigated with an experimental approach combined

with a computational analysis, in addition to the literature review.

Experimentation was performed on three different types of specimen: beams in bending, compact mixed-mode (CMM) specimens in tension and closed tubes under internal hydraulic pressure. The three point bend (3PB) beams were tested to investigate the relationship between the real and apparent critical values of the stress intensity factor in pure mode-I loading conditions, K_{IC} and K_{IC}^{APP} respectively. Therefore, the beams included two types of stress raisers: the narrow notch and the real crack which was grown controllably under fatigue vibration. The CMM specimens involved the same type of investigation differing only by having mixed-mode loading conditions. The 3PB and CMM specimens were dedicated for the study of the static mechanics of fracture. The dynamic side was examined by bursting the tubes under internal oil pressure after including semi-circular narrow notches on the outer surface, incurring a pure mode-I loading situation. The specimens were all destructively tested at ambient temperature.

The computational work was achieved using finite element analysis which eventually provided an accurate description of the peak stresses and the iso-stress contours at the tips of the different narrow notches in the 3PB and CMM specimens.

4.2. Material Preparation and Properties

The material conveniently chosen throughout this research was the epoxy resin: Araldite CT-200 with hardener HT-907. It is a brittle material which has been used

in the Department of Mechanical Engineering of the University of Nottingham for many years. It has unique photoelastic characteristics and can easily be obtained and cast into different shapes.

The resin and hardener are both obtained from Ciba-Geigy Plastics and Additives Company, Duxford, Cambridge. The Chemical name for the hardener HT-907 is dicarboxylic acid anhydride (solid).

The following procedure is followed carefully throughout the research in order to obtain an isotropic and homogeneous casting free from residual stresses and air bubbles.

Each aluminium and steel mould (described in detail in later chapters) is assembled and treated with the release agent hysol (a mixture of silicon oil in a petroleum carrier). One hundred weight units of the resin (Araldite CT-200) are placed in an oven at 128°C for 18 hours. Sixty weight units of the hardener HT-907 together with the prepared mould are placed in another oven at 100°C also for 18 hours. The hardener is then placed with the resin in the 128°C oven for 2 hours, after which they are mixed together thoroughly in a fume cabinet at room temperature using a stirring paddle. The mixture is placed once again in the oven at 128°C for 10 minutes, then carefully poured through a funnel into the mould which is still in the 100°C oven. This is left to cure for 120 hours at 100°C. The casting is stripped hot out of the mould and allowed to cool to room temperature (approximately 2 hours). It is placed on a glass surface in an oven to be finally cured at an elevated

temperature of 142°C for a period of 6 hours. The fully cured casting is slow-cooled to room temperature at a cooling rate of 2°C per hour. The casting is now ready to be machined to the required specimen dimensions.

The material, as already stated, is brittle, elastic, isotropic and homogeneous. Its modulus of elasticity, mass density, Poisson's ratio, tensile yield stress and ultimate tensile stress are respectively given below.

$E = 3900\ N/mm^2$ (appendix I)

$\delta = 1210\ kg/m^3$ (appendix I)

$\upsilon = 0.30$ (appendix I)

$\sigma_Y = 42.0\ N/mm^2$ (appendix II)

$\sigma_u = 90.8\ N/mm^2$ (appendix II)

CHAPTER FIVE

MODE-I EXPERIMENTATION

Pure mode-I investigation was carried out using the three-point bend (3PB) specimen or beam. To establish the relationship between the apparent and the real values of the pure mode-I stress intensity factor, tests included specimens with either a narrow notch or with a real crack respectively.

5.1. 3PB Specimen with a Notch

This type of specimen was produced by immersing a metal shim made of shim steel into the casting when the resin was poured into the mould. The effect was to produce a notch having a width equal to the thickness of the shim.

Two different shim shapes were used, the first of which had a flat edge involving three thicknesses: 0.20, 0.10 and 0.05 mm producing correspondingly-sized notches. The second shape was a sharpened edge belonging to a 0.10 mm shim producing a notch which effectively had a width of 0.02 mm. In other words, the process of sharpening the shim effectively reduced the width of the cast notch by a factor of 5.

The resulting notches with four different sizes were photographed under the microscope demonstrating their sizes and shapes from a practical point of view (Figs. 5.1(1-24)).

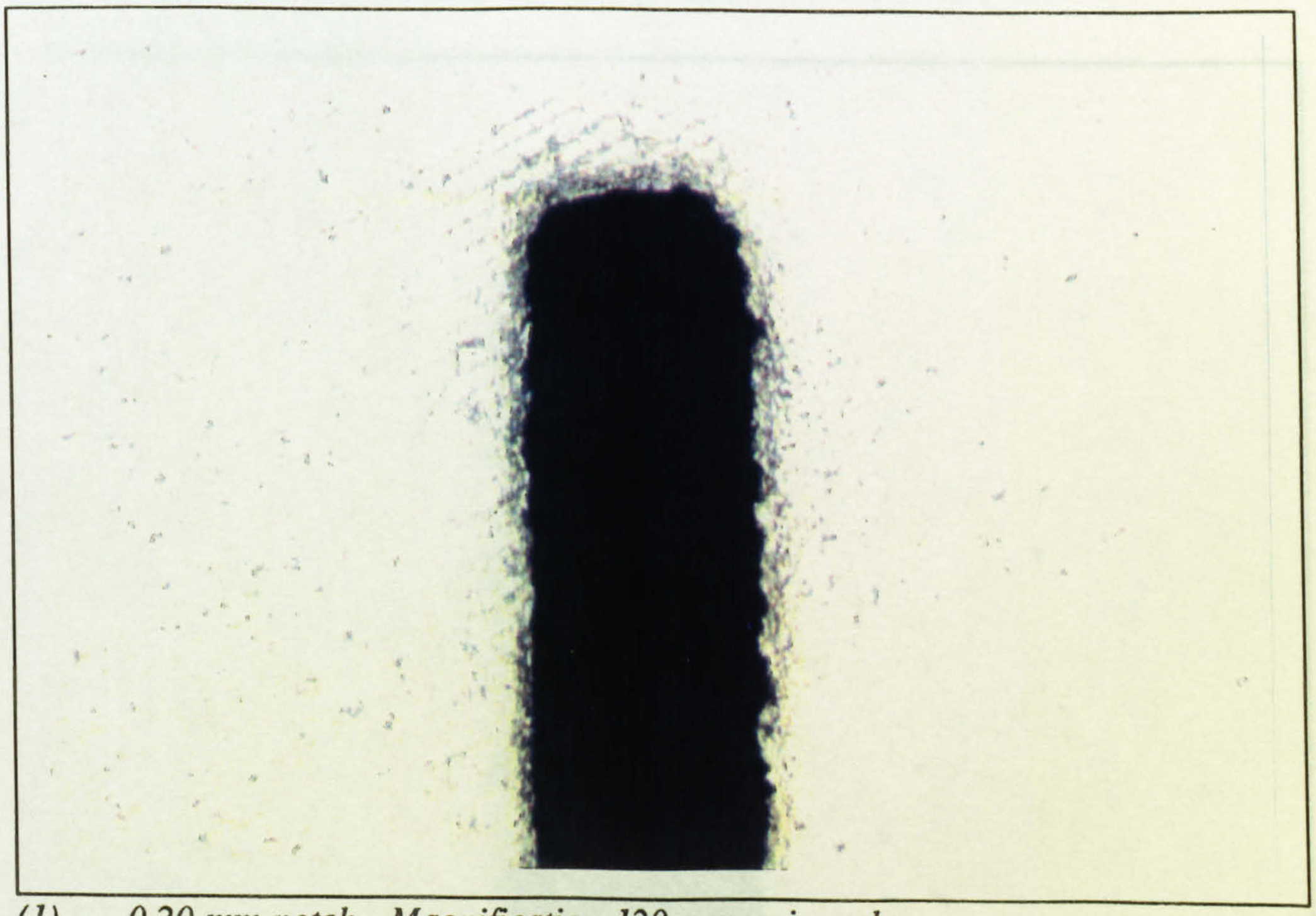

(1) 0.20 mm notch. Magnification 120 approximately.

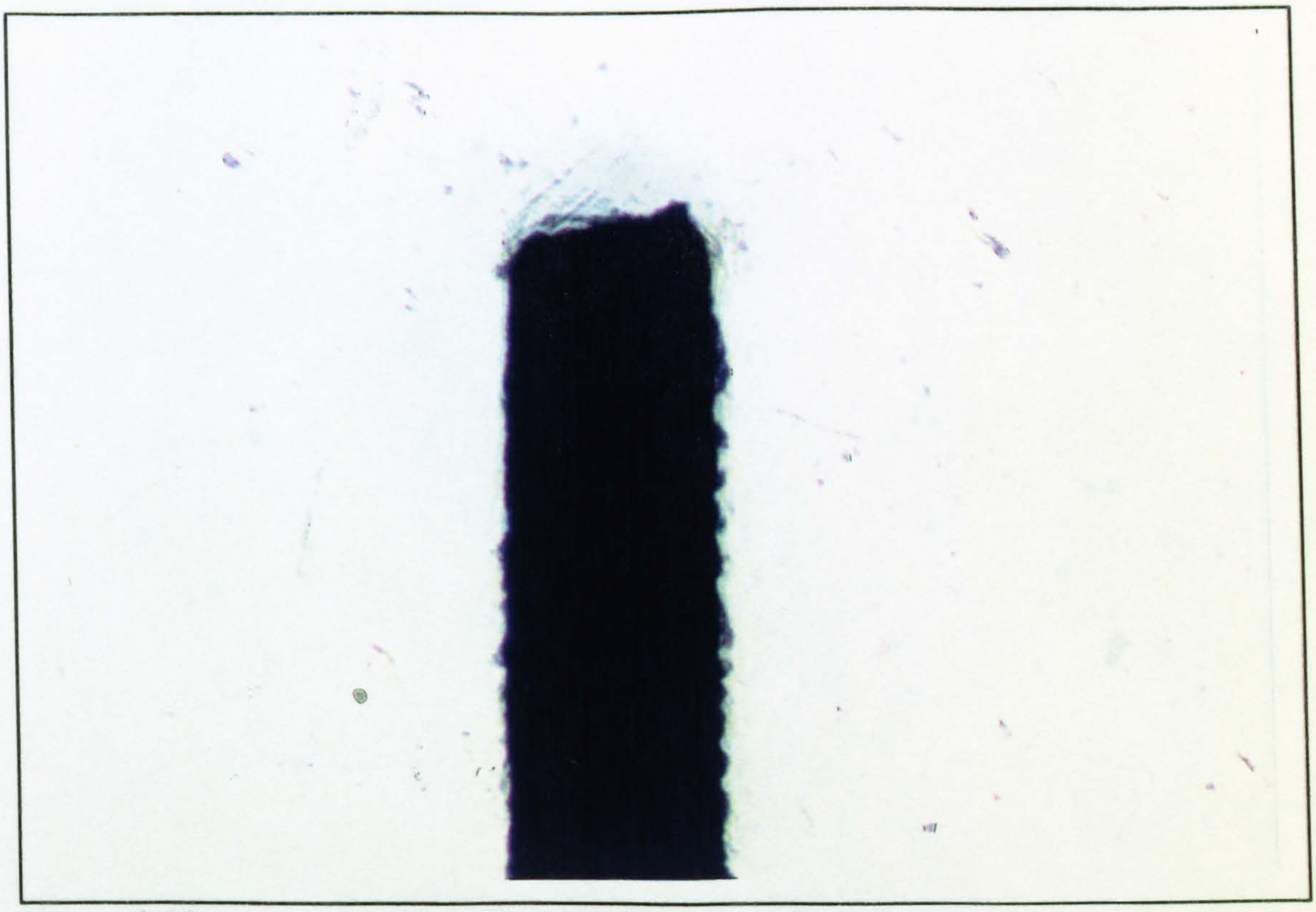

(2) 0.20 mm notch. Magnification 120 approximately.

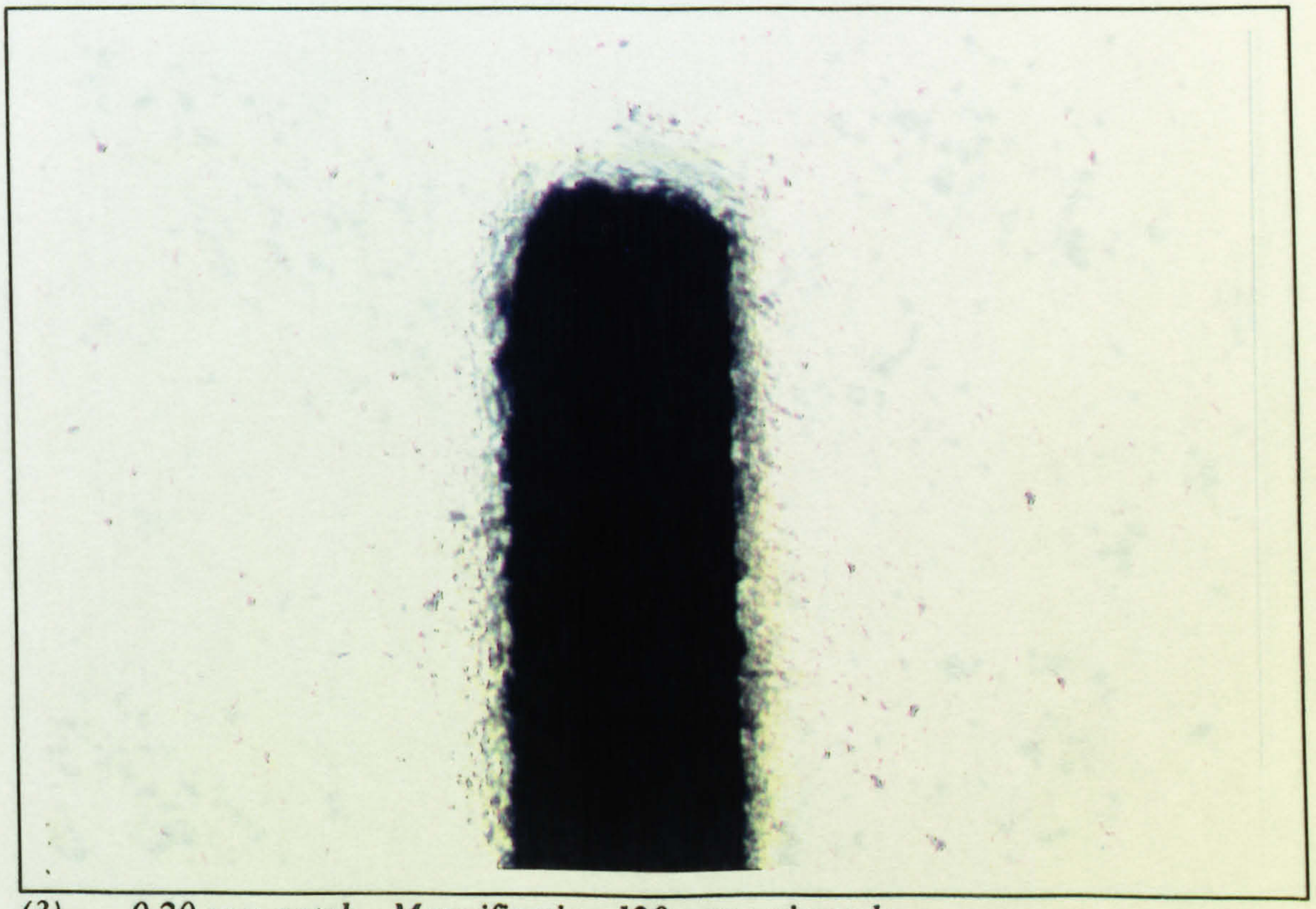

(3) 0.20 mm notch. Magnification 120 approximately.

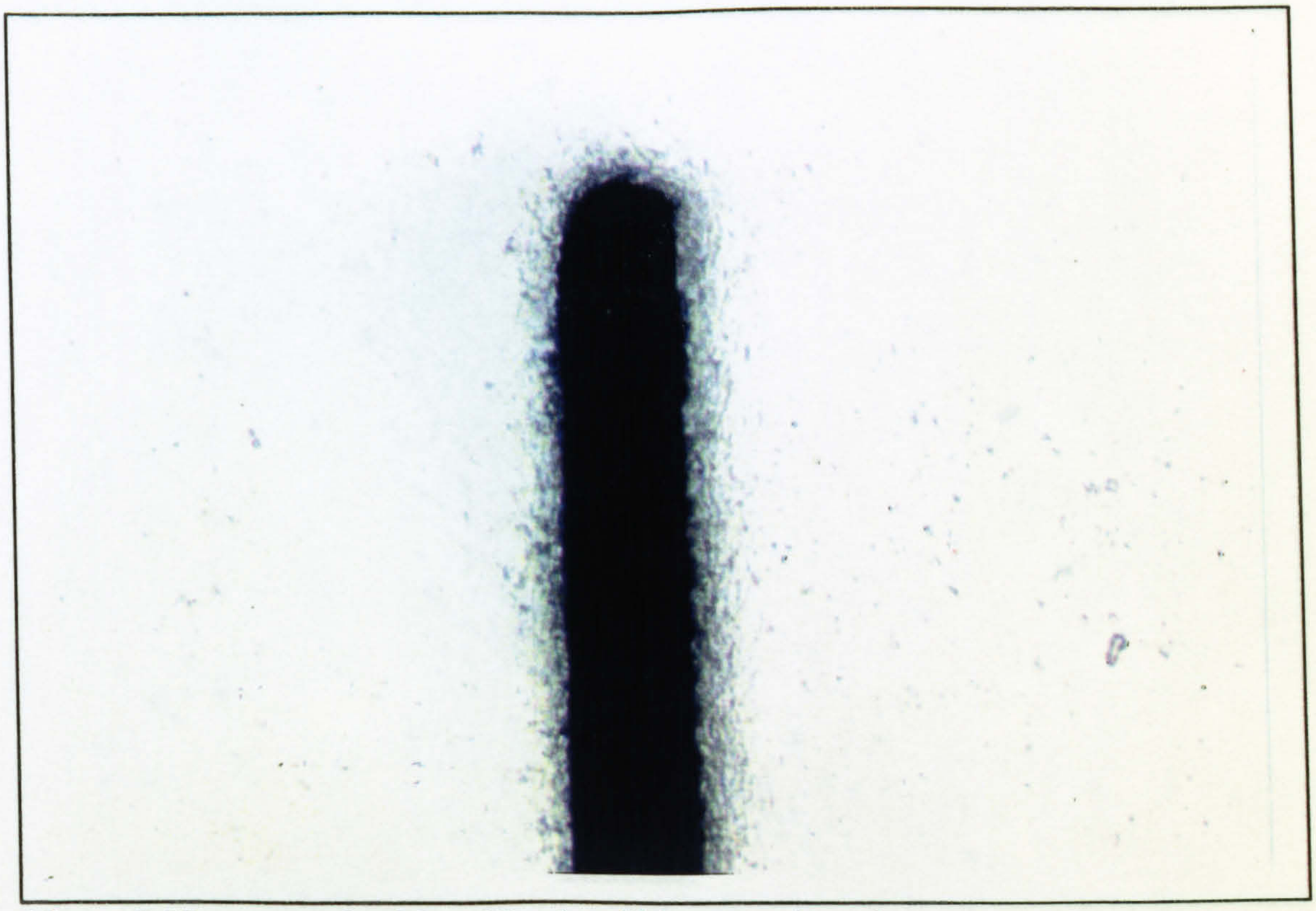

(4) 0.10 mm notch. Magnification 120 approximately.

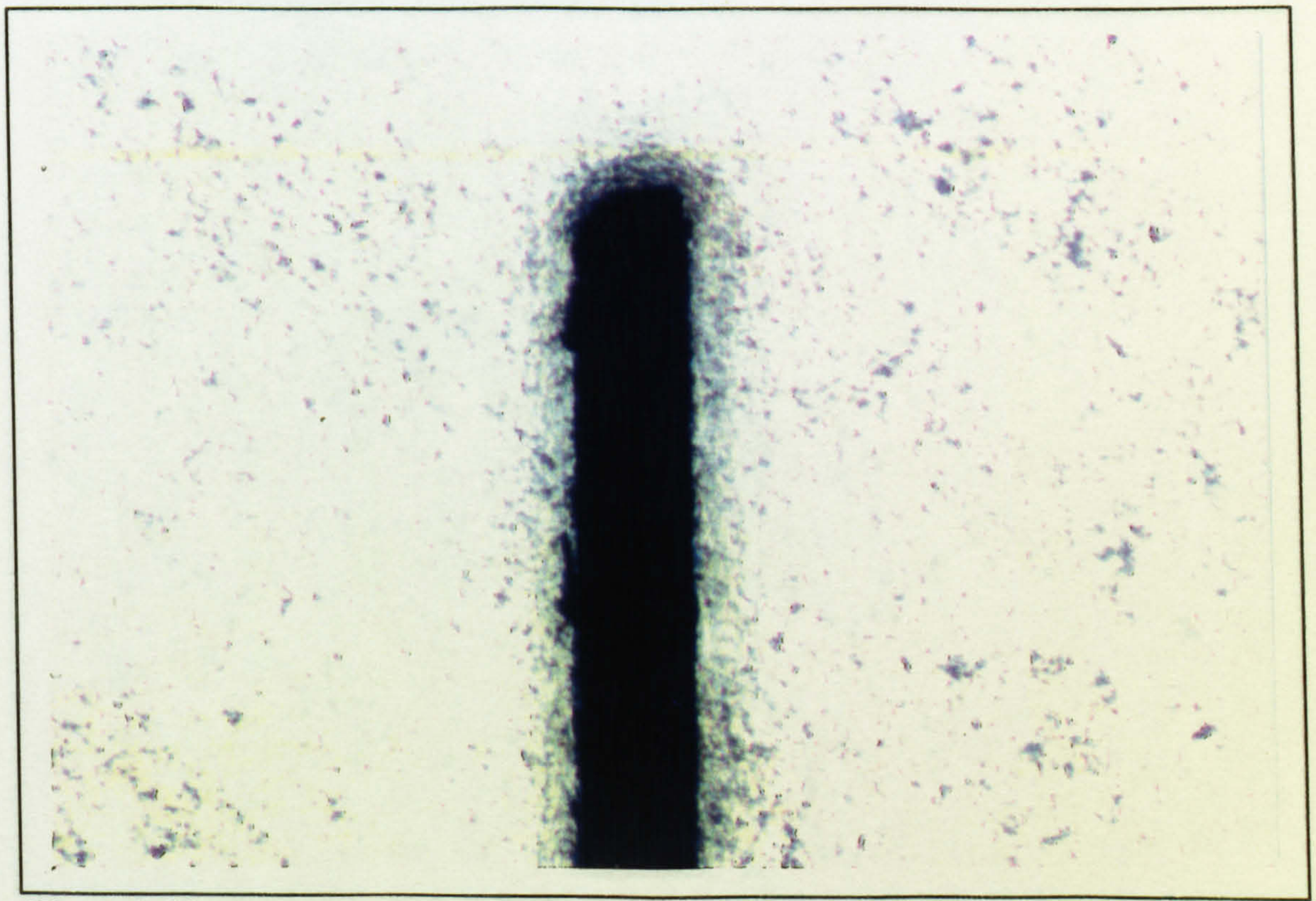

(5) 0.10 mm notch. Magnification 120 approximately.

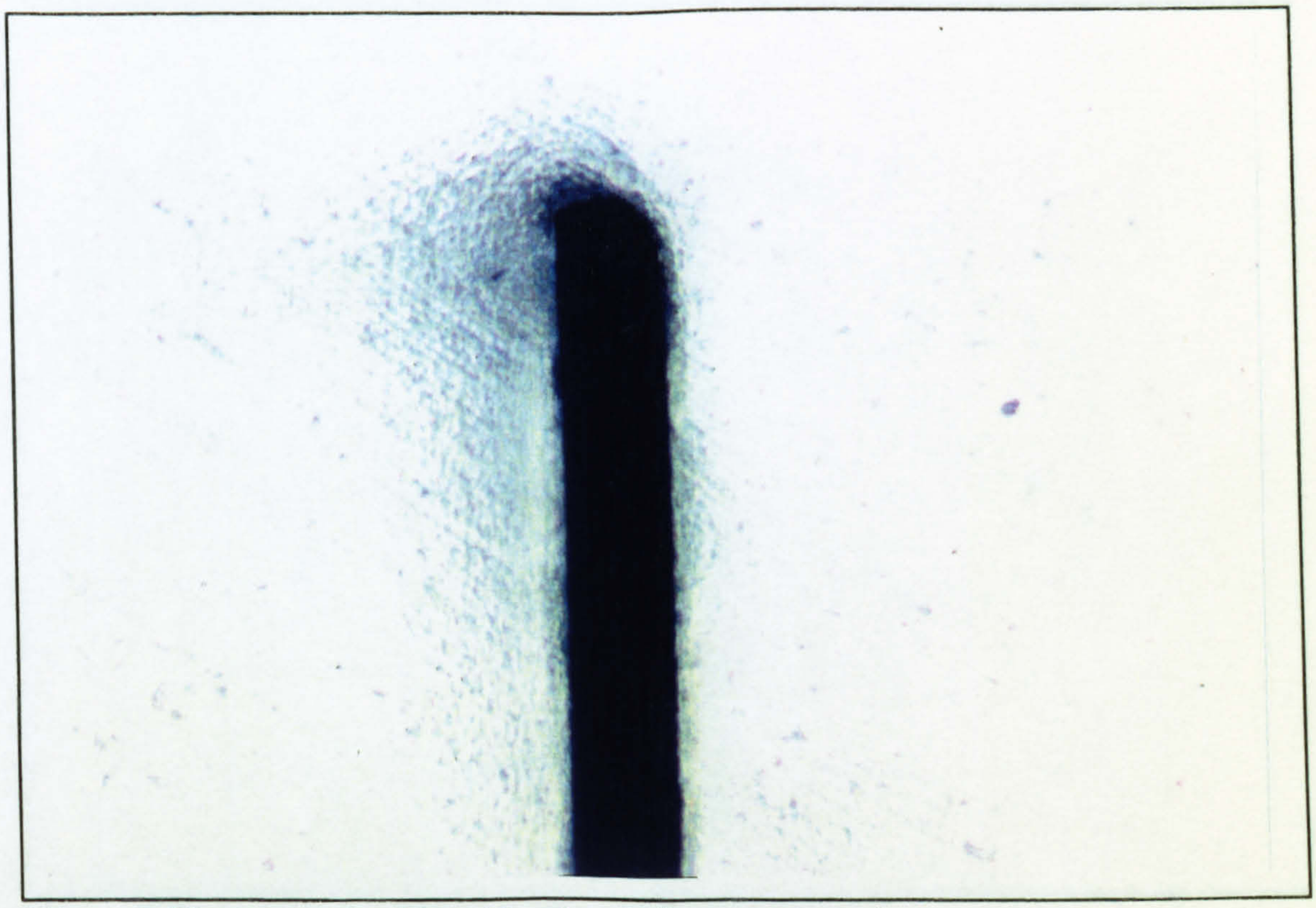

(6) 0.10 mm notch. Magnification 120 approximately.

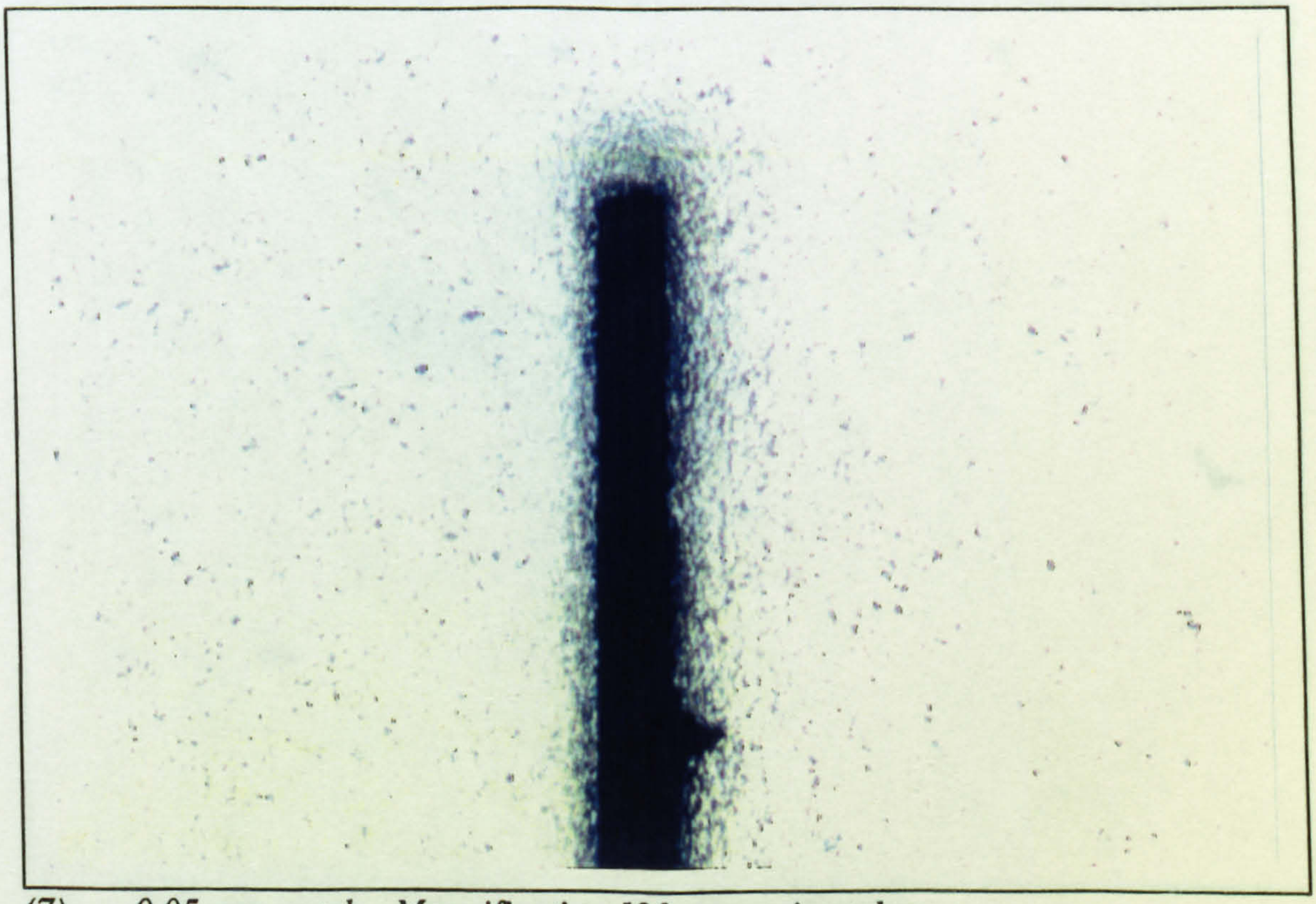

(7) 0.05 mm notch. Magnification 120 approximately.

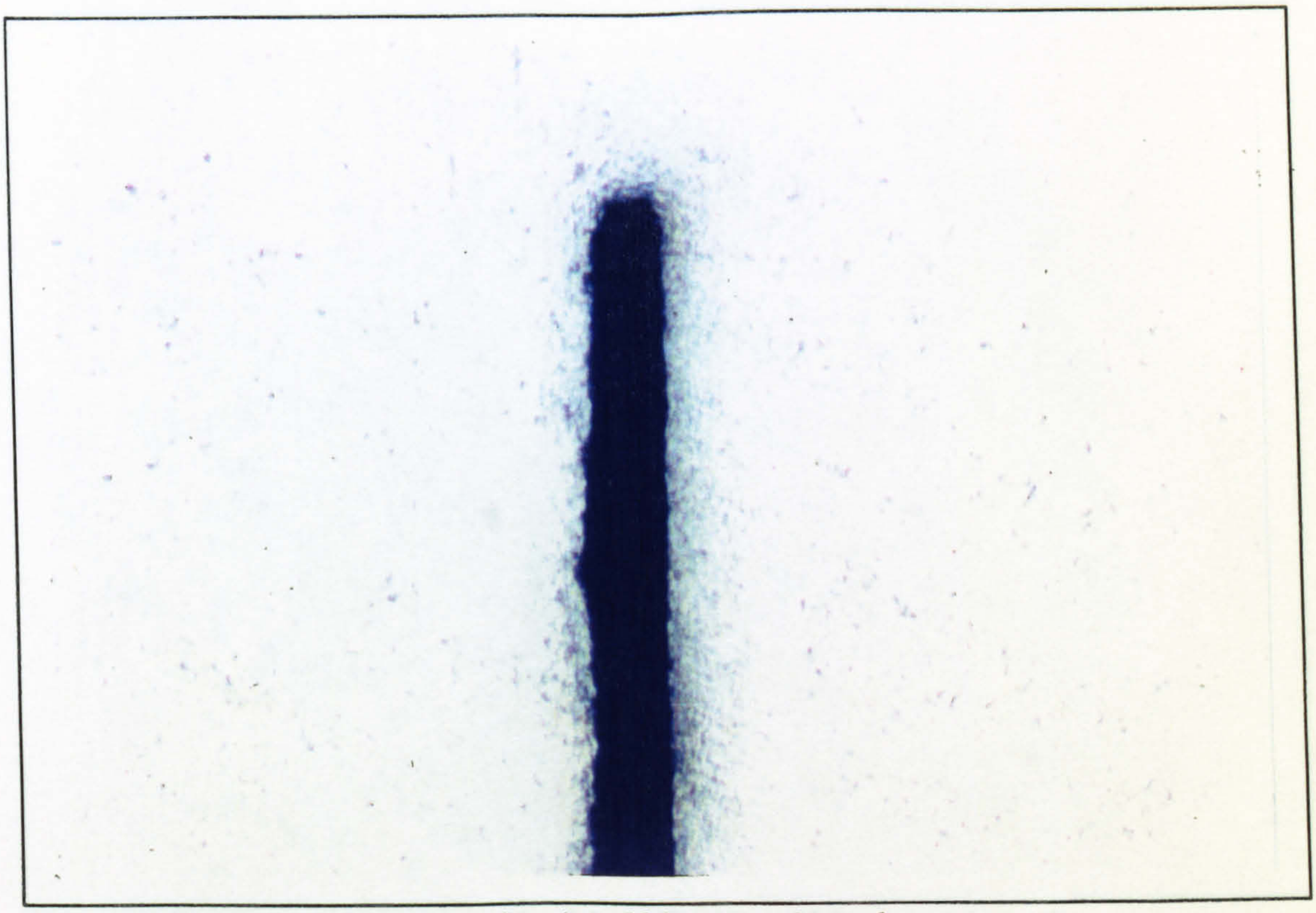

(8) 0.05 mm notch. Magnification 120 approximately.

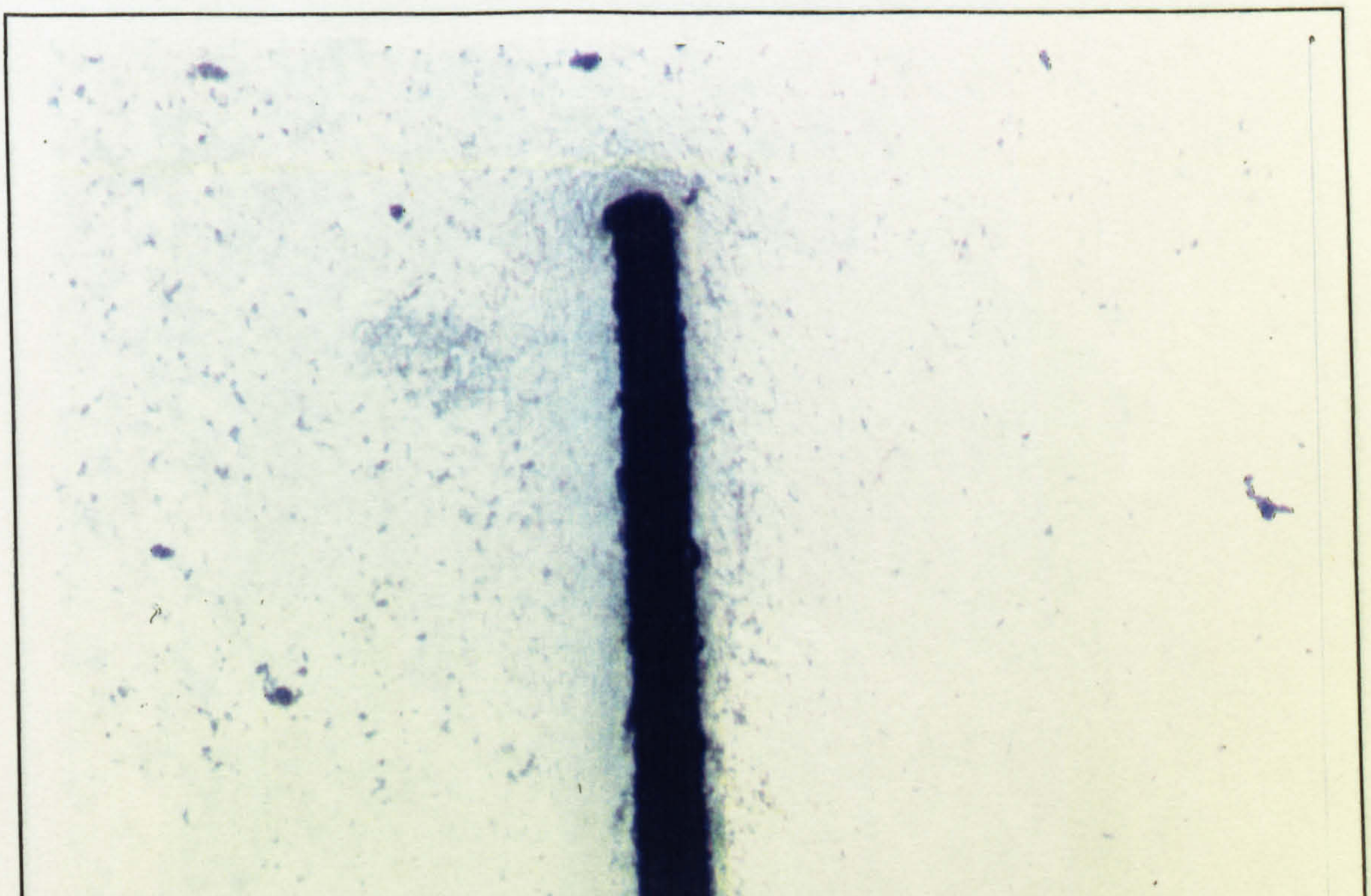

(9) 0.05 mm notch. Magnification 120 approximately.

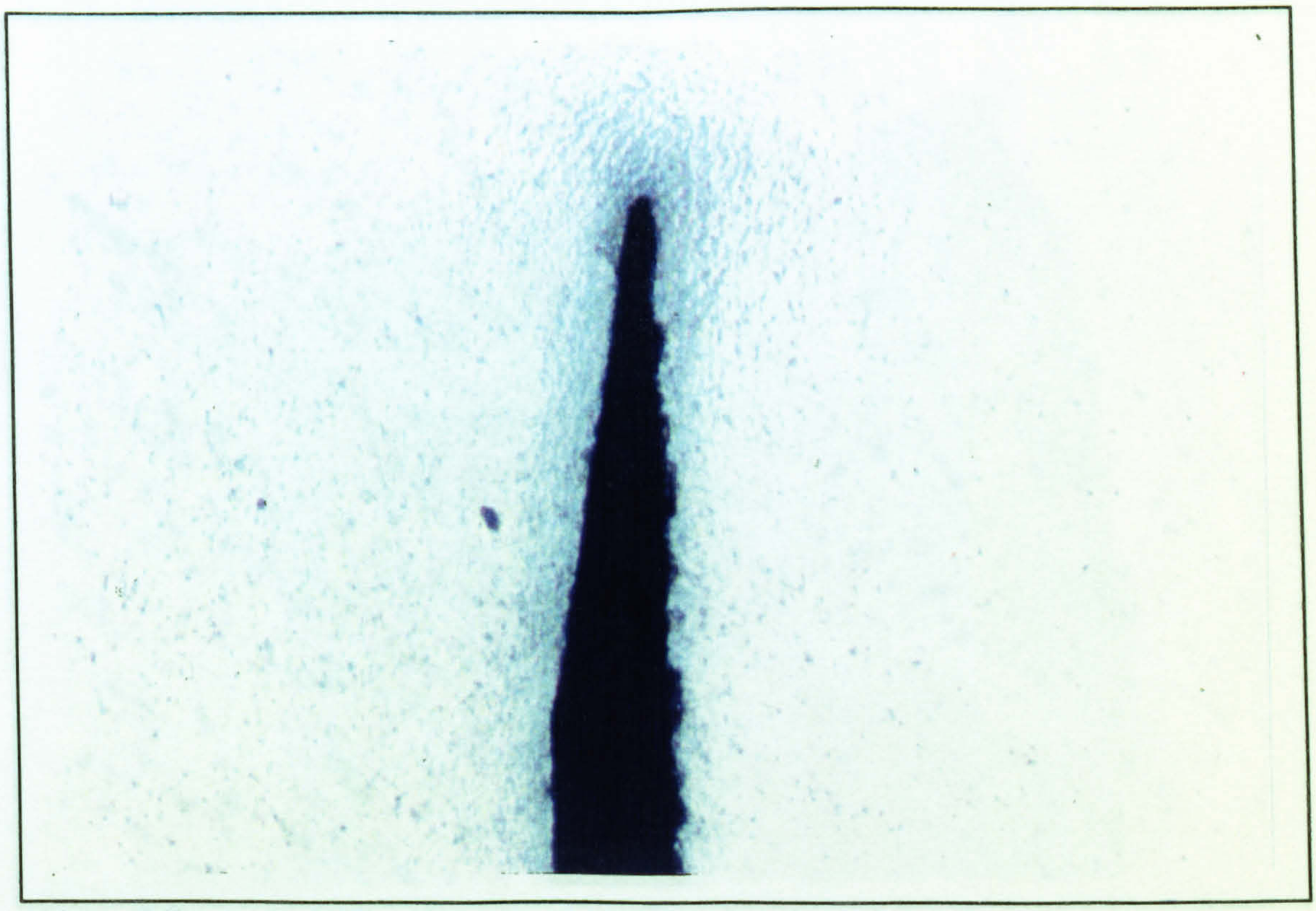

(10) Effectively 0.02 mm notch. Magnification 120 approximately.

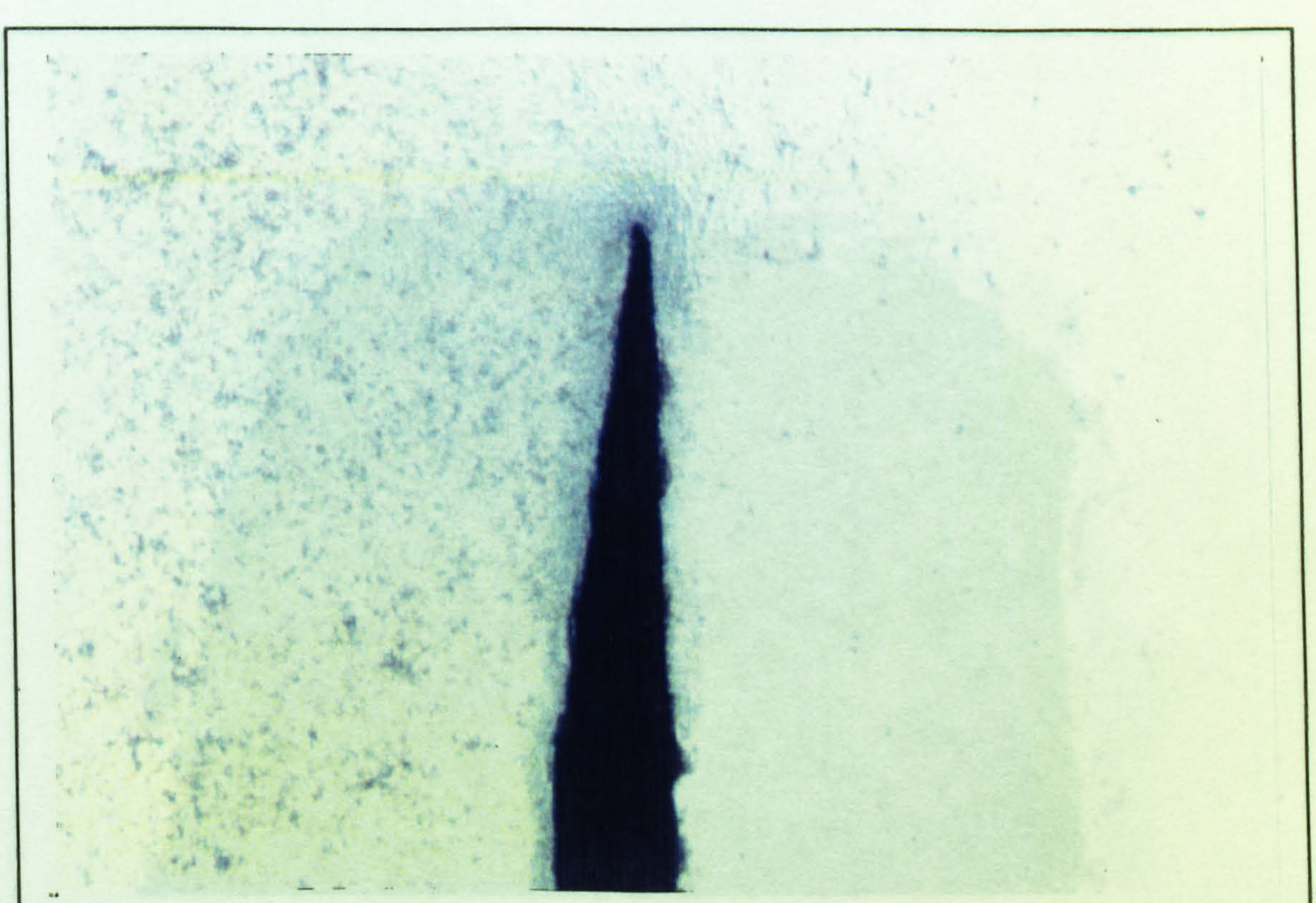

(11) Effectively 0.02 mm notch. Magnification 120 approximately.

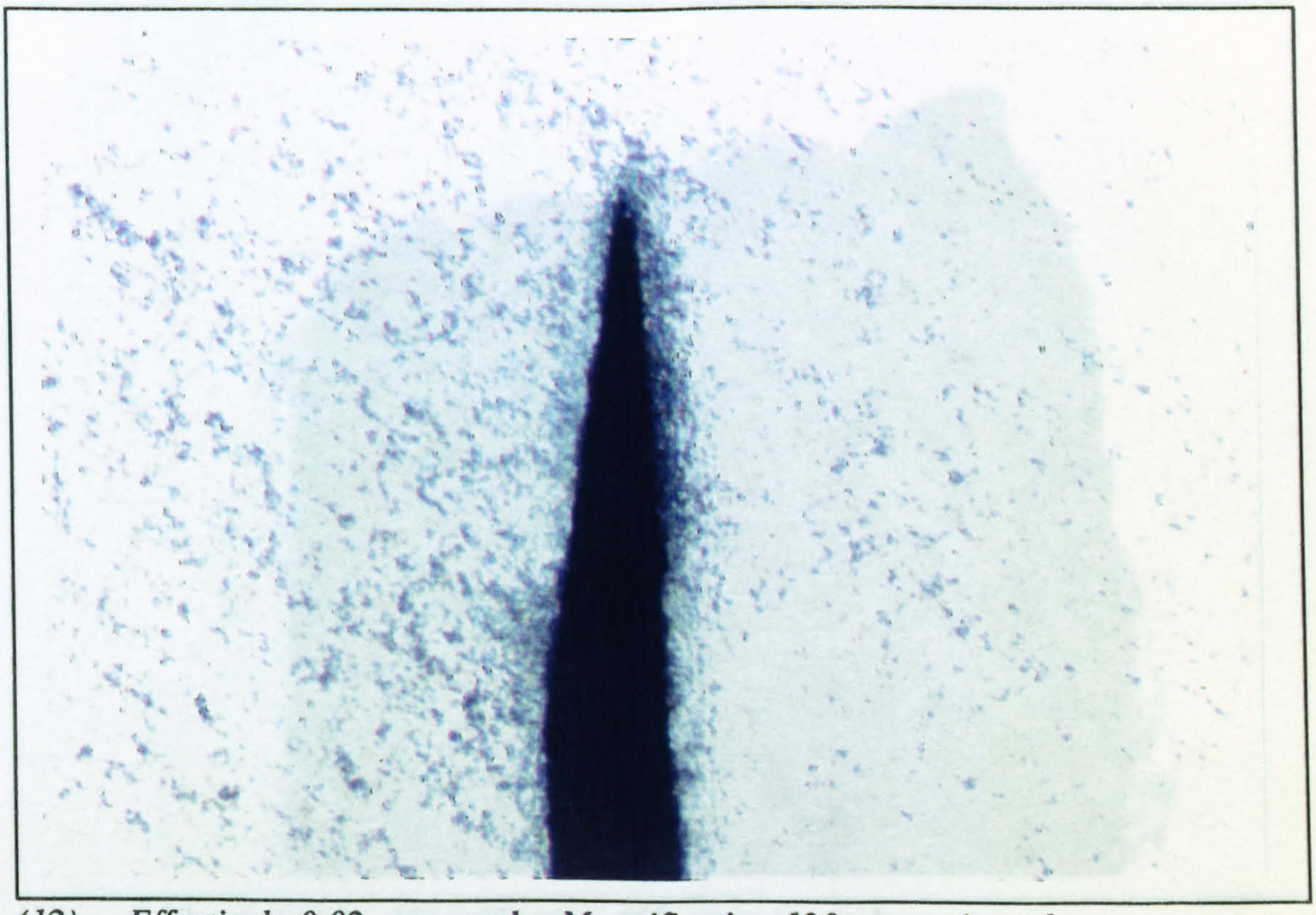

(12) Effectively 0.02 mm notch. Magnification 120 approximately.

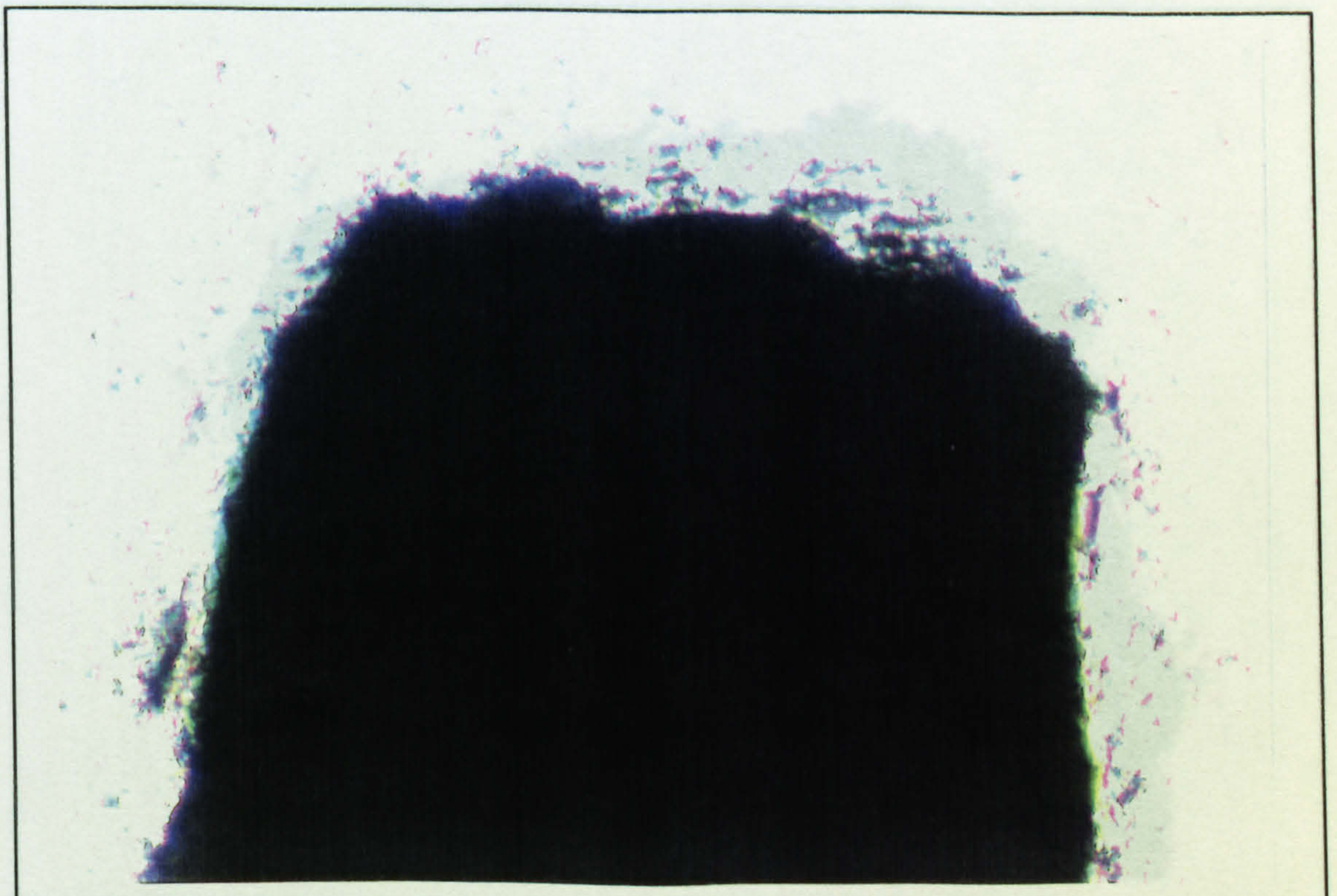

(13) 0.20 mm notch. Magnification 460 approximately.

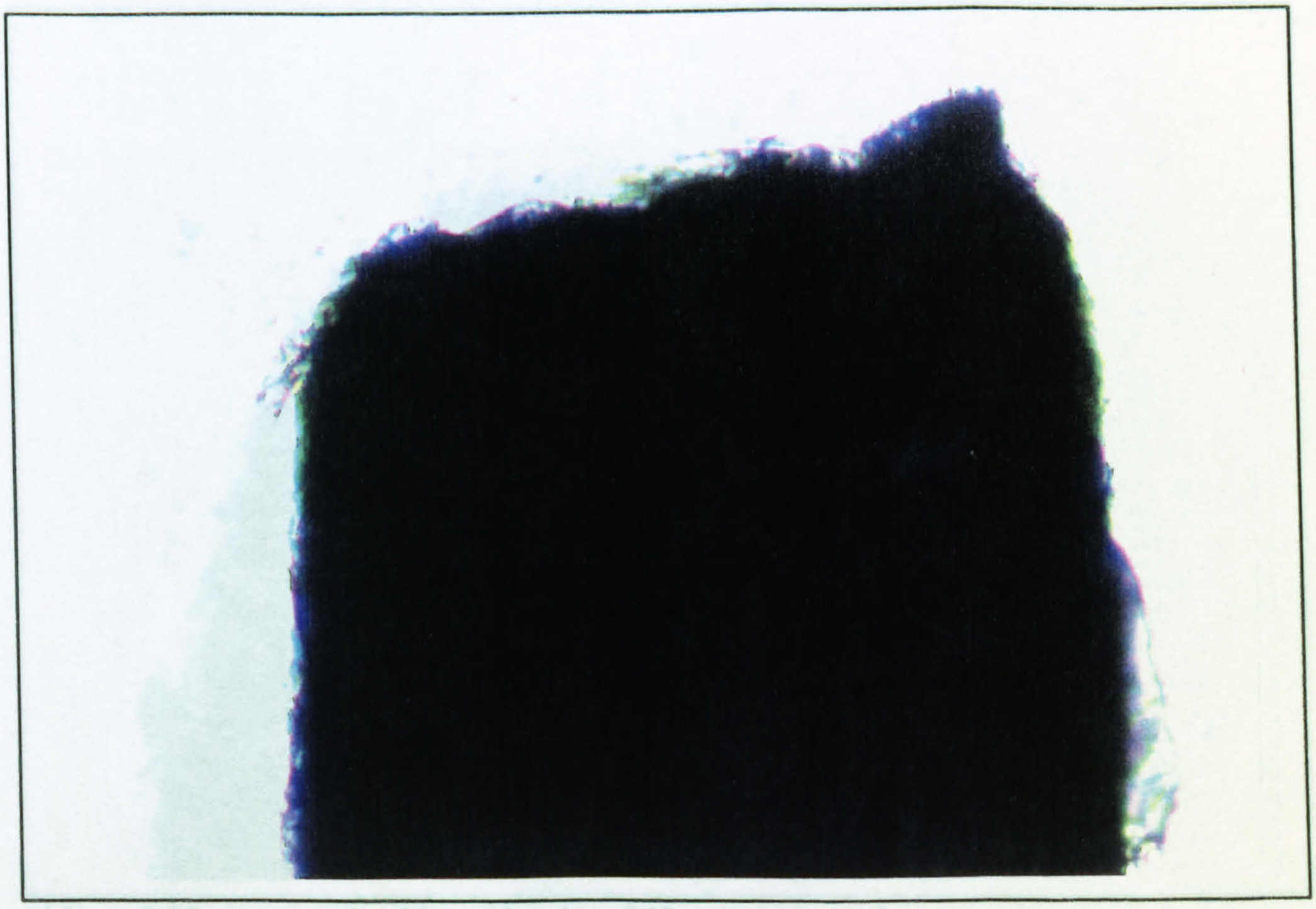

(14) 0.20 mm notch. Magnification 460 approximately.

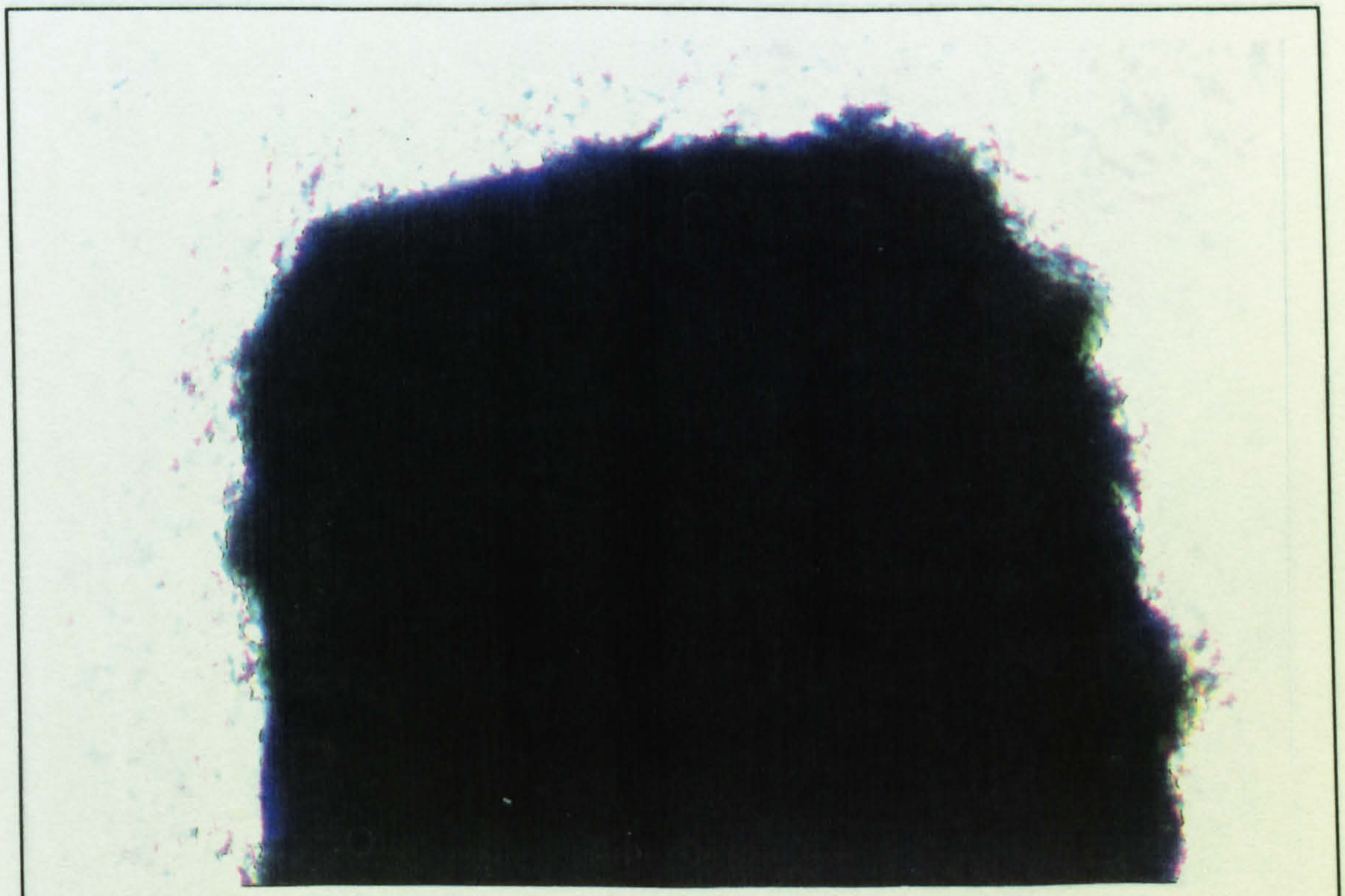

(15) 0.20 mm notch. Magnification 460 approximation.

(16) 0.10 mm notch. Magnification 940 approximately.

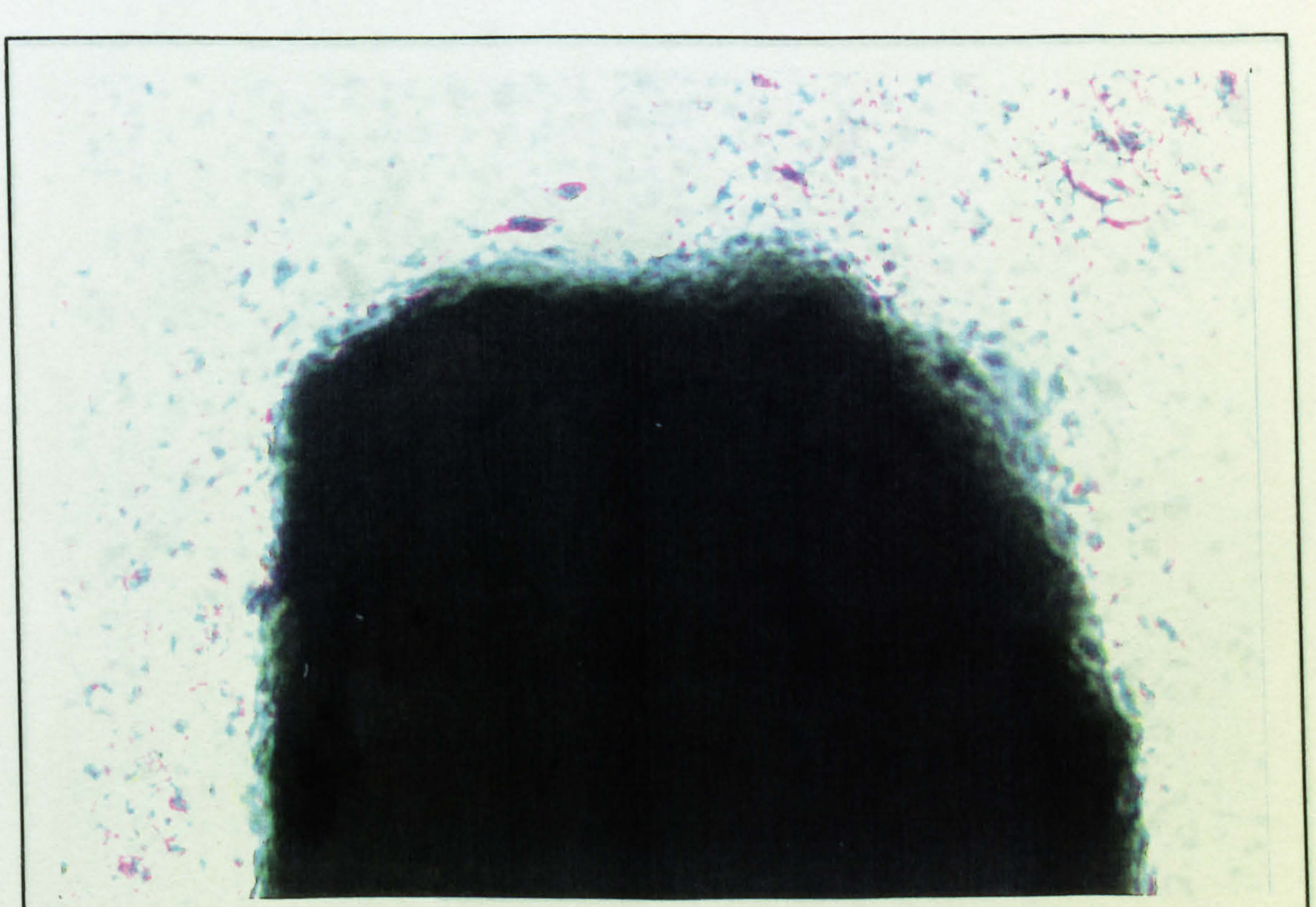

(17) 0.10 mm notch. Magnification 940 approximately.

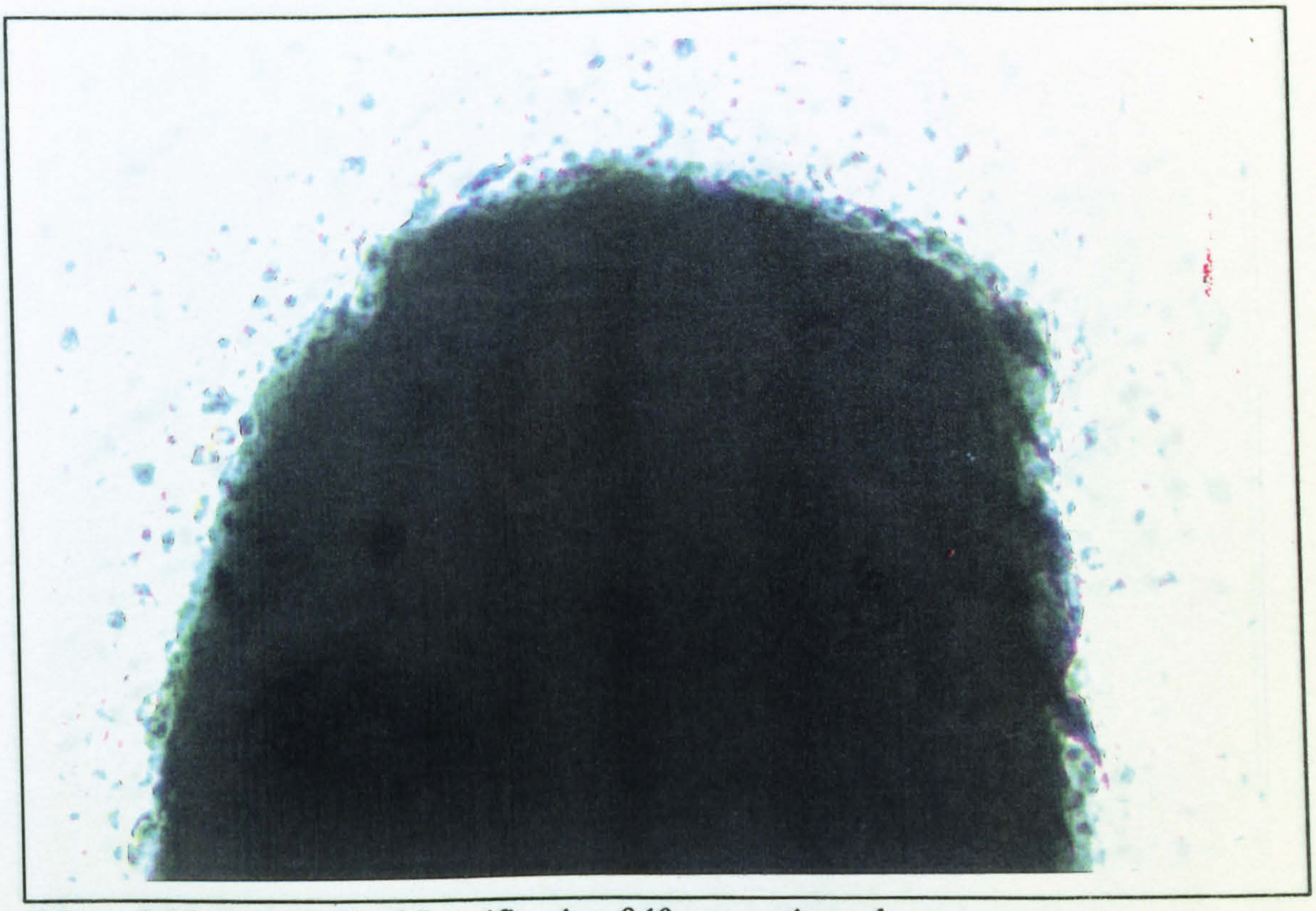

(18) 0.10 mm notch. Magnification 940 approximately.

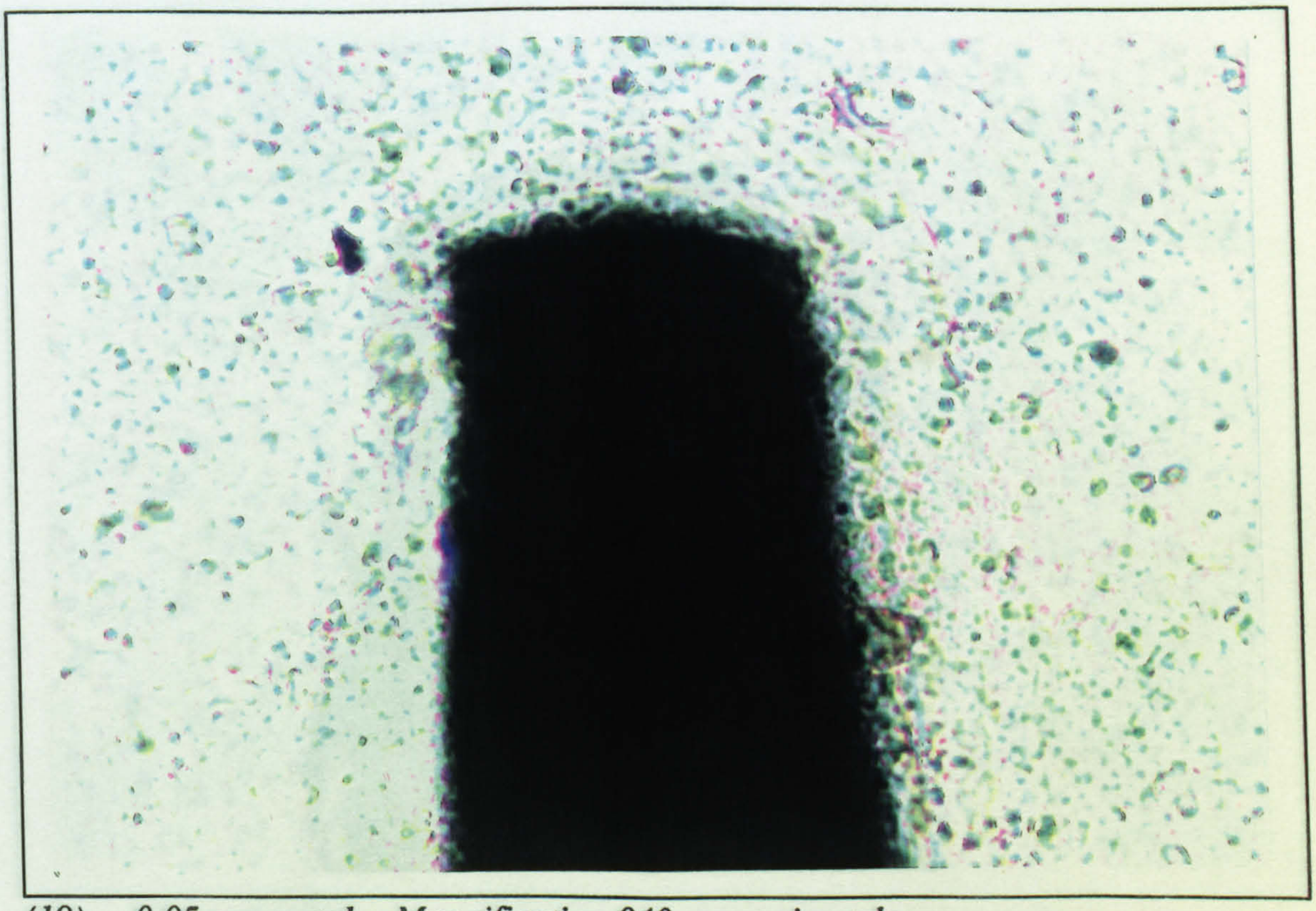

(19) 0.05 mm notch. Magnification 940 approximately.

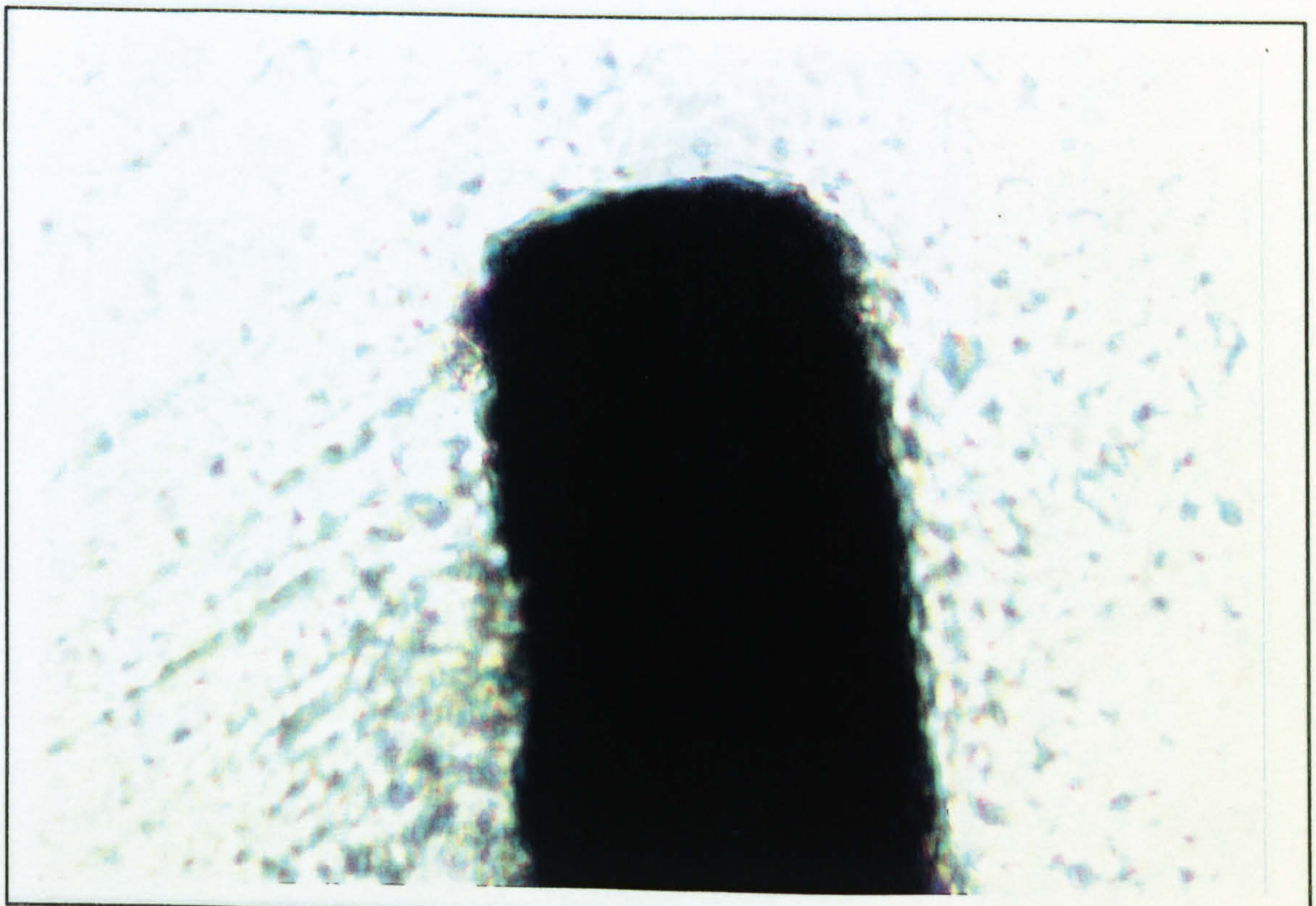

(20) 0.05 mm notch. Magnification 940 approximately.

(21) 0.05 mm notch. Magnification 940 approximately.

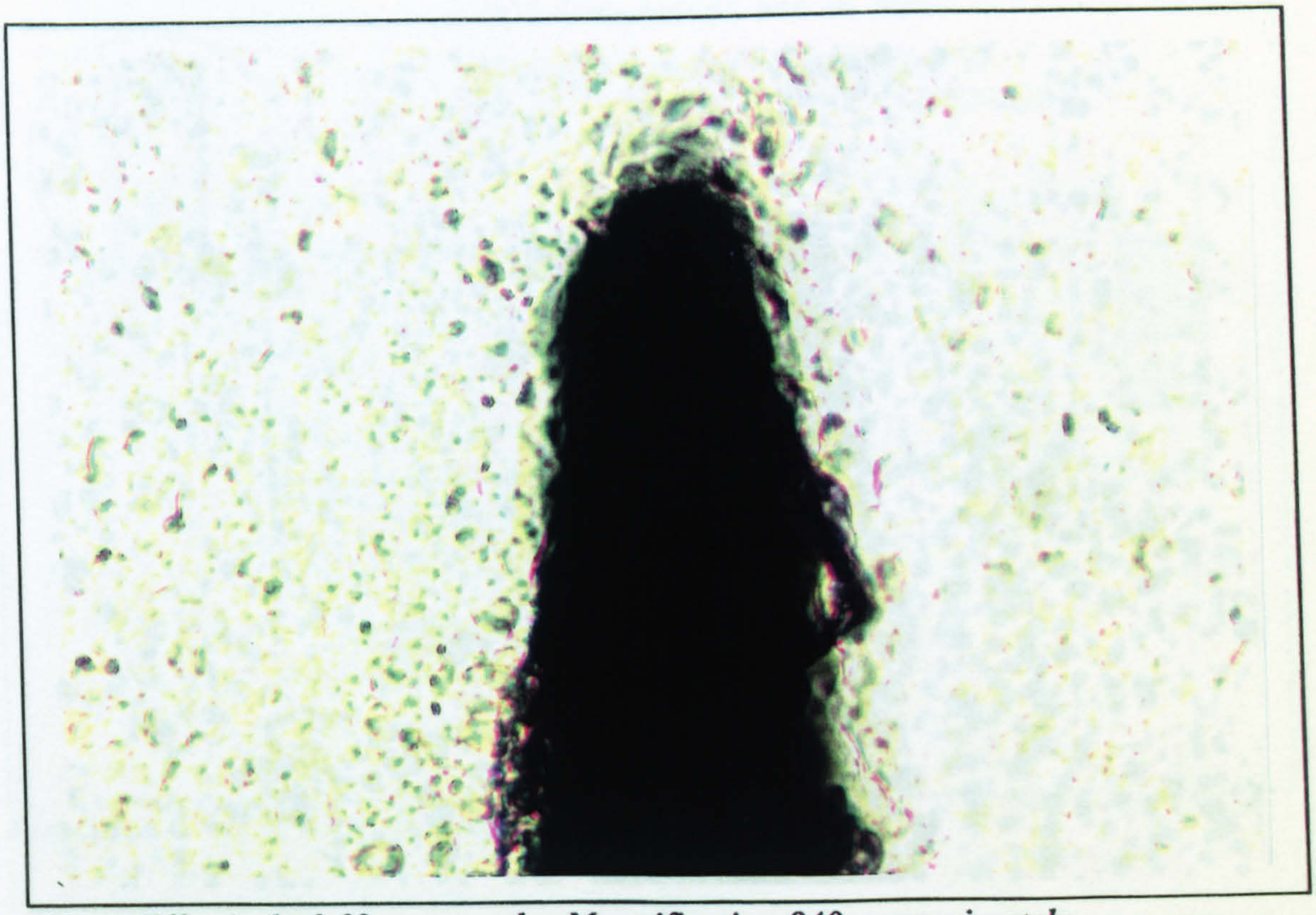

(22) Effectively 0.02 mm notch. Magnification 940 approximately.

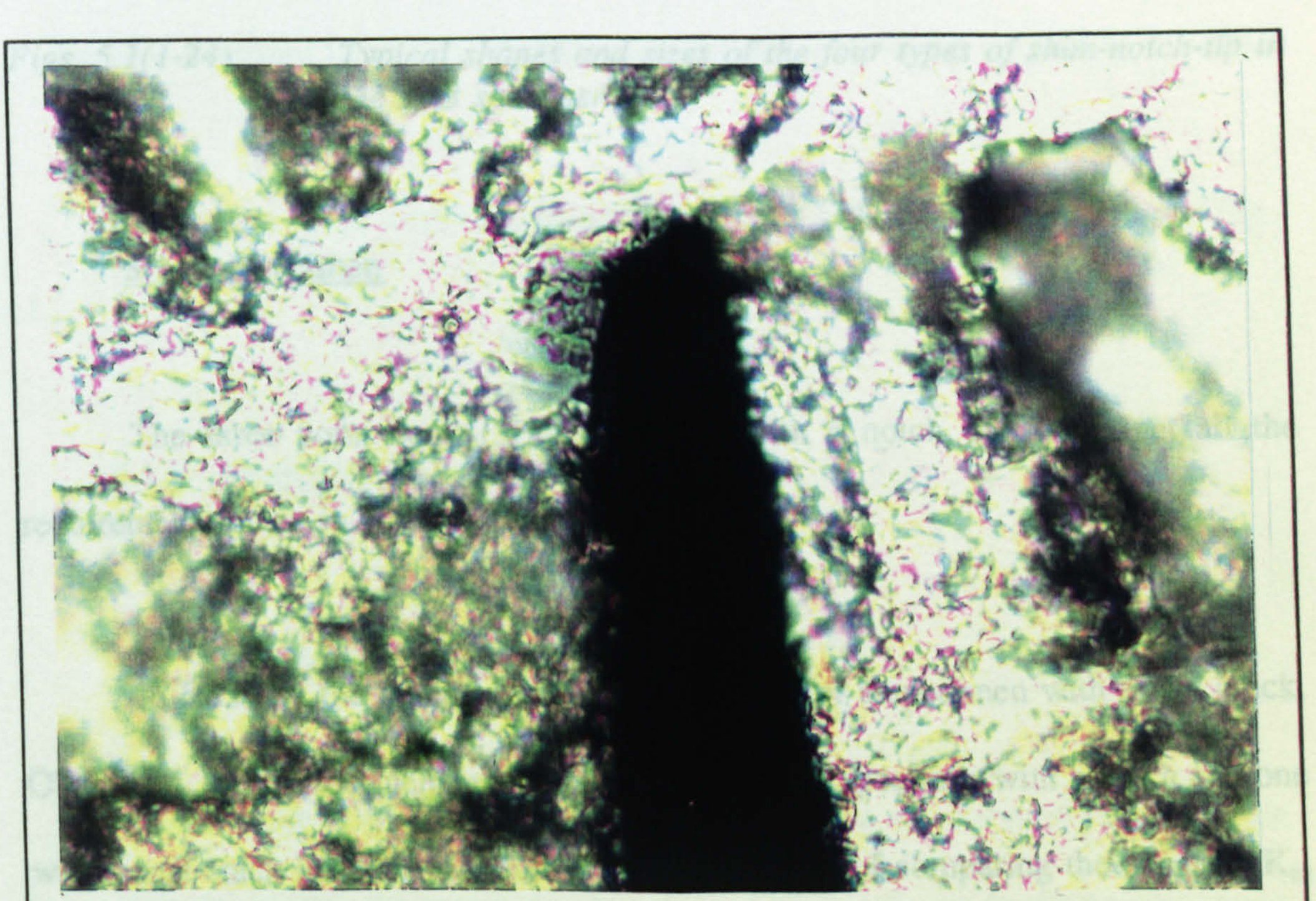

(23) Effectively 0.02 mm notch. Magnification 940 approximately.

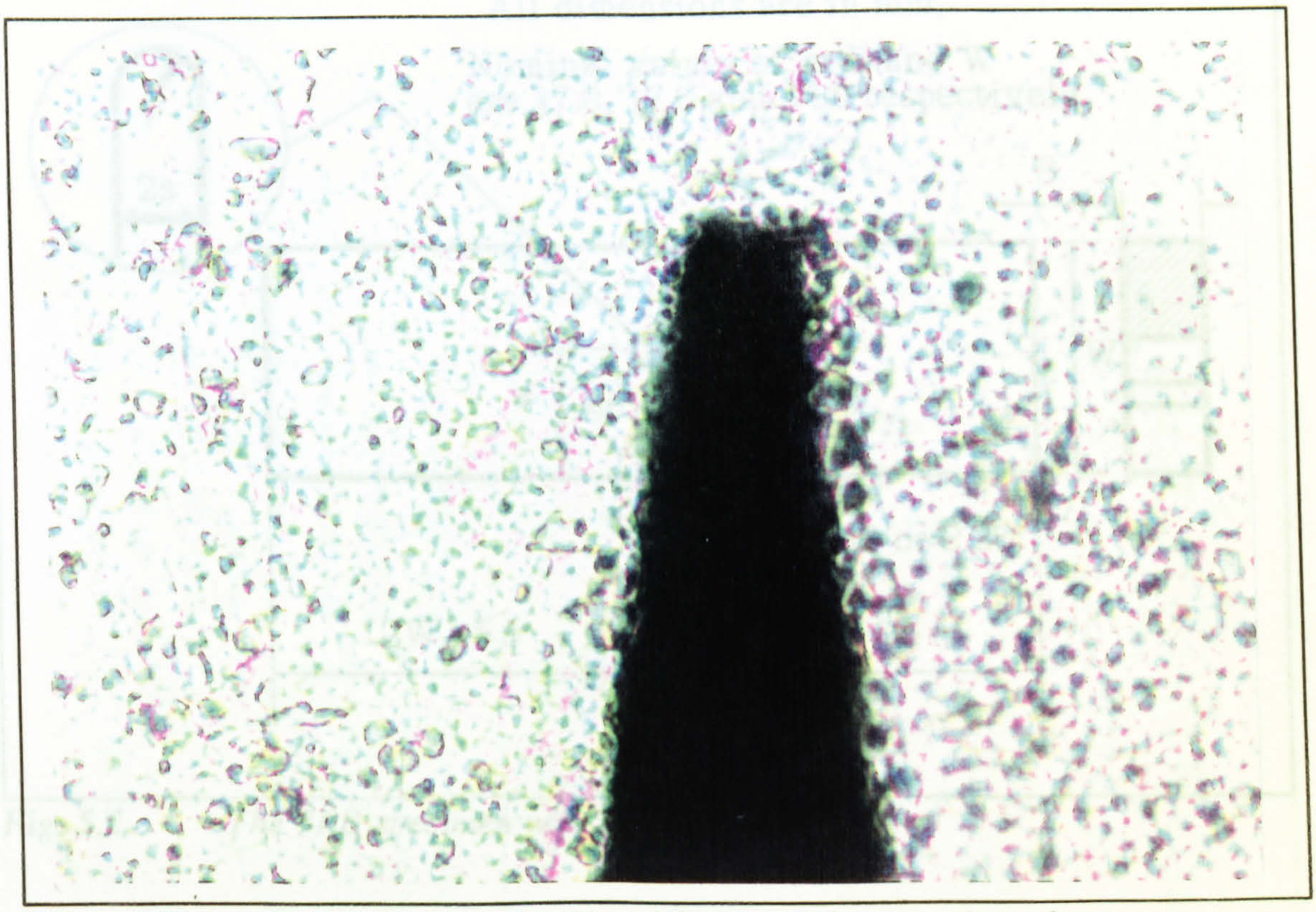

(24) Effectively 0.02 mm notch. Magnification 940 approximately.

Figs. 5.1(1-24). Typical shapes and sizes of the four types of shim-notch-tip in the 3PB specimen.

5.1.1. Specimen

The three point bend (3PB) specimen with a notch, Fig. 5.2, met all the requirements given in BS5447 [76].

In BS5447, the recommendations are given for a specimen with a real crack. Obviously, the same dimensions were used for both a specimen with a notch and one with a real crack in order to reduce the complications of comparing the apparent K_{IC} to the real K_{IC}. Such complications might have arisen due to plane strain considerations had the size of the specimens been different.

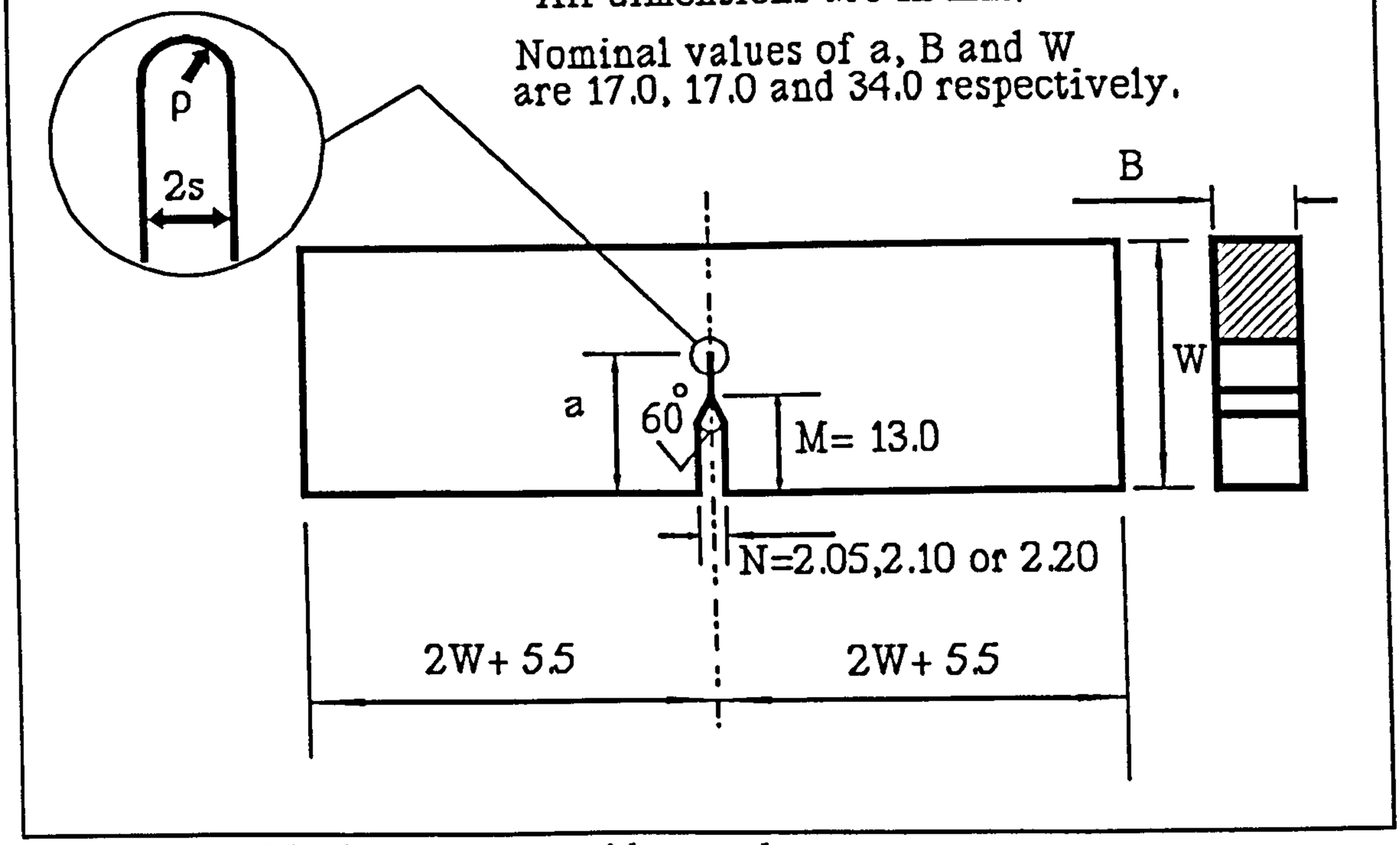

Fig. 5.2. The 3PB specimen with a notch.

In Fig. 5.2, the notch tip is shown to be semi-circular ($\rho/s = 1$). In reality the tip could be anything from a semi-circle to a flat end with sharp corners ($\rho/s \rightarrow 0$).

Four values of 2s were tested: 0.20, 0.10, 0.05 and 0.02 mm as shown in Fig. 5.1.

5.1.2. Manufacture

(a) Casting Technique

The production of the 3PB specimen involved the casting of a block of resin after which machining was required to transfer one block into ten or eleven specimens. Some thin slices were also machined out of each block and viewed through an

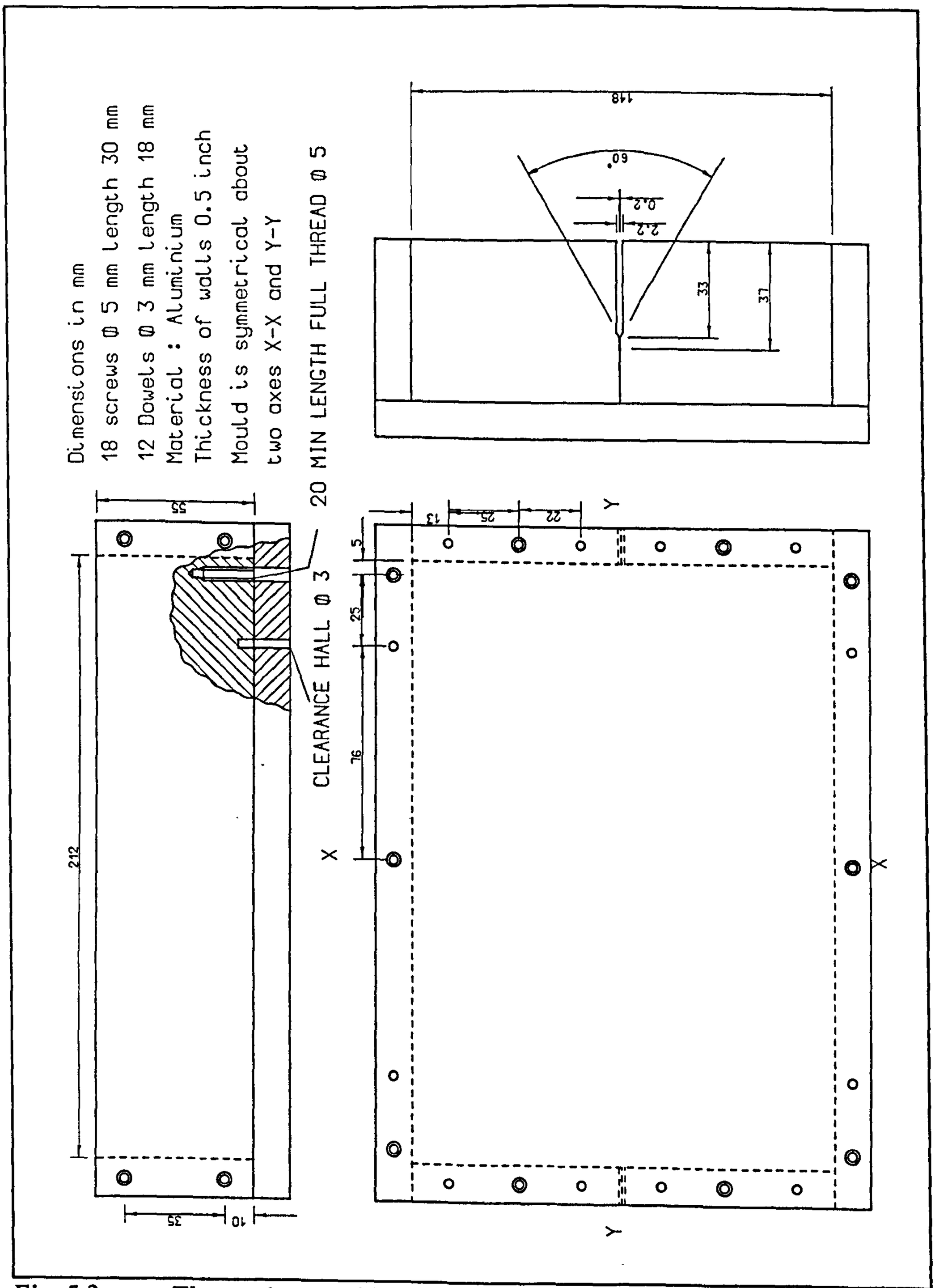

Fig. 5.3. The casting mould for the 3PB specimen, shown without the shim or the trapping plates.

polariscope to ensure the absence of residual stresses in the castings. Any casting

which had not acquired a "high quality standard" was rejected. What characterised a "high quality standard" were the absence of residual stresses and air bubbles, the achievement of the exact baking time periods and temperatures, the attaining of a uniform colour and homogeneity of the casting. In addition, the individual specimens were checked thoroughly, with the aid of a microscope and micrometers, for the dimensions and notch shapes.

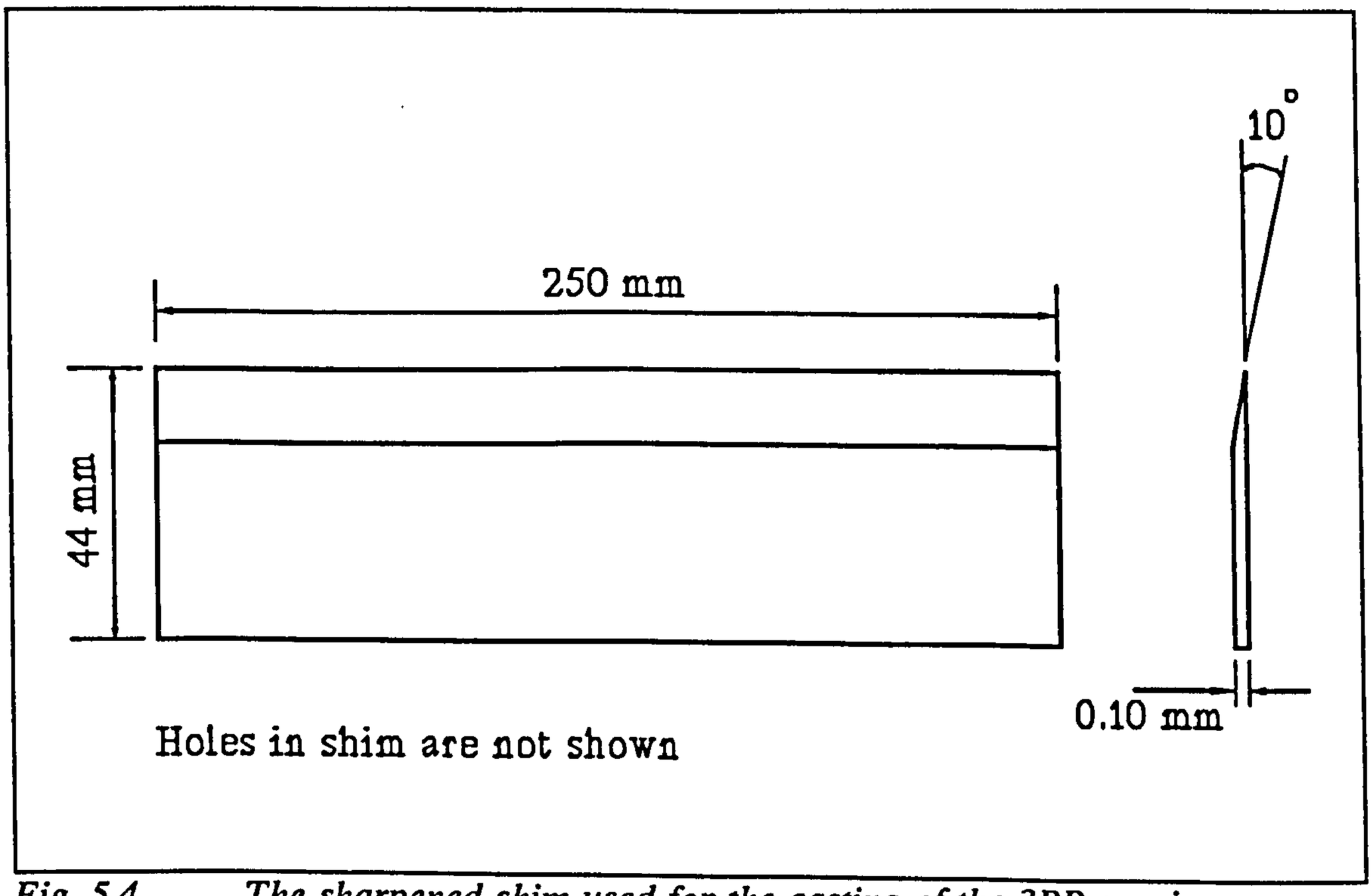

Fig. 5.4. The sharpened shim used for the casting of the 3PB specimen.

There were two identical moulds for casting the 3PB specimen blocks. They were made of aluminium, with the exception of the shim and the plates trapping the shim, being made of steel. Fig. 5.3 shows one of the two identical moulds separately. The sharpened shim and the trapping plates can be seen in Figs. 5.4. & 5.5 respectively. The above components are assembled together in Fig. 5.6.

The flat shims were produced by marking a straight line on the shim steel and cutting it with a pair of scissors. The burr on the edge was removed by rubbing it with a 320 grade wet and dry paper.

The sharpened shims were produced out of shim steel by trapping each of them between two flat 6mm-thick steel plates and grinding them at an angle of 10° to the plane of the plates.

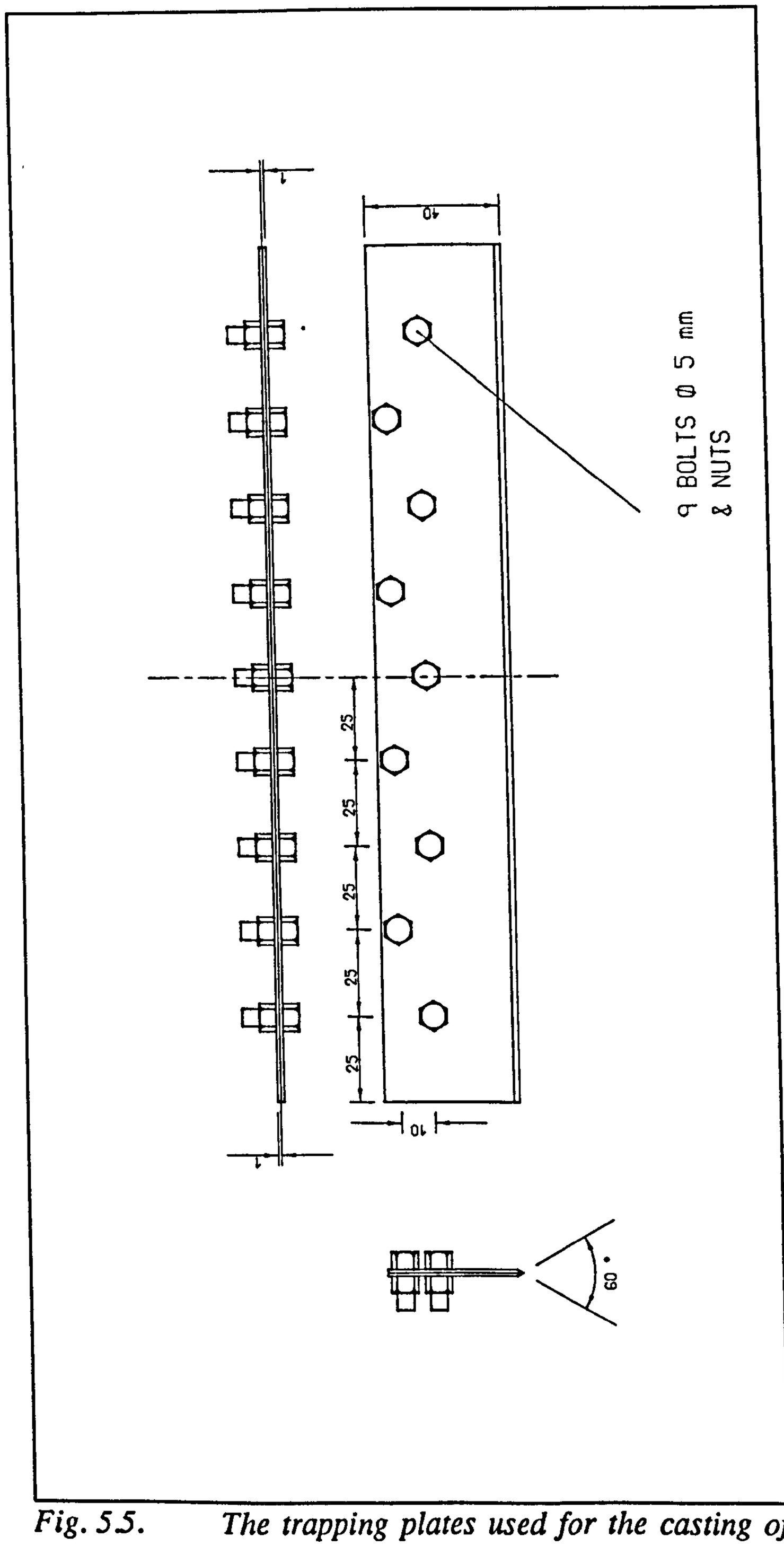

Fig. 5.5. The trapping plates used for the casting of the 3PB specimen.

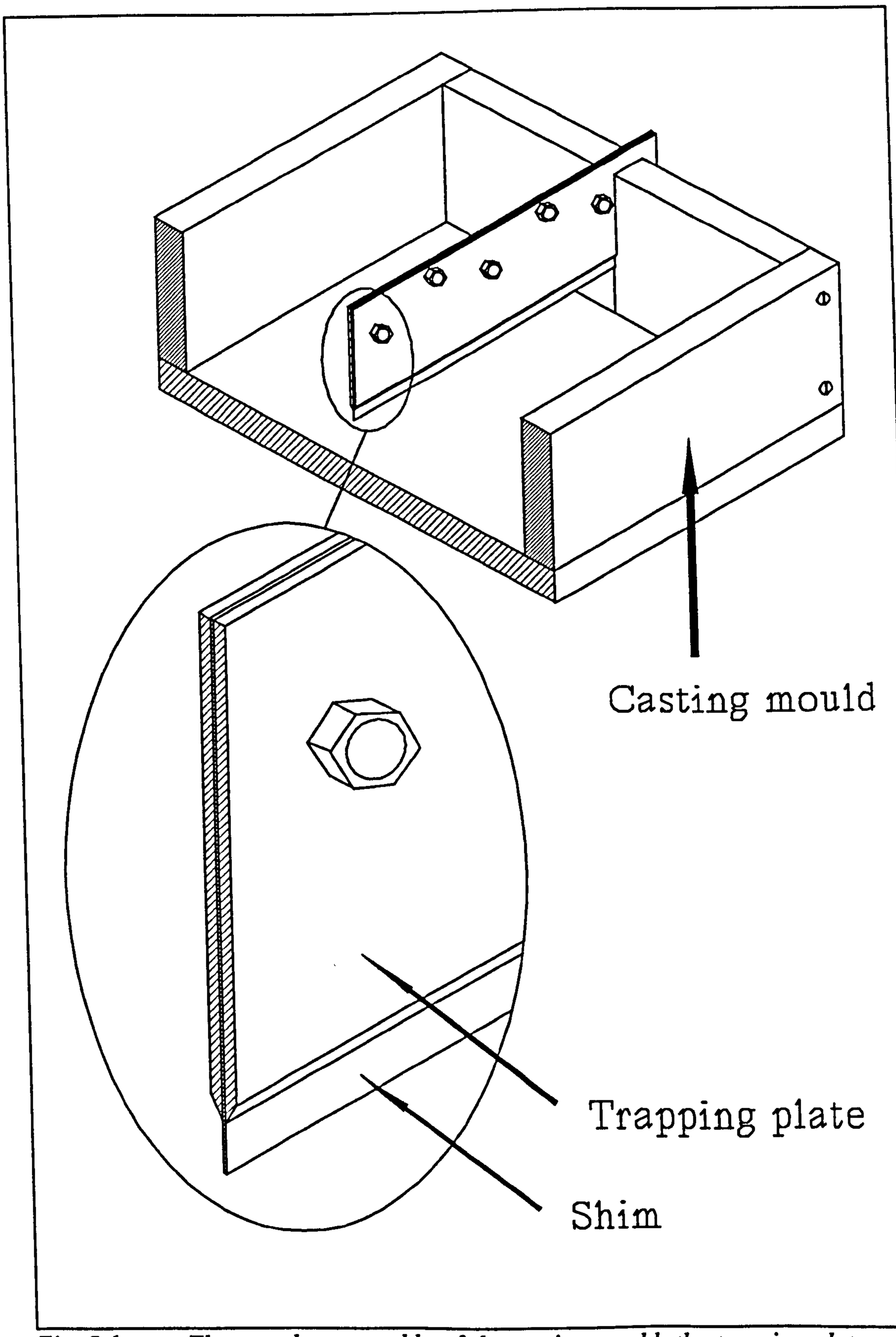

Fig. 5.6. *The complete assembly of the casting mould, the trapping plates and a flat-edged shim for the casting of the 3PB specimen.*

(b) Machining Technique

Each cast block was fly-cut on a milling machine to the required specimen width, W (Fig. 5.2). The block was then sliced into individual specimens of thickness B (Fig. 5.2) using a diamond impregnated cutting wheel. The slicing operation was carried out using copious quantities of cutting fluid in order to avoid any overheating of the material. The specimen with the final dimensions can be seen in Fig. 5.2.

5.1.3. Loading Apparatus

It was required to load the 3PB specimens in pure bending. The equipment used to achieve this was the Instron Instrument manufactured by Instron Limited (Coronation Rd, High Wycombe, Buckinghamshire). The Instron three point bend rollers, in conjunction with the Instron 1193 loading machine, provided the desired three point bending, as shown in Fig. 5.7. The upper roller was parallel to and of an equal distance from the two lower rollers (Fig. 5.8). The lower rollers had a loading span, L (= 4W), of 136.0 mm between their centres - a requirement given by BS5447 [76] for the size of the specimen in hand. The three rollers were 25.0 mm in diameter each.

An acceptable range for the dimensions of the rollers was recommended by BS5447 [76]. Also required was the ability of the lower rollers to roll away from each other, in the plane containing their axes, against a small spring force, if forced to do so, to trivialize any horizontal frictional force component between the specimen

and rollers. The rollers satisfied all the requirements.

The lower rollers were fixed to the base of the Instron 1193 loading machine while the upper roller was connected to its loading cross head having a controllable loading speed set at 1.0 mm/minute.

An Instron compression load cell was calibrated in accordance with the Instron manual, and used to measure the load exerted on the 3PB specimens.

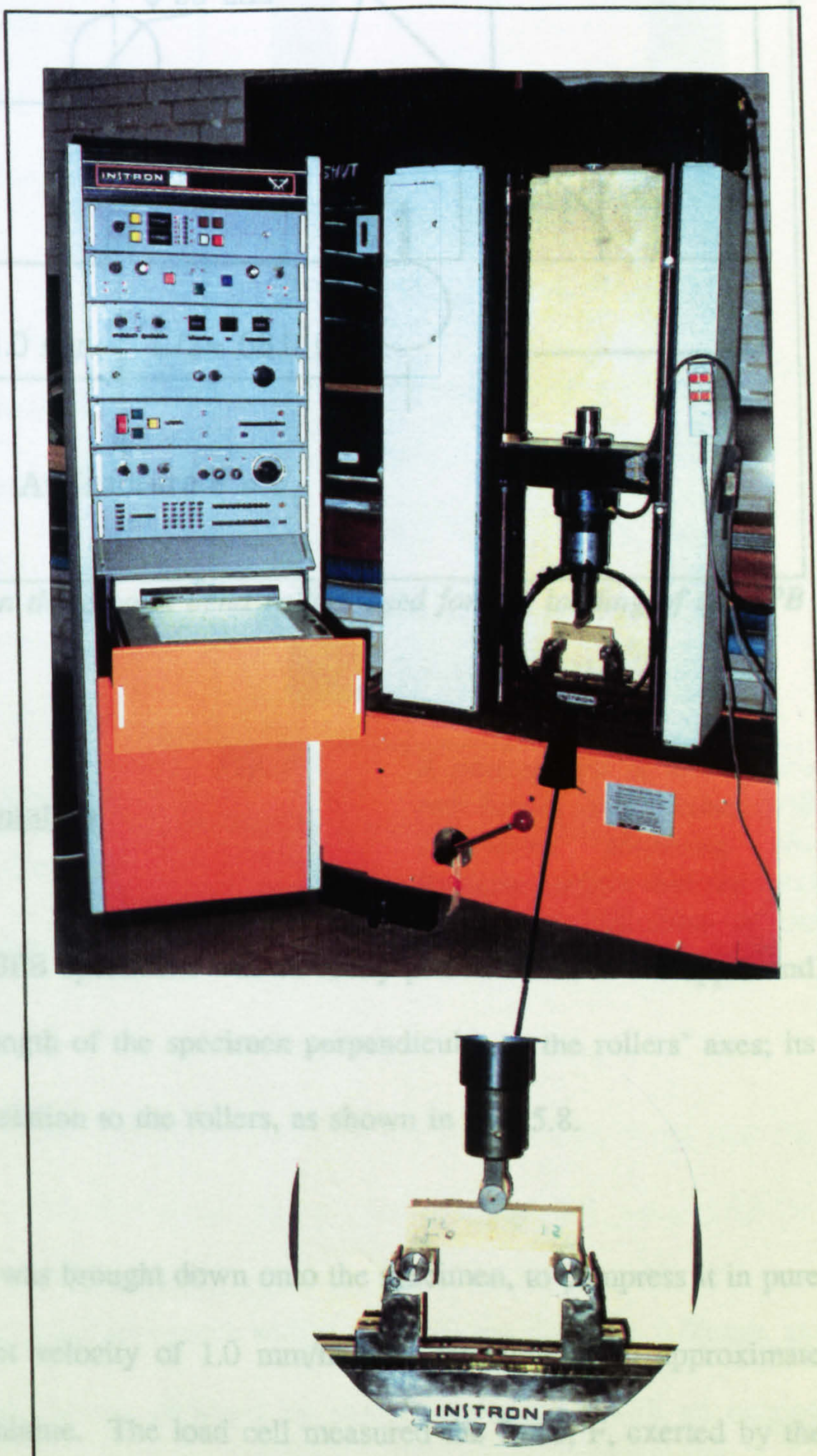

Fig. 5.7. *The Instron 1193 loading machine and three point bend rollers.*

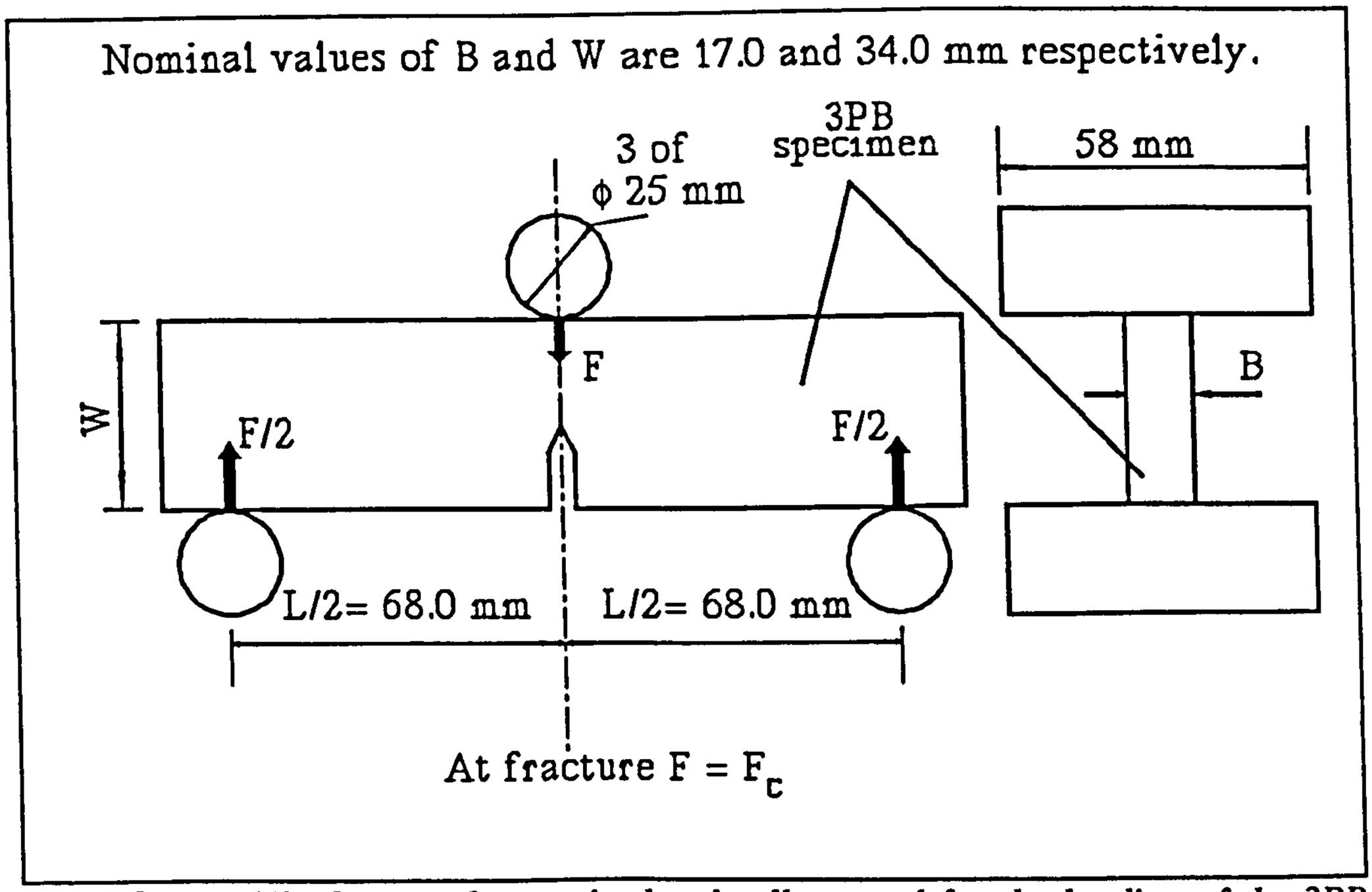

Fig. 5.8. *The Instron three point bend rollers used for the loading of the 3PB specimen.*

5.1.4. Experimentation

Each one of the 3PB specimens was carefully placed between the upper and lower rollers with the length of the specimen perpendicular to the rollers' axes; its location was central in relation to the rollers, as shown in Fig. 5.8.

The upper roller was brought down onto the specimen, to compress it in pure bending, with a constant velocity of 1.0 mm/minute, resulting in an approximate loading rate of 860 N/minute. The load cell measured the force, F, exerted by the upper roller at the point of contact with the specimen - see Fig. 5.8. The force at fracture, F_C, was recorded and used in the stress intensity factor calculations.

In every test, the specimen would break at the notch tip into two symmetric halves with the broken surface containing fine lines revealing the point along the notch tip at which the crack initiated, as can be seen in Fig. 5.9. Occasionally, when the crack initiated at either end of the notch tip, the results were rejected in case there was any asymmetric bending in the specimen due to uneven specimen dimensions caused by infrequent and unavoidable imbalance in machining tolerances.

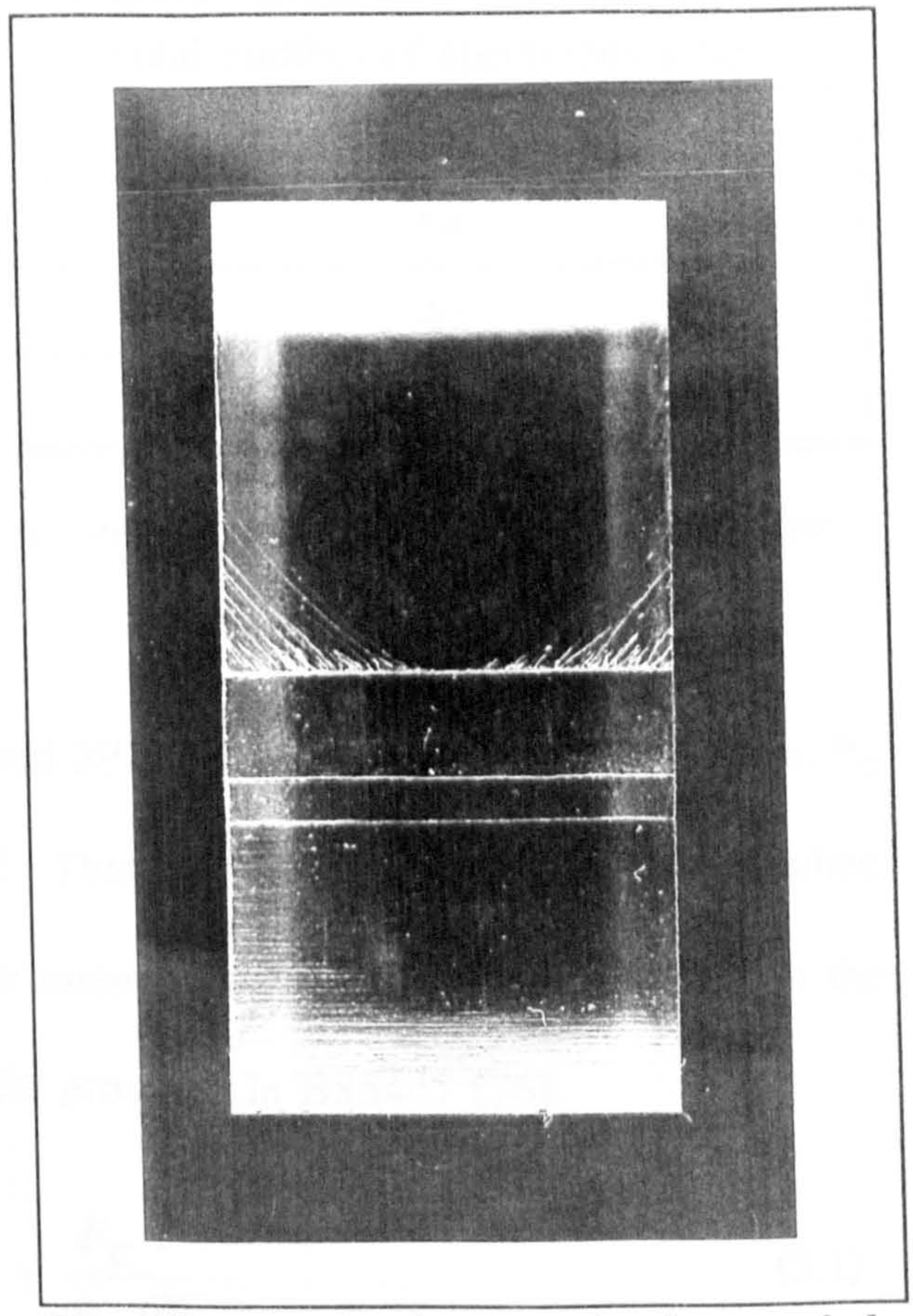

Fig. 5.9. A photograph of one of the two halves of a broken 3PB specimen showing the fracture surface and the lines which are indicative of the point of crack inception.

5.1.5. Results

The 3PB specimens had four notch widths, 2s: 0.20mm, 0.10mm, 0.05mm, and an effective 0.02mm which was obtained by sharpening a shim with an original thickness of 0.10mm. The total number of specimens tested with a valid outcome for each of the above four notch sizes is given in Table 5.1.

2s (mm)	Total number of specimens tested
0.20	47
0.10	58
0.05	46
0.02	147

Table 5.1. The number of valid tests for each notch size of the 3PB specimens.

The tests carried out on the notched 3PB specimens gave the critical force, F_C (see Fig. 5.8), at which fracture occurred. That value was in turn utilized to calculate the apparent critical values of the stress intensity factor, K_{IC}^{APP}, by referring to the relevant equation (equation 5.1) and table provided in BS5447 [76].

$$K_{IC} = \frac{F_C\, Y}{B\,\sqrt{W}} \qquad (5.1)$$

F_C being the critical value of F; F, B and W are defined in Fig. 5.8. Y is a dimensionless geometry factor tabulated in BS5447 [76] which depends on a/W, the ratio of the crack length to the specimen width, for the particular 3PB specimen.

The dimensions of the specimens and notches, the fracture loads and the apparent critical stress intensity factors can be seen in Tables 5.2, 5.3, 5.4 and 5.5 for the notch widths 0.20, 0.10, 0.05 and 0.02mm respectively.

The angle of crack propagation was zero for every 3PB specimen, producing two identical halves.

Specimen number	B(mm)	W(mm)	a/W	F_c(N)	K_{IC}^{APP}(N/mm$^{3/2}$)
1	17.02	33.95	0.487	467	47.9
2	17.03	33.96	0.488	488	50.2
3	17.05	33.96	0.488	645	66.2
4	17.06	33.97	0.499	653	69.5
5	17.02	33.98	0.499	600	64.0
6	17.05	33.97	0.499	618	65.8
7	17.04	34.00	0.498	538	57.1
8	17.02	34.00	0.499	563	60.0
9	17.06	34.00	0.500	516	55.0
10	16.99	34.01	0.499	512	54.7
11	17.00	34.00	0.500	495	53.0
12	17.06	34.00	0.507	630	68.8
13	17.07	34.00	0.508	513	56.0
14	17.06	33.99	0.508	564	61.7
15	17.02	33.99	0.507	592	64.7
16	17.01	33.98	0.507	531	58.0
17	17.09	33.98	0.508	464	50.6
18	17.06	33.99	0.509	508	55.7
19	17.05	33.99	0.509	557	61.3
20	17.11	34.00	0.509	516	56.4
21	17.05	34.01	0.508	499	54.7
22	17.06	33.91	0.494	620	65.0
23	17.10	33.92	0.494	605	63.2
24	17.04	33.91	0.494	690	72.4
25	17.12	33.91	0.494	581	60.7
26	17.03	33.90	0.494	575	60.4
27	17.12	33.90	0.494	703	73.3
28	17.06	33.90	0.493	482	50.3

29	16.98	33.95	0.507	665	72.3
30	16.99	33.96	0.504	567	61.6
31	16.95	33.97	0.505	711	77.6
32	16.97	34.00	0.490	627	65.0
33	16.96	34.00	0.489	676	70.1
34	17.00	34.00	0.489	637	65.8
35	16.99	33.99	0.488	632	65.1
36	16.97	33.99	0.487	600	61.7
37	16.99	33.99	0.488	621	63.9
38	16.96	33.99	0.487	649	66.8
39	17.04	34.00	0.490	697	72.0
40	17.03	34.00	0.488	760	78.0
41	17.04	33.99	0.500	681	72.7
42	17.00	33.98	0.499	690	73.5
43	17.01	33.98	0.500	631	67.4
44	17.00	33.98	0.501	757	81.2
45	16.96	34.00	0.505	690	75.2
46	16.95	33.98	0.499	693	74.1
47	17.01	34.00	0.507	776	84.9

Table 5.2. Results for the 3PB specimens with 0.20 mm notch width.

Specimen number	B(mm)	W(mm)	a/W	F_C(N)	K_{IC}^{APP}(N/mm$^{3/2}$)
1	17.08	34.00	0.504	554	59.7
2	17.04	33.99	0.503	491	53.0
3	17.02	33.98	0.502	500	53.8
4	17.04	33.96	0.501	502	53.8
5	17.06	33.96	0.501	527	56.5
6	17.08	33.96	0.502	489	52.4
7	17.07	33.96	0.501	524	56.1

8	17.04	33.97	0.503	564	60.8
9	17.01	33.96	0.501	495	53.1
10	17.04	33.95	0.500	542	57.9
11	16.97	33.95	0.499	524	56.0
12	16.95	33.94	0.498	539	57.5
13	17.04	34.00	0.512	501	55.6
14	17.04	34.00	0.511	525	58.1
15	17.05	33.99	0.511	570	63.1
16	17.08	33.99	0.512	569	63.0
17	17.09	33.98	0.512	470	52.0
18	17.03	33.98	0.512	398	44.2
19	16.97	33.97	0.513	517	57.8
20	17.07	33.97	0.513	575	63.9
21	17.06	33.96	0.512	464	51.5
22	17.08	34.01	0.492	602	62.4
23	17.12	33.99	0.489	593	60.9
24	17.08	33.99	0.487	536	54.8
25	17.12	33.98	0.488	605	61.8
26	17.13	33.97	0.488	642	65.7
27	17.13	33.97	0.488	605	61.9
28	17.11	33.97	0.487	671	68.5
29	17.00	33.97	0.488	564	58.0
30	17.13	33.98	0.488	700	71.6
31	17.11	33.98	0.487	563	57.4
32	17.01	34.00	0.494	444	46.6
33	16.98	33.99	0.493	582	60.9
34	17.01	33.98	0.497	506	53.7
35	16.96	33.98	0.494	473	49.8
36	16.95	33.98	0.494	414	43.6

37	17.06	33.98	0.500	618	65.9
38	17.00	33.99	0.500	627	67.1
39	17.01	34.00	0.500	617	65.9
40	17.03	34.01	0.499	625	66.6
41	17.00	34.02	0.500	556	59.4
42	17.02	34.02	0.499	671	71.5
43	17.03	34.03	0.500	605	64.5
44	17.02	34.03	0.499	705	75.1
45	17.02	34.04	0.499	710	75.5
46	17.01	34.05	0.498	611	64.9
47	17.05	34.04	0.498	571	60.4
48	17.08	34.07	0.508	508	55.5
49	16.99	34.07	0.506	540	58.9
50	17.02	34.07	0.506	511	55.6
51	17.03	34.07	0.505	498	54.0
52	17.02	34.07	0.504	541	58.5
53	17.06	34.07	0.504	456	49.2
54	17.01	34.07	0.503	490	52.9
55	17.06	34.07	0.503	451	48.4
56	17.07	34.07	0.502	611	65.5
57	17.04	34.07	0.502	475	51.0
58	17.07	34.07	0.502	476	51.0

Table 5.3. Results for the 3PB specimens with 0.10 mm notch width.

Specimen number	B(mm)	W(mm)	a/W	F_C(N)	K_{IC}^{APP}(N/mm$^{3/2}$)
1	17.07	34.04	0.494	569	59.5
2	17.07	34.03	0.497	561	59.2
3	17.07	34.02	0.498	513	54.3
4	17.05	34.02	0.502	528	56.5

5	17.08	34.02	0.499	545	57.9
6	17.12	34.02	0.500	546	58.0
7	17.06	34.02	0.503	445	47.9
8	17.04	34.02	0.503	522	56.2
9	17.09	33.96	0.503	457	49.1
10	17.05	33.96	0.501	428	45.8
11	17.03	33.97	0.500	533	56.9
12	17.06	33.97	0.501	591	63.2
13	17.10	33.98	0.501	574	61.3
14	17.06	33.98	0.500	524	55.8
15	17.02	34.00	0.502	530	56.6
16	17.03	34.01	0.502	452	48.6
17	17.01	33.97	0.517	380	43.0
18	17.08	33.98	0.511	389	43.0
19	17.02	33.97	0.512	376	41.8
20	17.04	33.97	0.514	437	48.8
21	17.08	33.97	0.514	383	42.7
22	17.10	33.97	0.513	409	45.4
23	17.04	33.97	0.514	406	45.4
24	17.01	33.98	0.513	382	42.6
25	16.93	34.01	0.509	370	40.9
26	16.94	34.01	0.509	522	57.8
27	16.96	34.01	0.509	485	53.6
28	16.99	34.02	0.508	457	50.2
29	17.03	34.02	0.509	400	43.9
30	16.99	34.02	0.512	486	54.0
31	16.98	34.02	0.512	408	45.4
32	16.99	34.02	0.511	484	53.6
33	16.99	34.02	0.512	460	51.2

34	17.01	34.02	0.514	443	49.5
35	16.96	34.02	0.515	360	40.5
36	17.01	34.01	0.513	410	45.8
37	17.04	34.01	0.512	432	48.0
38	17.01	34.00	0.512	414	46.0
39	17.00	34.00	0.511	451	50.0
40	17.02	34.00	0.511	505	55.9
41	17.02	34.00	0.510	437	48.3
42	17.02	33.99	0.508	471	51.6
43	17.00	33.99	0.508	400	43.9
44	16.99	33.99	0.508	455	49.9
45	17.01	33.99	0.508	524	57.4
46	17.06	33.98	0.506	436	47.4

Table 5.4. Results for the 3PB specimens with 0.05 mm notch width.

Specimen number	B(mm)	W(mm)	a/W	F_C(N)	K_{IC}^{APP}(N/mm$^{3/2}$)
1	16.97	33.97	0.493	275	28.9
2	16.97	33.96	0.489	288	29.9
3	16.98	33.95	0.492	333	34.8
4	17.02	33.95	0.494	294	30.9
5	17.07	33.95	0.493	317	33.1
6	16.92	33.95	0.494	293	30.9
7	16.91	33.95	0.494	304	32.1
8	16.90	33.96	0.492	292	30.7
9	17.02	33.96	0.491	300	31.2
10	16.98	33.96	0.491	305	31.8
11	17.07	34.01	0.480	306	30.6
12	17.00	34.00	0.475	318	31.5
13	17.01	34.00	0.479	311	31.1

14	17.05	34.00	0.481	298	29.9
15	17.00	33.99	0.481	277	27.9
16	17.01	33.99	0.480	290	29.1
17	17.07	33.99	0.480	316	31.6
18	17.07	33.99	0.480	307	30.7
19	17.04	34.00	0.479	321	32.1
20	17.01	34.00	0.479	321	32.1
21	16.87	33.99	0.485	349	35.9
22	17.02	33.99	0.488	375	38.6
23	17.02	33.99	0.486	349	35.7
24	17.01	33.98	0.487	349	35.8
25	17.00	33.98	0.487	350	36.0
26	16.89	33.98	0.486	335	34.5
27	16.95	33.98	0.487	324	33.4
28	16.95	33.98	0.487	365	37.6
29	16.97	33.98	0.483	345	35.1
30	16.96	33.98	0.479	344	34.6
31	17.00	33.95	0.480	351	35.3
32	16.98	33.94	0.481	435	43.9
33	16.94	33.93	0.483	344	35.1
34	17.01	33.93	0.486	347	35.5
35	16.92	33.92	0.488	372	38.5
36	17.01	33.92	0.490	411	42.6
37	17.04	33.91	0.493	350	36.6
38	16.97	33.91	0.494	392	41.3
39	17.02	33.92	0.493	368	38.5
40	16.98	33.92	0.492	377	39.4
41	16.97	33.97	0.504	295	32.1
42	17.02	33.96	0.502	319	34.3

43	16.98	33.95	0.501	301	32.4
44	17.00	33.95	0.500	307	32.9
45	17.01	33.94	0.499	323	34.5
46	17.03	33.94	0.498	310	32.9
47	17.00	33.94	0.498	330	35.1
48	17.01	33.95	0.497	340	36.1
49	17.00	33.95	0.493	373	39.1
50	17.04	33.94	0.493	316	33.0
51	16.98	33.95	0.499	295	31.5
52	17.01	33.95	0.499	320	34.2
53	16.95	33.94	0.499	313	33.5
54	17.03	33.93	0.499	309	33.0
55	16.99	33.93	0.499	314	33.6
56	17.05	33.93	0.498	318	33.7
57	17.00	33.92	0.498	336	35.8
58	16.98	33.92	0.497	339	36.0
59	17.02	33.93	0.496	322	34.0
60	17.03	33.94	0.492	323	33.7
61	16.95	33.95	0.498	255	27.2
62	17.00	33.94	0.498	324	34.5
63	17.03	33.93	0.501	367	39.4
64	16.96	33.92	0.504	337	36.7
65	17.00	33.93	0.502	310	33.4
66	17.01	33.93	0.502	305	32.9
67	17.02	33.94	0.502	290	31.2
68	17.03	33.94	0.502	300	32.3
69	16.97	33.94	0.502	274	29.6
70	17.00	33.94	0.502	270	29.1
71	17.01	33.92	0.501	282	30.3

72	17.01	33.91	0.500	318	34.1
73	16.90	33.90	0.503	335	36.5
74	16.98	33.90	0.508	300	33.0
75	17.01	33.90	0.504	314	34.1
76	17.00	33.88	0.505	276	30.1
77	17.03	33.90	0.505	303	32.9
78	17.04	33.90	0.505	352	38.2
79	17.03	33.91	0.505	330	35.9
80	16.95	33.91	0.503	275	29.8
81	17.03	33.95	0.498	314	33.4
82	16.99	33.95	0.501	345	37.1
83	16.97	33.95	0.503	337	36.5
84	16.95	33.95	0.504	331	36.0
85	16.97	33.95	0.504	301	32.7
86	16.92	33.95	0.504	335	36.5
87	16.92	33.95	0.504	330	36.0
88	16.97	33.96	0.504	390	42.4
89	16.95	33.97	0.504	355	38.6
90	16.95	33.98	0.504	337	36.7
91	17.00	33.98	0.502	398	42.9
92	17.03	33.98	0.501	362	38.8
93	17.00	33.97	0.503	381	41.2
94	17.01	33.97	0.504	397	43.0
95	17.02	33.96	0.504	375	40.6
96	17.03	33.96	0.504	355	38.5
97	17.07	33.96	0.505	375	40.6
98	16.98	33.96	0.504	368	40.0
99	17.03	33.96	0.501	381	40.9
100	17.01	33.96	0.498	384	40.8

101	17.00	33.96	0.491	312	32.5
102	16.97	33.96	0.489	333	34.5
103	16.97	33.97	0.490	621	64.5
104	17.00	33.97	0.492	421	39.9
105	16.96	33.97	0.494	426	40.6
106	16.99	33.98	0.495	343	32.8
107	16.96	33.98	0.494	376	35.9
108	17.01	33.98	0.495	352	33.6
109	16.90	33.99	0.495	402	38.6
110	16.99	33.99	0.490	306	31.8
111	17.02	33.99	0.490	443	45.9
112	17.00	33.99	0.492	409	42.7
113	16.97	33.98	0.495	591	62.4
114	16.98	33.98	0.496	370	39.2
115	16.98	33.98	0.497	325	34.5
116	16.94	33.98	0.498	441	47.1
117	17.00	33.97	0.497	400	42.4
118	17.03	33.97	0.497	332	35.2
119	16.98	33.96	0.498	366	39.0
120	17.02	34.02	0.491	360	37.4
121	17.01	34.02	0.491	392	40.7
122	17.00	34.02	0.492	430	44.8
123	16.98	34.02	0.495	485	51.1
124	16.99	34.02	0.495	474	49.9
125	17.01	34.02	0.495	340	35.8
126	16.98	34.02	0.496	381	40.3
127	17.01	34.02	0.493	435	45.5
128	17.01	34.02	0.492	370	38.6
129	17.02	34.02	0.490	306	31.7

130	16.97	34.01	0.500	435	46.6
131	16.97	34.00	0.499	468	50.0
132	16.99	33.99	0.500	337	36.1
133	16.99	33.99	0.501	376	40.4
134	17.03	33.99	0.501	470	50.4
135	16.96	33.98	0.501	385	41.5
136	16.99	33.98	0.502	418	45.1
137	17.00	33.97	0.498	460	48.9
138	17.00	33.96	0.496	341	36.1
139	16.95	33.95	0.500	295	31.7
140	17.02	33.95	0.498	397	42.2
141	17.00	33.95	0.498	395	42.0
142	16.98	33.95	0.497	474	50.4
143	16.97	33.96	0.496	338	35.8
144	16.99	33.97	0.497	335	35.6
145	17.02	33.97	0.494	380	39.9
146	16.97	33.98	0.492	313	32.7
147	17.00	33.98	0.490	276	28.6

Table 5.5. Results for the 3PB specimens with 0.02 mm notch width.

Table 5.6 presents some statistical parameters. The number of tested specimens, the mean value of the apparent critical stress intensity factor (K_{IC}^{APP}) and its standard deviation and 95% confidence limits are provided for each notch size.

A histogram of K_{IC}^{APP} for each notch size is shown in Fig. 5.10.

2s(mm)	Number of tested specimens	Mean value of K_{IC}^{APP} ($N/mm^{3/2}$)	Standard deviation of K_{IC}^{APP}($N/mm^{3/2}$)	95% confidence limits of K_{IC}^{APP}($N/mm^{3/2}$)
0.20	47	64.4	8.56	2.54
0.10	58	58.5	7.04	1.88
0.05	46	50.5	6.02	1.81
0.02	147	36.8	5.96	0.98

Table 5.6. Statistical analysis of the notched 3PB specimen results.

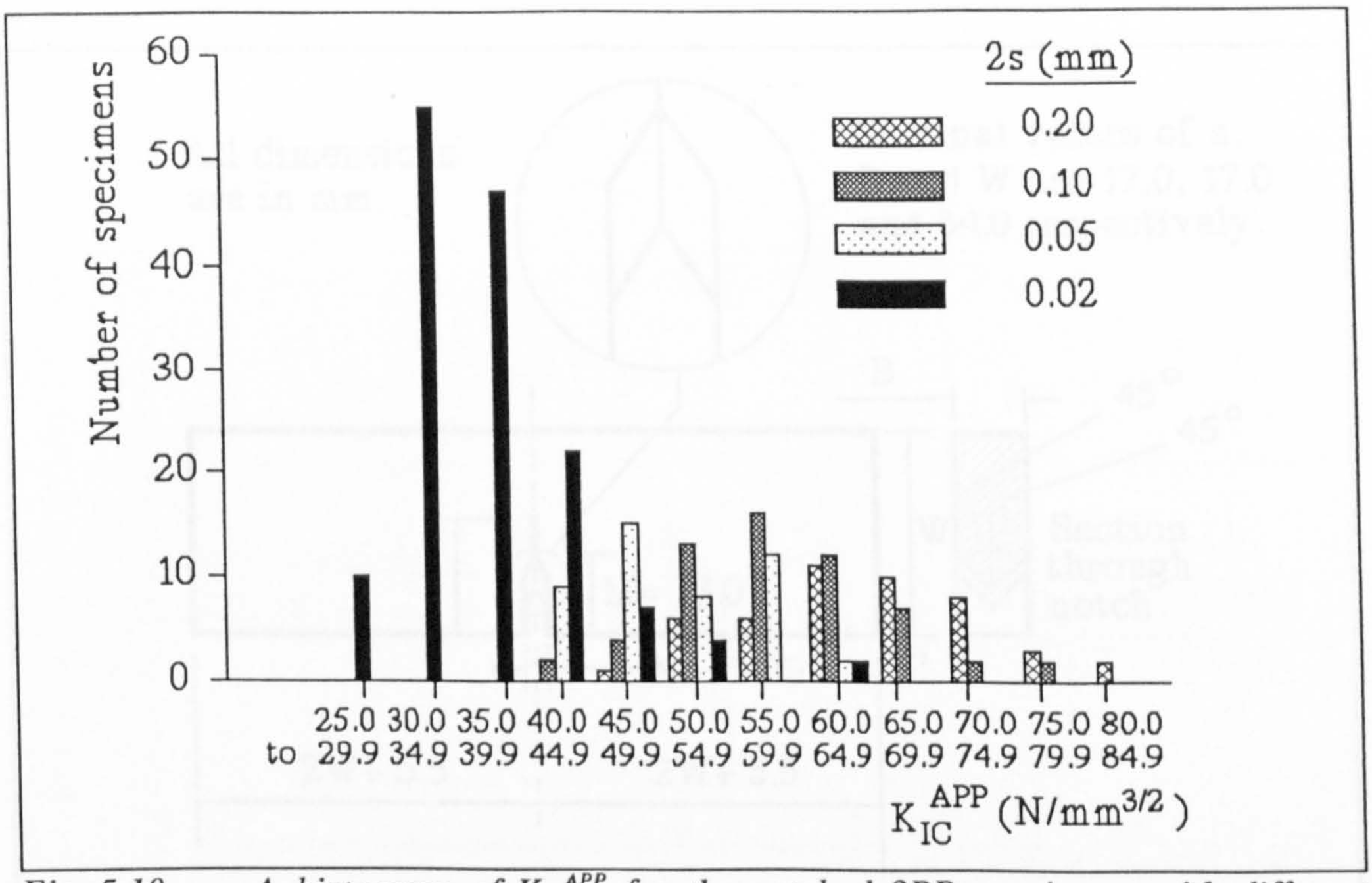

Fig. 5.10. A histogram of K_{IC}^{APP} for the notched 3PB specimens with different notch widths.

5.2. 3PB Specimen with a real crack

The 3PB specimen with a real crack was used to find the real critical stress intensity factor, K_{IC}.

Prior to the destructive testing of each specimen, it was fatigue loaded in order to produce a real crack of a certain length which initiated at the tip of a cast chevron notch.

5.2.1. Specimen

The 3PB specimen with a real crack, shown in Fig. 5.11, met all the requirements given in BS5447 [76].

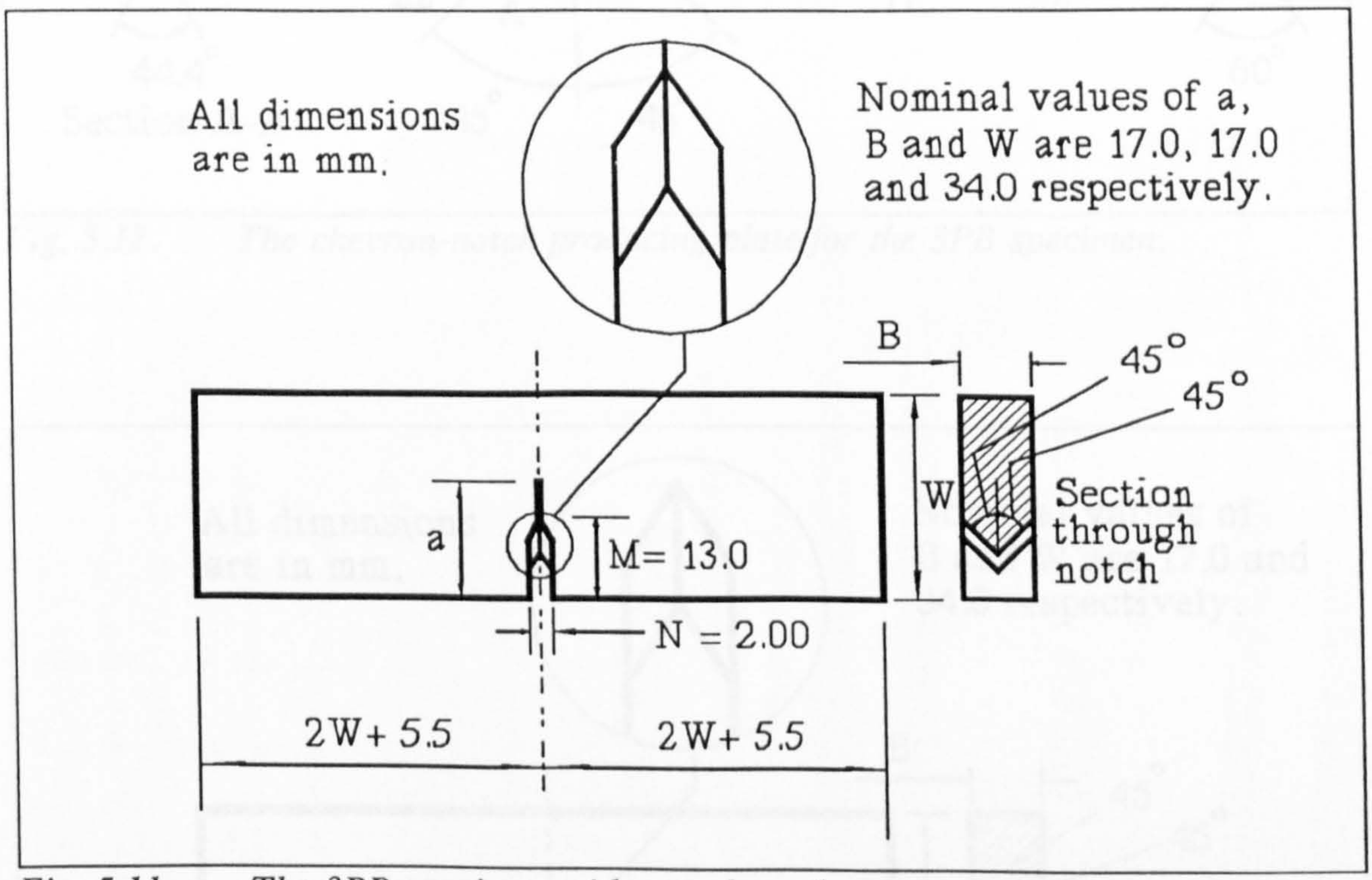

Fig. 5.11. The 3PB specimen with a real crack.

5.2.2. Manufacture

The two moulds used to produce the 3PB notched specimens, Fig. 5.3, were also employed to cast the 3PB specimens with a real crack, by replacing the shim and

the trapping plates with a chevron-notch producing plate, shown in Fig. 5.12.

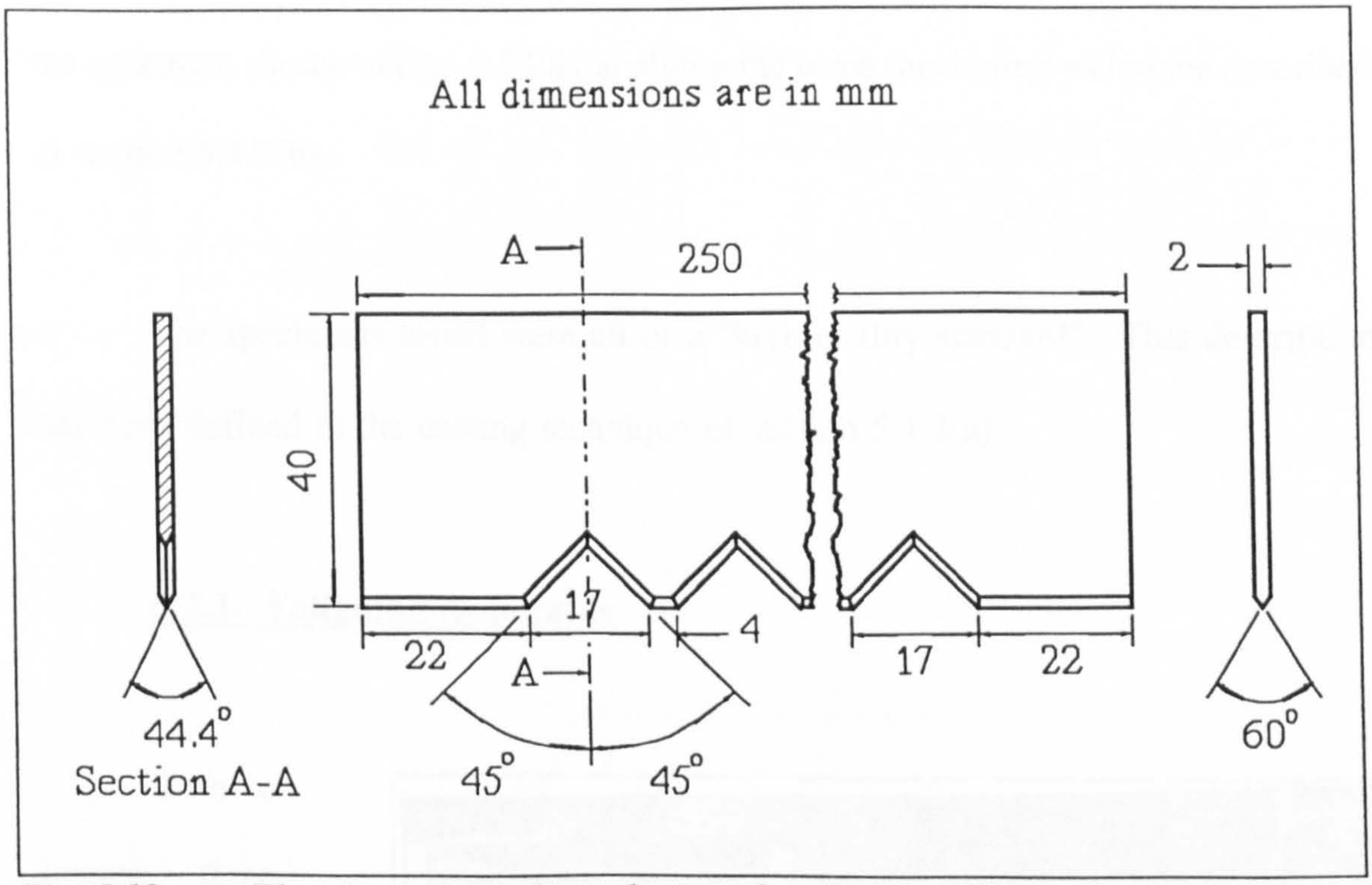

Fig. 5.12. The chevron-notch producing plate for the 3PB specimen.

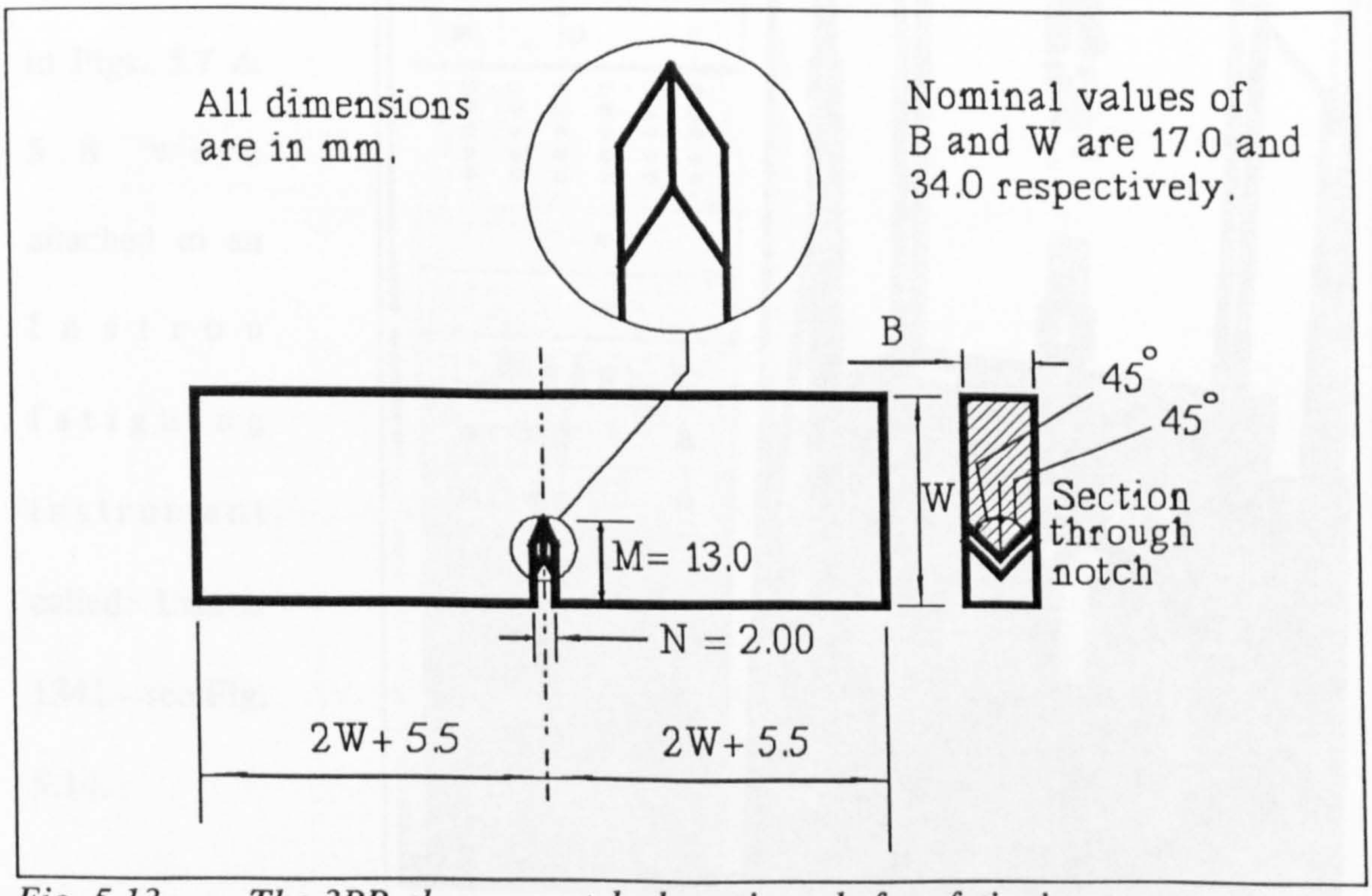

Fig. 5.13. The 3PB chevron-notched specimen before fatiguing.

The cast blocks of Araldite containing the chevron notches were machined into the specimen shown in Fig. 5.13 by applying the same machining technique described in section 5.1.2(b).

The specimens tested were all of a "high quality standard". This description has been defined in the casting technique of section 5.1.2(a).

5.2.3. Fatiguing Apparatus

The Instron three point bend rollers shown in Figs. 5.7 & 5.8 were attached to an Instron fatiguing instrument called: Instron 1341 - see Fig. 5.14.

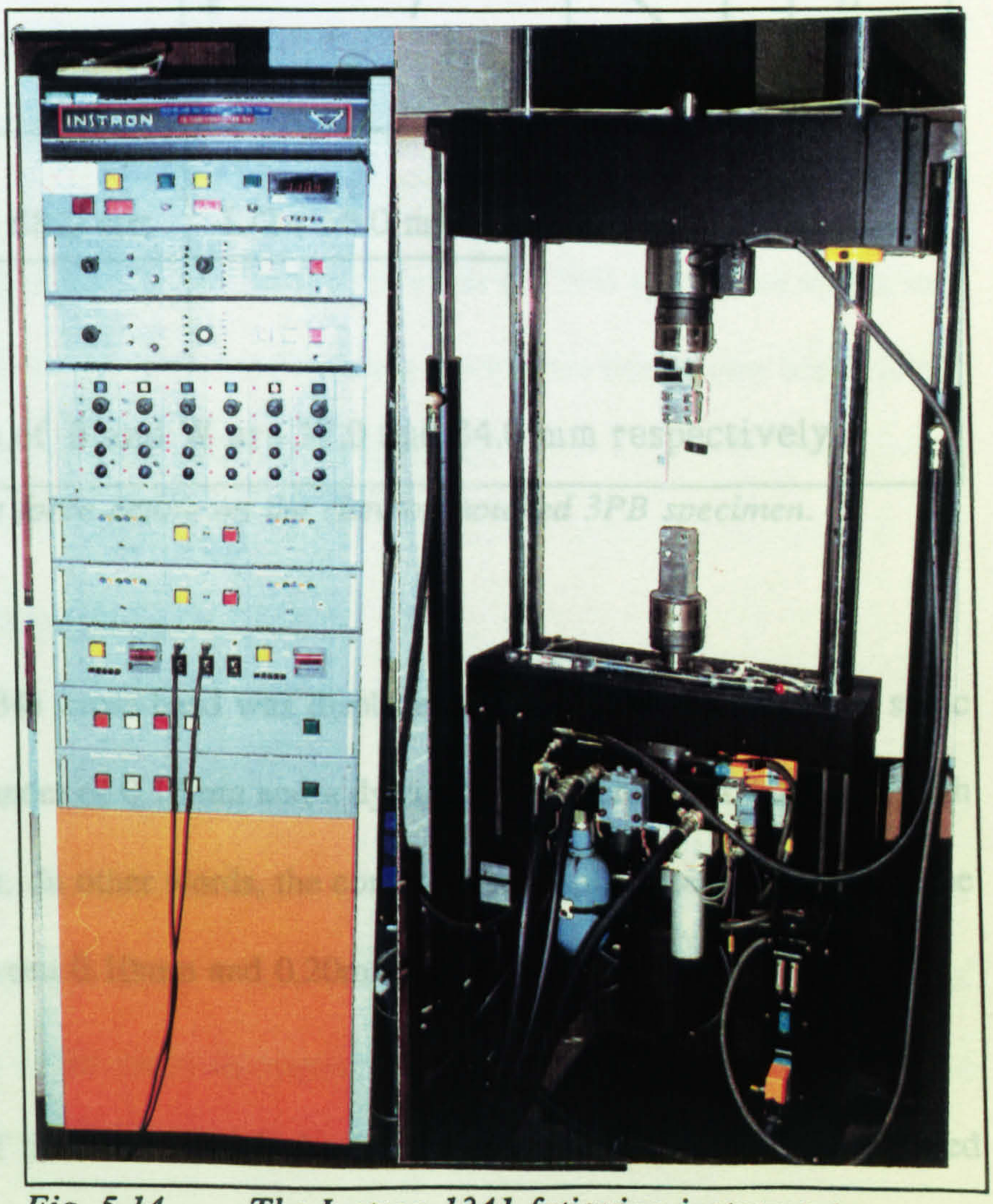

Fig. 5.14. The Instron 1341 fatiguing instrument.

5.2.4. Fatiguing Process

Each chevron-notched 3PB specimen was placed centrally between the upper and lower rollers with a fatiguing force applied by the Instron 1341 on the specimen through the rollers - see Fig. 5.15.

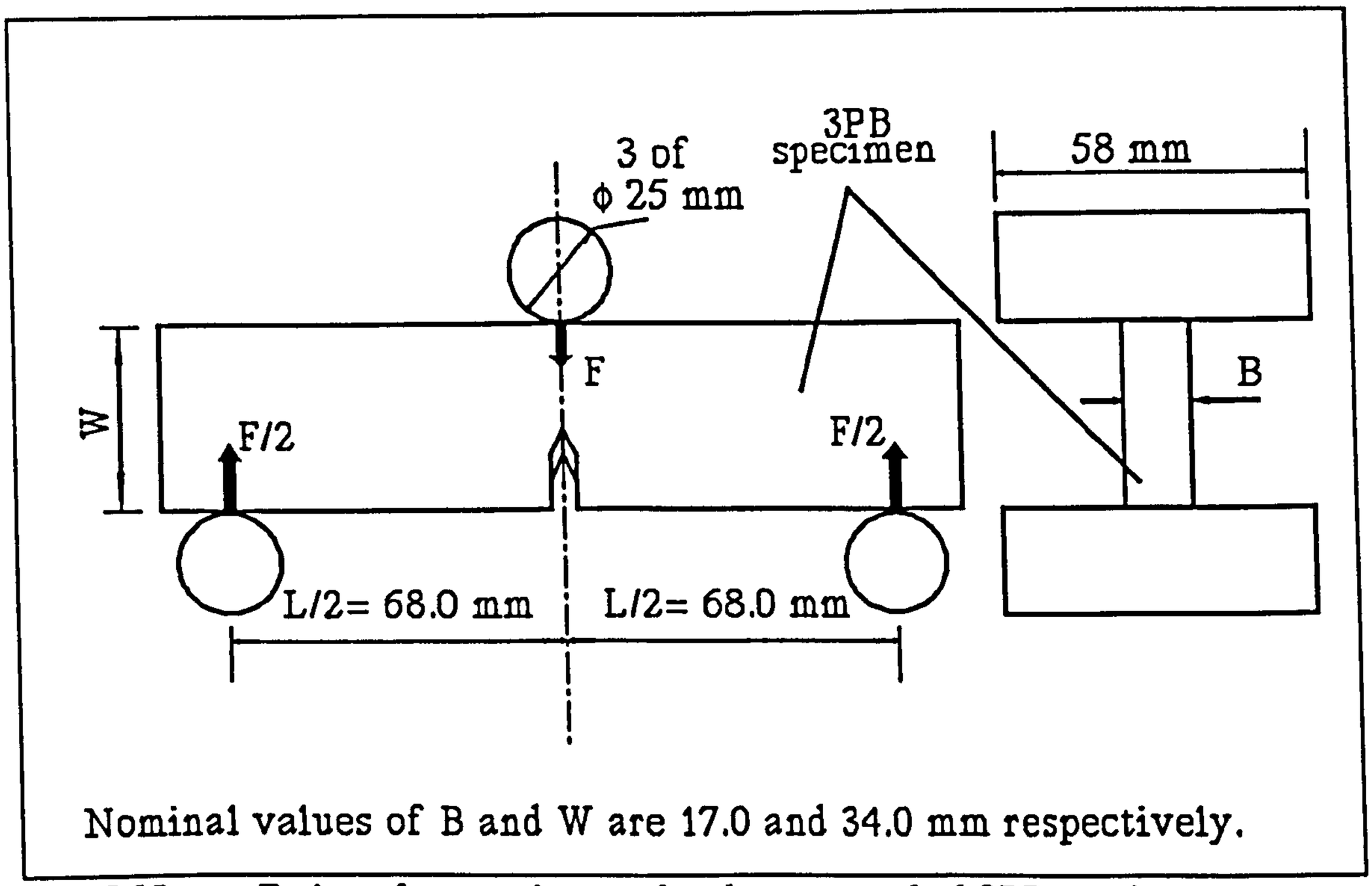

Fig. 5.15. Fatigue force acting on the chevron-notched 3PB specimen.

The Instron 1341 cross-head was displacement-controlled to provide a static compressive displacement of 0.15mm and a dynamic displacement of ±0.05mm with a frequency of 100Hz. In other words, the compressive displacement inflicted on the specimen varied between 0.10mm and 0.20mm with a frequency of 100Hz.

The period of time over which the fatigue crack propagated to the required length varied from a few minutes to a few hours. Therefore, a continuous monitoring

of each specimen during its fatigue loading was necessary. The fatigue crack was propagated until the total crack length, a, was approximately equal to W/2 - see Fig. 5.11.

The actual value of the fatiguing force was immaterial since it did not appear in any calculations, results or conclusions. The creation of a real crack in the specimen was vital regardless of the method. The same argument rendered the description of the crack propagation, of being either a fatiguing process or a set of consecutive short brittle propagation-incidents, as being indifferent.

5.2.5. Loading Apparatus

The loading apparatus used to destructively test the 3PB specimens with a real crack was fully described in section 5.1.3. It was the Instron three point bend rollers in conjunction with the Instron 1193 loading machine.

5.2.6. Experimentation

The testing of the 3PB specimens with a real crack was identical to that carried out on the 3PB notched specimens, a description of which is given in section 5.1.4. The specimens with a real crack would break in two symmetric halves with the propagation initiating at the crack tip rather than the notch tip as in the case of the notched specimens.

Another difference between the notched specimens and the specimens with a real crack was the smooth fracture surface in the latter case with the absence of any lines which would have otherwise indicated the point of crack initiation.

5.2.7. Results

The number of valid tests for the 3PB specimens with a real crack was 63. Prior to performing the destructive tests, the crack front which had been fatigue-produced had to satisfy specific requirements given by BS5447 [76] and ANSI/ASTM E 399 - 78a [77].

The process of checking the shape of the fatigued crack front had to be achieved after the breaking of each specimen into two halves, in order to be able to view the crack surfaces under the microscope. As expected, the crack front was a curve rather than a straight line, the centre point on the crack front travelling further than the end points. The curvature could not exceed certain limits [76 & 77] otherwise the test would be invalid.

The average crack length, a, was calculated by equating it to the arithmetic mean of the crack length at the following three locations: the centre of the crack front and the two midway points between the centre and each end of the crack front. The three points are denoted by the suffixes: "cen", "mid" and "mid" respectively. The suffix "end" denotes the end of the crack front from either side. Table 5.7 presents the different values of the crack length, for each specimen, at the above mentioned

five points on the crack front and the mean value, a, as defined above.

Table 5.7 also presents the thickness, B, and width, W, of each specimen, the ratio of the average crack length to the specimen width, a/W, the load at fracture, F_C, and finally the critical stress intensity factor, K_{IC}, which was obtained using the same equation, table and method of BS5447 [76] described in section 5.1.5.

The angle of propagation of the crack was zero in every 3PB specimen resulting in breaking the specimen in two halves.

Specimen number	a_{end} (mm)	a_{mid} (mm)	a_{cen} (mm)	a_{mid} (mm)	a_{end} (mm)	a (mm)
1	15.94	16.93	17.24	16.99	15.60	17.05
2	16.16	17.35	17.57	17.35	16.15	17.42
3	15.94	17.05	17.33	17.12	16.02	17.17
4	16.30	17.52	17.76	17.56	16.55	17.61
5	16.01	17.24	17.71	17.41	15.96	17.45
6	16.00	17.08	17.33	17.16	16.08	17.19
7	16.18	17.50	17.64	16.98	15.67	17.37
8	16.10	17.40	17.66	17.56	16.39	17.54
9	16.06	17.11	17.32	17.04	15.81	17.16
10	15.84	16.88	17.28	17.11	16.00	17.09
11	16.24	17.68	17.80	17.39	16.06	17.62
12	15.98	17.17	17.55	17.35	16.13	17.36
13	15.92	17.29	17.78	17.25	15.99	17.44
14	16.11	17.23	17.61	17.73	16.43	17.52
15	16.18	17.49	18.12	17.73	16.51	17.78

16	15.91	17.13	17.45	17.26	16.13	17.28
17	16.12	16.92	17.01	16.79	16.10	16.91
18	16.47	17.54	17.87	17.29	16.42	17.57
19	16.69	17.42	17.56	17.47	16.70	17.48
20	16.82	17.62	17.90	17.67	16.87	17.73
21	17.35	18.28	18.59	18.56	17.71	18.48
22	16.34	16.95	17.12	16.90	15.94	16.99
23	16.33	17.19	17.45	17.20	16.46	17.28
24	16.27	17.09	17.29	17.19	16.31	17.19
25	16.42	17.36	17.41	17.14	16.42	17.30
26	16.25	17.23	17.53	17.38	16.70	17.38
27	16.11	17.53	17.93	17.52	15.90	17.66
28	15.84	17.32	17.80	17.46	15.80	17.53
29	16.09	17.61	18.00	17.68	16.23	17.76
30	16.07	17.64	18.07	17.69	16.03	17.80
31	16.03	17.61	18.01	17.61	16.00	17.74
32	15.51	17.09	17.47	17.13	15.65	17.23
33	16.02	17.55	17.96	17.58	16.08	17.70
34	15.69	17.27	17.71	17.30	15.75	17.43
35	15.96	17.62	17.99	17.58	16.00	17.73
36	15.91	17.45	17.82	17.40	15.81	17.56
37	15.96	17.59	18.01	17.60	16.00	17.73
38	15.80	17.25	17.62	17.21	15.68	17.36
39	16.99	18.48	18.84	18.45	16.86	18.59
40	15.98	17.42	17.84	17.56	16.12	17.61
41	16.10	17.93	18.42	18.10	16.40	18.15
42	16.56	18.22	18.67	18.26	16.65	18.38
43	15.80	17.30	17.65	17.25	15.75	17.40
44	16.13	17.56	17.96	17.84	16.34	17.79

45	16.12	17.70	18.16	17.88	16.36	17.91
46	16.12	16.99	17.25	17.08	16.20	17.11
47	17.26	18.00	18.09	17.79	16.34	17.96
48	16.35	17.32	17.54	17.36	16.32	17.41
49	16.13	17.31	17.56	17.38	16.19	17.42
50	16.18	17.23	17.39	17.16	16.23	17.26
51	16.19	17.15	17.45	17.19	16.23	17.26
52	16.09	17.02	17.44	17.16	16.20	17.21
53	16.13	16.95	17.40	16.90	16.18	17.08
54	15.92	17.17	17.05	16.75	15.63	16.99
55	15.95	17.15	17.37	17.15	15.90	17.22
56	15.94	16.90	17.13	16.94	15.90	16.99
57	15.84	16.75	16.95	16.77	15.86	16.82
58	16.23	17.38	17.44	16.98	16.05	17.27
59	15.36	16.56	16.84	16.63	15.45	16.68
60	16.21	17.58	17.90	17.57	16.27	17.68
61	16.11	17.02	17.32	17.16	16.18	17.17
62	16.00	16.92	17.16	17.01	16.13	17.03
63	16.05	17.15	17.60	17.48	16.26	17.41

(a)

Specimen number	B(mm)	W(mm)	a/W	F_C(N)	K_{IC}(N/mm$^{3/2}$)
1	16.96	33.98	0.502	212	22.9
2	16.91	33.99	0.513	203	22.8
3	16.96	34.00	0.505	215	23.4
4	16.96	34.00	0.518	193	22.0
5	17.02	33.99	0.513	192	21.5
6	16.96	33.99	0.506	201	22.0
7	17.01	33.98	0.511	200	22.1

8	17.02	34.00	0.516	210	23.7
9	17.01	33.99	0.505	212	23.0
10	16.98	34.01	0.502	213	23.0
11	16.99	34.01	0.518	196	22.3
12	17.02	34.01	0.510	216	23.9
13	17.03	34.01	0.513	200	22.3
14	17.00	34.02	0.515	205	23.0
15	17.03	34.02	0.523	200	23.0
16	17.04	34.03	0.508	213	23.3
17	16.96	34.02	0.497	254	27.0
18	17.01	34.01	0.517	230	26.0
19	17.00	34.00	0.514	236	26.5
20	17.00	34.00	0.521	236	27.1
21	16.97	34.00	0.544	212	26.4
22	17.04	34.02	0.499	257	27.4
23	17.03	34.01	0.508	251	27.5
24	17.00	34.00	0.506	251	27.4
25	17.01	34.04	0.508	251	27.5
26	17.00	34.03	0.511	250	27.7
27	16.98	34.08	0.518	209	23.7
28	16.97	34.05	0.515	222	25.0
29	17.01	34.07	0.521	219	25.1
30	17.00	34.07	0.522	220	25.3
31	17.00	34.03	0.521	210	24.1
32	17.01	34.02	0.506	203	22.1
33	16.98	34.01	0.520	205	23.5
34	17.01	34.01	0.512	220	24.5
35	17.02	34.00	0.521	208	23.8
36	17.01	34.00	0.516	196	22.1

37	17.00	34.00	0.521	200	22.9
38	17.01	33.96	0.511	217	24.1
39	17.02	33.96	0.547	188	23.5
40	17.01	33.96	0.519	217	24.7
41	17.03	33.96	0.534	199	23.8
42	17.01	34.00	0.541	195	23.9
43	17.02	34.00	0.512	212	23.6
44	16.99	34.00	0.523	210	24.3
45	17.01	34.00	0.527	204	23.9
46	16.95	34.01	0.503	238	25.8
47	17.00	34.00	0.528	208	24.4
48	17.00	34.01	0.512	219	24.4
49	17.00	34.00	0.512	229	25.5
50	17.05	34.01	0.507	234	25.5
51	17.05	34.01	0.507	225	24.6
52	17.04	34.01	0.506	230	25.0
53	17.04	33.97	0.503	230	24.8
54	17.01	33.75	0.503	232	25.1
55	16.93	33.74	0.510	221	24.6
56	16.98	33.74	0.504	224	24.4
57	16.97	33.73	0.499	237	25.4
58	17.08	34.01	0.508	240	26.2
59	17.05	34.01	0.490	240	24.8
60	17.07	34.00	0.520	224	25.5
61	17.03	34.00	0.505	241	26.2
62	17.00	34.00	0.501	239	25.7
63	17.00	34.01	0.512	229	25.5

(b)

Table 5.7(a & b). Results for the 3PB specimens with a real crack.

The statistical analysis of the critical stress intensity factor values for the 63 3PB specimens containing a real crack can be seen in Table 5.8. It provides the number of tested specimens, the mean value of K_{IC} and its standard deviation and 95% confidence limits.

Number of tested specimens	Mean value of K_{IC} ($N/mm^{3/2}$)	Standard deviation of K_{IC}($N/mm^{3/2}$)	95% confidence limits of K_{IC}($N/mm^{3/2}$)
63	24.5	1.59	0.41

Table 5.8. Statistical analysis of the 3PB specimens with a real crack.

A histogram of K_{IC} for this type of specimen is shown in Fig. 5.16.

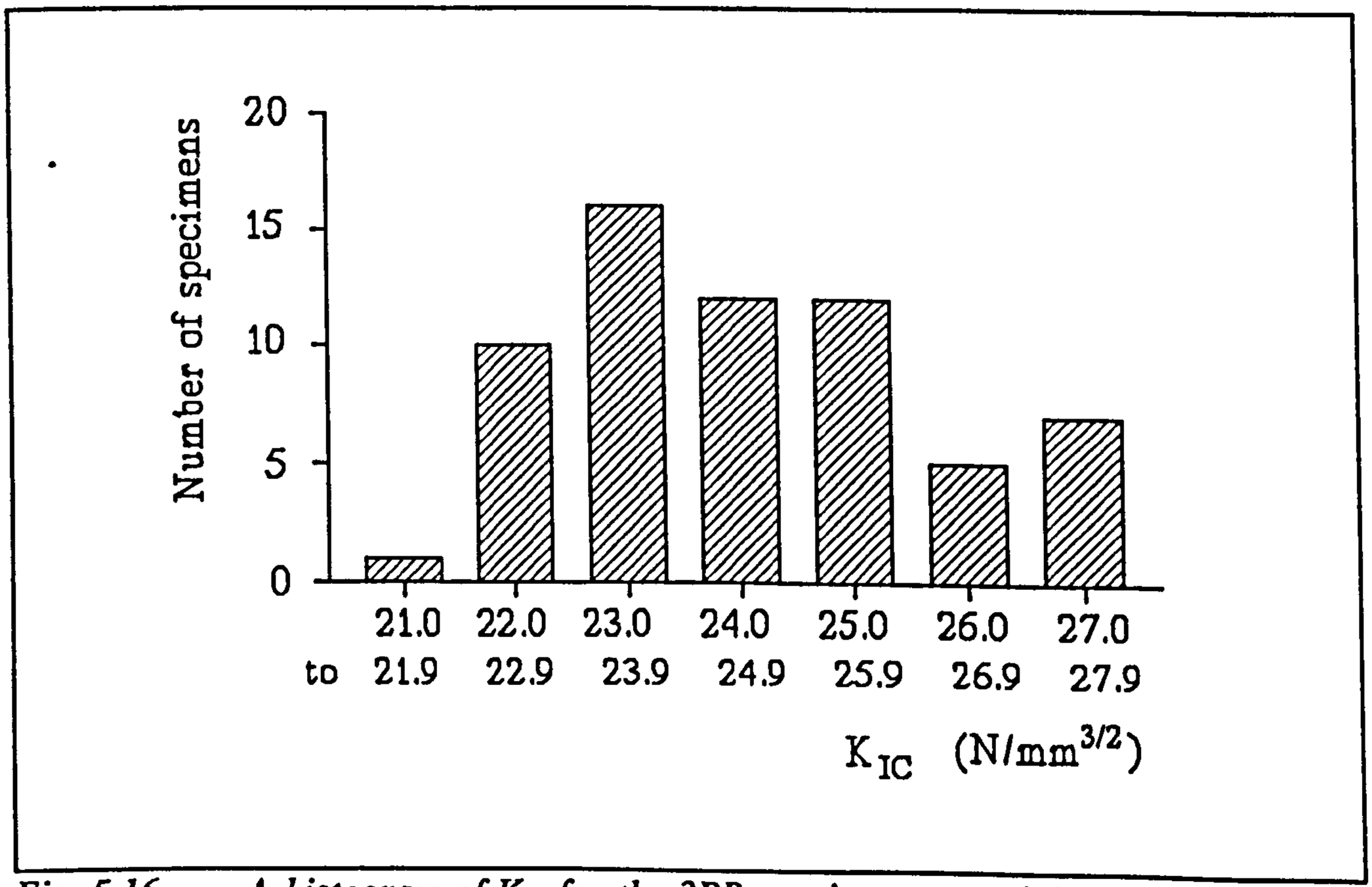

Fig. 5.16. A histogram of K_{IC} for the 3PB specimens containing a real crack.

A comparison of the distribution of the K_{IC} for the 3PB specimens containing a real crack with that of the K_{IC}^{APP} for the notched 3PB specimens is presented in Fig. 5.17.

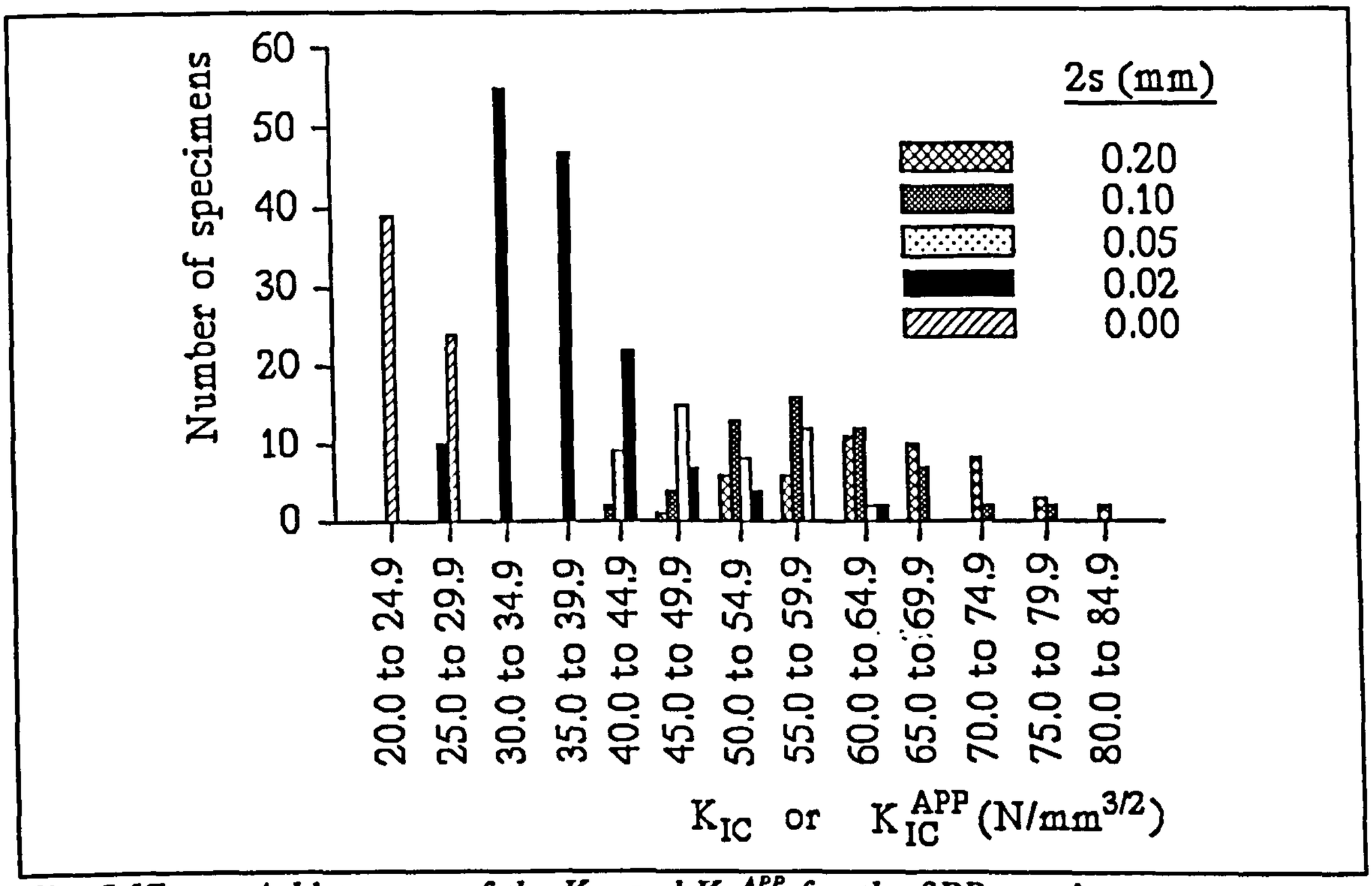

Fig. 5.17. A histogram of the K_{IC} and K_{IC}^{APP} for the 3PB specimens.

Fig. 5.17 is the same as Fig. 5.10 with only two columns of data added from the specimens with a real crack.

5.3. Conclusions

The need to compare the behaviour of a notched specimen to that of one with a real crack was explained in section 4.1. Thus, the ratio of the apparent critical stress intensity factor for a notch, K_{IC}^{APP}, to the critical stress intensity factor for a real crack, K_{IC}, is significant for modelling a crack in an engineering component with a casting

that contains a narrow notch which represents the crack.

Using the average values of the stress intensity factors stated in sections 5.1.5 and 5.2.7, Table 5.9 was produced. It presents the ratio K_{IC}^{APP}/K_{IC} for the four different values of notch width in the 3PB specimens.

2s(mm)	K_{IC}^{APP}/K_{IC}
0.20	2.63
0.10	2.39
0.05	2.06
0.02	1.50

Table 5.9. K_{IC}^{APP}/K_{IC} for the notched 3PB specimens.

The real and apparent critical stress intensity factors obtained by testing 63 3PB specimens with a real crack and 298 notched 3PB specimens respectively are all plotted against half the notch width, s, in Fig. 5.18 - assuming s (half the crack width) to be zero for a real crack. The figure represents the mean values with a solid line, the standard deviation with two dashed lines, and the 95% confidence limits with two dotted lines.

A graph of K_{IC} obtained from the 3PB specimen tests together with K_I and K_{II} at fracture obtained from the CMM specimen tests can be seen in Fig. 6.11 of section 6.3.

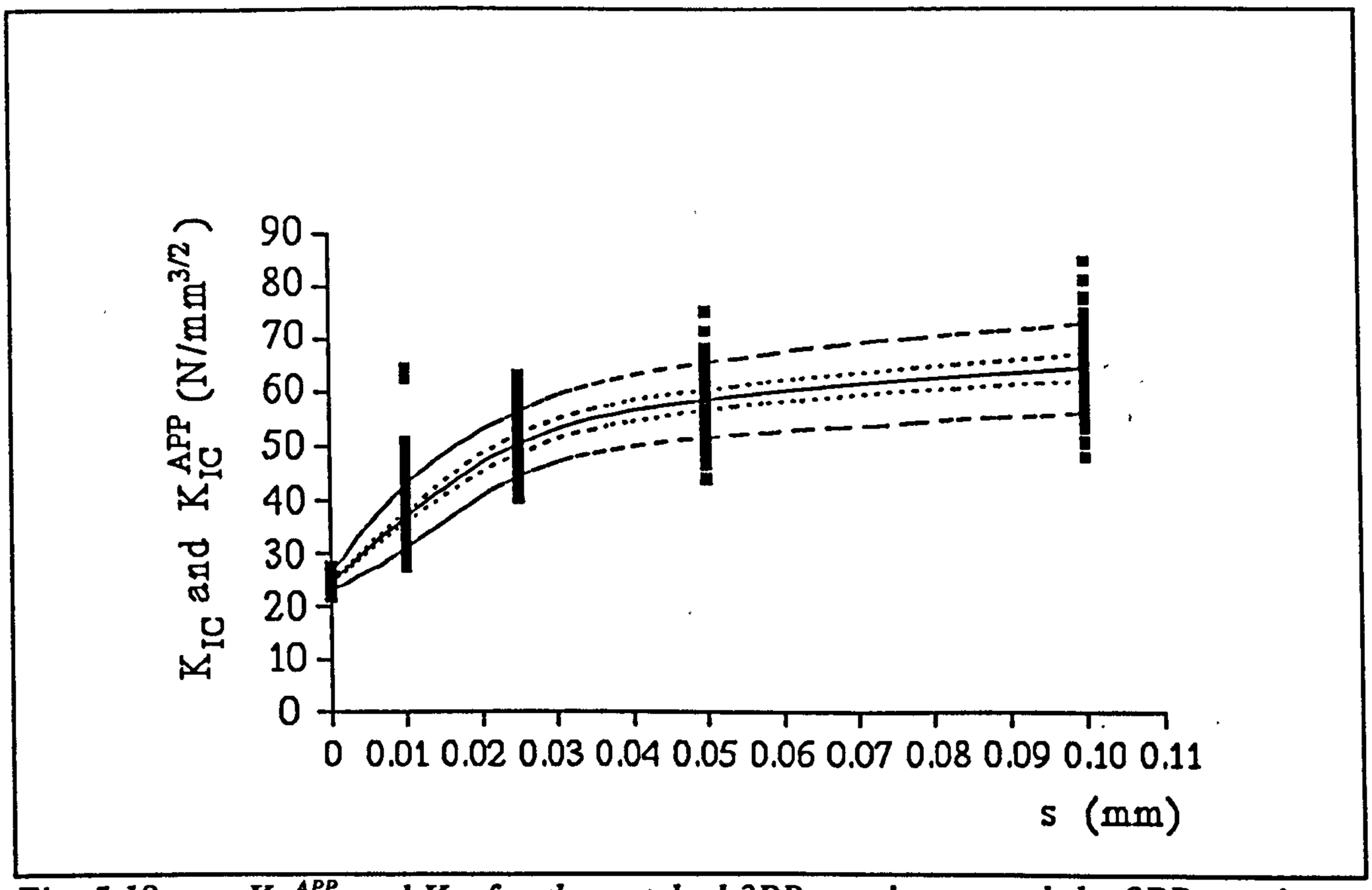

Fig. 5.18. *K_{IC}^{APP} and K_{IC} for the notched 3PB specimens and the 3PB specimens with a real crack respectively, plotted against half the notch width, s.*

CHAPTER SIX

MIXED-MODE EXPERIMENTATION

The problem of failure and the mechanics of fracture are not limited to mode-I loading conditions in real life. Mixed-mode loading is often the case, combining mode-I and mode-II in different ratios. Thus, the importance of including mixed-mode study was apparent, covering a wide range of mode-mixity.

The experimentation on mixed-mode loading was performed using the compact mixed mode (CMM) specimen, shown in Fig. 6.1, which had been used in the Department of Mechanical Engineering at the University of Nottingham to investigate creep, fatigue, and fracture problems [78]. Equations describing K_I and K_{II} in the vicinity of the crack tip had been obtained by the finite element method and confirmed photoelastically [78].

Similar to that described in chapter 5, the experimentation on the CMM specimen was comprised of the testing of specimens containing narrow notches as well as others with real cracks. The notched specimens were employed to establish the apparent critical values of K_I and K_{II} at which fracture occurred, while the specimens containing real cracks established the real critical values of K_I and K_{II} at

fracture.

6.1. CMM Specimen with Two Notches

The notched CMM specimen was cast in the form of a block and then machined to size. Each one of the two moulds used had two shims producing the narrow notches. Four different shims were employed. The first three had thicknesses, 2s, of 0.20, 0.10 and 0.05mm producing notch widths of 0.20, 0.10 and 0.05mm respectively. An effective notch width of 0.02mm was obtained with a sharpened shim having an original thickness of 0.10mm. The method of sharpening the shims was described in section 5.1.2(a).

6.1.1. Specimen

The notched CMM specimen is shown in Fig. 6.1.

Hyde and Chambers [78] analyzed the CMM specimen containing two real cracks by finite element and photoelastic methods; equations describing K_I and K_{II} for different loading conditions were presented.

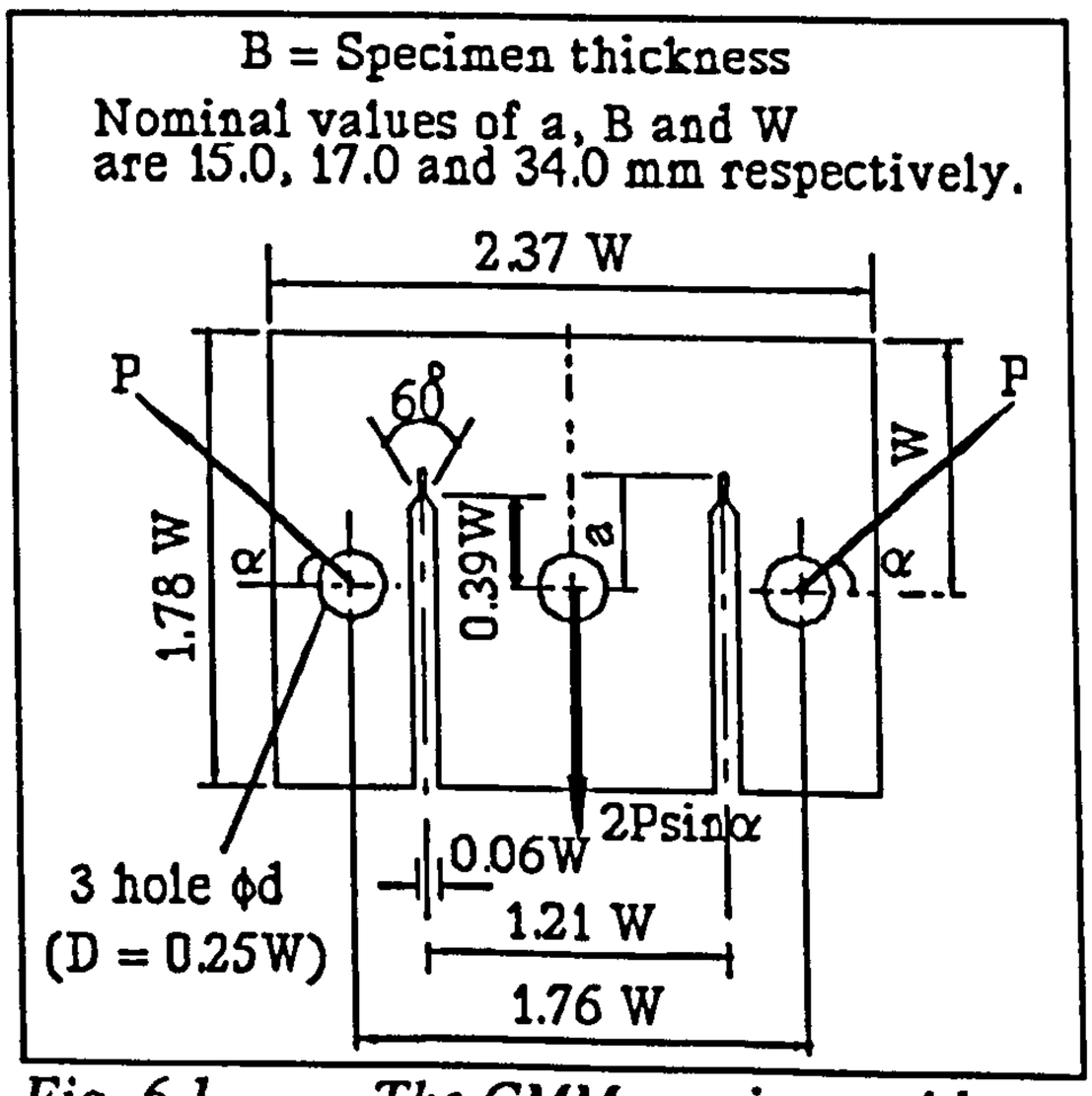

Fig. 6.1. The CMM specimen with two notches. At fracture $P = P_C$.

The thickness of the specimen, B, and the dimension W were chosen to be approximately equal to those of the 3PB specimen of chapter 5, in order to ensure a plain-strain prevailing condition.

The notch tip was similar to that of the 3PB specimen described in section 5.1. The tip might be a semi-circle ($\rho/s = 1$), a flat end with sharp corners ($\rho/s \rightarrow 0$), or anything in between. Also, four values of 2s were tested: 0.20, 0.10, 0.05 and 0.02mm.

6.1.2. Manufacture

The casting and machining techniques were identical to those of the 3PB

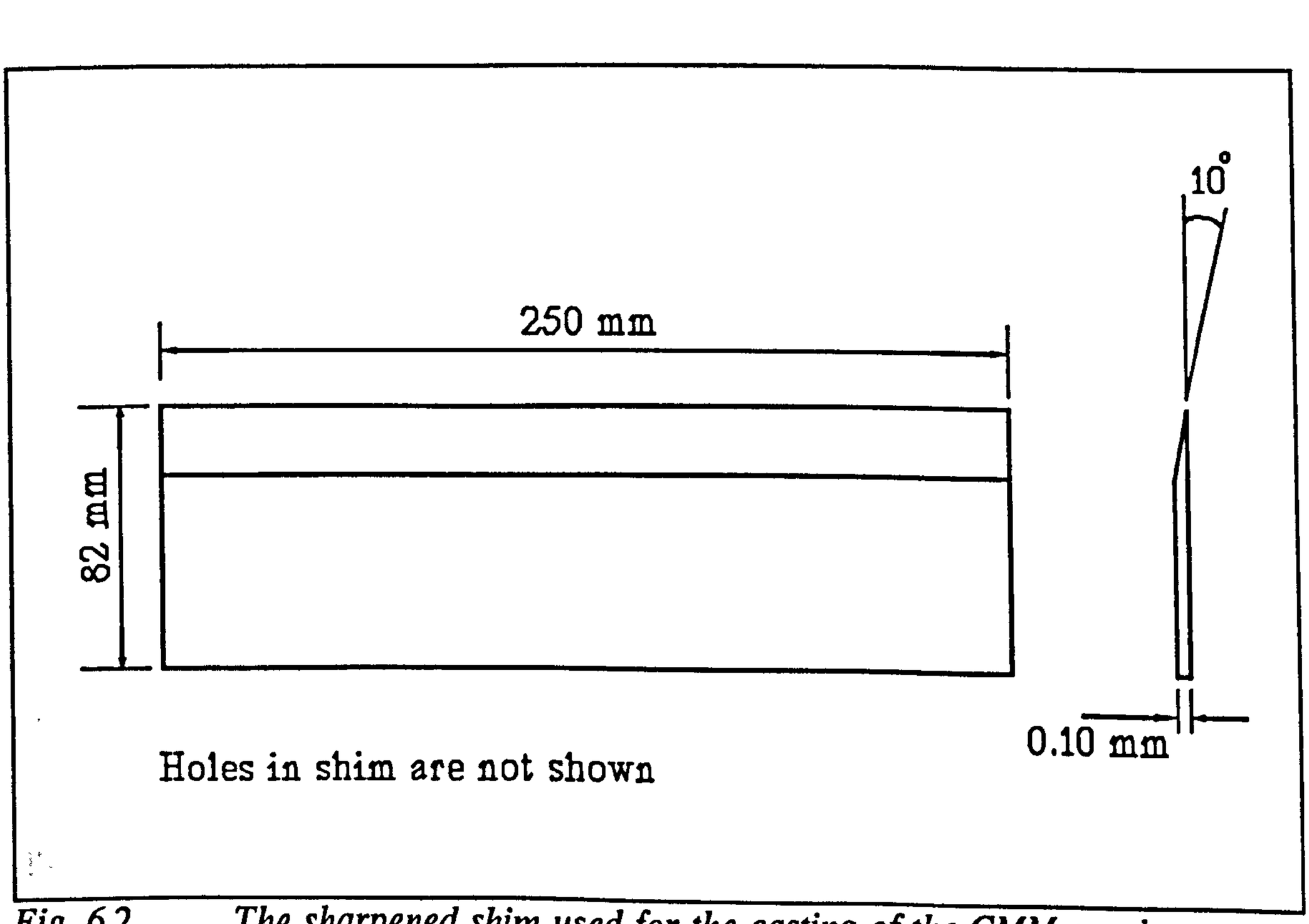

Fig. 6.2. The sharpened shim used for the casting of the CMM specimen.

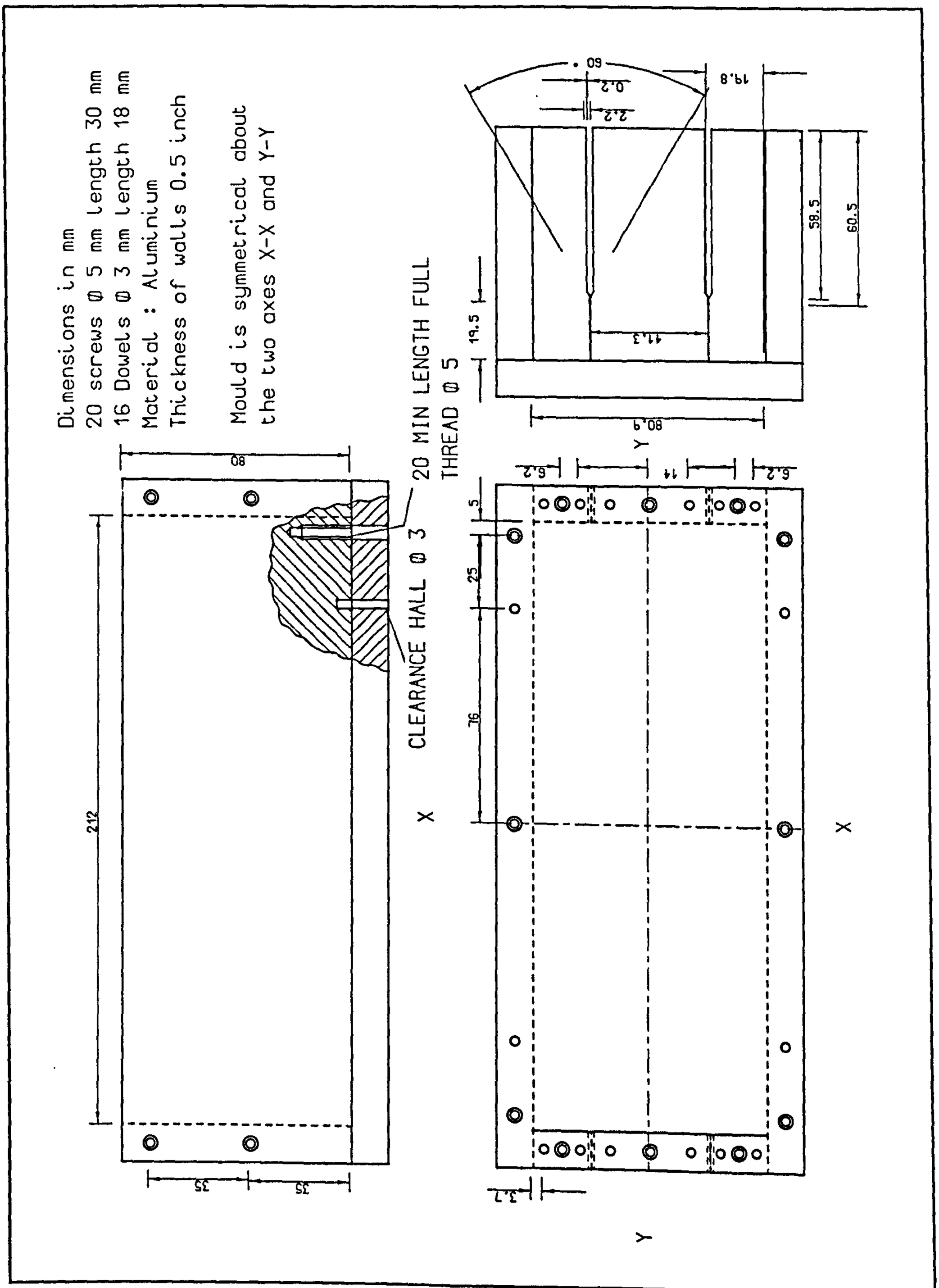

Fig. 6.3. The casting mould for the CMM specimen, shown without the shim or the trapping plates.

specimen described in section 5.1.2, with the exception of the shape of the mould.

One of the two identical moulds used to cast the CMM specimens is shown in Fig. 6.3. The sharpened shim and trapping plates are shown in Figs. 6.2 & 6.4 respectively. The flat and sharpened shims were produced as described in section 5.1.2(a).

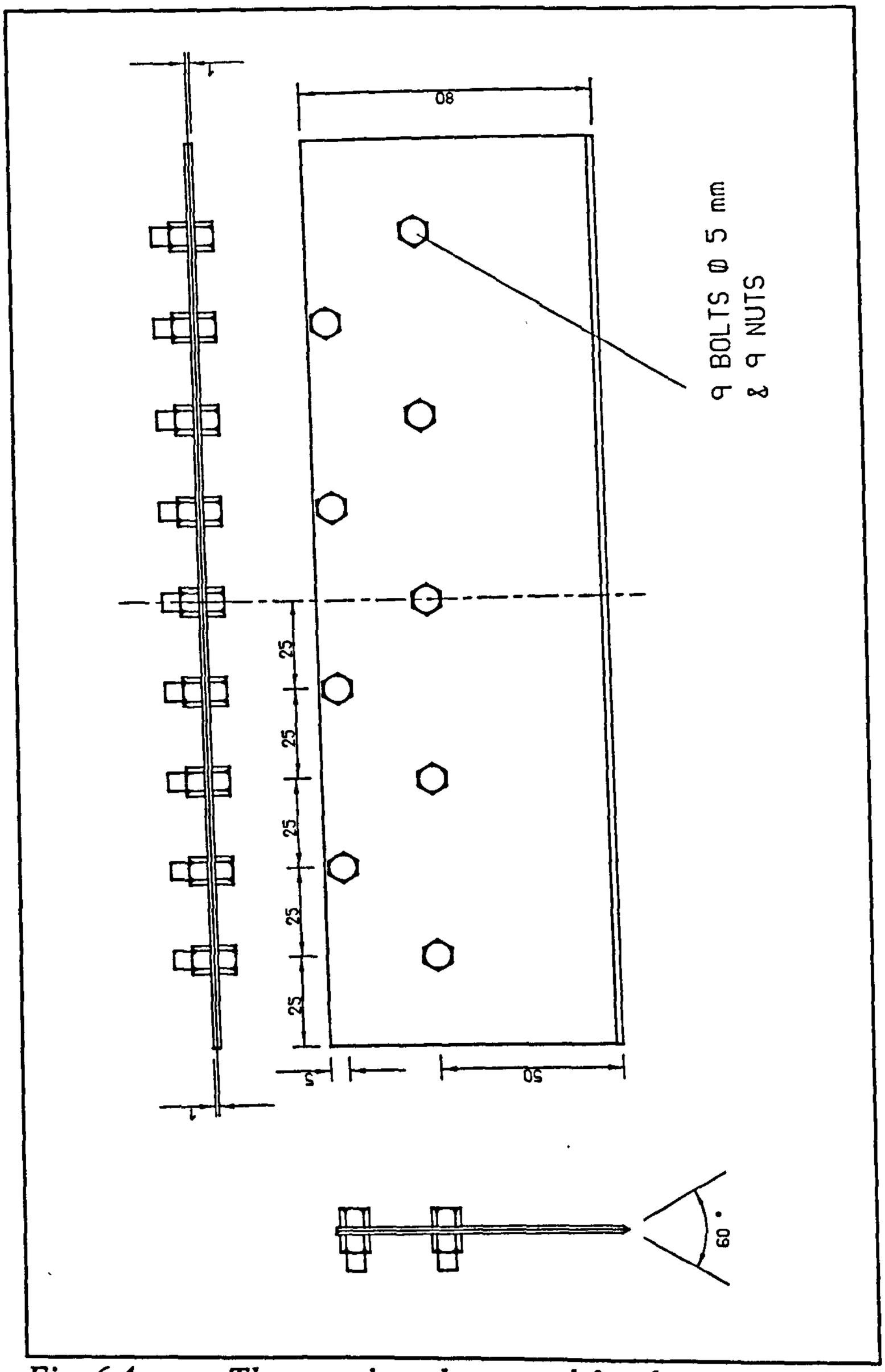

Fig. 6.4. The trapping plates used for the casting of the CMM specimen.

6.1.3. Loading Apparatus

The CMM specimens were loaded under tension at different angles by using the Instron 1193, shown in Fig. 5.7, having a tension load cell, in conjunction with the

tension loading rig made of aluminium and steel - see Fig. 6.5. The rig could provide a loading angle, α (Fig. 6.5), of 16, 50, 70, 90, 100, and 105 degrees, covering a wide range of mode-mixity of loading modes I and II.

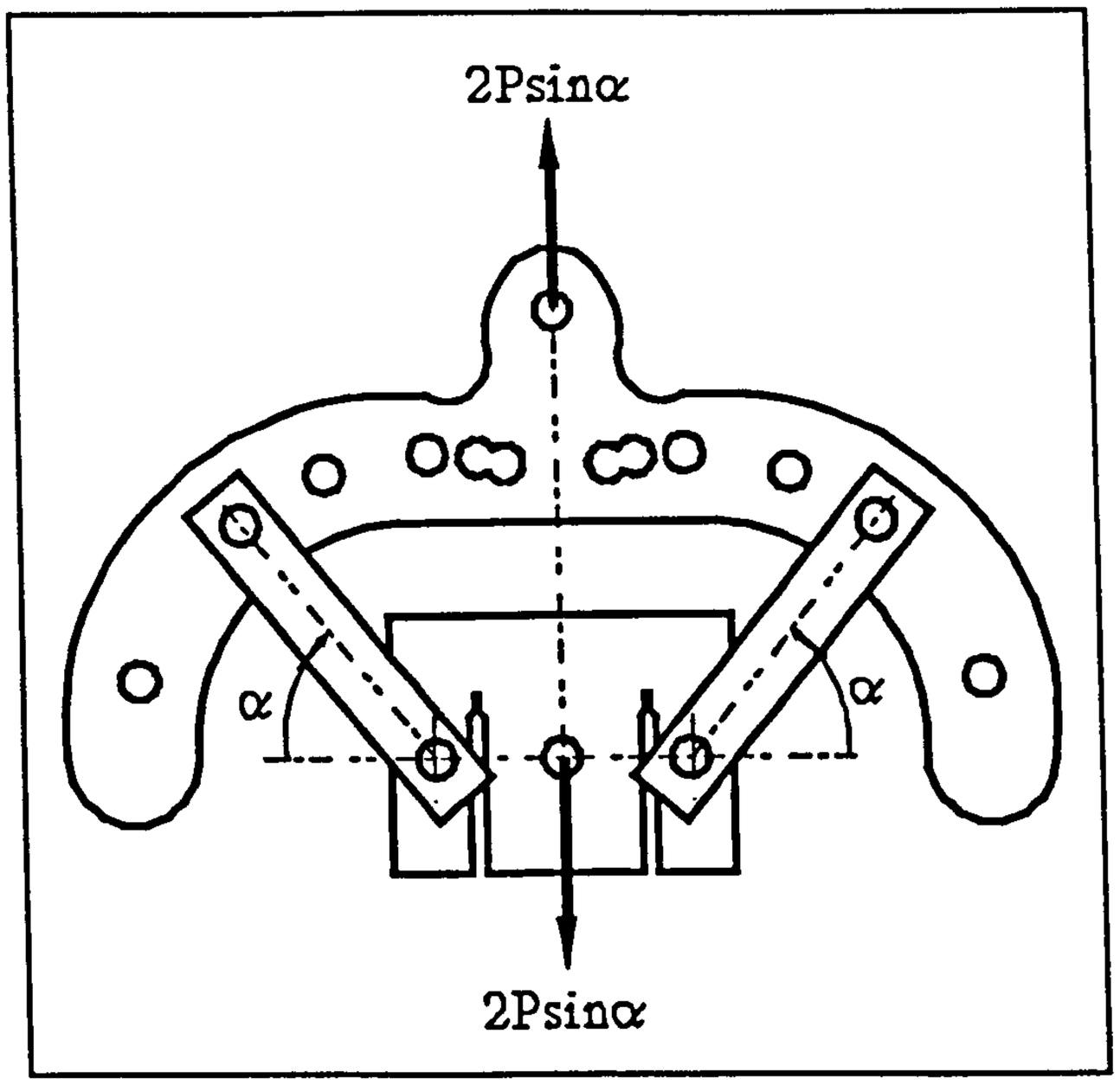

Fig. 6.5. The tension loading rig used for the CMM specimen.

The Instron tension load cell was electrically calibrated in accordance with the Instron manual instructions.

6.1.4. Experimentation

Each CMM specimen was carefully broken into two pieces in the above described loading apparatus. The angle of crack propagation, measured from a line parallel to the symmetry line of the specimen, depended on the loading mode-mixity.

The broken surfaces (surfaces of fracture) contained fine lines indicating the point of fracture inception along the notch tip. The very few specimens having the crack initiating at the edge of the notch were considered to provide invalid data and therefore were rejected. This excluded any specimens which might have had an imbalance in the machining tolerances which could have caused twisting or bending.

6.1.5. Results

A total of 83 notched CMM specimens were tested which provided valid results. Table 6.1 states the number of specimens for each notch size.

2s(mm)	Number of valid tests
0.20	21
0.10	21
0.05	21
0.02	20

Table 6.1. The number of valid notched CMM specimens tested for each notch width.

The critical value of the loading force, P_c (see Fig. 6.1), was obtained from the above tests. Referring to a paper written by Hyde and Chambers [78], equations which calculated K_I and K_{II} from P for different a/W and different loading angles, α, were derived (refer to appendix III for details).

The dimensions of the specimens and notches, the loading angles, the fracture loads, the angles of crack propagation and the stress intensity factors at fracture are presented in Tables 6.2, 6.3, 6.4 and 6.5 for the notch widths 0.20, 0.10, 0.05 and 0.02mm respectively.

Specimen number	B(mm)	W(mm)	a/W	α(°)
1	16.86	34.08	0.442	90
2	16.83	34.22	0.441	90
3	17.06	34.23	0.440	100
4	16.90	34.07	0.441	100
5	17.03	34.23	0.442	105
6	17.03	34.29	0.438	105
7	16.97	34.25	0.445	105
8	16.91	34.20	0.434	16
9	16.99	34.26	0.435	16
10	17.07	34.21	0.433	70
11	16.93	34.30	0.447	70
12	17.00	34.18	0.450	70
13	17.04	34.22	0.449	70
14	17.00	34.22	0.448	105
15	17.04	34.28	0.443	105
16	16.97	34.29	0.448	100
17	19.96	33.92	0.442	100
18	16.99	34.28	0.448	90
19	16.98	34.17	0.445	90
20	17.03	34.23	0.448	16
21	17.05	34.28	0.448	16

(a)

Specimen number	P_C(kN)	Propagation angle (°)	K_I at fracture ($N/mm^{3/2}$)	K_{II} at fracture ($N/mm^{3/2}$)
1	0.90	51.5	22.3	15.4
2	1.31	49.0	32.3	22.1
3	1.91	61.0	19.5	33.5
4	1.79	57.0	18.6	31.8

5	1.80	-	5.4	32.2
6	1.91	67.0	5.6	33.8
7	2.15	66.0	6.7	38.8
8	0.80	1.5	65.6	-1.2
9	0.85	2.0	69.9	-1.3
10	1.11	29.5	54.1	14.8
11	0.83	31.0	42.6	11.5
12	1.13	31.5	58.5	15.8
13	1.08	31.5	55.4	15.0
14	2.63	65.5	8.2	47.4
15	2.81	66.0	8.5	50.3
16	2.02	60.5	21.3	36.0
17	2.39	60.0	24.8	42.7
18	1.35	47.5	33.8	22.9
19	1.50	47.5	37.3	25.5
20	0.89	1.0	75.8	-1.2
21	1.50	1.0	89.2	-1.4

(b)

Table 6.2(a & b). Results for the CMM specimens with 0.20mm notch width.

Specimen number	B(mm)	W(mm)	a/W	α(°)
1	16.97	34.21	0.426	105
2	16.98	34.32	0.429	105
3	17.02	34.22	0.425	100
4	16.99	34.26	0.427	100
5	16.78	34.19	0.429	90
6	17.02	34.20	0.426	90
7	17.00	34.13	0.430	70
8	16.94	34.13	0.430	70
9	17.01	34.14	0.431	16

10	16.82	34.14	0.431	16
11	17.05	34.11	0.431	105
12	17.05	34.21	0.458	100
13	17.05	34.19	0.455	100
14	17.01	34.15	0.455	105
15	17.05	34.15	0.457	105
16	17.07	34.24	0.460	90
17	17.03	34.26	0.459	90
18	16.95	34.23	0.459	70
19	16.99	34.21	0.457	70
20	17.08	34.26	0.460	16
21	17.07	34.35	0.461	16

(a)

Specimen number	P_C(kN)	Propagation angle (°)	K_I at fracture ($N/mm^{3/2}$)	K_{II} at fracture ($N/mm^{3/2}$)
1	1.44	-	4.0	25.2
2	1.65	-	4.6	28.9
3	1.90	57.5	18.5	32.7
4	1.48	57.5	14.5	25.6
5	1.12	49.0	26.7	18.7
6	1.03	-	23.9	16.8
7	0.92	31.5	44.6	12.2
8	0.78	31.5	38.2	10.5
9	0.61	2.0	49.5	-0.9
10	0.55	-0.5	44.9	-0.9
11	1.35	67.0	3.9	23.6
12	1.72	56.0	18.9	31.1
13	1.30	57.5	14.1	23.5
14	1.47	66.5	4.8	26.8

15	1.65	65.5	5.7	31.0
16	1.16	46.5	30.2	20.0
17	1.25	47.0	32.5	21.6
18	0.65	32.0	34.6	9.2
19	0.68	30.5	36.0	9.6
20	0.66	2.0	57.7	-0.7
21	0.65	1.0	57.5	-0.7

(b)

Table 6.3(a & b). Results for the CMM specimens with 0.10mm notch width.

Specimen number	B(mm)	W(mm)	a/W	α(°)
1	17.17	34.01	0.437	105
2	16.95	34.04	0.437	90
3	16.98	33.99	0.446	70
4	17.02	34.05	0.448	105
5	17.03	33.98	0.447	105
6	17.05	34.02	0.449	90
7	17.07	34.05	0.448	90
8	17.04	34.05	0.448	70
9	17.04	34.05	0.447	70
10	14.98	34.07	0.446	16
11	16.86	34.17	0.456	105
12	16.97	34.12	0.444	105
13	17.01	34.15	0.448	105
14	16.92	34.19	0.453	90
15	16.99	34.34	0.455	90
16	17.04	34.21	0.453	90
17	17.05	34.24	0.454	70
18	17.04	34.23	0.452	70
19	17.02	34.24	0.451	70

20	16.99	34.23	0.452	16
21	16.14	34.22	0.448	50

(a)

Specimen number	P_C(kN)	Propagation angle (°)	K_I at fracture ($N/mm^{3/2}$)	K_{II} at fracture ($N/mm^{3/2}$)
1	2.41	66.0	7.2	42.6
2	1.07	49.0	26.1	18.0
3	0.81	29.0	41.4	11.2
4	1.56	66.5	4.0	28.2
5	1.48	66.0	4.6	26.6
6	0.89	46.5	22.3	15.2
7	0.89	42.5	22.1	15.0
8	0.76	32.0	39.1	10.5
9	0.67	29.0	34.3	9.3
10	0.51	0.5	49.0	-0.8
11	2.53	67.0	8.4	46.4
12	2.30	67.0	7.1	41.5
13	2.34	65.5	7.3	42.2
14	1.23	47.5	31.3	21.2
15	1.36	51.0	34.8	23.4
16	1.13	48.5	28.6	19.3
17	0.85	32.5	44.1	11.8
18	0.93	31.5	48.0	12.9
19	0.90	31.0	46.8	12.6
20	0.57	3.0	49.3	-0.7
21	0.64	18.5	48.0	6.1

(b)

Table 6.4(a & b). Results for the CMM specimens with 0.05mm notch width.

Specimen number	B(mm)	W(mm)	a/W	α(°)

1	17.07	33.83	0.449	105
2	17.11	33.85	0.448	100
3	17.04	33.83	0.447	90
4	17.06	33.80	0.448	70
5	17.05	33.83	0.450	16
6	17.15	33.92	0.449	105
7	16.94	33.86	0.442	100
8	16.94	33.86	0.445	90
9	17.03	33.75	0.444	70
10	16.99	33.86	0.448	50
11	17.00	33.84	0.443	105
12	17.06	33.92	0.442	105
13	17.06	33.80	0.443	100
14	17.05	33.93	0.440	100
15	17.02	33.85	0.440	90
16	17.01	33.89	0.444	90
17	17.00	33.79	0.442	70
18	16.96	33.82	0.444	70
19	17.06	33.94	0.444	50
20	16.96	33.75	0.445	16

(a)

Specimen number	P_C(kN)	Propagation angle (°)	K_I at fracture ($N/mm^{3/2}$)	K_{II} at fracture ($N/mm^{3/2}$)
1	1.89	66.0	5.8	34.3
2	1.42	58.5	15.0	25.3
3	0.92	47.0	22.9	15.6
4	0.56	30.0	28.8	7.8
5	0.44	1.0	37.3	-0.6
6	1.97	66.5	6.0	35.5

7	1.25	58.5	13.0	22.3
8	1.00	47.5	24.9	17.1
9	0.60	30.5	30.7	8.3
10	0.42	20.5	30.0	3.8
11	1.85	66.0	5.6	33.4
12	1.76	67.0	5.3	31.6
13	1.39	58.5	14.4	24.7
14	1.35	58.5	13.9	23.9
15	0.99	48.0	24.2	16.6
16	0.95	44.5	23.5	16.0
17	0.50	-	25.4	6.9
18	0.53	31.0	27.2	7.4
19	0.43	21.0	30.5	3.8
20	0.44	2.5	37.1	-0.6

(b)

Table 6.5(a & b). Results for the CMM specimens with 0.02mm notch width.

Tables 6.2, 6.3 and 6.5 contain a few specimens with no value for the angle of crack propagation. Some specimens displayed practical difficulties in measuring the propagation angle due to the inability to determine the exact point of crack inception or the exact direction of crack propagation. Nevertheless, the large number of tests and the consistency of the propagation angles rendered this problem, if described as such, insignificant.

The K_I and K_{II} values of the notched CMM specimen tests at fracture can be seen, together with those of the tests of the CMM specimens with a real crack, in Fig. 6.10 of section 6.3.

6.2. CMM Specimen with a Real Crack

The CMM specimens with a real crack were destructively tested to obtain K_I and K_{II} at fracture for different mode-mixities of mode-I and mode-II loading conditions.

Unlike the notched CMM specimens which contained two identical notches each, the CMM specimens with a real crack each contained two identical chevron notches of which only one was extended into a real crack. This difference did not have any effect on the stress field in the vicinity of the crack tip since the other chevron notch was too distant and the existence of a second real crack rather than just a chevron notch would have had a local effect not affecting the first crack tip. This can be confirmed by looking at the finite element analysis and the stress contours presented in chapter 8 and appendix V.

The method of extending a chevron notch into a real crack was achieved by fatigue loading each specimen.

6.2.1. Specimen

The CMM specimen with a real crack met all the requirements specified by Hyde and Chambers in their published paper [78] which gave a precise method of obtaining K_I and K_{II} for different loading conditions (see appendix III).

Each specimen had two chevron notches from which a real crack could be extended by fatigue loading. Had there been two real cracks in each specimen, the local stress field at each crack tip would not have affected the other due to the adequate distance between them. Therefore the existence of one real crack in each specimen was sufficient for the purpose of the test.

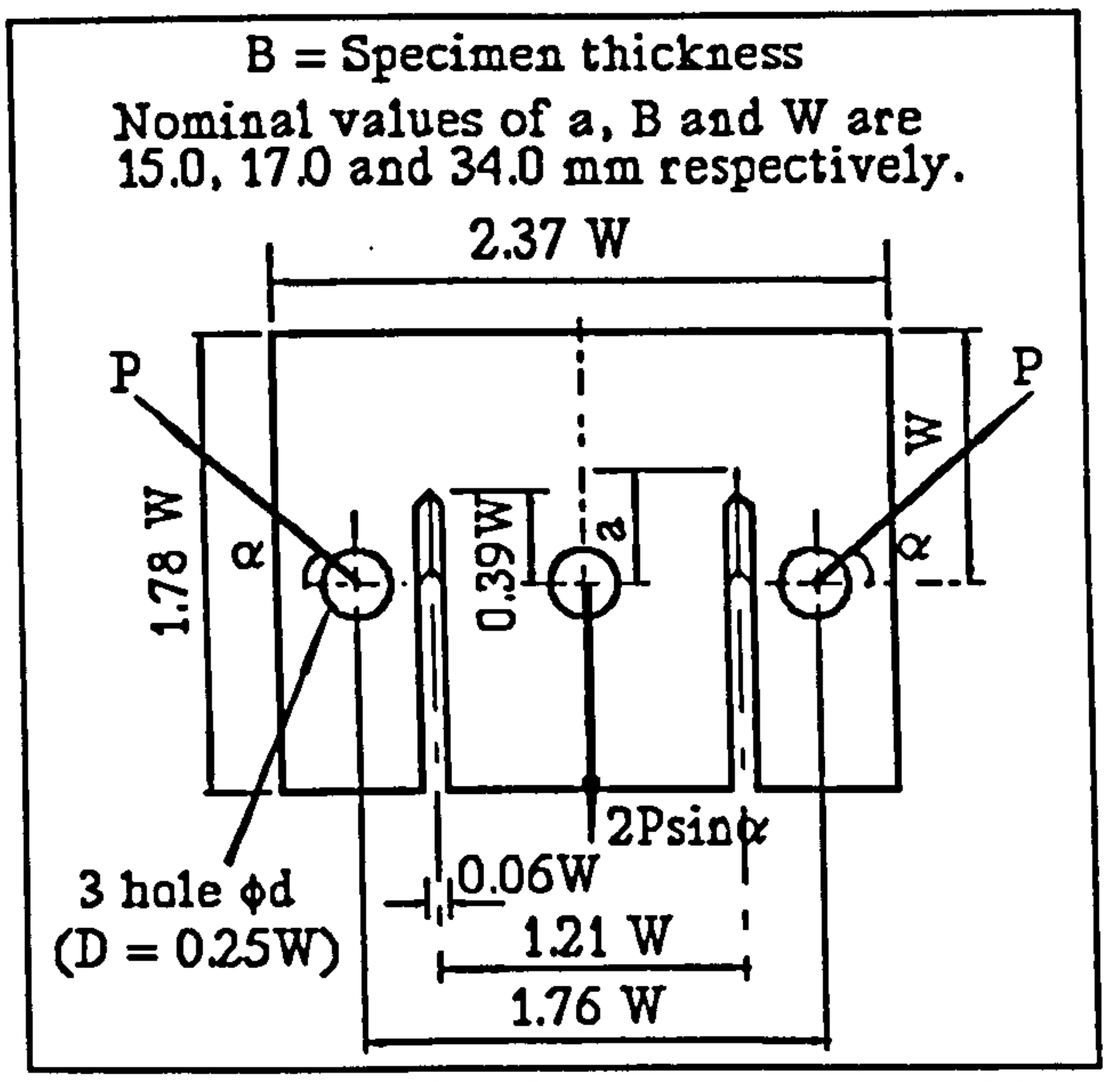

Fig. 6.6. The CMM specimen with a real crack. At fracture, $P = P_c$.

The specimen can be seen in Fig. 6.6. The real crack is shown to extend from one chevron notch only.

6.2.2. Manufacture

The CMM specimens with a real crack were produced by firstly casting blocks of resin in the same moulds used to produce the notched CMM specimens (see Fig. 6.3), with the exchange of shims and trapping plates with chevron-notch producing plates (see Fig. 6.7).

Secondly, the cast blocks were machined by applying the technique described in section 5.1.2(b). Specimens with two chevron notches each, were produced with

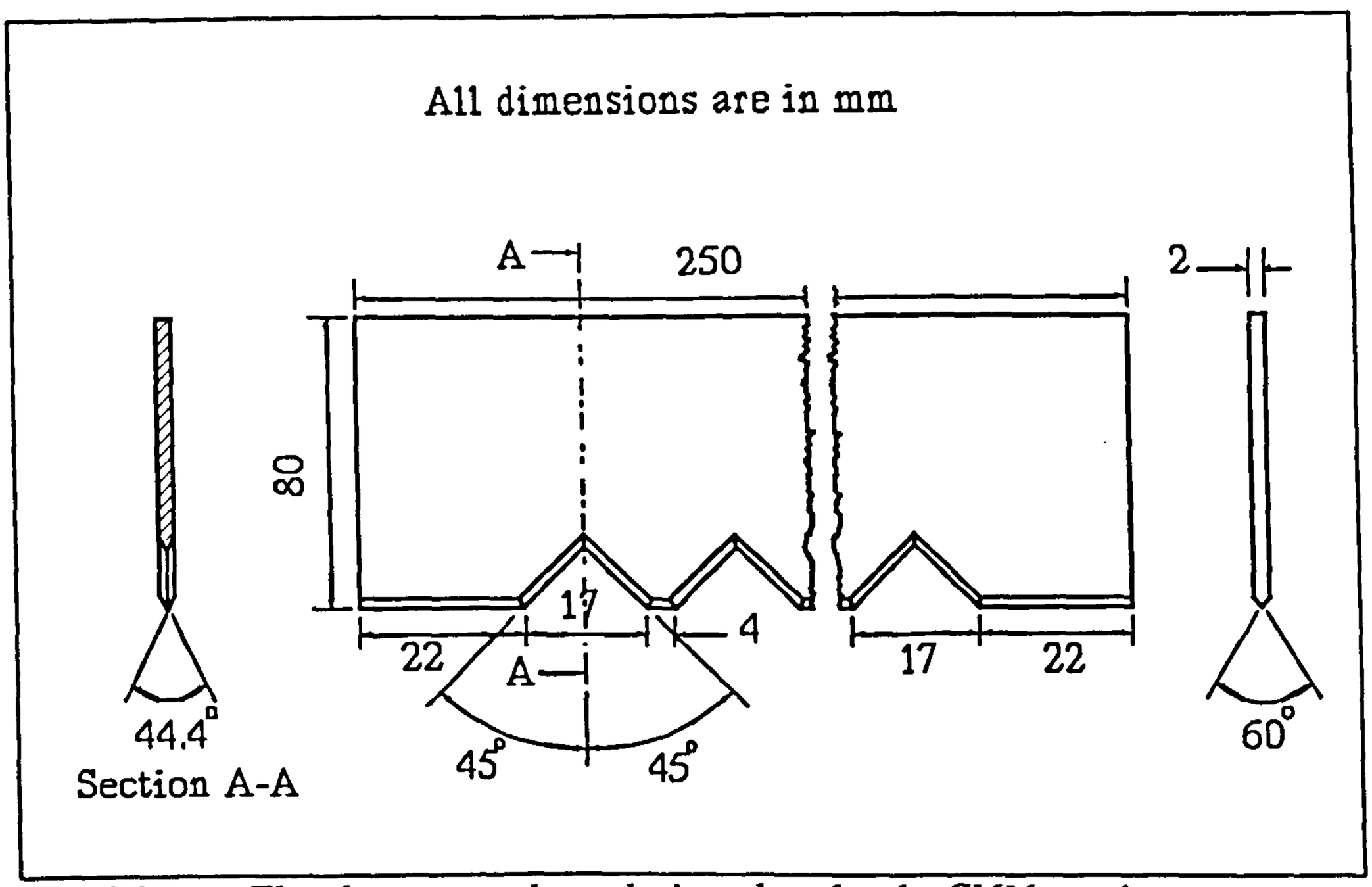

Fig. 6.7. The chevron-notch producing plate for the CMM specimens.

a "high quality standard" - as defined in section 5.1.2(a), (see Fig. 6.8), and later fatigued to produce one real crack of a certain length which was necessary for the final test (see Fig. 6.6).

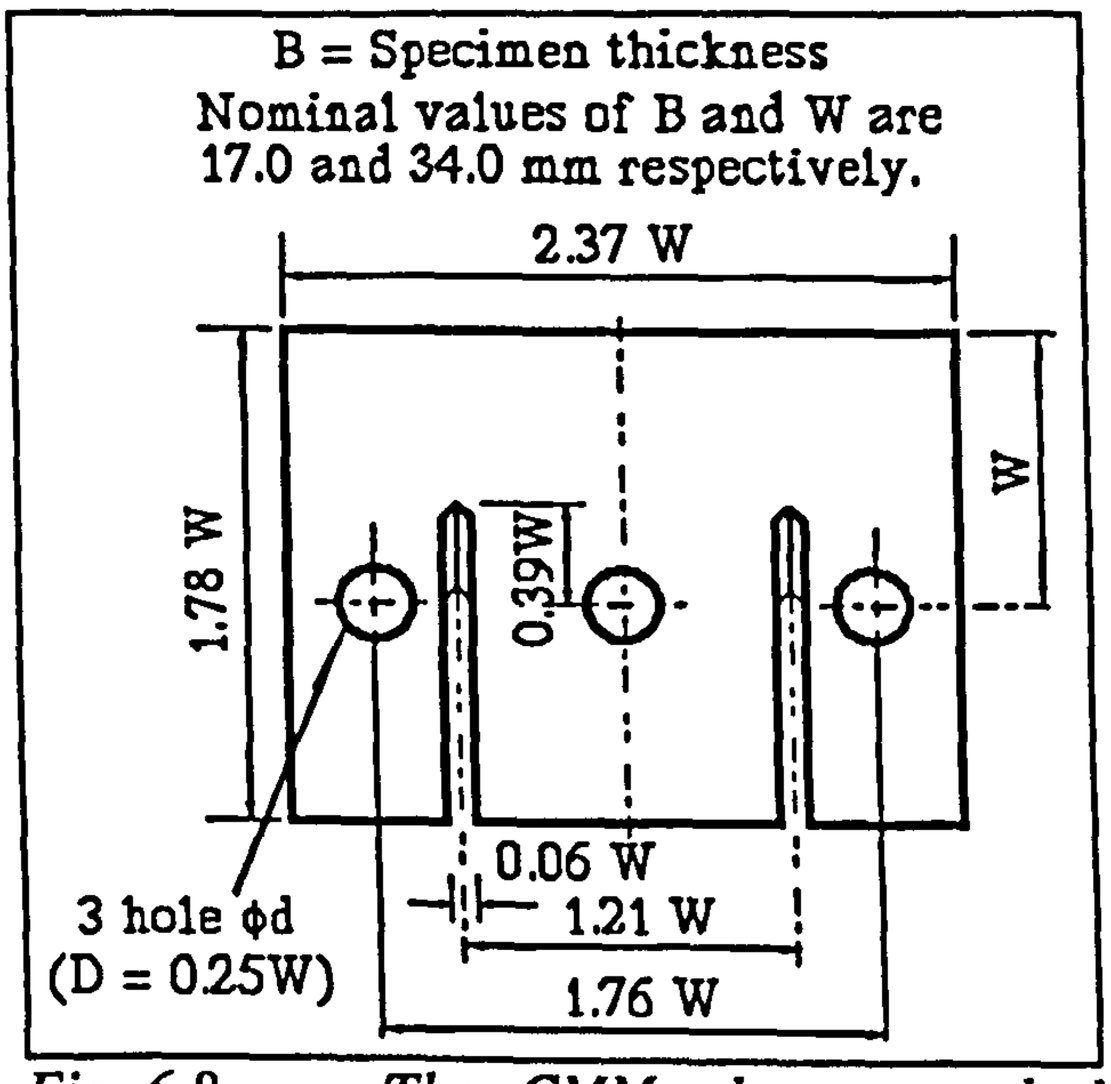

Fig. 6.8. The CMM chevron-notched specimen before fatiguing.

6.2.3. Fatiguing Apparatus

The Instron 1341 Fatiguing Instrument, Fig. 5.14 was employed in conjunction with the loading rig shown in Fig. 6.9.

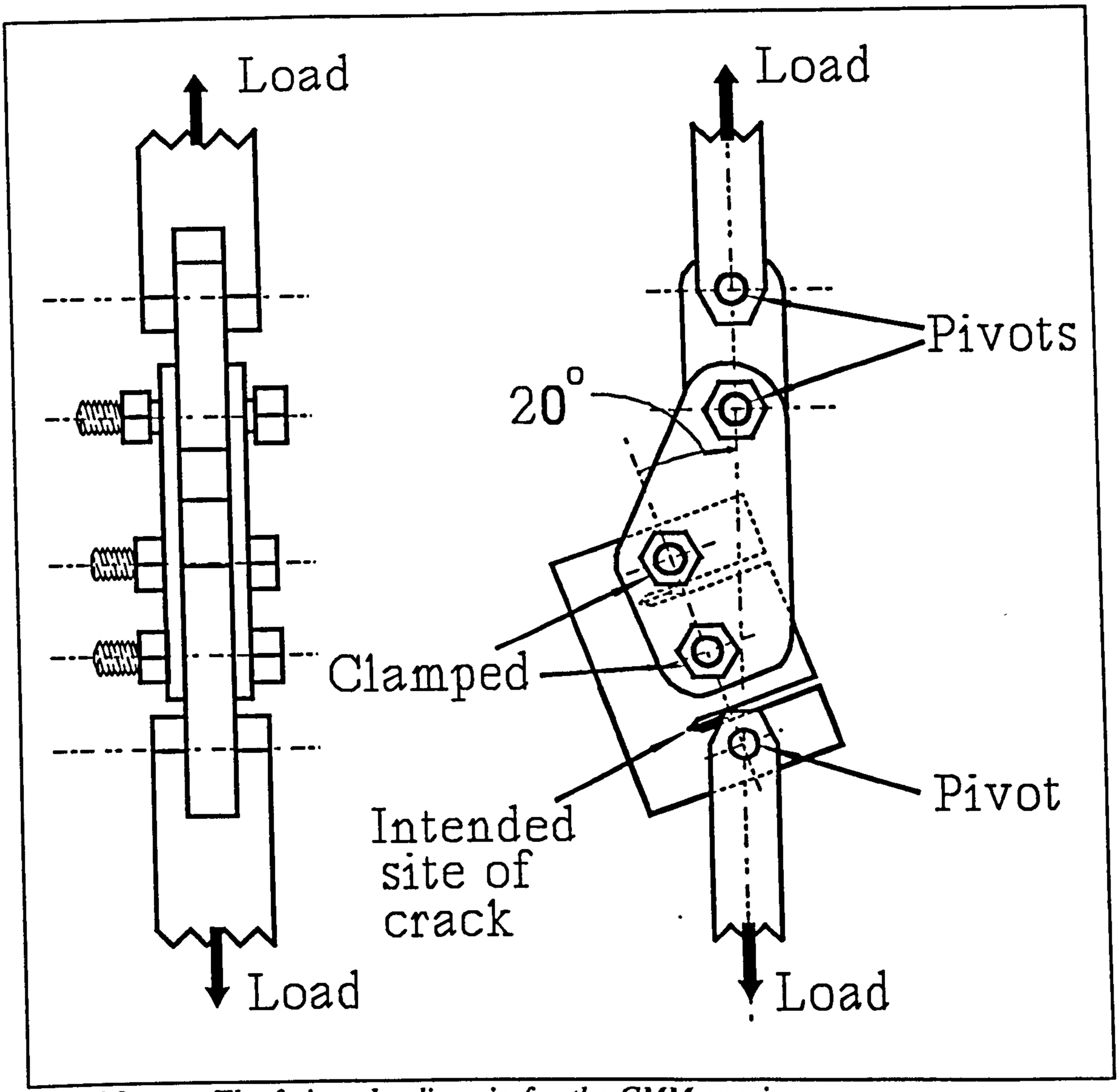

Fig. 6.9. The fatigue loading rig for the CMM specimen.

6.2.4. Fatiguing Process

The fatiguing apparatus described in the previous section was used to fatigue load the CMM specimens containing chevron notches. Only one of the two chevron notches in each specimen was fatigued.

The Instron 1341 cross-head was displacement-controlled to provide a static

tensile displacement of 0.10mm and a dynamic displacement of ± 0.05mm, with a frequency of 100Hz. In other words, the tensile displacement acting upon the specimen varied between 0.05mm and 0.15mm with a frequency of 100Hz.

The time of fatiguing the CMM specimens varied from a few minutes to a few hours. The fatigue crack was propagated until the total crack length, a, was approximately 0.45W, as shown in Fig. 6.6.

The fatigue crack was not absolutely straight. But the plane containing the cracked surfaces was within 10 degrees from the desired plane which would be perpendicular to the line joining the centres of the three holes of the specimen. The accuracy to within ±10 degrees was recommended in BS5447 [76] for other types of specimen.

The length of crack, a, was obtained by measuring the projected length along the plane perpendicular to the line joining the centres of the three holes in the specimen.

The specimens were ready to be destructively tested after being fatigued.

6.2.5. Loading Apparatus

The same apparatus was used for testing all the CMM specimens with notches and with real cracks. It was described in section 6.1.3.

6.2.6. Experimentation

The destructive testing was carried out on the CMM specimens with a real crack, breaking each specimen into two pieces. The angle of propagation depended on the mode-mixity of mode-I and mode-II loading.

The fracture surfaces did not contain any fine lines which would have otherwise indicated the point of fracture inception.

6.2.7 Results

The number of valid tests for the CMM specimen with a real crack was 13. The criteria given by BS5447 [76] and ANSI/ASTM E 399 - 78a [77] were consulted to establish the validity of the curved fatigued crack front, although no reference was made to this particular type of specimen. It was considered sufficient that the above two papers referred to other specimens containing cracks used to evaluate the plane strain fracture toughness of the tested material.

The shape of the fatigued crack front could not be checked until the final testing of the specimens had been performed: the fatigued crack front could not be seen clearly until each specimen broke into two pieces. The specimens which did not satisfy the crack front criteria provided in BS5447 [76] and ANSI/ASTM E 399 - 78a [77], regarding the curvature of the crack tip, were rejected.

The average crack length for each specimen was calculated as described in section 5.2.7. The average crack length, a, together with a_{cen} and the two values of each of a_{mid} and a_{end}, is presented in Table 6.6. The crack length at each end of the crack front was denoted by a_{end}, while a_{cen} represented the crack length in the centre of the crack front. At the mid-point between the centre and each end, the crack length was denoted by a_{mid}.

The method employed in section 6.1.5 and described in appendix III determined the values of K_I and K_{II} for the tests of the CMM specimens with a real crack. Table 6.6 presents the values of K_I and K_{II} at fracture, the angle of crack propagation, the loading angle and the dimensions of the specimens.

Specimen number	B (mm)	W (mm)	a_{end} (mm)	a_{mid} (mm)	a_{cen} (mm)	a_{mid} (mm)	a_{end} (mm)
1	17.03	34.00	14.99	16.16	16.89	16.48	14.98
2	17.03	34.13	18.65	19.96	20.57	20.37	19.59
3	17.06	33.99	16.42	17.56	17.77	17.81	17.08
4	17.03	34.03	17.02	18.30	19.05	18.93	17.74
5	17.01	34.05	17.37	18.18	18.46	18.12	17.23
6	17.01	34.07	16.81	17.65	17.90	17.92	16.95
7	17.02	34.13	18.90	19.86	20.69	19.98	18.76
8	17.02	34.11	16.22	17.60	17.99	17.80	16.32
9	17.05	34.12	17.38	18.20	18.51	17.94	16.65
10	16.99	34.13	18.66	19.58	19.64	18.92	17.67
11	17.06	34.11	16.60	17.55	17.75	17.18	16.01
12	17.03	33.97	16.17	17.50	17.98	17.74	16.16

13	17.02	34.08	15.34	16.61	16.60	17.13	15.91

(a)

Specimen number	a (mm)	a/W	α (°)	P_c (kN)	Propaga-tion angle (°)	K_I at fracture ($N/mm^{3/2}$)	K_{II} at fracture ($N/mm^{3/2}$)
1	16.51	0.486	90	0.71	50.0	20.3	12.8
2	20.30	0.595	105	0.89	68.5	4.2	19.6
3	17.71	0.521	105	1.04	68.0	4.9	20.6
4	18.76	0.551	70	0.28	30.5	20.4	4.8
5	18.25	0.536	50	0.28	20.5	27.3	3.3
6	17.82	0.523	90	0.63	48.0	20.5	12.0
7	21.18	0.591	90	0.49	48.5	20.2	10.5
8	17.80	0.522	100	0.78	59.5	11.1	15.5
9	18.22	0.534	16	0.25	3.5	28.4	0.1
10	19.38	0.568	16	0.26	5.0	33.8	0.3
11	17.49	0.513	90	0.67	52.5	21.1	12.6
12	17.74	0.522	70	0.32	30.0	21.0	5.1
13	16.78	0.492	50	0.36	25.0	29.2	3.6

(b)

Table 6.6(a & b). Results for the CMM specimens with a real crack.

The K_I and K_{II} values have been plotted with other results from different sections in section 6.3.

6.3. Conclusions

The stress intensity factor results of all the CMM specimens, which were 96 specimens, have been plotted in Fig. 6.10.

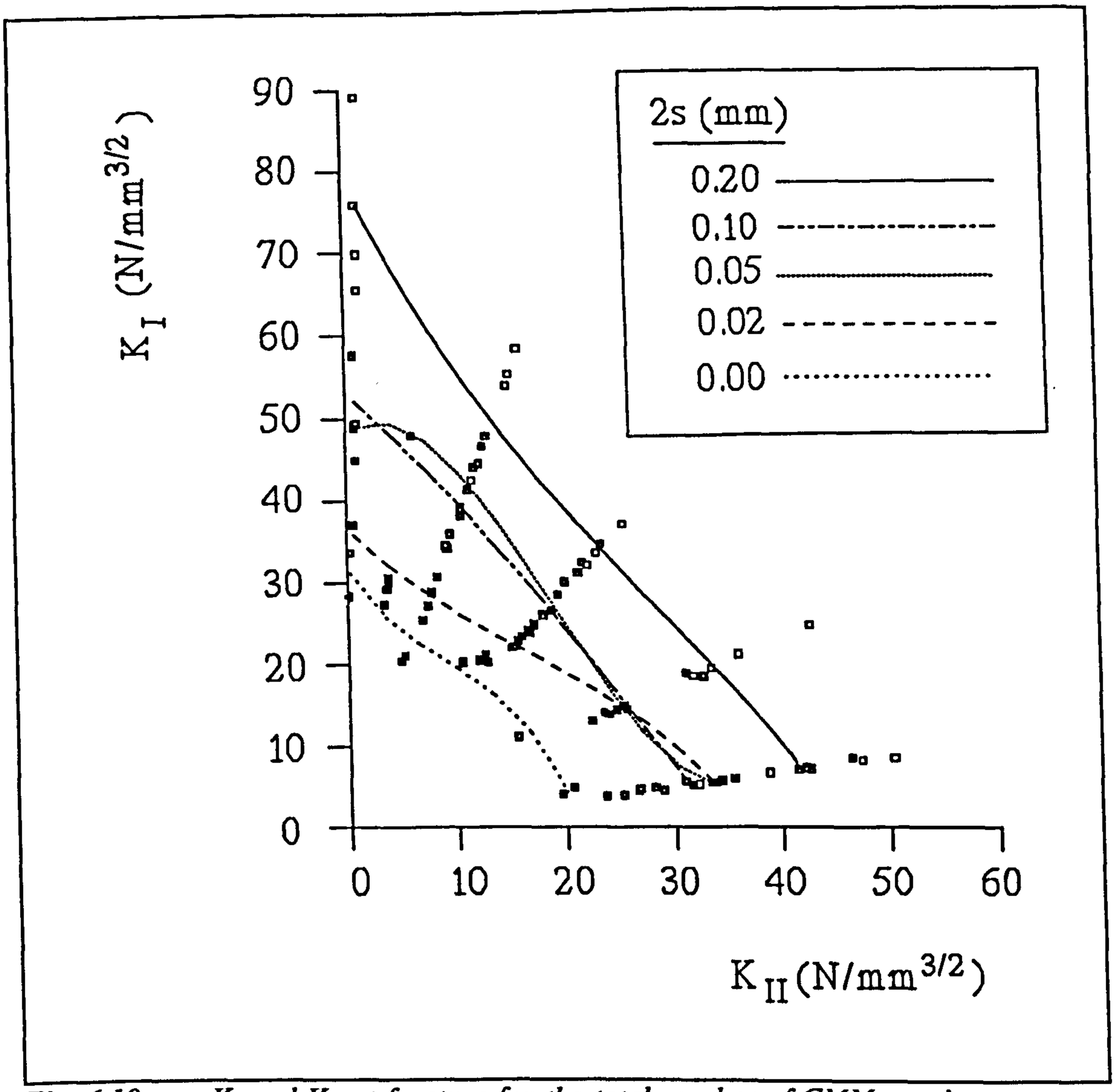

Fig. 6.10. K_I and K_{II} at fracture for the total number of CMM specimens.

The K_{IC} results obtained from the 361 3PB specimen tests were considered with the 96 CMM specimen results to plot the graph in Fig. 6.11 which contained a total number of 457 results.

A graph of the angle of crack propagation against $K_I/(K_I+K_{II})$, for all the CMM specimens, has been plotted and shown in Fig. 6.12. The graph demonstrates a very close agreement with the results obtained by Maccagno and Knott [60] in their brittle

fracture experimentation on PMMA (the amorphous glassy polymer Polymethylmethacrylate) at room temperature. They [60] also presented three curves predicting the angle of propagation using the three well known hypotheses: the maximum tangential tensile stress, the maximum elastic energy release rate and the minimum strain energy density hypotheses. The results of Fig. 6.12 show the closest agreement with the maximum tangential tensile stress criterion.

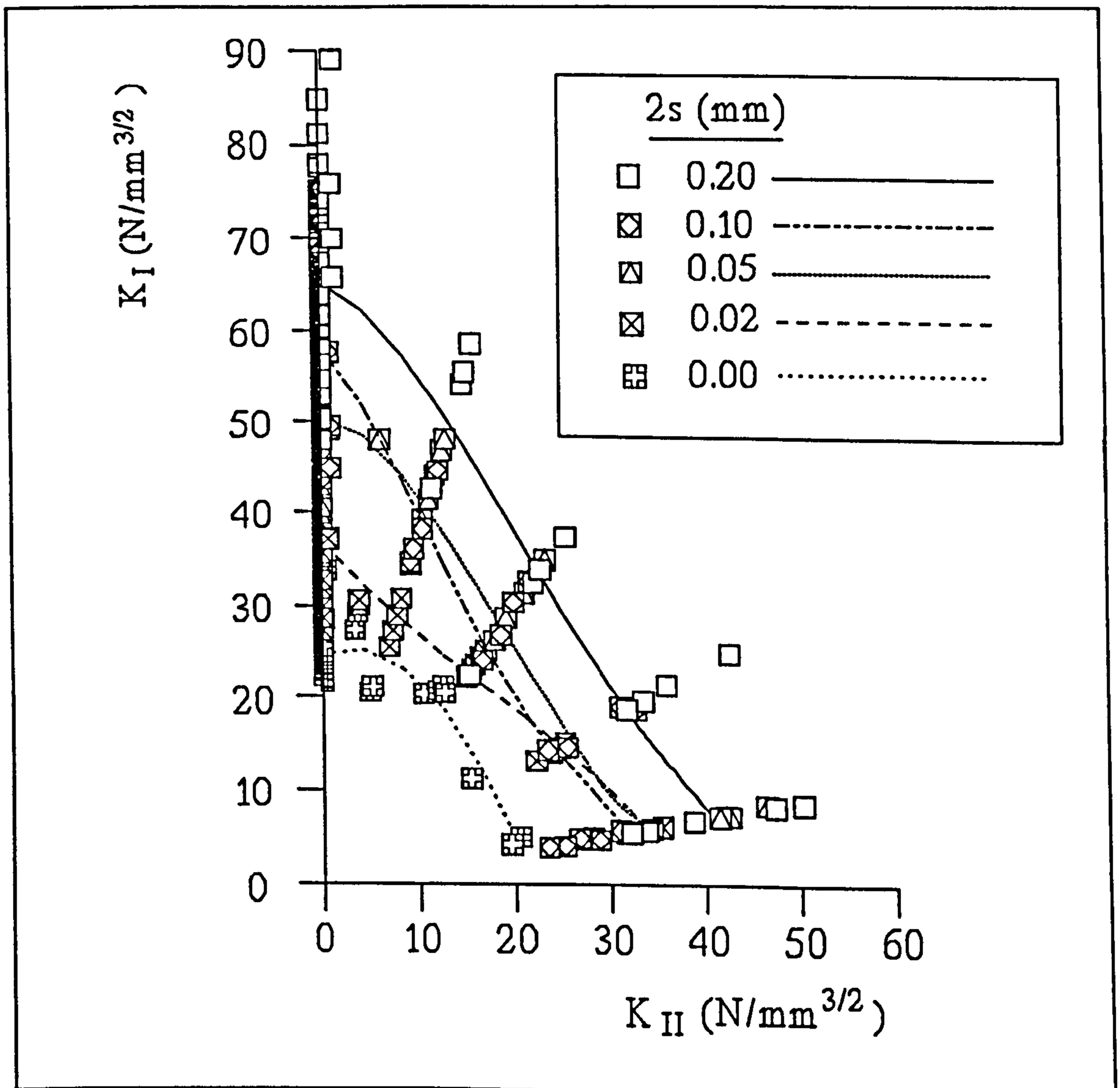

Fig. 6.11. K_I and K_{II} at fracture for the total number of 3PB and CMM specimens.

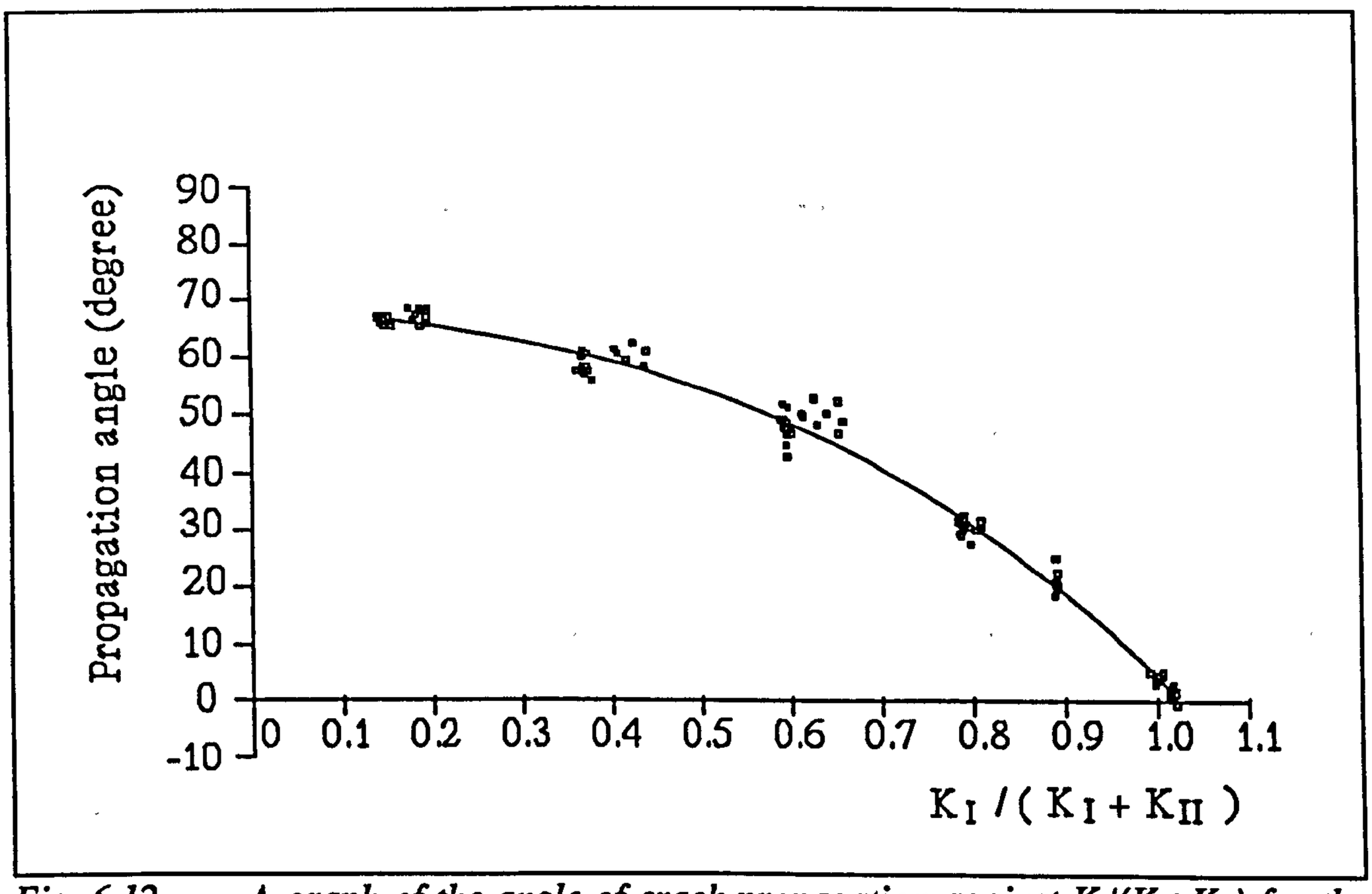

Fig. 6.12. A graph of the angle of crack propagation against $K_I/(K_I+K_{II})$ for the CMM specimens.

CHAPTER SEVEN

MODE-I FINITE ELEMENT ANALYSIS

The previous two chapters examined the stress intensity factors for specimens with cracks or narrow notches. The method of examination was experimental. The stress intensity factors described the magnitude of the stress fields in the vicinity of the tips of the cracks and notches.

This chapter has a complementary approach to the previous ones. The stress contours and in particular the actual peak stresses, which are of most significance, have been acquired for a range of semi-circular and rectangular narrow notches or cut-outs subjected to mode-I loading conditions. The rectangular cut-outs have rounded corners. The method of finite element analysis has been utilized to achieve the above.

For very narrow cut-outs, approaching the shape of a crack, with elliptically and hyperbolically shaped ends, Creager and Paris [79] has derived solutions for the stress fields near the ends of the cut-outs when they are in uniformly stressed (tension or shear) infinite plates. Creager and Paris [79] presented the solutions in terms of the stress intensity factors related to the stress fields in the vicinity of the tips of cracks [6] which are the same length as the narrow cut-outs. It seems likely that

Creager's solutions can be used to estimate the magnitudes of the stresses in narrow slots with more complex end shapes and in non-uniform stress fields, in components of finite size.

In this chapter, the finite element method has been used for the same 3PB specimen of chapter 5. Solutions for the stresses near the ends of narrow rectangular slots with rounded corners in a beam subjected to three-point bending, see Fig. 7.1, have been obtained. The solutions are compared with those for cracks [6] and with predictions based on Creager's analysis. The three-point bend specimen has a non-uniform stress field and can therefore be used to assess the applicability of Creager's solutions [79] for more complex shapes of the ends of slots in non-uniform stress fields.

7.1. The Geometry, Loading and Finite Element Analyses

The general dimensions of the three-point bend specimen, shown in Fig. 7.1, are those of a standard fracture toughness specimen [76]. The loading is conveniently characterised by the nominal maximum bending stress, σ_{nom}, on the central ligament of the component, i.e.

$$\sigma_{nom} = \frac{3FL}{2B(W-a)^2} \qquad (7.1)$$

The geometry at the end of the notch is shown in Fig. 7.2. It is characterised by two dimensions, i.e., the notch width, 2s, and the corner radii, ρ.

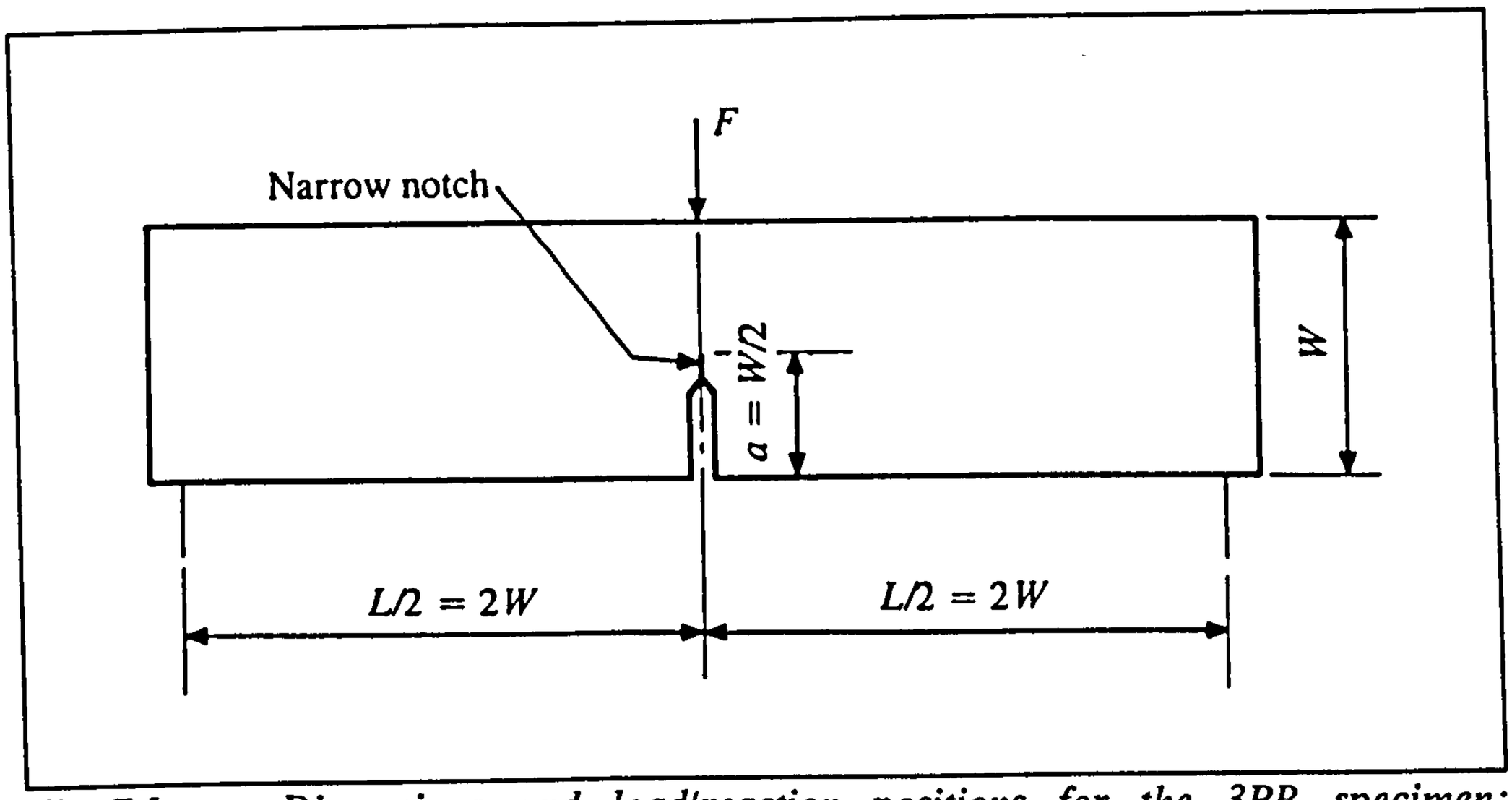

Fig. 7.1. *Dimensions and load/reaction positions for the 3PB specimen; thickness B = W/2.*

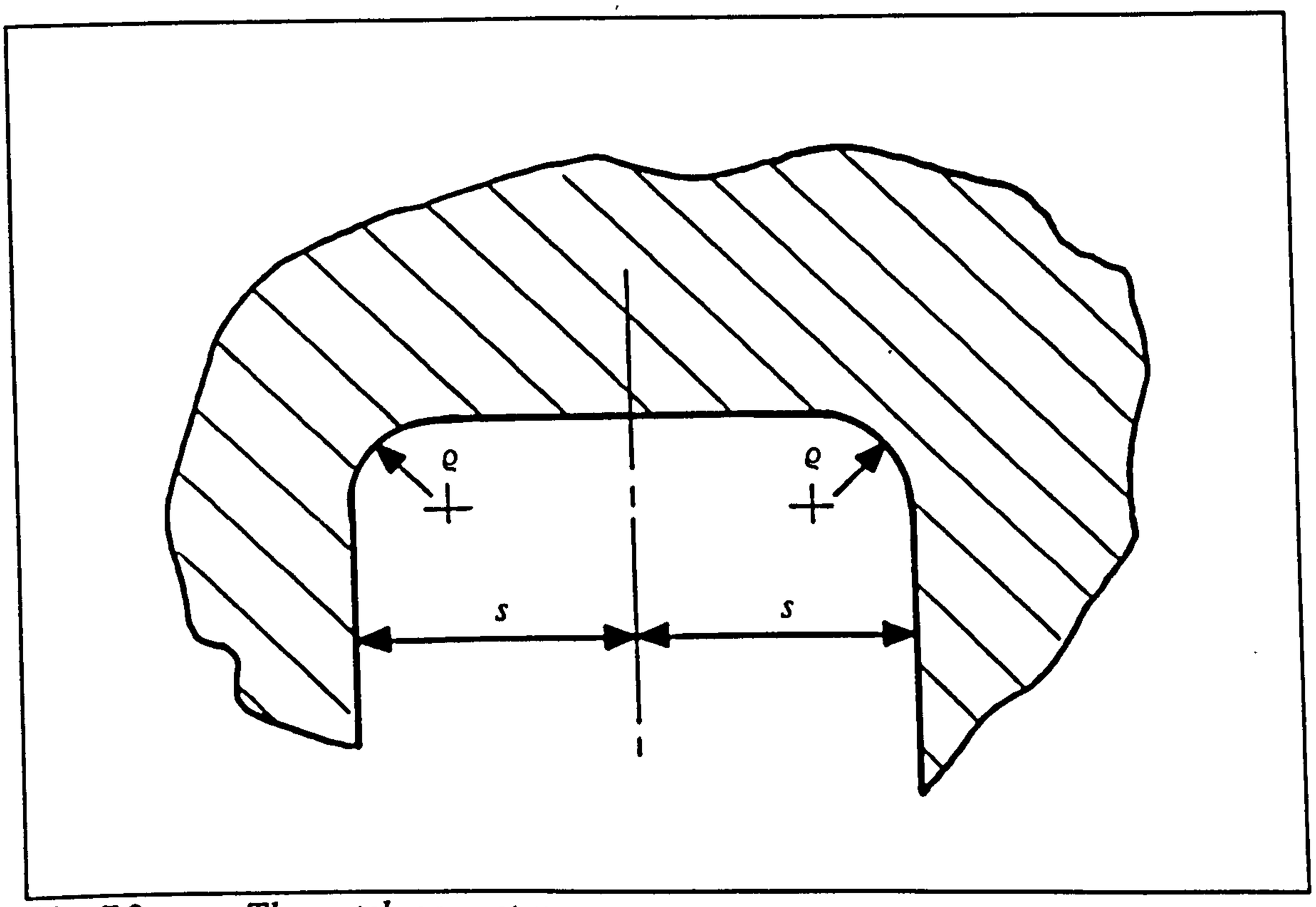

Fig. 7.2. *The notch geometry.*

In this chapter, results are presented for values of s/W in the range 7.35×10^{-4} to 2.35×10^{-2} and s/ρ values between 1 (semi-circular) and 256.

The finite element results were obtained using PAFEC finite element package [80]. Eight-noded, plane strain, isoparametric finite elements were used throughout.

A symmetric half of the component was modelled; typical meshes are shown in Figs. 7.3(a-c). The suitability of the meshes was established by ensuring that discontinuities of stress, at corresponding nodes, in adjacent elements were negligible. Although more sophisticated methods for determining the suitability of finite element meshes exist [e.g. 81], these were not available in the finite element package used [80]. However, if care is taken, the relatively tedious method of checking to ensure that stress discontinuities are negligible is reliable.

s/W	s/ρ
7.35×10^{-4}	1, 2, 4, 8
1.47×10^{-3}	1, 2, 4, 8, 16
2.94×10^{-3}	1, 2, 4, 8, 16, 32
5.88×10^{-3}	64
1.18×10^{-2}	128
2.35×10^{-2}	256

Table 7.1. Notch geometries for which finite element results were obtained.

A total of eighteen analyses were performed with the notch dimensions defined in Table 7.1. Iso-stress contours have been plotted for each case. Numerous examples have been included in appendix IV.

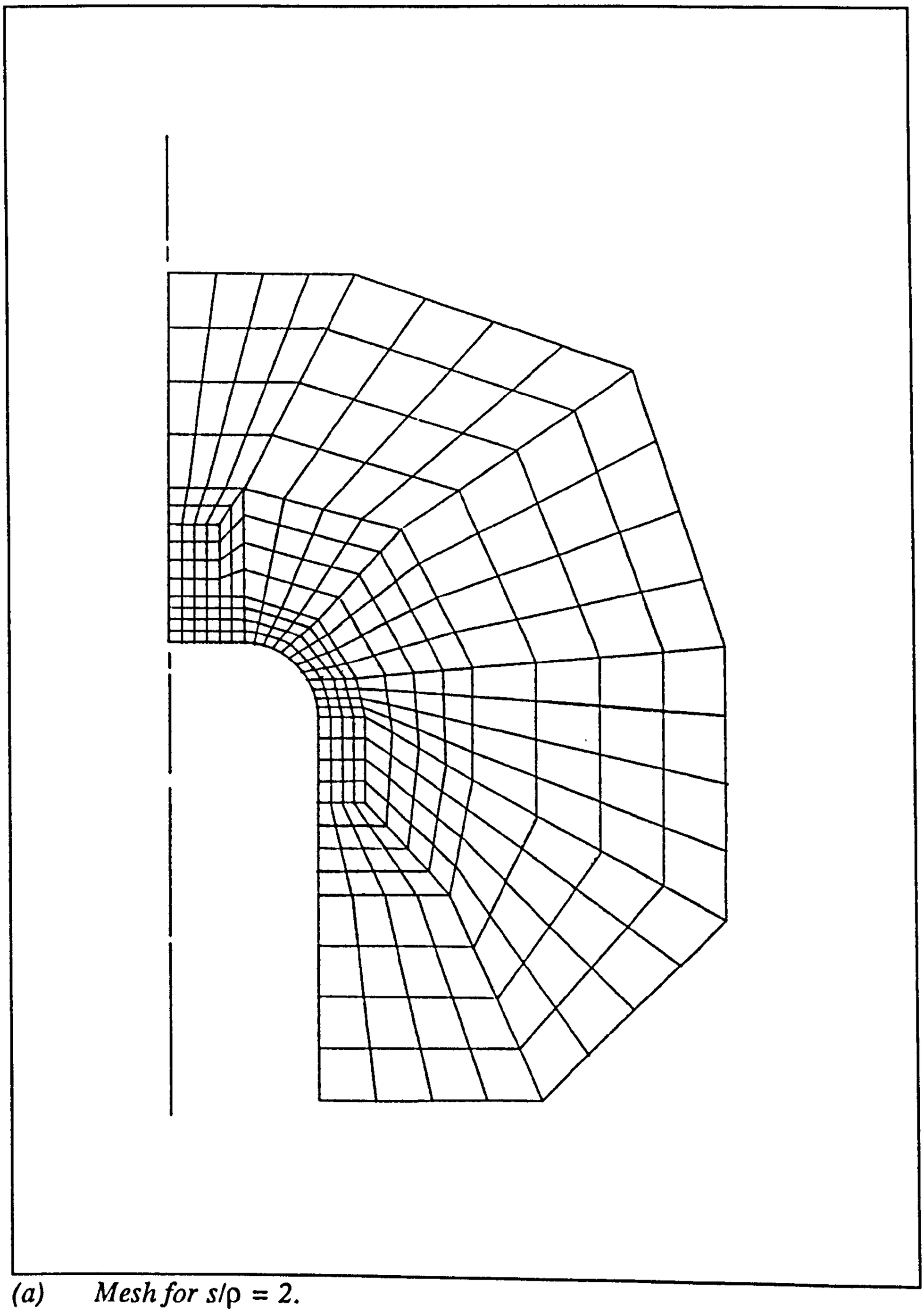

(a) *Mesh for* $s/\rho = 2$.

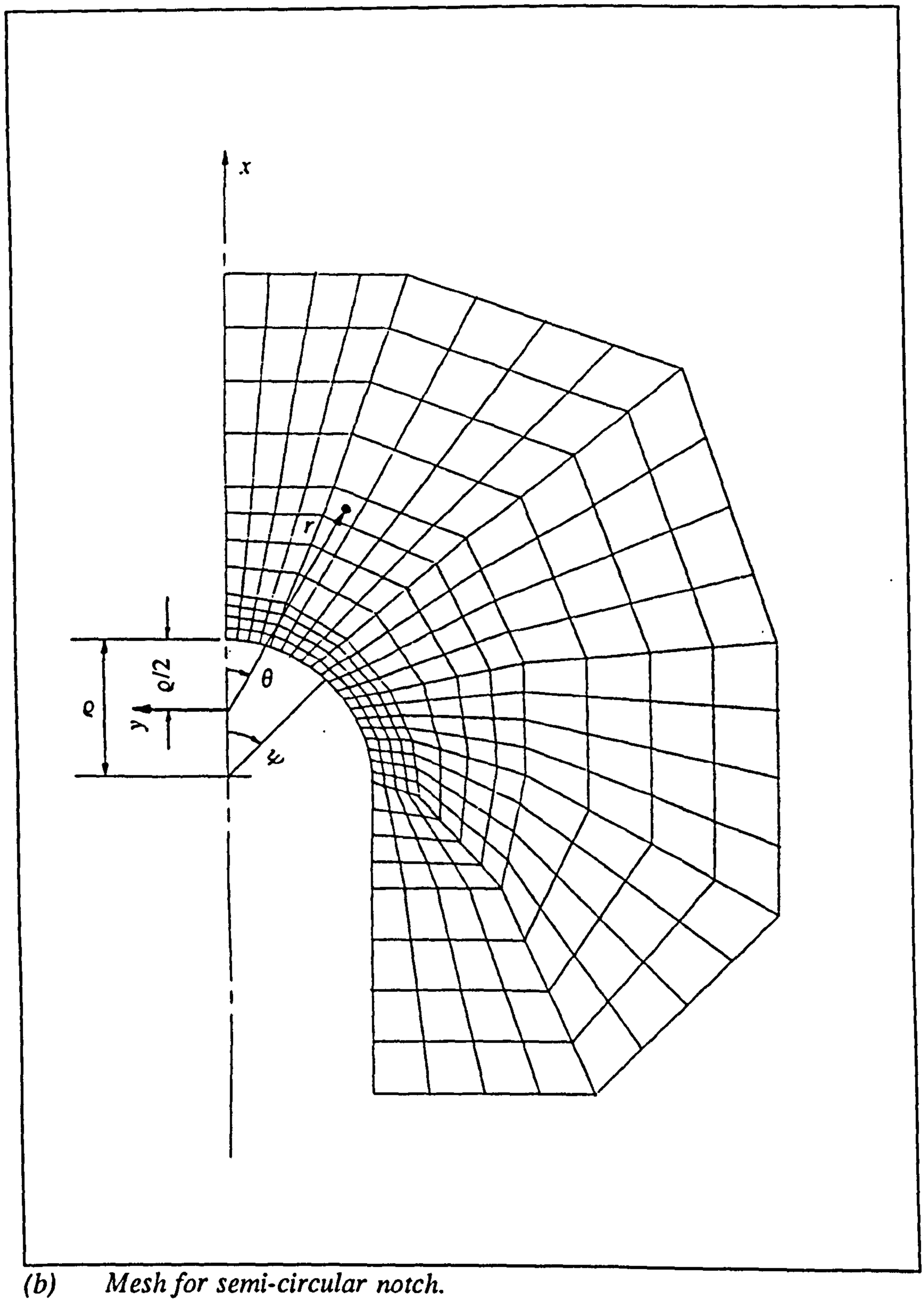

(b) Mesh for semi-circular notch.

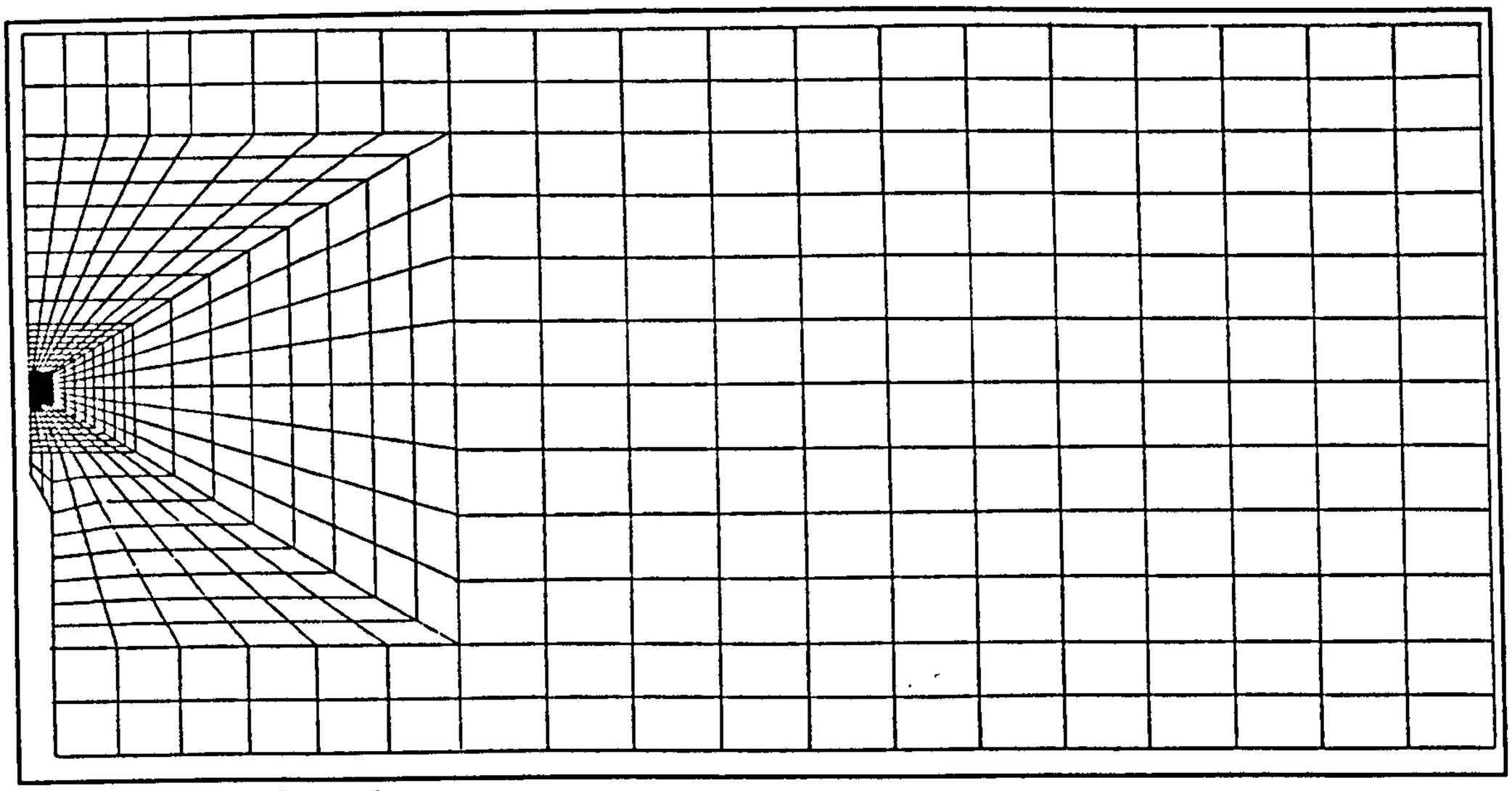

(c) General mesh.

Figs. 7.3(a-c). Typical meshes used in the finite element analyses.

7.2. Results

The results in this chapter are presented in two sub-sections. The first mainly talks about semi-circular notches while the second covers rectangular notches with rounded corners.

7.2.1. Semi-Circular ($s/\rho = 1$) Notch Ends

The distributions of the normalised maximum principal stresses obtained from the finite element analyses on the surfaces of the semi-circular notches (the tangential stress) with angular position, ψ (defined in Fig. 7.3(b)), for $s/W = 7.35 \times 10^{-4}$, 1.47×10^{-3} and 2.94×10^{-3}, are shown in Fig. 7.4. It can be seen that the peak stress occurs at $\psi = 0$ and that the stress increases with reducing notch width, 2s.

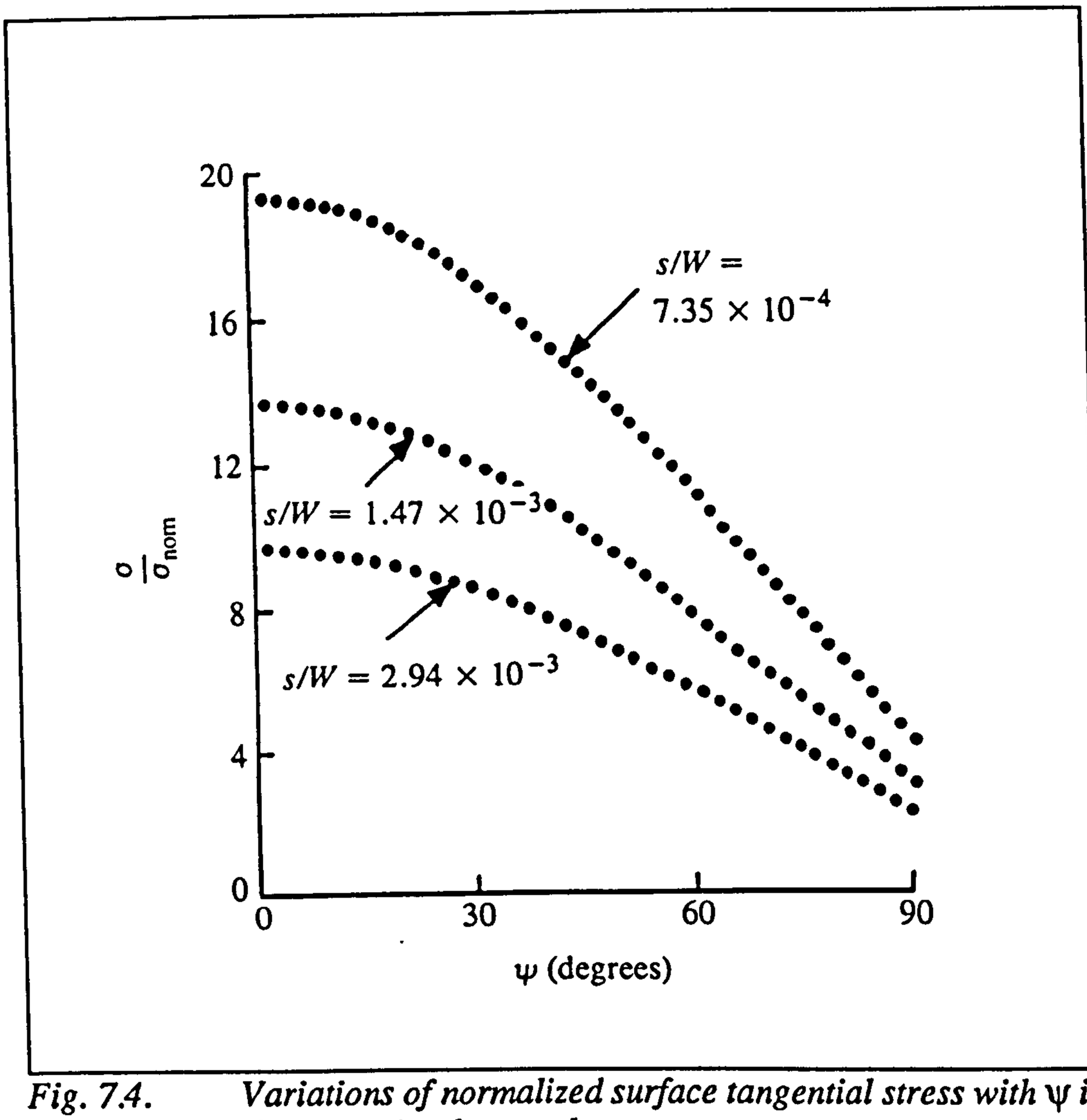

Fig. 7.4. Variations of normalized surface tangential stress with ψ in the semi-circular notches.

Creager's analysis [79] for elliptical and hyperbolic notches, with notch tip radius of curvature, ρ, gives

$$\sigma_x = \frac{K_I}{\sqrt{2\pi r}}\left[\cos\frac{\theta}{2}\left(1 - \sin\frac{\theta}{2}\sin\frac{3\theta}{2}\right) - \frac{\rho}{2r}\cos\frac{3\theta}{2}\right] \tag{7.2}$$

$$\sigma_y = \frac{K_I}{\sqrt{2\pi r}}\left[\cos\frac{\theta}{2}\left(1 + \sin\frac{\theta}{2}\sin\frac{3\theta}{2}\right) + \frac{\rho}{2r}\cos\frac{3\theta}{2}\right] \tag{7.3}$$

and

$$\tau_{xy} = \frac{K_I}{\sqrt{2\pi r}}\left[\sin\frac{\theta}{2}\cos\frac{\theta}{2}\cos\frac{3\theta}{2} - \frac{\rho}{2r}\sin\frac{3\theta}{2}\right] \tag{7.4}$$

where r and θ are measured from a point ρ/2 from the centre of curvature, on ψ = 0, (x,y) is a coordinate system having the same origin as the (r,θ) system, as indicated in Fig. 7.3(b), and K_I is the mode-I stress intensity factor for an equivalent sharp crack. The peak stress predicted, is σ_y (ρ/2,0) at r = ρ/2 and θ = 0, i.e. on the surface, in the centre of the notch. Substituting r = ρ/2 and θ = 0 into equation (7.3) gives

$$\hat{\sigma}\sqrt{\pi\rho} = 2K_I \qquad (7.5)$$

This predicts that for elliptical and hyperbolic notches, with different notch tip radii of curvature, the product of $\hat{\sigma}$ and $\sqrt{\rho}$ is a constant. The $\hat{\sigma}\sqrt{\rho}$ values from the three, semi-circular notch, finite element analyses were found to be the same to within 0.5%. Also, the $\hat{\sigma}\sqrt{(\pi\rho)}$ values agreed with that obtained using equation (7.5) to within 5%, the finite element results being slightly higher than the Creager predictions (equation (7.5)).

The variations of the normalised stresses, σ_x/σ_{nom} and σ_y/σ_{nom}, along θ = 0, with dimensionless distance from the notch tip, for $s/W = 7.35 \times 10^{-4}$, are shown in Fig. 7.5; τ_{xy} along this line of symmetry is zero. Also shown in Fig. 7.5 are predictions based on Creager's solution [79], i.e. equations (7.2) and (7.3), and on Westergaard's [6] equations, which apply to a sharp crack tip. The Westergaard equations are the same as equations (7.2) and (7.3) with the last term (containing ρ/2r) omitted. It can be seen that the predictions based on equations (7.2) and (7.3) are very close to the finite element results. The σ_y/σ_{nom} values approach each other and for distances greater than ρ/s the difference between them is less than 10%. Beyond this point, the

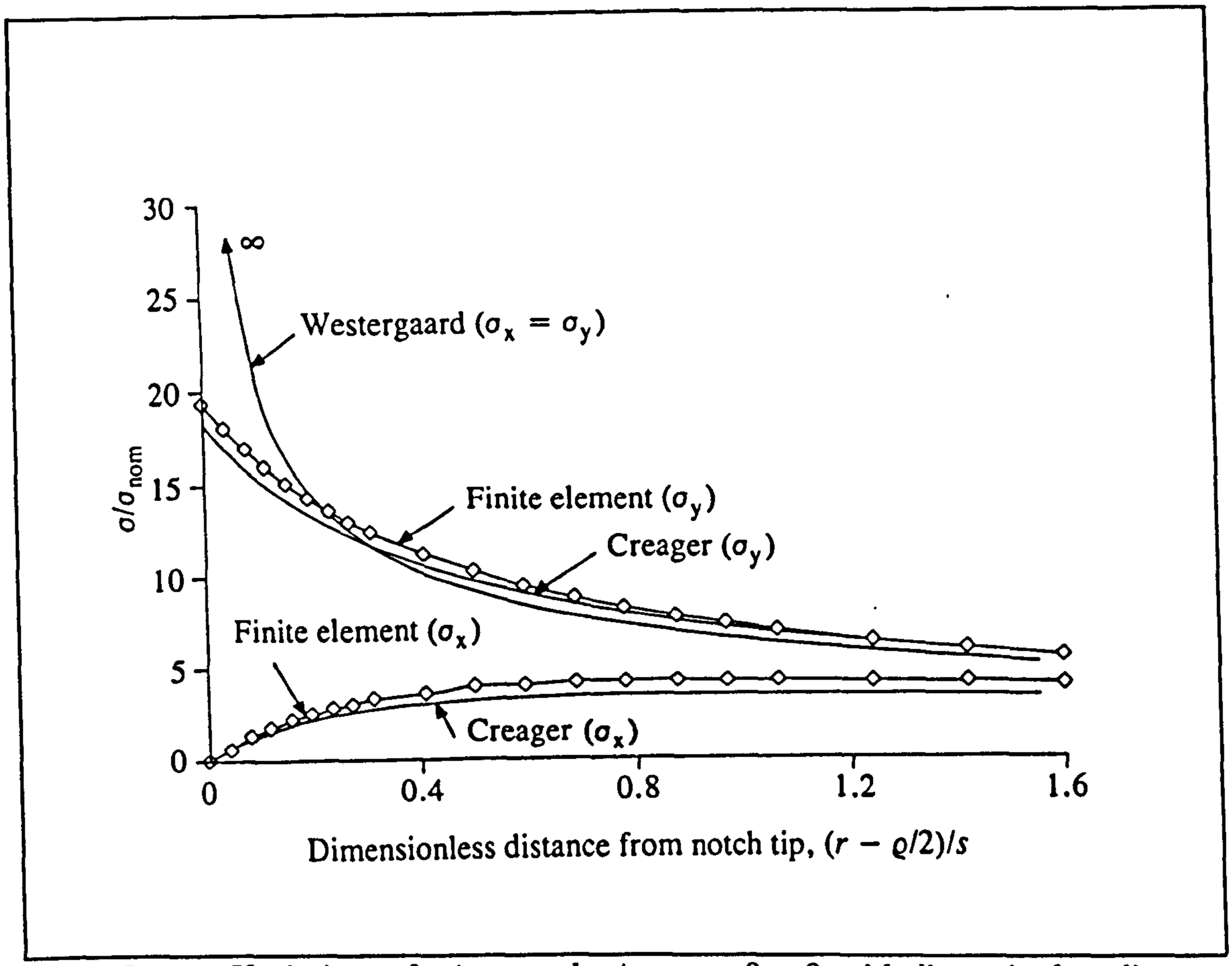

Fig. 7.5. Variations of σ_x/σ_{nom} and σ_y/σ_{nom}, on $\theta = 0$, with dimensionless distance from the notch tip; $s/W = 7.35 \times 10^{-4}$.

crack tip stress predictions (σ_x and σ_y) are accurate. However, the σ_x value obtained from the finite element analysis and from equation (7.2) is zero at the notch (because there are no tractions applied to the notch surface) whereas a value of ∞ is predicted for a sharp crack. For distances greater than 0.2 (i.e., $0.2\rho/s$) the crack tip solution for σ_y is reasonably accurate. However as the notch tip is approached, for distances less than $0.2\rho/s$, the crack tip solution becomes progressively worse. Comparison between the finite element results, predictions based on Creager's analysis [79] (equations (7.2) and (7.3)), and the sharp crack analysis [6] for $s/W = 1.47 \times 10^{-3}$ and 2.94×10^{-3} lead to the same conclusions. This is to be expected since the dimensions which characterise the notch geometry, i.e. s and ρ, are very small compared with all

other component dimensions for s/W = 1.47×10^{-3} and 2.94×10^{-3} as well as for s/W = 7.35×10^{-4}.

The contours in Figs. 7.6(a-b) , which join points with equal maximum principal stress in the vicinity of the notch tip with s/W = 7.35×10^{-4}, were obtained by finite element analysis. Similar results were obtained for s/W = 1.47×10^{-3} and 2.94×10^{-3}. Equations (7.2), (7.3) and (7.4) can be used to obtain the maximum principal stress at any position in the vicinity of the notch tip. Similarly, by omitting the terms in $\rho/2r$ in equations (7.2), (7.3) and (7.4), maximum principal

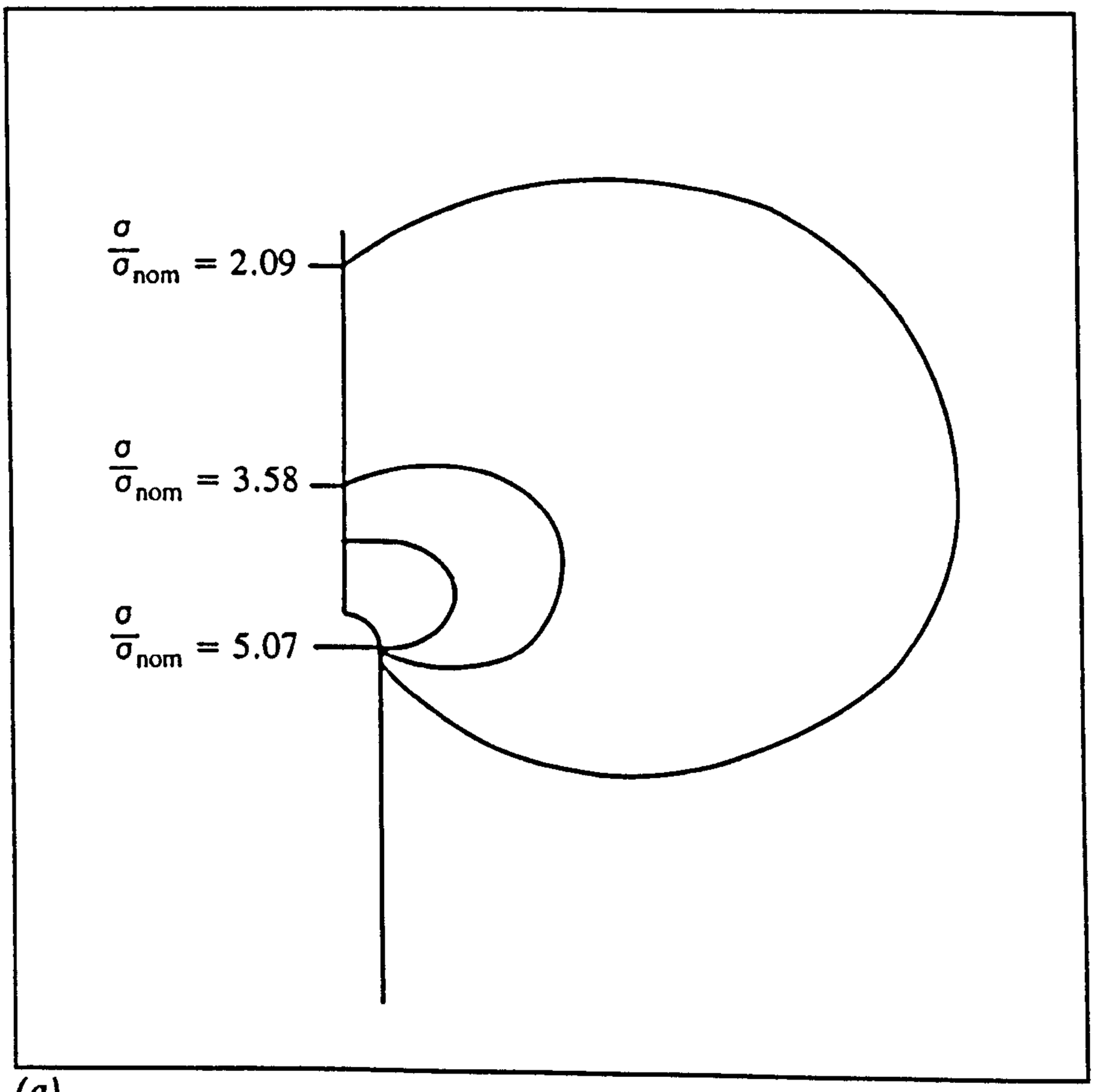

(a)

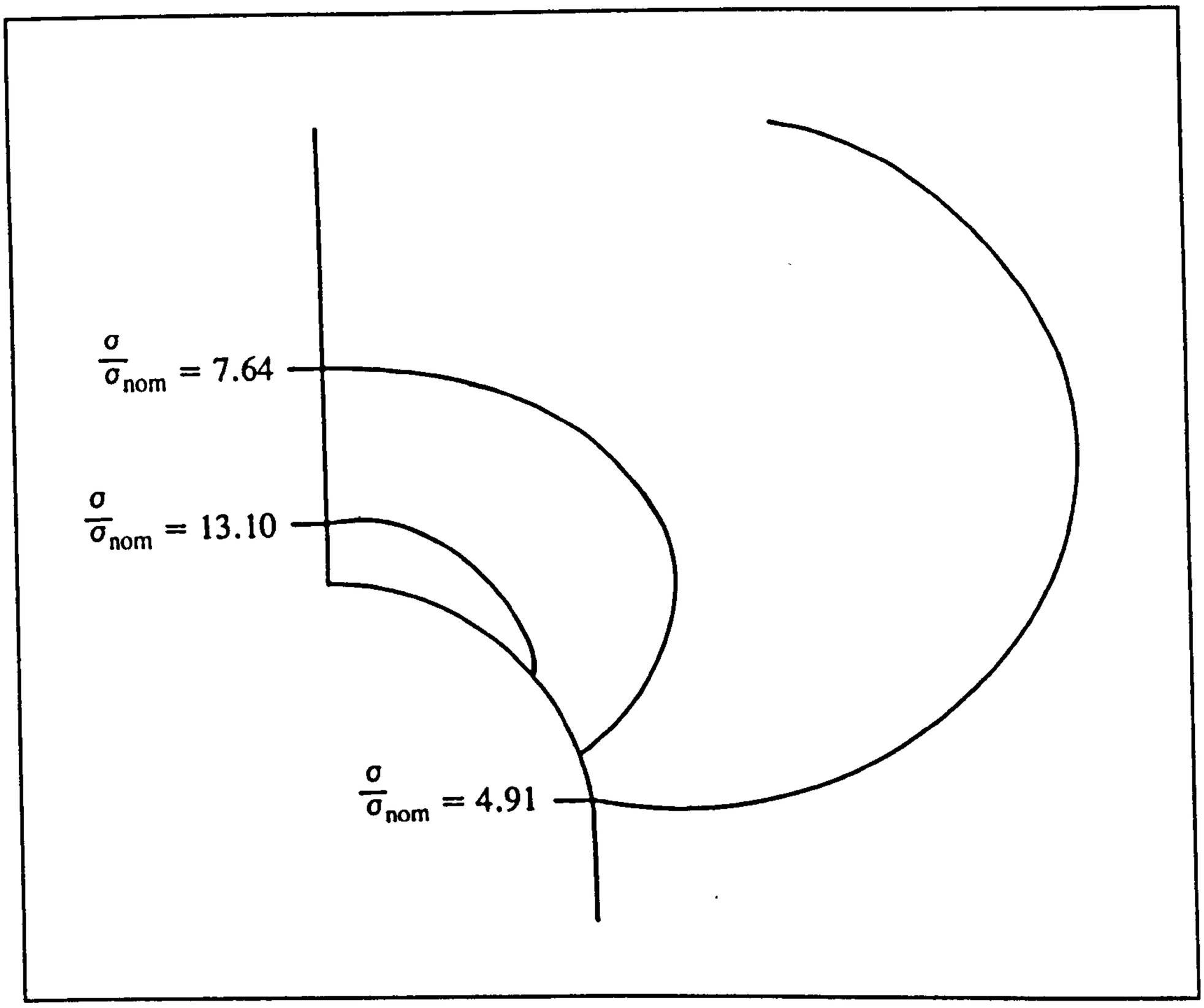

(b)

Figs. 7.6(a-b). *Contours joining points of equal maximum principal stress in the vicinity of a semi-circular notch ($s/W = 7.35 \times 10^{-4}$) obtained by finite element analysis; the contours correspond to those in Figs. 7.7(a-b) and 7.8(a-b).*

stresses in the vicinity of a crack tip can be obtained. Contours of maximum principal stress in the vicinity of a notch based on Creager's analysis (equations (7.2), (7.3) and (7.4) are shown in Figs. 7.7(a-b) and those for a sharp crack, are shown in Figs. 7.8(a-b). The contours in Figs. 7.7 and 7.8 correspond to the finite element results in Figs. 7.6.

From Figs. 7.6(a), 7.7(a) and 7.8(a) it can be seen that the iso-stress contours, which are at distances greater than 2ρ from the notch tip, obtained by finite element,

Creager's, and an actual crack analyses, have shapes and sizes which are practically the same for the semi-circular notch. Closer to the notch tip, the Creager results, Fig. 7.7(b), are still in good agreement with the finite element results, Fig. 7.6(b), for the semi-circular notch. However, as Fig. 7.8(b) shows, the iso-stress contours predicted for a crack tip are not in good agreement with those for a semi-circular notch.

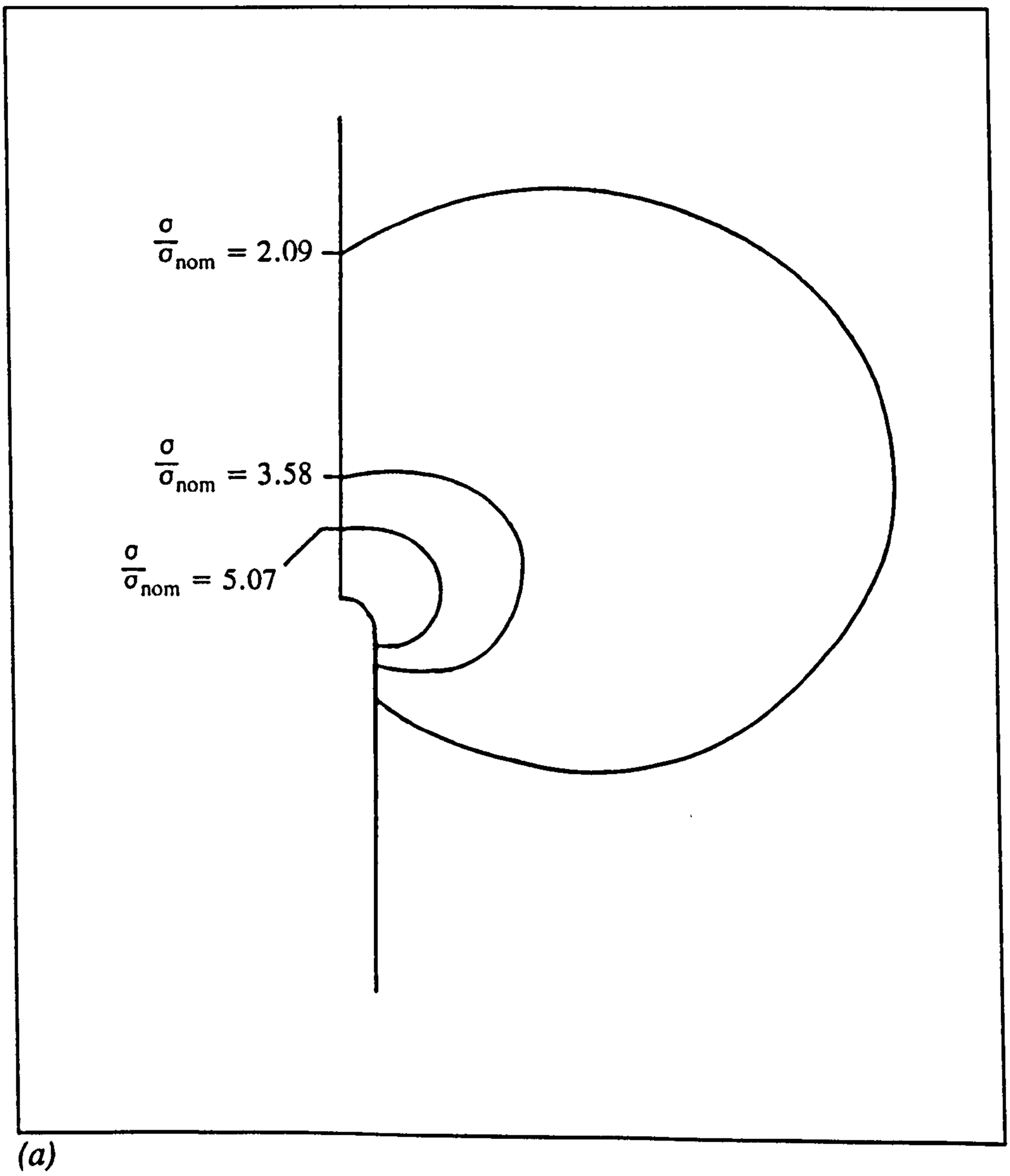

(a)

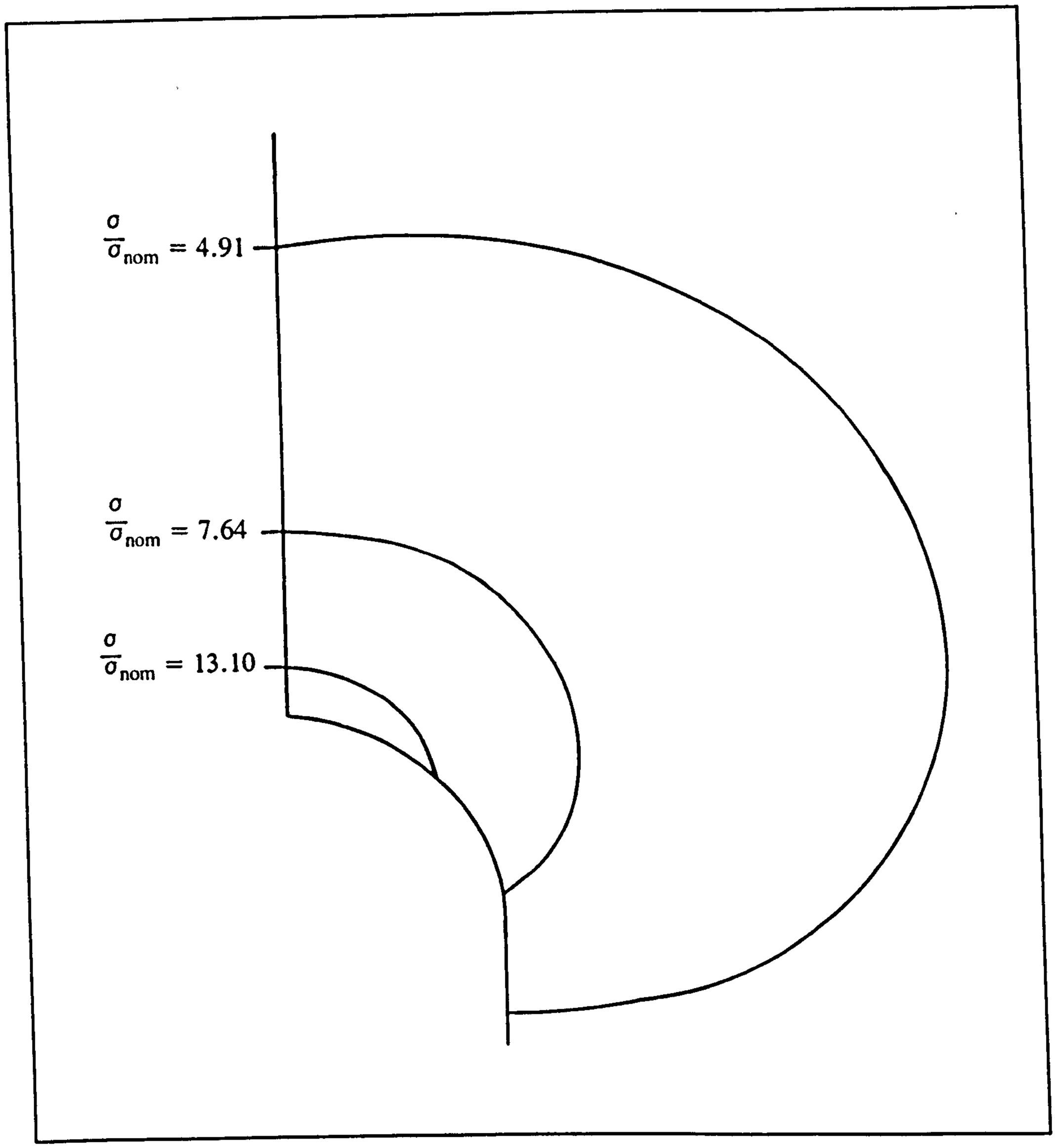

(b)

Figs. 7.7(a-b). *Contours joining points of equal maximum principal stress predicted by Creager's analysis [79] for s/W = 7.35 × 10⁻⁴; the contours correspond to those of Figs. 7.6(a-b) and 7.8(a-b).*

Comparisons of the results obtained by finite element analysis for semi-circular notches (e.g. Figs. 7.4, 7.5 and 7.6) with those predicted by equations (7.2, 7.3 and 7.4), obtained by Creager for elliptical and hyperbolic notches, show that equations

(7.2, 7.3 and 7.4) give a good representation of the stresses near a semi-circular notch. However, even though the notches are very narrow, crack tip stress fields do not accurately represent the stress fields at a distance less than 2ρ from the notch tip; at a greater distance, predictions obtained for an equivalent crack tip are reasonably accurate.

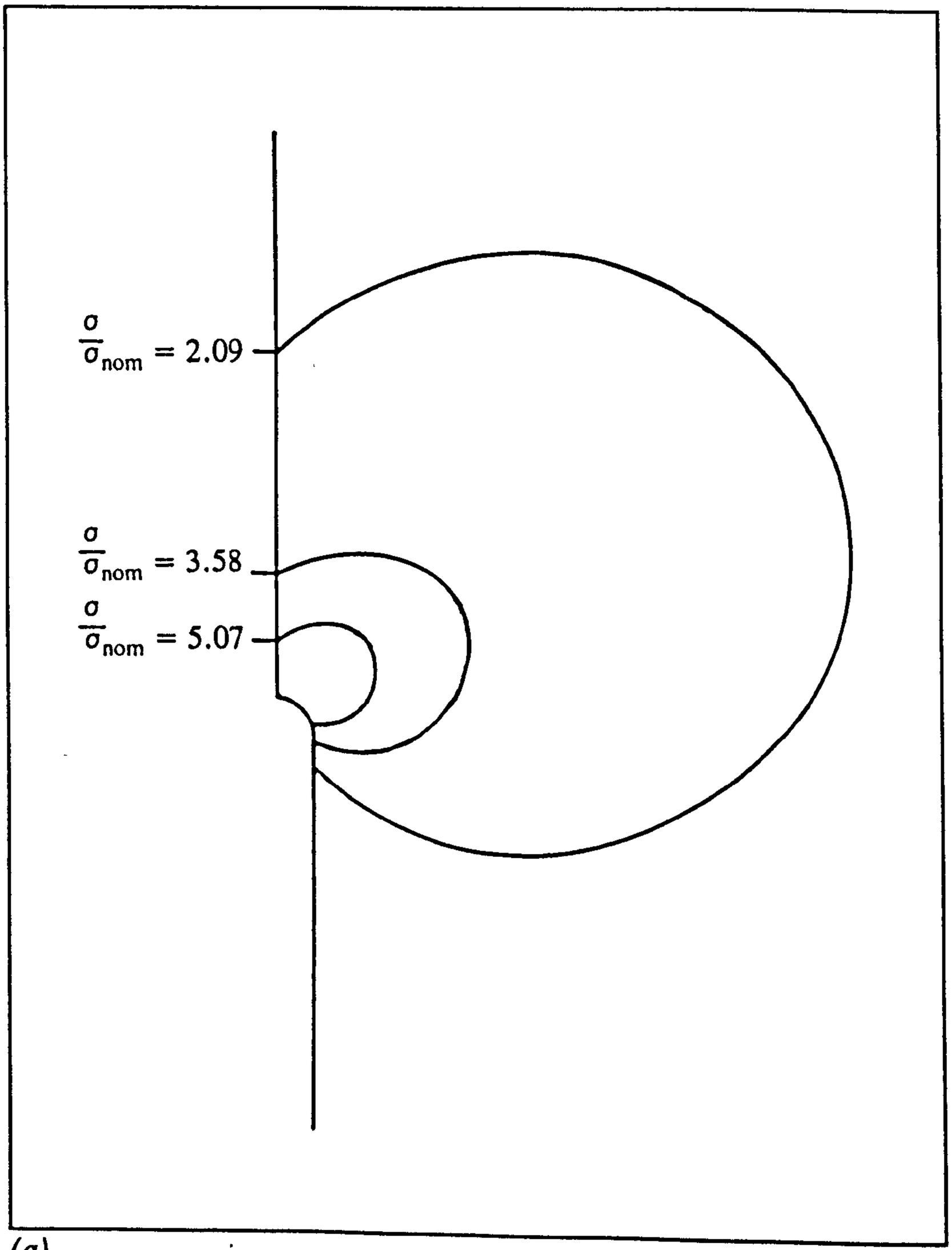

(a)

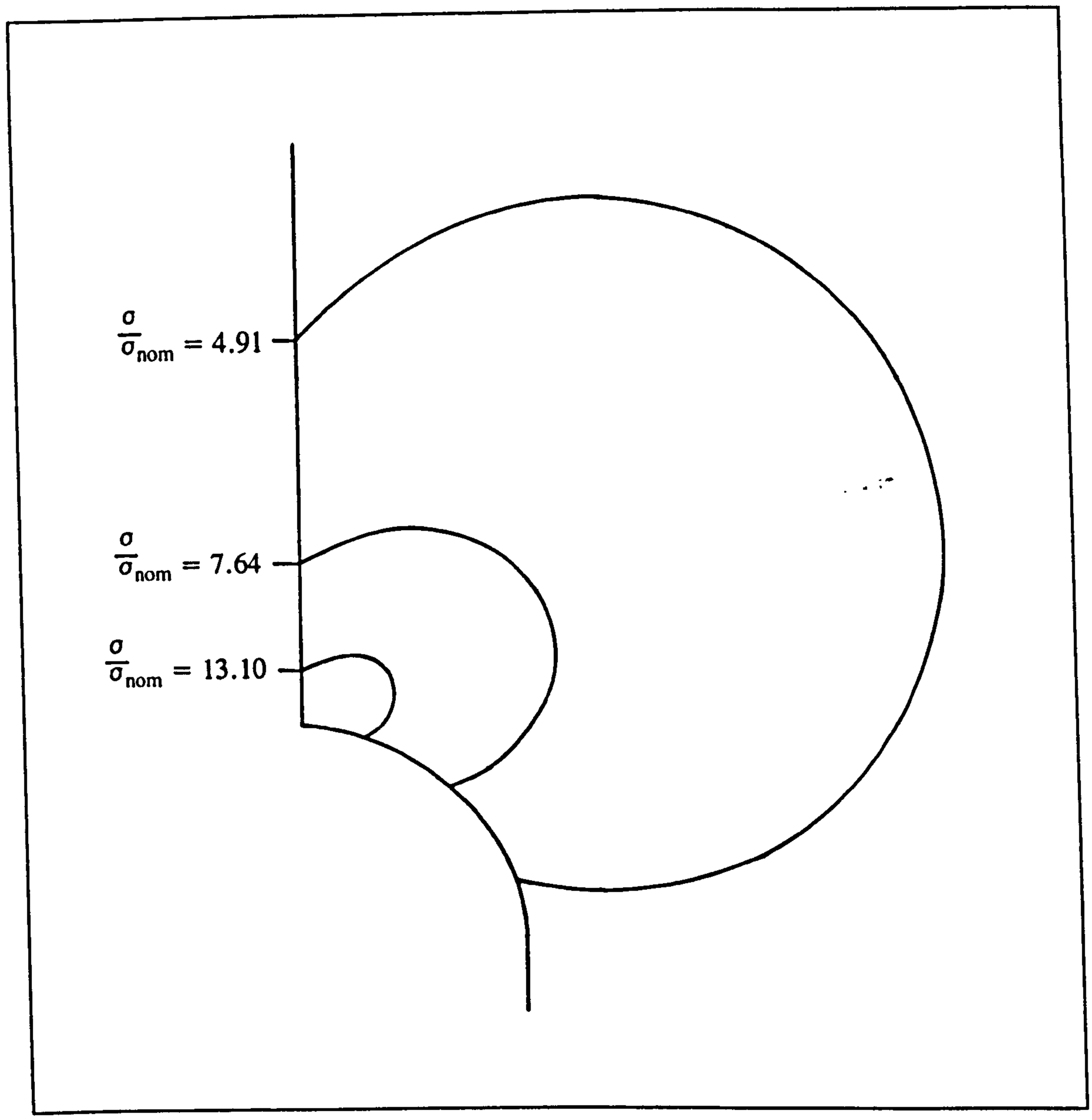

(b)

Figs. 7.8(a-b). *Contours joining points of equal maximum principal stress in the vicinity of a crack tip [6]; the contours correspond to those in Figs. 7.6(a-b) and 7.7(a-b).*

7.2.2. Rectangular Notches with Rounded Corners ($s/\rho > 1$)

The distribution of the normalised maximum principal stress (the tangential stress), obtained by the finite element analysis, on the surface of a rectangular

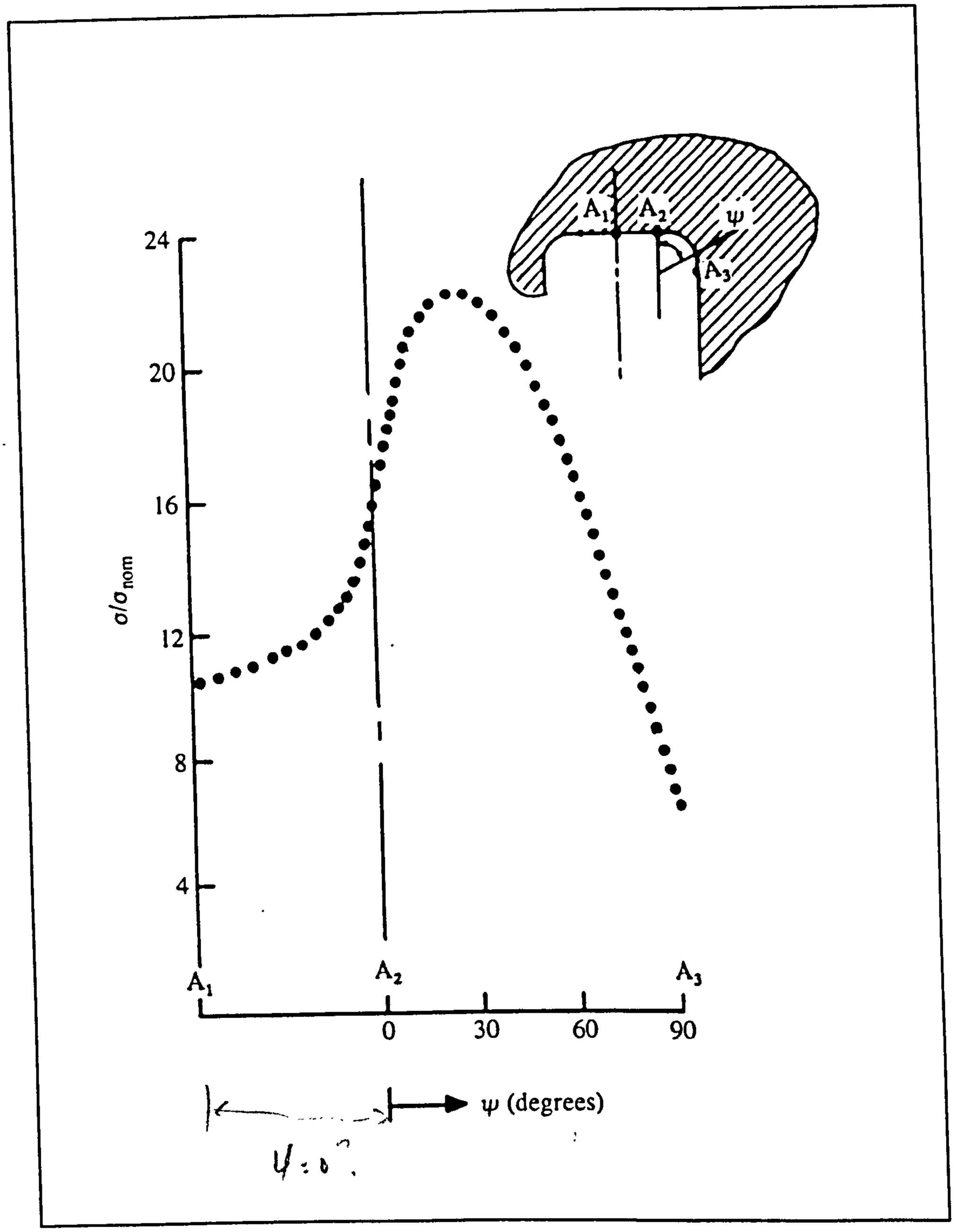

Fig. 7.9. The variation of normalised surface tangential stress with position (see inset drawing) for a rectangular notch with rounded corners ($s/\rho = 7.35 \times 10^{-4}$).

notch, with $s/\rho = 2$, is shown in Fig. 7.9; the particular results are for $s/W = 7.35 \times 10^{-4}$. The form of this stress distribution is similar to that obtained for all of the

notches with $s/\rho > 1$ which are analyzed (see Table 7.1 for details). The peak stress was always found to be in the corner radius at a position nearer to A_2 than A_3. The variation of the angular position, ψ_{peak}, at which the maximum stress was obtained, with ρ/s, is shown in Fig. 7.10. The position, ψ_{peak}, of the peak stress was found to be insensitive to the actual values of ρ and s and only dependent on their ratio. However, the magnitude of the peak stress, $\hat{\sigma}$, was found to increase, for any particular value of ρ/s, as ρ (or s) decreased. This is to be expected because as ρ and s tend to zero, the notch geometry approaches that of a sharp crack, for which the theoretical peak stress is infinite.

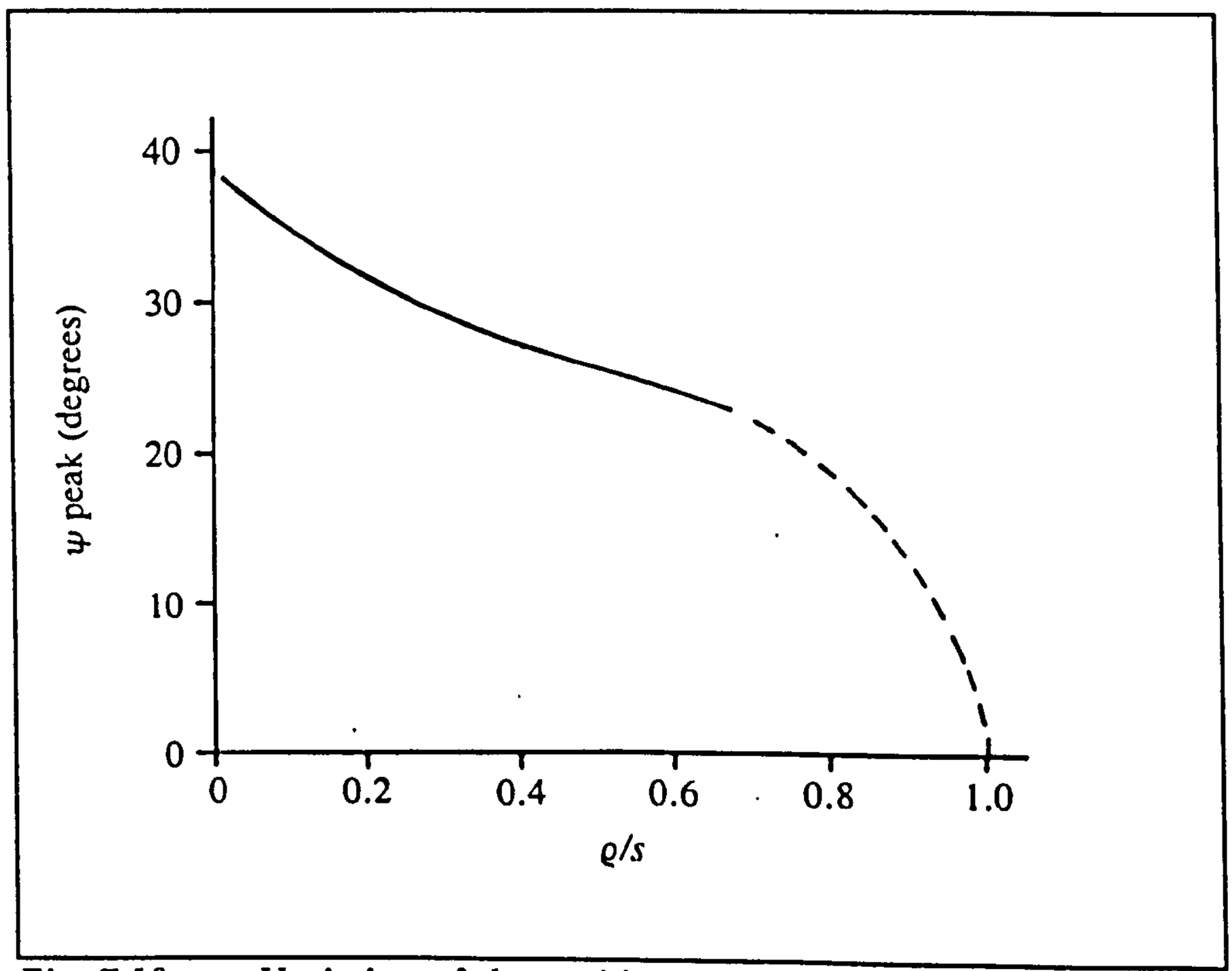

Fig. 7.10. Variation of the position at which the peak stress occurs, ψ_{peak}, with ρ/s.

Although equation (7.5) does not apply to rectangular notches with rounded corners, it was found that an effectively constant value of $\hat{\sigma}\sqrt{\rho}$ was obtained from the

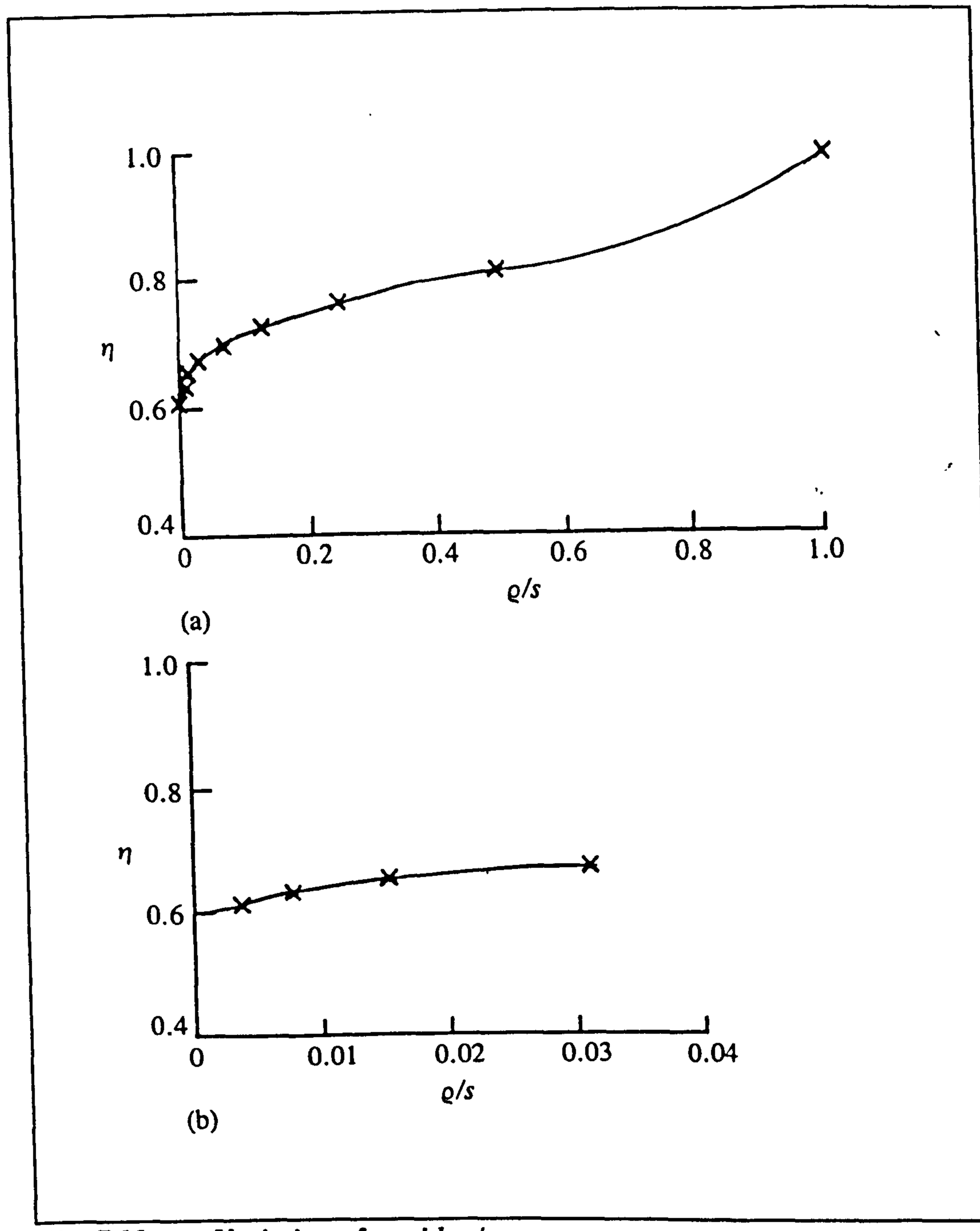

Fig. 7.11. Variation of η with ρ/s.

finite element analyses with different values of s, but with the same value of s/ρ.

These results are conveniently normalised by dividing them by $\hat{\sigma}\sqrt{\rho}$ obtained for semi-circular notches. The results are presented in Fig. 7.11, which shows the $\hat{\sigma}\sqrt{\rho}$ values obtained from the analyses of the rectangular notches with rounded (radius, ρ) corners divided by $\hat{\sigma}\sqrt{\rho}$ obtained for semi-circular notches (the ratio is given the symbol η),

each other. The σ_x/σ_{nom} distributions only converge to the same degree at a depth of about 1.6. Up to this depth the σ_x/σ_{nom} values are significantly smaller that the corresponding σ_y/σ_{nom} values. This general behaviour is similar for all the rectangular notches defined in Table 7.1.

Finite element contours joining points which have the same value of maximum principal stress are shown in Figs. 7.13(a)-(e) for a range of s/ρ values with $s/W = 1.47 \times 10^{-3}$. As ρ decreases, for the same value of s, it can be seen (Figs. 7.13(a-e)) that the highest stress regions become more localised.

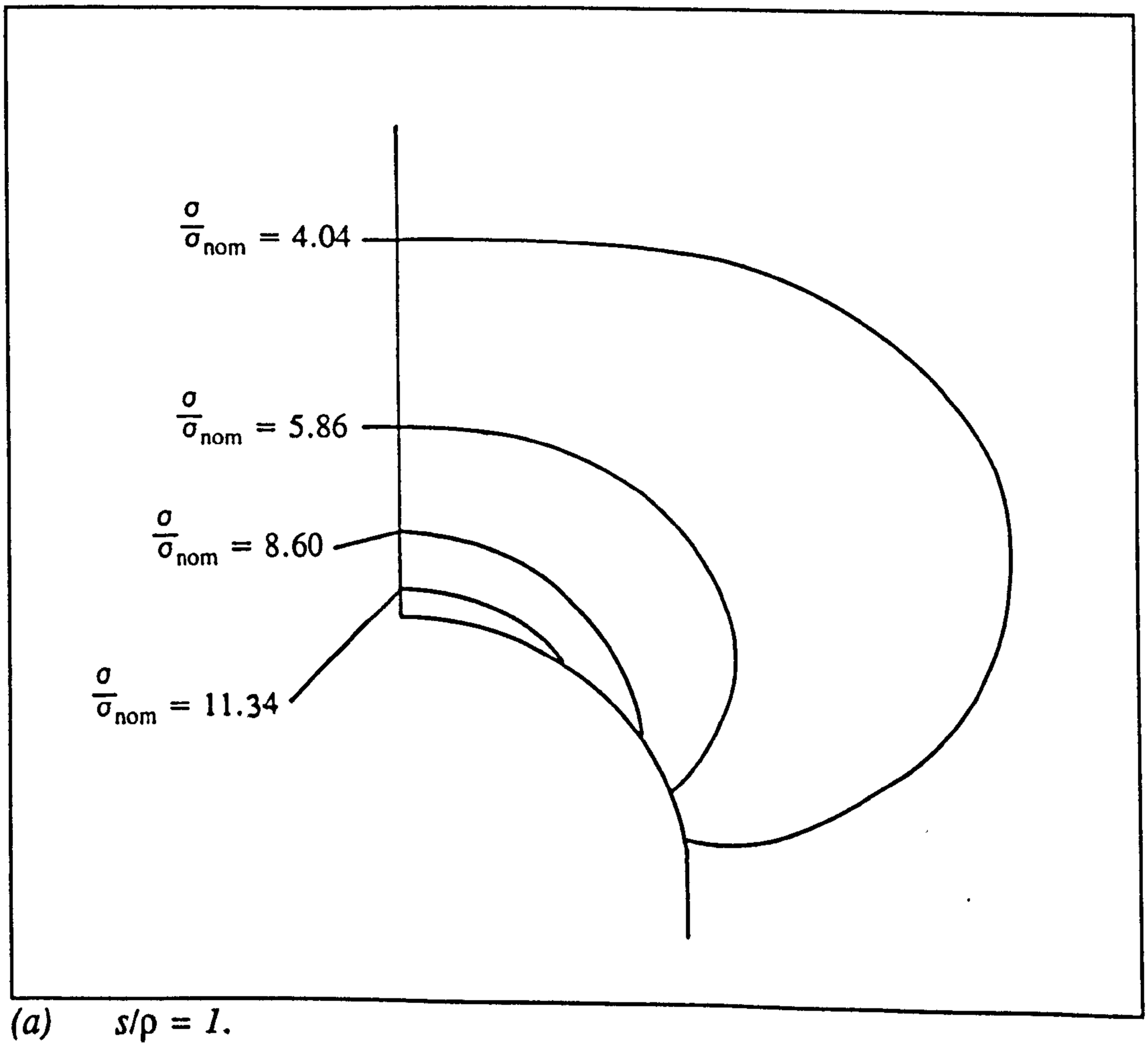

(a) $s/\rho = 1$.

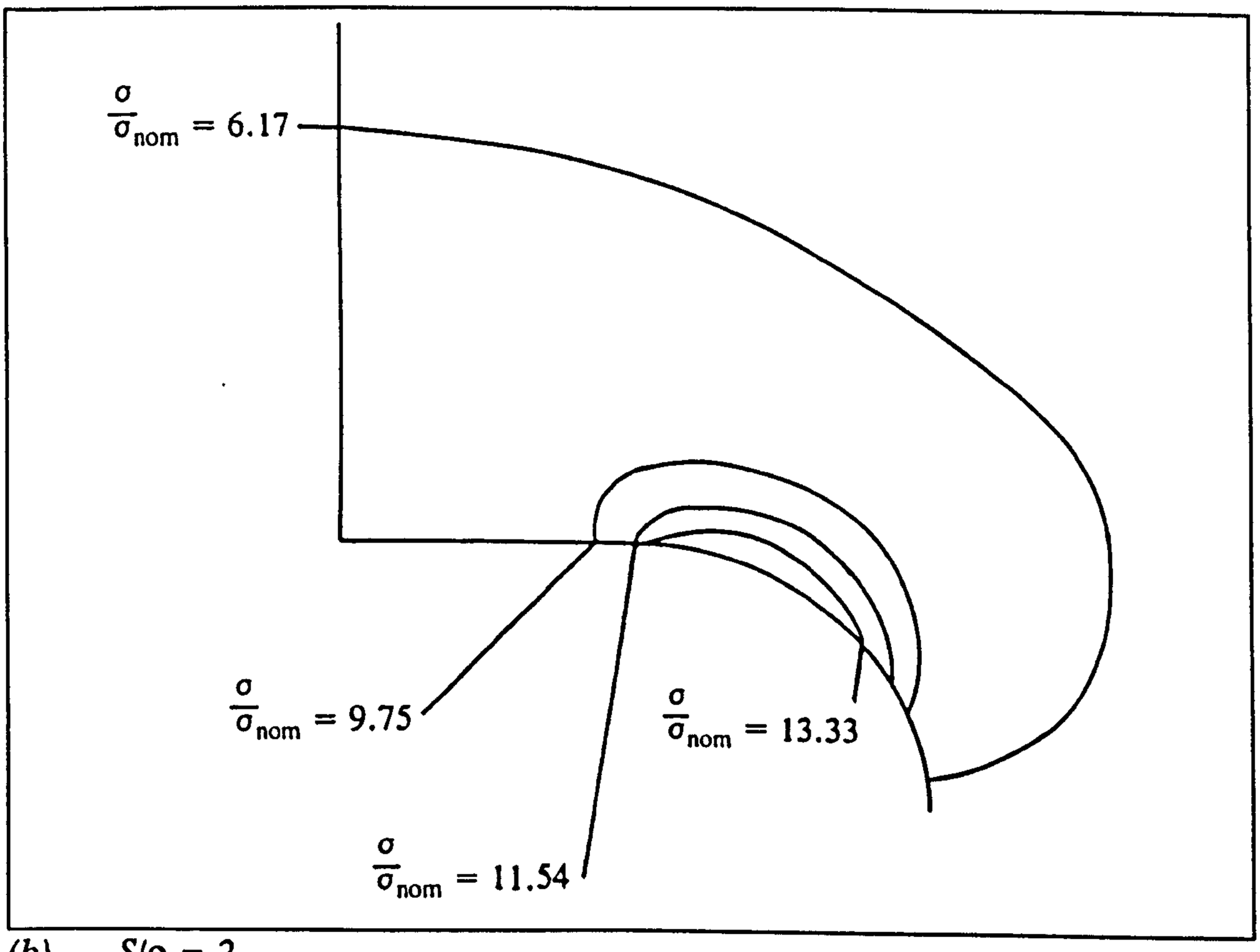

(b) $S/\rho = 2.$

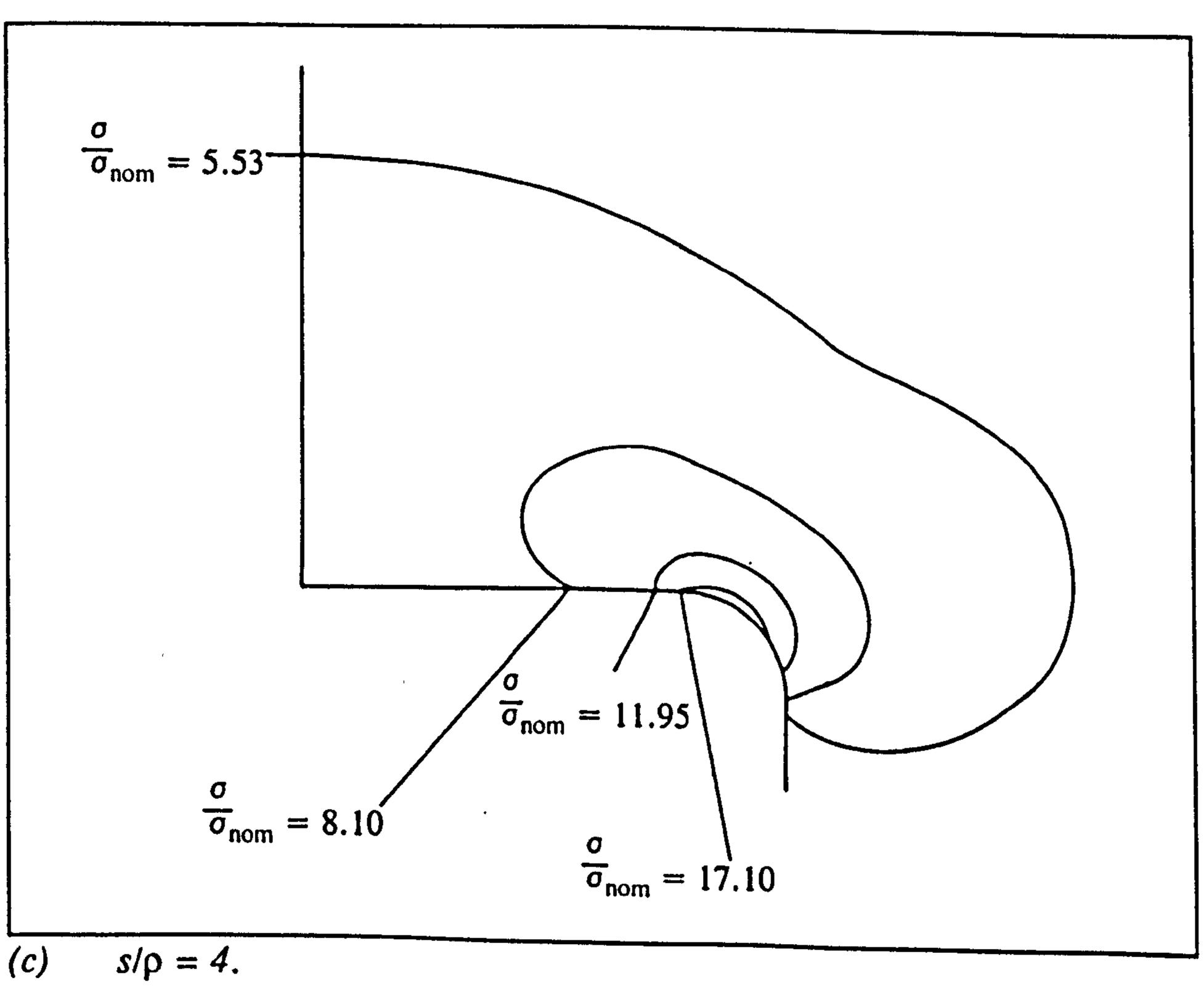

(c) $s/\rho = 4.$

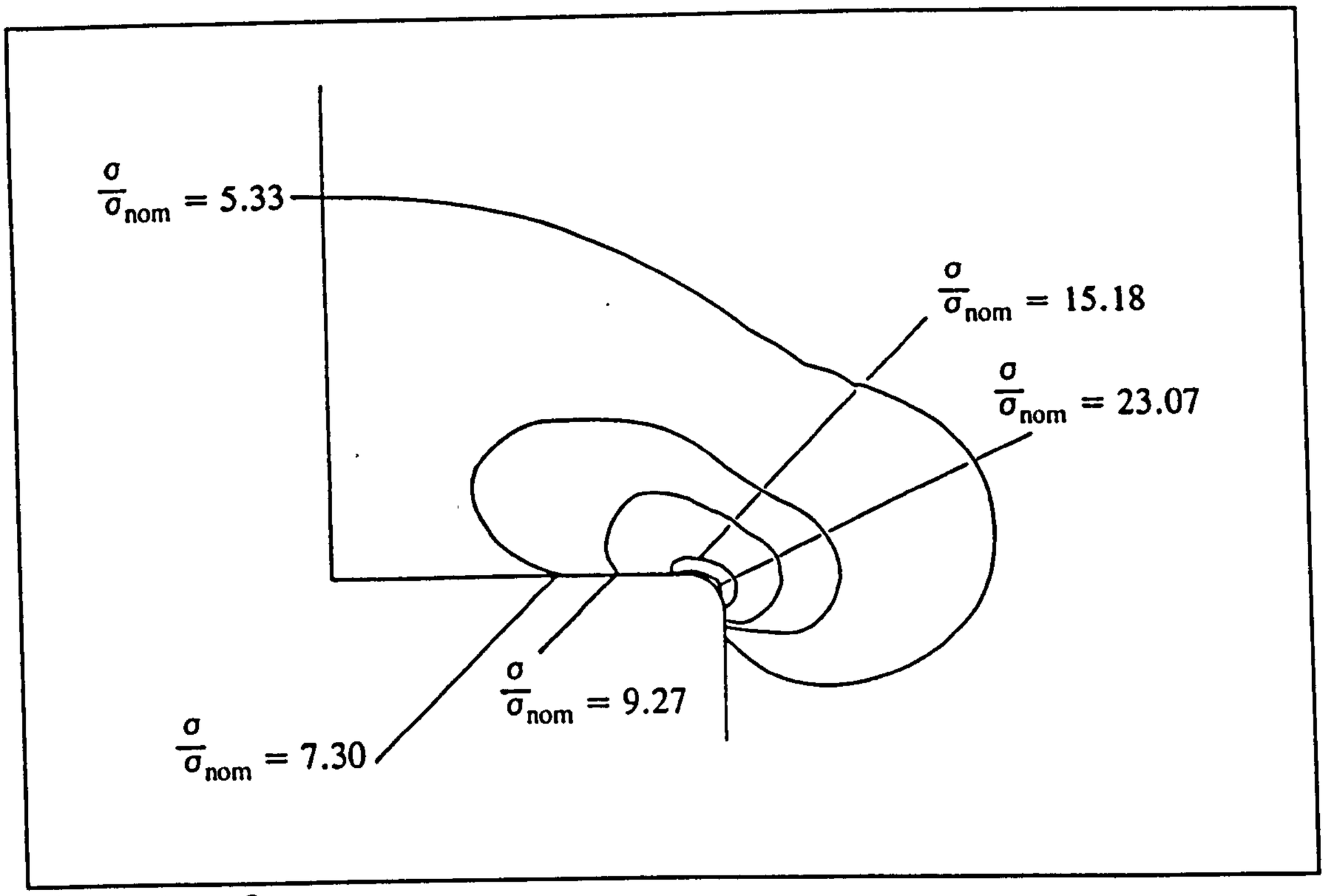

(d) $s/\rho = 8.$

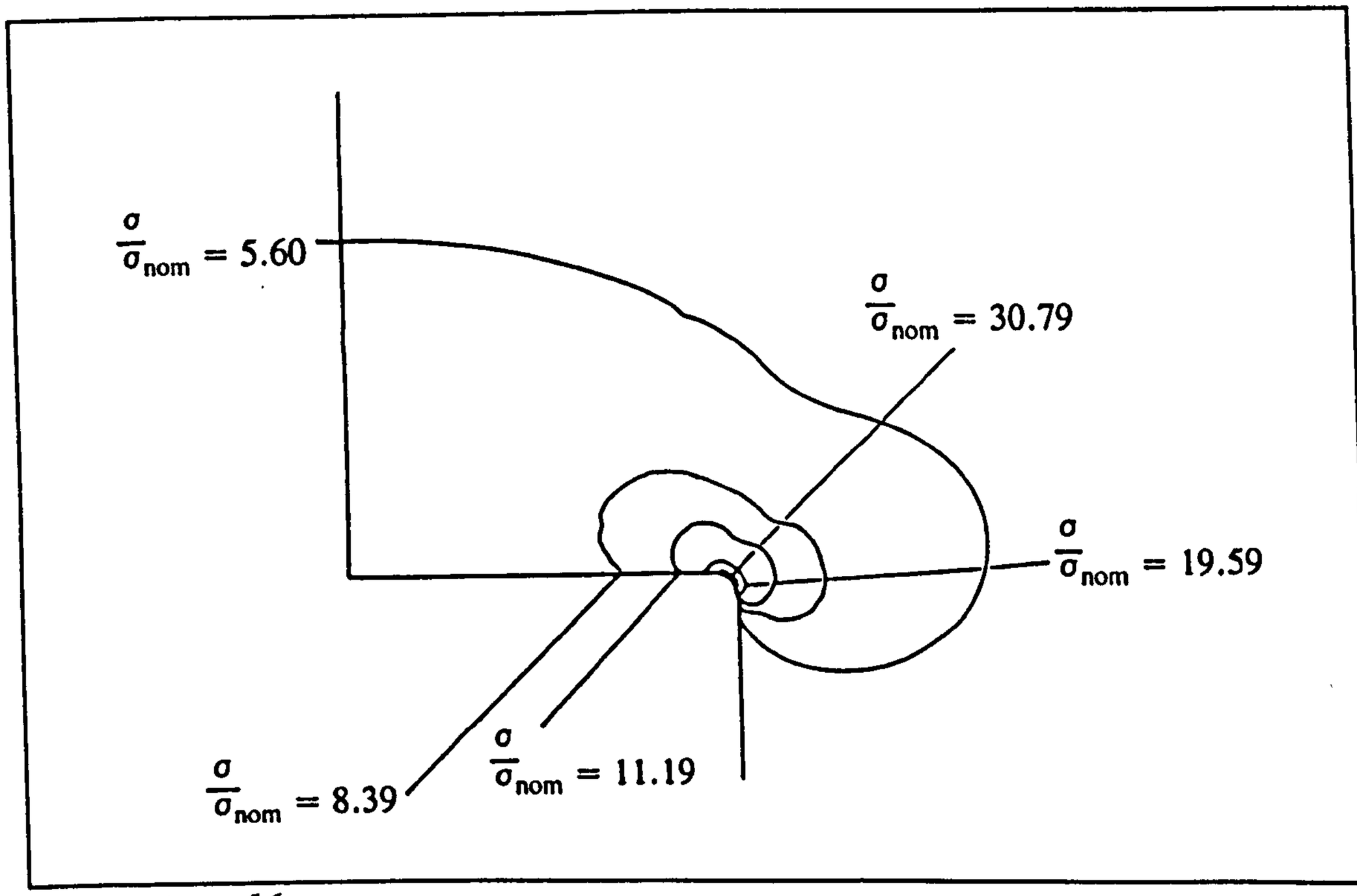

(e) $s/\rho = 16.$

Figs. 7.13(a-e). *Maximum principal stress contours for notches with $s/W = 1.47 \times 10^{-3}$, obtained by finite element analyses.*

7.3. Discussion and Conclusions

The solutions due to Creager, for elliptical and hyperbolic notches, were found to give accurate predictions of peak stress for semi-circular ended, narrow cut-outs, approaching the shape of a crack. In the finite element analyses a bending stress distribution was produced whereas Creager's solution is for a uniform applied stress field. Thus the agreement implies that only the local, nominal stress field affects the stresses near the ends of the sharp notches. Hence Creager's solutions can be applied in other loading situations and also, the finite element solutions for the rectangular notches with rounded corners ($s/\rho > 1$) as well as those for semi-circular notches ($s/\rho = 1$), can be applied in loading situations other than the bending case for which they were derived. Thus the stress concentration factor data presented in this paper can be used to predict the stresses in combined bending and tension situations provided the appropriate stress field can be determined. The above argument applies to mode-I loading. Mode-II and mixed-mode loading will be discussed in the next chapter.

For a wide range of geometries containing cracks, stress intensity factors (in terms of loads, component and crack dimensions), K_I, have been determined [e.g. 37, 82, 83 and 84]. The peak stresses at the tips of semi-circular notches can be obtained by using equation (7.5) (i.e., $\hat{\sigma} = 2K_I/(\pi\rho)^{1/2}$). For rectangular notches with rounded corners, the peak stresses can be determined from the result for a semi-circular notch together with the results presented in Fig. 7.11. Hence the peak stress is obtained from the value of the stress intensity factor for an equivalent crack, equation (7.5) and Fig. 7.11. Also, the position of the peak stress, ψ_{peak}, can be obtained for any value

of ρ/s from Fig. 7.10.

CHAPTER EIGHT

MIXED-MODE FINITE ELEMENT ANALYSIS

In the previous chapter, a method for determining the stresses in narrow rectangular notches with rounded corners, in beams in bending, was presented. Initially, the mode-I stress intensity factor, K_I, for the equivalent crack is obtained [76]. Then, the peak stress, $\hat{\sigma}$, for a narrow rectangular notch, having semi-circular end, with radius ρ, is obtained using the equations derived by Creager and Paris [79] for elliptical and hyperbolic notches, i.e. $\hat{\sigma} = 2K_I/(\pi\rho)^{1/2}$, where ρ is taken to be the radius of curvature at the tip of the elliptical or hyperbolic notches. Finally, a notch shape factor, η, is used to modify the peak stress for a semi-circular ended notch; the shape factor, obtained from the results of finite element analyses, depends exclusively on the ratio of half the notch width to corner radius, s/ρ. This method can be used to obtain the peak stresses in components which contain narrow rectangular notches with rounded corners, provided the notch is subjected to a purely opening mode of loading and that the mode-I stress intensity factor for the equivalent crack in the same component can be obtained. Since stress-intensity factor solutions exist for a wide range of cracked geometries [e.g. 37, 82, 83 and 84], peak stresses for a wide range of rectangular notches can be easily determined.

The above method is successful for an opening mode of loading. Therefore an extension of the method has been developed to deal with the more general case of components containing rectangular notches with rounded corners, subjected to shear as well as opening loading. This is the subject of this chapter.

As in the case of opening loading modes, for which stress solutions exist for various shapes of cut-outs in plates and pressure vessels, including rectangular cut-outs with rounded corners [e.g. 3, 33, 34, 35 and 36], some solutions exist for shear loading of components with cut-outs [e.g. 36]. However, less data exist for the shear loading case. In both the opening and shear loading cases, the results which exist are not applicable to very narrow cut-outs. Creager's solution [79] for the stresses in the vicinity of crack like features, with elliptical or hyperbolic shaped ends, can be applied in a shear loading situation as well as in the opening mode case. In this case, the mode-II stress intensity factor, K_{II}, for the equivalent crack, is required, as well as the mode-I stress intensity factor.

In this chapter, the finite element method has been used to obtain the stress distributions near narrow rectangular notches, with rounded corners, under opening and shear loading modes, with s/ρ ratios in the range 1 to 256. By superposition of the stress distributions of the pure opening and pure shear loading, the positions and magnitudes of the peak stresses can be determined for any combination of the two loading modes. The magnitudes of the opening and shear loading stresses at the notch tips are characterised by the mode-I and mode-II stress intensity factors for an equivalent crack, i.e. K_I and K_{II}. This is similar to the approach used in the previous

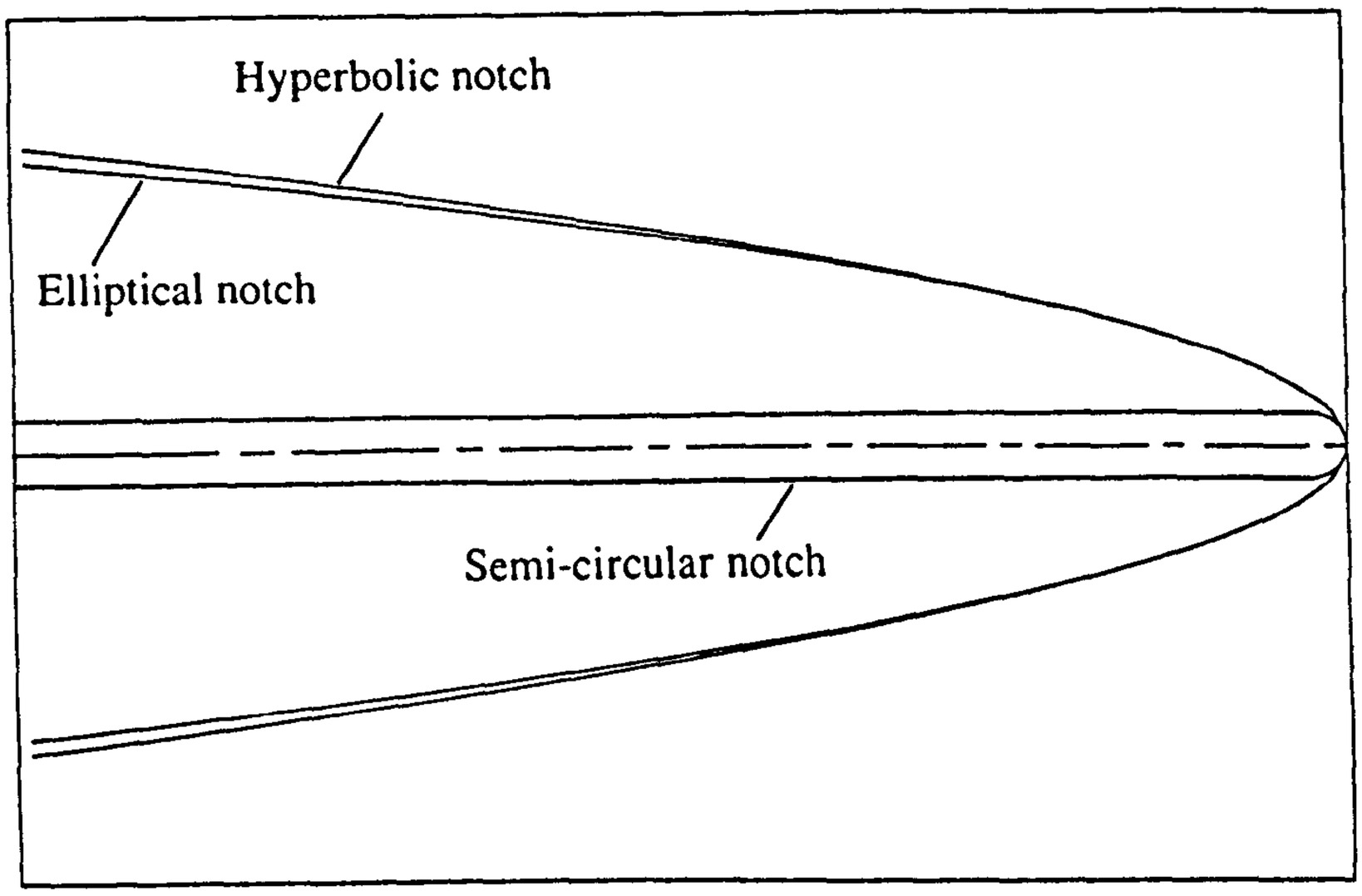

(a) General view.

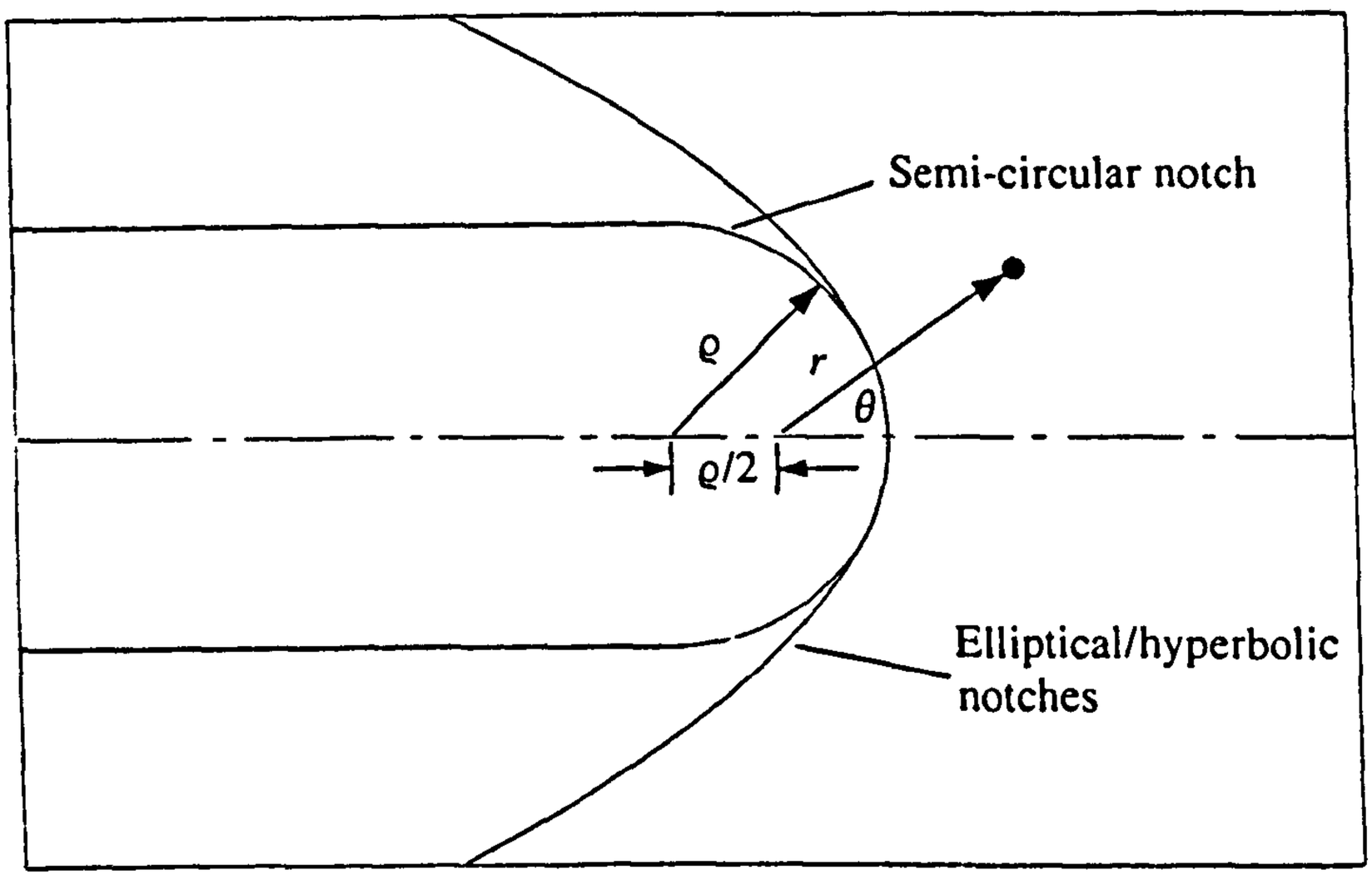

(b) Notch tip view.

Fig. 8.1. Comparison between the semi-circular, elliptical and hyperbolic notches, with the same radius of curvature, ρ, at the notch tip.

chapter for a pure opening mode situation, where the peak stress for a semi-circular

notch could be obtained from Creager's solution [79] which was derived for elliptical and hyperbolic notches. The prediction accuracy of the peak stress in this case is due to the peak stress occurring on the line of symmetry (see Fig. 8.1) where the local geometry in all cases is characterised by the tip radius, ρ. Under mode-II conditions, the peak stresses do not occur on the line of symmetry. Hence, the radial distance from the origin, as defined by Creager and Paris [79], (see Fig. 8.1), to the peak surface stress position, for the semi-circular notch and for the hyperbolic or elliptical notches, is significantly different. This results in the magnitude of the peak stress on the surface of the semi-circular notch being significantly different from Creager's theoretical prediction under mode-II conditions; preliminary finite element calculations showed this to be the case. Hence, unlike the pure mode-I case, it was found that the peak stress under mode-II conditions could not be simply obtained from an analytical solution. Therefore, an alternative method for obtaining the peak stress positions and magnitudes under pure mode-II and mixed-mode conditions is proposed.

8.1. The Geometry, Loading and Finite Element Analyses

The actual geometry used to obtain the finite element results is not particularly important since the results are presented in terms of the mode-I and mode-II stress intensity factors, K_I and K_{II} respectively. Hence the results can be applied to any narrow rectangular notches, with rounded corners, provided the K_I and K_{II} values can be determined for the equivalent crack in the same component. However, an experimental investigation, carried out in parallel with the finite element study, was conducted on the compact mixed-mode (CMM) specimen (chapter 6) shown in Fig.

8.2. Therefore, the CMM specimen was chosen as the component to be used to obtain mode-I, mode-II and mixed-mode finite element results for narrow rectangular notches with rounded corners. In addition, the finite element results for pure mode-I obtained previously and presented in chapter 7 have been included in this chapter.

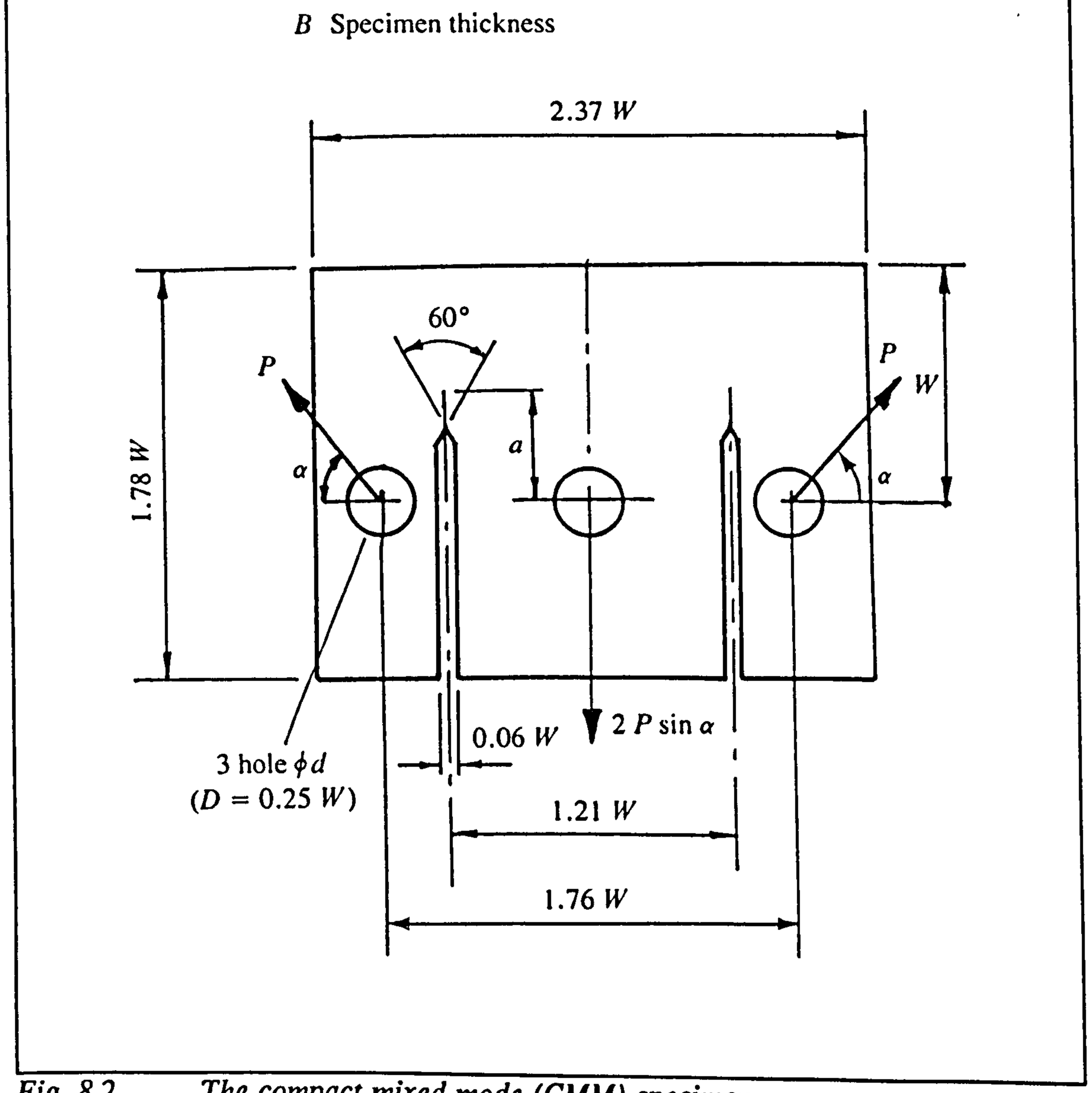

Fig. 8.2. The compact mixed-mode (CMM) specimen.

The CMM specimen and the relationships between either K_I or K_{II} and the component dimensions, characterised by the dimensions W, B and a, the load, P, and the loading angle, α, see Fig. 8.2, have been fully described in chapter 6. The specimen has been successfully used to investigate the fatigue, creep and creep/fatigue mode-II and mixed-mode crack growth of metallic alloys [e.g. 85, 86 and 87]. For a/W = 0.45, as used in the present investigation, K_I and K_{II} are given by [78]

$$K_I = \frac{P}{B\sqrt{W}}(7.93\cos\alpha + 2.67\sin\alpha) \qquad (8.1)$$

and

$$K_{II} = \frac{P}{B\sqrt{W}}(1.71\sin\alpha - 0.63\cos\alpha) \qquad (8.2)$$

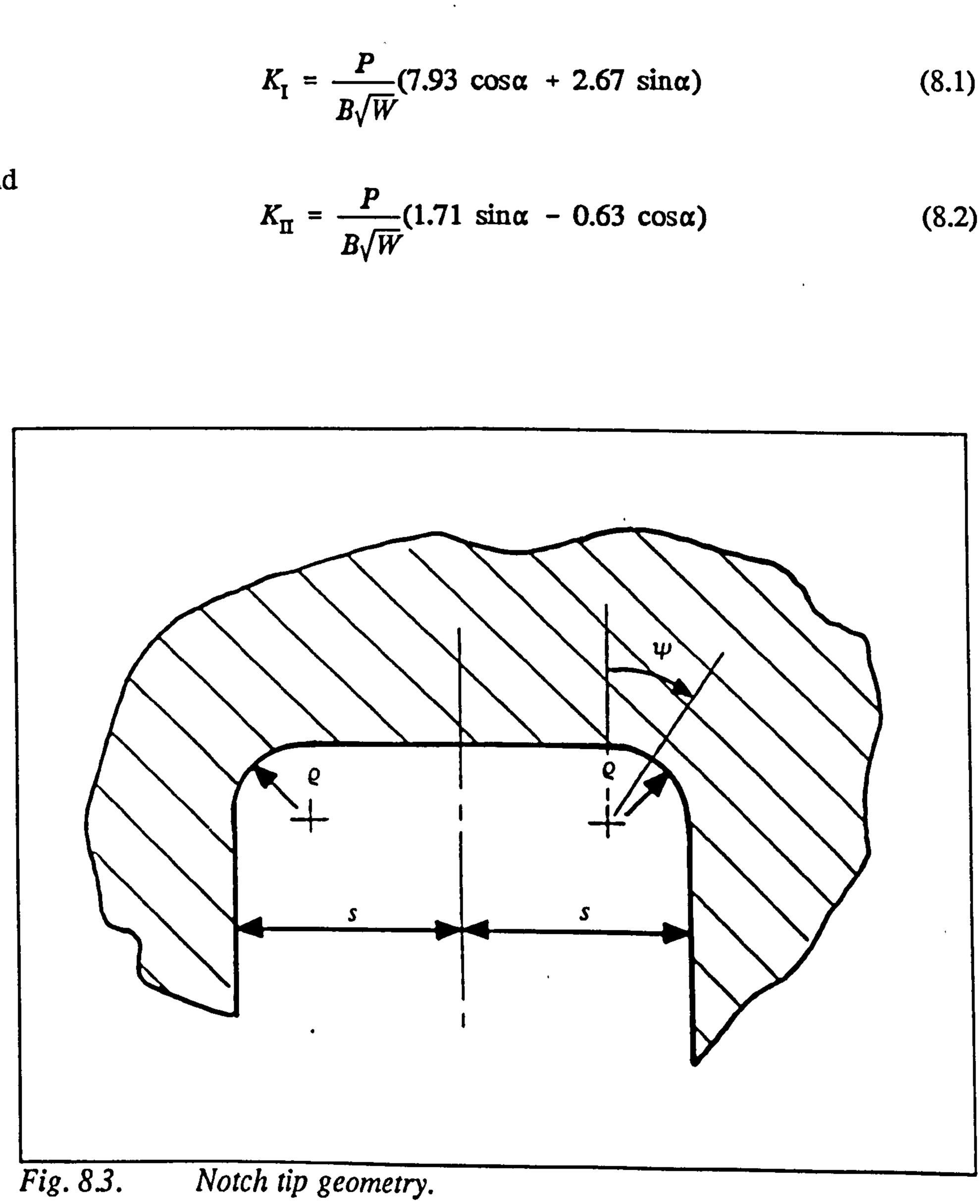

Fig. 8.3. Notch tip geometry.

The geometry at the end of the notch is shown in Fig. 8.3. It is characterised by two dimensions: the notch width, 2s, and the radius of the two corners, ρ. In this chapter, results are presented for s/ρ values in the range 1 to 256, with s/W = 7.35×10^{-4}, and for s/ρ = 1, with s/W = 2.94×10^{-3}. The study has included mainly one value of s/W since in the previous chapter it was shown that the only ratio which influenced the peak stress results for narrow rectangular notches, with rounded corners, was s/ρ. The other value of s/W was considered to reconfirm this observation for pure mode-II and mixed-mode loading conditions. Indeed, for the same value of s/ρ, the peak stress results, $\hat{\sigma}\sqrt{\rho}$, were constant to within 1%, for different values of s/W.

The finite element results were obtained using the PAFEC finite element

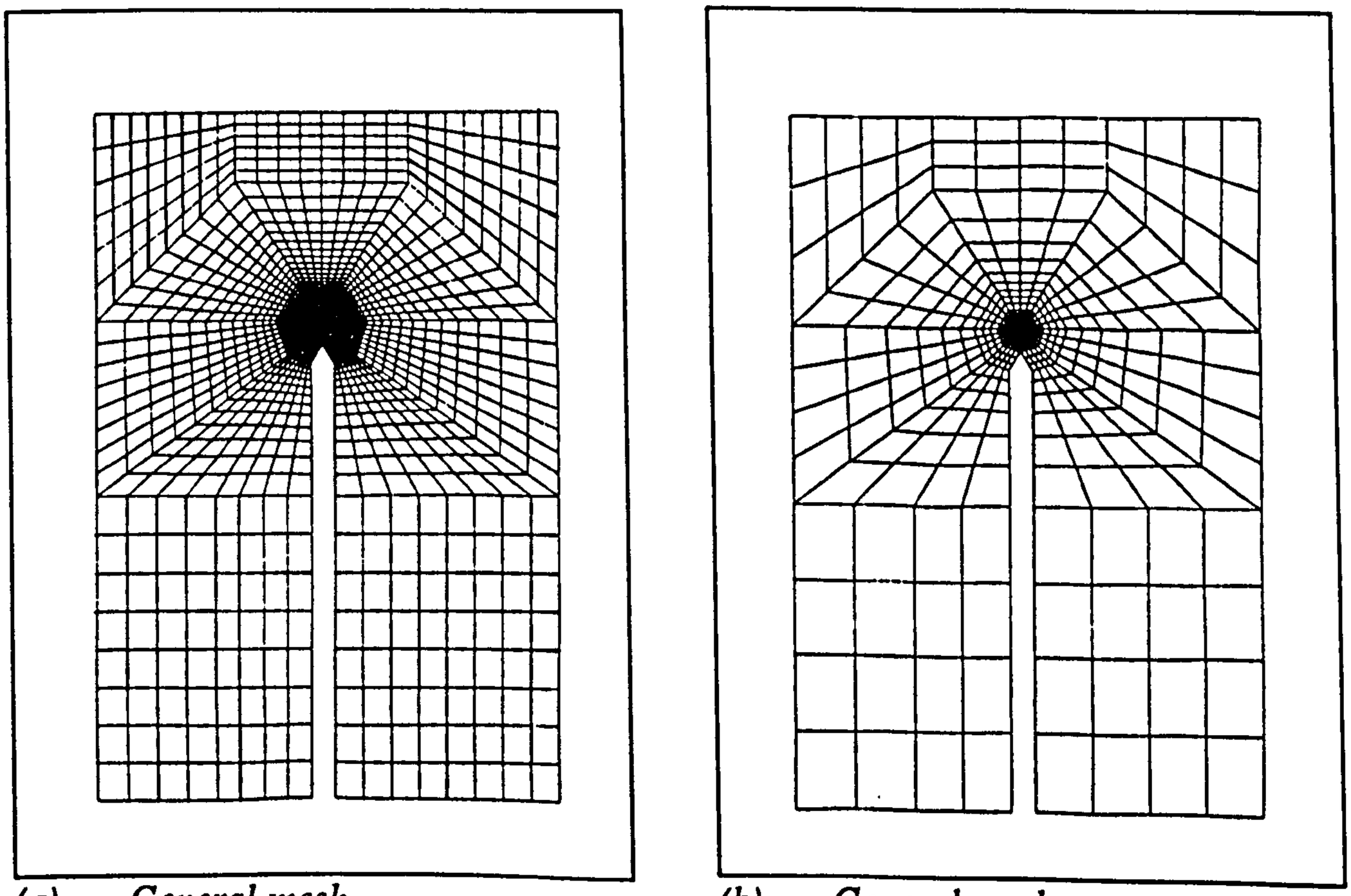

(a) General mesh.

(b) General mesh.

package [80]. Eight-noded, plane strain, isoparametric finite elements were used throughout. A symmetric half of the component was modelled; typical meshes are shown in Figs. 8.4(a-e). The suitability of the meshes was established by ensuring that stress discontinuities at corresponding nodes in adjacent elements were negligible.

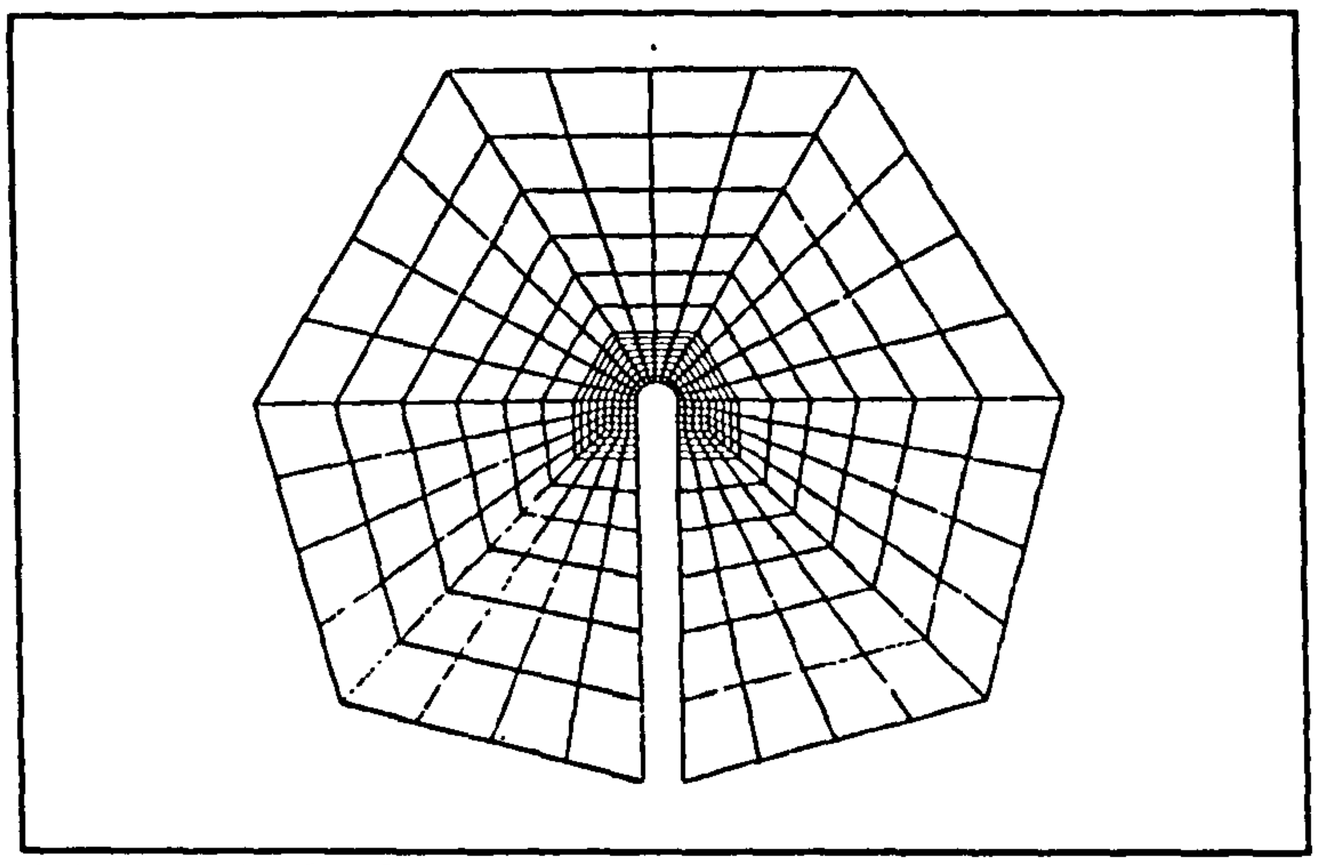

(c) Mesh close to a semi-circular notch tip.

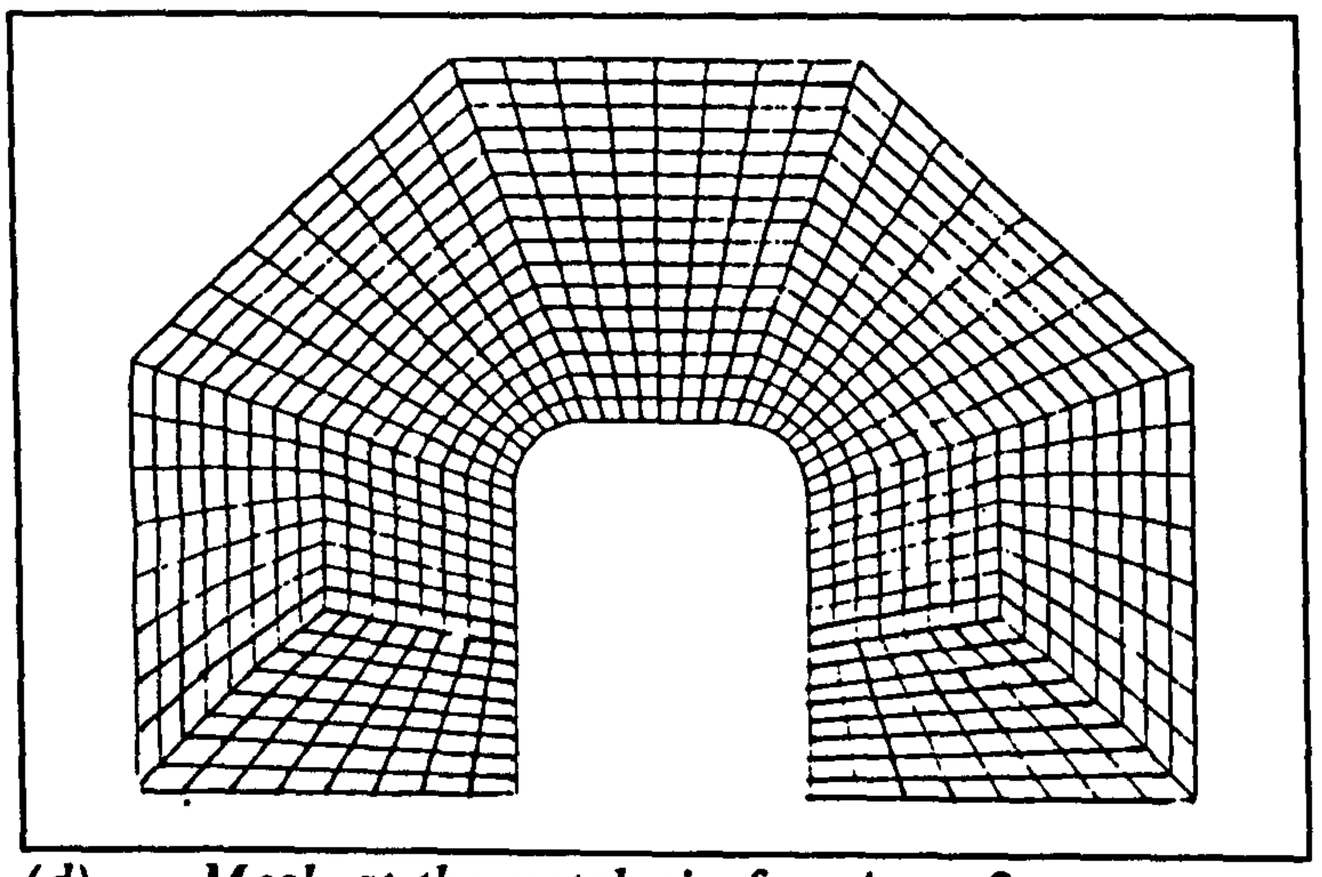

(d) Mesh at the notch tip for s/ρ = 2.

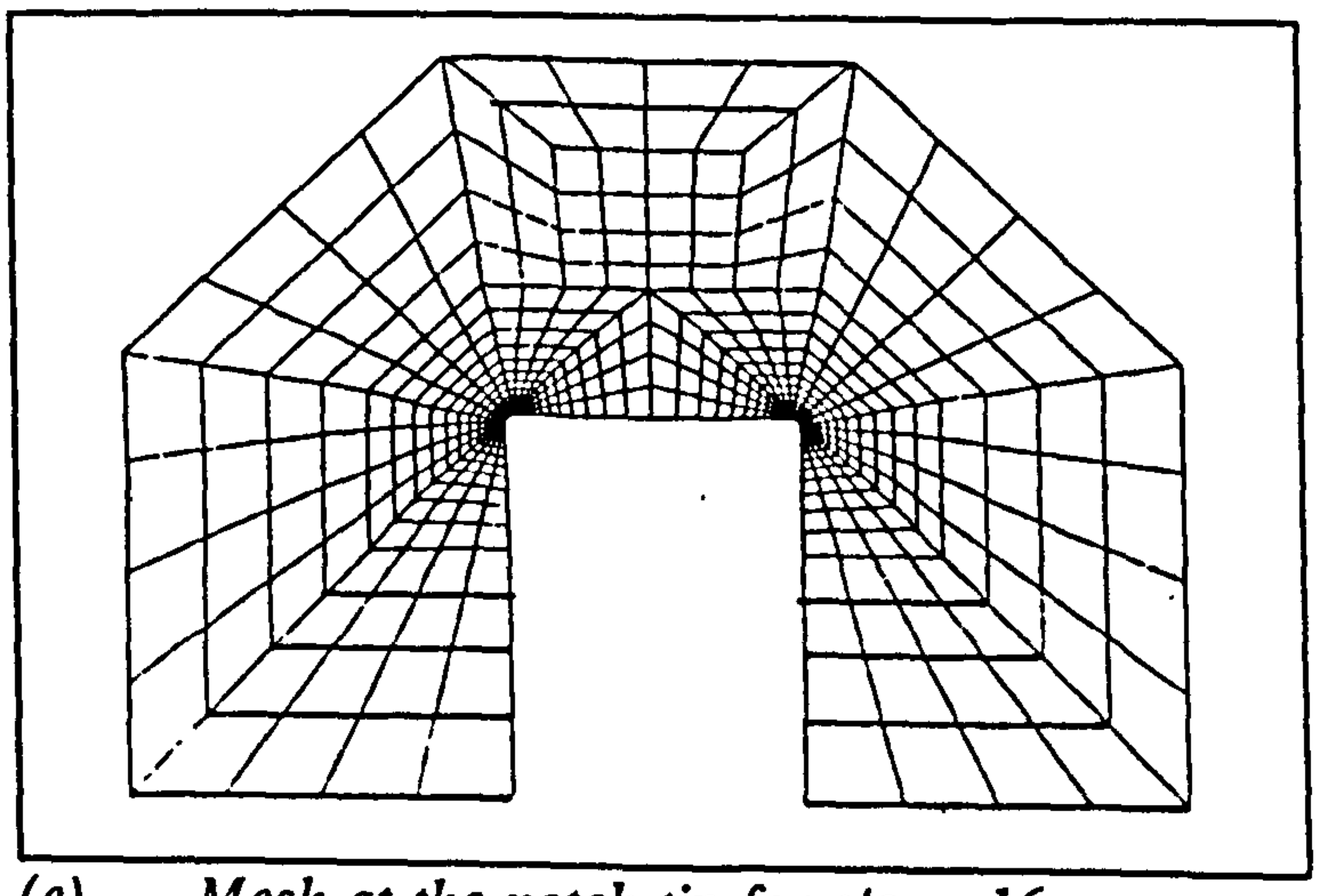

(e) Mesh at the notch tip for s/ρ = 16.

Figs. 8.4(a-e). Typical finite element meshes.

Although more sophisticated methods for determining the suitability of finite element meshes exist [e.g. 81], these were not available in the finite element package used [80]. However, if care is taken, the

relatively tedious method of checking to ensure that stress discontinuities are negligible is reliable, as have already been mentioned in chapter 7.

A total of 65 analyses were performed out of which 63 analyses were carried out with $s/W = 7.35 \times 10^{-4}$. With s/ρ values 1, 2, 16, 64 and 256, solutions were obtained for $K_I/(K_I + K_{II})$ values of 1.086, 1.041, 0.971, 0.907, 0.790, 0.610, 0.411, 0.225, 0.047, 0.001, -0.032 and -0.125. Additional solutions were obtained for $s/\rho = 1$ with $K_I/(K_I + K_{II})$ values of 1.016 and 1.001 and for $s/\rho = 2$ with a $K_I/(K_I + K_{II})$ value of 1.001.

Two of the 65 analyses were performed with $s/W = 2.94 \times 10^{-3}$ and $s/\rho = 1$, with $K_I/(K_I + K_{II})$ values of 0.411 and 0.001.

Iso-stress contours were plotted for many of the above cases. Numerous examples have been given in appendix V.

In order to complement this study, the results obtained in the previous chapter, for pure mode-I loading conditions, have been employed.

8.2. Results

The results are presented under two categories. The semi-circular notch comes first. It is followed by the rectangular notch with rounded corners.

8.2.1. Semi-Circular ($s/\rho = 1$) Notch Ends

The distributions of normalised maximum principal stresses, σ_{max}, obtained from the finite element analyses on the surfaces of the semi-circular notches (the tangential stress), with angular position, ψ, under pure mode-I and pure mode-II conditions, are shown in Fig. 8.5. The results apply for any value of s, as have

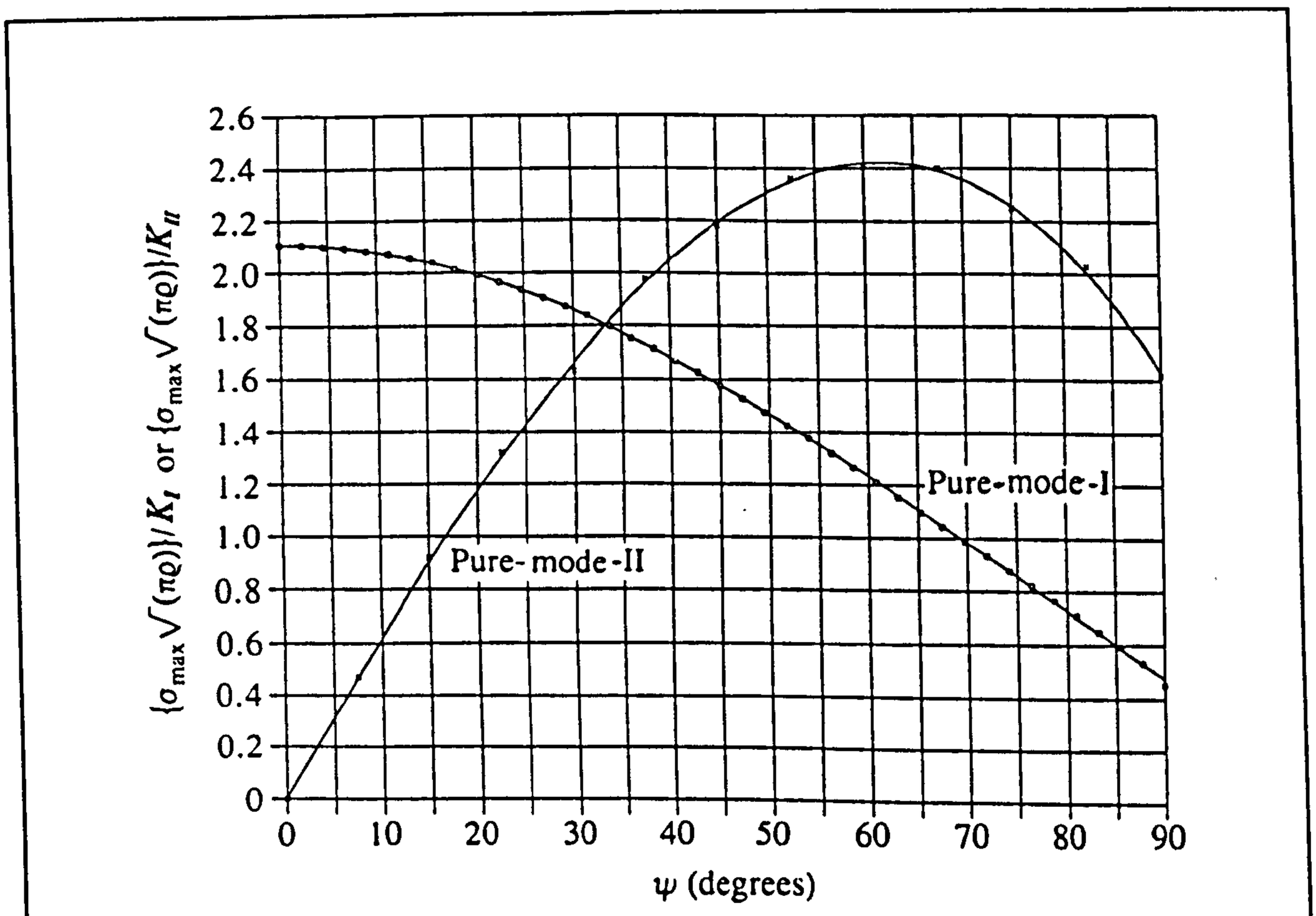

Fig. 8.5. Non-dimensional stress distributions for the semi-circular notch.

already been shown in the previous chapter and reconfirmed in this one, provided s is small in comparison to the notch length, a, and the other component dimensions (Fig. 8.2); results have been obtained for $7.35 \times 10^{-4} \leq s/W \leq 2.35 \times 10^{-2}$. The polynomial fits to the data, shown in Fig. 8.5, for mode-I and mode-II conditions, are

$$\sigma_{max}\frac{\sqrt{\pi\rho}}{K_I} = 2.107 + 5.8\times10^{-4}\psi - 3.4\times10^{-4}\psi^2 + 1.47\times10^{-6}\psi^3 \qquad (8.3)$$

and

$$\sigma_{max}\frac{\sqrt{\pi\rho}}{K_{II}} = 6.34\times10^{-2}\psi - 1.49\times10^{-4}\psi^2 - 3.94\times10^{-6}\psi^3 \qquad (8.4)$$

respectively, where ψ, the angular position in degrees, is in the range $0° \leq \psi \leq 90°$. Symmetry and skew-symmetry conditions, for mode-I and mode-II situations, respectively, can be used to obtain the appropriate values for ψ in the range $-90° \leq \psi \leq 0°$.

Equations (8.3) and (8.4) can be used for a semi-circular notch with any small radius, ρ, in any component for which K_I and K_{II} can be obtained for an equivalent crack. The resulting variations of σ_{max} values with ψ for the mode-I and mode-II load components can then be added to obtain the resultant variation of σ_{max} with ψ. In particular, the position and magnitude of the peak value of stress can be obtained. It should be noted that attempts to obtain the variations of stress with ψ, around the surface of the semi-circular notch, using the analytical solutions derived by Creager and Paris [79] gave large errors when compared with those obtained by the finite element method.

The mode-mixity is conveniently described by $K_I/(K_I + K_{II})$ because it lies between 0 and 1 for positive values of K_I and K_{II}. The variation of the position of the peak stress, ψ_{peak}, with mode-mixity is given in Fig. 8.6. The slight scattering of the finite element results about the cubic fit to them is due to the finite element peak stresses being obtained at discrete nodes of elements. Nodal points are 7.5° apart and

therefore the positions are only likely to be accurate to within about ± 4°.

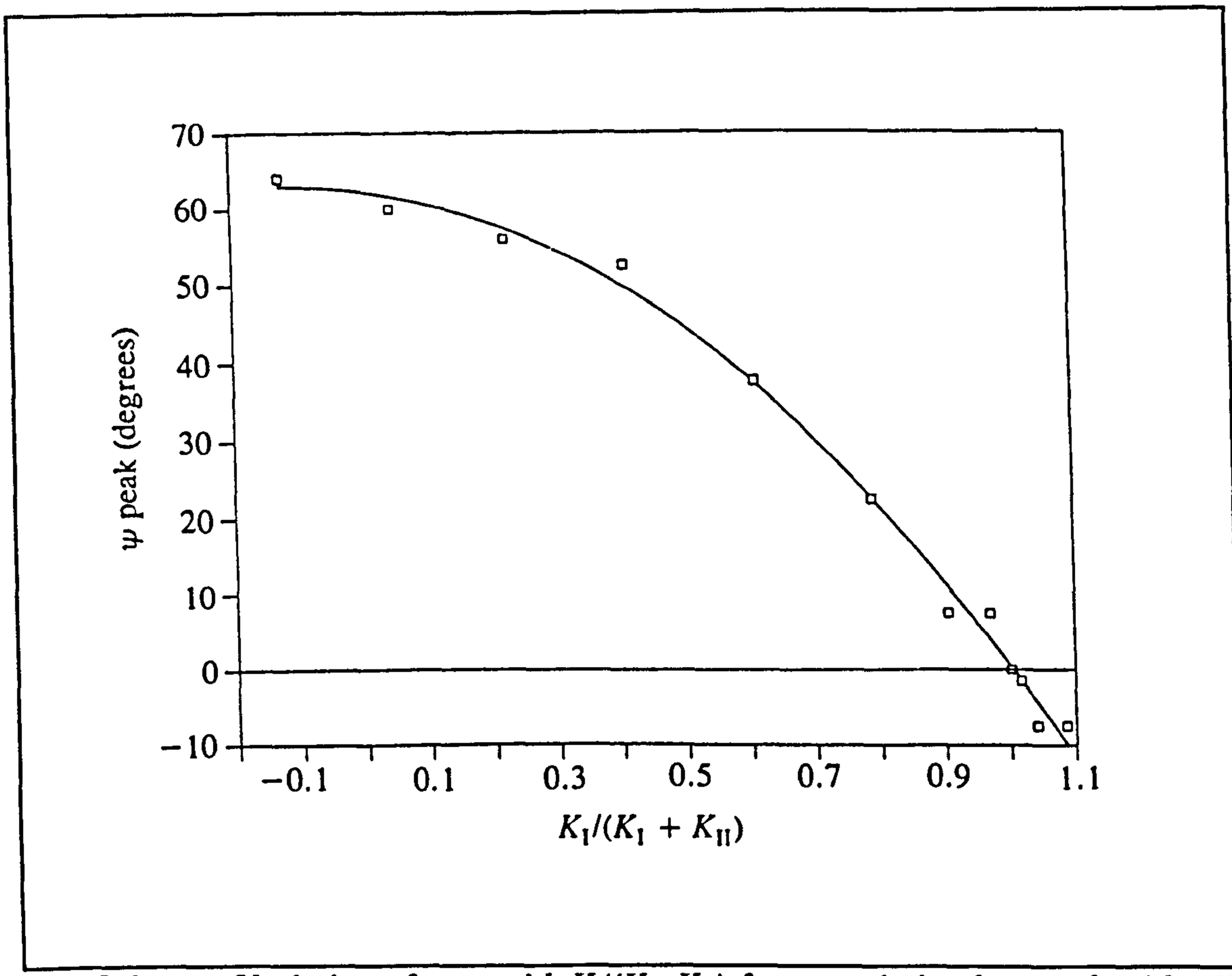

Fig. 8.6. Variation of ψ_{peak} with $K_I/(K_I+K_{II})$ for a semi-circular notch with s/W = 7.35 × 10⁻⁴.

8.2.2. Rectangular Notches with Rounded Corners (s/ρ > 1)

The distributions of the normalised maximum principal stress (the tangential stress), obtained from the finite element analyses, on the surface of a rectangular notch, with $s/\rho = 2$, for various mode-mixities, $K_I/(K_I + K_{II})$ are shown in Fig. 8.7. The stresses were conveniently normalised by dividing them by $(K_I + K_{II})$. The smooth distributions of stress obtained, together with the low stress discontinuities at element boundaries, indicate that the meshes are producing accurate results. The

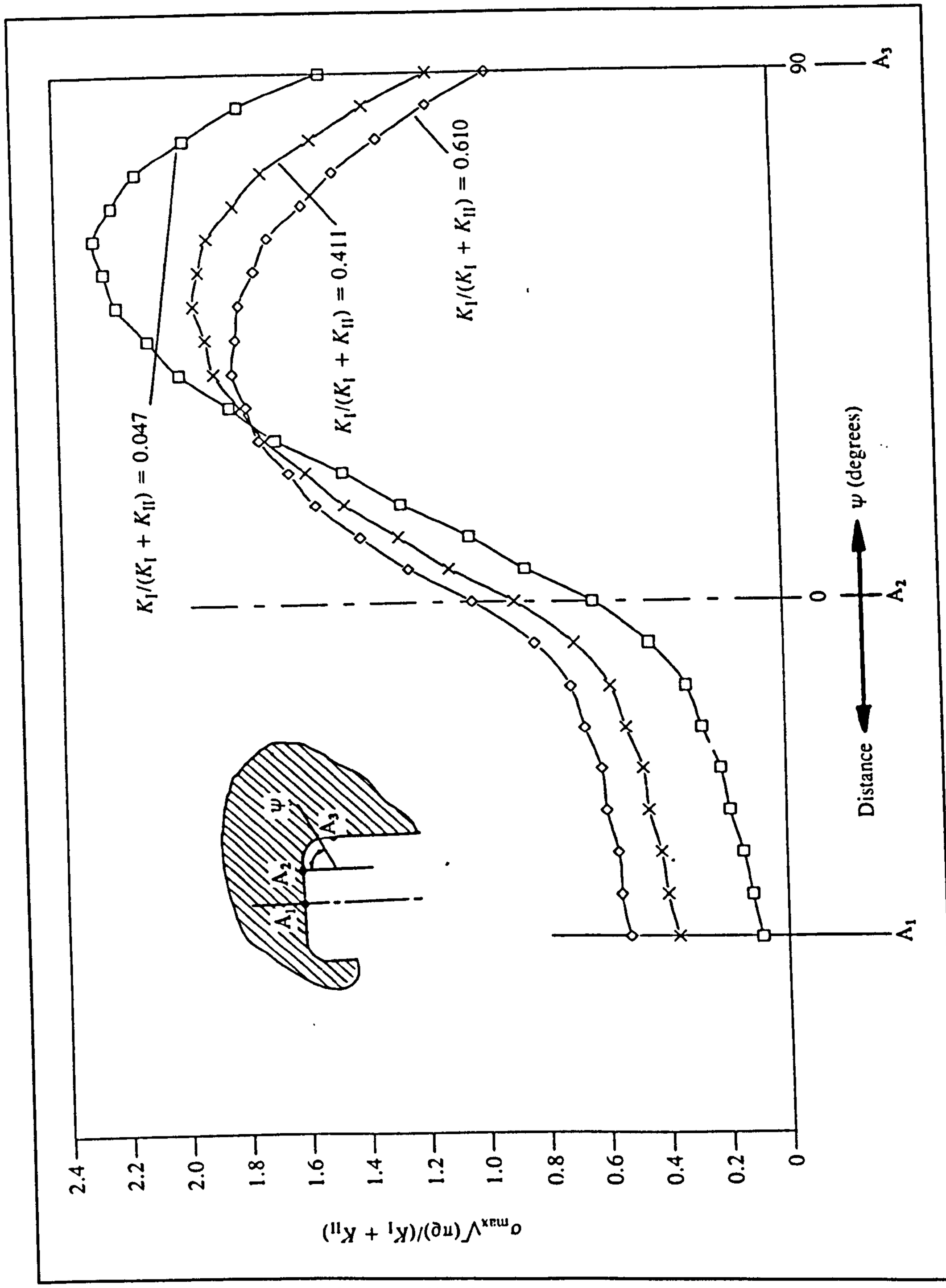

Fig. 8.7. *Variation of normalized maximum surface tangential stress with position (see inset drawing) for a rectangular notch with rounded corners in mixed-mode loading conditions; $s/\rho = 2$ and $s/W = 7.35 \times 10^{-4}$.*

forms of these stress distributions are similar to those obtained for all the other notches with $s/\rho > 1$ which were analyzed. The variations of the positions, ψ_{peak}, of the nodes having the peak stress, with mode-mixity, are shown in Figs. 8.8(a-d). Two factors affect the position and magnitude of the peak stress. These are the ratio s/ρ and the mode-mixity $K_I/(K_I + K_{II})$. However, although the position of the peak stress was found to be insensitive to the actual values of ρ and s, the magnitude of the peak stress increased for any particular value of s/ρ as ρ (or s) decreased. This is to be expected because when ρ and s tend to zero, the notch geometry approaches that of a sharp crack for which the theoretical peak stress is infinite. However, an effectively constant value of $\hat{\sigma}\sqrt{\rho}$ is obtained with different values of s, but with the same value of s/ρ under mode-I, mode-II and mixed-mode conditions.

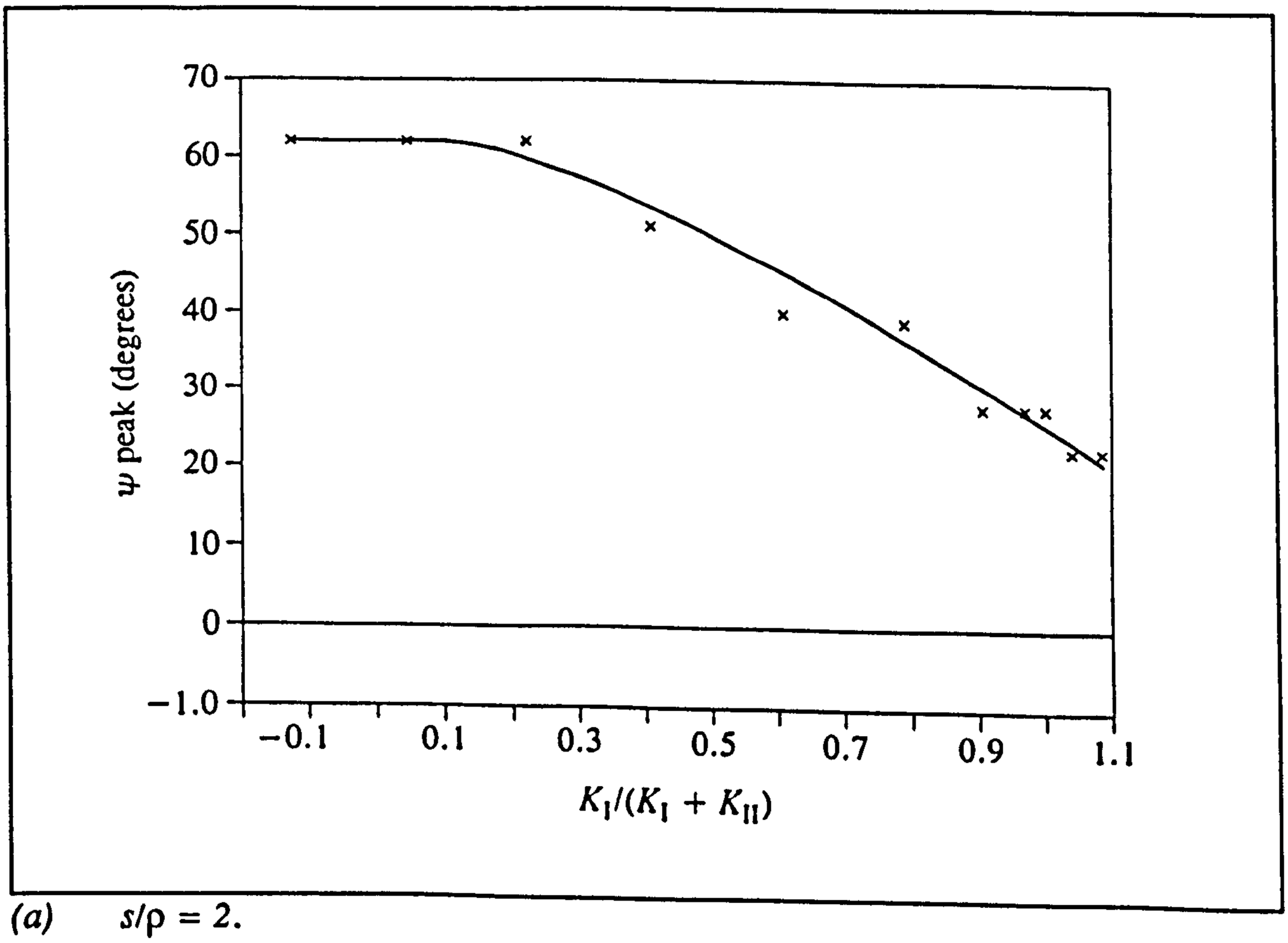

(a) $s/\rho = 2.$

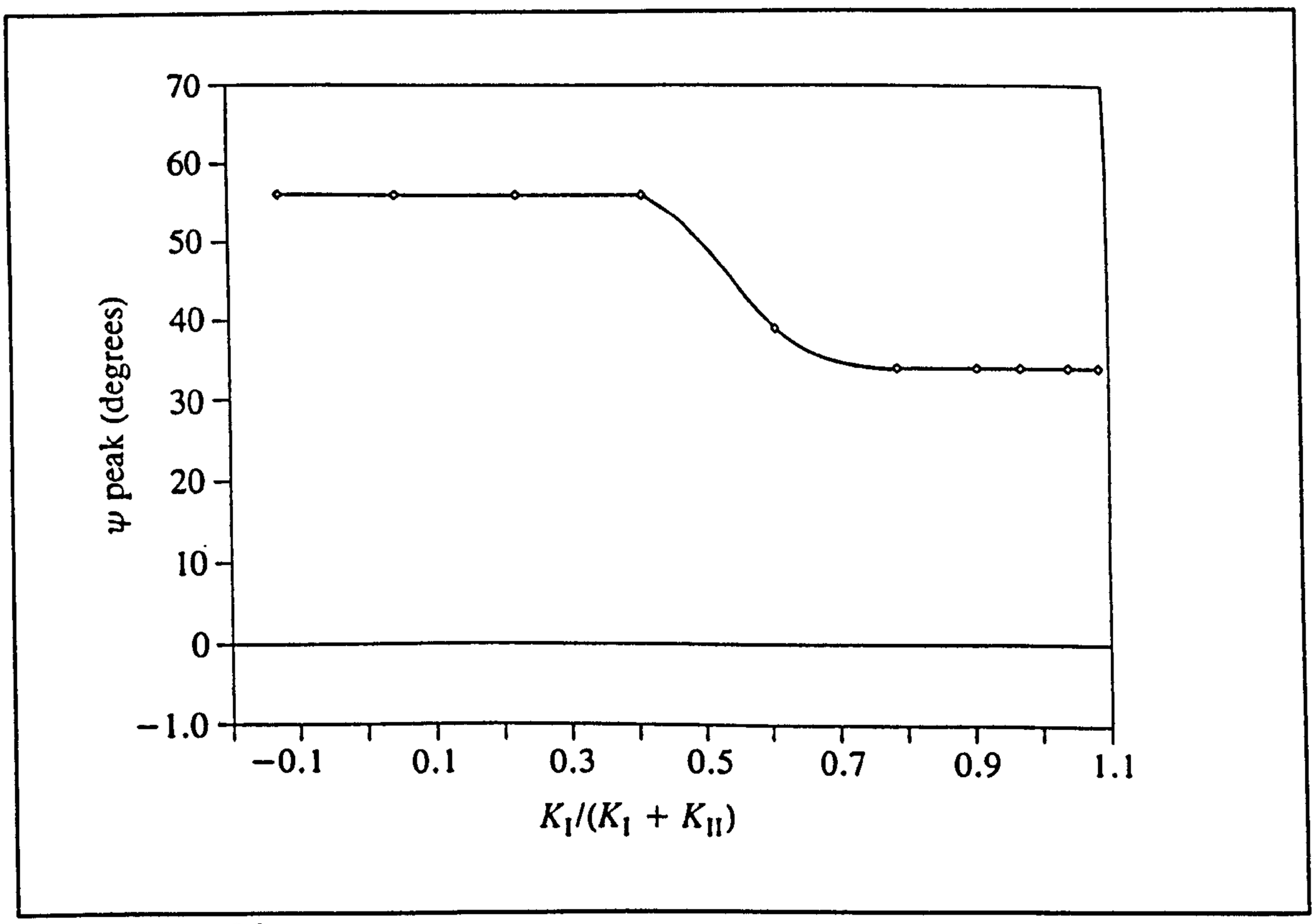

(b) $s/\rho = 16$.

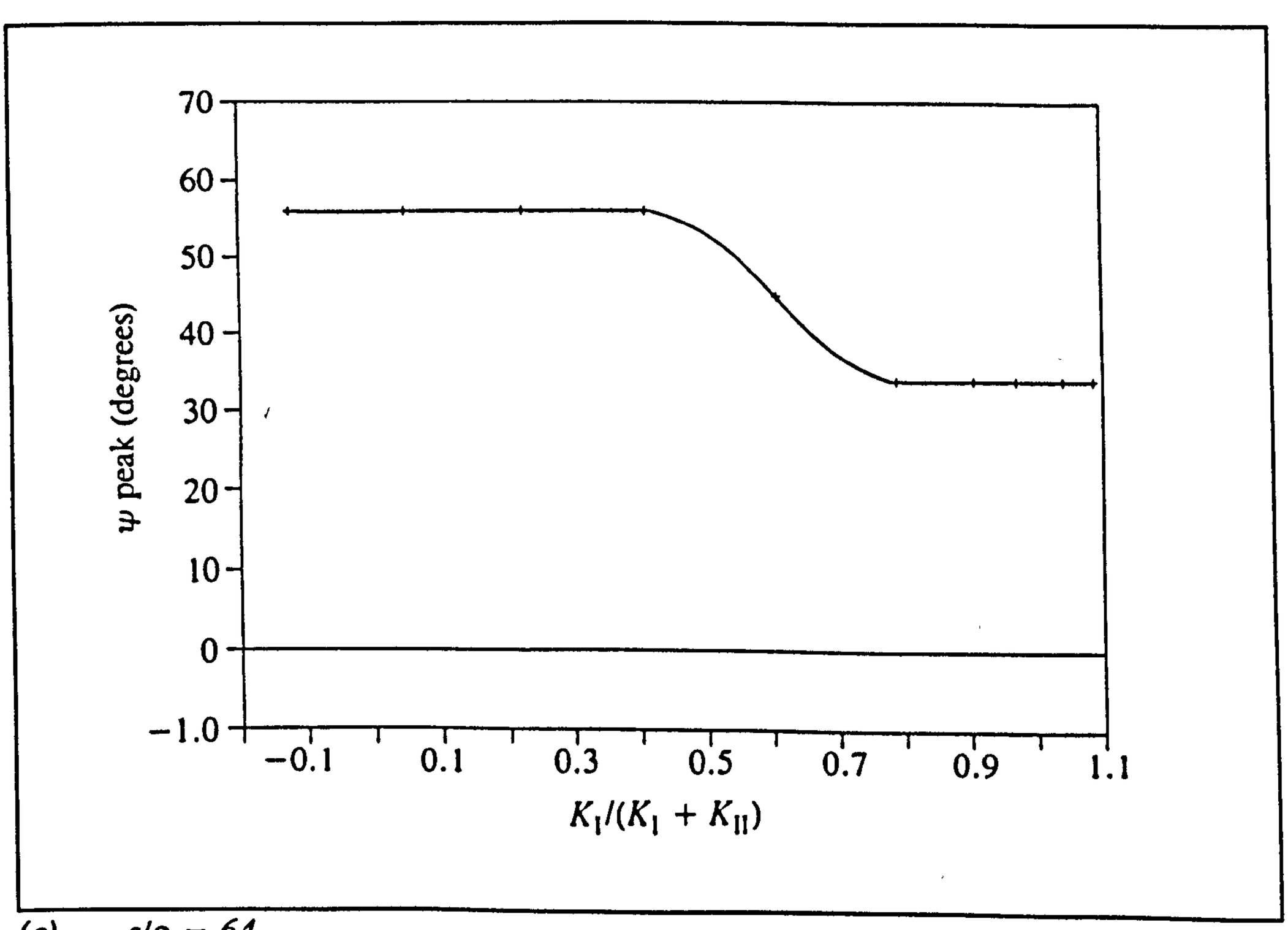

(c) $s/\rho = 64$.

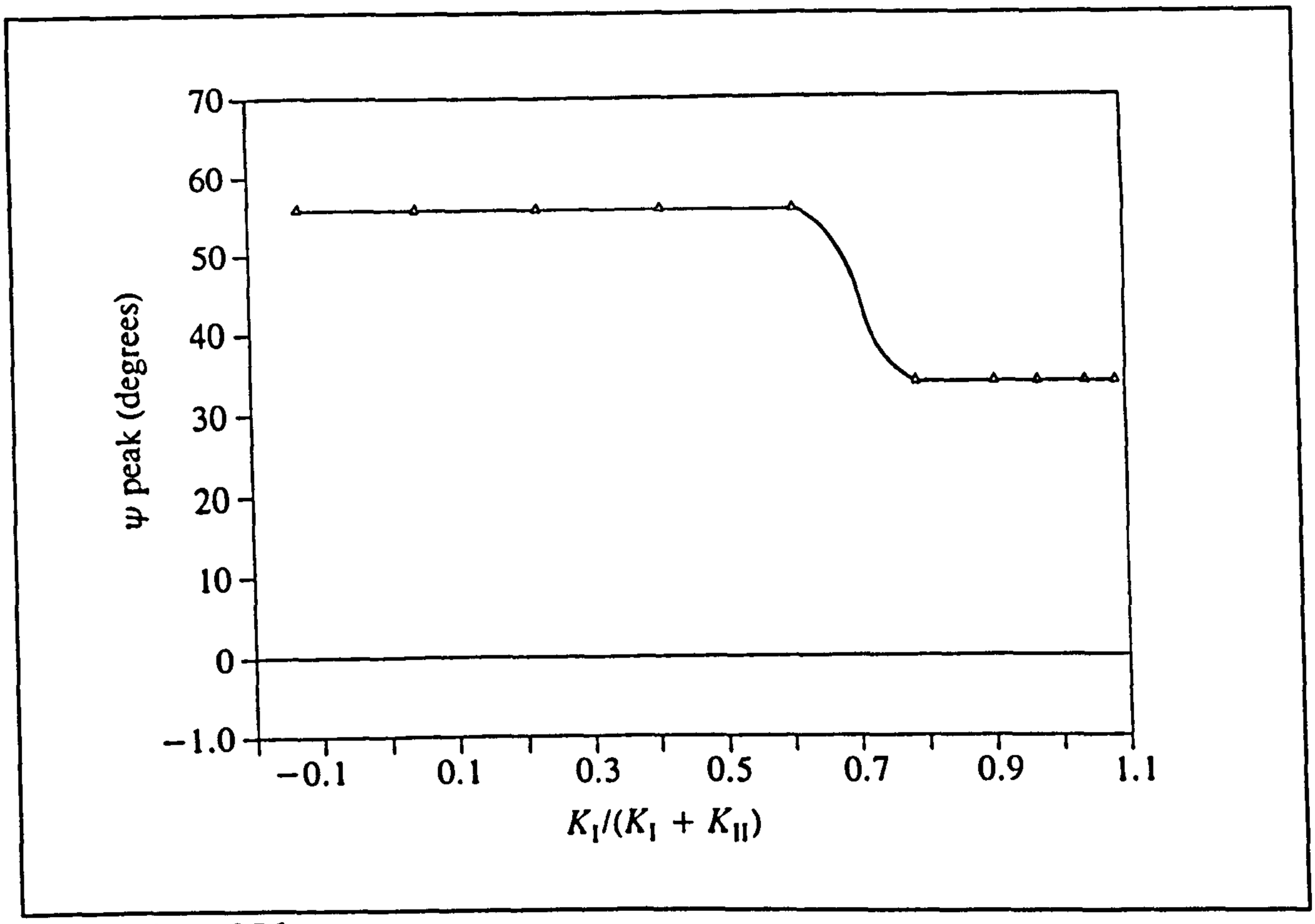

(d) $s/\rho = 256$.

Figs. 8.8(a-d). *Variation of ψ_{peak} with $K_I/(K_I+K_{II})$; $s/W = 7.35 \times 10^{-4}$.*

The $\hat{\sigma}\sqrt{\rho}$ results obtained for the narrow rectangular notches, with rounded corners, are conveniently normalised by dividing them by the $\hat{\sigma}\sqrt{\rho}$ value obtained for semi-circular notches subjected to the same mode-mixity conditions. The results are shown in Fig. 8.9, which shows the $\hat{\sigma}\sqrt{\rho}$ values obtained from the analyses of the rectangular notches with rounded (radius, ρ) corners divided by $\hat{\sigma}\sqrt{\rho}$ obtained for semi-circular notches (the ratio is given the symbol η), plotted against mode-mixity, $K_I/(K_I + K_{II})$, for various s/ρ ratios.

In order to obtain the peak stress in the case of a rectangular notch with rounded corners ($s/\rho > 1$), the procedure described in the semi-circular notch section

should be adopted, followed by multiplying the calculated $\hat{\sigma}\sqrt{\rho}$ value by the relevant value of η from Fig. 8.9. When consulting Fig. 8.9 for a value of η, the notch geometry, i.e. s/ρ, and the loading conditions, i.e. $K_I/(K_I + K_{II})$, should be known.

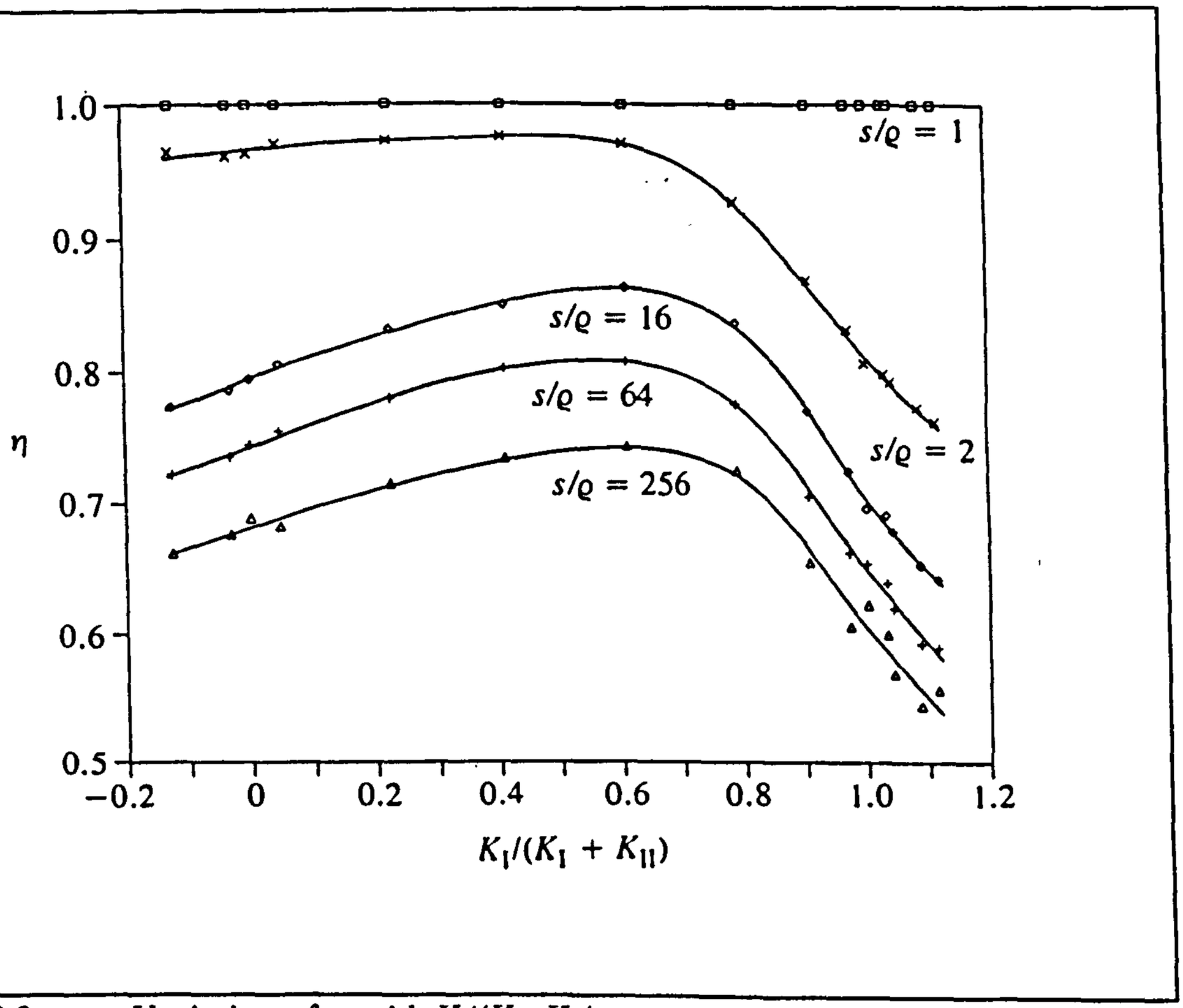

Fig. 8.9. Variation of η with $K_I/(K_I+K_{II})$.

8.3. Discussion and Conclusions

Under pure opening (mode-I) loading conditions for narrow rectangular notches, with rounded corners, it was found in the previous chapter that the stress fields, and in particular the peak stresses, in the vicinity of the notch tips, could be simply related to the local geometry, i.e. s/ρ, and to the mode-I stress intensity factor,

K_I, for the equivalent crack. In this chapter, it has been shown that under mixed-mode conditions, the peak stress is again simply related to the local geometry, i.e. s/ρ, and to the magnitudes of the mode-I and mode-II stress intensity factors obtained for an equivalent crack. First, the mode-I and mode-II stress intensity factors for an equivalent crack are obtained. The variations of the surface tangential stresses, σ_{max}, with angular positions, ψ, for a narrow semi-circular notch can be obtained by using equations (8.3) and (8.4). Fig. 8.5 is an alternative to equations (8.3) and (8.4). Superposition of these two stress distributions will allow the position, ψ_{peak}, and magnitude, $\hat{\sigma}$, of the peak stress to be obtained. Hence, the $\hat{\sigma}\sqrt{\rho}$ value for a narrow semi-circular notch with the appropriate K_I and K_{II} values can be obtained. For the mode-mixity ratio, $K_I/(K_I + K_{II})$, the information in Fig. 8.9 can be interpolated to obtain the η value for the required s/ρ ratio. From this η value and the $\hat{\sigma}\sqrt{\rho}$ value obtained for a semi-circular notch, the $\hat{\sigma}\sqrt{\rho}$ value for the narrow rectangular notch, with rounded corners (radius, ρ) can be obtained. Hence the peak stress, $\hat{\sigma}$, is determined for the particular radius, ρ, which has taken into account the important local geometry ratio, s/ρ, the local loading conditions, characterised by the stress intensity factors, K_I and K_{II}, and the actual notch size, characterised by the radius, ρ. The position of the peak stress, ψ_{peak}, is also easily obtained for an s/ρ value and mode-mixity by using Fig. 8.8.

For a wide range of geometries containing cracks, mode-I and mode-II stress intensity factors (in terms of loads, component dimensions and crack lengths), K_I and K_{II}, have been determined [e.g. 37, 82, 83 and 84]. Using these solutions for the stress intensity factors, together with the information contained in this chapter, it is

now possible to obtain the peak stresses, and their positions, in narrow, rectangular notches, with rounded corners, having any s/ρ ratio. If necessary, K_I and K_{II} values could be obtained, relatively easily, by finite element or boundary element techniques using special crack tip elements, and these single solutions could be used to obtain the peak stresses, and their positions, for narrow rectangular notches, with rounded corners, having a wide range of s/ρ ratios. The method therefore provides a cheap and efficient way of obtaining stress concentration factors.

CHAPTER NINE

PRESSURE TUBES

The static study of modelling cracks was presented in the previous chapters. This chapter investigates the dynamic side of the subject. In order to model a crack successfully and accurately, not only the period before failure should be investigated, but also those during and after failure. Attention should be given to both the direction and speed of crack propagation. Another important aspect is the phenomenon of crack branching: when and how does it occur ? All these concerns create an urge to dedicate part of the research to the dynamic side of fracture.

Bearing in mind the complexity of dynamic fracture compared to static fracture, the results and obvious conclusions are presented in this chapter, leaving the less simple matters to be approached in the tenth chapter.

9.1. Specimen

The specimen utilised to study the dynamics of fracture was the pressure tube. It was comprised of three Araldite cast cylinders glued together to form one open tube. Araldite caps were glued to both ends of the resulting tube sealing it for an

internal hydraulic pressure to be applied. The middle cylinder contained a semi-circular narrow notch, at which failure initiated during the destructive testing of the specimens - see Fig. 9.1.

Fig. 9.1. Photograph of a pressure tube prior to testing.

A diagram of the specimen is given in Fig. 9.2. The specimen included two small openings at the top, one connected to an oil pump to provide the hydraulic pressure and the other linked to a pressure gauge. The notch was always semi-circular, central, radial and parallel to the tube axis, and on the external surface of the tube. Its radius, a, had three different values: 7, 5 and 3mm (see Fig. 9.2). It had two effective thicknesses produced by two different types of shim. Both types were 0.10mm thick. One of them had a flat tip while the other had a sharpened tip producing an effective thickness of 0.02mm - see Fig. 9.3(c). Therefore, in total, there were six different notch sizes. The shape of the shim tips will be discussed in chapter 10 with particular reference to any discrepancy between straight shims used for the 3PB and CMM specimens on one hand and semi-circular shims used for the pressure tubes on the other.

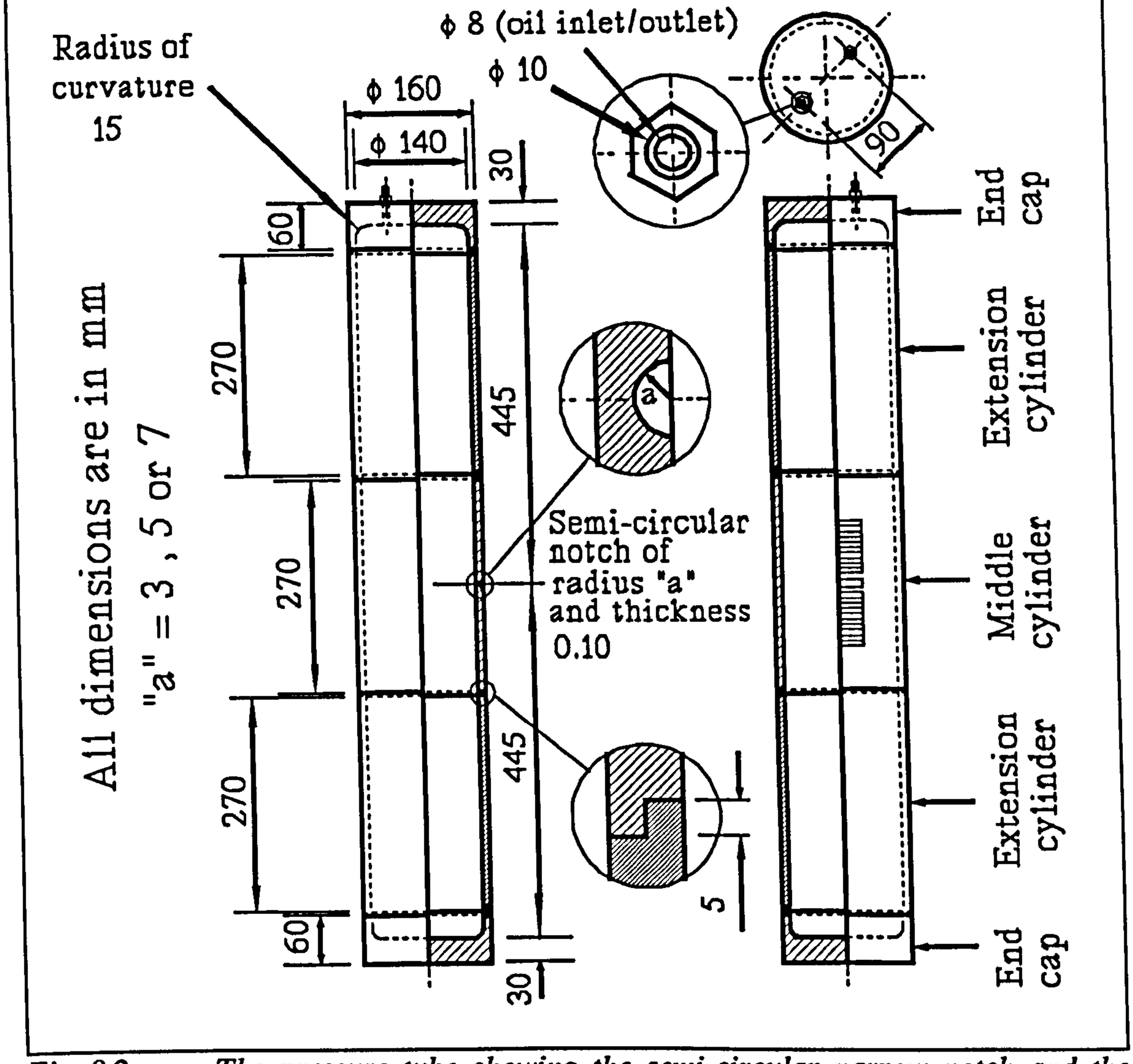

Fig. 9.2. The pressure tube showing the semi-circular narrow notch and the electrically-conductive grig.

An electrically conductive grid was painted on each specimen for the purpose of measuring crack propagation velocity. The grid and the specimen dimensions can be seen in Fig. 9.2.

9.2. Manufacture

The pressure tubes were manufactured by casting and machining the different components which were then glued together; Fig. 9.3 shows the casting moulds. The middle cylinder containing the notch was produced using the mould in Fig. 9.3(a). The extension cylinders were cast using the moulds in Fig. 9.3(b). The casting technique is described fully in section 4.2.

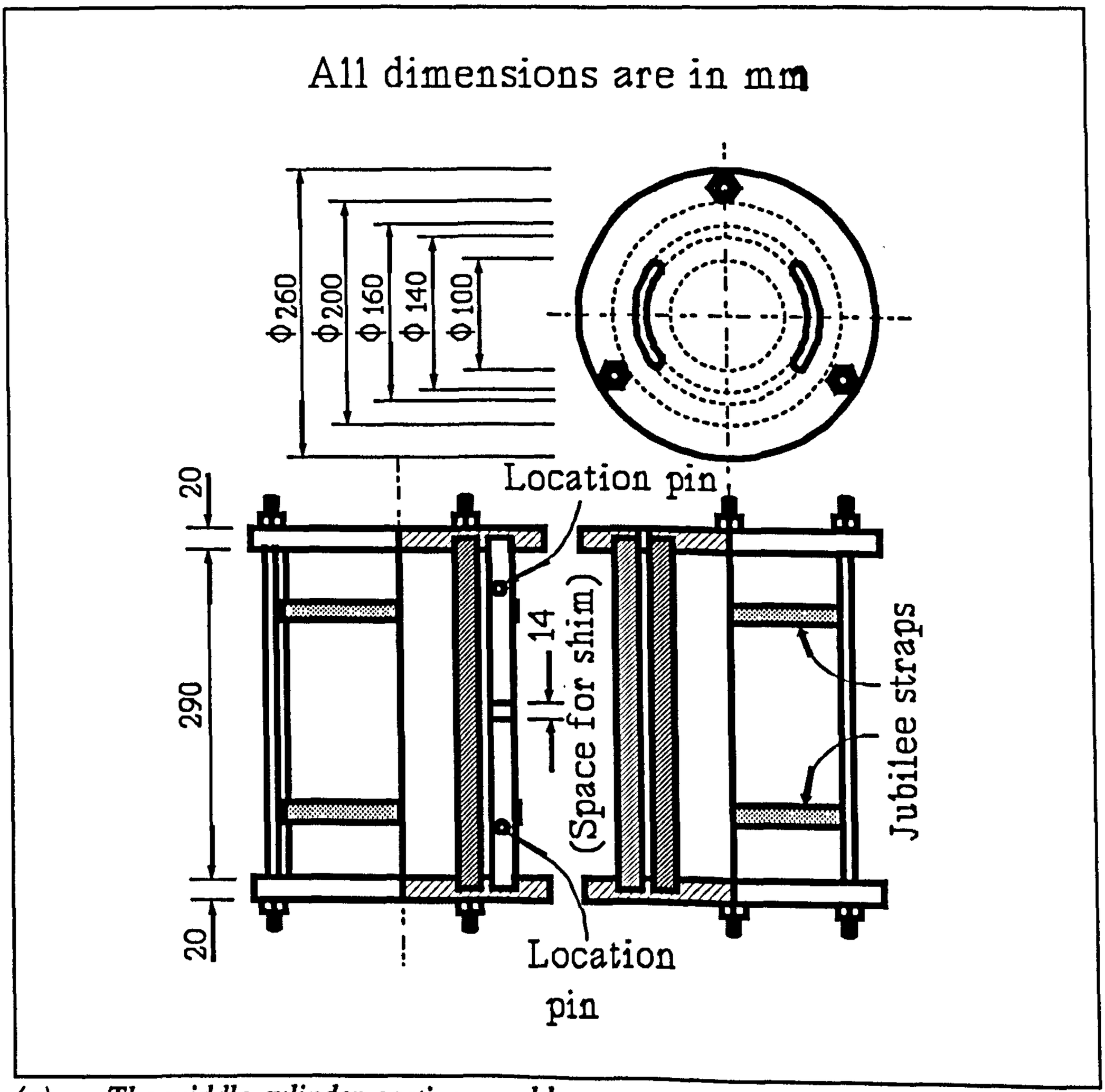

(a) The middle-cylinder casting mould.

All dimensions are in mm

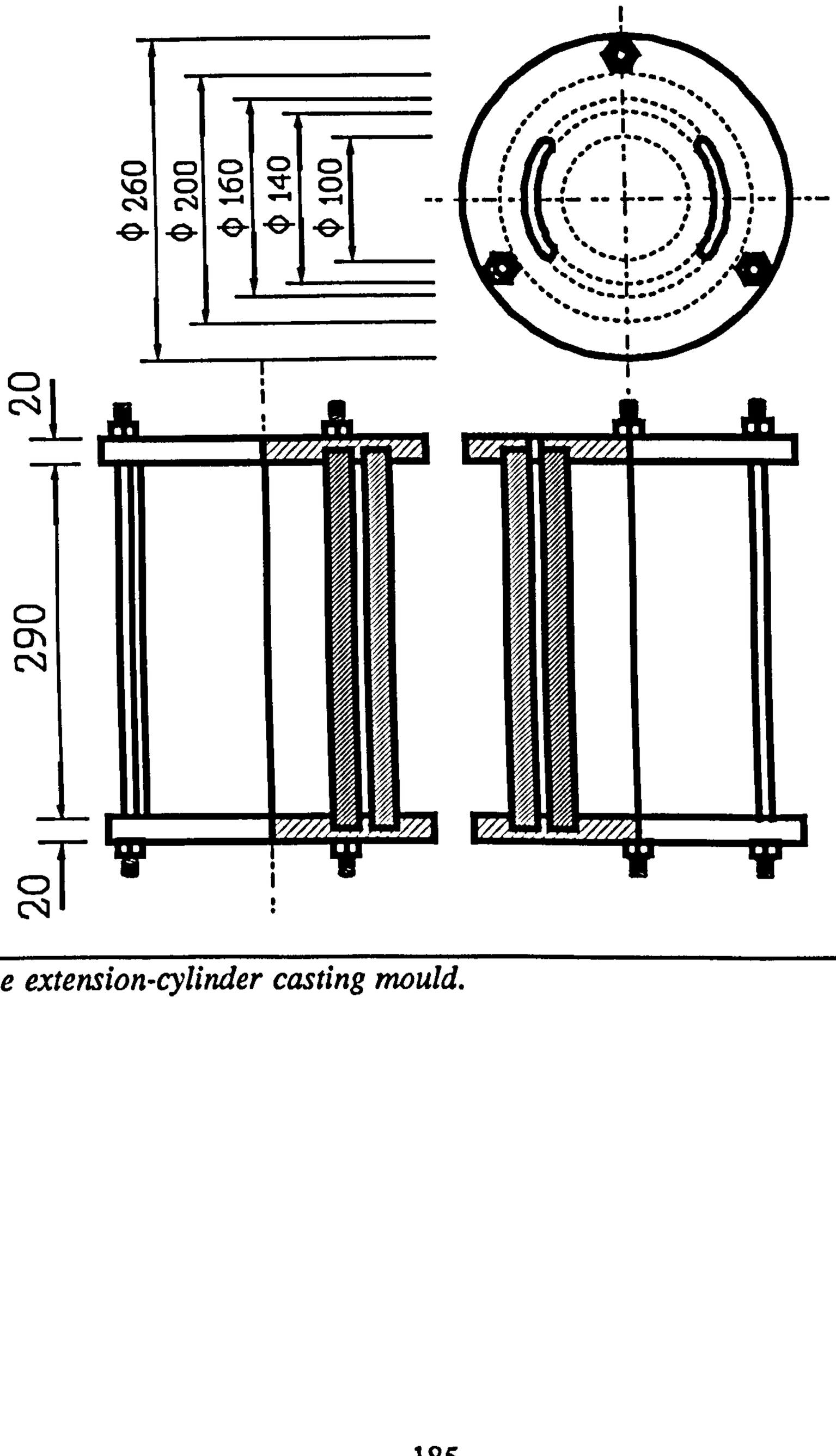

(b) The extension-cylinder casting mould.

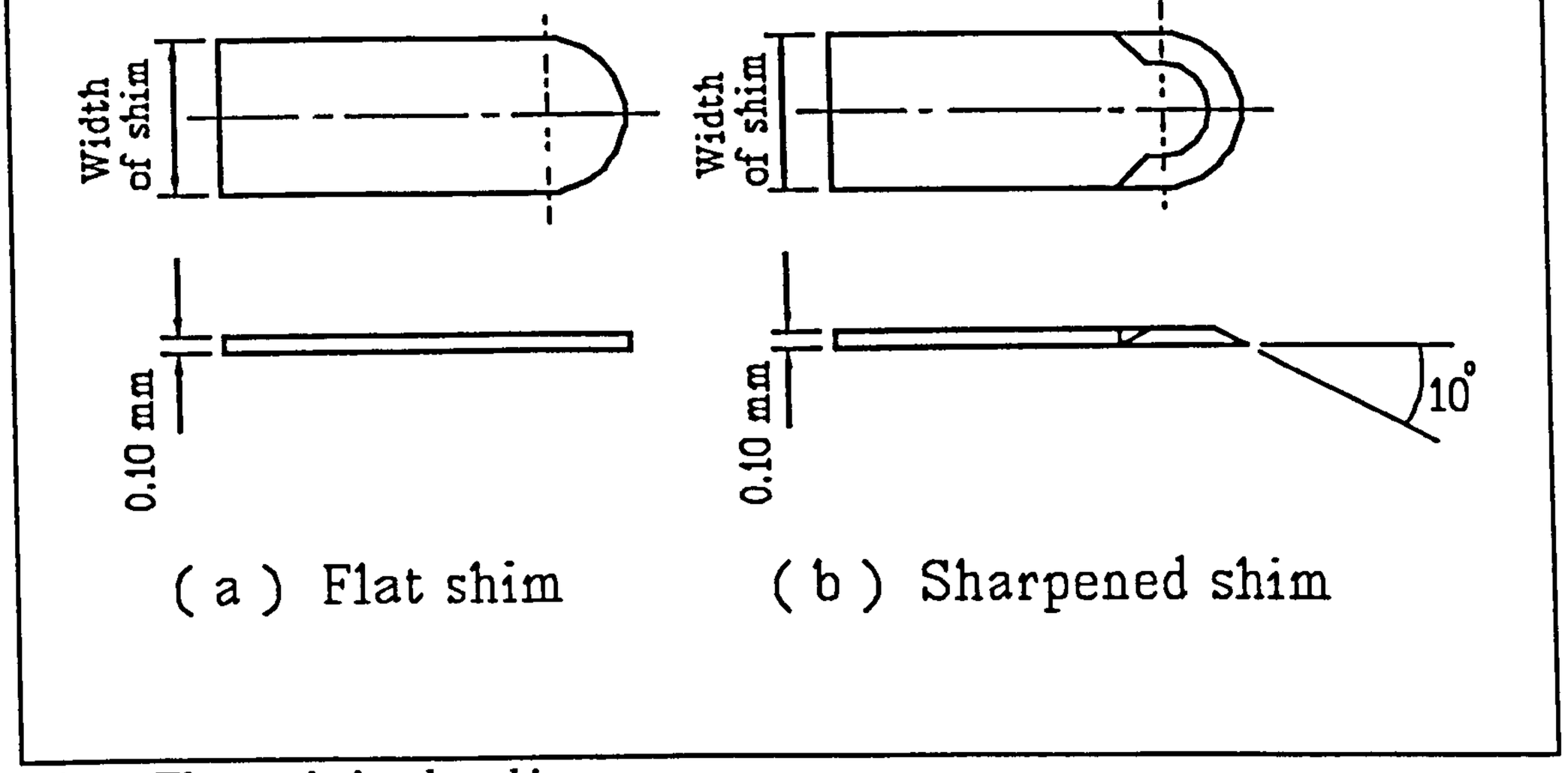

(c) The semi-circular shims.

Figs. 9.3(a-c). The pressure tube casting moulds and shims.

Both end caps were machined out of rectangular Araldite blocks. They were employed repeatedly in all the pressure tube tests. On the other hand, the three cylinders of each tube fractured in every test and therefore could only be used once. Hence, one middle notched cylinder and two extension cylinders had to be cast for each tube test.

After casting the notched cylinder, it was machined on both ends to produce 5mm long spigots. The extension cylinders were also machined to produce a corresponding recess to accommodate the spigots. The recess was 0.1mm over the spigot size to allow for the glued joint. Finally, the end caps were similarly machined to fit the extension cylinders.

The flat semi-circular shims were manufactured by cutting a rectangular piece of shim steel to the correct width and trapping it between two 15mm thick steel blocks. They were placed on a rotary table and machined with an end mill through 180 degrees in order to produce the semi-circular profile.

The sharpened semi-circular shims were produced similarly with the milling machine head inclined at an angle of 10 degrees to the vertical while the shim lay in the horizontal plane.

The finished shims are shown in Fig. 9.3(c).

Prior to connecting the different parts of the tubes together they were cleaned with propanone and then an electrically conductive grid was applied on each notched cylinder symmetrically at both ends of the notch as shown in Figs. 9.2 & 9.11. The material applied was a silver electrically-conductive paint supplied by RS Components Ltd, P O Box 99, Corby, Northants.

The paint was applied in accordance with the manufactures instructions. The volume resistivity of the paint when completely dry (12 hours after application) was given as 0.001Ωcm.

The grid lines perpendicular to the notch (and to the cylinder axis) were 0.5mm wide and initially 0.05mm thick. They were then manually and carefully filed to a smaller thickness until each individual line had a resistance in the range 50 to 300Ω

preferably in an ascending sequence in the direction away from the notch. A digital voltmeter was used to measure the resistance. The total resistance of each grid of eleven lines was between 10 and 15Ω. The trigger lines (Figs. 9.2 & 9.11) were not filed; the resistance of each two in series was 10Ω approximately. All the electric contacts on the grids were soldered to electric wires. The electric circuit which operated in conjunction with the girds is fully described in section 9.4.

Following the preparation of the electric grids on the specimens, each set of components (two end caps, one notched cylinder and two extension cylinders) was placed in an oven at a temperature of 75°C for 24 hours to remove the moisture on the Araldite surfaces and hence increase the strength of the glued joints when the components were subsequently joined together. On removal from the oven, the cylinders and end caps were immediately glued together using Ciba-Geigy Araldite 2004 two-part (A and B) epoxy paste. Each specimen (Figs. 9.1 & 9.2) was then pressed together with dead weights (approximately 10kg) for a period of 24 hours. The specimen was then given at least another 24 hours to ensure full curing and maximum strength of the glued joints. At that stage the pressure tubes were ready to be destructively tested.

9.3. Loading Apparatus

The loading apparatus consisted of several litres of hydraulic oil, a manual oil pump and a pressure gauge which could measure up to a pressure of 600 psi. The pressure gauge was checked with a dead weight tester and found to be very accurate

before conducting any tests.

The specimen to be tested was filled with oil and both the oil pump and the pressure gauge were connected to the specimen. In every test, the absence of any air in the specimen, the pump and any of the connection tubes was confirmed before the specimen could be pressurized, in order to eliminate the danger of compressed air.

The specimens were placed in a closed metal tank during each test. The tank contained the bursting of the tubes and the consequent fragmentation and oil spillage.

9.4. Apparatus for the Measurement of Crack Propagation Velocity

The method of measuring the velocity of crack propagation in the fractured pressure tubes was based on the breakage of the electrically conductive lines in the painted grids. Each grid had an overall electric resistance which underwent a step increase in value every time one of the grid lines broke due to the passage of the crack.

The grid was part of an electric circuit shown in Fig. 9.6. The circuit transferred the step increase of the grid resistance into an output voltage step increase, which was fed into a digitizing oscilloscope. It was the Hewlett-Packard 54501A Digitizing Oscilloscope (Fig. 9.4) which displayed the output voltage from both grids of each notch on the same screen. A copy of the displayed output voltage was then produced by the Hewlett-Packard Think Jet Printer. The printout was a plot of the

output voltage against time, covering the time period from 0 to 500µs, as shown in Figs. 9.7.

Fig. 9.4. The Hewlett-Packard 54501A Digitizing Oscilloscope.

The equation relating the output voltage to the grid resistance, which is stated below, was easily derived from first principles. Referring to Fig. 9.5, and assuming that the resistance per line has the same magnitude for all the grid lines,

$$V_o = \frac{V_i}{\frac{R_1}{R_2} + \frac{N_* R_1}{R_*} + 1} \qquad (9.1)$$

where V_o and V_i are the output and input voltages respectively, R_1 and R_2 are the resistances of the resistors shown in Fig. 9.5, R_* is the resistance per painted grid line,

and N_* is the number of unbroken grid lines ranging from 0 to 11. Fig. 9.5 explains the basic circuit on which the actual circuit used in the testing of the pressure tubes was based. The latter circuit, shown in Fig. 9.6, specifies the actual values of the resistance and voltages applied in the tests. The choice of these values was entirely based on providing a clearly noticeable step change in the output voltage.

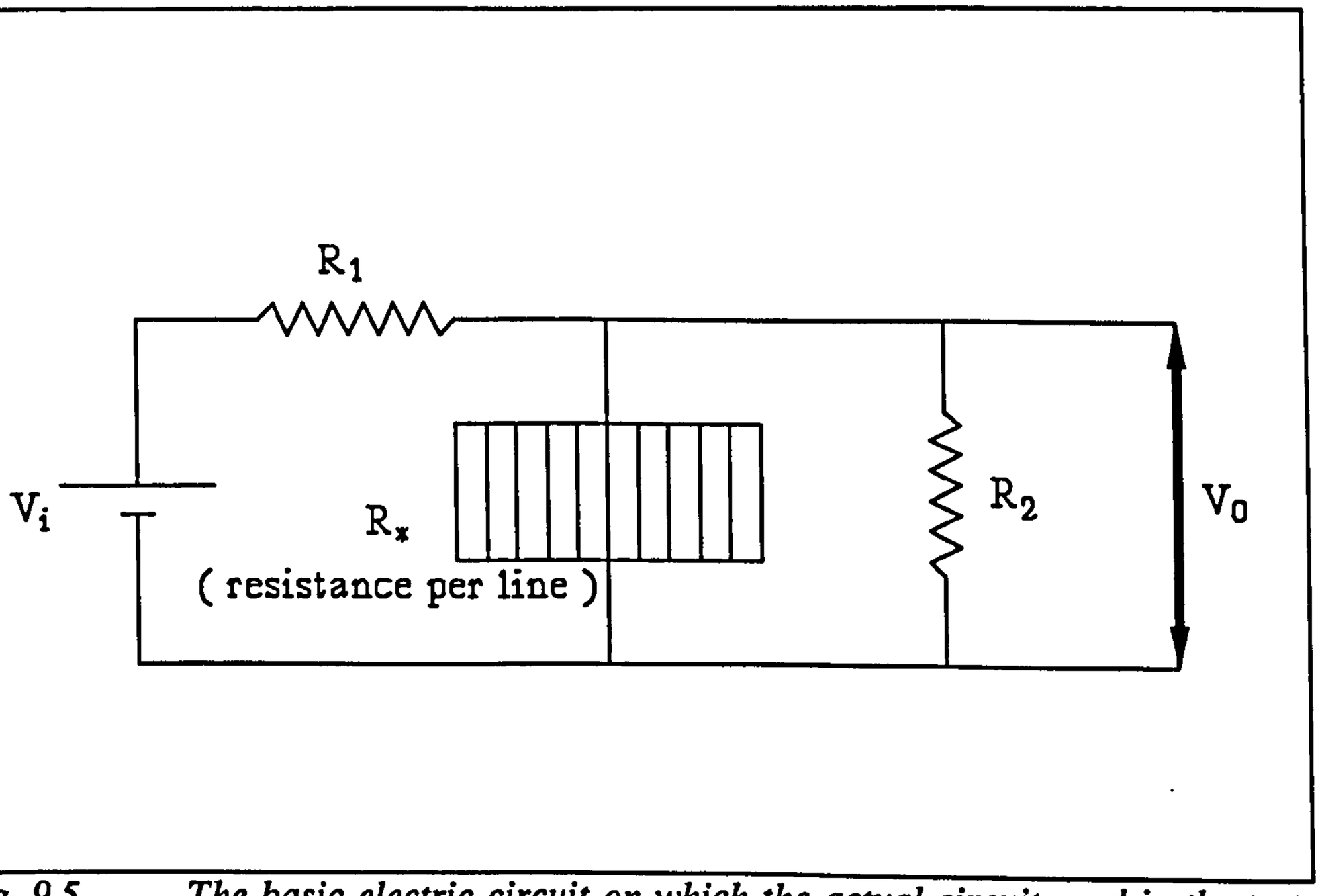

Fig. 9.5. The basic electric circuit on which the actual circuit used in the tests was based.

The digitizing oscilloscope had to be triggered off every time a crack propagated. That was achieved by two electric lines painted at both ends of the notch, preceding the lines of the grids. The two lines were connected together to form a single triggering mechanism, which operated when either of the two lines was broken, setting the digitizing oscilloscope off. The triggering mechanism, which was part of the utilized electric circuit, can be seen in Fig. 9.6(b).

The testing of the pressure tubes was performed while they rested on their bases with their axis being vertical. The top painted electric grid was connected to channel 1 on the digitizing oscilloscope while the bottom one was connected to channel 4. Channel 3 was designated for the trigger circuit. The signals of channel 1 and 4 were displayed in the top and bottom halves of the printouts of Figs. 9.7(a-j) respectively. Three of the printouts also displayed the signal of channel 3 in the bottom half.

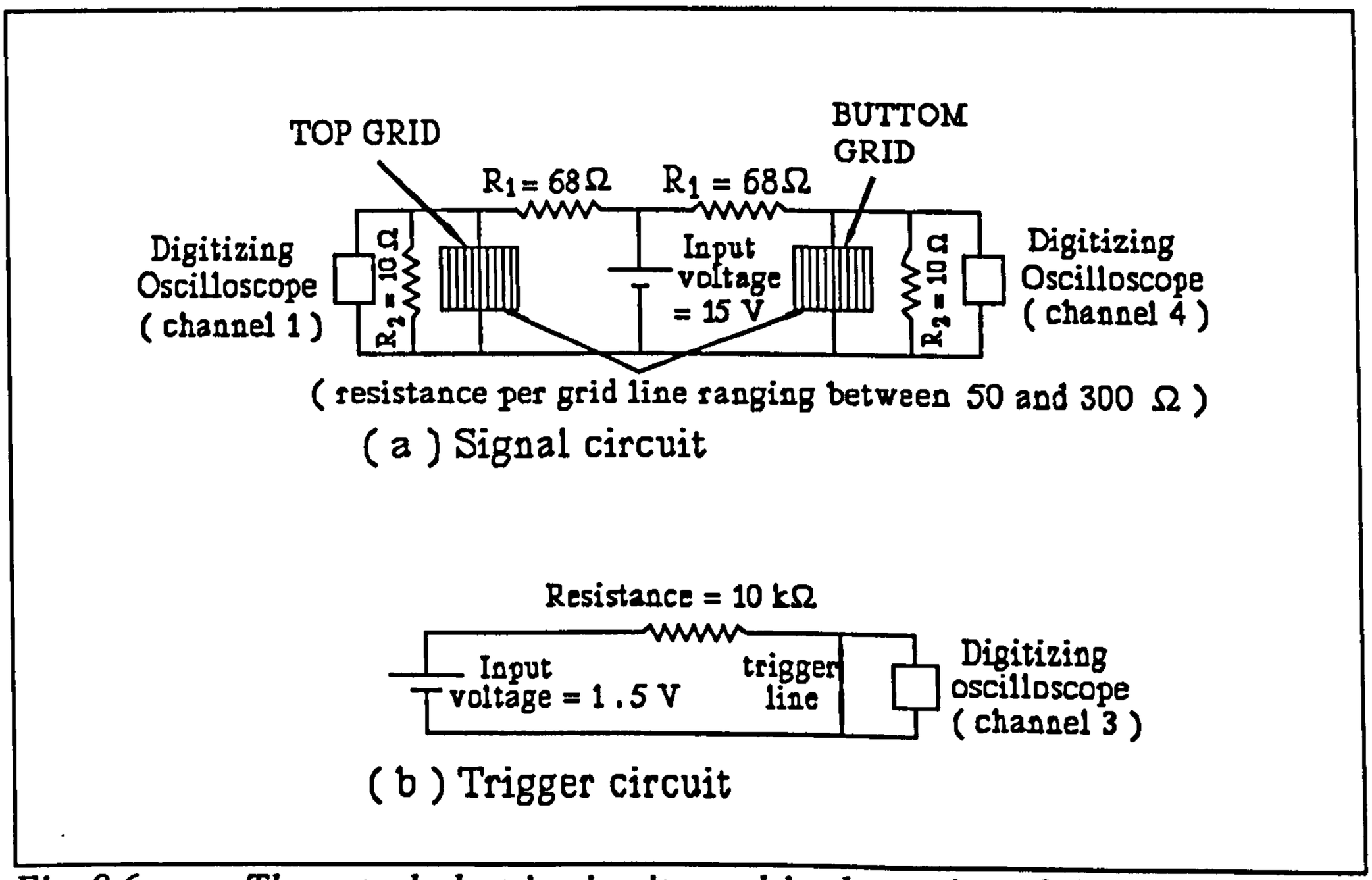

Fig. 9.6. The actual electric circuit, used in the testing of the pressure tubes, comprising of the signal and trigger circuits.

The 15V input voltage in the signal circuit of Fig. 9.6(a) was delivered by Farnell Instruments Ltd stabilised voltage supply, while the 1.5V input voltage in the trigger circuit of Fig. 9.6(b) was provided by a dry 1.5V battery.

The actual values of the resistances and output voltages were not significant in any of the subsequent calculations of the crack velocities. The important parameters were the displacements between the centres of the grid lines and the corresponding time changes on the digitizing oscilloscope printouts. These are presented in Figs. 9.8(a-f).

The time change between the breakage of the trigger line and the first grid line was not used in any calculations. This precaution was taken to avoid any errors arising from the possibility of the digitizing oscilloscope not responding with sufficient speed to the triggering action.

9.5. Experimentation

The testing of the pressure tubes was carried out in a number of stages. The individual resistances of the grid lines were checked. The triggering lines and grids on the specimen to be tested were electrically connected to the electric circuit of Fig. 9.6. The digitizing oscilloscope and the printer were also connected to the circuit. The oscilloscope was set in order to achieve a clear, large and complete display of the stepped output voltage. The specimen was then placed inside the protective metal tank with the lid still open. After completely filling the tube with oil, the oil pump and pressure gauge were attached to the tube, making sure that the system was free of any air bubbles. The protective tank was then covered and the tube was pressurized to failure, which occupied a time period between two and four minutes. The process of pressurizing the tubes was achieved manually, paying attention to the

increase in pressure to be as steady as possible.

The tubes failed with a loud bang, the crack initiating at the tip of the semi-circular notch and travelling vertically in both directions, cutting through the trigger lines and then the grid lines, until branching took place. The digitizing oscilloscope displayed a stepped presentation of the output voltage which corresponded to the propagation of the crack through the grid lines.

9.6. Results

The results obtained from the pressure tube tests covered a few topics in the field of fracture mechanics. Consideration has been given to the apparent static K_{IC} values which led to fracture. As the cracks propagated from the narrow semi-circular notch tips, breaking through the painted grid lines, the corresponding time change at each line was registered. That facilitated the displacements and velocities of the cracks to be plotted against time. In addition, the branching process has been studied giving particular attention to the dynamic stress intensity factor, K_D. The surface texture of the fracture surfaces has been another subject of scrutiny, for which some photographs were taken - see Figs. 9.13.

A total of ten successful tests were carried out on the pressure tubes. They were all destructive tests with the cracks initiating at the tip of the narrow semi-circular notches. Table 9.1 states the number of valid tests for each notch radius, a, and effective width, 2s.

Notch radius, a (mm)	Notch width, 2s (mm)	Number of valid tests
7	0.02	2
7	0.10	2
5	0.02	1
5	0.10	2
3	0.02	2
3	0.10	1

Table 9.1. The number of valid tests for each notch radius and width for the pressure tubes.

9.6.1. Apparent Static K_{IC}

The value of the oil pressure inside the tubes was used to calculate the apparent static stress intensity factor, K_{IC}^{APP}, at the tip of the narrow semi-circular notch at the point of fracture. The loading of the material at the notch tip was the mode-I type, the nominal stress being the hoop stress.

Two methods were employed to calculate the K_{IC}^{APP}: the first method provided a value which was considered to be accurate, and the second method confirmed that value but was only approximate.

The first method followed the equations and tables provided by Murakami [84] on pages 751-757 of his second volume for internal and external surface cracks in cylindrical vessels. It was stated in that reference that the method provided an accuracy less than 10%. It is interesting to note that the analysis presented in the

reference was based on a cylinder with two diametrically located cracks. Although Murakami [84] states that in general the stress intensity factor for a single crack is about 4% lower than that for two cracks, but this percentage is seen to be much smaller in the particular case of this thesis by referring to the original source of the analysis [88]. The fact that the tubes have semi-circular notches rather than semi-elliptical ones reduces the above mentioned percentage significantly. Another factor which have a reducing effect on the percentage is the actual choice of the notch-radius sizes. Although Raju and Newman,Jr. [88] do not quantify the above percentage for each possibility, nevertheless from the general description it is concluded that the above percentage is negligible for this particular case.

The final results of this method are given in Table 9.2, which presents the oil pressure at failure, p, the K_{IC}^{APP}, the notch radius, a, and the notch width, 2s.

Specimen number	a (mm)	2s (mm)	Pressure at failure, p (psi)	K_{IC}^{APP} (N/mm$^{3/2}$)	
				First method (accurate)	Second method (approximate)
1	7	0.02	165	31.7	33.5
2	7	0.02	170	32.6	34.5
3	7	0.10	205	39.4	41.6
4	7	0.10	220	42.2	44.7
5	5	0.02	265	38.7	41.7
6	5	0.10	275	40.2	43.3
7	5	0.10	290	42.3	45.6
8	3	0.02	320	33.9	36.3
9	3	0.02	330	35.0	37.4

10	3	0.10	375	39.8	42.5

Table 9.2. The pressure-tube K_{IC}^{APP} values obtained by Murakami's methods [84] on internal and external surface cracks in cylindrical vessels [88] (more accurate), and on a semi-elliptical surface crack in finite-thickness plates [89] (less accurate).

The second method followed the equations and tables provided by Murakami [84] on pages 692-696 of his second volume for a semi-elliptical surface crack in finite-thickness plates. An accuracy of 3% was associated with the second method. But since treating the tubes as flat plates is a rough approximation, the second method was considered to give approximate K_{IC}^{APP} values destined merely to reconfirm the more accurate values obtained by the first method. The K_{IC}^{APP} values obtained by using the less accurate second method are given in Table 9.2.

Although the two methods concern the general case of the semi-elliptical crack, nonetheless they also deal with the particular case of the semi-circular crack. The maximum value of K_{IC}^{APP} was associated with the tip of the notch at the external surface of the tube for both methods. Moreover, the cracks initiated more or less at the notch tips at the external surface, as explained at the end of section 9.6.5. Therefore the calculations were done at the same location.

The derived equations of Murakami [84] assumed a uniform tensile stress distribution throughout the cross-section of the plate of the second method, and an average hoop stress in the cylinder of the first method. Therefore, for both cases, the hoop stress was calculated assuming the tubes to be thin cylinders, i.e.,

$$\sigma_\theta = \frac{pd}{2t} \qquad (9.2)$$

where σ_θ is the hoop stress, p is the internal hydraulic pressure, t is the side wall thickness of the tubes and d is their internal diameter.

9.6.2. Displacements of the Cracks

The printouts of the digitizing oscilloscope display are shown in Figs. 9.7(a-j). Using these printouts, the displacement against time graphs were plotted. They are shown in Figs. 9.8(a-f). The curves drawn are cubic fits.

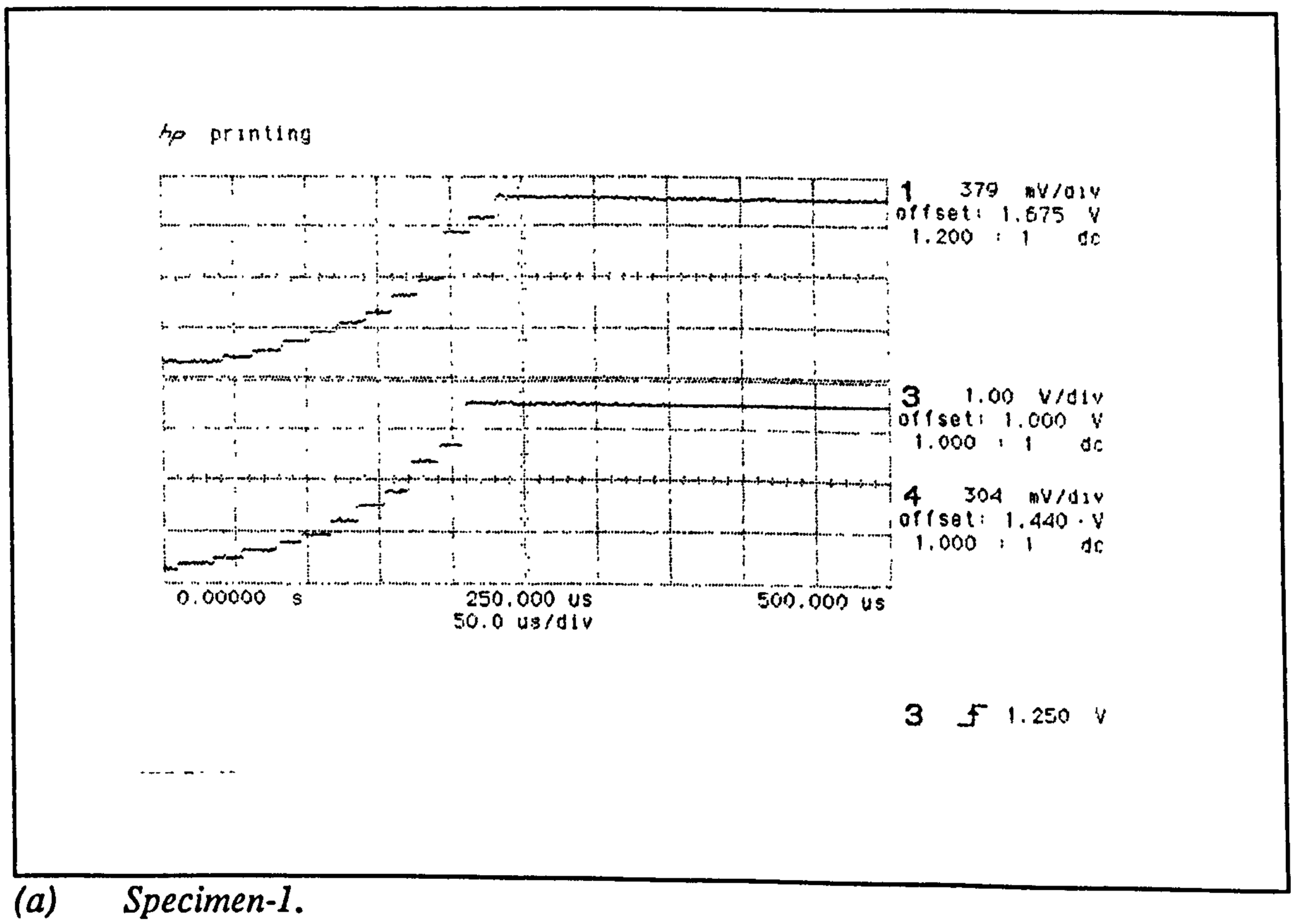

(a) Specimen-1.

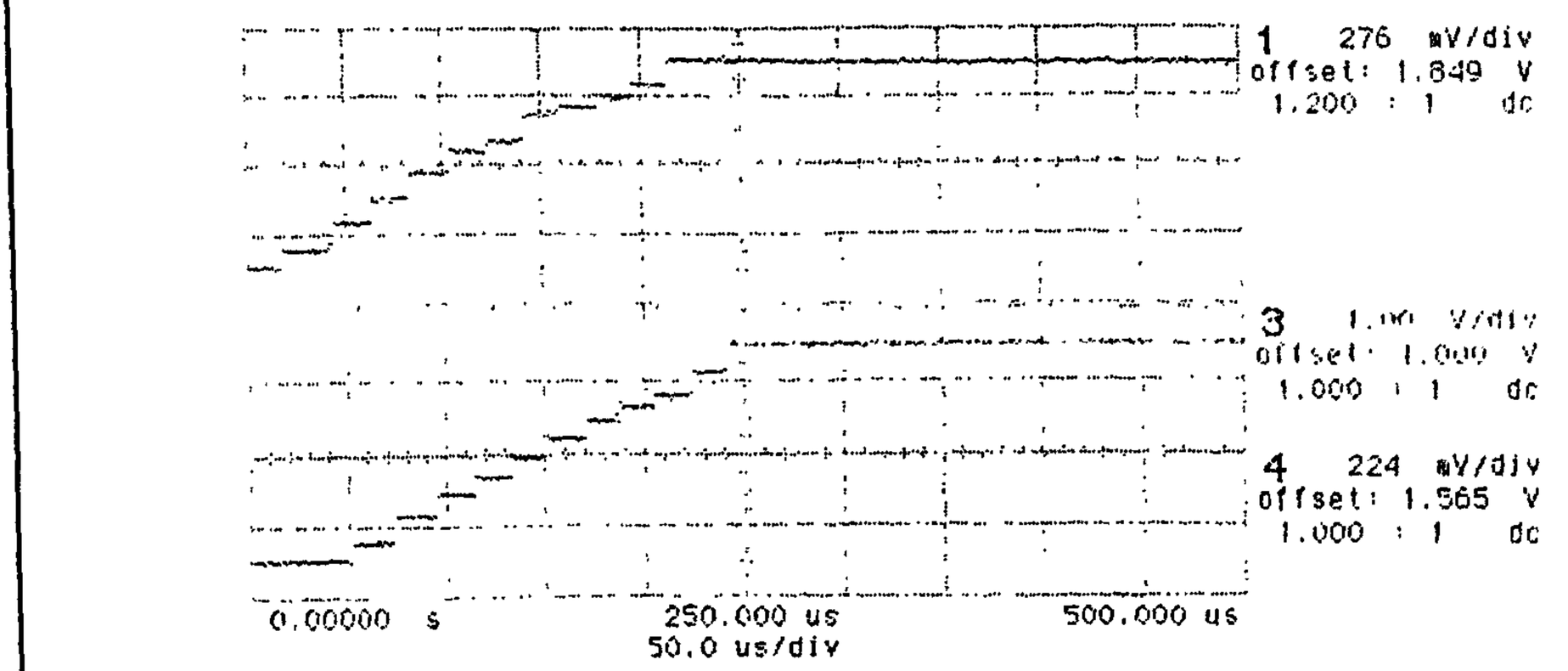

(b) Specimen-2.

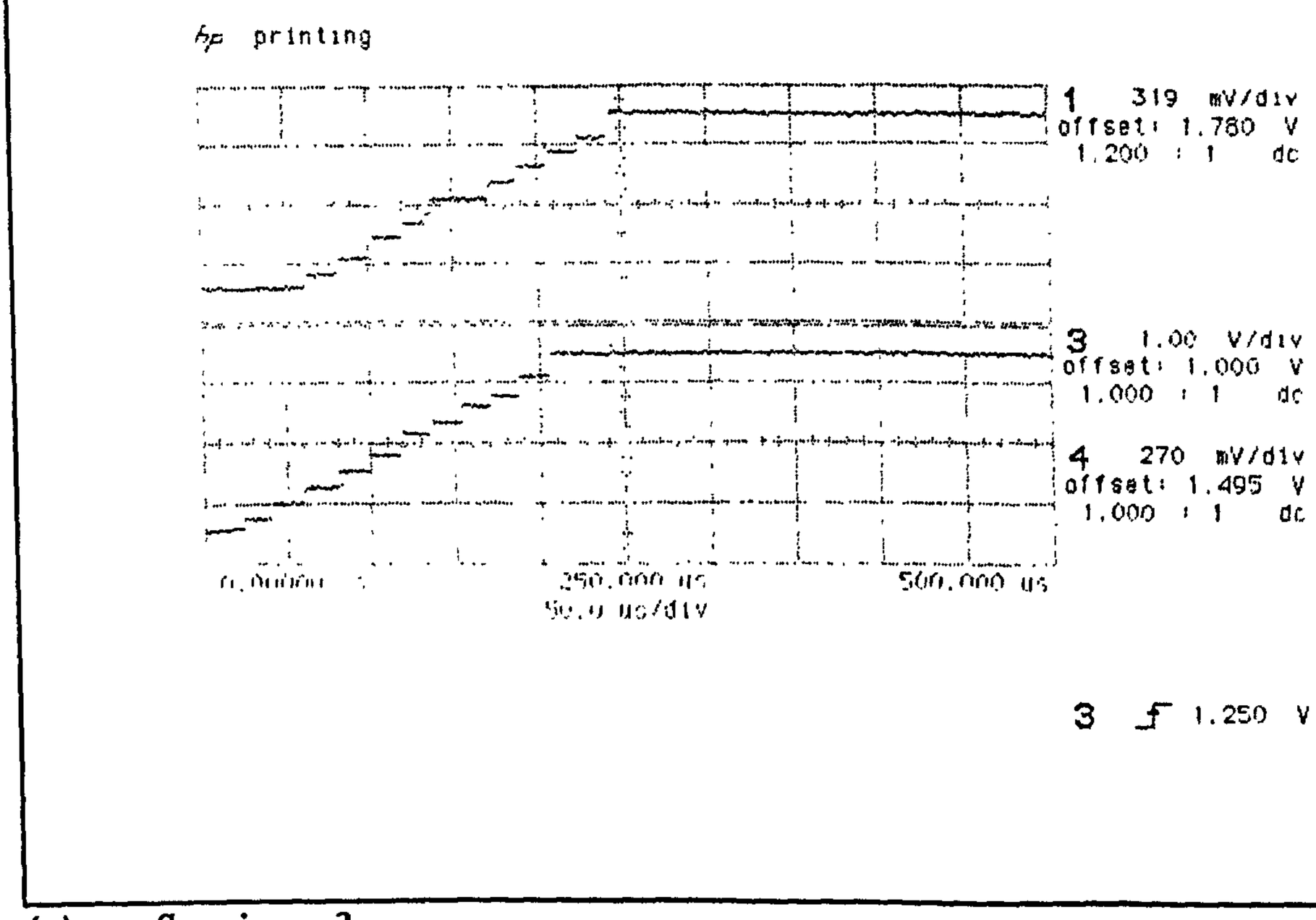

(c) Specimen-3.

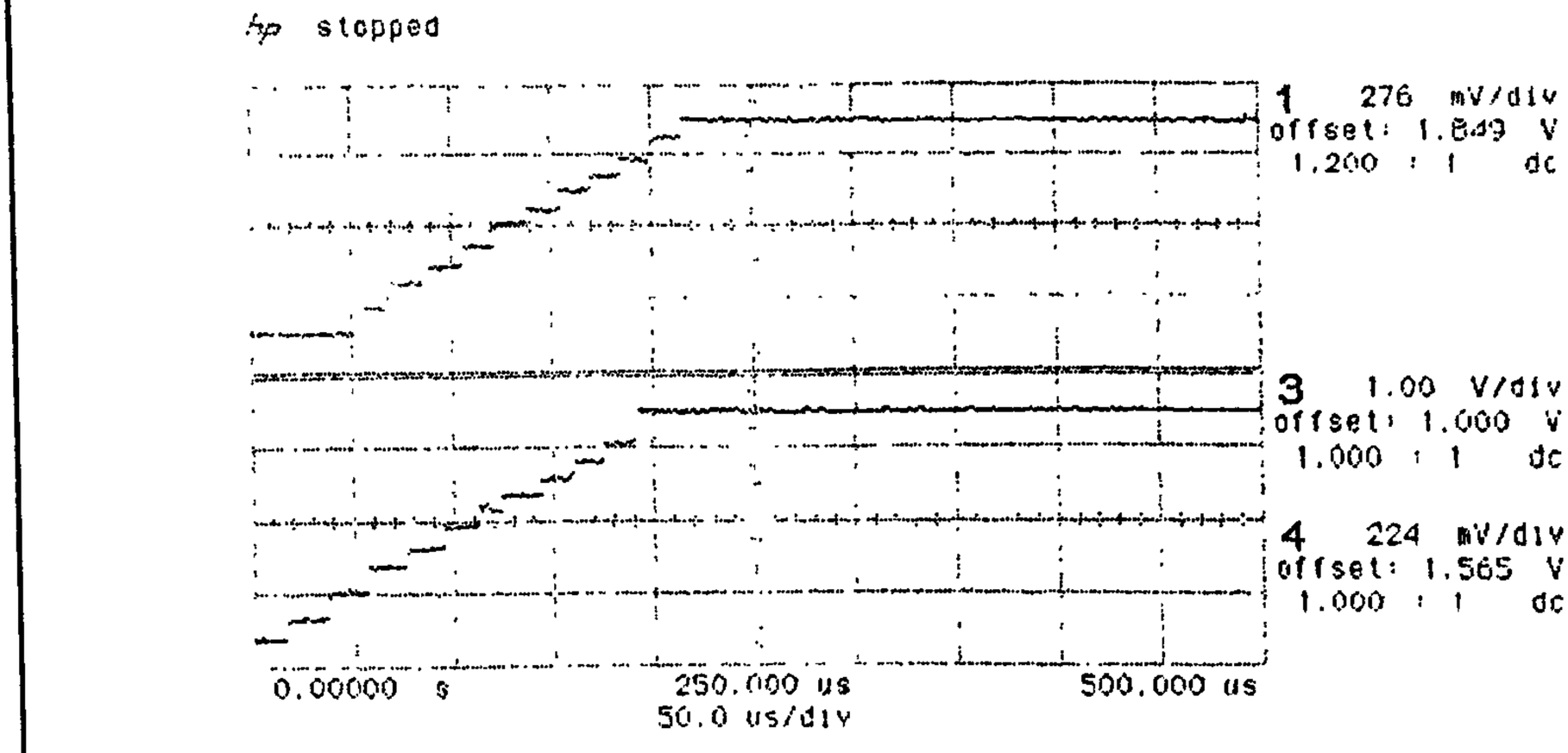

(d) Specimen-4.

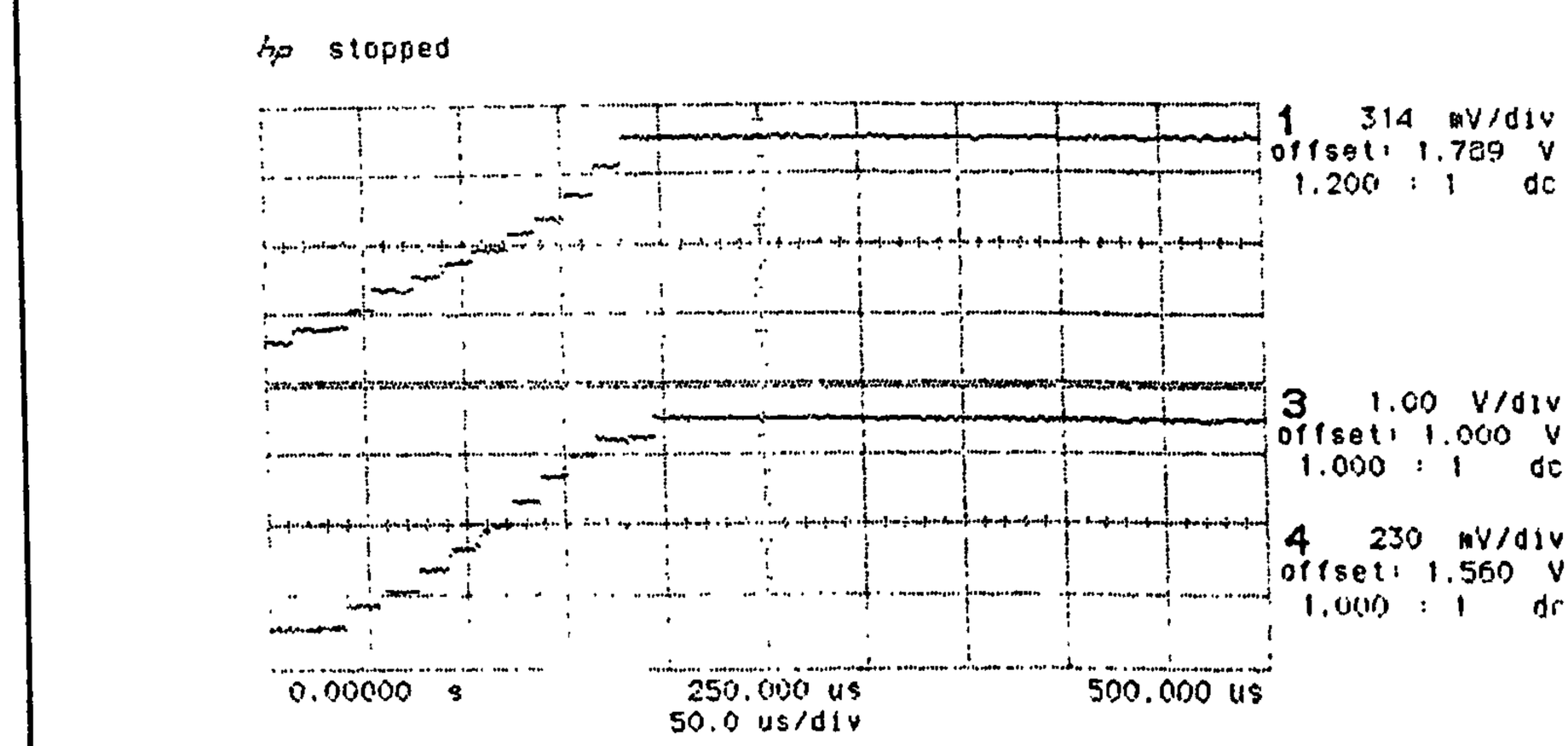

(e) Specimen-5.

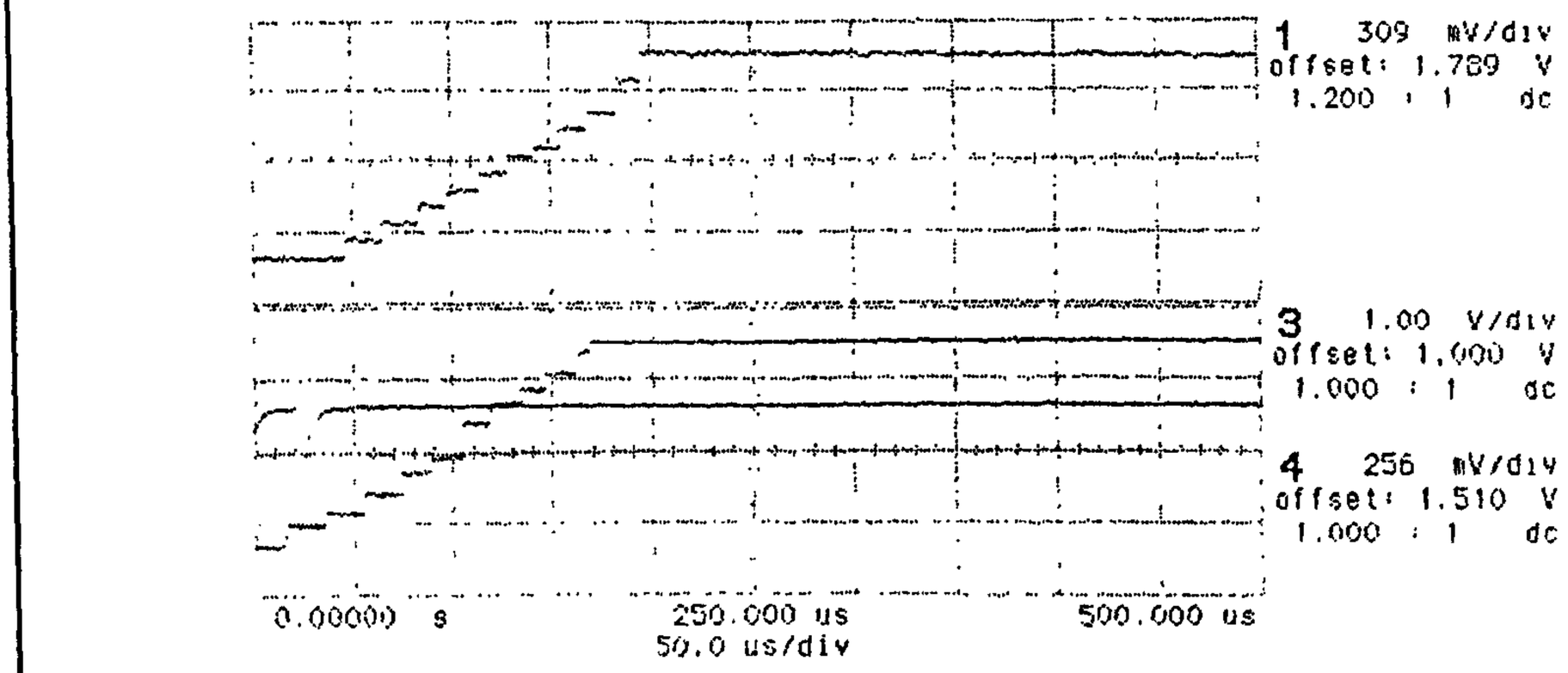

(f) Specimen-6.

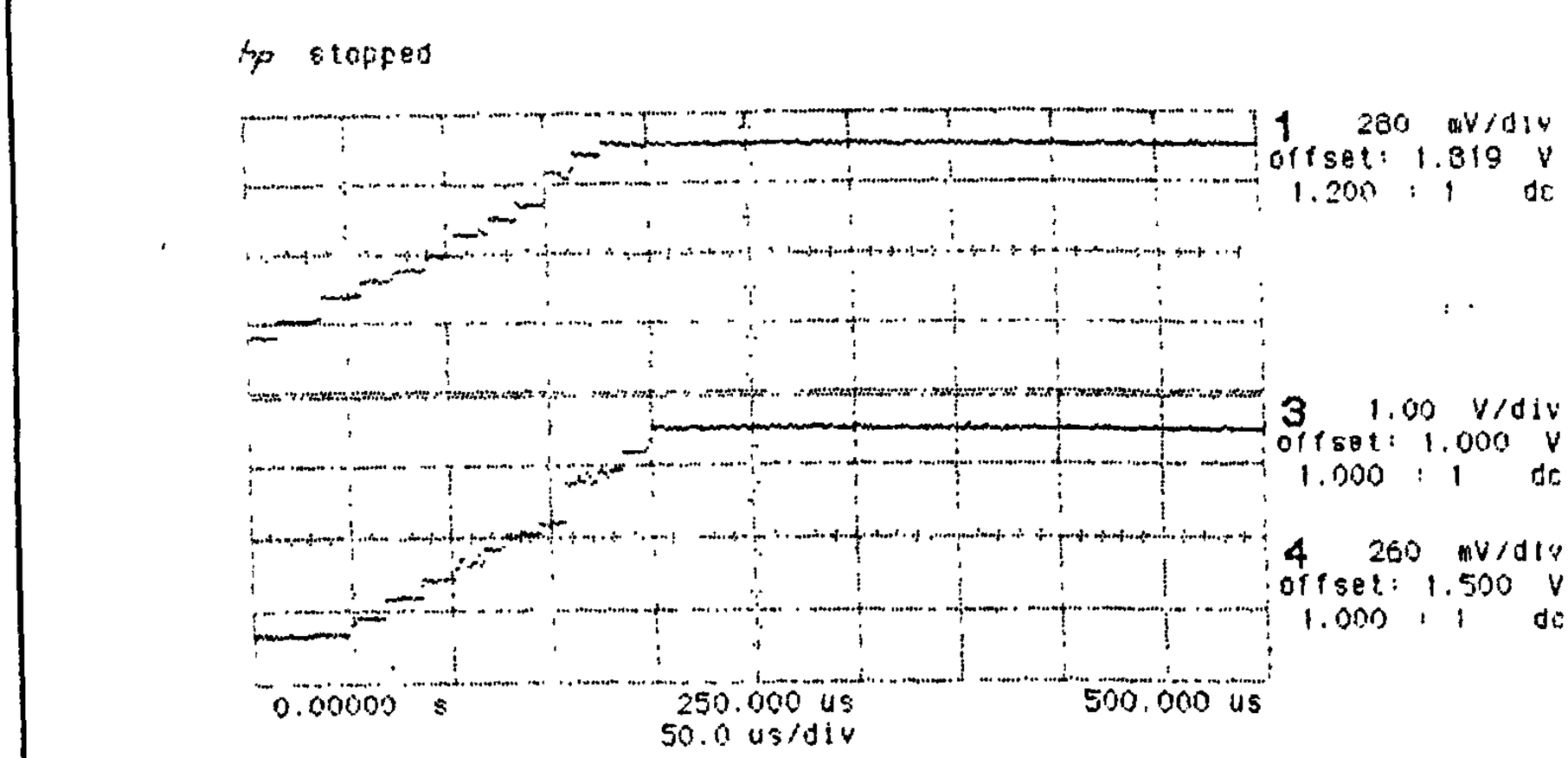

(g) Specimen-7.

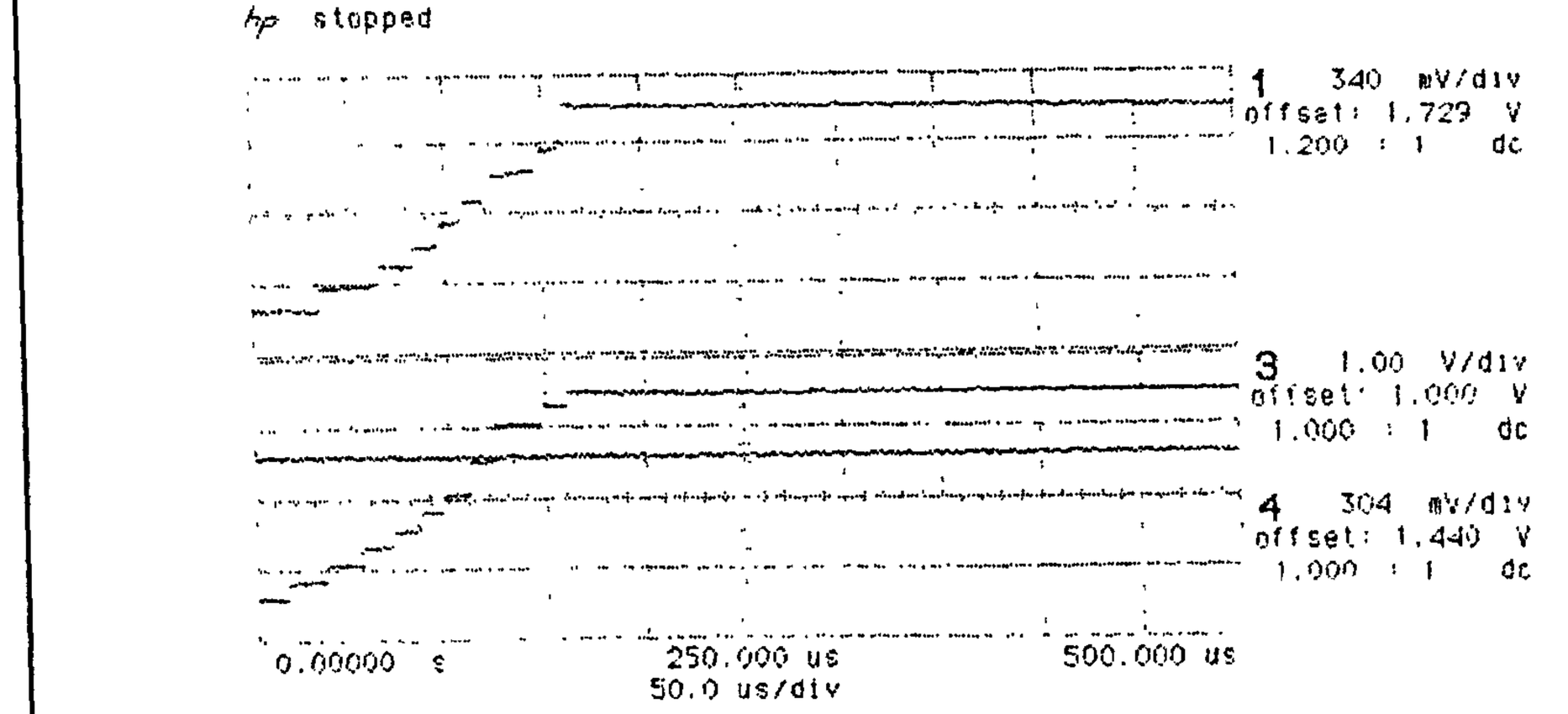

(h) Specimen-8.

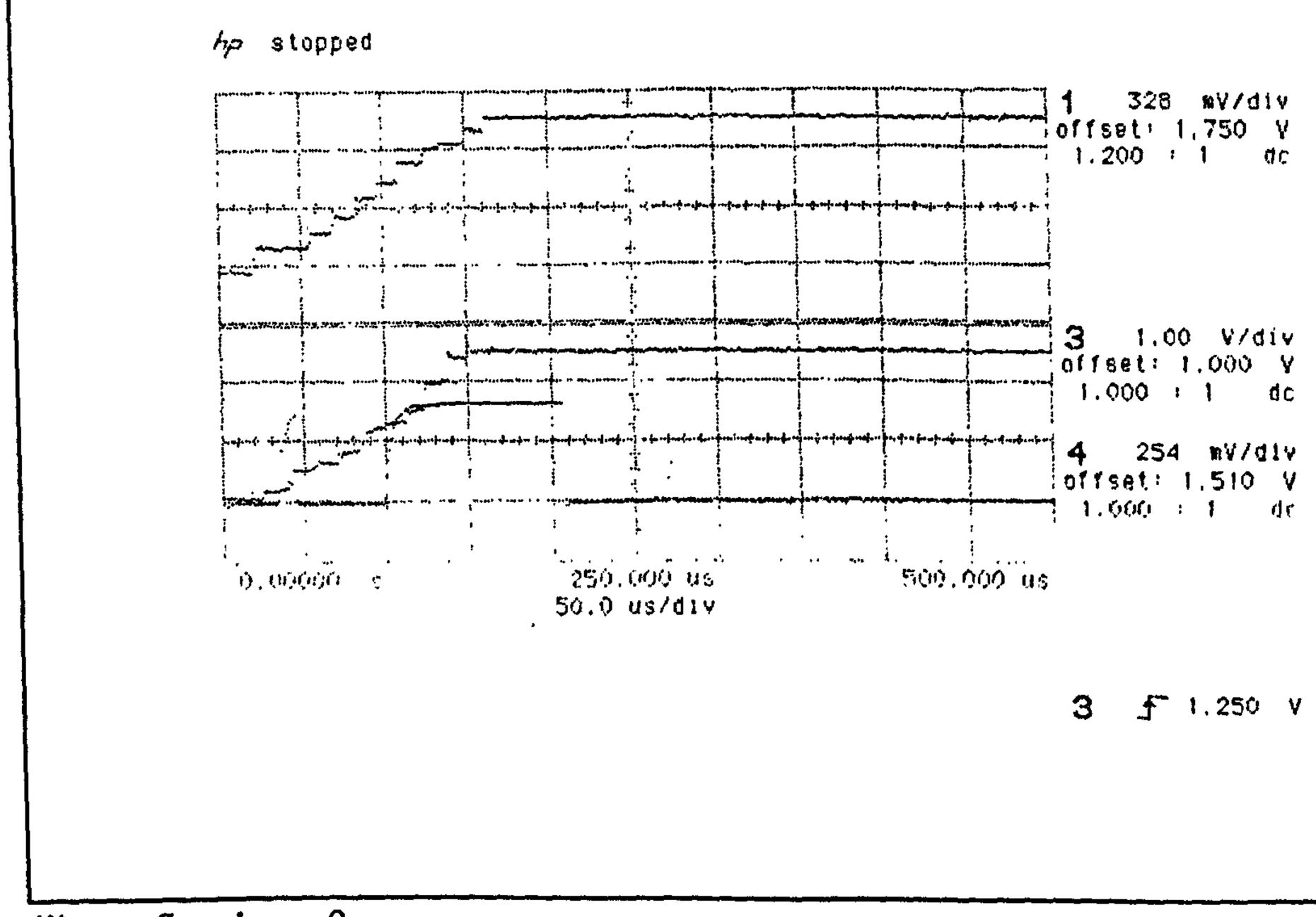

(i) Specimen-9.

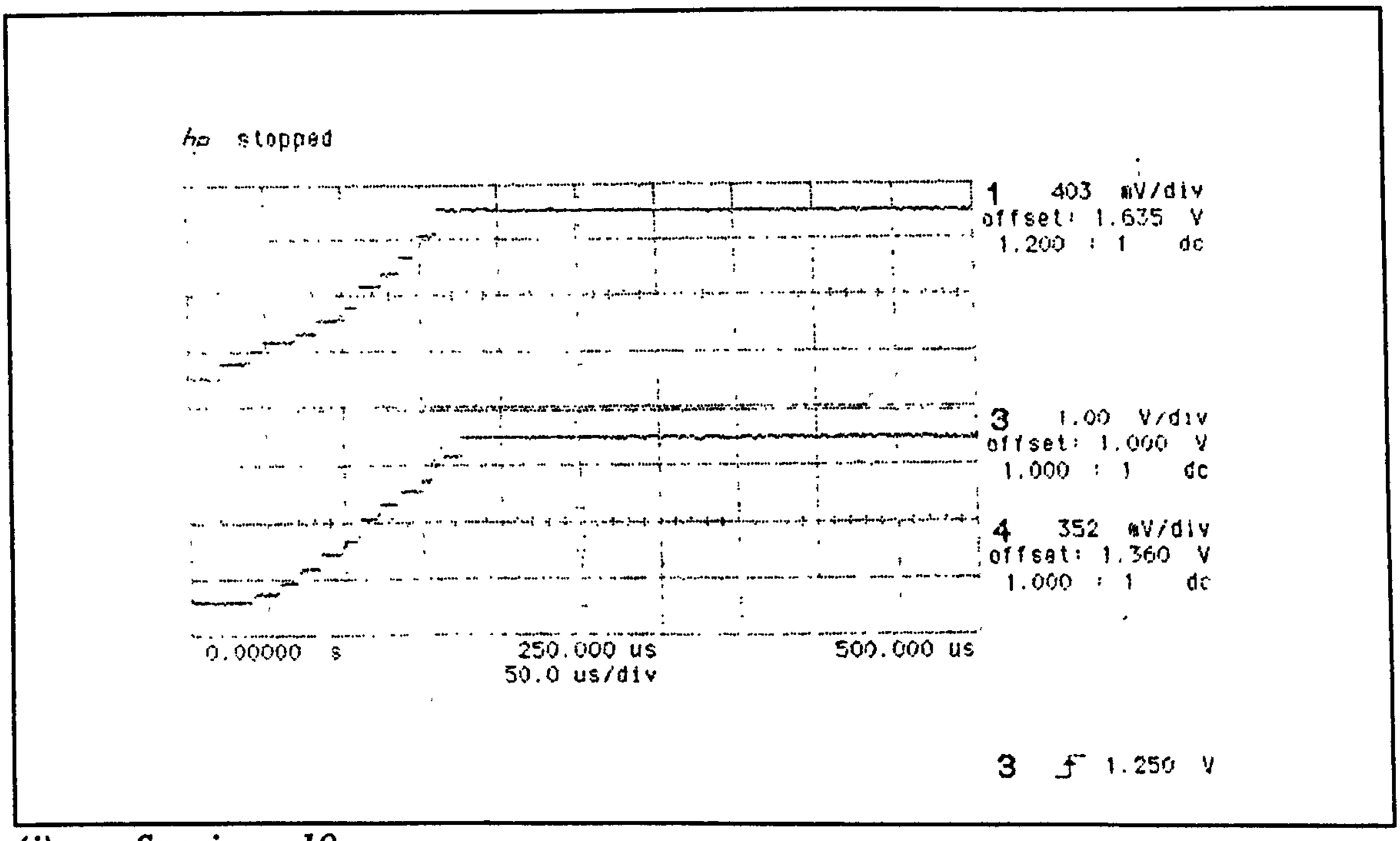

(j) Specimen-10.

Figs. 9.7(a-j). Printouts of the digitizing-oscilloscope display.

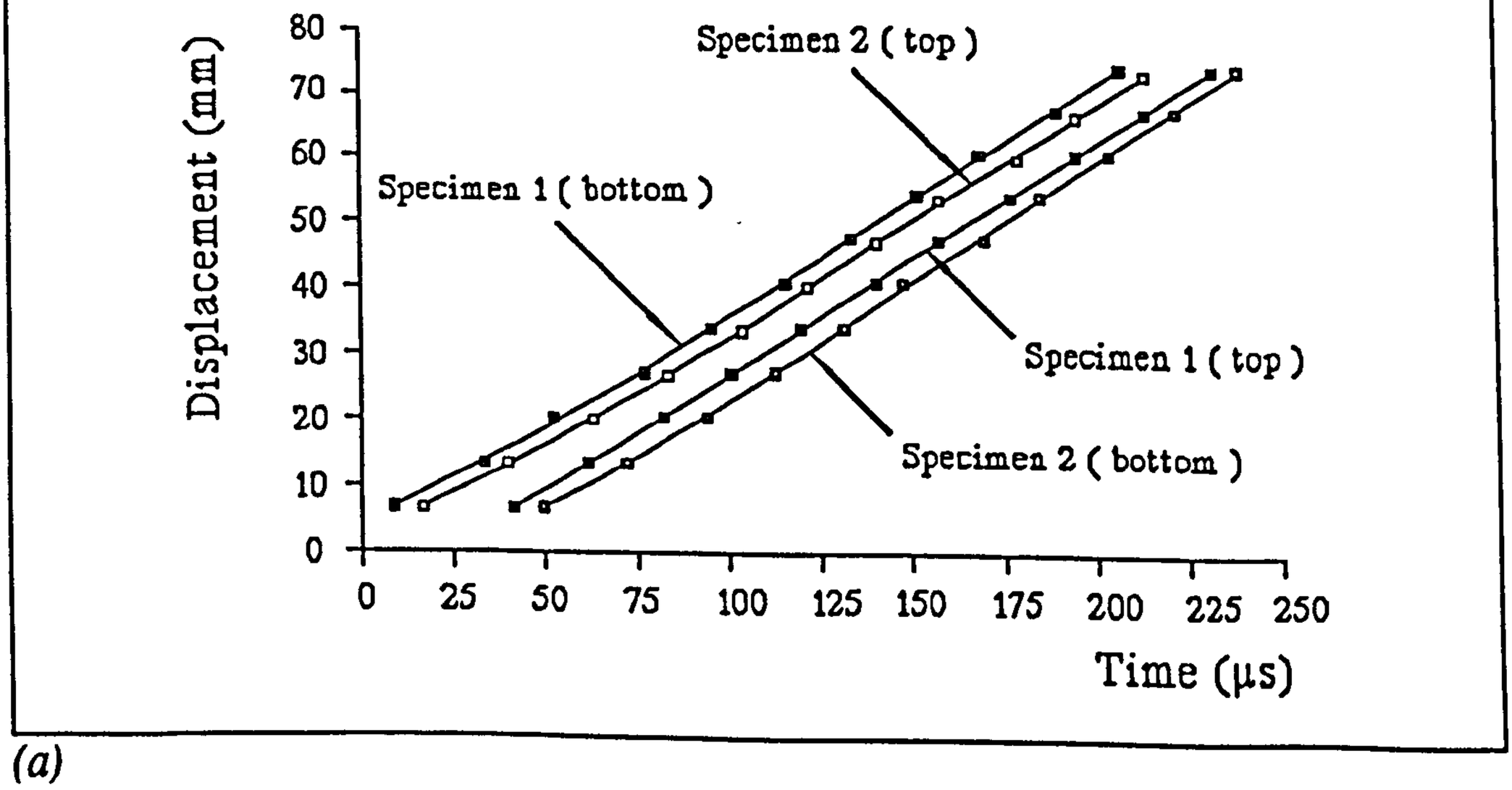

(a)

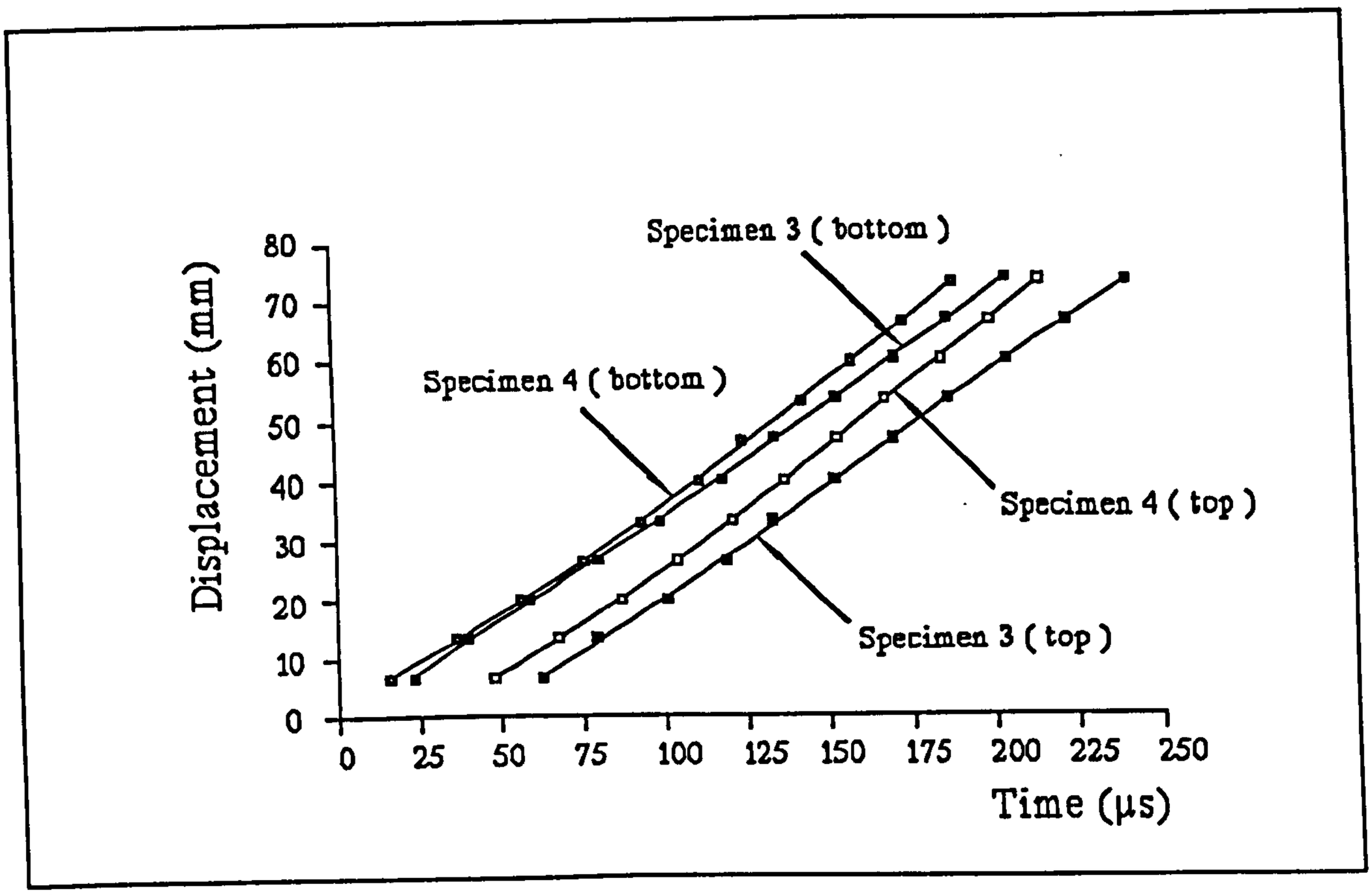
Specimen 3 (bottom)
Specimen 4 (bottom)
Specimen 4 (top)
Specimen 3 (top)
Displacement (mm)
80
70
60
50
40
30
20
10
0
0
25
50
75
100
125
150
175
200
225
250
Time (μs)

(b)

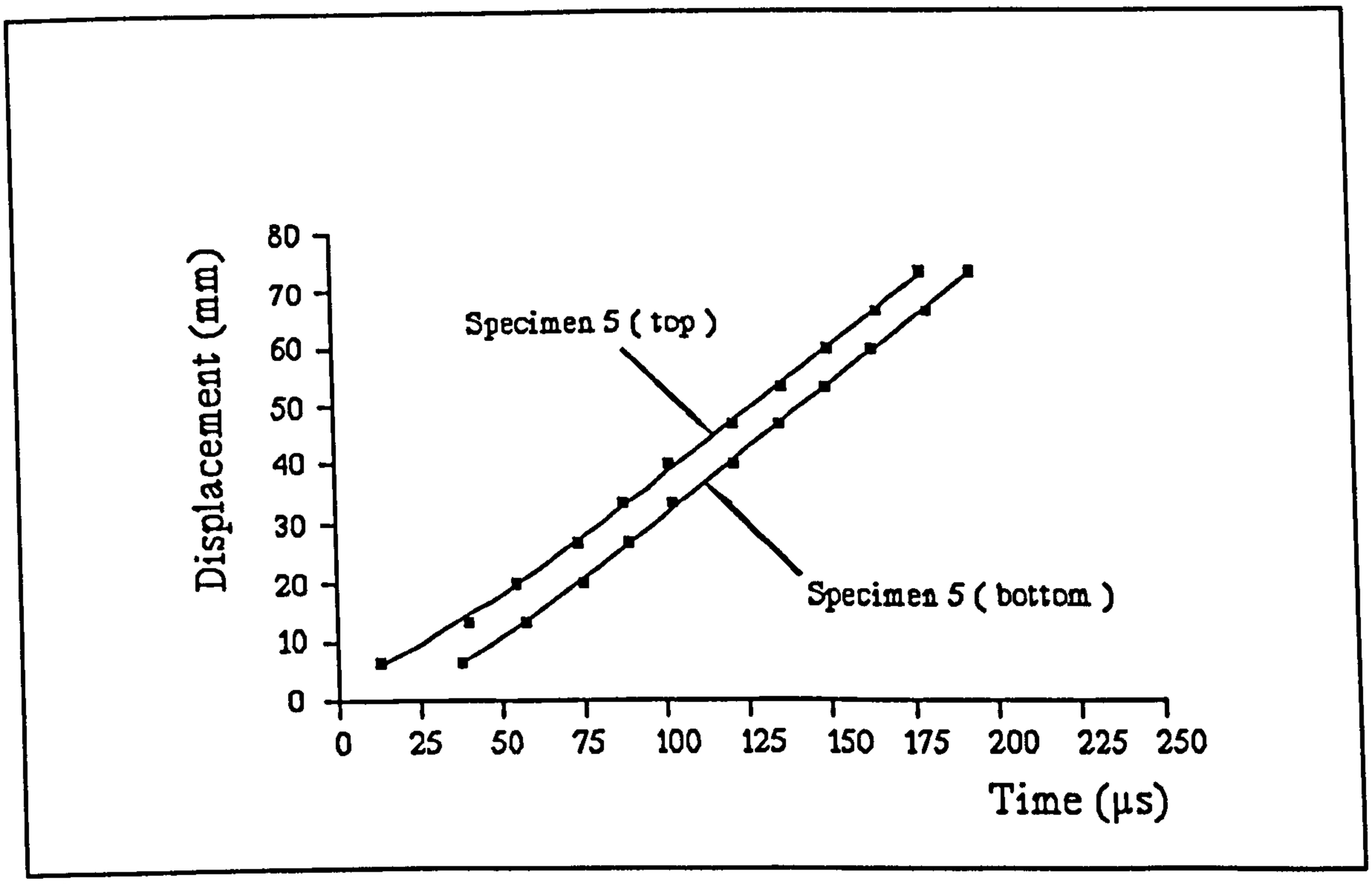
Specimen 5 (top)
Specimen 5 (bottom)
Displacement (mm)
80
70
60
50
40
30
20
10
0
0
25
50
75
100
125
150
175
200
225
250
Time (μs)

(c)

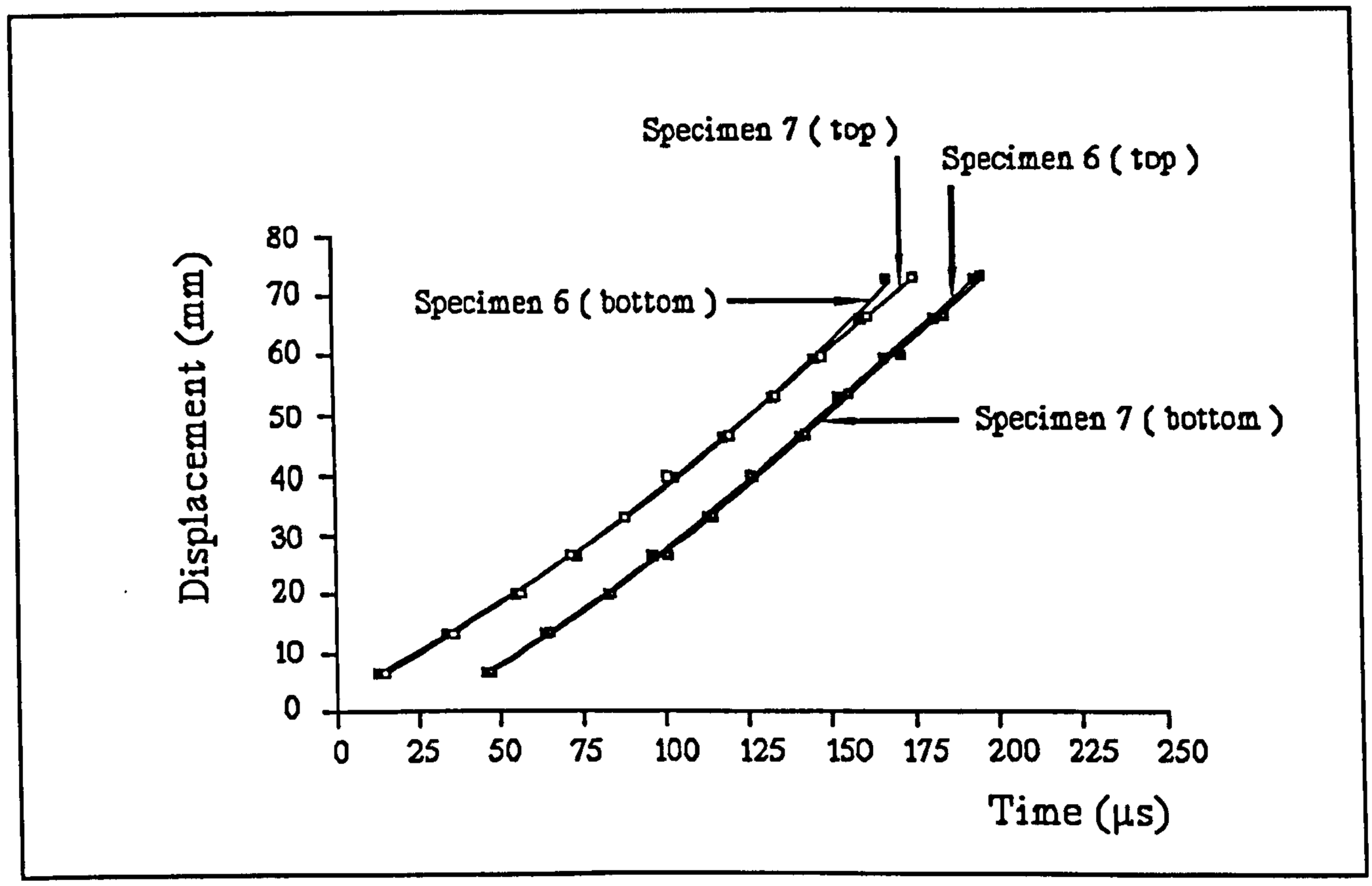
Specimen 7 (top)
Specimen 6 (top)
Specimen 6 (bottom)
Specimen 7 (bottom)
Displacement (mm)
80
70
60
50
40
30
20
10
0
0
25
50
75
100
125
150
175
200
225
250
Time (μs)

(d)

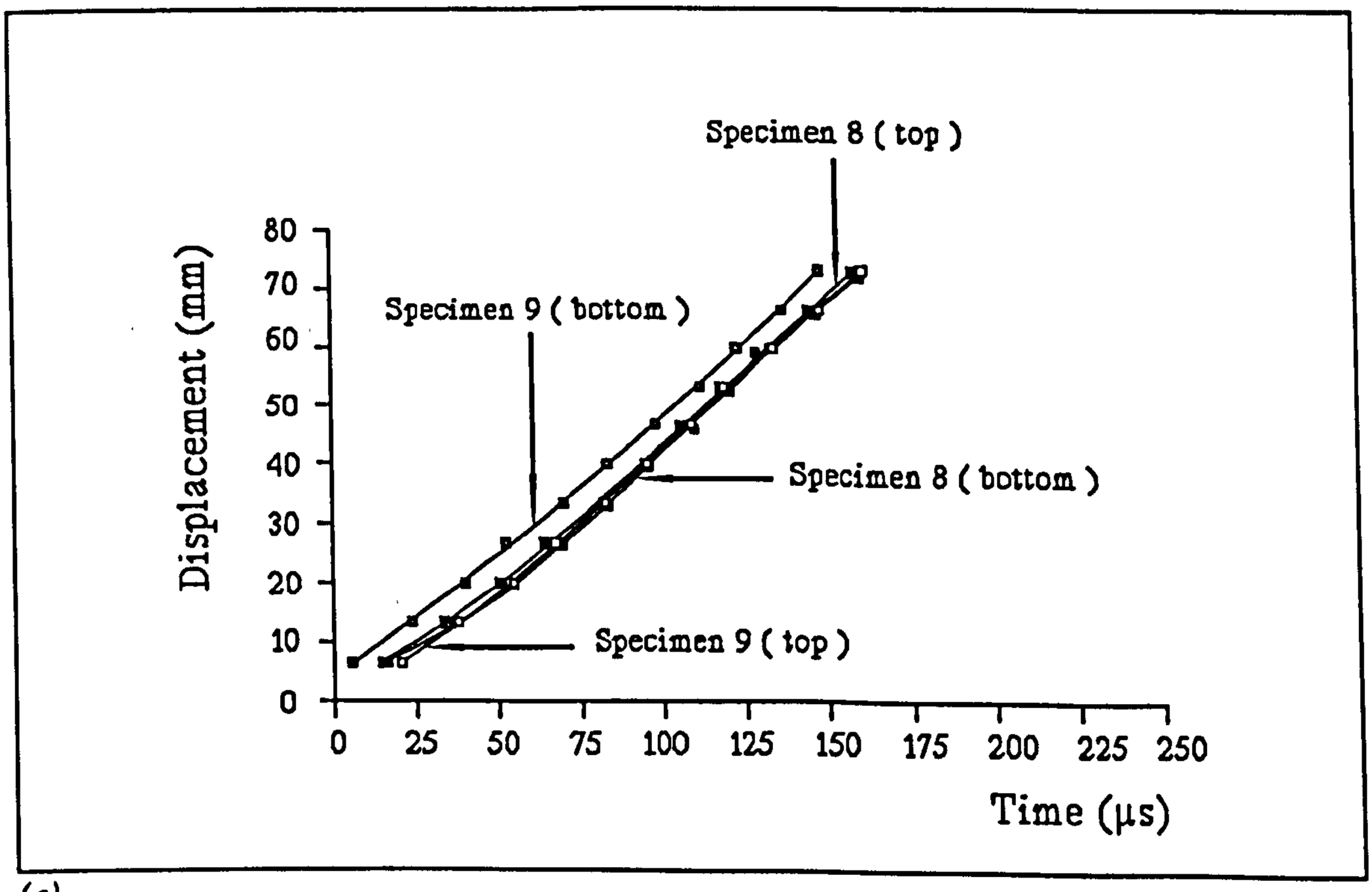
Specimen 8 (top)
Specimen 9 (bottom)
Specimen 8 (bottom)
Specimen 9 (top)
Displacement (mm)
80
70
60
50
40
30
20
10
0
0
25
50
75
100
125
150
175
200
225
250
Time (μs)

(e)

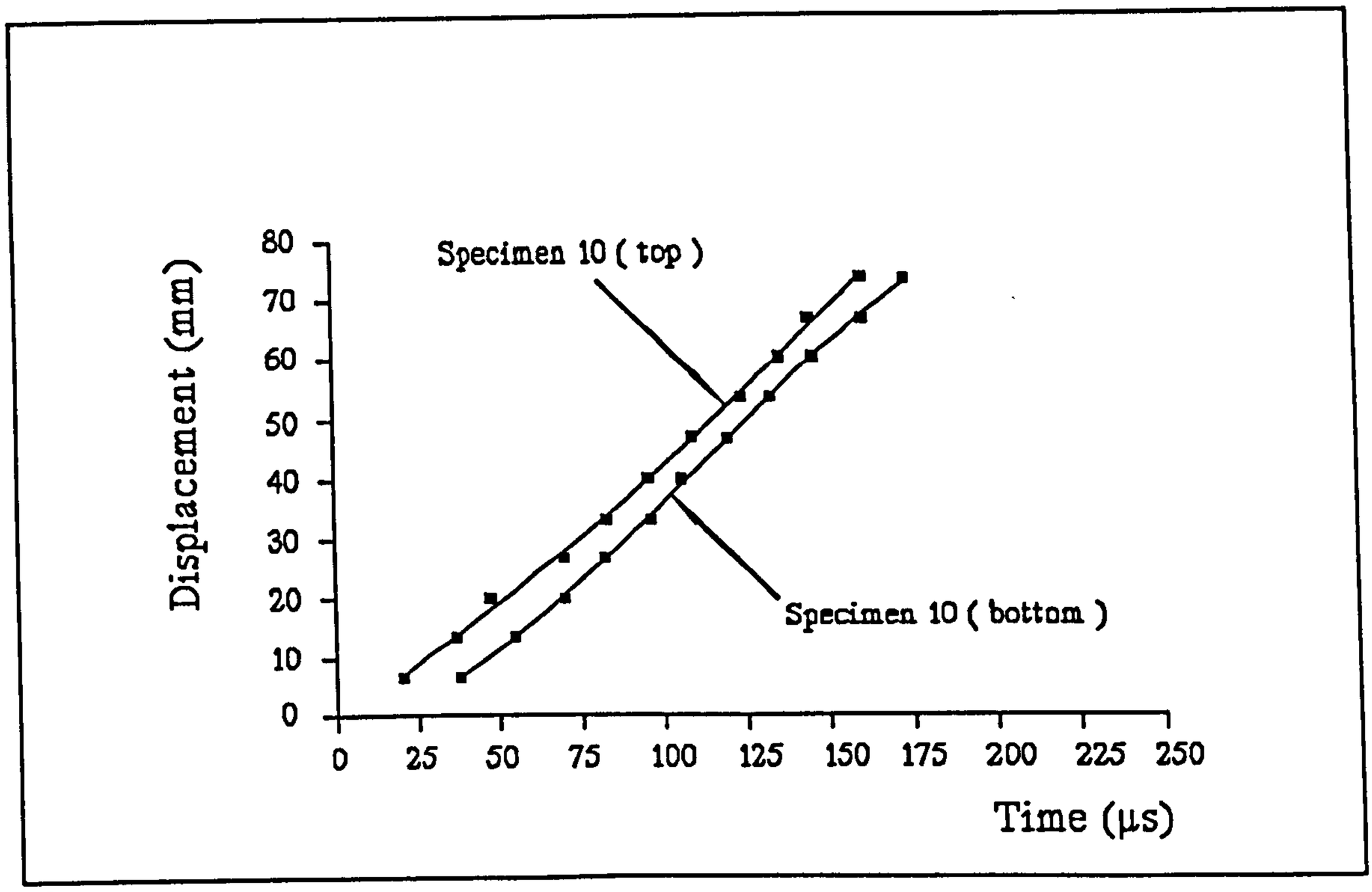

(f)

Figs. 9.8(a-f). Displacement against time graphs of the cracks travelling through the painted grid lines.

9.6.3. Velocities of the Cracks and their Branching

The velocity of crack propagation, v, in the direction perpendicular to the grid lines was calculated by measuring the gradient of the tangent on the displacement-time graphs half way between every consecutive two points. The velocities were then plotted against displacement in Figs. 9.9(a-f) and against time in Figs. 9.10(a-f). The curve fit to the graphs was cubic.

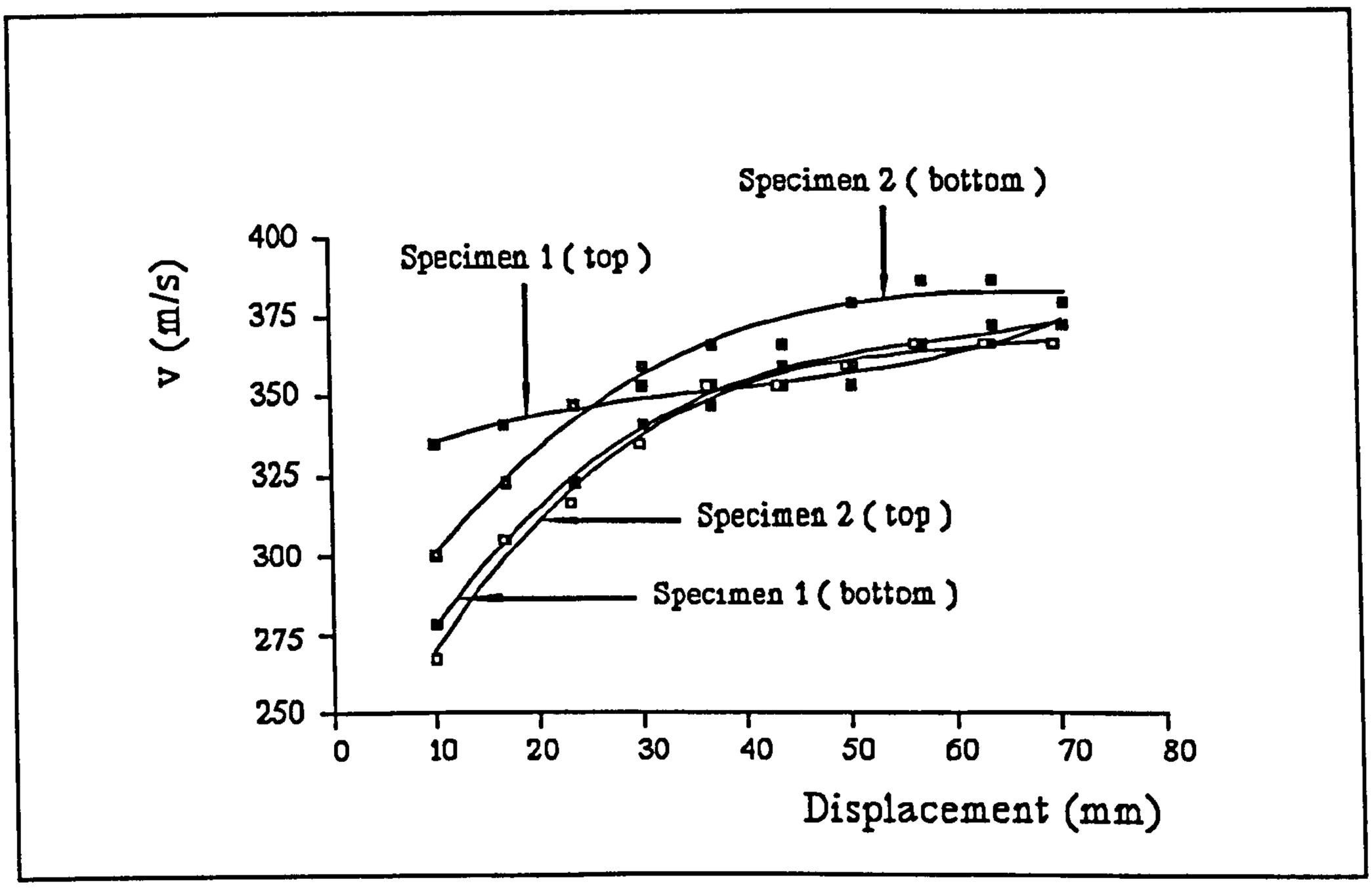
Specimen 2 (bottom)
Specimen 1 (top)
Specimen 2 (top)
Specimen 1 (bottom)
v (m/s)
400
375
350
325
300
275
250
0
10
20
30
40
50
60
70
80
Displacement (mm)

(a)

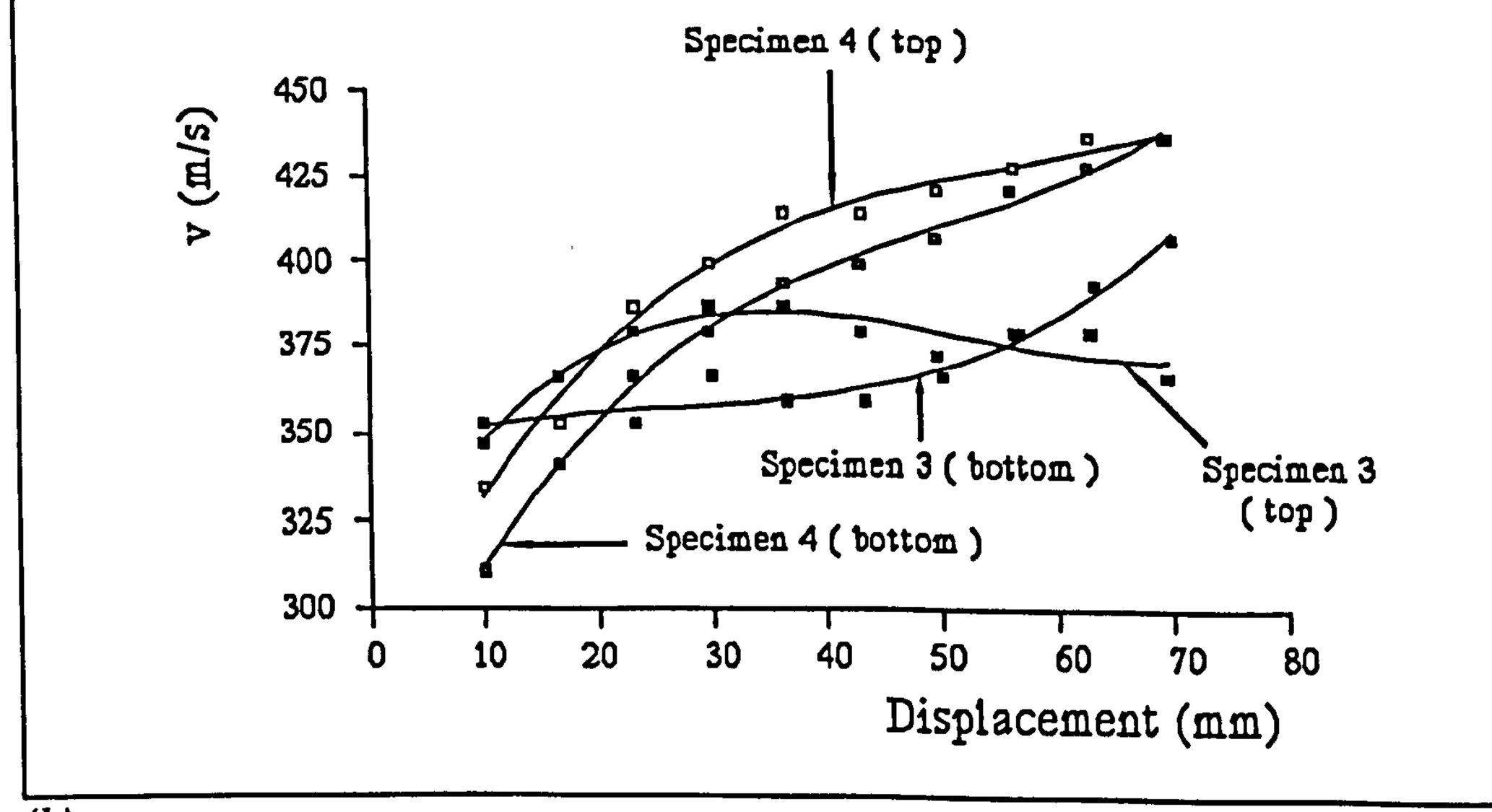
Specimen 4 (top)
v (m/s)
450
425
400
375
350
325
300
Specimen 3 (bottom)
Specimen 3
(top)
Specimen 4 (bottom)
0
10
20
30
40
50
60
70
80
Displacement (mm)

(b)

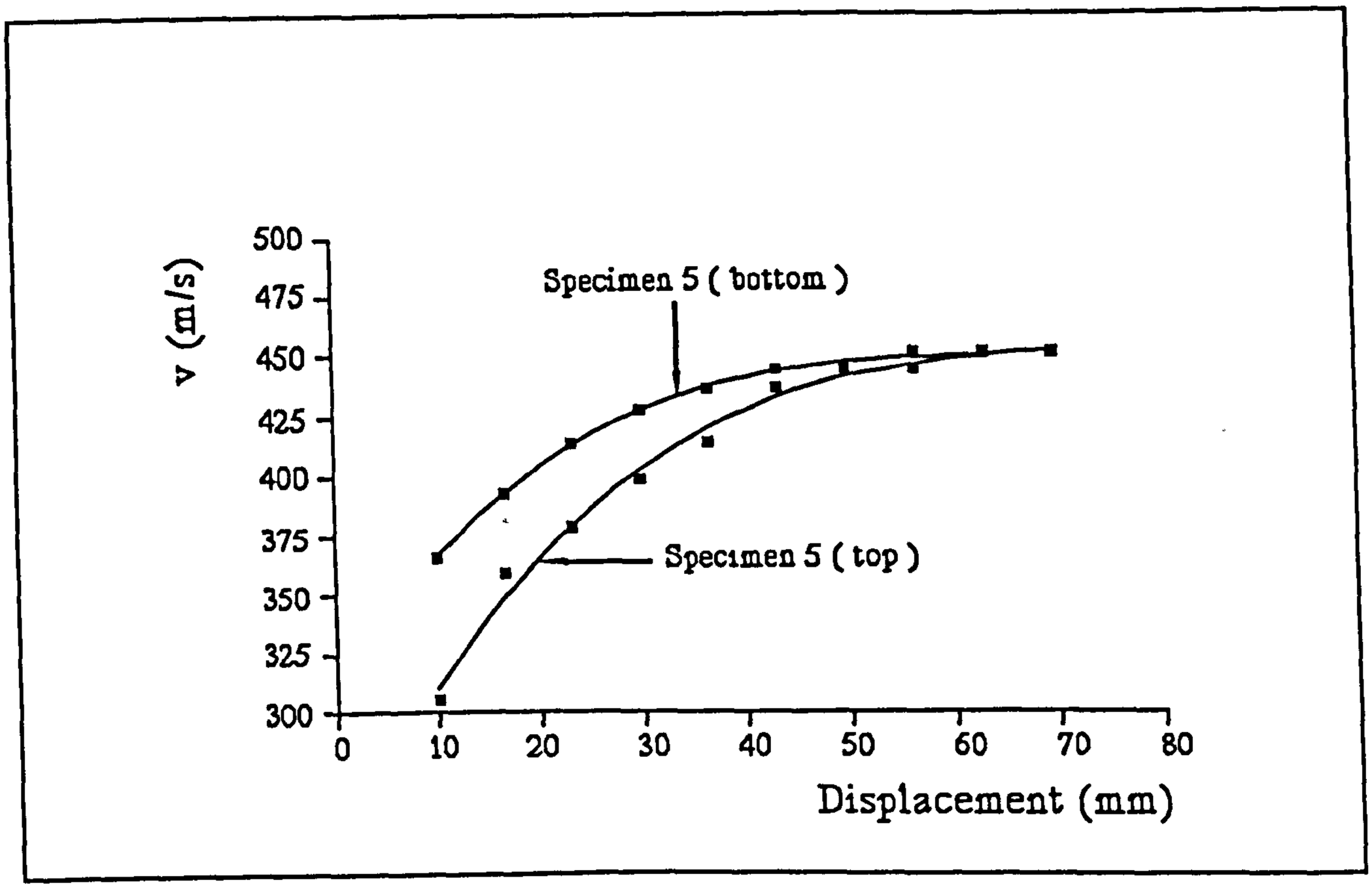
v (m/s)
500
475
450
425
400
375
350
325
300
0
10
20
30
40
50
60
70
80
Specimen 5 (bottom)
Specimen 5 (top)
Displacement (mm)

(c)

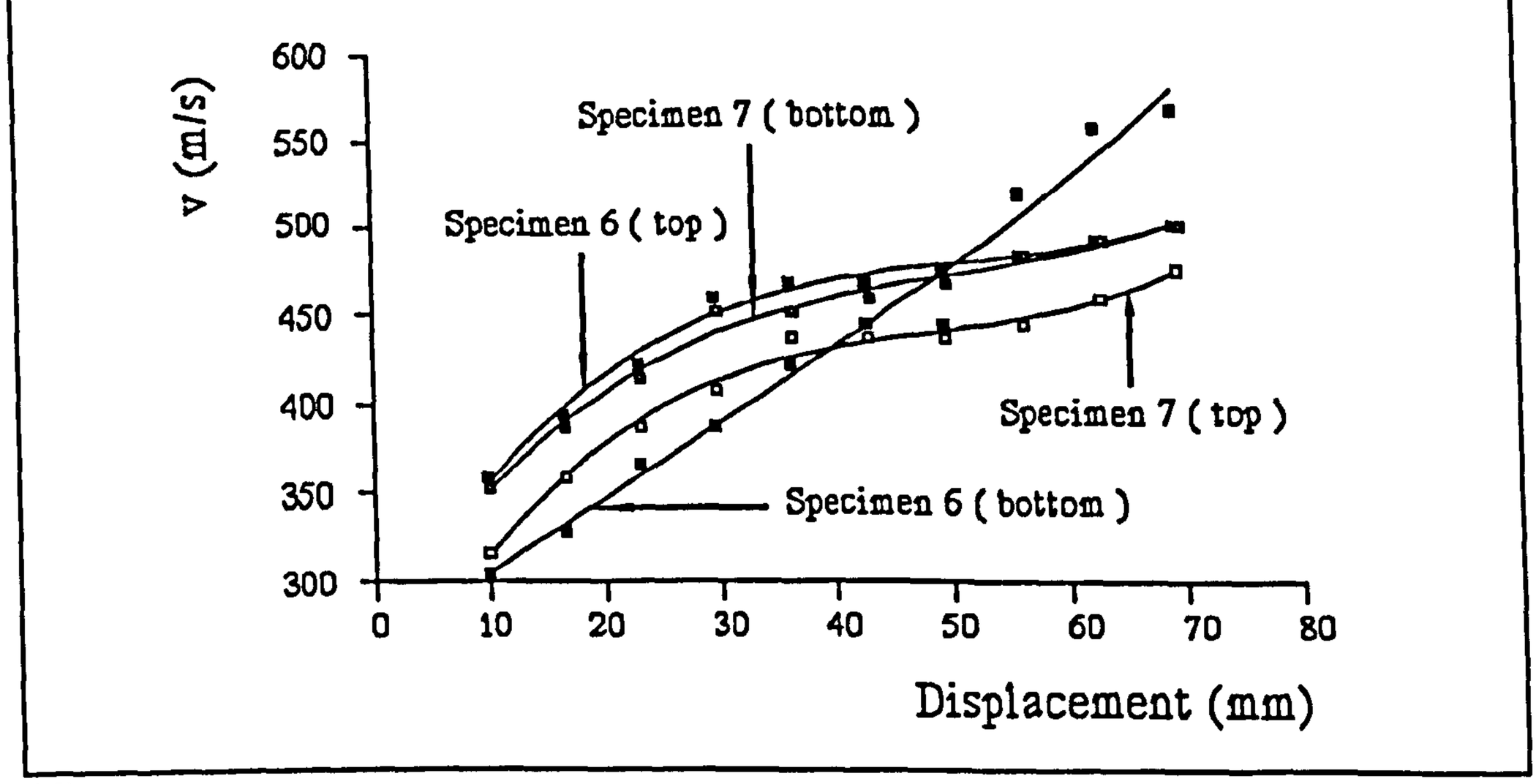
v (m/s)
600
550
500
450
400
350
300
0
10
20
30
40
50
60
70
80
Specimen 7 (bottom)
Specimen 6 (top)
Specimen 7 (top)
Specimen 6 (bottom)
Displacement (mm)

(d)

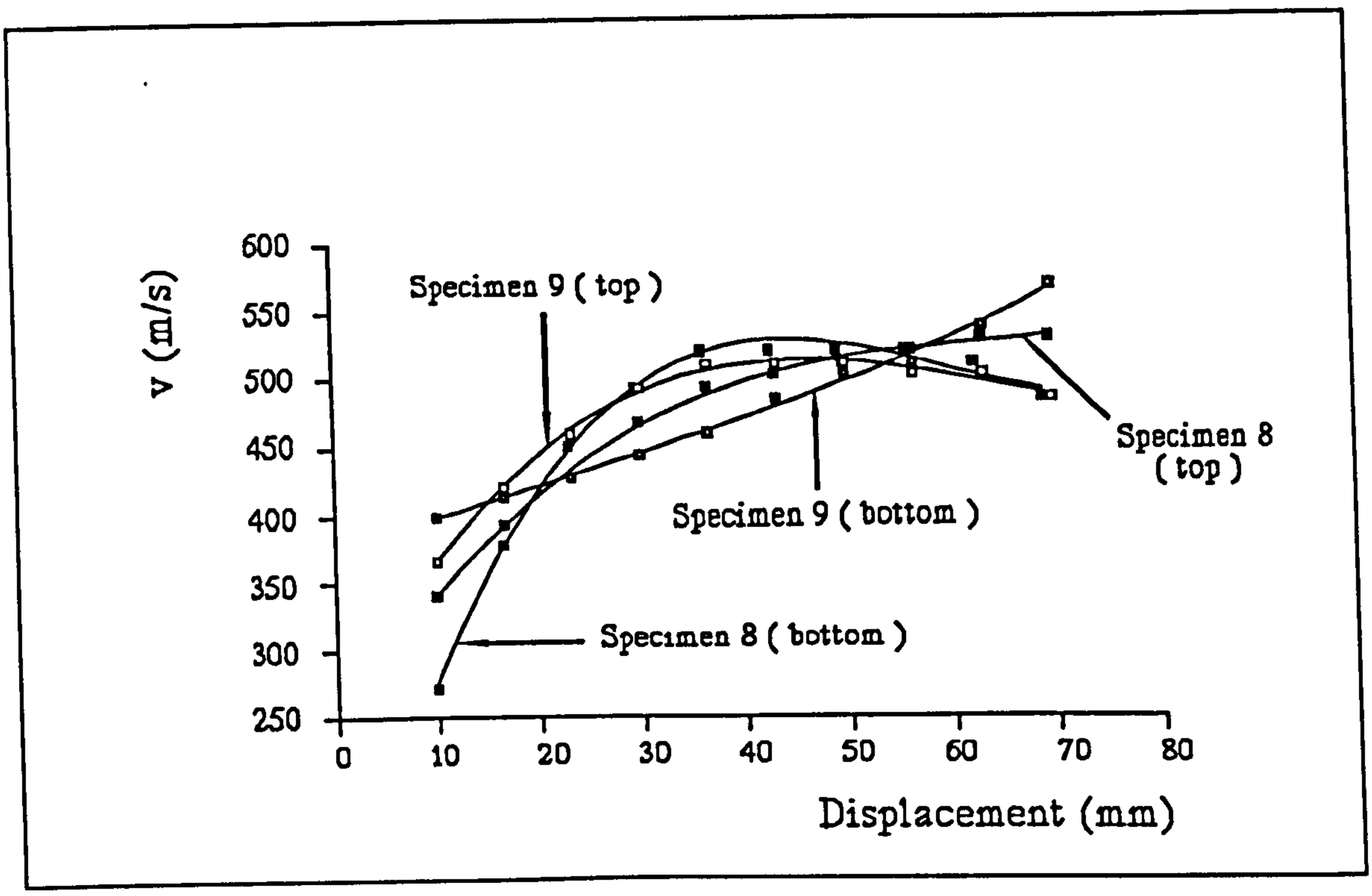

(e)

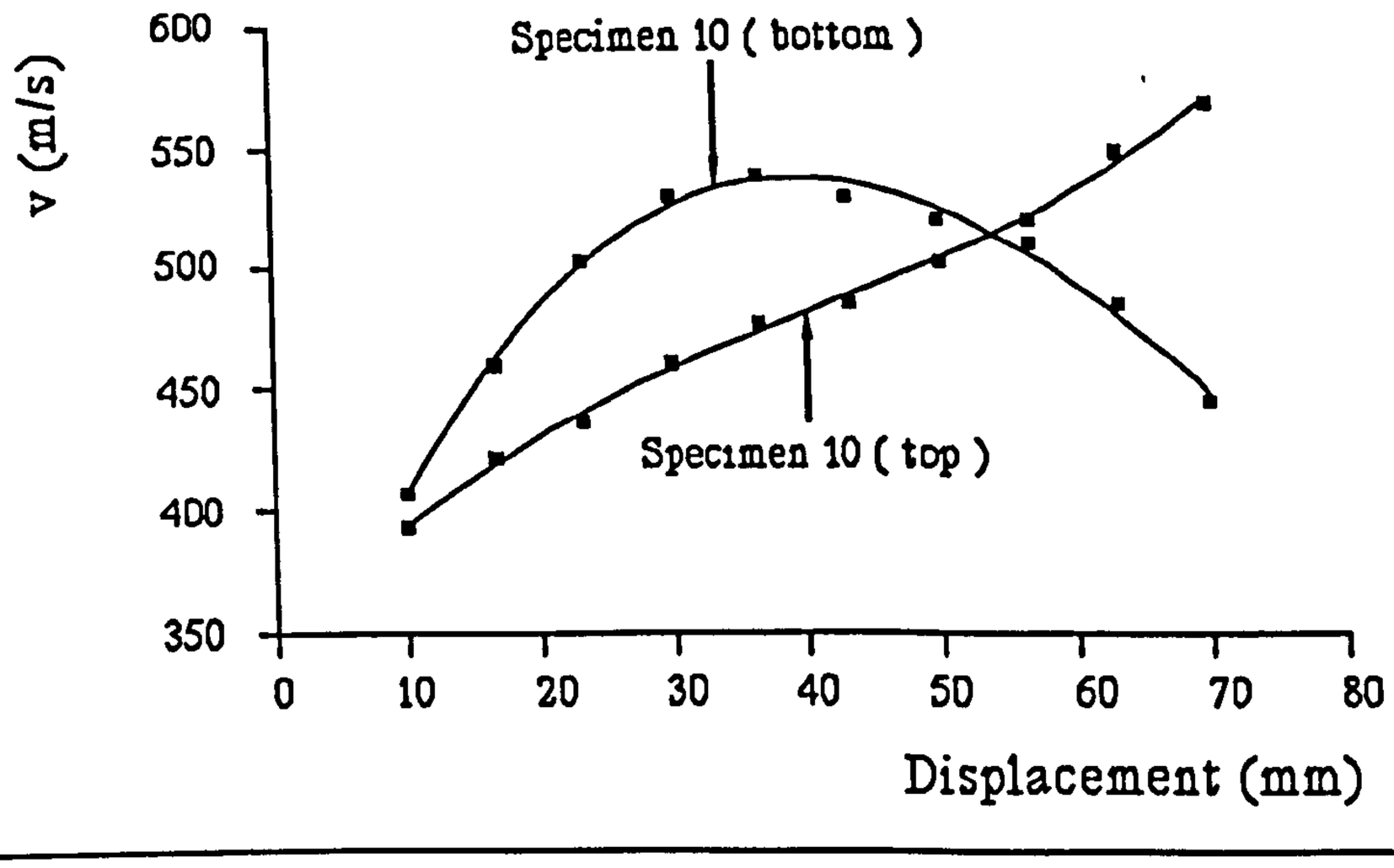

(f)

Figs. 9.9(a-f). Velocity against displacement graphs of the crack propagating through the grid lines.

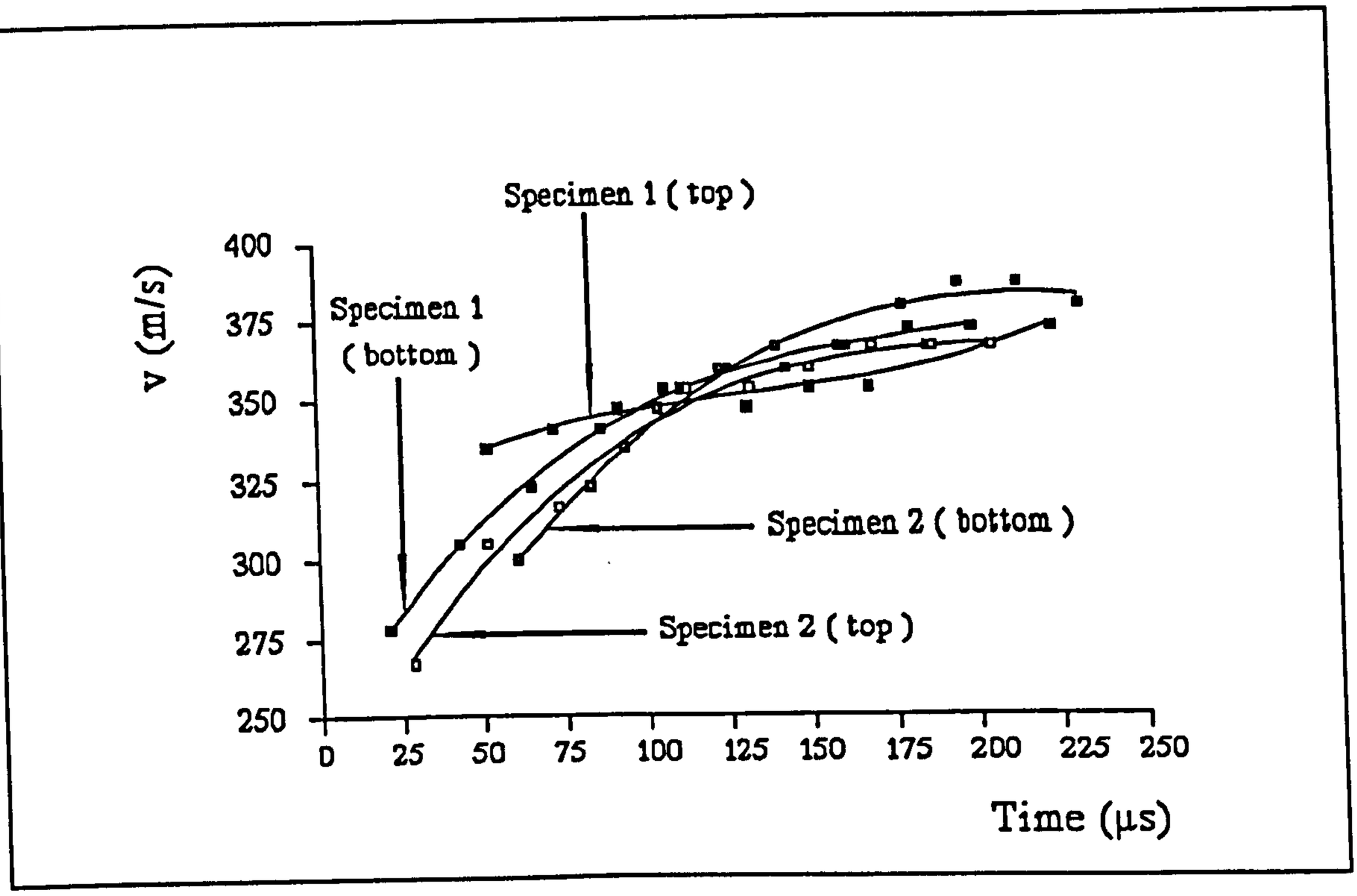
Specimen 1 (top)
Specimen 1
(bottom)
v (m/s)
400
375
350
325
300
275
250
Specimen 2 (bottom)
Specimen 2 (top)
0
25
50
75
100
125
150
175
200
225
250
Time (μs)

(a)

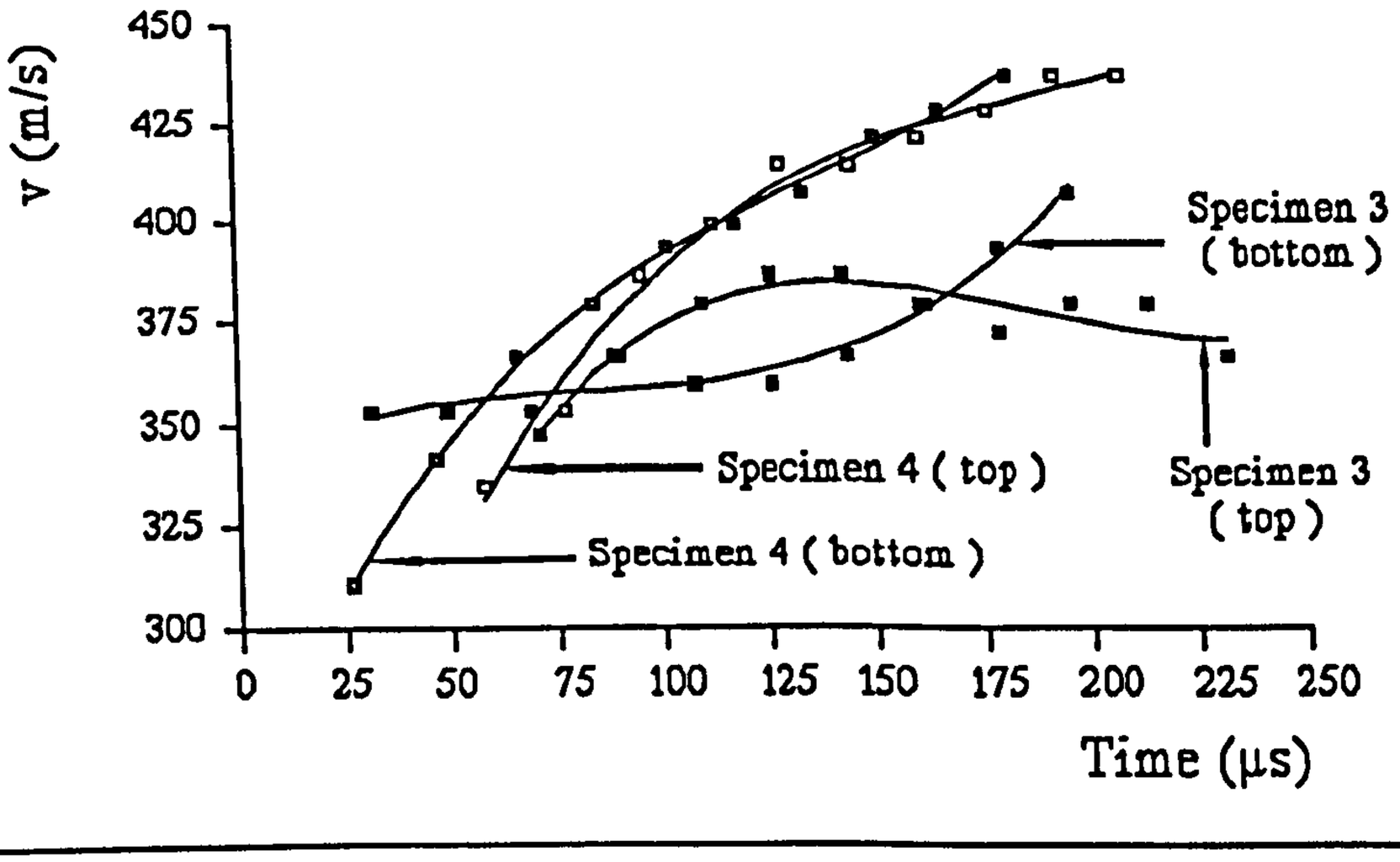
v (m/s)
450
425
400
375
350
325
300
Specimen 3
(bottom)
Specimen 4 (top)
Specimen 3
(top)
Specimen 4 (bottom)
0
25
50
75
100
125
150
175
200
225
250
Time (μs)

(b)

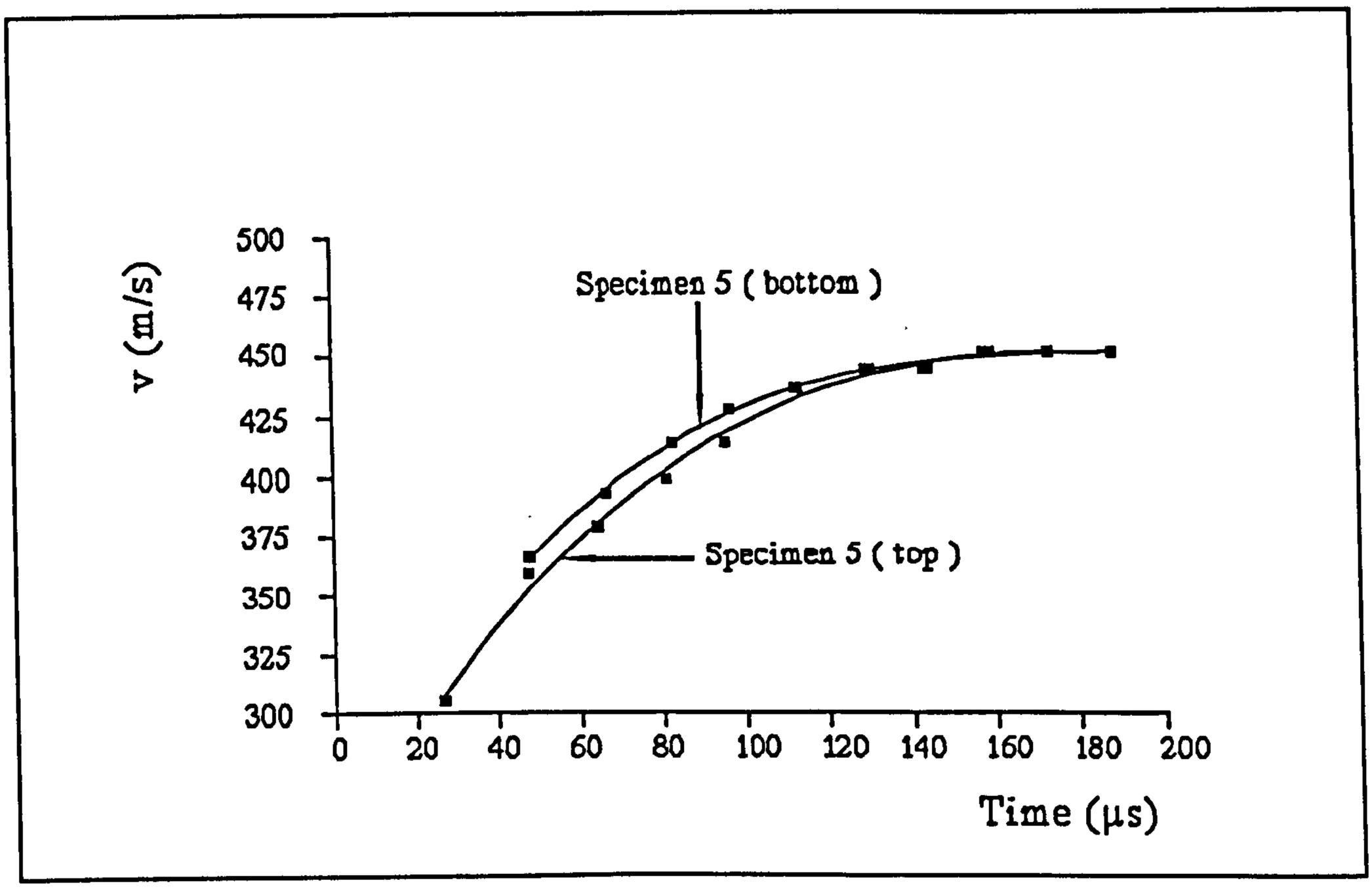
v (m/s)
500
475
450
425
400
375
350
325
300
0
20
40
60
80
100
120
140
160
180
200
Time (μs)
Specimen 5 (bottom)
Specimen 5 (top)

(c)

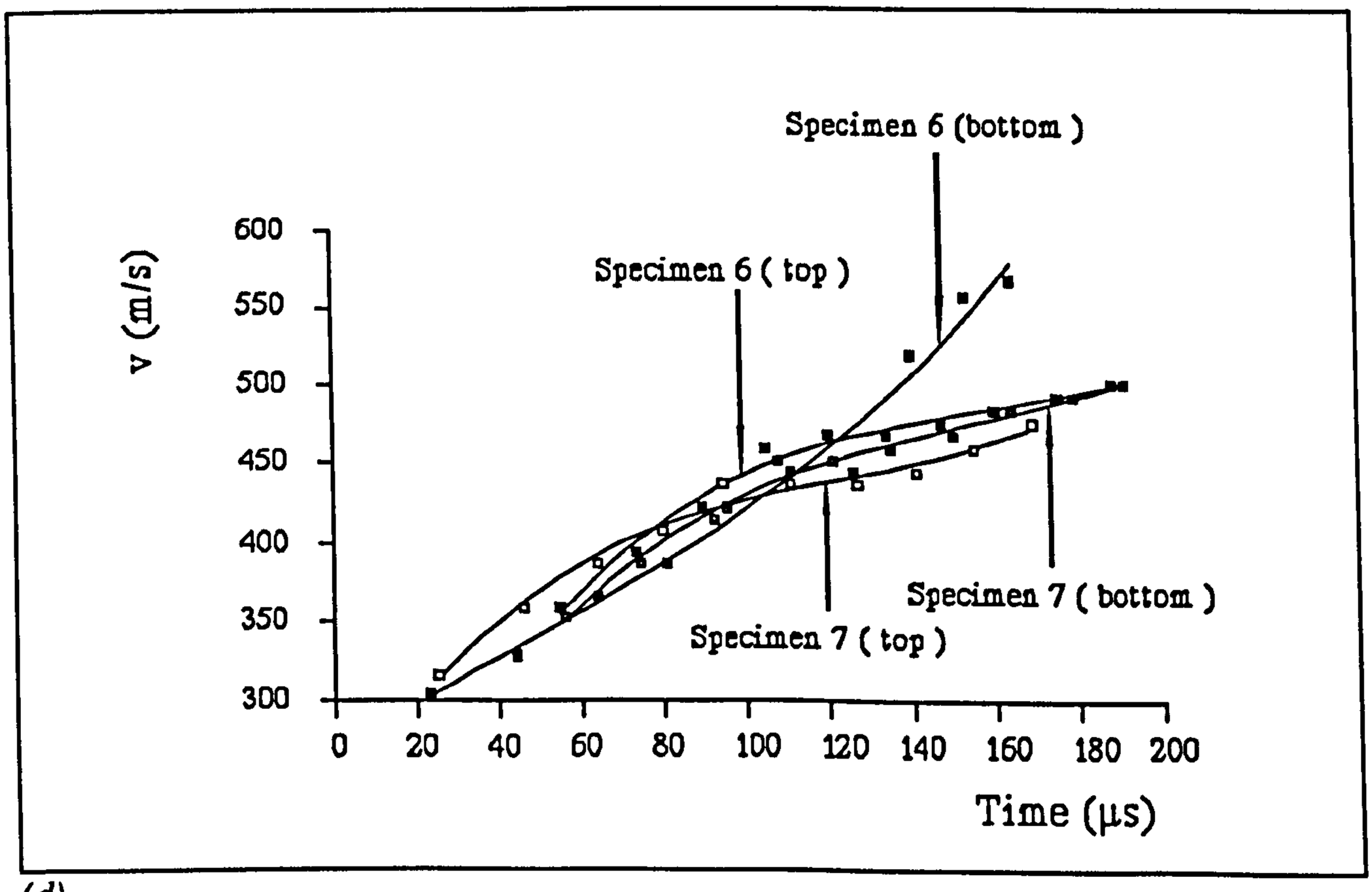
v (m/s)
600
550
500
450
400
350
300
0
20
40
60
80
100
120
140
160
180
200
Time (μs)
Specimen 6 (bottom)
Specimen 6 (top)
Specimen 7 (bottom)
Specimen 7 (top)

(d)

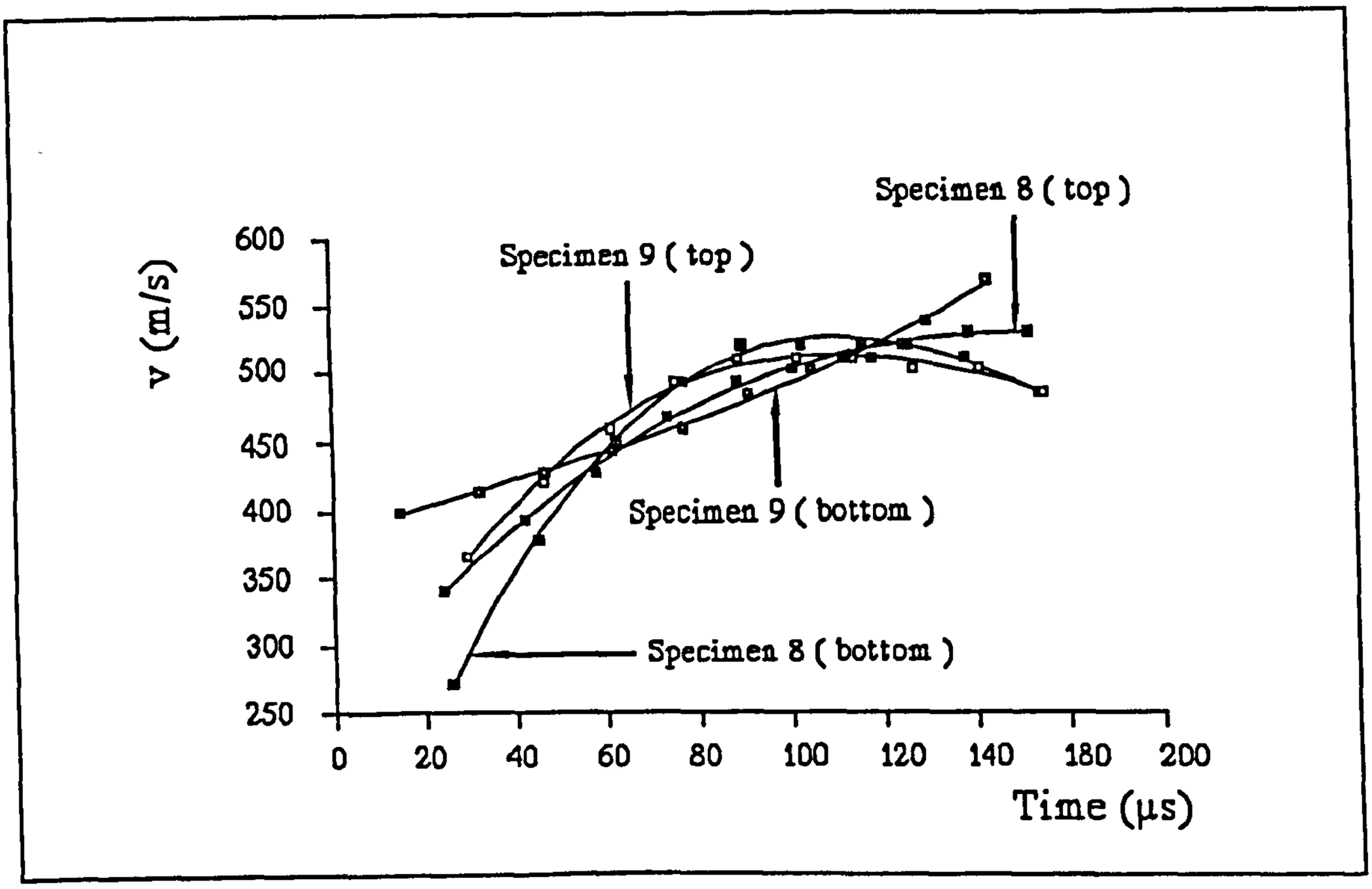

(e)

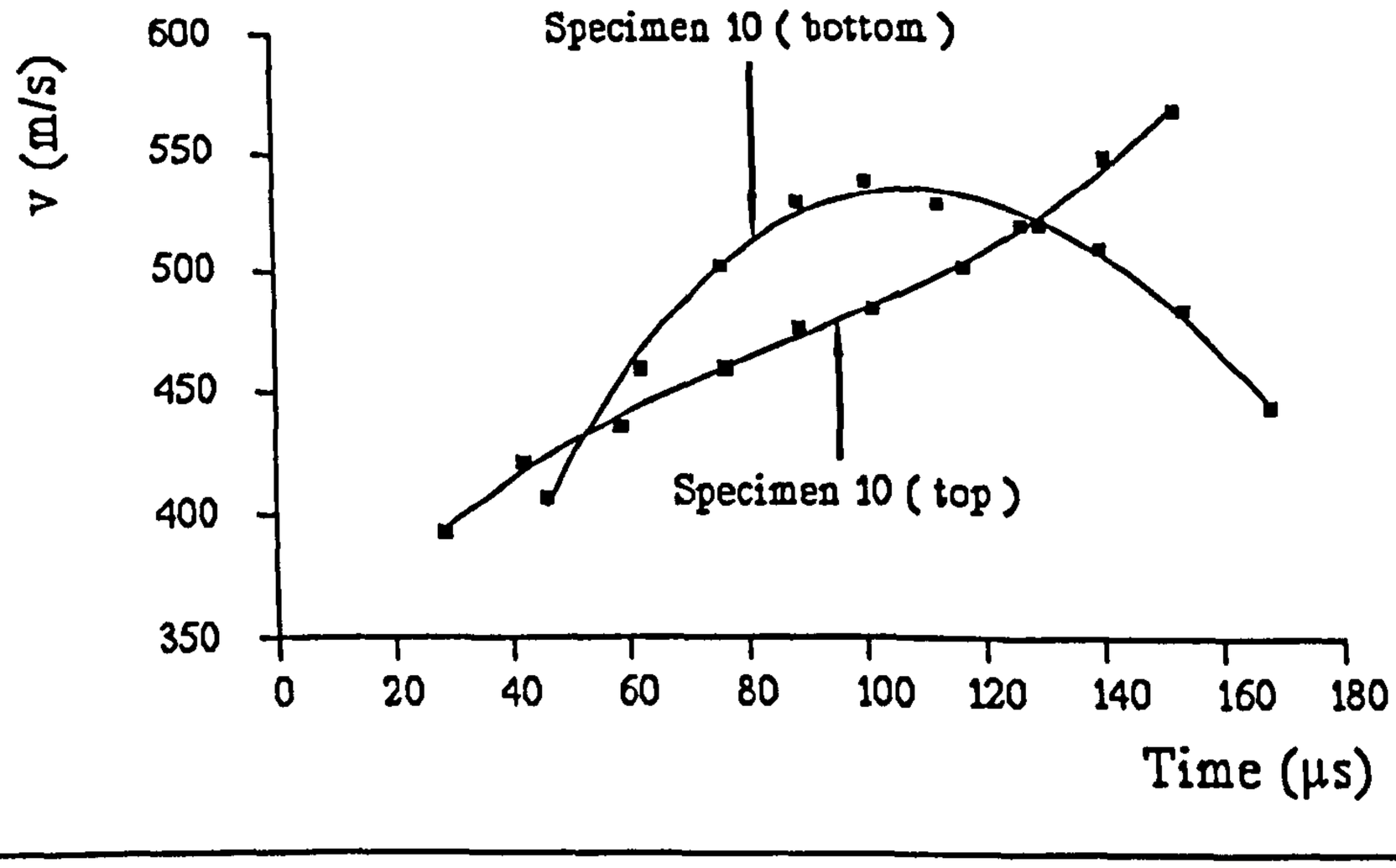

(f)

Figs. 9.10(a-f). *Velocity against time graphs of the crack propagating through the grid lines.*

In addition, it is useful to show the velocities of the crack propagating at each

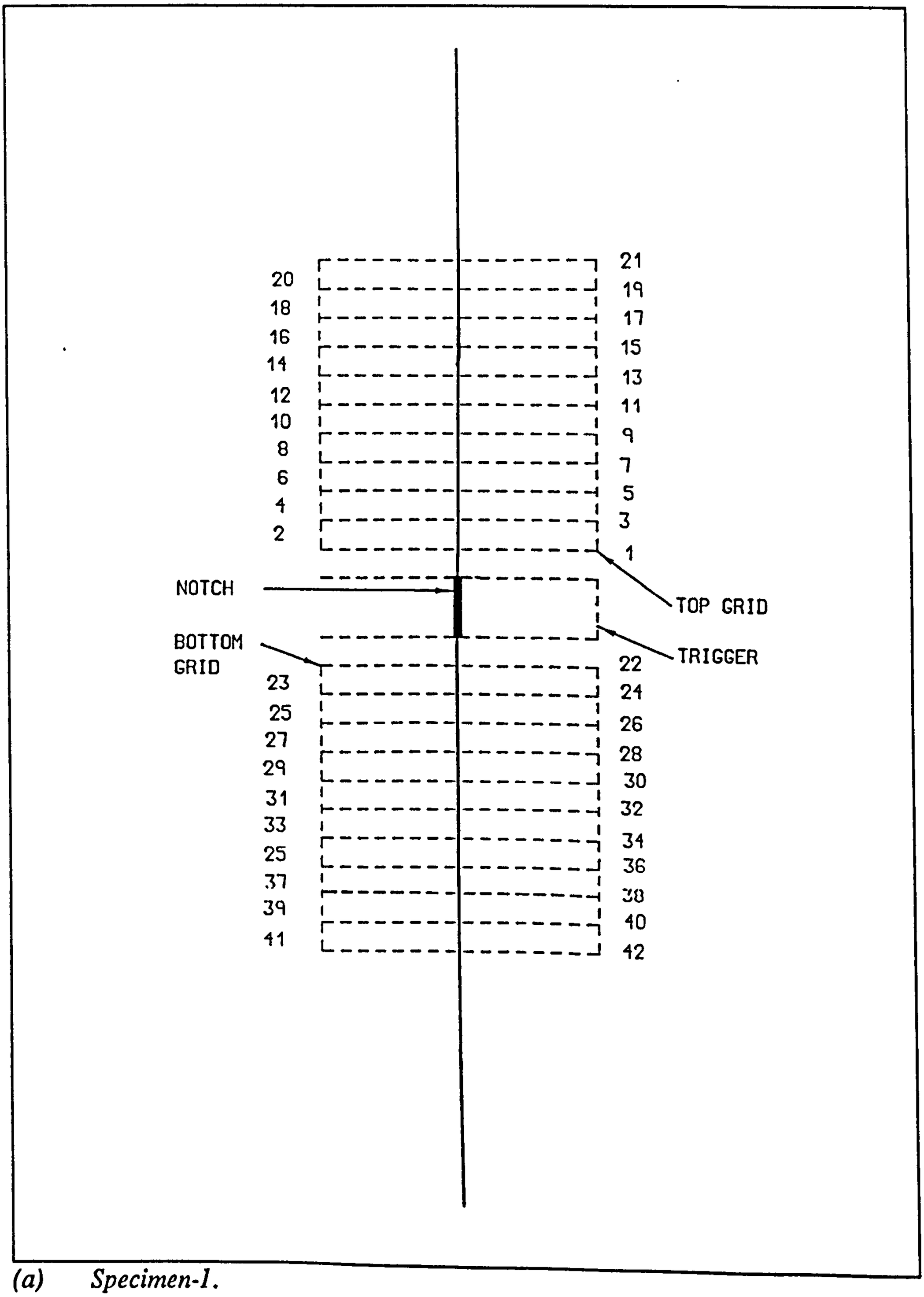

(a) Specimen-1.

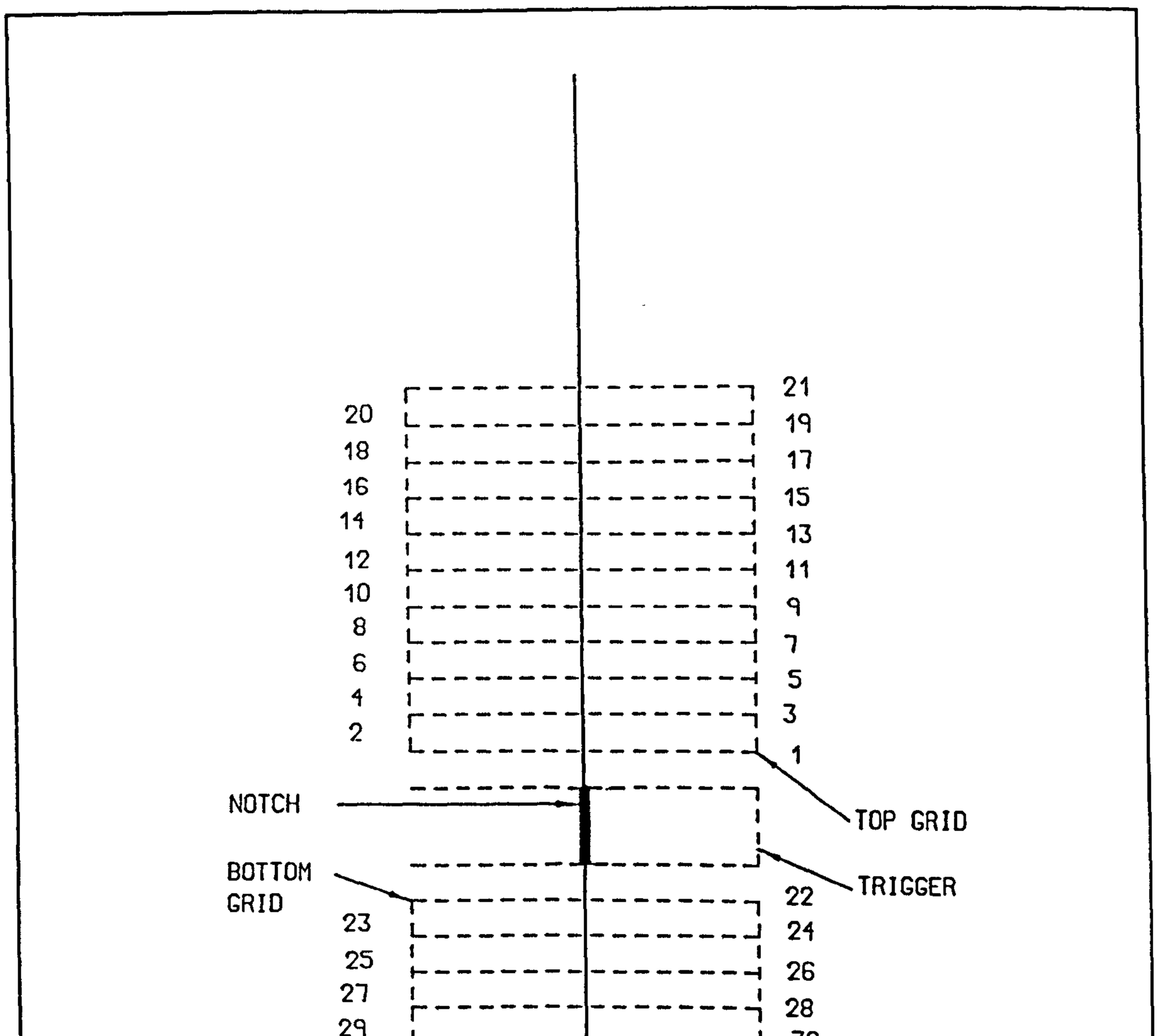
21
20
19
18
17
16
15
14
13
12
11
10
9
8
7
6
5
4
3
2
1
NOTCH
TOP GRID
BOTTOM GRID
TRIGGER
22
23
24
25
26
27
28
29
30
31
32
33
34
25
36
37
38
39
40
41
42

(b) Specimen-2.

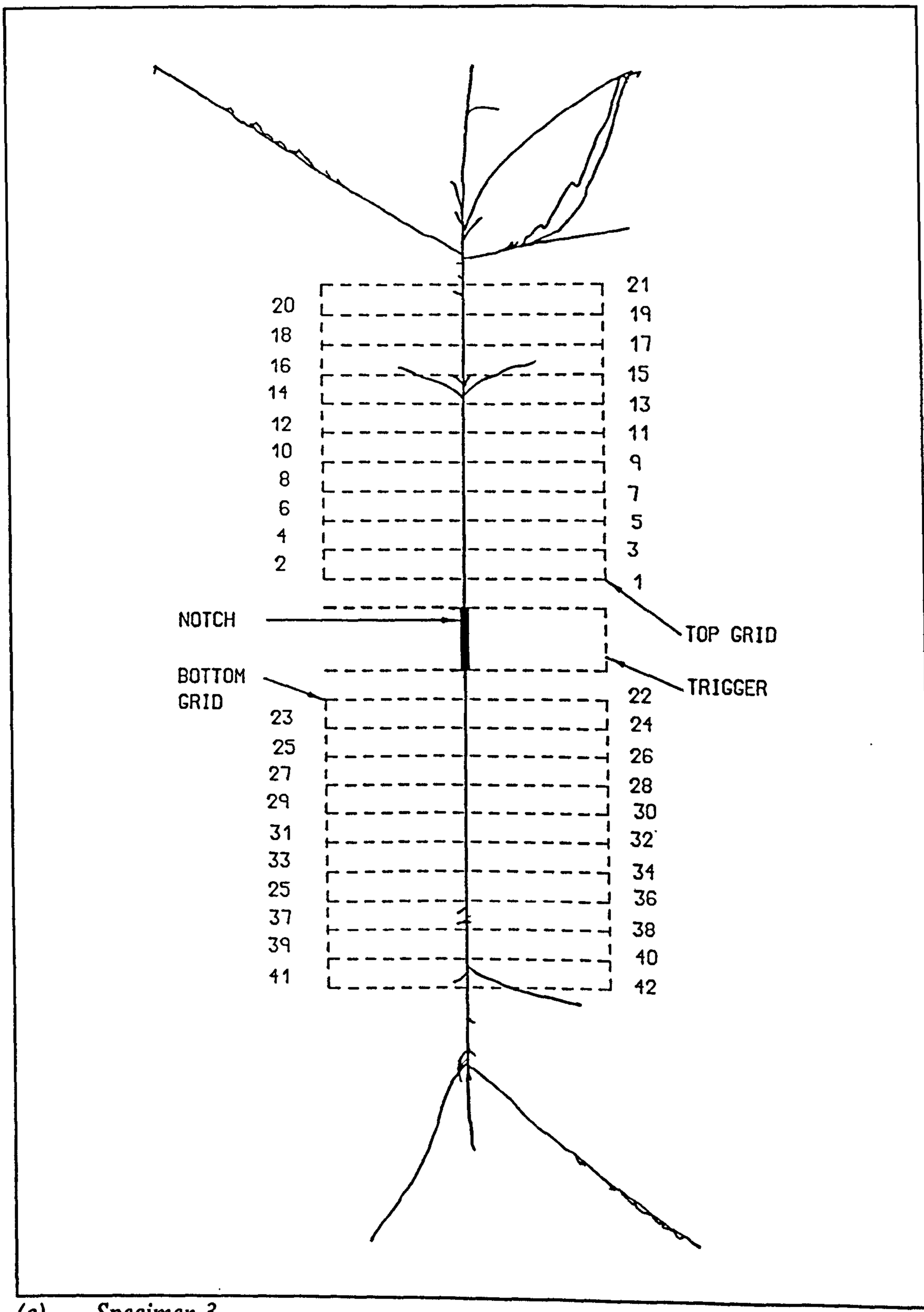
21
20
19
18
17
16
15
14
13
12
11
10
9
8
7
6
5
4
3
2
1
NOTCH
TOP GRID
BOTTOM
GRID
TRIGGER
22
23
24
25
26
27
28
29
30
31
32
33
34
25
36
37
38
39
40
41
42

(c) Specimen-3.

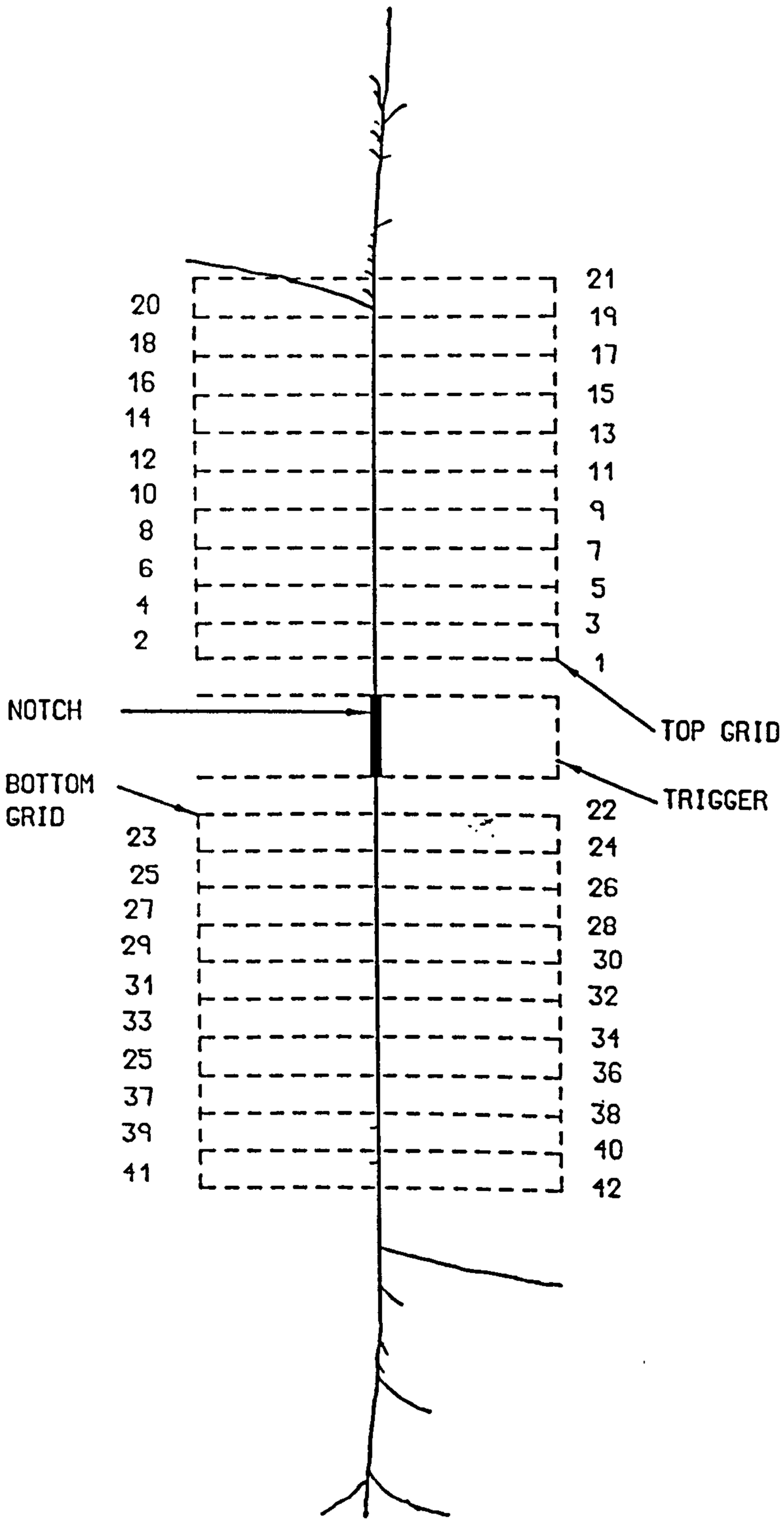
20
18
16
14
12
10
8
6
4
2
21
19
17
15
13
11
9
7
5
3
1
NOTCH
TOP GRID
BOTTOM GRID
TRIGGER
23
25
27
29
31
33
25
37
39
41
22
24
26
28
30
32
34
36
38
40
42

(d) Specimen-4.

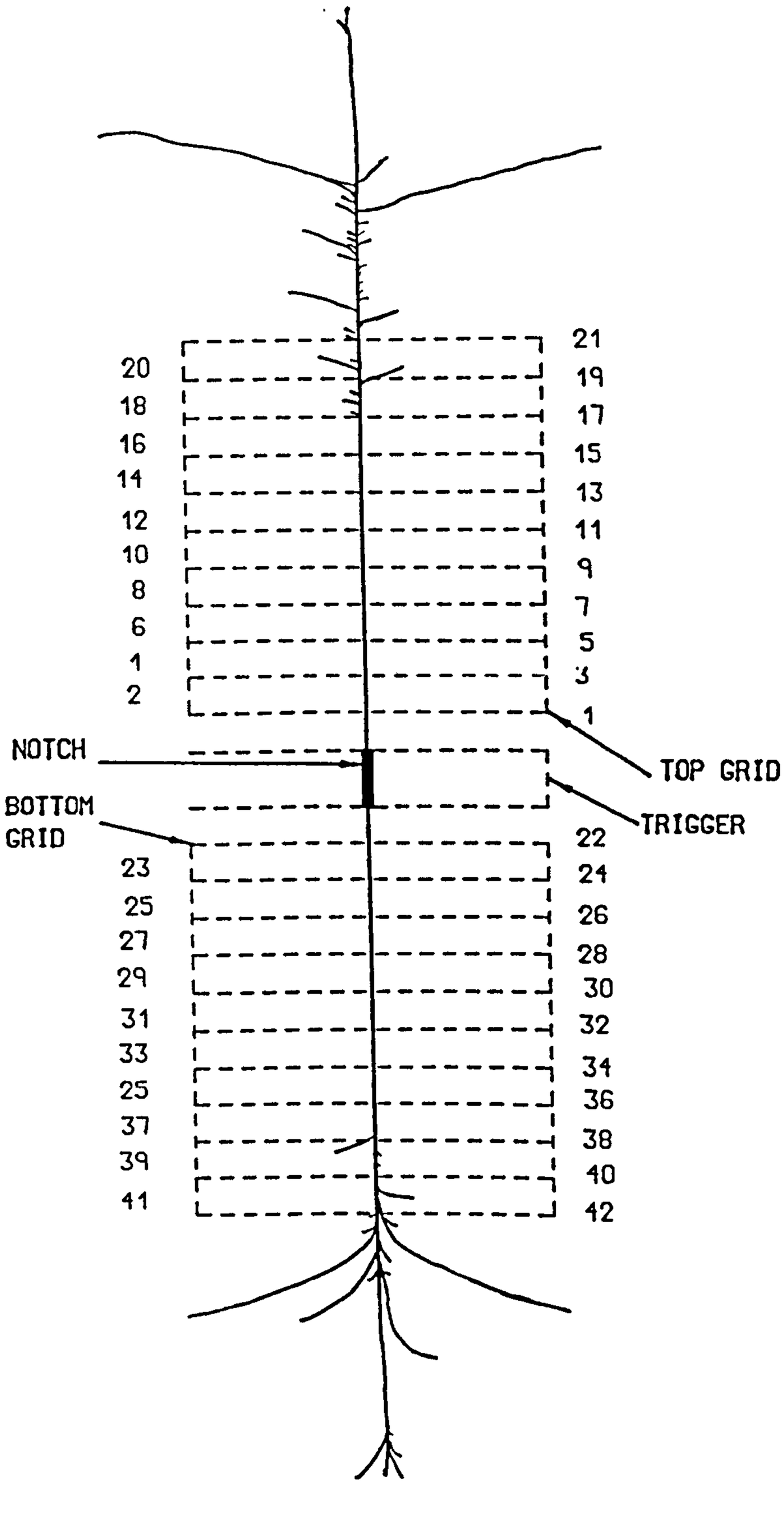
21
20
19
18
17
16
15
14
13
12
11
10
9
8
7
6
5
1
3
2
1
NOTCH
TOP GRID
BOTTOM
GRID
TRIGGER
22
23
24
25
26
27
28
29
30
31
32
33
34
25
36
37
38
39
40
41
42

(e) Specimen-5.

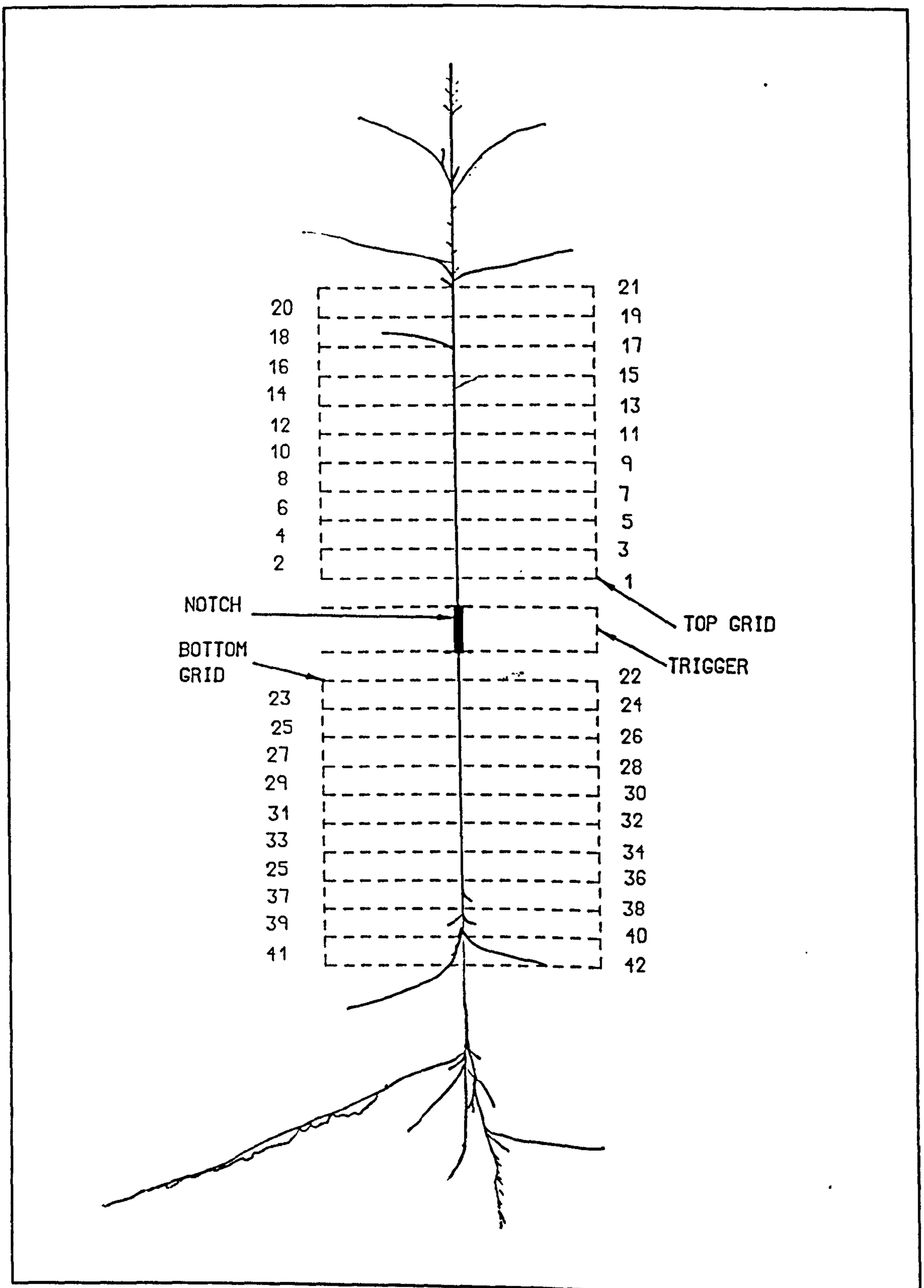
21
20
19
18
17
16
15
14
13
12
11
10
9
8
7
6
5
4
3
2
1
NOTCH
TOP GRID
BOTTOM GRID
TRIGGER
22
23
24
25
26
27
28
29
30
31
32
33
34
25
36
37
38
39
40
41
42

(f) Specimen-6.

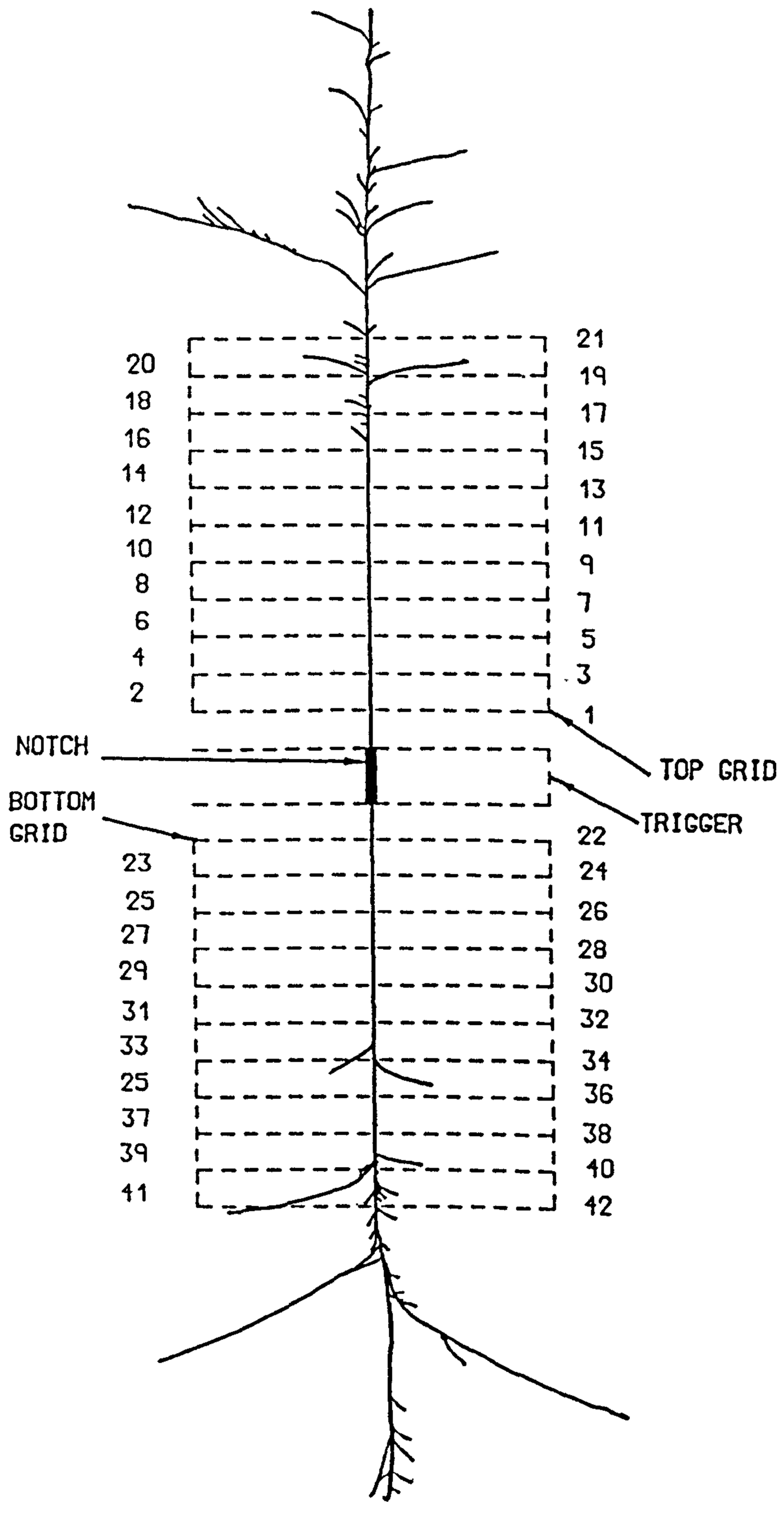
21
20
19
18
17
16
15
14
13
12
11
10
9
8
7
6
5
4
3
2
1
NOTCH
TOP GRID
BOTTOM GRID
TRIGGER
22
23
24
25
26
27
28
29
30
31
32
33
34
25
36
37
38
39
40
41
42

(g) Specimen-7.

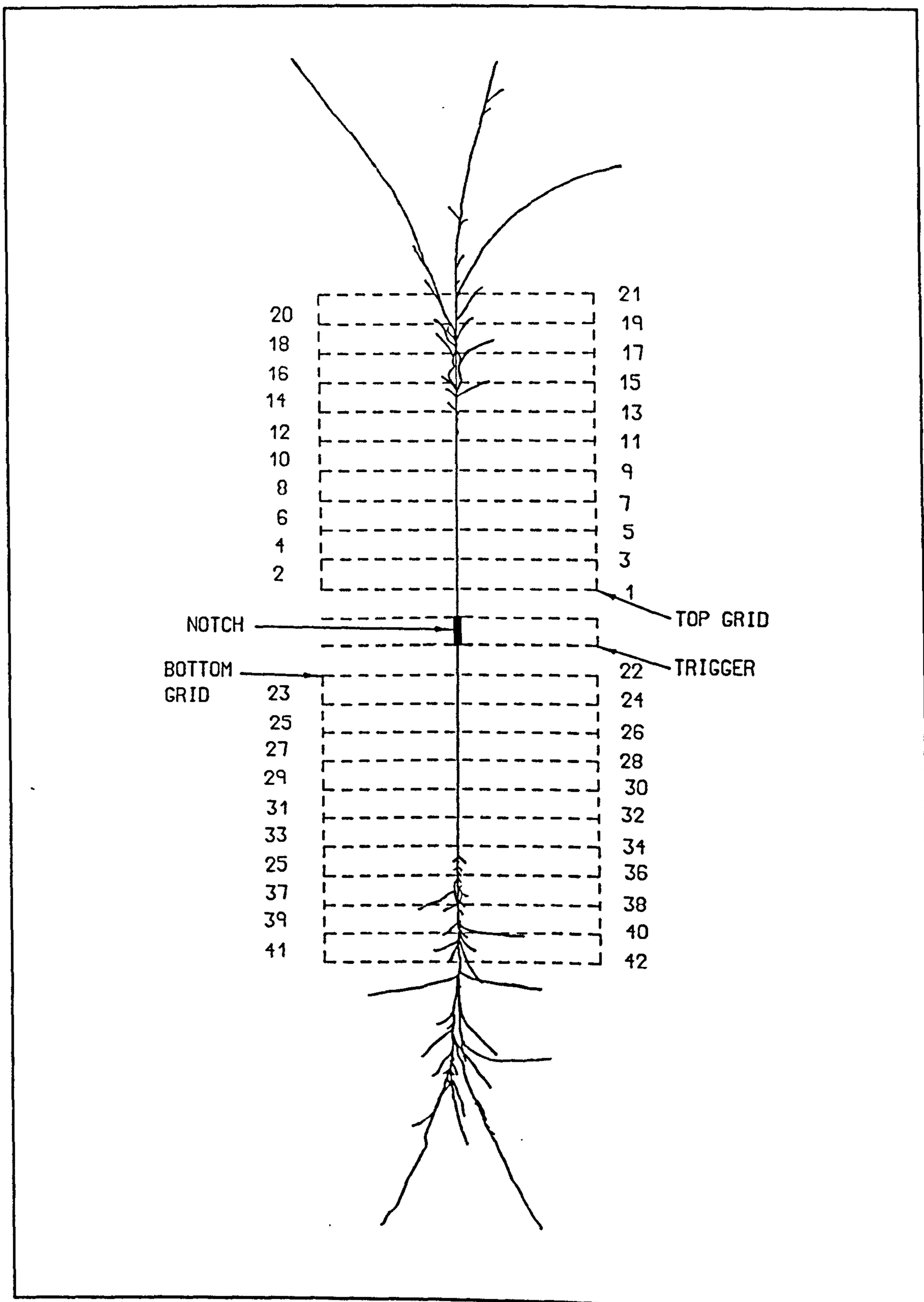
21
20
19
18
17
16
15
14
13
12
11
10
9
8
7
6
5
4
3
2
1
TOP GRID
NOTCH
TRIGGER
22
BOTTOM
GRID
23
24
25
26
27
28
29
30
31
32
33
34
25
36
37
38
39
40
41
42

(h) Specimen-8.

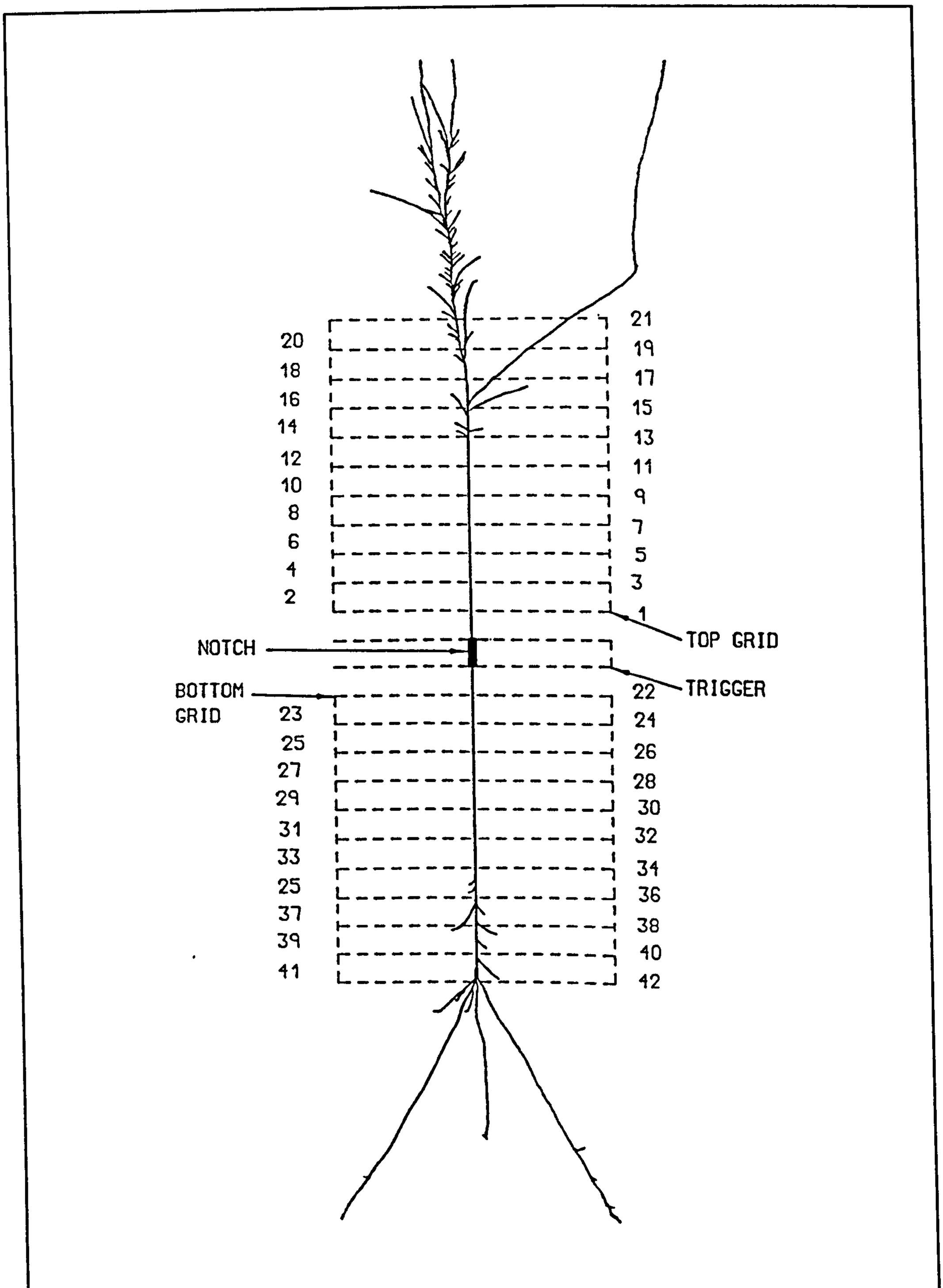
20
18
16
14
12
10
8
6
4
2
21
19
17
15
13
11
9
7
5
3
1
TOP GRID
NOTCH
TRIGGER
BOTTOM
GRID
23
25
27
29
31
33
25
37
39
41
22
24
26
28
30
32
34
36
38
40
42

(i) Specimen-9.

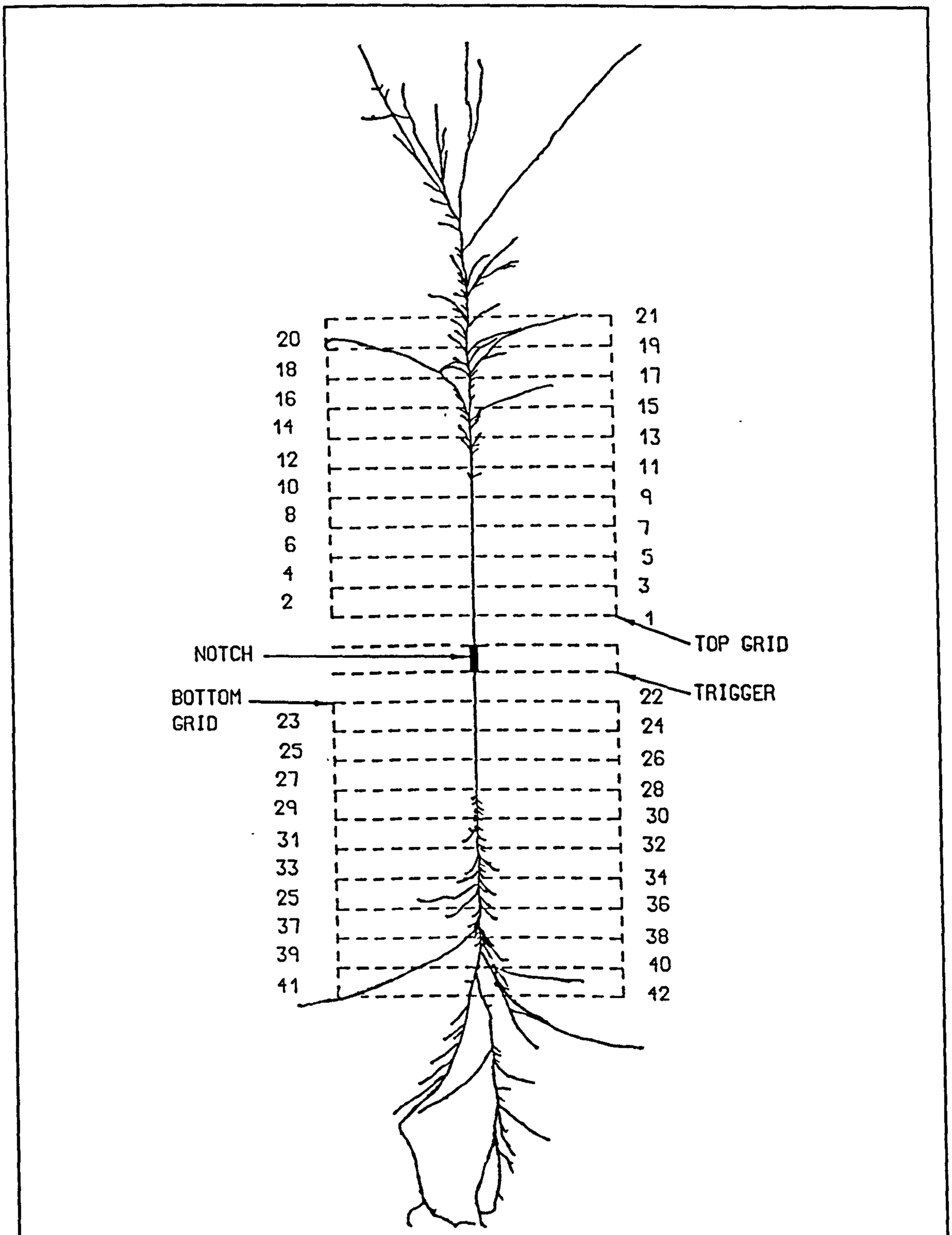

(j) Specimen-10.

Figs. 9.11(a-j). *The crack, the branching phenomenon, the top and bottom grids (dashed line), the trigger (dashed line) and the location numbers unfolded and shown in the plane of the paper to a scale of 1 : 1.43.*

point half way between every two consecutive grid lines, and the time of occurrence of fracture at each grid line. Therefore, these locations were numbered from 1 to 21 for the grid above the semi-circular notch (top grid), and from 22 to 42 for the grid below the notch (bottom grid) - see Figs. 9.11(a-j). The instantaneous velocities and time of occurrences corresponding to the locations on the grids are given in Tables 9.3(a-j).

Figs. 9.11 also display the crack and all the branches which developed in the middle cylinder of each pressure tube.

Location at the grid - Fig. 9.11	Instantaneous crack velocity, v (m/s)	Fracture occurrence time (μs)
1	-	42
2	335	-
3	-	62
4	341	-
5	-	82
6	347	-
7	-	101
8	353	-
9	-	120
10	347	-
11	-	141
12	353	-
13	-	158
14	353	-
15	-	177

16	366	-
17	-	195
18	366	-
19	-	214
20	372	-
21	-	232
22	-	9
23	278	-
24	-	34
25	305	-
26	-	53
27	323	-
28	-	77
29	341	-
30	-	95
31	353	-
32	-	116
33	359	-
34	-	134
35	359	-
36	-	152
37	366	-
38	-	169
39	372	-
40	-	190
41	372	-
42	-	207

(a) Specimen-1.

Location at the grid - Fig. 9.11	Instantaneous crack velocity, v (m/s)	Fracture occurrence time (μs)
1	-	34
2	267	-
3	-	40
4	305	-
5	-	63
6	317	-
7	-	84
8	335	-
9	-	104
10	353	-
11	-	122
12	353	-
13	-	141
14	359	-
15	-	158
16	366	-
17	-	179
18	366	-
19	-	195
20	366	-
21	-	214
22	-	50
23	300	-
24	-	72
25	323	-
26	-	94
27	347	-
28	-	113

29	359	-
30	-	132
31	366	-
32	-	148
33	366	-
34	-	170
35	379	-
36	-	185
37	386	-
38	-	204
39	386	-
40	-	222
41	379	-
42	-	239

(b) Specimen-2.

Location at the grid - Fig. 9.11	Instantaneous crack velocity, v (m/s)	Fracture occurrence time (μs)
1	-	63
2	347	-
3	-	79
4	366	-
5	-	101
6	379	-
7	-	119
8	386	-
9	-	133
10	386	-

11	-	152
12	379	-
13	-	170
14	372	-
15	-	187
16	379	-
17	-	205
18	379	-
19	-	223
20	366	-
21	-	241
22	-	23
23	353	-
24	-	40
25	353	-
26	-	59
27	353	-
28	-	80
29	366	-
30	-	99
31	359	-
32	-	118
33	359	-
34	-	134
35	366	-
36	-	153
37	379	-
38	-	171
39	393	-

40	-	187
41	407	-
42	-	205

(c) Specimen-3.

Location at the grid - Fig. 9.11	Instantaneous crack velocity, v (m/s)	Fracture occurrence time (μs)
1	-	48
2	335	-
3	-	68
4	353	-
5	-	87
6	386	-
7	-	104
8	399	-
9	-	121
10	414	-
11	-	137
12	414	-
13	-	153
14	421	-
15	-	168
16	428	-
17	-	185
18	436	-
19	-	200
20	436	-
21	-	215

22	-	16
23	311	-
24	-	37
25	341	-
26	-	56
27	366	-
28	-	76
29	379	-
30	-	93
31	393	-
32	-	111
33	399	-
34	-	124
35	407	-
36	-	143
37	421	-
38	-	158
39	428	-
40	-	174
41	436	-
42	-	189

(d) Specimen-4.

Location at the grid - Fig. 9.11	Instantaneous crack velocity, v (m/s)	Fracture occurrence time (μs)
1	-	13
2	305	-
3	-	40

4	359	-
5	-	55
6	379	-
7	-	74
8	399	-
9	-	88
10	414	-
11	-	102
12	436	-
13	-	122
14	444	-
15	-	137
16	444	-
17	-	151
18	451	-
19	-	166
20	451	-
21	-	179
22	-	38
23	366	-
24	-	58
25	393	-
26	-	75
27	414	-
28	-	89
29	428	-
30	-	103
31	436	-
32	-	122

33	444	-
34	-	136
35	444	-
36	-	150
37	451	-
38	-	164
39	451	-
40	-	181
41	451	-
42	-	194

(e) Specimen-5.

Location at the grid - Fig. 9.11	Instantaneous crack velocity, v (m/s)	Fracture occurrence time (μs)
1	-	46
2	359	-
3	-	64
4	393	-
5	-	83
6	421	-
7	-	96
8	459	-
9	-	113
10	468	-
11	-	127
12	468	-
13	-	141
14	476	-

15	-	153
16	484	-
17	-	167
18	493	-
19	-	182
20	502	-
21	-	194
22	-	13
23	305	-
24	-	34
25	329	-
26	-	55
27	366	-
28	-	74
29	386	-
30	-	88
31	421	-
32	-	103
33	444	-
34	-	118
35	444	-
36	-	133
37	520	-
38	-	146
39	558	-
40	-	160
41	568	-
42	-	168

(f) Specimen-6.

Location at the grid - Fig. 9.11	Instantaneous crack velocity, v (m/s)	Fracture occurrence time (μs)
1	-	15
2	317	-
3	-	36
4	359	-
5	-	56
6	386	-
7	-	72
8	407	-
9	-	88
10	436	-
11	-	101
12	436	-
13	-	120
14	436	-
15	-	134
16	444	-
17	-	148
18	459	-
19	-	162
20	476	-
21	-	176
22	-	47
23	353	-
24	-	65
25	386	-
26	-	84
27	414	-
28	-	101

29	451	-
30	-	115
31	451	-
32	-	126
33	459	-
34	-	143
35	468	-
36	-	156
37	484	-
38	-	172
39	493	-
40	-	185
41	502	-
42	-	196

(g) Specimen-7.

Location at the grid - Fig. 9.11	Instantaneous crack velocity, v (m/s)	Fracture occurrence time (μs)
1	-	15
2	341	-
3	-	34
4	393	-
5	-	51
6	428	-
7	-	64
8	468	-
9	-	82
10	493	-

11	-	95
12	502	-
13	-	106
14	510	-
15	-	118
16	520	-
17	-	133
18	529	-
19	-	145
20	529	-
21	-	158
22	-	16
23	272	-
24	-	35
25	379	-
26	-	55
27	451	-
28	-	70
29	493	-
30	-	84
31	520	-
32	-	96
33	520	-
34	-	110
35	520	-
36	-	121
37	520	-
38	-	129
39	510	-

40	-	147
41	484	-
42	-	160

(h) Specimen-8.

Location at the grid - Fig. 9.11	Instantaneous crack velocity, v (m/s)	Fracture occurrence time (μs)
1	-	21
2	366	-
3	-	38
4	421	-
5	-	55
6	459	-
7	-	68
8	493	-
9	-	83
10	510	-
11	-	95
12	510	-
13	-	109
14	510	-
15	-	119
16	502	-
17	-	134
18	502	-
19	-	148
20	484	-
21	-	161

22	-	5
23	399	-
24	-	24
25	414	-
26	-	40
27	428	-
28	-	53
29	444	-
30	-	70
31	459	-
32	-	84
33	484	-
34	-	98
35	502	-
36	-	112
37	510	-
38	-	123
39	538	-
40	-	137
41	568	-
42	-	148

(i) Specimen-9.

Location at the grid - Fig. 9.11	Instantaneous crack velocity, v (m/s)	Fracture occurrence time (μs)
1	-	21
2	393	-
3	-	37

4	421	-
5	-	47
6	436	-
7	-	70
8	459	-
9	-	83
10	476	-
11	-	96
12	484	-
13	-	109
14	502	-
15	-	124
16	520	-
17	-	137
18	548	-
19	-	145
20	568	-
21	-	161
22	-	38
23	407	-
24	-	55
25	459	-
26	-	70
27	502	-
28	-	82
29	529	-
30	-	97
31	538	-
32	-	106

33	529	-
34	-	120
35	520	-
36	-	133
37	510	-
38	-	146
39	484	-
40	-	161
41	444	-
42	-	174

(j) Specimen-10.

Tables 9.3(a-j). *The instantaneous velocity of crack propagation and the time of fracture occurrence at consecutive locations at the grid - see Figs. 9.11.*

The velocities were nondimensionalized by dividing them by the velocity of sound in the tubes, v_s, which is given by

$$v_s = \sqrt{\frac{E}{\delta}} \tag{9.3}$$

where E is the modulus of elasticity and δ is the mass density of the material. Referring to section 4.2 or appendix I,

$$v_s = 1800 \text{ m/s}$$

The dimensionless velocity plotted against time is shown in Figs. 9.12(a-f).

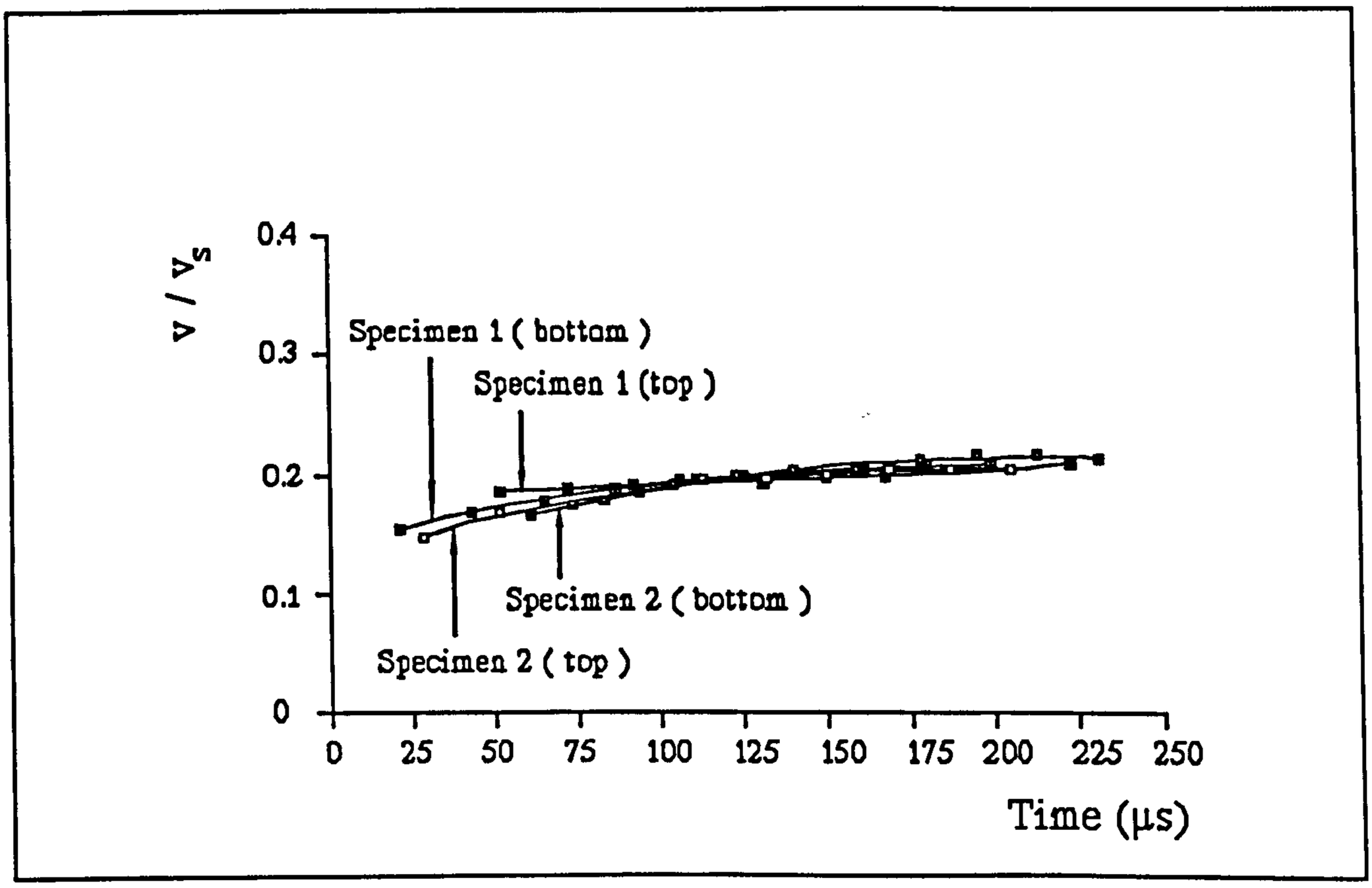
V / Vs
0.4
0.3
0.2
0.1
0
Specimen 1 (bottom)
Specimen 1 (top)
Specimen 2 (bottom)
Specimen 2 (top)
0
25
50
75
100
125
150
175
200
225
250
Time (μs)

(a)

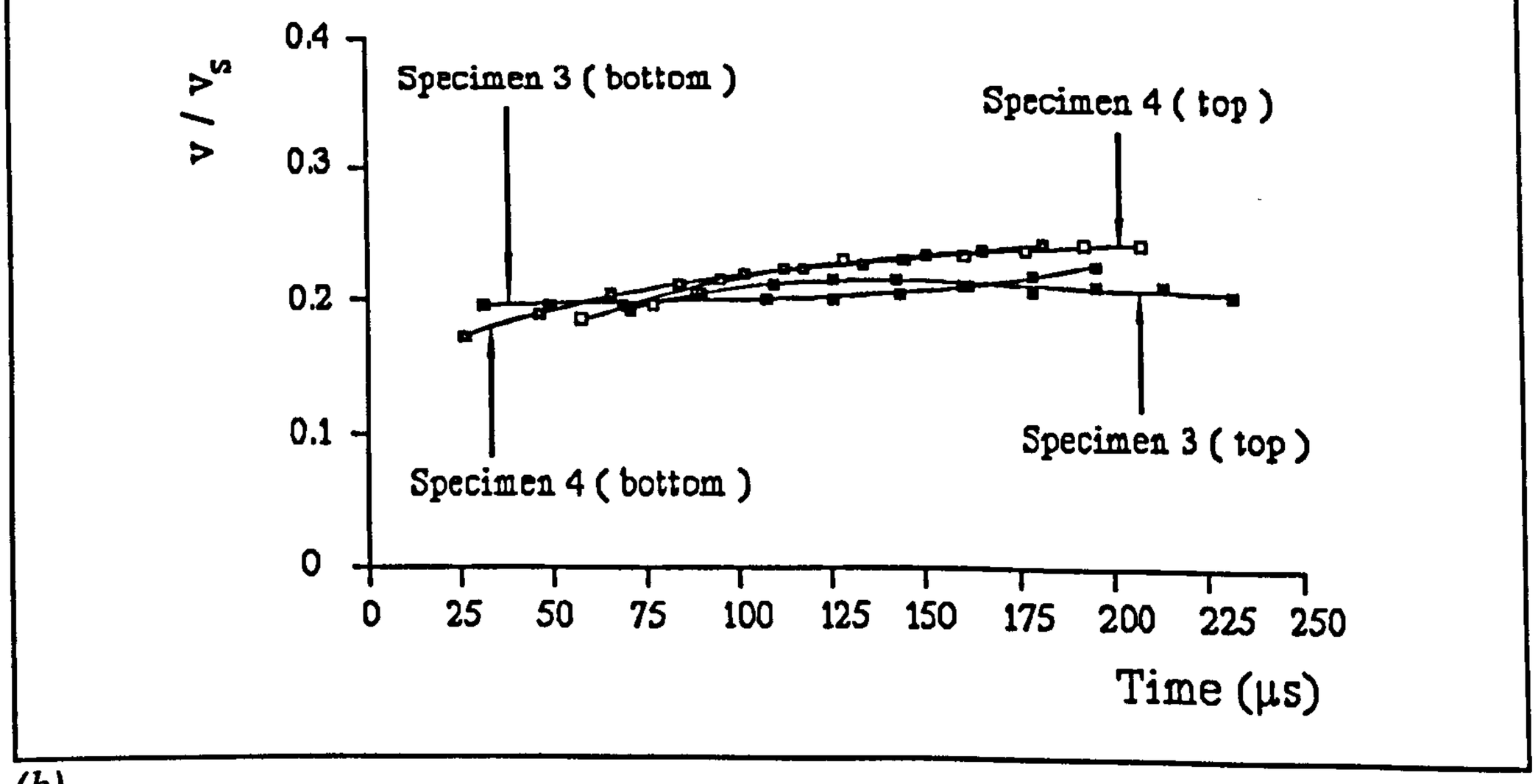
V / Vs
0.4
0.3
0.2
0.1
0
Specimen 3 (bottom)
Specimen 4 (top)
Specimen 4 (bottom)
Specimen 3 (top)
0
25
50
75
100
125
150
175
200
225
250
Time (μs)

(b)

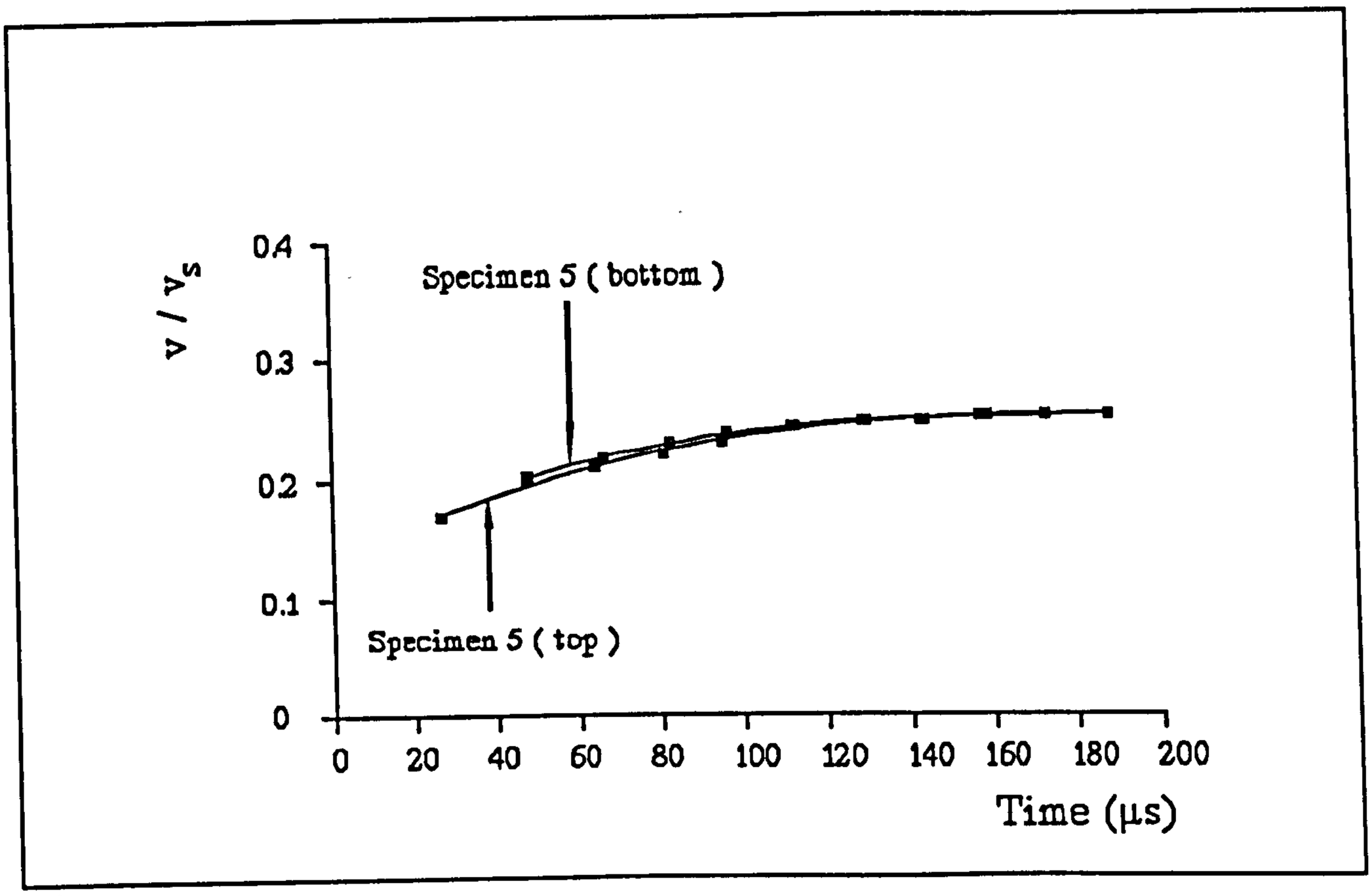
V / Vs
0.4
0.3
0.2
0.1
0
Specimen 5 (bottom)
Specimen 5 (top)
0
20
40
60
80
100
120
140
160
180
200
Time (μs)

(c)

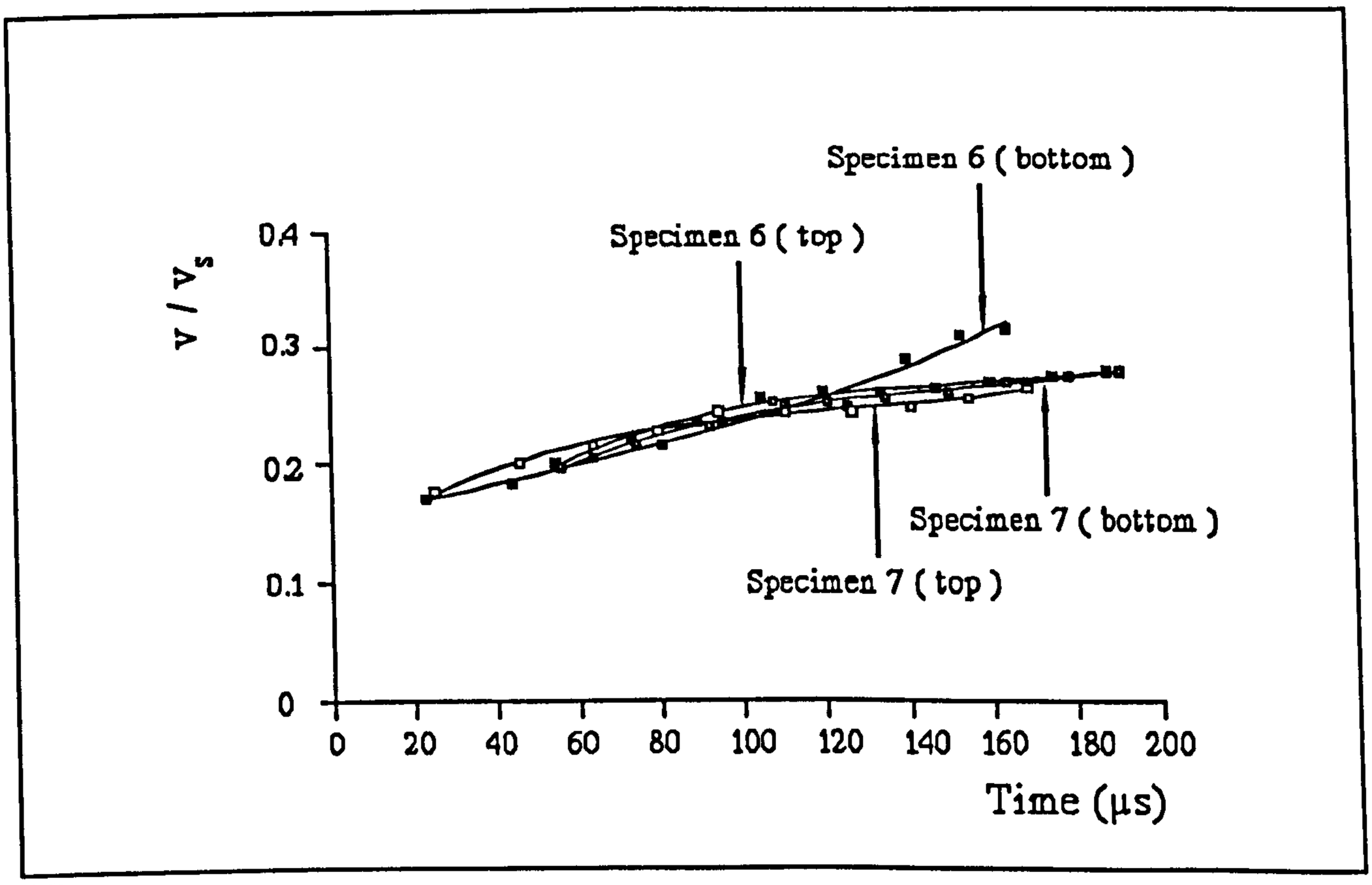
Specimen 6 (bottom)
Specimen 6 (top)
V / Vs
0.4
0.3
0.2
0.1
0
Specimen 7 (bottom)
Specimen 7 (top)
0
20
40
60
80
100
120
140
160
180
200
Time (μs)

(d)

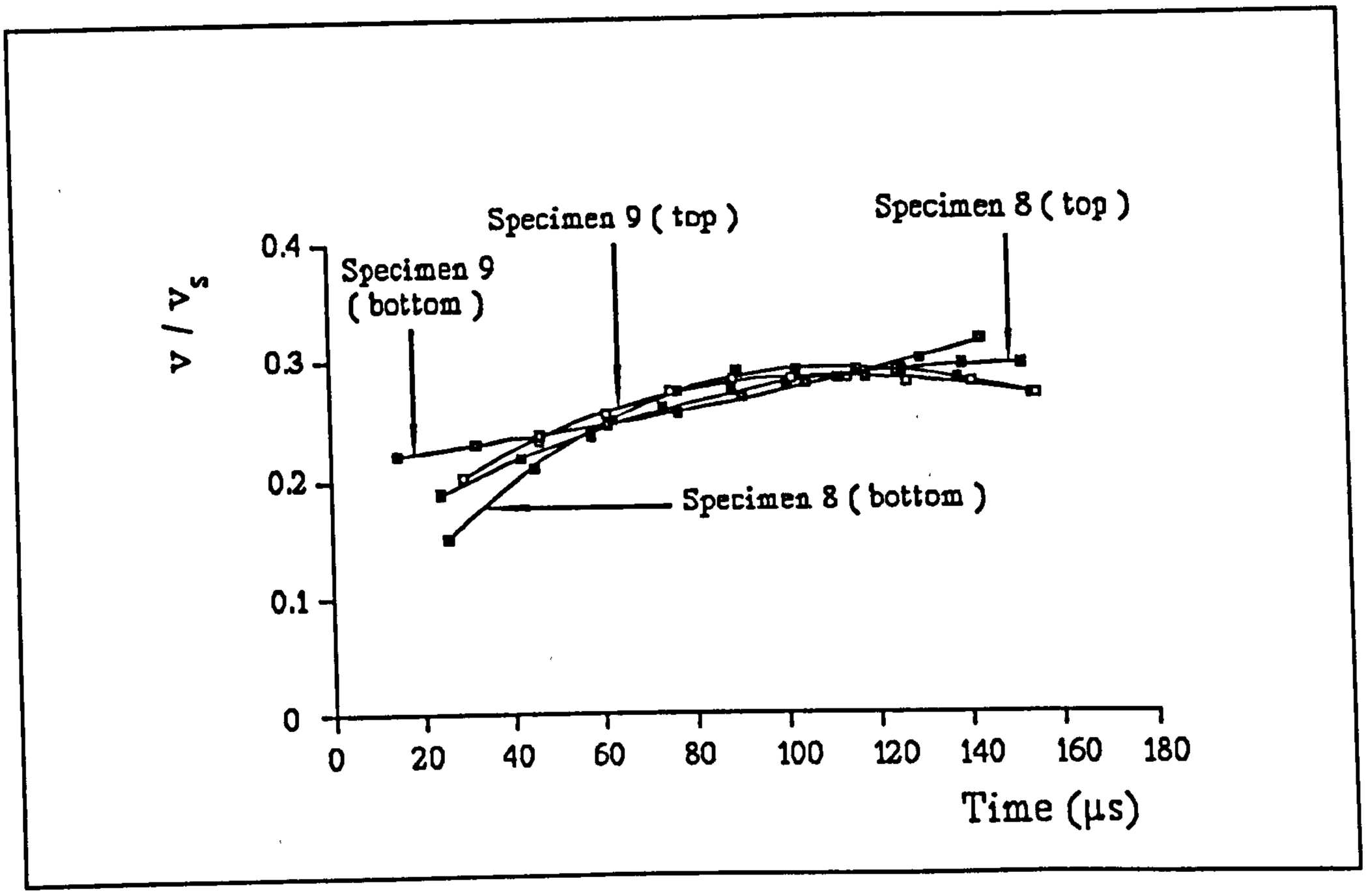

(e)

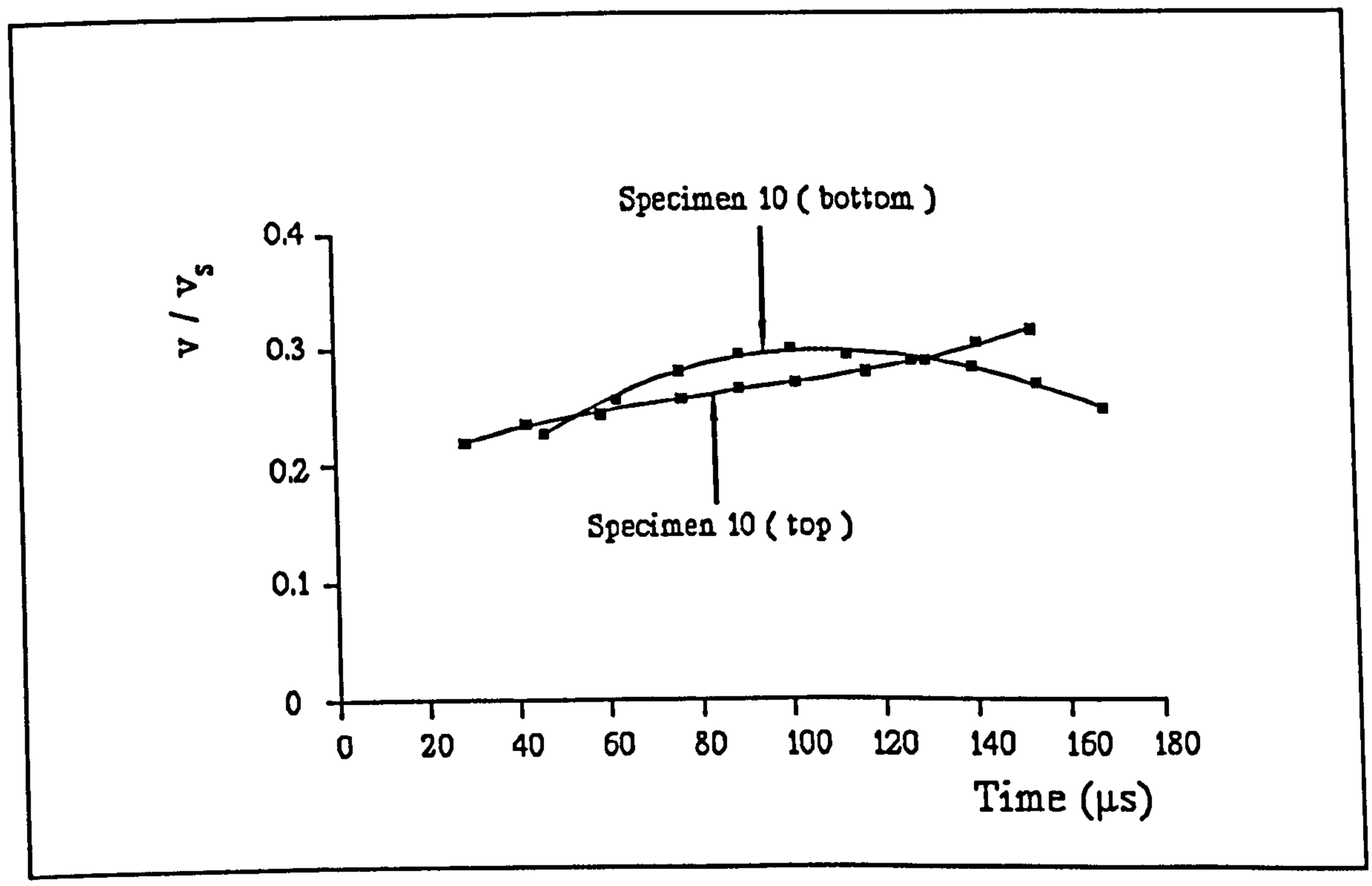

(f)

Figs. 9.12(a-f). *Dimensionless velocity against time graphs of the crack propagating through the grid lines.*

9.6.4. Branching and the Dynamic Stress Intensity Factor, K_D

Fracture mechanics is a fairly young field of science. Its pioneers strived at establishing the basic theories in the first few decades of this century. The concept of the stress intensity factor describing the stress field emerged gradually, and had been derived only for the static case until recently. The derivation for the dynamic case is more complex and came with some simplifying assumptions. Nilsson [25] produced a useful graph in his paper, published in 1972, plotting the ratio of the dynamic stress intensity factor for a propagating crack, K_{ID}, to the static K_I for an equivalent stationary crack against the dimensionless velocity of crack propagation. His calculations were based on a crack propagating at a constant velocity. He considered a crack propagating at one end in a semi-infinite plate, while the other end extended to infinity. The pressure tubes which were investigated in this chapter had propagating cracks of finite lengths. Therefore, a more applicable model is the one presented by Freund [50] with the resulting graph on page 336 of his book, published in 1990. The graph plotted the ratio K_{ID}/K_I against the dimensionless velocity of crack propagation. The calculations were based on an infinite plate with a crack of finite length propagating at a constant velocity at both tips. The velocities at both tips are not necessarily equal in magnitude. It is assumed that in this case Freund [50] gives a better approximation compared to that of Nilsson [25] since the finite length of the crack is a more realistic assumption.

The static stress intensity factor for an equivalent stationary crack had to be found prior to obtaining a value for the dynamic stress intensity factor of a

propagating crack. Referring to pages 1348-1350 in the second volume of Murakami [84], the K_I value was calculated for the different pressure tubes at the point of initial branching, assuming the pressure to be the same as that at the point of failure. Using each value of K_I and referring to Nilsson's [25] and Freund's [50] graphs, two values of K_{ID} were obtained. Table 9.4 presents the pressure, p, the assumed length of the crack, 2a (measured from the point of initial branching at one end of the crack to the point of initial branching at the other end), the average value of the two velocities at the crack tips, v_{avg}, and the corresponding two values of K_{ID}.

p (psi)	2a (mm)	v_{avg} (m/s)	K_{ID} (N/mm$^{3/2}$)	
			obtained with reference to Nilsson [25]	obtained with reference to Freund [50]
205	118	378	205	189
220	146	432	269	241
265	131	450	286	256
275	117	498	266	228
290	110	452	267	229
320	103	513	266	227
330	103	506	275	237
375	72	503	217	185

Table 9.4. K_{ID} at the point of initiation of branching assuming the crack length to be the distance between the point of initiation of branching at one end of the crack and the point of initiation of branching at the other end.

There are two components of every resultant value of K_{ID}. The membrane component is the major one ranging from 82% to 95%, while the bending component is the minor one ranging from 5% to 18% of the resultant value of K_{ID} [84].

The length of the crack at the point of initial branching can be defined differently. In Table 9.5, the crack length, 2a, has been defined as the distance between the point of initiation of branching at one end of the crack where branching occurred first and the corresponding point at the other end occurring at the same incident of time. In other words, referring to Figs. 9.11 and Tables 9.3, the point at which branching initiated was determined paying attention to the crack end at which it occurred. The corresponding incident of time was observed and the point at the other end of the crack existing at the same incident of time was identified. Thereafter, the length of the crack could be measured between the two identified points. Table 9.5 also provides the internal pressure, p, the instantaneous velocity of the crack at the point of initial branching, v, and the corresponding values of K_{ID}.

p (psi)	2a (mm)	v (m/s)	K_{ID} (N/mm$^{3/2}$)	
			obtained with reference to Nilsson [25]	obtained with reference to Freund [50]
205	112	379	195	179
220	130	428	241	216
265	125	448	274	245
275	113	520	255	216
290	109	459	261	231
320	98	506	256	220
330	101	502	275	235
375	68	516	203	173

Table 9.5. K_{IC} at the point of initiation of branching assuming the crack length to be the distance between the point of initiation of branching at one end of the crack where branching occurred first and the corresponding point at the other end occurring at the same incident of time.

The two pressure tubes with the largest semi-circular notches produced with sharpened shims failed at pressures of 165 and 170 psi and their cracks did not contain any branching in the notched middle cylinder. Therefore Tables 9.4 and 9.5 present the results of the remaining eight tubes only.

9.6.5. Fracture Surfaces and the Dynamic Stress Intensity Factor

The fracture surfaces of the pressure tubes can be seen in Figs. 9.13(a-j). Due to similarity between the fracture surfaces of the two broken parts of each tube, only one surface was shown for each tube.

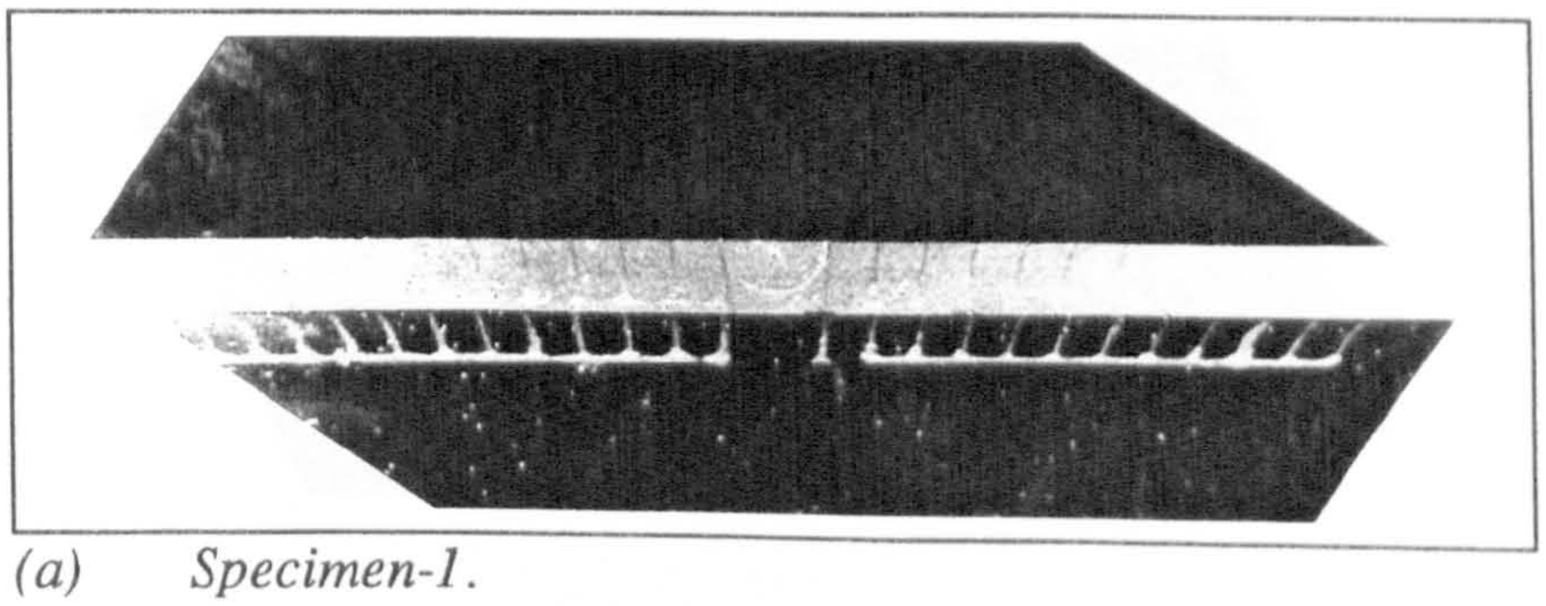

(a) Specimen-1.

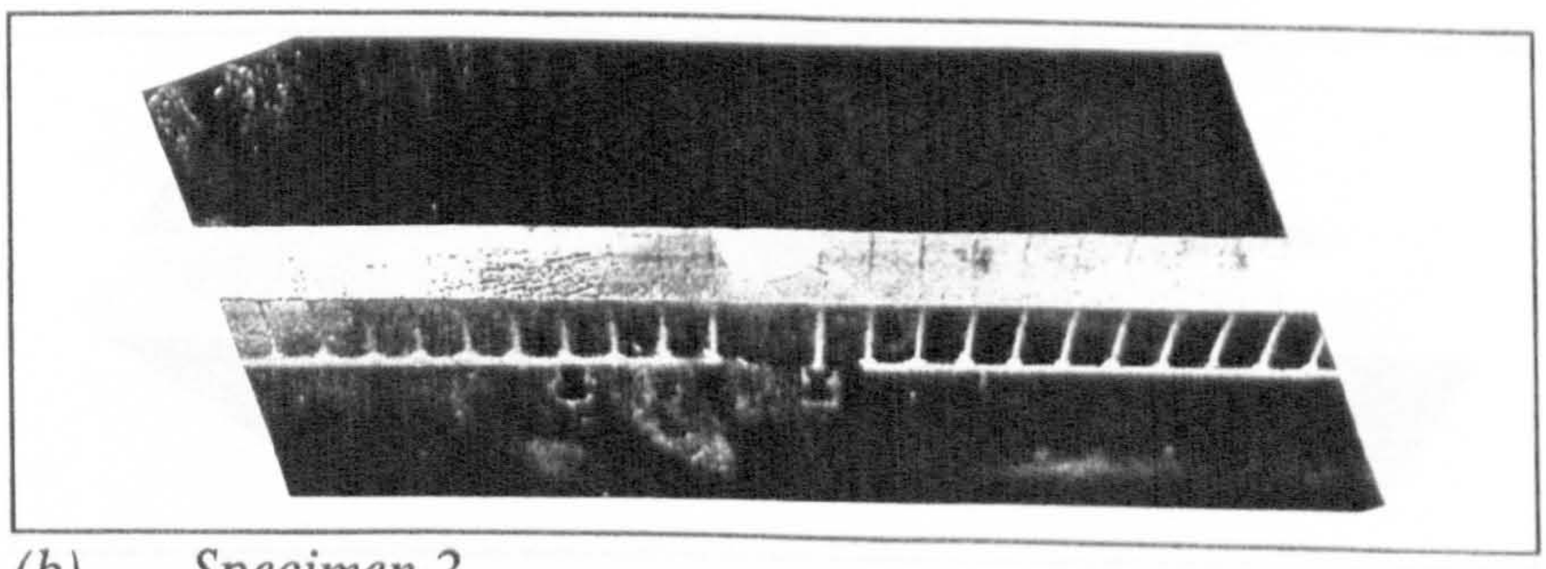

(b) Specimen-2.

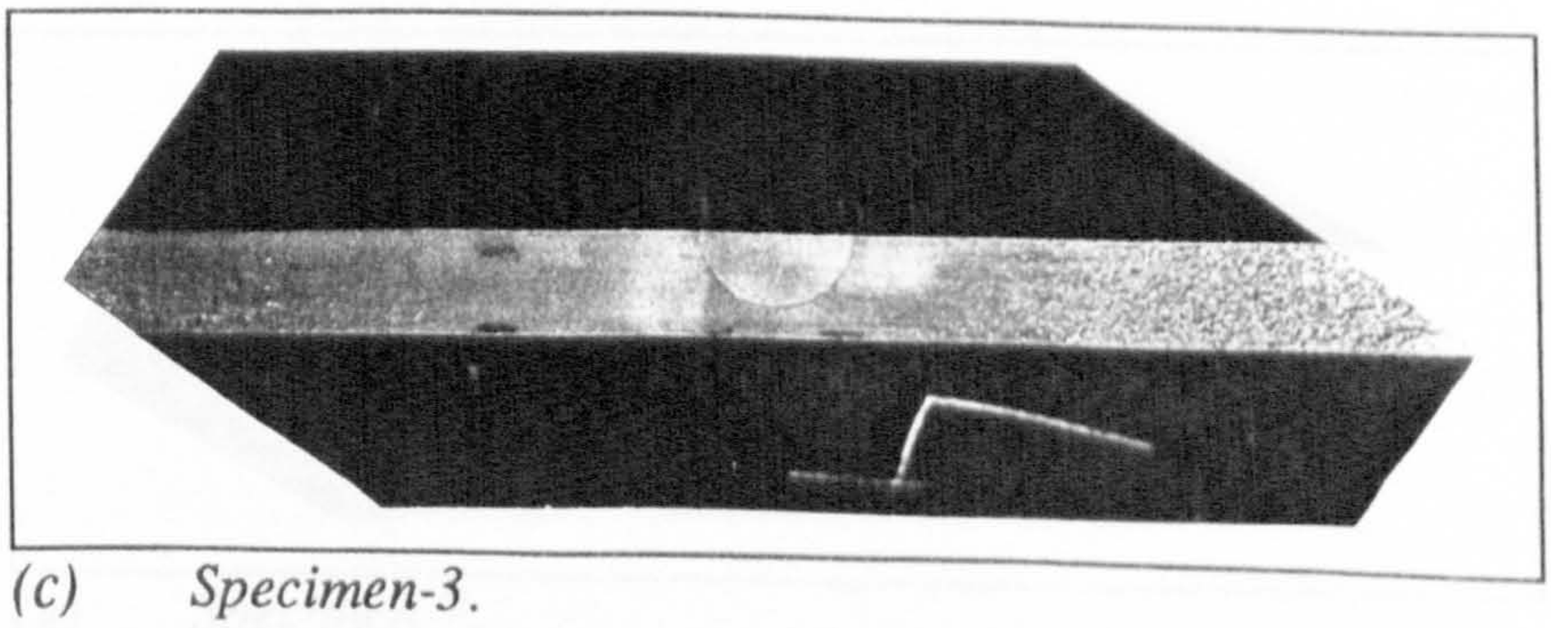

(c) Specimen-3.

The fracture surfaces displayed clear characteristics. Starting at the tip of the semi-circular notches, shown in Figs. 9.13(a-j), the crack propagated giving a smooth mirror surface. This was followed by a less-smooth mist region. Finally a rough hackle region developed with the degree of

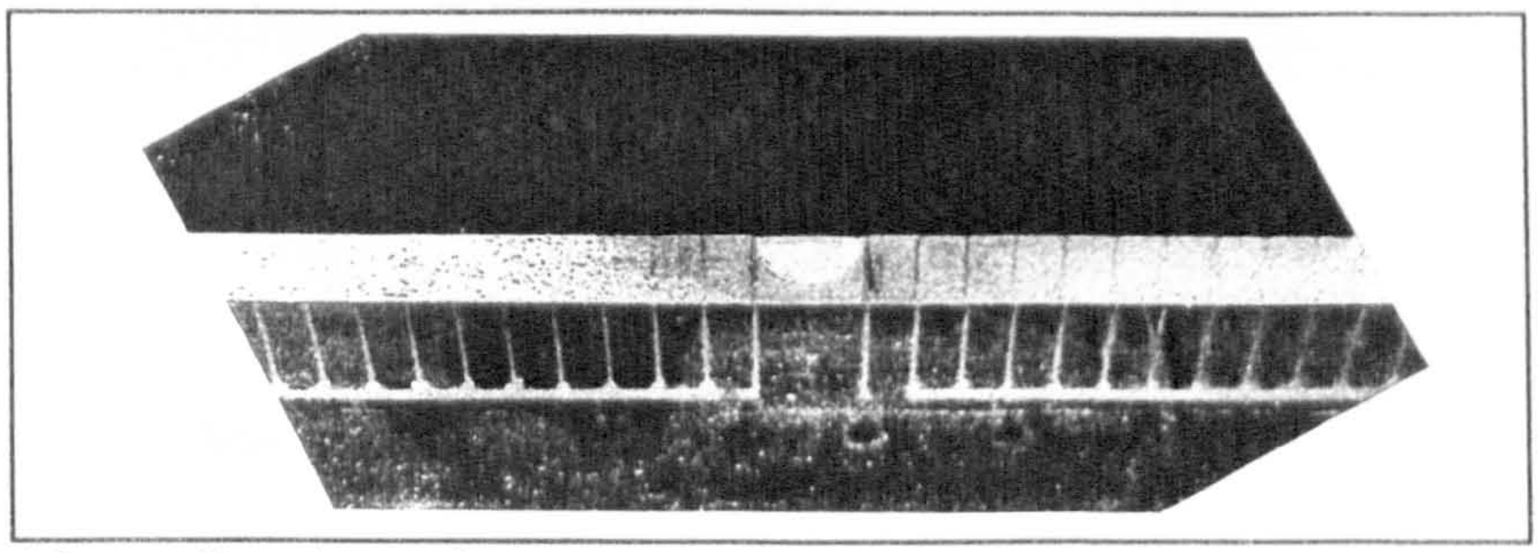

(d) Specimen-4.

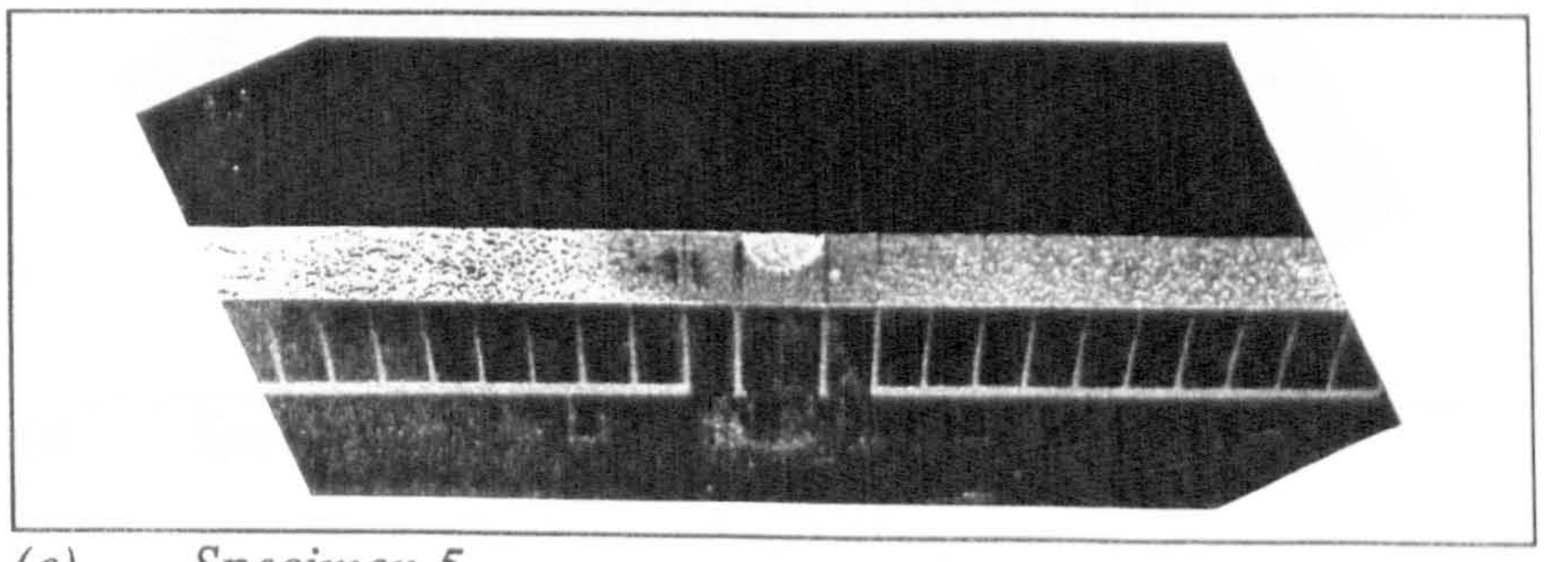

(e) Specimen-5.

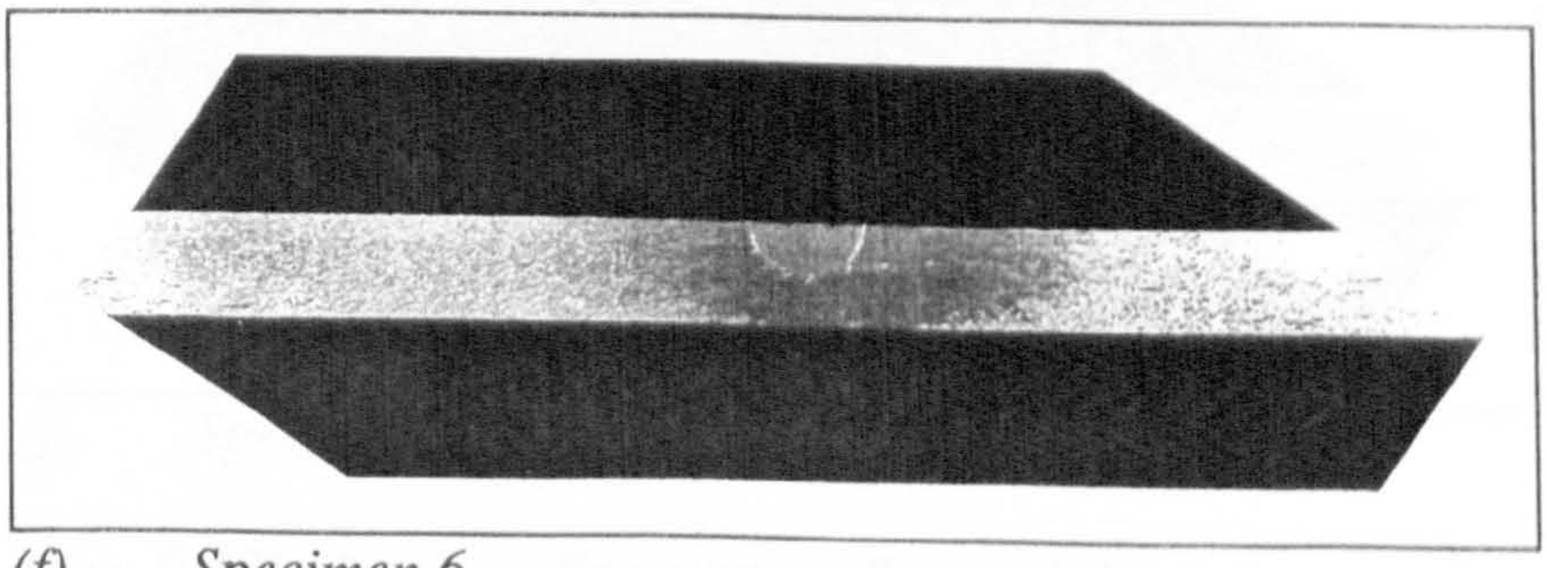

(f) Specimen-6.

(g) Specimen-7.

roughness increasing with distance away from the notch. The first two regions were small compared to the hackle region as depicted in Figs. 9.13. One photograph exhibits the process of branching - Fig. 9.13(i).

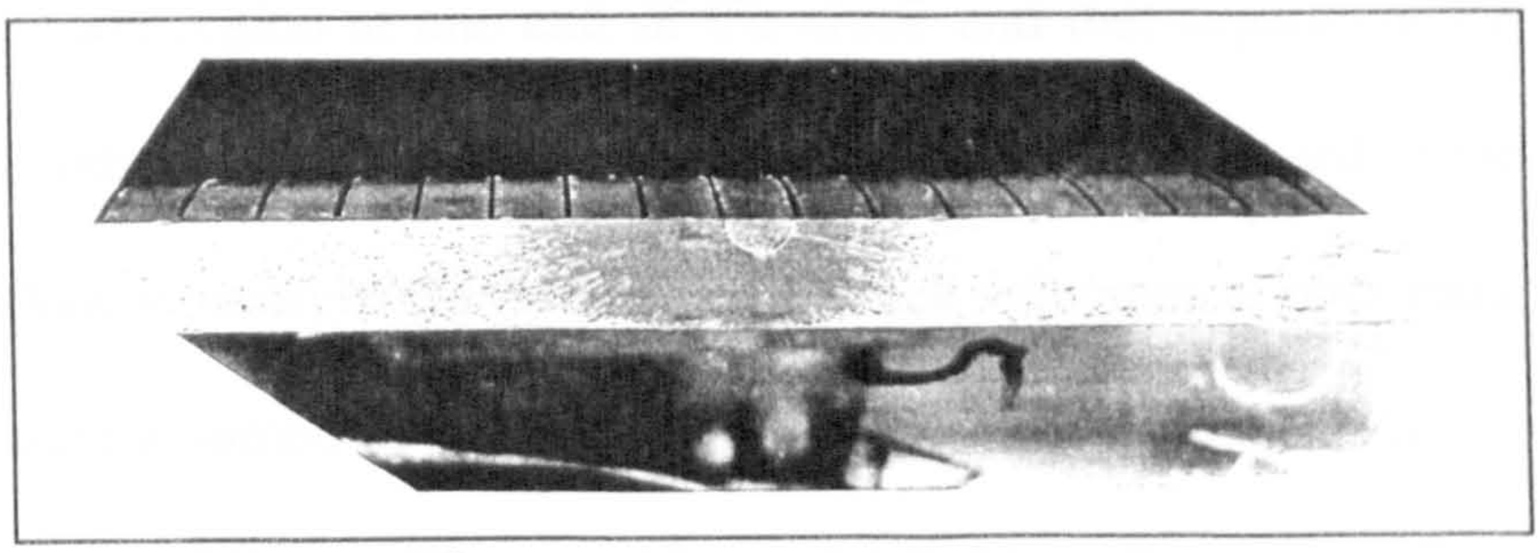

(h) Specimen-8.

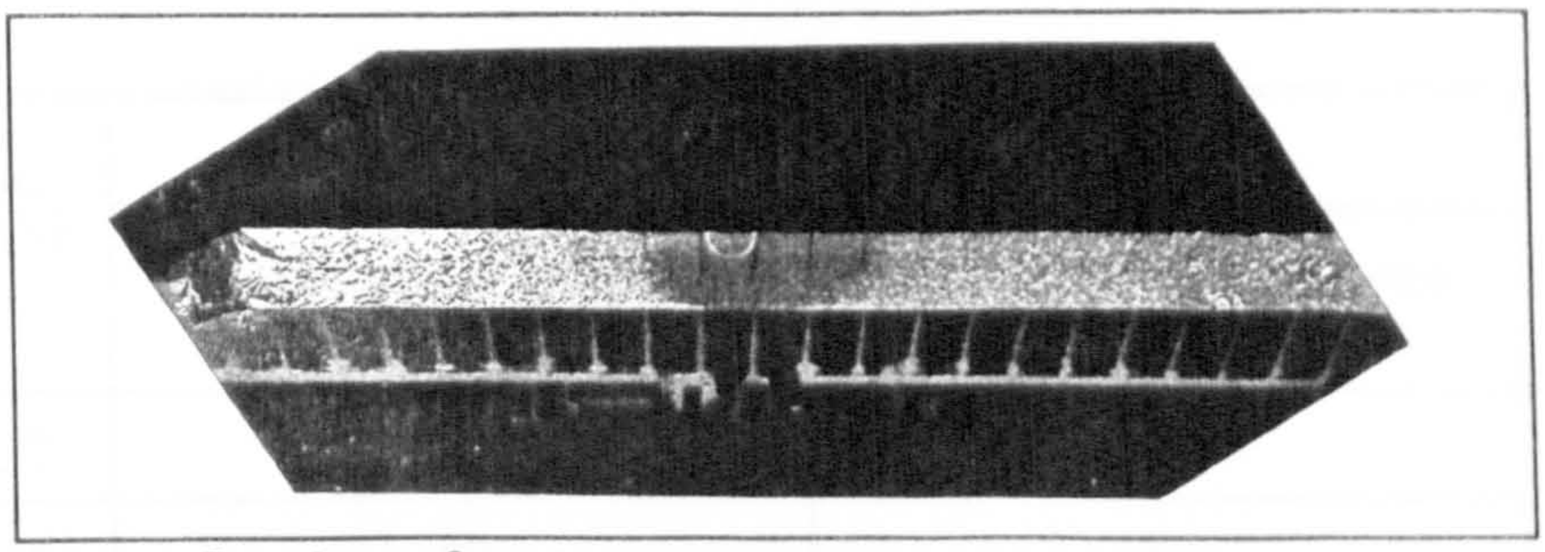

(i) Specimen-9.

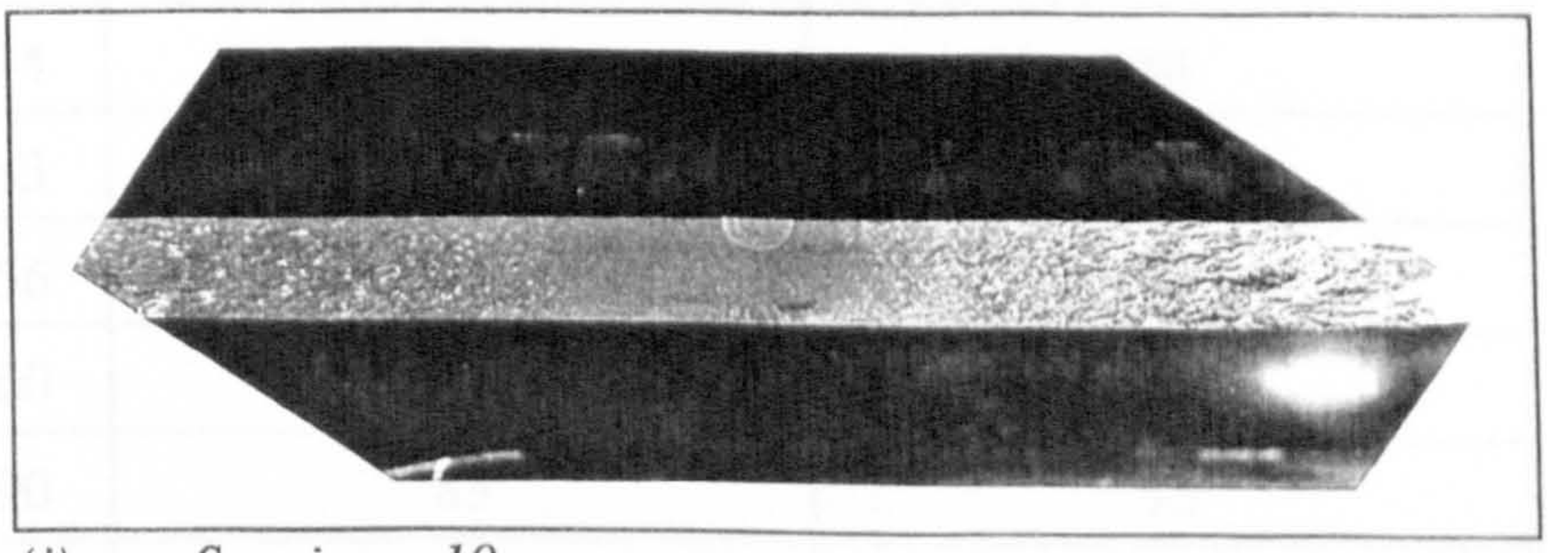

(j) Specimen-10.

Figs. 9.13(a-j). Fracture surfaces of the pressure tubes.

The inception of both hackle regions in each pressure tube occurred simultaneously. This was concluded from observing the fracture surfaces and referring to Figs. 9.11 and Tables 9.3. The dynamic stress intensity factor was calculated for the tubes as the crack tips were at the commencement of the hackle regions. The length of the crack, 2a, was defined to be the distance between the line separating the

mist region from the hackle region at one end of the crack and that separating the same two regions at the other end of the crack. The velocity of the crack used in the calculation was the arithmetic mean of the instantaneous crack velocities at both ends, v_{avg}. The internal pressure assumed in the calculation of the membrane stress in the tubes was that occurring at failure. The procedure of obtaining K_{ID} was the one followed in section 9.6.4. The results are presented in Table 9.6.

p (psi)	2a (mm)	v_{avg} (m/s)	K_{ID} (N/mm$^{3/2}$)	
			obtained with reference to Nilsson [25]	obtained with reference to Freund [50]
165	60	337	83	77
170	64	335	89	84
205	54	357	91	84
220	51	351	92	85
265	44	374	95	88
275	41	363	93	86
290	36	356	86	80
320	34	360	89	82
330	30	390	83	75
375	28	407	86	78

Table 9.6. K_{ID} at the point of inception of the hackle region.

A close scrutiny of the semi-circular notch tips revealed the point at which the cracks initiated. There were fine lines indicative of the point of initiation of the cracks, as shown in Fig. 9.14. The figure also defines the angle at which the cracks initiated, γ, which ranged between 0 and 10 degrees.

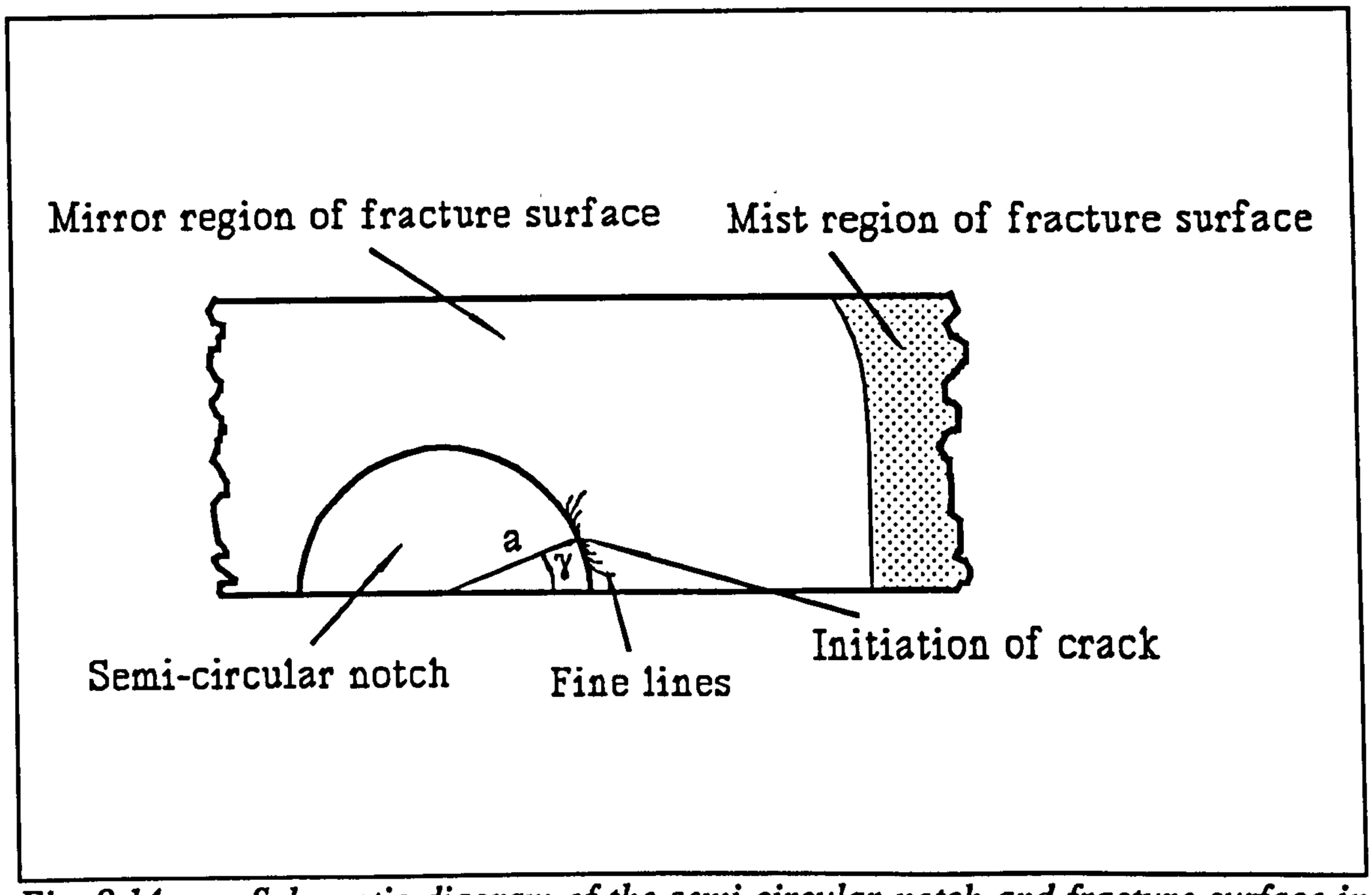

Fig. 9.14. Schematic diagram of the semi-circular notch and fracture surface in the pressure tubes.

It may be interesting to the reader to compare the fine lines of Fig. 9.14 which are indicative of the point of inception of fracture to those of Fig. 5.9.

CHAPTER TEN

DISCUSSION AND CONCLUSIONS

The main area of research for this thesis was carried out experimentally to find different values of the stress intensity factor. Both the static and dynamic stress intensity factors were scrutinised. The investigation considered pure mode-I and mixed-mode (I and II) loading conditions in the static study which involved real and apparent stress intensity factors for cracks and narrow notches respectively. The dynamic study was limited to the examination of narrow semi-circular notches under pure mode-I loading conditions.

The number of specimens tested in each case was governed by the difficulty of manufacture together with the need to achieve statistically reliable results. The complexity of producing specimens containing real cracks combined with the consistency of their results rendered the testing of a few specimens sufficient. While the relative ease of manufacture of notched specimens together with the scatter in the results necessitated the testing of a large number of specimens.

The experimental study was complemented by a finite element computational analysis, which described the stress contours and, in particular, the peak stresses at the

tips of narrow notches with semi-circular tips or with rectangular tips with rounded corners. The investigation involved pure mode-I, pure mode-II and mixed-mode (I and II) loading conditions. The results of the study would enable the reader to obtain the peak stresses in any component containing a narrow notch with a semi-circular or rectangular (with rounded corners) tip under any combination of mode-I and mode-II loading conditions, provided the notch geometry was known and the stress intensity factors K_I and K_{II} for an equivalent crack could be obtained.

10.1. Static Stress Intensity Factors and the Static Modelling of Cracks

The real and apparent static stress intensity factors for cracks and narrow notches respectively were documented in the previous chapters, for the different specimens of the project. The results covered almost any combination of mode-I and mode-II loading conditions. Four different notch sizes were investigated.

The results facilitate the modelling of a crack in a real engineering component by using a narrow notch in a model. Since the research has exclusively dealt with brittle fracture, the modelling of components containing cracks can be achieved provided their behaviour is brittle.

The modelling process is carried out by measuring the exact dimensions of the component and the crack. The dimensions of the model and its narrow notch (which represents the crack) are thus decided. The model can be of any size, bearing in mind that failure must be brittle, and maintaining a proportional relationship between the

model and the component. The notch and the crack must also be proportionate, with the exception of their thicknesses, and hence the existence of an apparent value of the stress intensity factor. The model is cast with the introduction of a narrow notch using a shim. The material and casting procedure are described fully in chapter 4. The shim can have any one of the four thicknesses considered in this thesis. The apparent stress intensity factor used in the calculations must correspond to the selected thickness of the notch (referred to as the notch width in earlier chapters: 2s).

From basic equations it can be shown that

$$\left(\frac{K}{\sigma_{nom}\sqrt{a}}\right)_{component} = \left(\frac{K^{APP}}{\sigma_{nom}\sqrt{a}}\right)_{model} \qquad (10.1)$$

where K and K^{APP} are the real and apparent stress intensity factors respectively, σ_{nom} is the nominal stress, and a is the crack or notch length. If the model is taken to failure, the critical value of K^{APP} is substituted in the equation. Also, the value of σ_{nom} at failure is substituted in the model-side of the equation.

K^{APP} can take the form of pure mode-I, pure mode-II or any combination of the two modes, depending on the loading conditions. At failure, the critical value of K^{APP} is considered. K_{IC}^{APP} is documented in chapter 5. Fig. 6.11 plots the value of K_C^{APP} for almost any combination of mode-I and mode-II loading conditions.

The actual loading condition on the model, which must be identical to that on the component, dictates which value of K_C^{APP} to use. Subsequently, this value is

substituted in equation (10.1).

The material of the component must be known. K_{IC} or K_{IIC} for the material must be obtained from published tables. Thereafter, it is assumed that K_c for the material in any combination of mode-I and mode-II loading conditions follows the same shape of graph for a real crack which is shown in Fig. 6.11. The appropriate value of K_c is thus chosen, corresponding to the actual loading condition. It substitutes for K in the component-side of equation (10.1). $\sqrt{a}$ is substituted for in both sides of the equation. The only residual unknown is $(\sigma_{nom})_{component}$. By solving the equation, a value for $(\sigma_{nom})_{component}$ can be obtained and used to calculate the load at which failure by brittle fracture is predicted.

10.2. Discrepancy between the Apparent Critical Static Stress Intensity Factors, K_c^{APP}

The narrow notches in all the specimens being tested were introduced by casting the specimens with a shim being present in the mould. In general, the shape of the shims has a direct effect on that of the notches. Since the manufacture and machining of the shims influence their shape, particularly at the tip, then the subsequent test results will be affected by the process of production of the shims.

A scanning electron microscope was employed to elucidate the different shapes of the shims. The tips were viewed under high magnification as shown in Figs. 10.1(a-d). Twenty four photographs for four different types of shim were taken. Two

of the shims had a straight edge, with either a flat or sharpened tip; the other two had a semi-circular edge, also with either type of tip. The straight-edge shims were used for the 3PB and CMM specimens, while the semi-circular-edge shims were used for the pressure tubes. The shims shown in Figs. 10.1 had a thickness of 0.10mm each.

Six photographs were taken for each of the four shims: three were of a low magnification and the other three were of a high magnification. The direction of viewing the shims was almost perpendicular to their plane from either side or parallel to it. Sixteen photographs pointed up and eight pointed down for configuration reasons inside the scanning electron microscope.

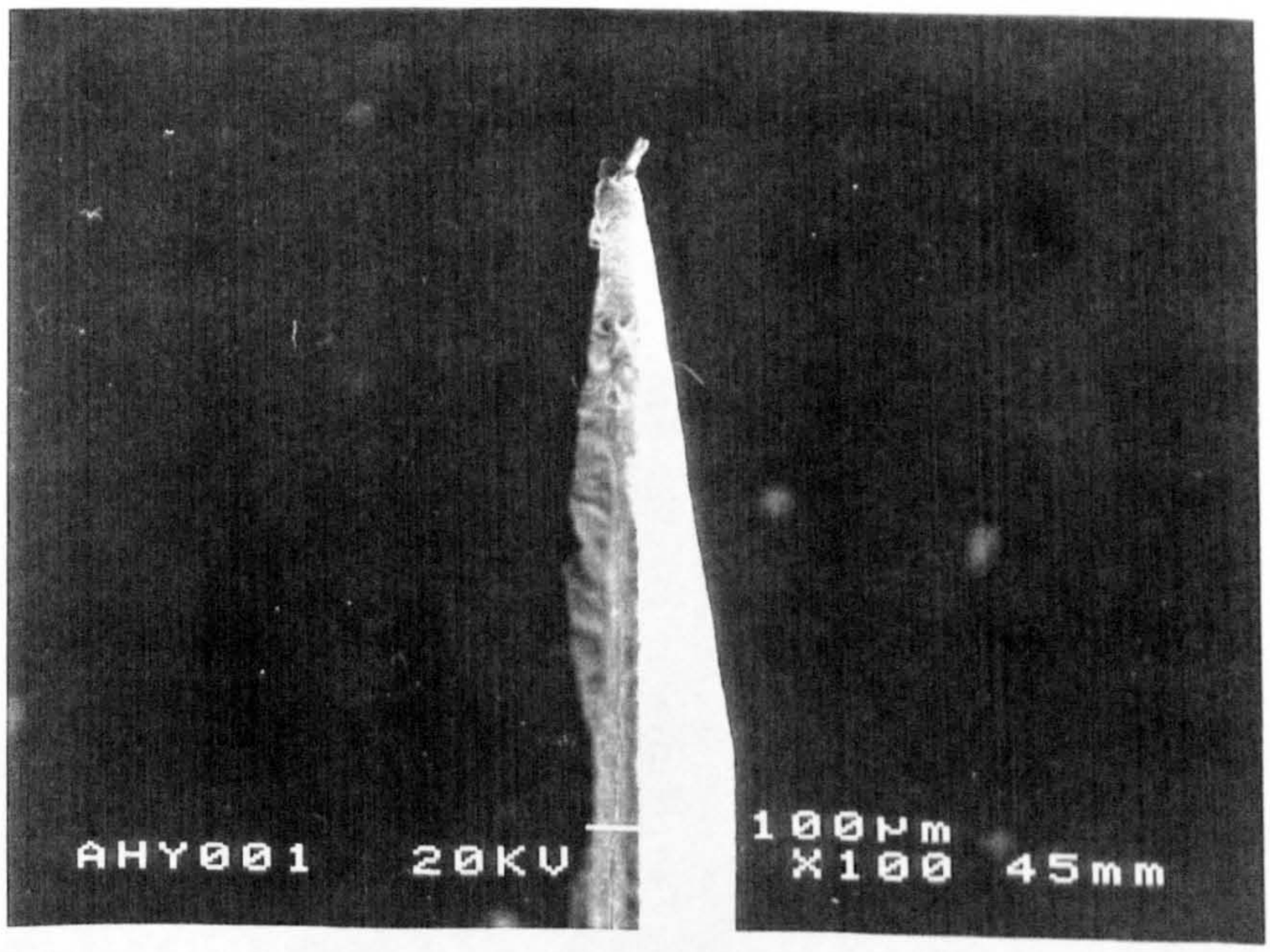

(a.1) Magnification ≈ 100.

(a.2) Magnification ≈ 1000.

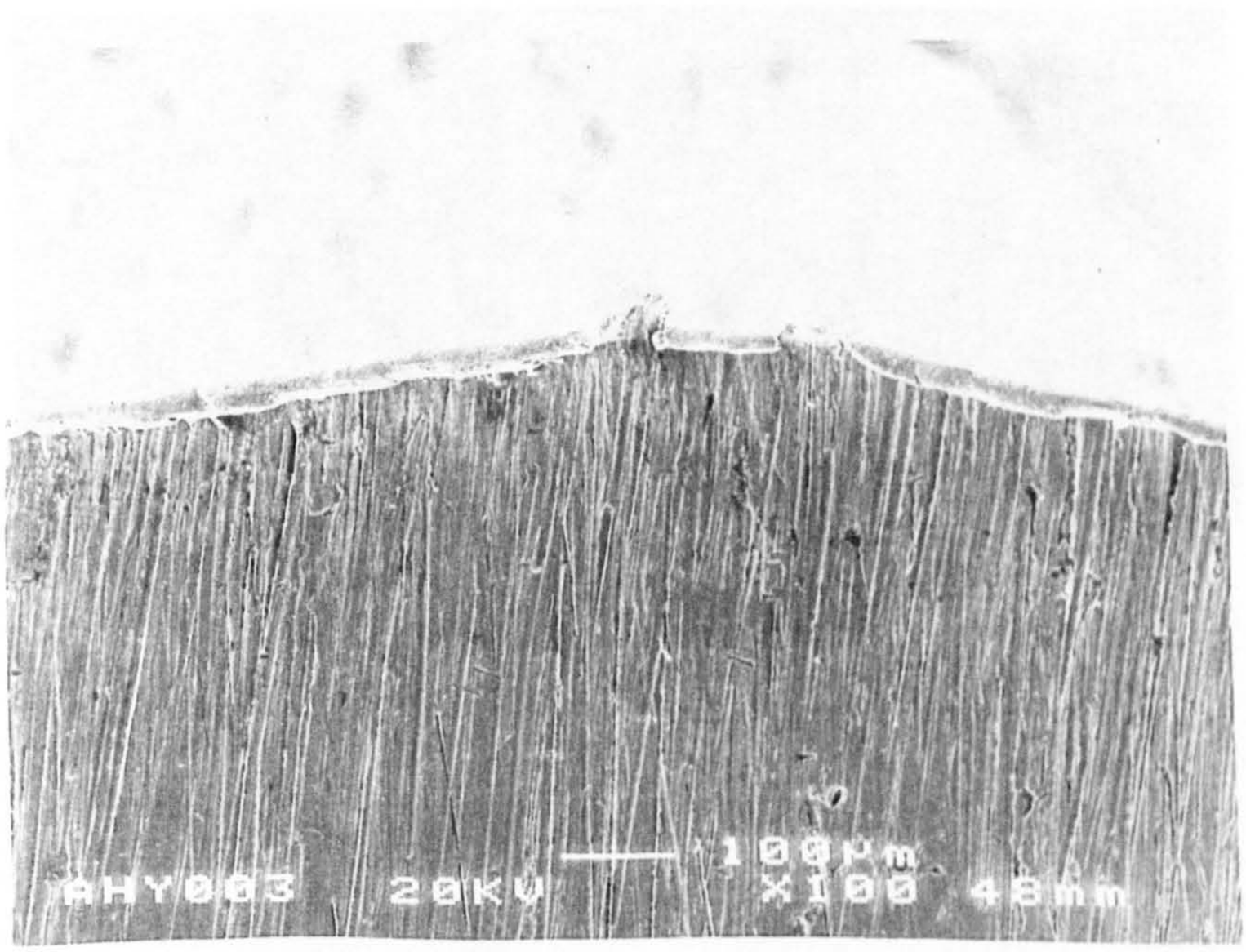

(a.3) Unsharpened side, magnification ≈ 100.

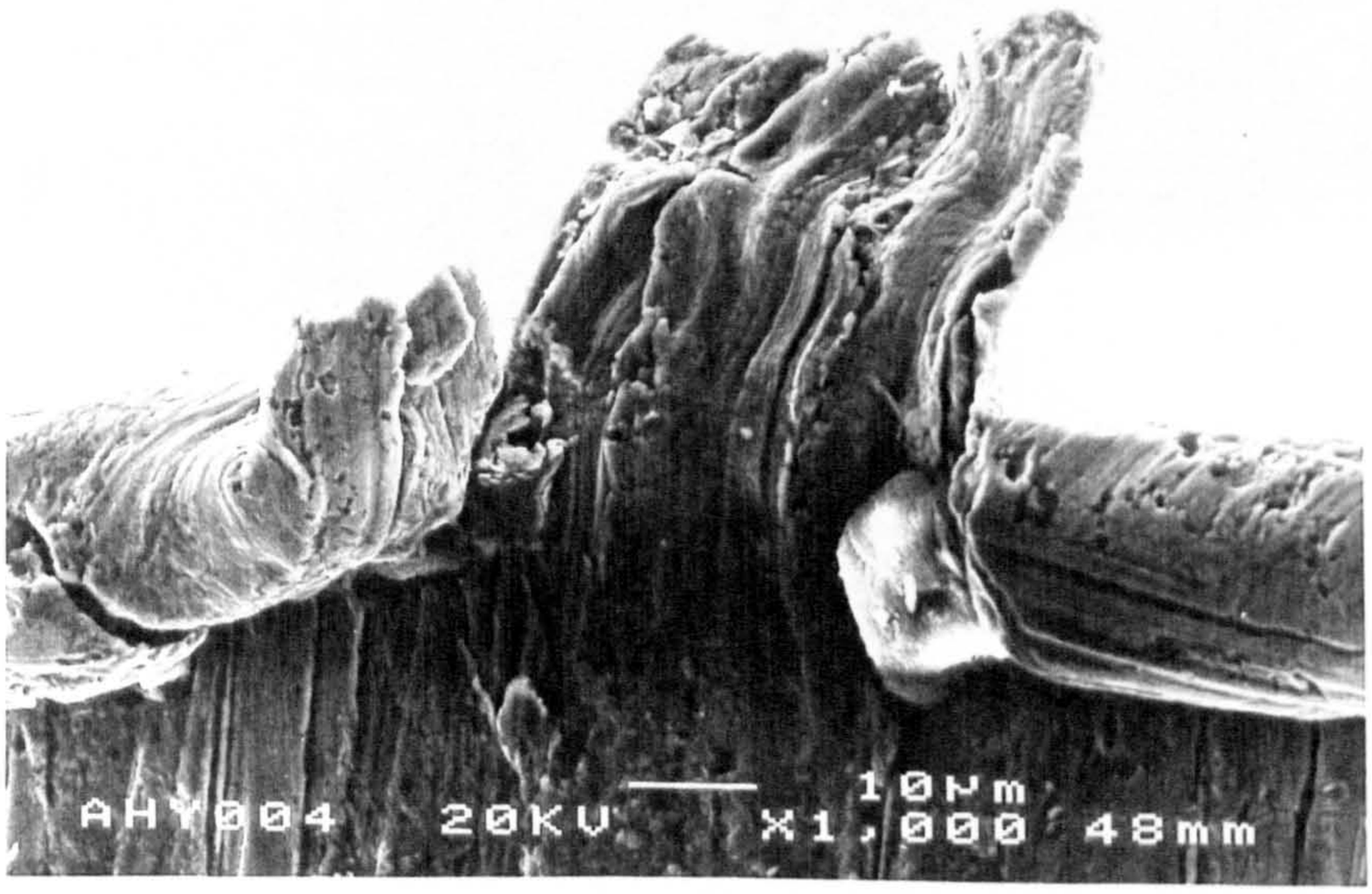

(a.4) Unsharpened side, magnification ≈ 1000.

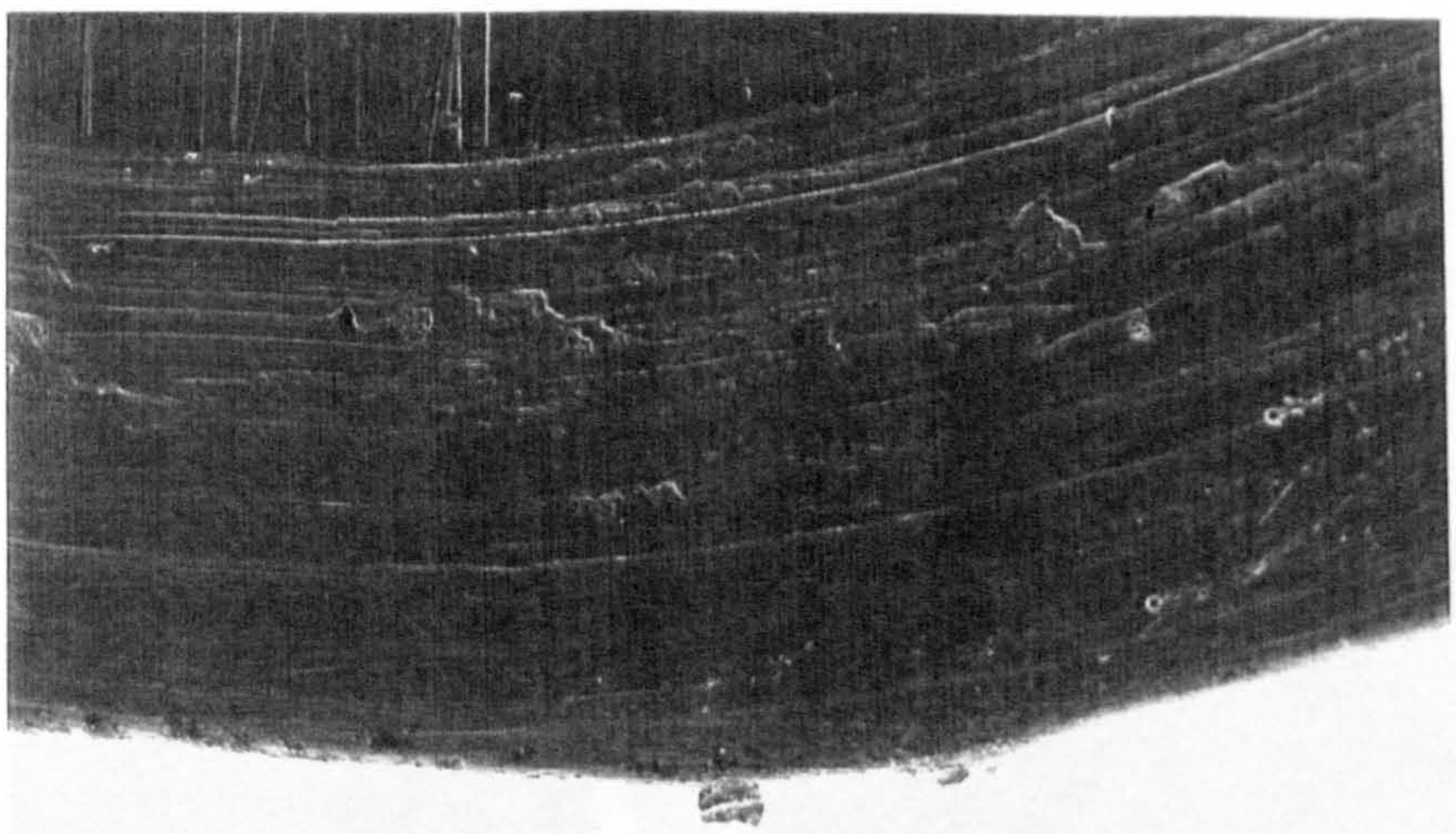

(a.5) Sharpened side, magnification ≈ 100.

(a.6) *Sharpened side, magnification ≈ 1000.*

(a) *0.10mm-thick semi-circular 3mm-radius sharpened shim.*

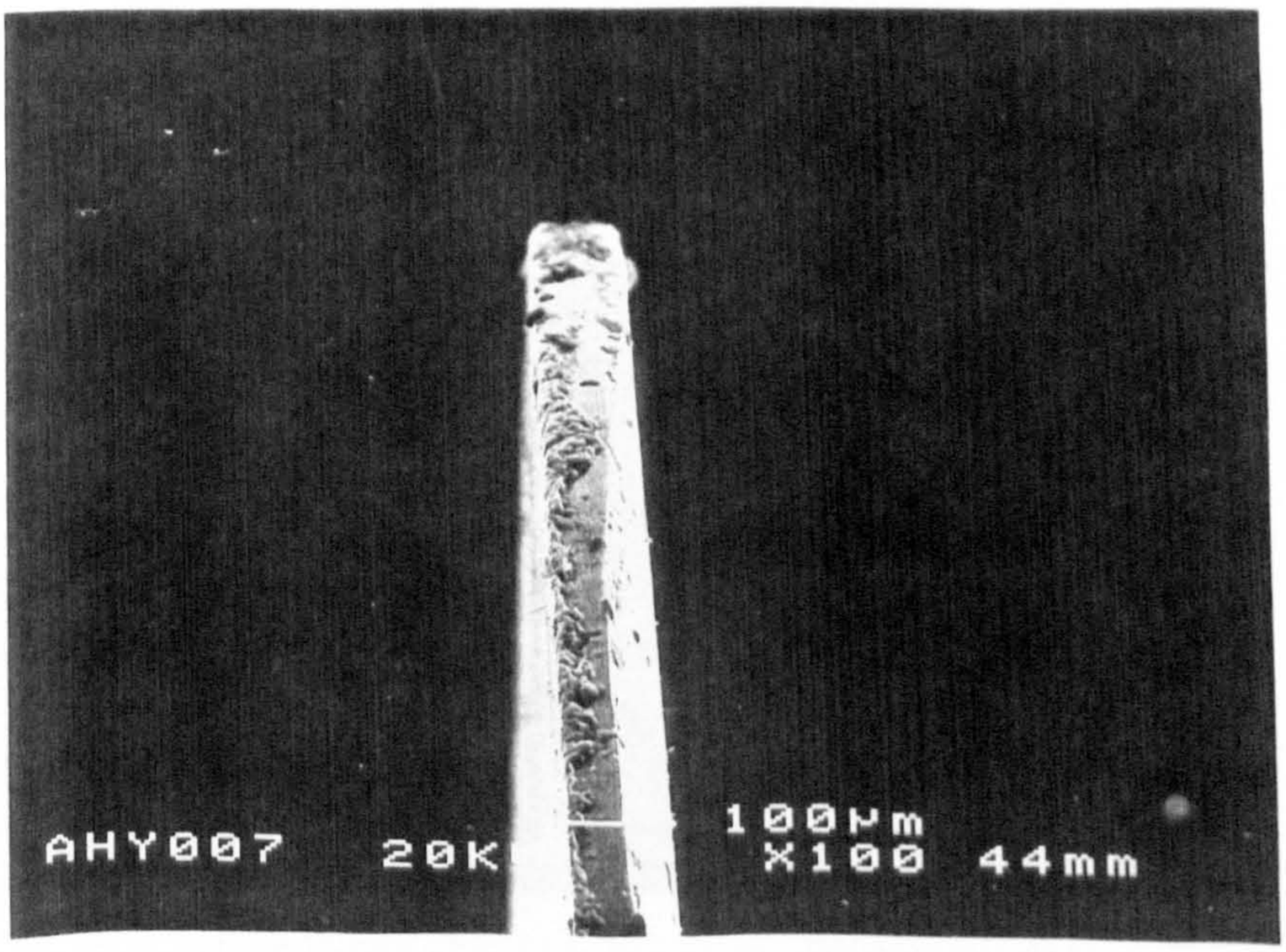

(b.1) *Magnification ≈ 100.*

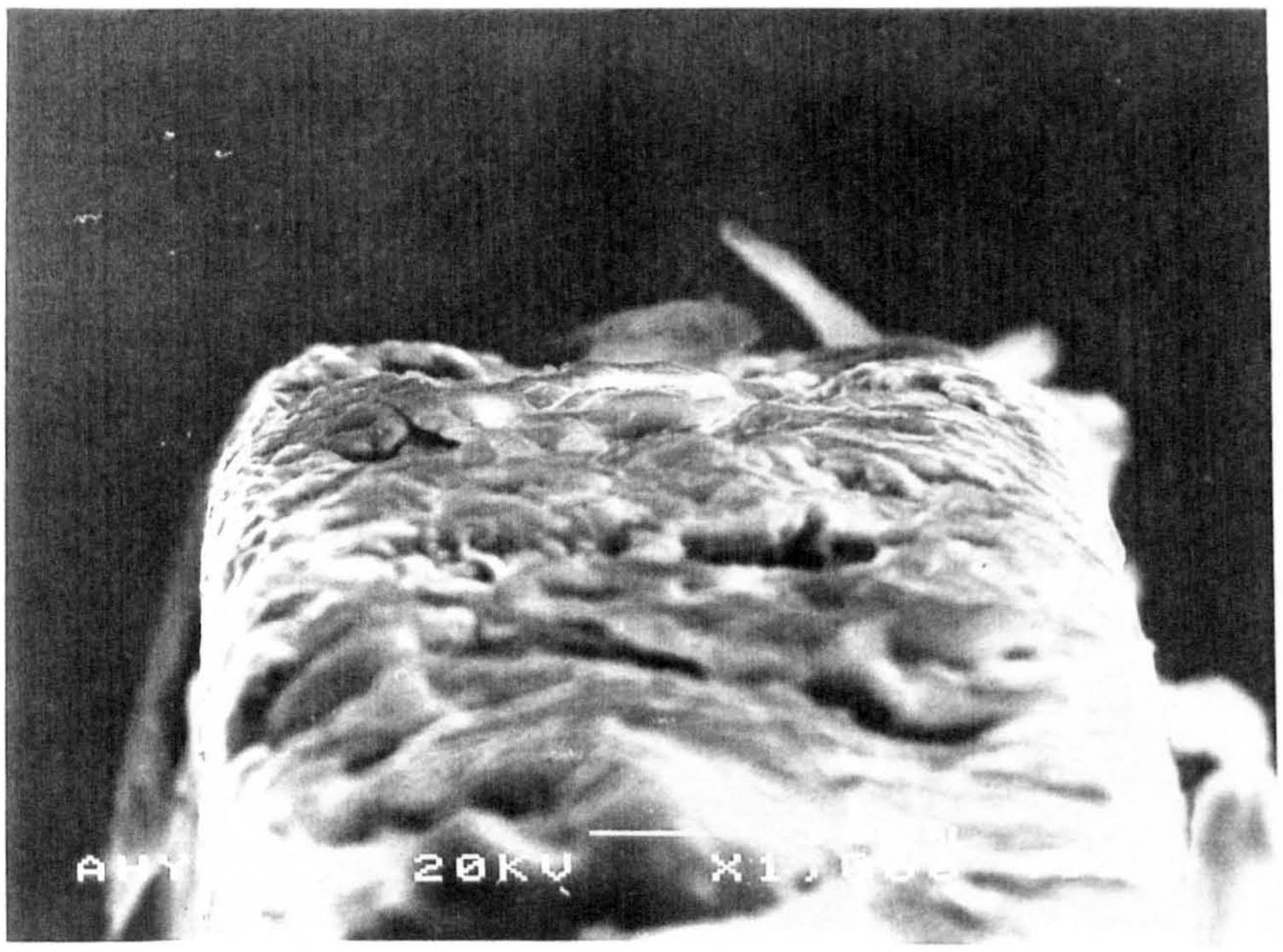

(b.2) Magnification ≈ 1000.

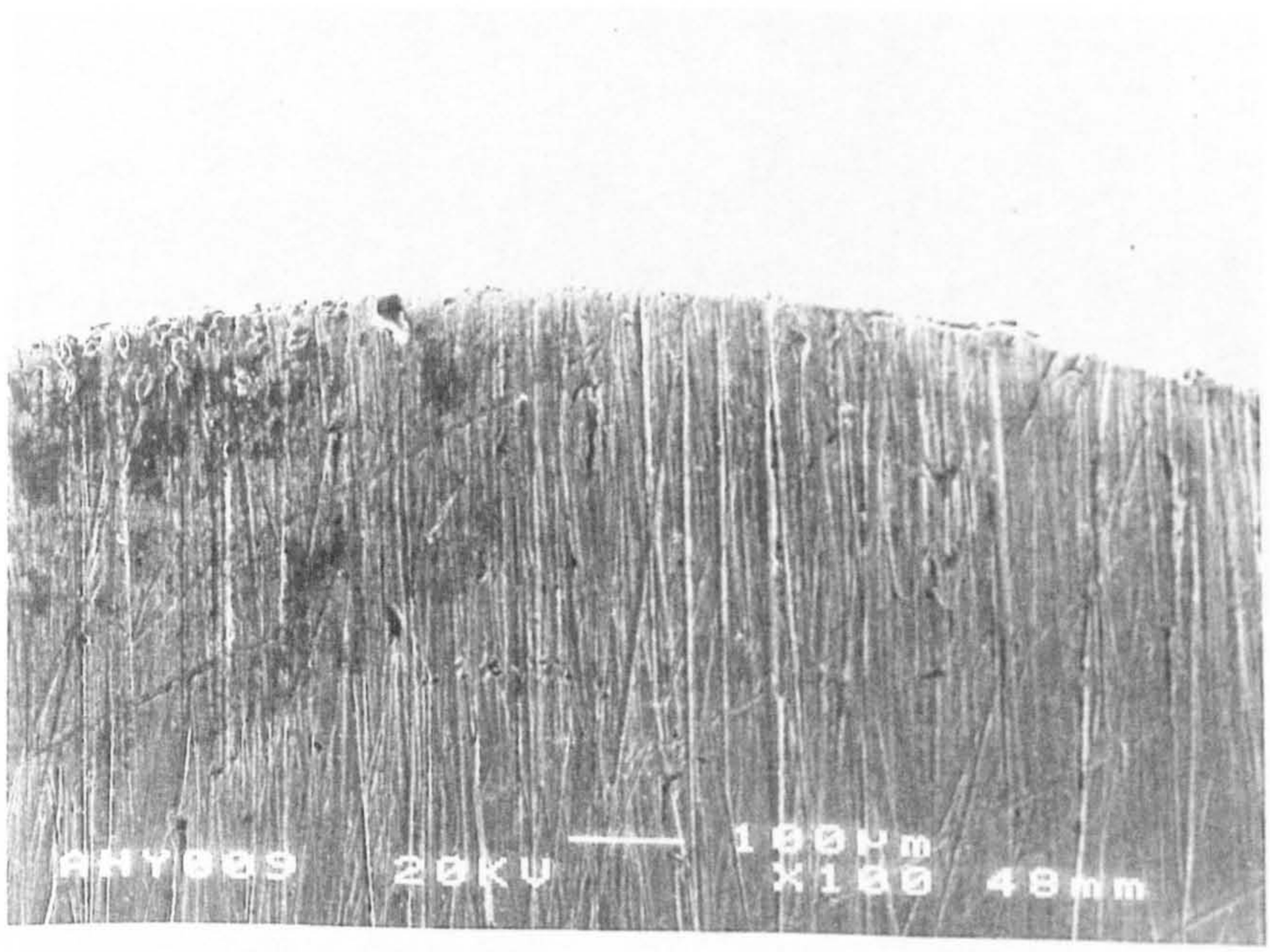

(b.3) Magnification ≈ 100.

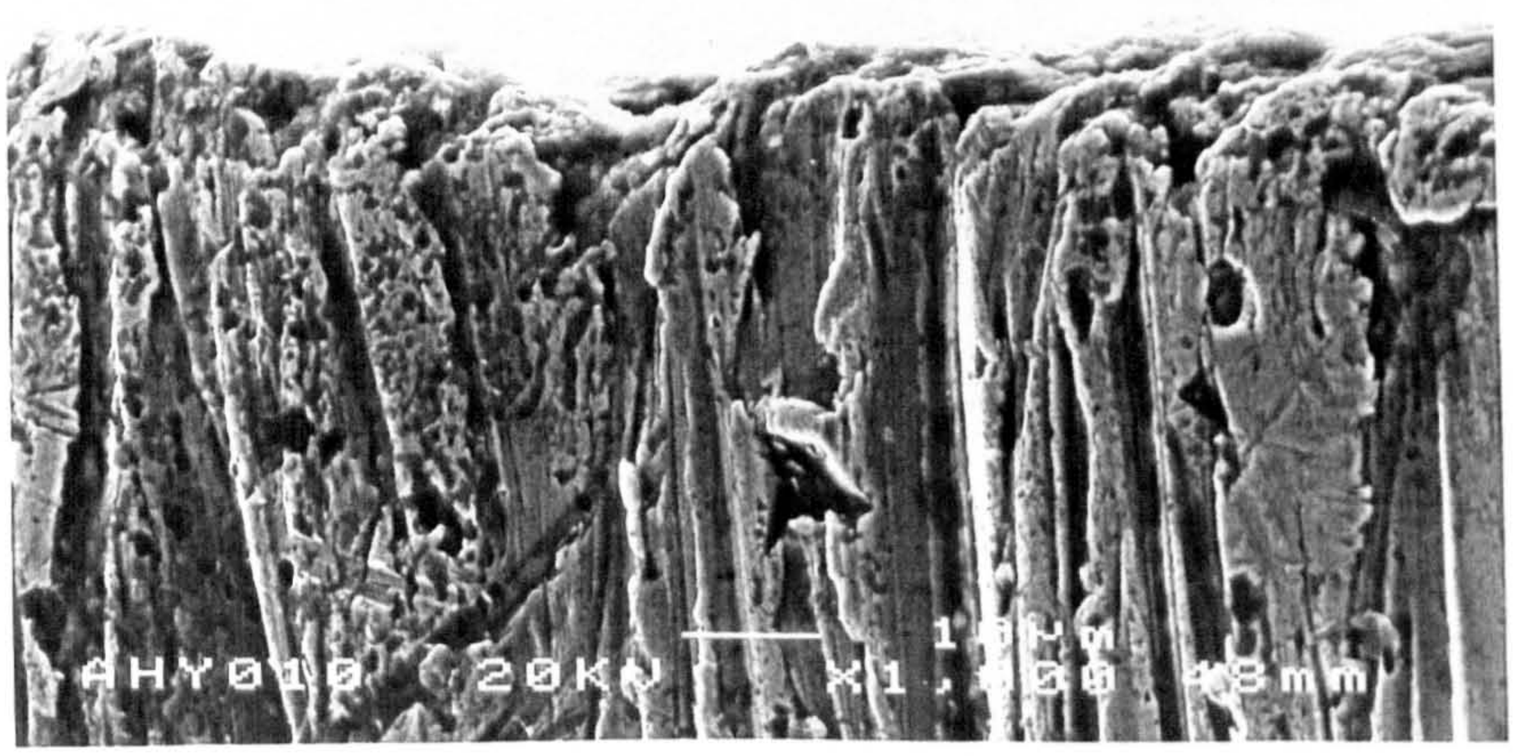

(b.4) Magnification ≈ 1000.

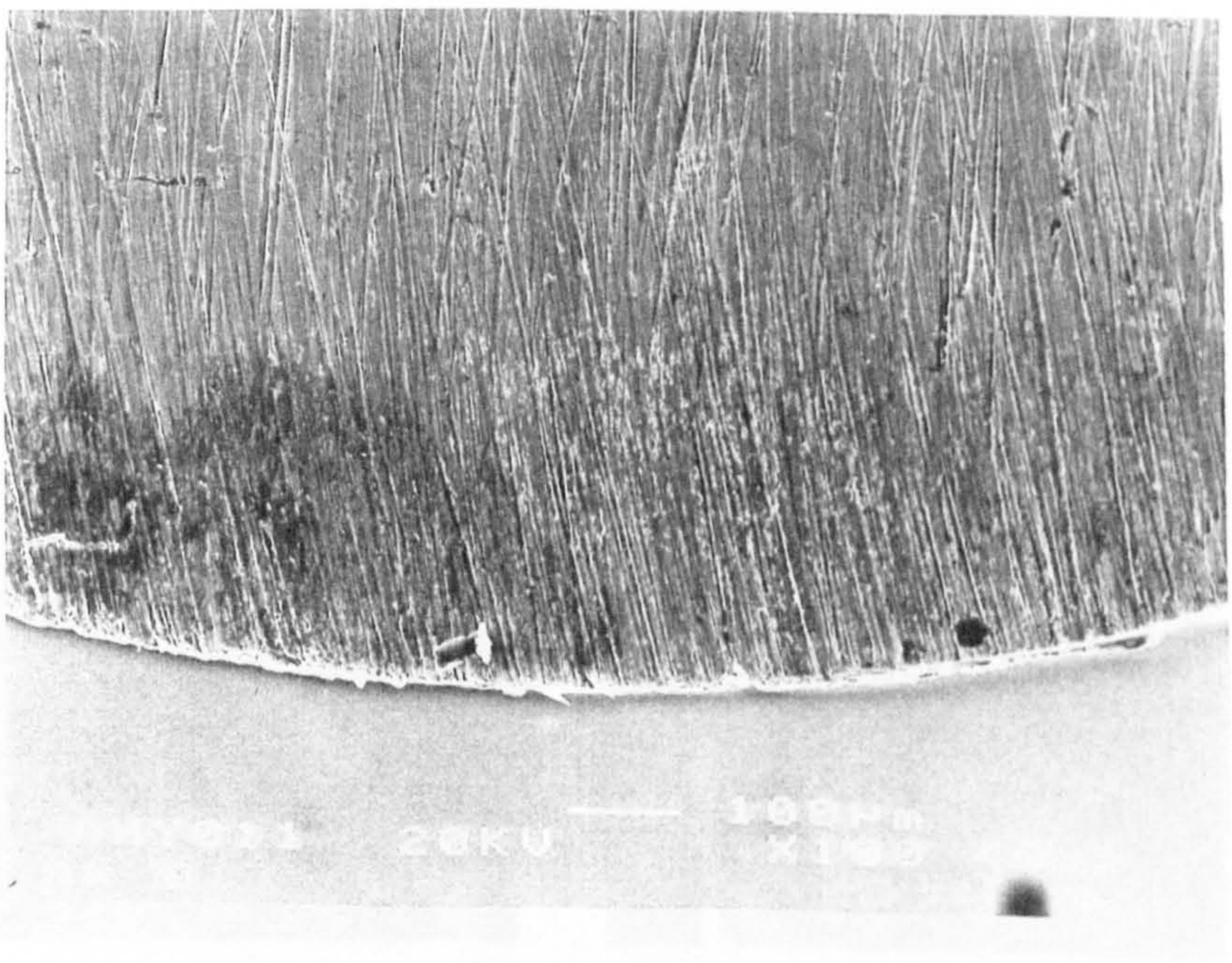

(b.5) Magnification ≈ 100.

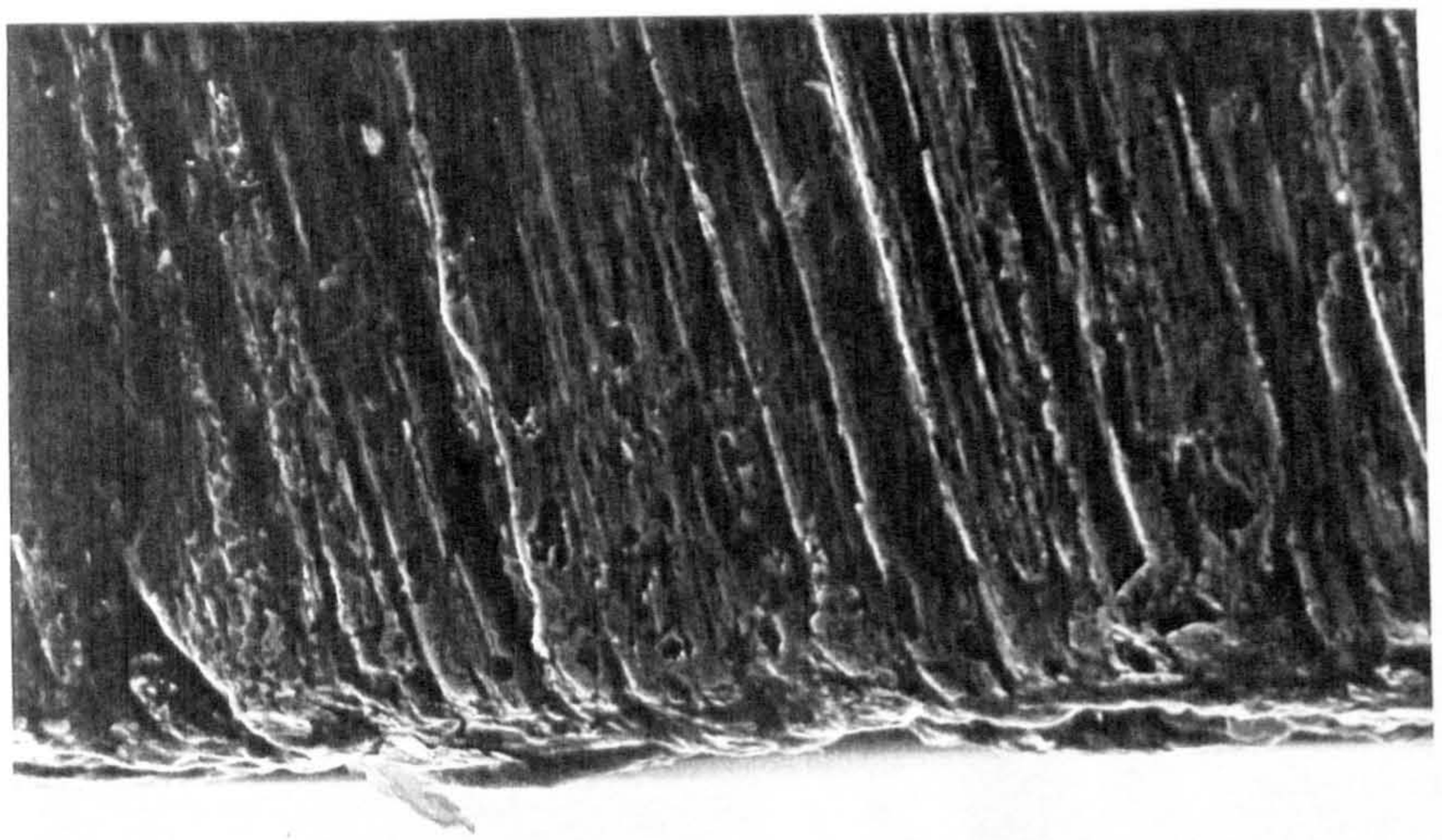

(b.6) Magnification ≈ 1000.

(b) 0.10mm-thick semi-circular 3mm-radius flat shim.

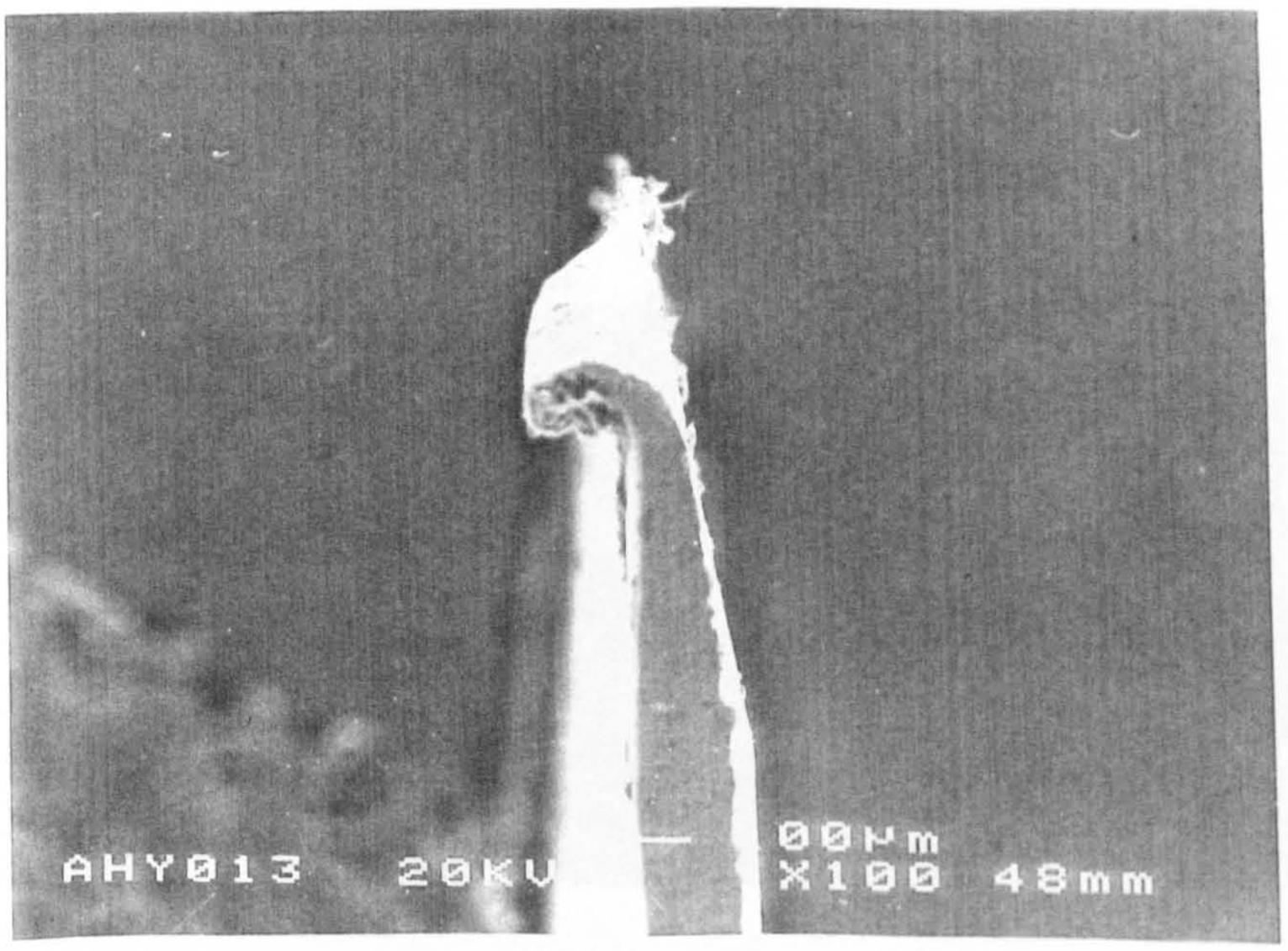

(c.1) Magnification ≈ 100.

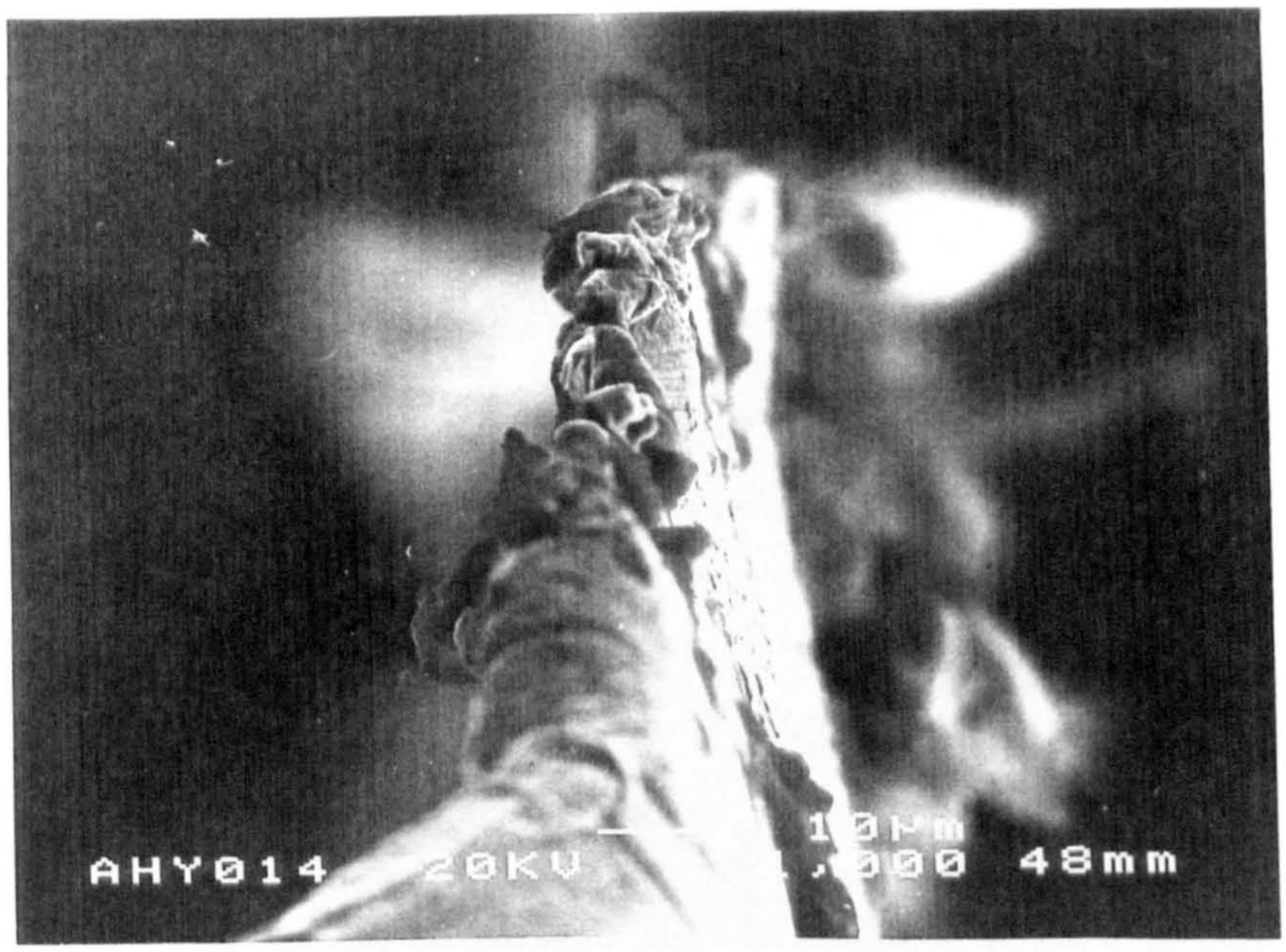

(c.2) Magnification ≈ 1000.

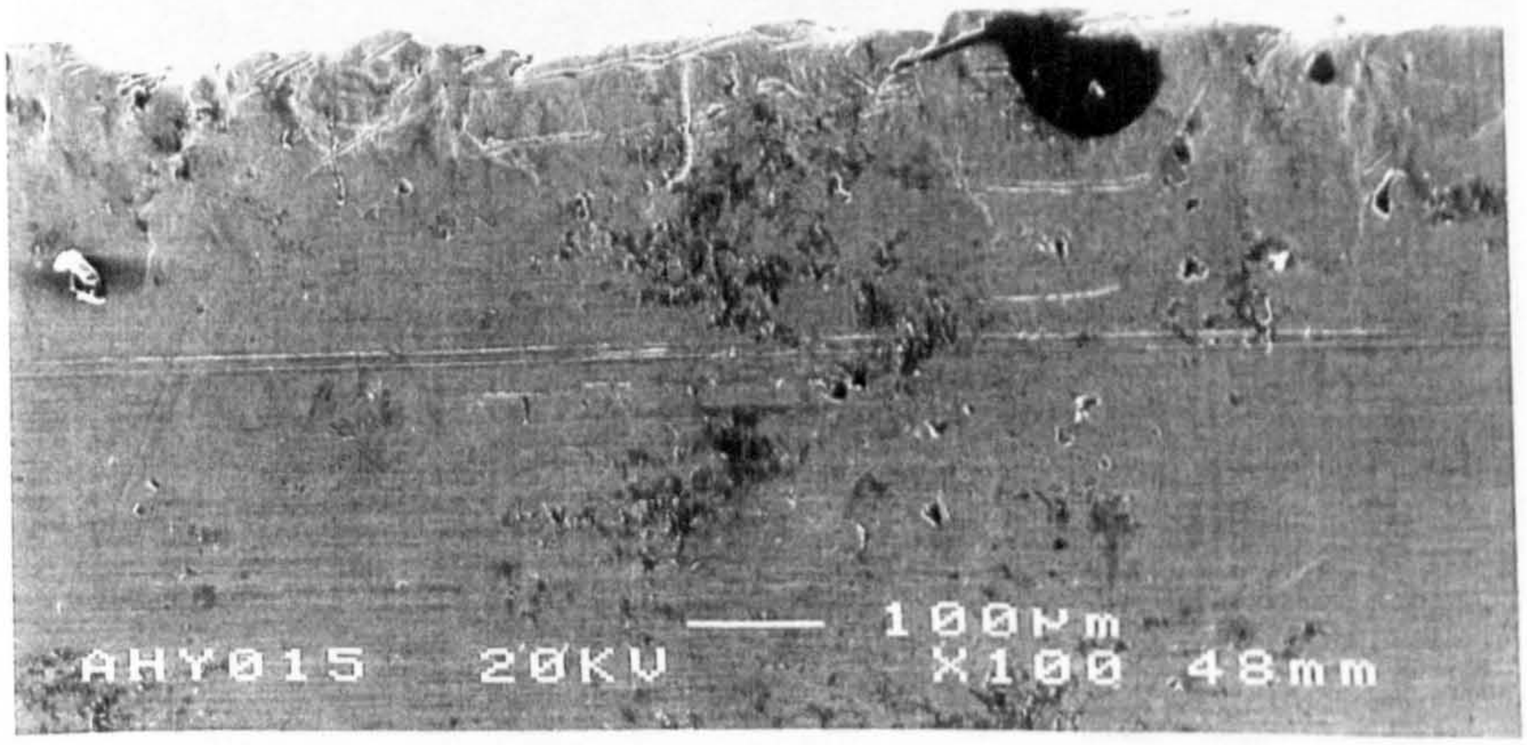

(c.3) Unsharpened side, magnification ≈ 100.

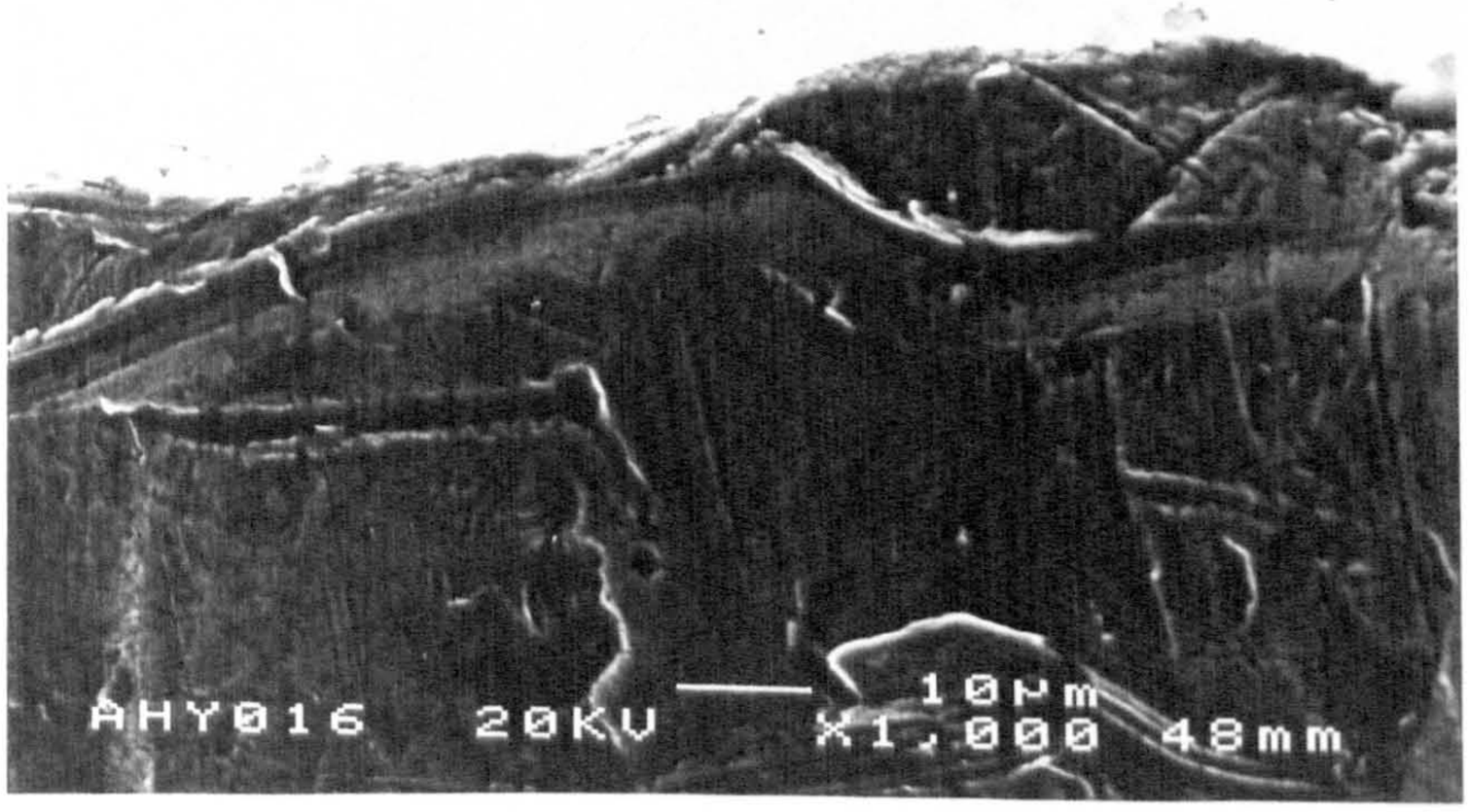

(c.4) Unsharpened side, magnification ≈ 1000.

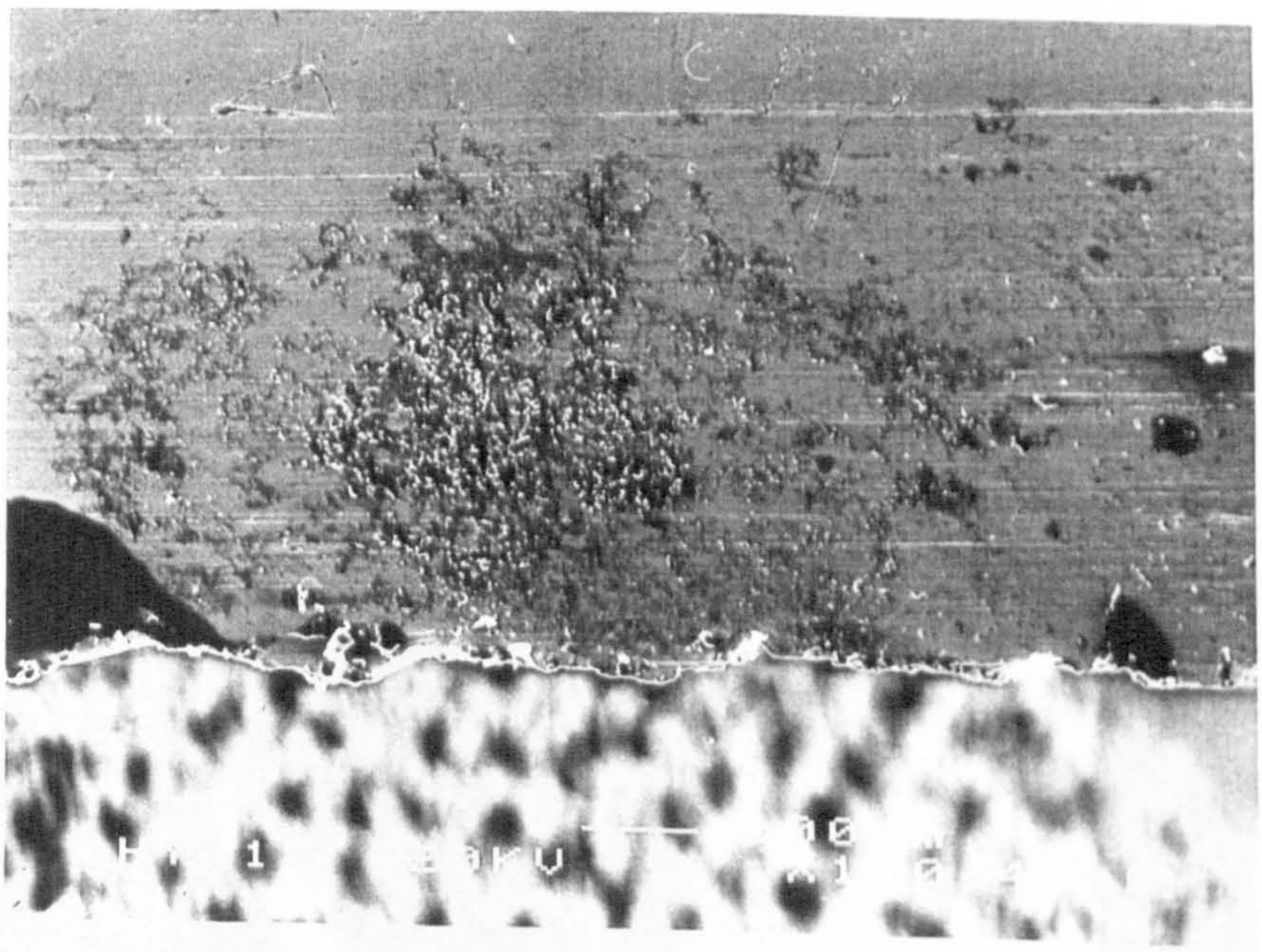

(c.5) Sharpened side, magnification ≈ 100.

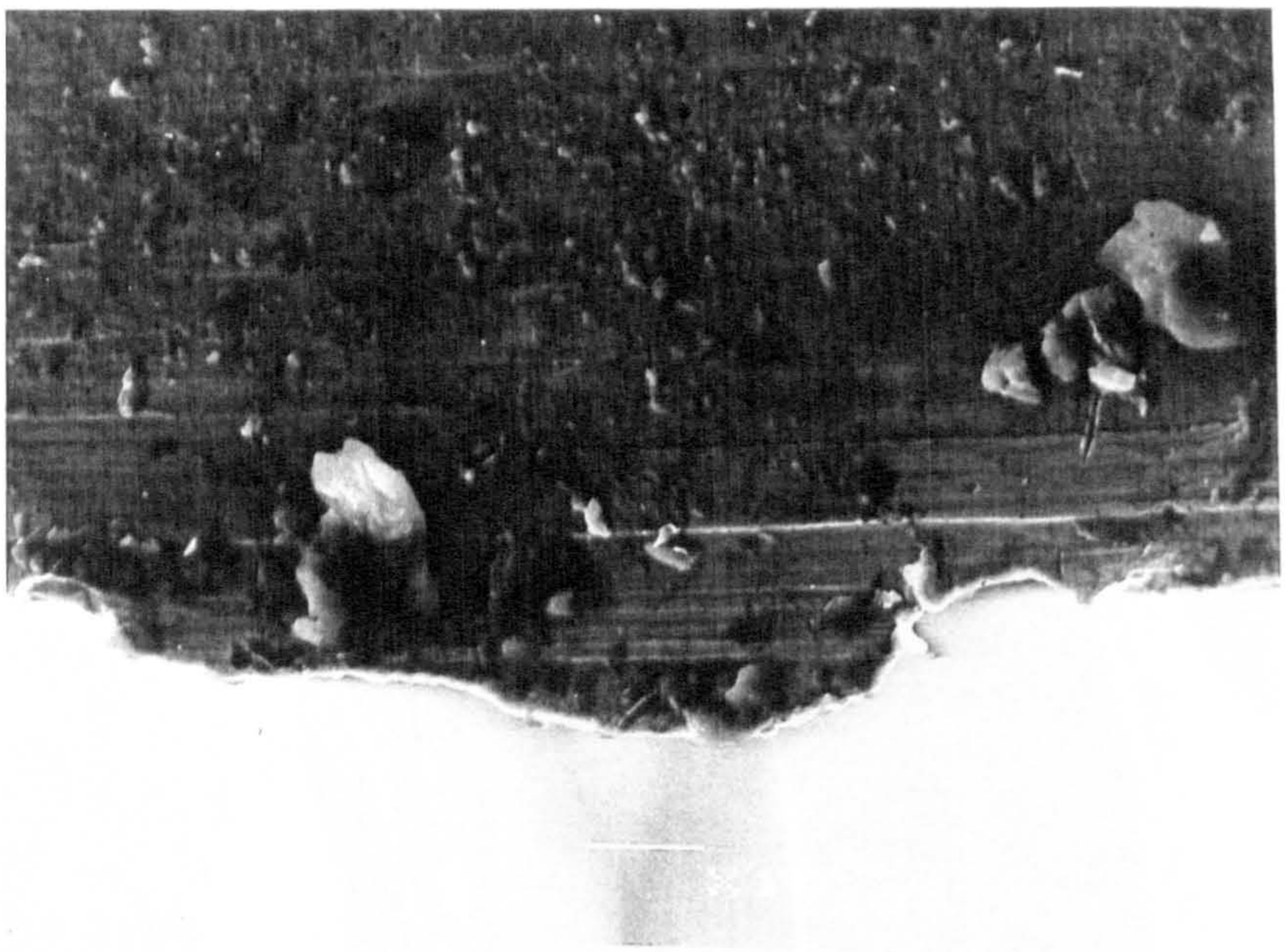

(c.6) Sharpened side, magnification ≈ 1000.
(c) 0.10mm-thick straight sharpened shim.

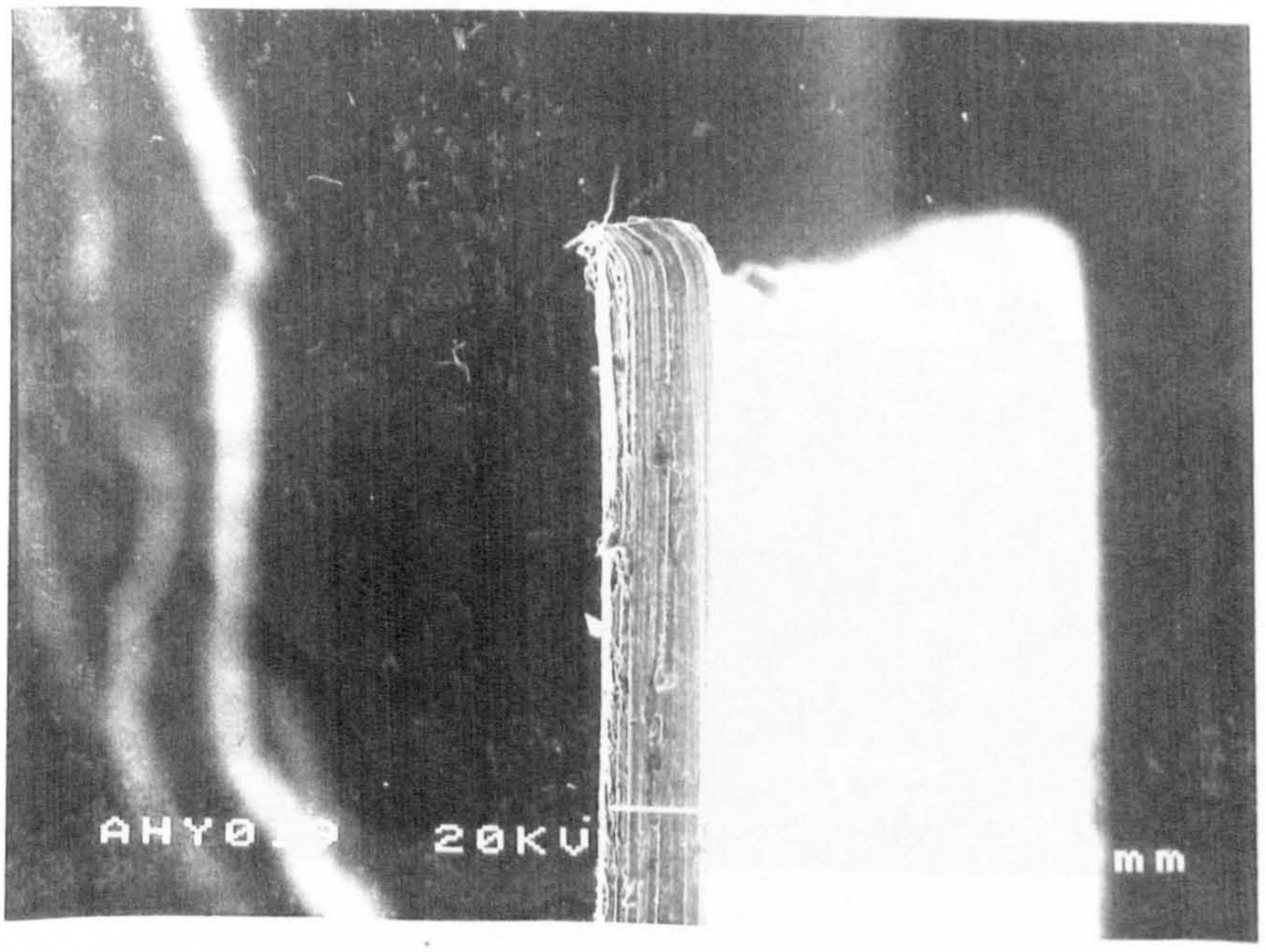

(d.1) Magnification ≈ 100.

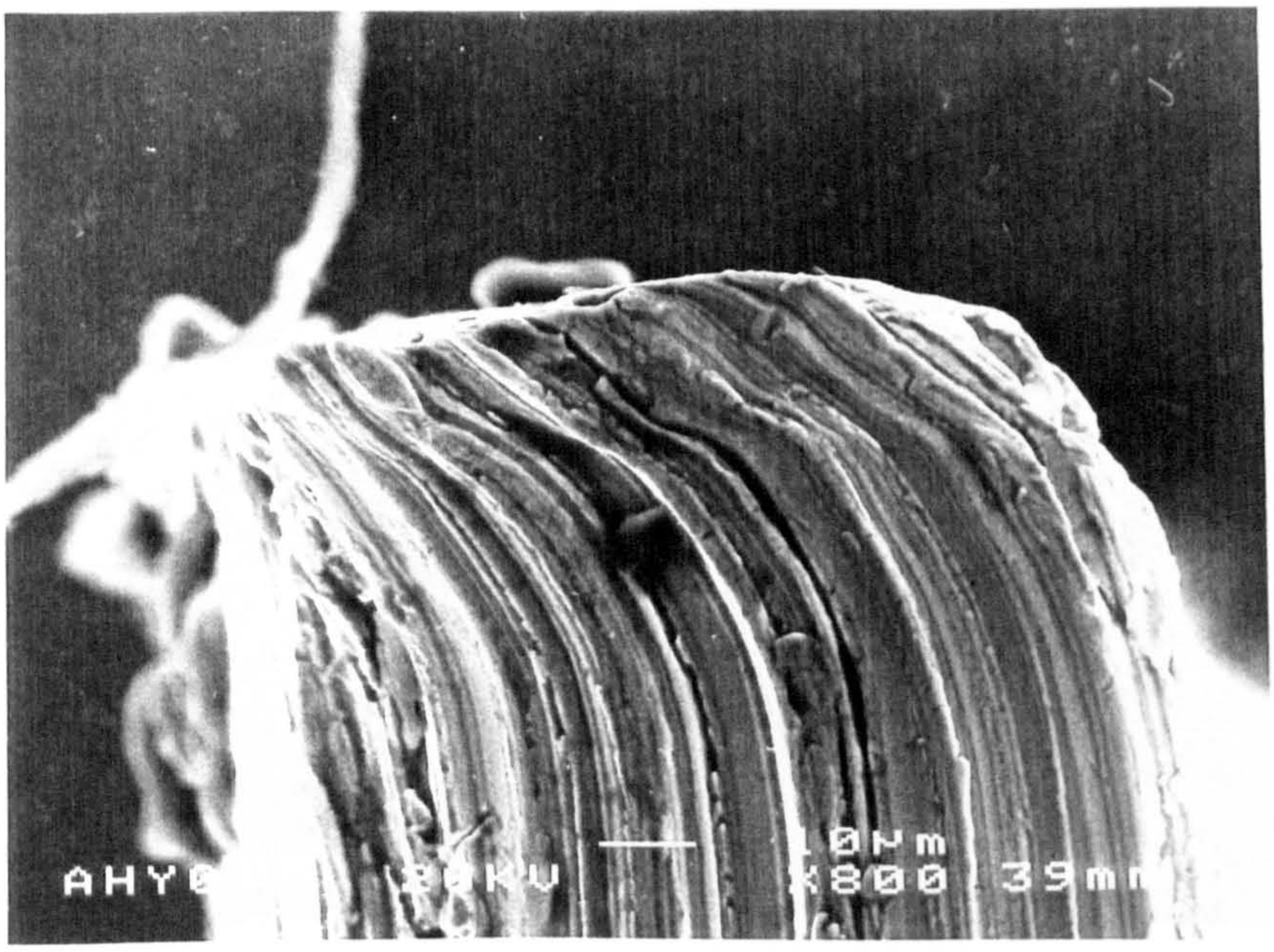

(d.2) Magnification ≈ 800.

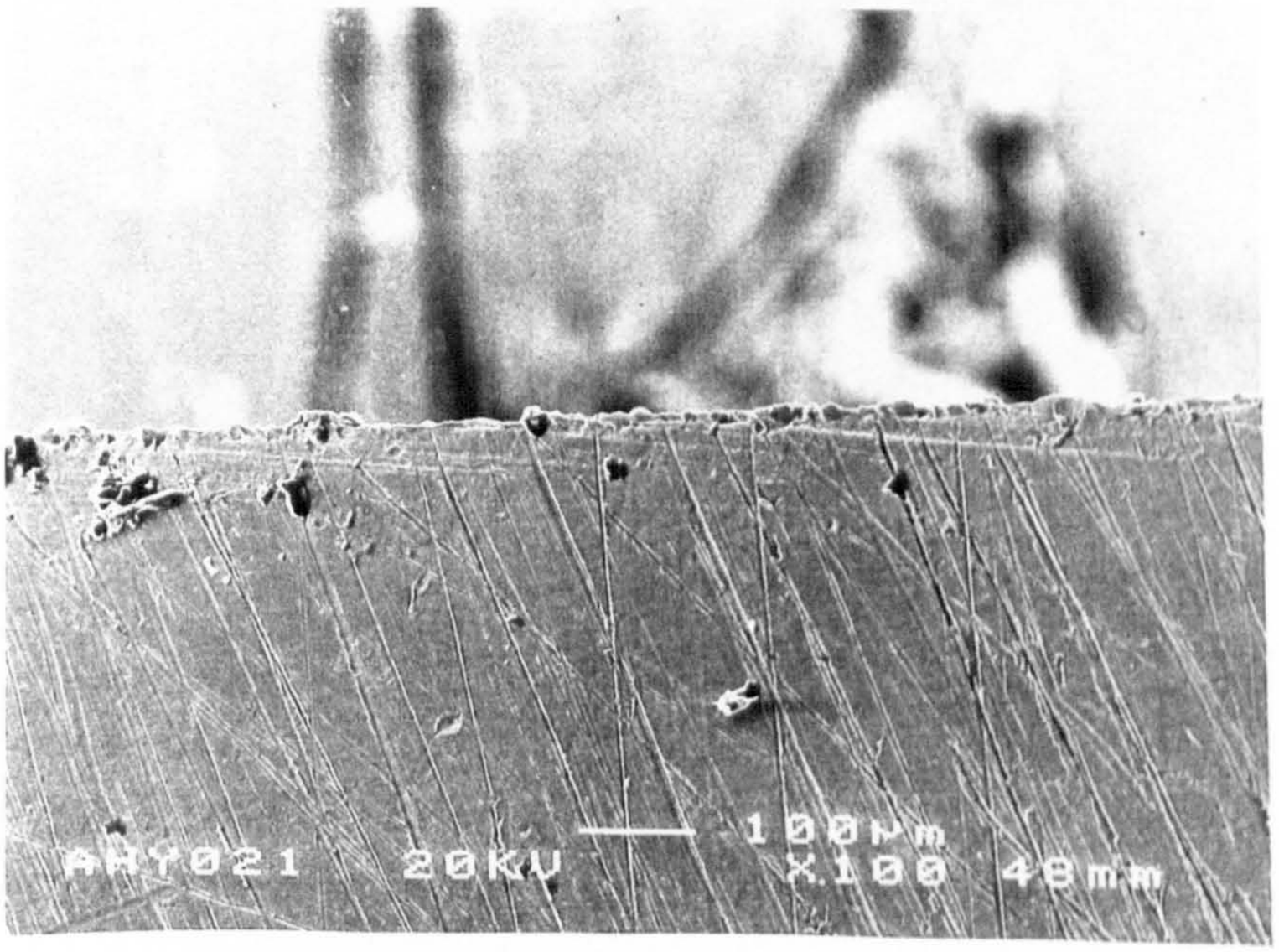

(d.3) Magnification ≈ 100.

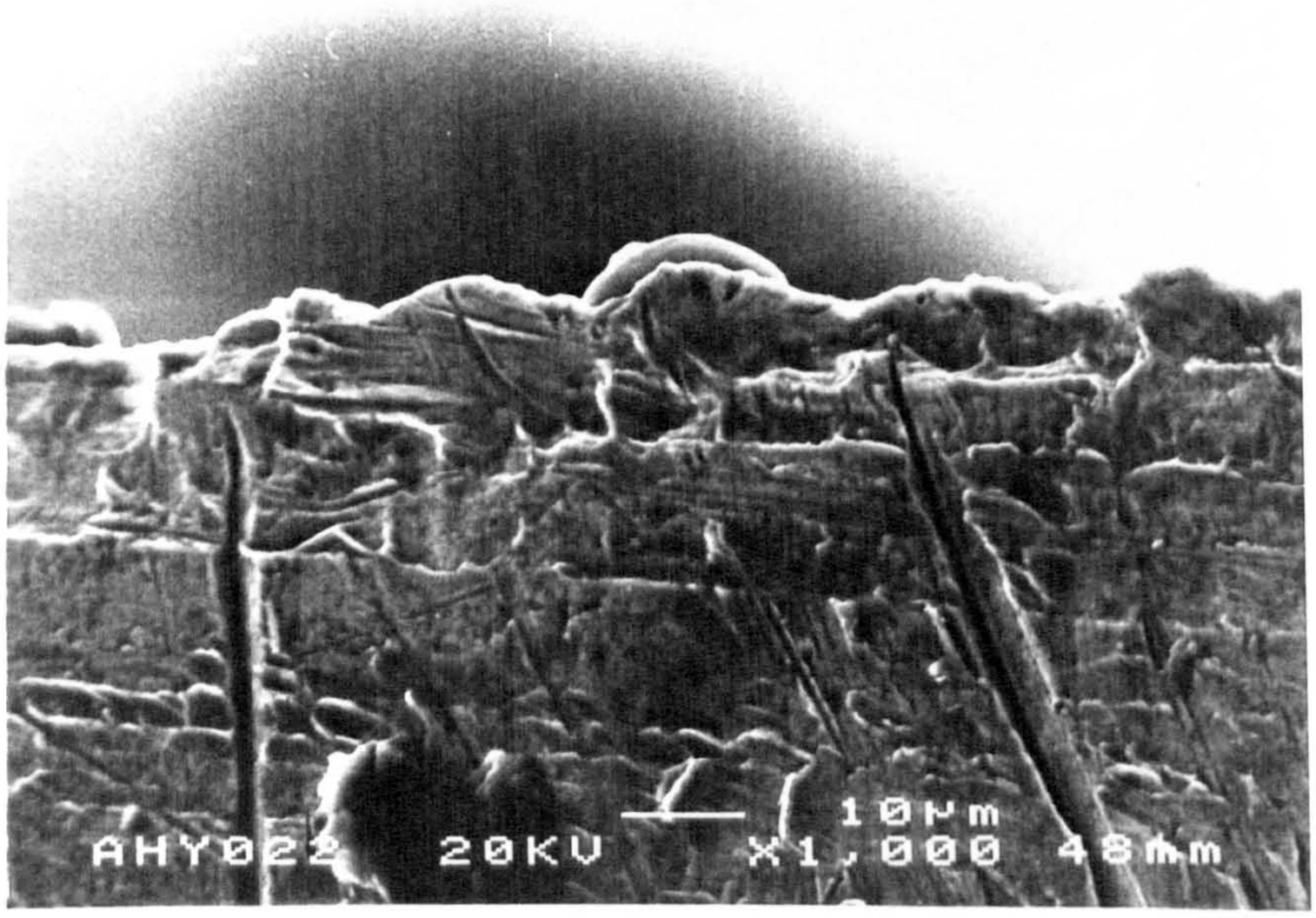

(d.4) Magnification ≈ 1000.

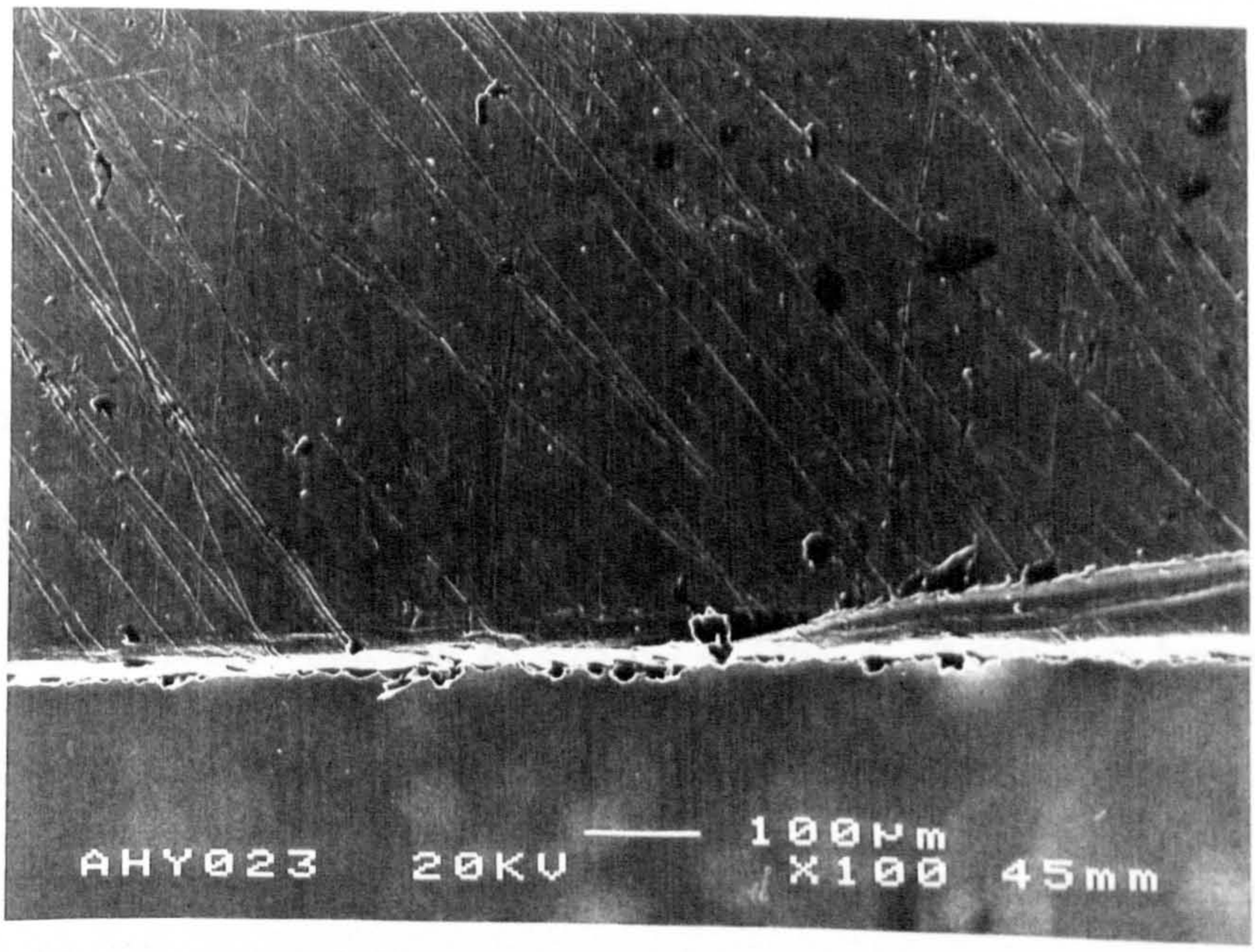

(d.5) Magnification ≈ 100.

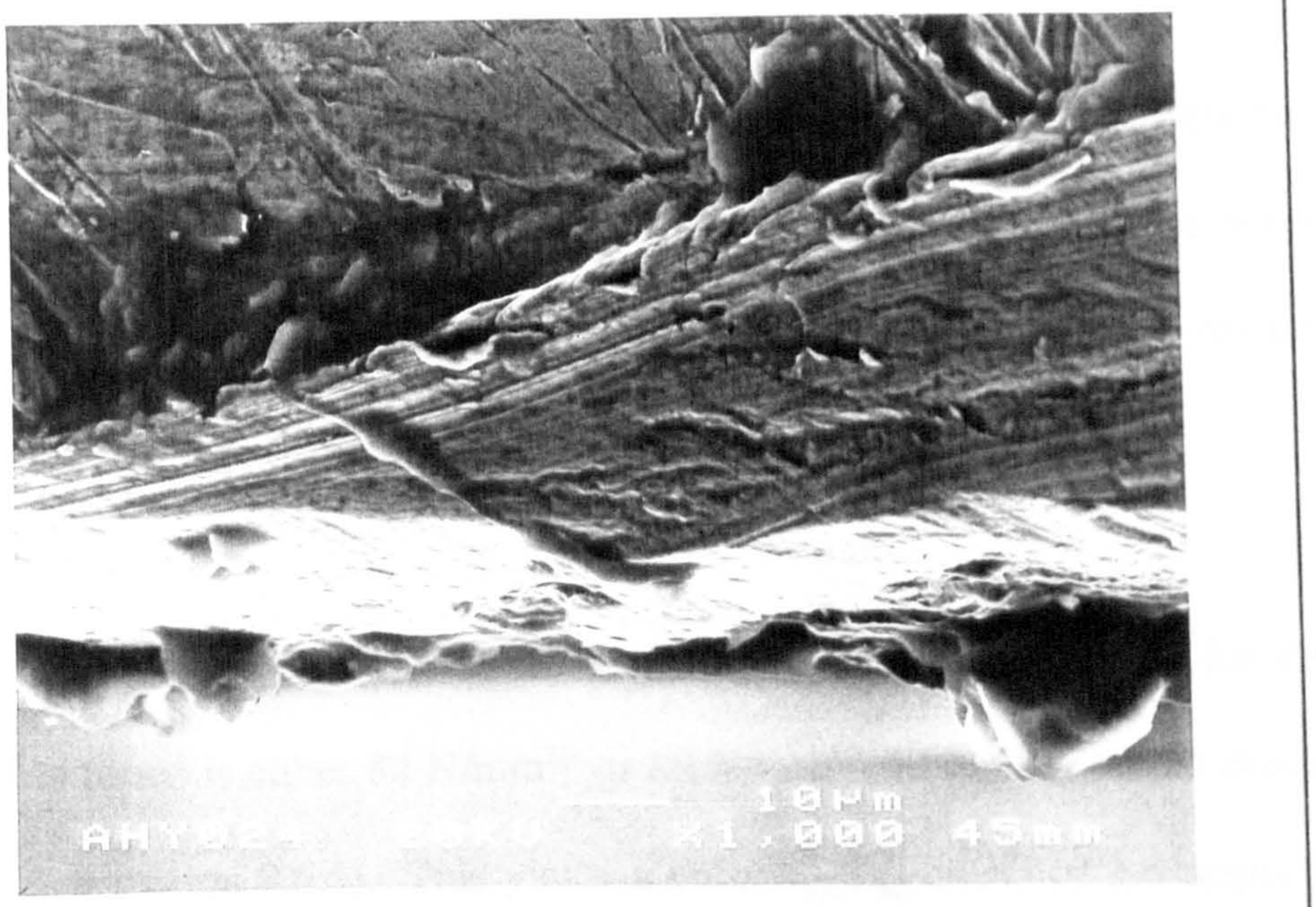

(d.6) Magnification ≈ 1000.
(d) 0.10mm-thick straight flat shim.

Figs. 10.1(a-d). *Photographs of straight and semi-circular shims which have flat or sharpened tips. Each one of the four different shims was photographed almost perpendicularly to its plane from both sides and also parallel to it. This was done at both the low and high magnifications.*

In spite of the high quality standard to which the shims were manufactured and machined, the photographs show irregularities and roughness at the tips. This may explain the scatter in the values of K_I and K_{II} at failure. It can also be seen that the method of machining significantly affects the shape of the tips, which may explain the difference between the K_{IC} values in the 3PB specimen testing on one hand and those in the testing of the pressure tubes on the other. Both sets of the K_{IC} values are tabulated in chapters 5 and 9 respectively. Therefore, the need to give a description of the machining process of the shims is prominent.

10.3. Dynamic Stress Intensity Factor, K_D

The dynamic stress intensity factor, K_{ID}, was obtained for the pressure tube tests at two locations during crack propagation: the inception of the hackle region on the fracture surfaces and the commencement of branching. All the results are tabulated in chapter 9.

The average value of K_{ID} at the inception of the hackle region for the ten pressure tubes tested is either 82 $N/mm^{3/2}$ or 89 $N/mm^{3/2}$ depending on the method of calculation (see section 9.6.5). This yields a ratio K_{ID}/K_{IC} of 3.3 or 3.6 respectively. If the hackle region is indicative of the instability of a crack, then the instability of the crack commences when K_{ID}/K_{IC} is greater than 3.

The value of K_{ID} ranged from 75 to 95 $N/mm^{3/2}$ at the inception of the hackle region. The corresponding range of K_{ID}/K_{IC} is from 3.1 to 3.9.

The total range of K_{ID} at the initiation of branching is 173 to 286 $N/mm^{3/2}$ including both methods of calculation (see section 9.6.4). This gives a range of 7.1 to 11.7 for the ratio K_{ID}/K_{IC}.

10.4. The Uniqueness of the Dynamic Stress Intensity Factor - Instantaneous Crack Velocity Relationship

The existence of a unique relationship between the dynamic stress intensity

factor, K_{ID}, and the instantaneous crack propagation velocity, v, has been debated in section 3.2. The Kobayashi and Dally [90] unique relationship of K_{ID}/K_{IC} versus v/c_1 has been reported by several researchers [e.g. 67 and 66]. It covered a range of K_{ID}/K_{IC} up to a value of less than 4. Similar graphs of K_{ID} versus v have been plotted by other authors [e.g. 74, 75 and 72].

The research conducted in this project has revealed a range of K_{ID}/K_{IC} between 3 and 12 which corresponds to a range of v between 0.18 and 0.29. The values of K_{ID} and v have been presented in Tables 9.4, 9.5 and 9.6. The investigated range is an extension of the above-described Kobayashi and Dally relationship. In Fig. 10.2, the dimensionless K_{ID}/K_{IC} has been plotted against the dimensionless v/v_s using the values

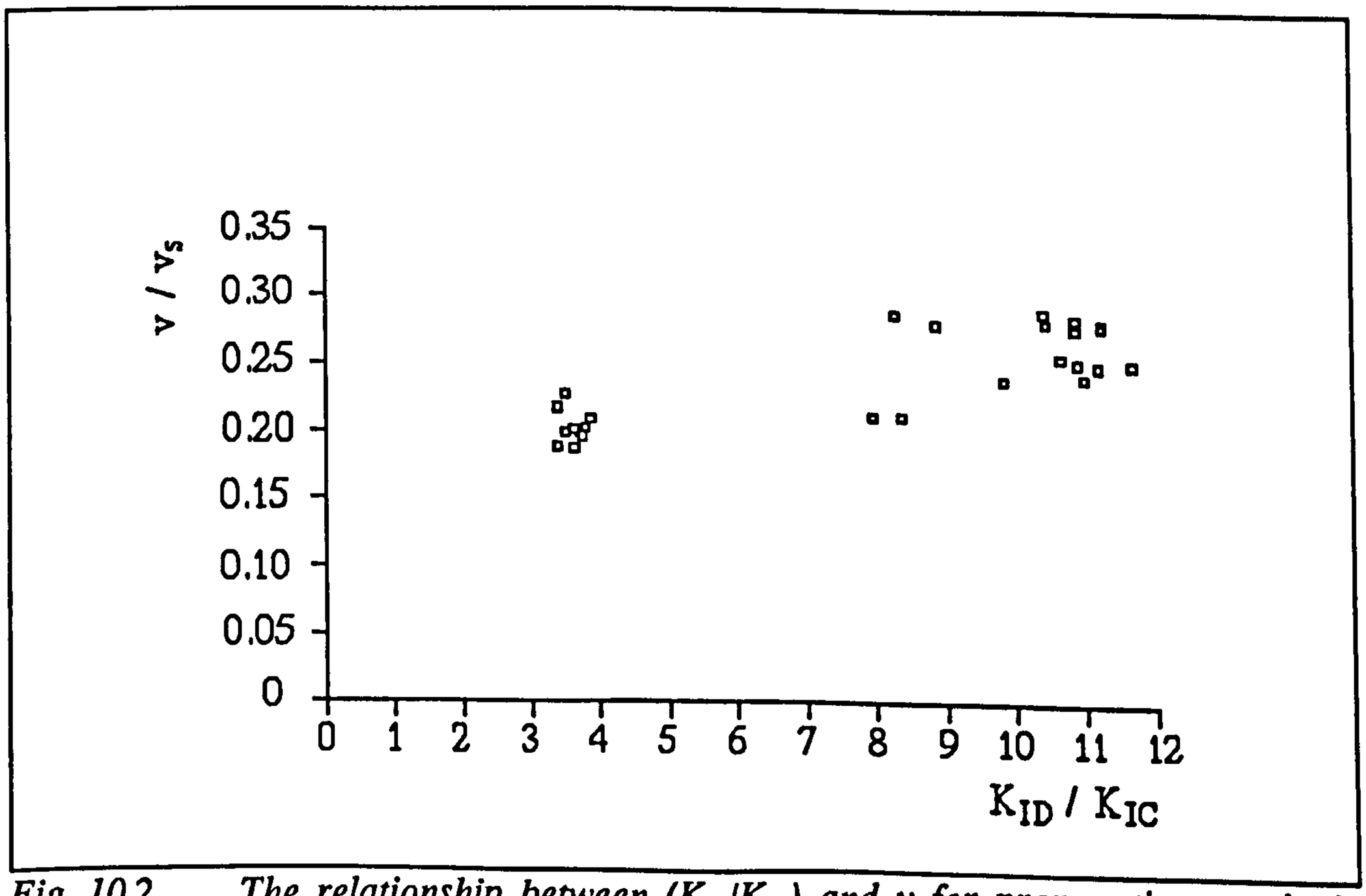

Fig. 10.2. The relationship between (K_{ID}/K_{IC}) and v for propagating cracks in pressure tubes with reference to Nilsson [25] for the calculation of K_{ID}.

of K_{ID} obtained by referring to Nilsson [25], while Fig. 10.3 shows the same dimensionless parameters using the values of K_{ID} obtained by referring to Freund [50] - see section 9.6.4. The scatter in the results underlines the uncertainty of the uniqueness of the K_{ID} versus v relationship.

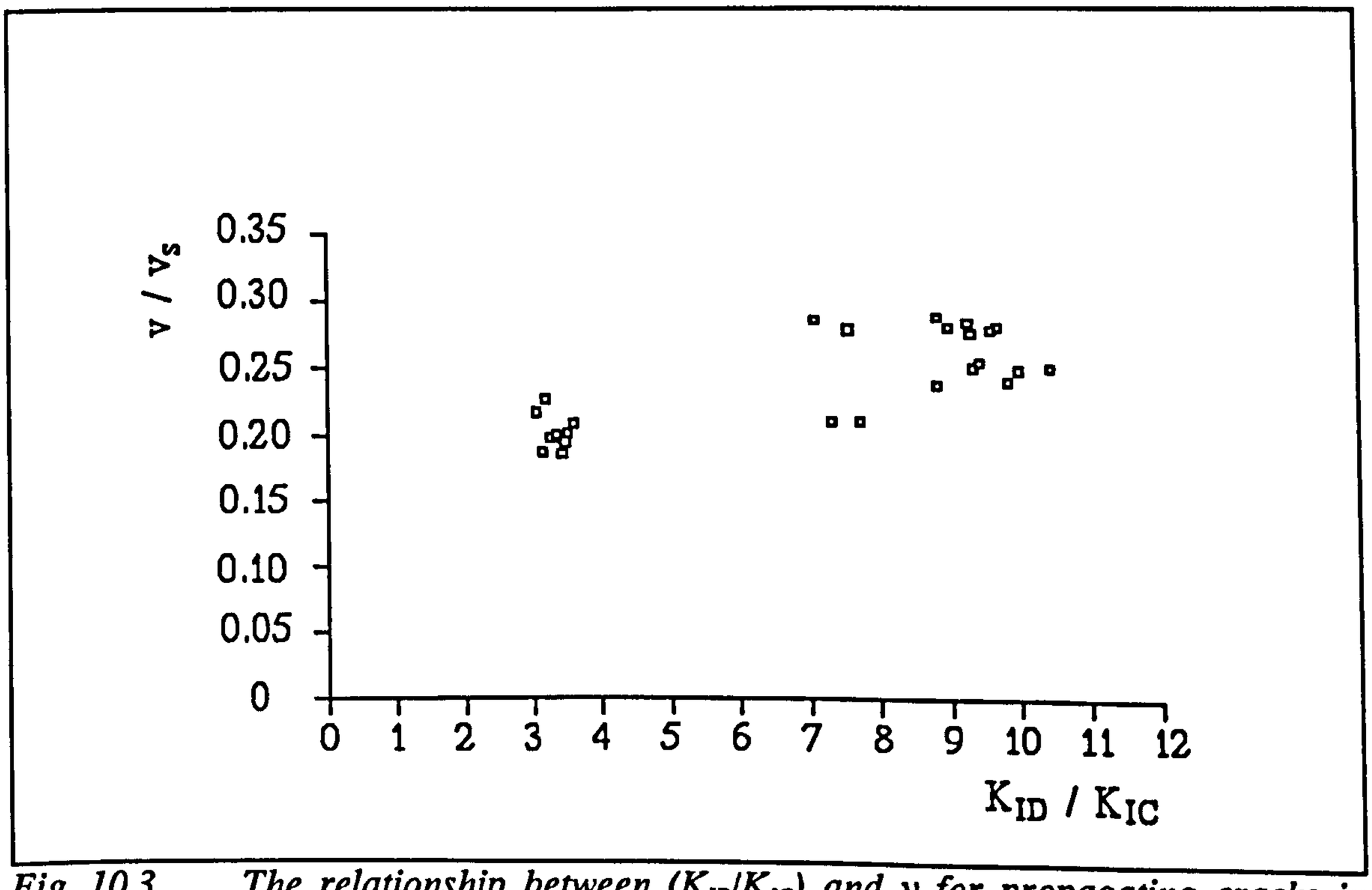

Fig. 10.3. The relationship between (K_{ID}/K_{IC}) and v for propagating cracks in pressure tubes with reference to Freund [50] for the calculation of K_{ID}.

10.5. Dynamic Modelling of Cracks

The modelling of a crack in a structural component in the static stage was discussed in section 10.1. The destructive testing of a model containing a narrow notch predicts the magnitude of the force which may cause the failure of the modelled component.

In the dynamic stage, although the propagation of the crack in the model, and the subsequent instability of the crack including branching, may give an approximate representation of how the actual component would dynamically break, nevertheless the representation may not be sufficiently accurate. The real and apparent static stress intensity factors of the component and model respectively can be utilized to predict the failure load of the component, depending on the dimensions of the component and model and the forces acting on them (see section 10.1). But the dynamic stress intensity factor depends on the velocity of crack propagation. Assuming that the stability of crack propagation is dependent upon the ratio K_{ID}/K_{IC}, and since the crack propagation may not have the same velocity in both the component and model, then the instability of propagation may occur at different locations in the component and model. This dynamic consideration is the subject of the next chapter.

Other dynamic factors which can affect the stability of a propagating crack are stress waves which may travel through a component and its model at different speeds.

CHAPTER ELEVEN

FUTURE WORK

The previous chapter describes the method of modelling cracks in an engineering component by using a model with a narrow notch, provided that the behaviour is brittle. The modelling process is accurate for the static stage. However, the dynamic stage of fracture, where the crack propagates with a certain velocity, may be different in the component and the model, due to the dependence of the dynamic stress intensity factor upon the velocity of crack propagation.

The future work recommended in this chapter is suggested in the following three points.

Firstly, it should be established further whether the instability and the subsequent branching of a crack are dependent upon the ratio K_{ID}/K_{IC} (see section 10.3). This can be achieved by investigating the dynamic fracture of different specimens for a number of materials.

Secondly, it may be rewarding to experiment further with the velocity of crack propagation as an attempt to create equations and numerical tables which can be used

to predict the velocity of propagation of any crack.

Thirdly, it is advised to gather enough information from the previous two points to enable a reasonably accurate modelling of cracks in the static and dynamic stages by using a model with a narrow notch. The dynamic modelling of a crack may require either the K_{ID}/K_{IC} versus v/c_1 relations of both the model and component to coincide in addition to the use of scaled geometries as has been suggested by Kobayashi [72], or the dimensions of the model to be proportionate to those of the component in such a ratio that will incite crack instability and branching to occur at proportionate locations in both the model and component.

REFERENCES

1. Anderson, W. E., An engineer views brittle fracture history, Boeing rept., 1969.

2. Broek, D., Elementary engineering fracture mechanics, 1986, Martinus Nijhoff Publishers.

3. Inglis, C. E., "Stresses in a plate due to the presence of cracks and sharp corners", Proceedings, Inst. Naval Architects, 1913, Vol. 60, pp. 219-230.

4. Griffith, A. A., "The phenomena of rupture and flow in solids", Transactions, Royal Soc. London, 1920, Vol. 221, pp. 163-198.

5. Love, A. E. H., Mathematical theory of elasticity, 1920, Cambridge: University Press.

6. Westergaard, H. M., "Bearing pressures and cracks", Transactions, Am. Soc. Mechanical Engrs., Journal of Applied Mechanics, June 1939, pp. A-49 - A-53.

7. Sneddon, I. N., "The distribution of stress in the neighbourhood of a crack in an elastic solid", Proceedings, Royal Soc. London, 1946, Vol. A-187, pp. 229-260.

8. Irwin, G. R., "Analysis of stresses and strains near the end of a crack traversing a plate", Transactions, Am. Soc. Mechanical Engrs., Journal of Applied Mechanics, September 1957, pp. 361-364.

9. Orowan, E., "Fundamentals of brittle behavior in metals", Fatigue and Fracture

of Metals (MIT Symposium, June 1950), John Wiley & Sons, Inc., New York, N. Y., 1952, pp. 139-167.

10. Irwin, G. R., Fracture, Handbuch der Physik, 1958, Vol. VI, Springer, Berlin, pp. 551-590.

11. Paris, P. C. and Sih, G. C., "Stress analysis of cracks", ASTM STP 381, 1965, pp. 30-81.

12. Knott, J. F., Fundamentals of fracture mechanics, 1973, Butterworth, London.

13. Parker, A. P., The mechanics of fracture and fatigue, 1981, E. & F. N. Spon Ltd.

14. Weiss, V. and Yukawa, S., "Critical appraisal of fracture mechanics", ASTM STP 381, 1965, pp. 1-29.

15. Fuchs, H. O. and Stephens, R. I., Metal fatigue in engineering, 1980, John Wiley & Sons.

16. Mott, N. F., "Fracture of metals: theoretical considerations", Engineering, 1948, Vol. 165, pp. 16-18.

17. Yoffe, E. H., "The moving Griffith crack", Philosophical Mag., 1951, Ser. 7, Vol. 42, pp. 739-750.

18. Roberts, D. K. and Wells, A. A., "The velocity of Brittle Fracture", Engineering, 1954, Vol. 178, pp. 820-821.

19. Craggs, J. W., "On the propagation of a crack in an elastic-brittle material", Journal of Mechanics and Physics of Solids, 1960, Vol. 8, pp. 66-75.

20. McClintock, F. A. and Sukhatme, S. P., "Travelling cracks in elastic materials under longitudinal shear", Journal of Mechanics and Physics of Solids, 1960, Vol. 8, pp. 187-193.

21. Bilby, B. A. and Bullough, R., 1954, Phil. Mag., 45, 631.

22. Baker, B. R., "Dynamic stresses created by a moving crack", Journal of Applied Mechanics, 1962, Vol. 29, pp. 449-458.

23. Williams, M. L., "On the stress distribution at the base of a stationary crack", Transactions, Am. Soc. Mechanical Engrs., Journal of Applied Mechanics, March 1957, pp. 109-114.

24. Cotterell, B., "On the nature of moving cracks", Journal of Applied Mechanics, March 1964, pp. 12-16.

25. Nilsson, F., "Dynamic stress-intensity factors for finite strip problems", Int. J. Fracture Mech., 1972, Vol. 8, No. 4, pp. 403-411.

26. Willis, J. R., "A comparison of the fracture criteria of Griffith and Barenblatt", Journal of the Mechanics and Physics of Solids, 1967, Vol. 15, pp. 151-162.

27. Sih, G. C. and Chen, E. P., "Moving cracks in a finite strip under tearing action", Journal of the Franklin Institute, 1970, Vol. 290, pp. 25-35.

28. Freund, L. B., "The motion of a crack in an elastic solid subjected to general loading", Dynamic Crack Propagation, (Sih, ed.), 1973, pp. 553-562, Noordhoff.

29. Hartranft, R. J. and Sih, G. C., "Application of the strain energy density fracture criterion to dynamic crack problems", Prospects of Fracture Mechanics, (Sih, Van Elst, Broek, ed.), 1974, pp. 281-297, Noordhoff.

30. Achenbach, J. D., "Elastodynamic stress intensity factors for a bifurcating crack", Prospects of Fracture Mechanics, (Sih, Van Elst, Broek, ed.), 1974, pp. 319-336, Noordhoff.

31. Atkinson, C., "Some aspects of dynamic crack propagation: a review and some

generalizations", Prospects of Fracture Mechanics, (Sih, Van Elst, Broek, ed.), 1974, pp. 337-350, Noordhoff.

32. Peterson, R. E., Stress concentration factors: charts and relations useful in making strength calculations for machine parts and structural elements, 1974, New York: Wiley-Interscience.

33. Heller, S. R., Brock, J. S. and Bart, R., "The stresses around a rectangular opening with rounded corners in a uniformly loaded plate", Proceedings of the Third US National Congress of Applied Mechanics, 1958, ASME, pp. 357-368.

34. Sobey, A. J., "Stress concentration factors for rounded rectangular holes in infinite sheets", 1965, ARC R and M 3407.

35. Mansfield, E. H., "Stress concentrations in the design of pressurised shells", 1955, ARC CP217.

36. Engineering Sciences Data Item Number 80027, "Elastic stress concentration factors. Single reinforced and unreinforced holes in infinite plates of isotropic material", 1980, Engineering Sciences Data Unit, London.

37. Rooke, D. P. and Cartwright, D. J., Compendium of stress intensity factors, 1976, HMSO, London.

38. Griffith, A. A., "The theory of rupture", Proc. 1st Int. Congress Appl. Mech., 1924, pp. 55-63.

39. Rice, J. R., "A path independent Integral and the approximate analysis of strain concentration by notches and cracks", Journal of Applied Mechanics, June 1968, pp. 379-386.

40. Dugdale, D. S., "Yielding of steel sheets containing slits", J. Mech Phys. Sol., 1960, Vol. 8, pp. 100-108.

41. Graff, K. F., Wave motion in elastic solids, 1975, Clarendon Press, Oxford.

42. Kolsky, H., Stress waves in solids, 1953, Clarendon Press, Oxford.

43. Schardin, H. and Struth, W., Glastech, Ber., 1938, Vol. 16, No. 7, p. 219.

44. Hudson, G. and Greenfield, M., Jl. Applied Physics., 1947, Vol. 18, p. 405.

45. Edgerton, H. E. and Barstow, F. E., Jl. Amer. Ceramic Soc., 1941, Vol. 24, p. 131.

46. Smith, H. L. and Ferguson, W. J., N.R.L. Progress Report, April 1950.

47. Kennedy, H. E., Welding Res. Suppt., 1945, Vol. 10, No. 11, p. 597-s.

48. Boodberg, A. and collaborators, Welding Res. Suppt., 1948, Vol. 13, No. 4, p.186-s.

49. Robertson, T. S., Jl. Iron and Steel Inst., 1953, Vol. 175, page 361.

50. Freund, L. B., Dynamic fracture mechanics, 1990, Cambridge University Press.

51. Broberg, K. B., "The propagation of a brittle crack", Arkiv Fysik, 1960, Vol. 18, pp. 159-192.

52. Andrews, E. H., Fracture in Polymers, 1968, Oliver and Boyd, Edinburgh and London.

53. Stanley, P. and Chan, W. K., "The determination of stress intensity factors and crack-tip velocities from thermoelastic infra-red emissions", IMechE C262, 1986, pp. 105-114.

54. Cartwright, D. J. and Rooke, D. P., "Evaluation of stress intensity factors", Journal of Strain Analysis, 1975, Vol. 10, No. 4, pp. 217-224.

55. Evans, W. T. and Barr, B.I.G., "Experimental evaluation of the fracture toughness (K_{Ic}) of an epoxy resin", Journal of Strain Analysis, 1974, Vol. 9, No. 3, pp. 166-171.

56. Hollmann, K. and Hahn, H. T., "Plane-strain fracture toughness of epoxies at different loading rates", Polymer Engineering and Science, 1989, Vol. 29, No. 8, pp. 523-530.

57. Breslauer, M., Voloshin, A. S. and Manson, J. A., "Casting compact-tension specimens from brittle epoxy", Experimental Techniques, 1986, Vol. 10, No. 5, pp. 26-27.

58. Harada, S., Endo, T., Harada Y. and Murakami, Y., "A simple method for the experimental K-value evaluation of the cracked body using brittle fracture characteristic of epoxy resin", Application of Fracture Mechanics to Materials and Structures, Proceedings, Int. Conf., 1984, Martinus Nijhoff Publ., pp. 1095-1108.

59. Narisawa, I., Murayama, T and Ogawa, H., "Internal fracture of notched epoxy resins", Polymer, 1982, Vol. 23, No. 2, pp. 291-294.

60. Maccagno, T. M. and Knott, J. F., "The fracture behaviour of PMMA in mixed modes I and II", Engineering Fracture Mechanics, 1989, Vol. 34, No. 1, pp. 65-86.

61. Erdogan, F. and Sih, G. C., "On the crack extension in plates under plane loading and transverse shear", Transactions ASME, Journal of Basic Engineering, December 1963, pp. 519-527.

62. Lo, K. K., " Analysis of branched cracks", Transactions ASME, Journal of Applied Mechanics, 1978, Vol. 45, pp. 797-802.

63. Takahashi, K. and Arakawa, K., "Dependence of crack acceleration on the dynamic stress-intensity factor in polymers", Experimental Mechanics, June 1987, pp. 195-200.

64. Glover, A. P., Johnson, F. A. and Radon, J. C., "Crack velocity measurements in the toughness testing of polymers", Int. Conf. on Dynamic Crack Propagation, 1972, Lehigh University.

65. Ramulu, M., Kobayashi, A. S. and Kang, B. S.-J., " Dynamic crack branching - a photoelastic evaluation", Fracture Mechanics: Fifteenth Symposium, ASTM STP 833, R. J. Sanford, Ed., American Society for Testing and Materials, 1984, pp. 130-148.

66. Knauss, W. G., "Fundamental problems in dynamic fracture", Proceedings of the 6th International Conference on Fracture, December 1984.

67. Kobayashi, A. S. and Mall, S., "Dynamic fracture toughness of Homalite-100", Experimental Mechanics, January 1978, pp. 11-18.

68. Dempsey, J. P. and Burgers, P., "Dynamic crack branching in brittle solids", Int. Jl. of Fracture, 1985, Vol. 27, pp. 203-213.

69. Knauss, W. G. and Ravi-Chandar, K., "Some basic problems in stress wave dominated fracture", International Journal of Fracture, 1985, Vol. 27, pp. 127-143.

70. Ramulu, M. and Kobayashi, A. S., "Criteria for dynamic crack curving and branching", Proceedings of the 6th International conference on Fracture, December 1984.

71. Ramulu, M. and Kobayashi, A. S., "Mechanics of crack curving and branching - a dynamic fracture analysis", International Journal of Fracture, 1985, Vol. 27, pp. 187-201.

72. Kobayashi, A.S., "Dynamic crack propagation in brittle and ductile materials", Structural Impact and Crashworthiness, (Vol. 1: Keynote Lectures), July 1984,

Elsevier Applied Science Publ., London, USA.

73. Popelar, C. H. and Gehlen, P. C., "Modelling of dynamic crack propagation: II. Validation of two-dimensional analysis", International Journal of Fracture, 1979, Vol. 15, No. 2, pp. 159-177.

74. Kobayashi, A. S. and Mall, S., "Rapid crack propagation and arrest in polymers", Polymer Engineering and Science, 1979, Vol. 19, No. 2, pp. 131-135.

75. Dally, J. W., Fourney, W. L. and Irwin, G. R., "On the uniqueness of the stress intensity factor - crack velocity relationship", International Journal of Fracture, 1985, Vol. 27, pp. 159-168.

76. BS5447: British Standard Methods of test for plane strain fracture toughness (K_{IC}) of metallic materials, 1977, British Standards Institution.

77. ANSI/ASTM E 399 - 78a: American Standard Test Method for plane-strain fracture toughness of metallic materials, 1978, The American Society for Testing and Materials.

78. Hyde, T. H. and Chambers, A. C., "A compact mixed-mode (CMM) fracture specimen", J. Strain Analysis, 1988, Vol. 23, p. 61.

79. Creager, M. and Paris, P. C., "Elastic field equations for blunt cracks with reference to stress corrosion cracking", Int. J. Fracture, 1967, Vol. 3, p. 246.

80. PAFEC 75 Data Preparation Manual, Pafec 1st Edition, 1978, Nottingham.

81. Zienkiewicz, O. C. and Zhu, J. Z., "A simple error estimator and adaptive procedure for practical engineering analysis", Int. J. numer Methods Engng, 1987, Vol. 24, pp. 337-357.

82. Sih, G. C., Handbook of stress intensity factors for researchers and engineers,

1973, Institute of Fractures and Solid Mechanics, Lehigh University of Bethlehem, PA.

83. Tada, H., Paris, P. and Irwin, G. R., The stress analysis of cracks handbook, 1973, Del Research Corp., Hillertown, PA.

84. Murakami, Y., Stress intensity factors handbook, 1988, Pergamon Press, Oxford.

85. Chambers, A. C., Hyde, T. H. and Webster, J. J., "Mixed-mode fatigue crack growth at 550°C under plane stress conditions in Jethete M152", Engng Fracture Mech., 1991, Vol. 39, p. 603.

86. Hyde, T. H. and Chambers, A. C., "An experimental investigation of mixed-mode creep crack growth in Jethete M152 at 550°C", Maters High Temp., 1991, Vol. 9, p. 127.

87. Hyde, T. H. and Chambers, A. C., "Creep-fatigue crack growth in Jethete M152 at 550°C under mixed-mode conditions", J. Strain Analysis, 1992, Vol. 27, p. 49.

88. Raju, I. S. and Newman, Jr., J. C., "Stress-intensity factors for internal and external surface cracks in cylindrical vessels", Trans. ASME, Ser. J, J. Pressure Vessel Technology, 1982, Vol. 104, pp. 293-298.

89. Raju, I. S. and Newman, Jr., J. C., "Stress-intensity factors for a wide range of semi-elliptical surface cracks in finite-thickness plates", Engng Frac. Mech., 1979, Vol. 11, pp. 817-829.

90. Kobayashi, T. and Dally J. W., "The relationship between crack velocity and stress intensity factor in birefringent polymers", Fast Fracture and Crack Arrest, ASTM STP 627, July 1977, pp. 257-273.

APPENDIX I

MATERIAL PROPERTIES I

(ARALDITE CT-200 WITH HARDENER HT-907)

The modulus of elasticity, E, for the epoxy resin Araldite CT-200 with Hardener HT-907 was obtained experimentally by testing a beam under three point bending, as shown in Fig. I.1.

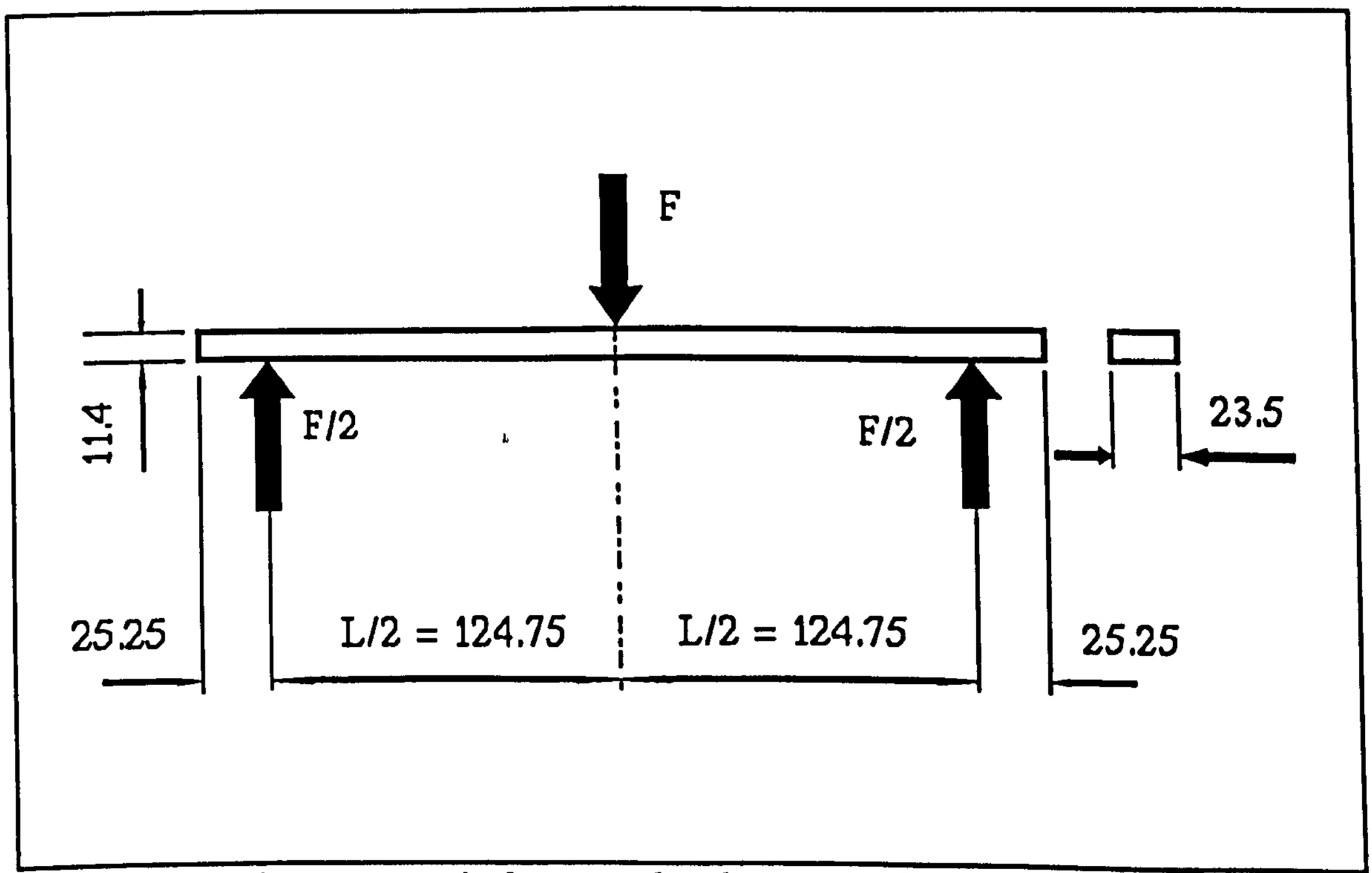

Fig. I.1. An epoxy resin beam under three point bending - all the dimensions are in mm.

The Instron 1193, shown in Fig. 5.7, which has a displacement-controlled

loading cross-head, was used to provide the bending force. The beam was loaded from 0 to a maximum of 500 N under a constant loading speed of 5 mm/minute. The plot of the force F against the displacement of the cross-head (i.e., F versus the deflection of the beam) was a straight line with a gradient ξ of 35.0 N/mm. It can be shown from first principles that the modulus of elasticity is given by

$$E = \frac{\xi L^3}{48I} \qquad \text{(I.1)}$$

where I is the second moment of area of the beam. E was calculated to be 3900 N/mm^2 (accurate to two significant figures).

The mass density, δ, of the epoxy resin was found by accurately weighing a known volume of the material. The volume was decided by using a micrometer to measure the dimensions of any weighed sample, and the method of water displacement confirmed the calculated volume. δ was calculated to be 1210 kg/m^3 (accurate to three significant figures).

The material's Poisson's ratio, υ, has been well established in the Department of Mechanical Engineering of the University of Nottingham after the experimentation of several researchers. υ was found to be 0.30.

APPENDIX II

MATERIAL PROPERTIES II

(ARALDITE CT-200 WITH HARDENER HT-907)

The tensile yield stress, σ_Y, and the ultimate tensile stress, σ_u, of the epoxy resin were obtained experimentally by loading the specimen shown in Fig. II.1 to failure.

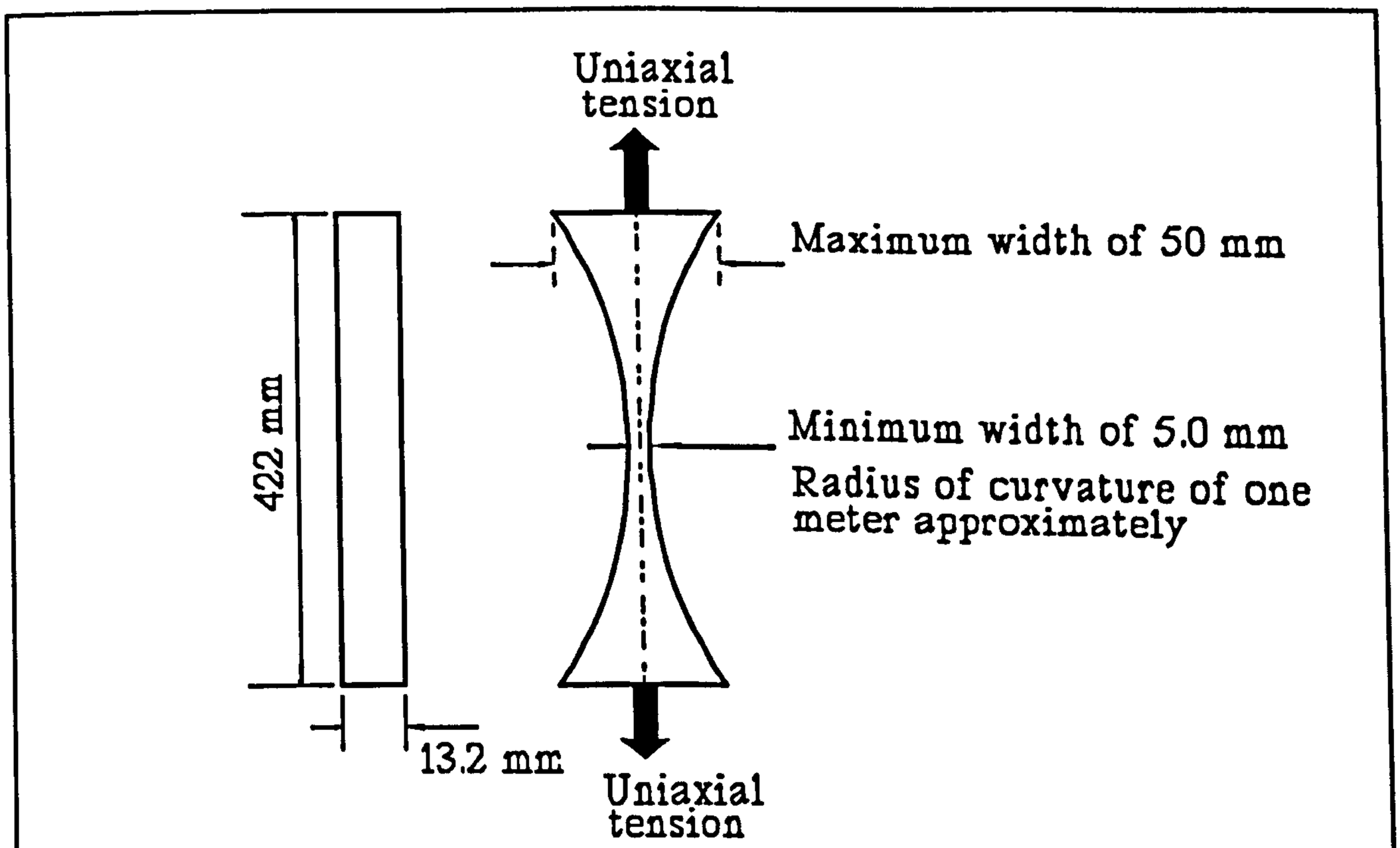

Fig. II.1. Uniaxial tensile loading of a specimen.

The Instron 1193 in conjunction with the Instron gripping jaws provided the uniaxial tension required to test the specimen. The speed of the loading cross-head

was 1 mm/minute. A plot of the uniaxial tensile stress (at the minimum cross-sectional area) against the cross-head displacement is shown in Fig. II.2.

The plot of σ against displacement is a straight line up to a σ value of 42.0 N/mm^2, and therefore the σ_Y of the material is 42.0 N/mm^2. It can also be seen that the σ_u of the material is 90.8 N/mm^2. The graph reveals a small drop in σ before final fracture occurs.

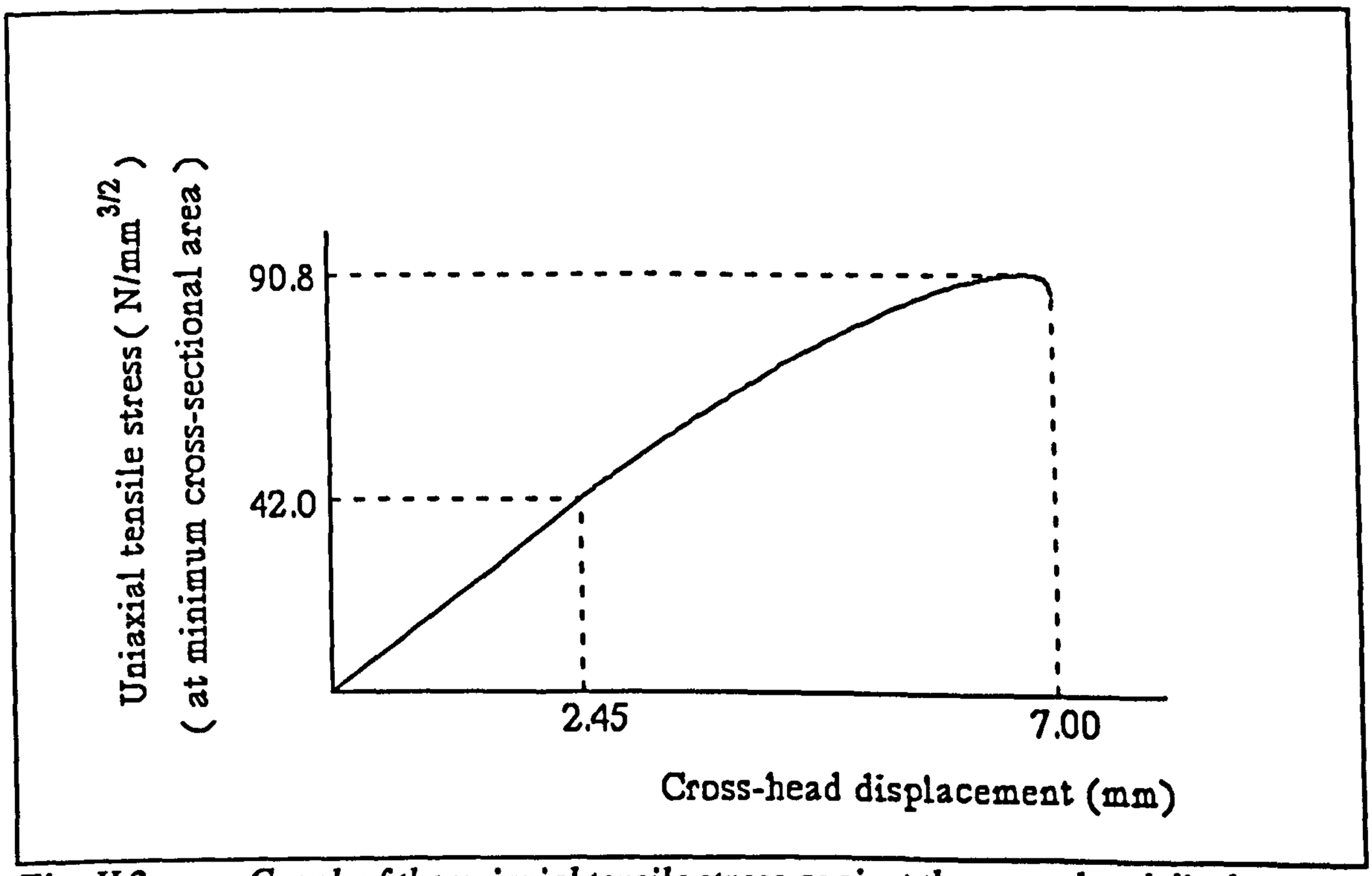

Fig. II.2. Graph of the uniaxial tensile stress against the cross-head displacement for the specimen shown in Fig. II.1.

The specimen broke at the minimum cross-sectional area. The fracture surface was flat and perpendicular to the uniaxial tensile stress, which is typical of a brittle fracture. The fracture surface texture and lines indicated that fracture initiated at one of the corners of the broken surface.

APPENDIX III

K_I AND K_{II} EVALUATION METHOD

Hyde and Chambers [78] employed the finite element and photoelastic techniques to obtain the mode-I and mode-II static stress intensity factors for the CMM specimen. Their results were presented in the form of four graphs of $K_I^0/(P/BW^{1/2})$, $K_I^{90}/(P/BW^{1/2})$, $K_{II}^0/(P/BW^{1/2})$ and $K_{II}^{90}/(P/BW^{1/2})$ against a/W. K_I^0 and K_I^{90} are the mode-I stress intensity factors for the loading angle, α, of 0° and 90° respectively. The parameters α, a, P, B and W are all defined in chapters 6 and 8. K_{II}^0 and K_{II}^{90} are the mode-II stress intensity factors for the loading angle, α, of 0° and 90° respectively. The stress intensity factors for any loading angle, α, are given [78] by

$$K_I = K_I^0 \cos\alpha + K_I^{90} \sin\alpha \qquad \text{(III.1)}$$

and

$$K_{II} = K_{II}^0 \cos\alpha + K_{II}^{90} \sin\alpha \qquad \text{(III.2)}$$

The four graphs presented by Hyde and Chambers [78] have been used to obtain the values of $K_I^0/(P/BW^{1/2})$, $K_I^{90}/(P/BW^{1/2})$, $K_{II}^0/(P/BW^{1/2})$ and $K_{II}^{90}/(P/BW^{1/2})$ for different values of a/W in Table III.1.

The two values of the loading angle, α, predicted by Hyde and Chambers [78]

to give pure mode-I and pure mode-II loading conditions for (a/W = 0.45) agreed with those obtained by the author, for the same loading conditions, in the finite element analysis presented in chapter 8, which were 20.2° and 108.6° respectively.

a/W	$K_I^0/(P/BW^{1/2})$	$K_I^{90}/(P/BW^{1/2})$	$K_{II}^0/(P/BW^{1/2})$	$K_{II}^{90}/(P/BW^{1/2})$
0.300	5.61	1.70	-0.67	1.32
0.350	6.25	1.86	-0.67	1.43
0.369	6.54	1.96	-0.66	1.48
0.400	7.02	2.13	-0.65	1.57
0.410	7.24	2.20	-0.64	1.59
0.420	7.46	2.28	-0.64	1.62
0.421	7.48	2.29	-0.64	1.62
0.422	7.50	2.29	-0.64	1.62
0.423	7.53	2.30	-0.64	1.63
0.424	7.55	2.31	-0.64	1.63
0.425	7.57	2.32	-0.64	1.63
0.426	7.59	2.32	-0.63	1.63
0.427	7.61	2.33	-0.63	1.63
0.428	7.64	2.34	-0.63	1.64
0.429	7.66	2.34	-0.63	1.64
0.430	7.68	2.35	-0.63	1.64
0.431	7.70	2.36	-0.63	1.64
0.432	7.73	2.37	-0.63	1.65
0.433	7.75	2.37	-0.63	1.65
0.434	7.77	2.38	-0.63	1.65
0.435	7.80	2.39	-0.63	1.66
0.436	7.82	2.40	-0.63	1.66
0.437	7.84	2.41	-0.63	1.66

0.438	7.86	2.41	-0.63	1.66
0.439	7.89	2.42	-0.63	1.67
0.440	7.91	2.43	-0.63	1.67
0.441	7.93	2.44	-0.63	1.67
0.442	7.95	2.44	-0.63	1.68
0.443	7.98	2.45	-0.63	1.68
0.444	8.00	2.46	-0.63	1.68
0.445	8.02	2.47	-0.62	1.69
0.446	8.04	2.47	-0.62	1.69
0.447	8.06	2.48	-0.62	1.69
0.448	8.09	2.49	-0.62	1.69
0.449	8.11	2.49	-0.62	1.70
0.450	8.13	2.50	-0.62	1.70
0.451	8.16	2.51	-0.62	1.70
0.452	8.18	2.52	-0.62	1.70
0.453	8.21	2.53	-0.62	1.71
0.454	8.23	2.54	-0.62	1.71
0.455	8.26	2.55	-0.62	1.71
0.456	8.29	2.56	-0.61	1.71
0.457	8.31	2.57	-0.61	1.71
0.458	8.34	2.58	-0.61	1.72
0.459	8.36	2.59	-0.61	1.72
0.460	8.39	2.60	-0.61	1.72
0.461	8.42	2.61	-0.61	1.72
0.462	8.44	2.62	-0.61	1.73
0.463	8.47	2.63	-0.61	1.73
0.464	8.49	2.64	-0.61	1.73
0.465	8.52	2.65	-0.61	1.74
0.466	8.55	2.66	-0.60	1.74

0.467	8.57	2.67	-0.60	1.74
0.468	8.60	2.68	-0.60	1.74
0.469	8.62	2.69	-0.60	1.75
0.470	8.65	2.70	-0.60	1.75
0.471	8.68	2.71	-0.60	1.75
0.472	8.70	2.72	-0.60	1.76
0.473	8.73	2.73	-0.60	1.76
0.474	8.75	2.74	-0.60	1.76
0.475	8.78	2.75	-0.60	1.77
0.476	8.81	2.76	-0.60	1.77
0.477	8.83	2.77	-0.60	1.77
0.478	8.86	2.78	-0.60	1.77
0.479	8.88	2.79	-0.60	1.78
0.480	8.91	2.80	-0.60	1.78
0.481	8.94	2.81	-0.60	1.78
0.482	8.96	2.82	-0.60	1.79
0.483	8.99	2.83	-0.60	1.79
0.484	9.01	2.84	-0.60	1.79
0.485	9.04	2.85	-0.60	1.80
0.486	9.07	2.86	-0.59	1.80
0.487	9.09	2.87	-0.59	1.80
0.488	9.12	2.88	-0.59	1.80
0.489	9.14	2.89	-0.59	1.81
0.490	9.17	2.90	-0.59	1.81
0.491	9.20	2.91	-0.59	1.81
0.492	9.22	2.92	-0.59	1.82
0.493	9.25	2.93	-0.59	1.82
0.494	9.27	2.94	-0.59	1.82
0.495	9.30	2.95	-0.59	1.83

0.496	9.33	2.95	-0.58	1.83
0.497	9.35	2.96	-0.58	1.83
0.498	9.38	2.97	-0.58	1.83
0.499	9.40	2.98	-0.58	1.84
0.500	9.43	2.99	-0.58	1.84
0.501	9.47	3.00	-0.58	1.84
0.502	9.50	3.01	-0.58	1.85
0.503	9.54	3.02	-0.57	1.85
0.504	9.58	3.03	-0.57	1.85
0.505	9.62	3.05	-0.57	1.86
0.506	9.65	3.06	-0.57	1.86
0.507	9.69	3.07	-0.57	1.86
0.508	9.73	3.08	-0.56	1.86
0.509	9.76	3.09	-0.56	1.87
0.510	9.80	3.10	-0.56	1.87
0.511	9.84	3.11	-0.56	1.87
0.512	9.88	3.12	-0.56	1.88
0.513	9.91	3.14	-0.56	1.88
0.514	9.95	3.15	-0.56	1.88
0.515	9.99	3.16	-0.56	1.89
0.516	10.03	3.17	-0.55	1.89
0.517	10.07	3.18	-0.55	1.89
0.518	10.10	3.20	-0.55	1.89
0.519	10.14	3.21	-0.55	1.90
0.520	10.18	3.22	-0.55	1.90
0.521	10.22	3.23	-0.55	1.90
0.522	10.25	3.24	-0.55	1.91
0.523	10.29	3.25	-0.54	1.91
0.524	10.33	3.26	-0.54	1.91

0.525	10.37	3.28	-0.54	1.92
0.526	10.40	3.29	-0.54	1.92
0.527	10.44	3.30	-0.54	1.92
0.528	10.48	3.31	-0.53	1.92
0.529	10.51	3.32	-0.53	1.93
0.530	10.55	3.33	-0.53	1.93
0.531	10.59	3.34	-0.53	1.93
0.532	10.62	3.35	-0.53	1.94
0.533	10.66	3.36	-0.53	1.94
0.534	10.70	3.37	-0.53	1.95
0.535	10.74	3.39	-0.53	1.95
0.536	10.77	3.40	-0.52	1.95
0.537	10.81	3.41	-0.52	1.96
0.538	10.85	3.42	-0.52	1.96
0.539	10.88	3.43	-0.52	1.97
0.540	10.92	3.44	-0.52	1.97
0.541	10.96	3.45	-0.52	1.97
0.542	10.99	3.46	-0.52	1.98
0.543	11.03	3.47	-0.51	1.98
0.544	11.07	3.48	-0.51	1.98
0.545	11.11	3.50	-0.51	1.99
0.546	11.14	3.51	-0.51	1.99
0.547	11.18	3.52	-0.51	1.99
0.548	11.22	3.53	-0.50	1.99
0.549	11.25	3.54	-0.50	2.00
0.550	11.29	3.55	-0.50	2.00
0.551	11.34	3.56	-0.50	2.00
0.552	11.40	3.58	-0.50	2.01
0.553	11.45	3.59	-0.49	2.01

0.554	11.51	3.61	-0.49	2.01
0.555	11.56	3.62	-0.49	2.02
0.556	11.61	3.63	-0.49	2.02
0.557	11.67	3.65	-0.49	2.02
0.558	11.72	3.66	-0.48	2.02
0.559	11.78	3.68	-0.48	2.03
0.560	11.83	3.69	-0.48	2.03
0.561	11.88	3.70	-0.48	2.03
0.562	11.94	3.72	-0.48	2.04
0.563	11.99	3.73	-0.48	2.04
0.564	12.05	3.74	-0.48	2.04
0.565	12.10	3.76	-0.48	2.05
0.566	12.15	3.77	-0.47	2.05
0.567	12.21	3.78	-0.47	2.05
0.568	12.26	3.79	-0.47	2.05
0.569	12.32	3.81	-0.47	2.06
0.570	12.37	3.82	-0.47	2.06
0.571	12.43	3.83	-0.47	2.06
0.572	12.48	3.85	-0.47	2.07
0.573	12.54	3.86	-0.46	2.07
0.574	12.59	3.88	-0.46	2.08
0.575	12.65	3.89	-0.46	2.08
0.576	12.70	3.90	-0.46	2.08
0.577	12.76	3.92	-0.46	2.09
0.578	12.81	3.93	-0.45	2.09
0.579	12.87	3.95	-0.45	2.10
0.580	12.92	3.96	-0.45	2.10
0.581	12.97	3.97	-0.45	2.10
0.582	13.03	3.99	-0.45	2.11

0.583	13.08	4.00	-0.45	2.11
0.584	13.14	4.01	-0.45	2.11
0.585	13.19	4.03	-0.45	2.12
0.586	13.24	4.04	-0.44	2.12
0.587	13.30	4.05	-0.44	2.12
0.588	13.35	4.06	-0.44	2.12
0.589	13.41	4.08	-0.44	2.13
0.590	13.46	4.09	-0.44	2.13
0.591	13.51	4.10	-0.44	2.13
0.592	13.57	4.12	-0.44	2.14
0.593	13.62	4.13	-0.43	2.14
0.594	13.68	4.15	-0.43	2.14
0.595	13.73	4.16	-0.43	2.15
0.596	13.78	4.17	-0.43	2.15
0.597	13.84	4.19	-0.43	2.15
0.598	13.89	4.20	-0.42	2.15
0.599	13.95	4.22	-0.42	2.16
0.600	14.00	4.23	-0.42	2.16

Table III.1. *The dimensionless mode-I and mode-II stress intensity factors for 0° and 90° loading angles for different values of a/W for the CMM specimen [78].*

APPENDIX IV

MODE-I STRESS CONTOUR PLOTS

The iso-stress contours presented in this appendix have all been obtained for the 3PB specimen - see Figs. IV.1(1-36). The notch tip is shown in every figure. The force, F, has been given the value 472 N throughout the analysis. All the dimensions and definitions have been given in chapter 7. The s/W and s/ρ ratios are provided for each iso-stress figure. The contours have been produced using the PAFEC Interactive Graphics Suite (PIGS) computer package. Half of the 3PB specimen has been modelled since both halves are symmetrical. The maximum stresses are all given in N/mm^2.

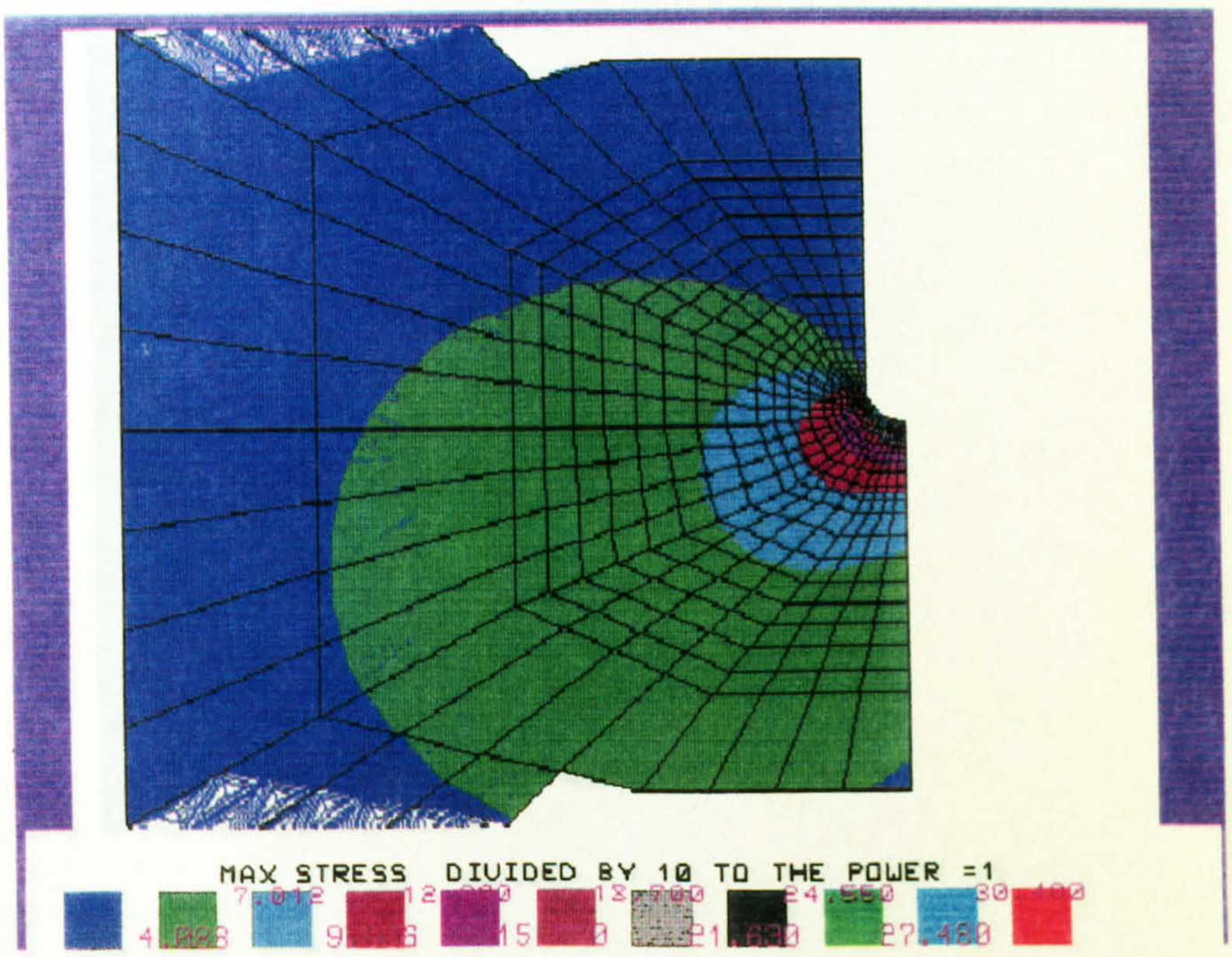

(1) $s/W = 7.35 \times 10^{-4}$ and $s/\rho = 1$.

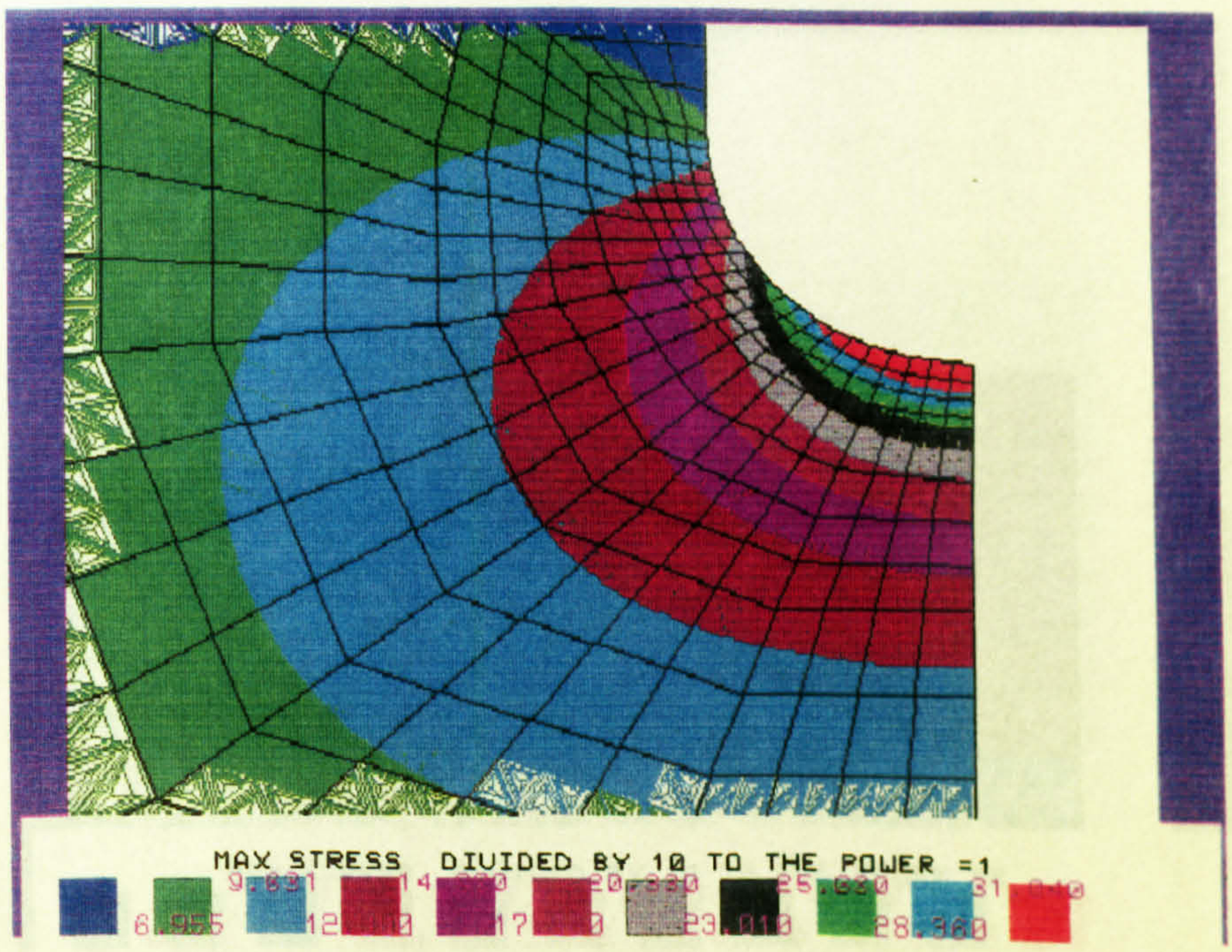

(2) $s/W = 7.35 \times 10^{-4}$ and $s/\rho = 1$.

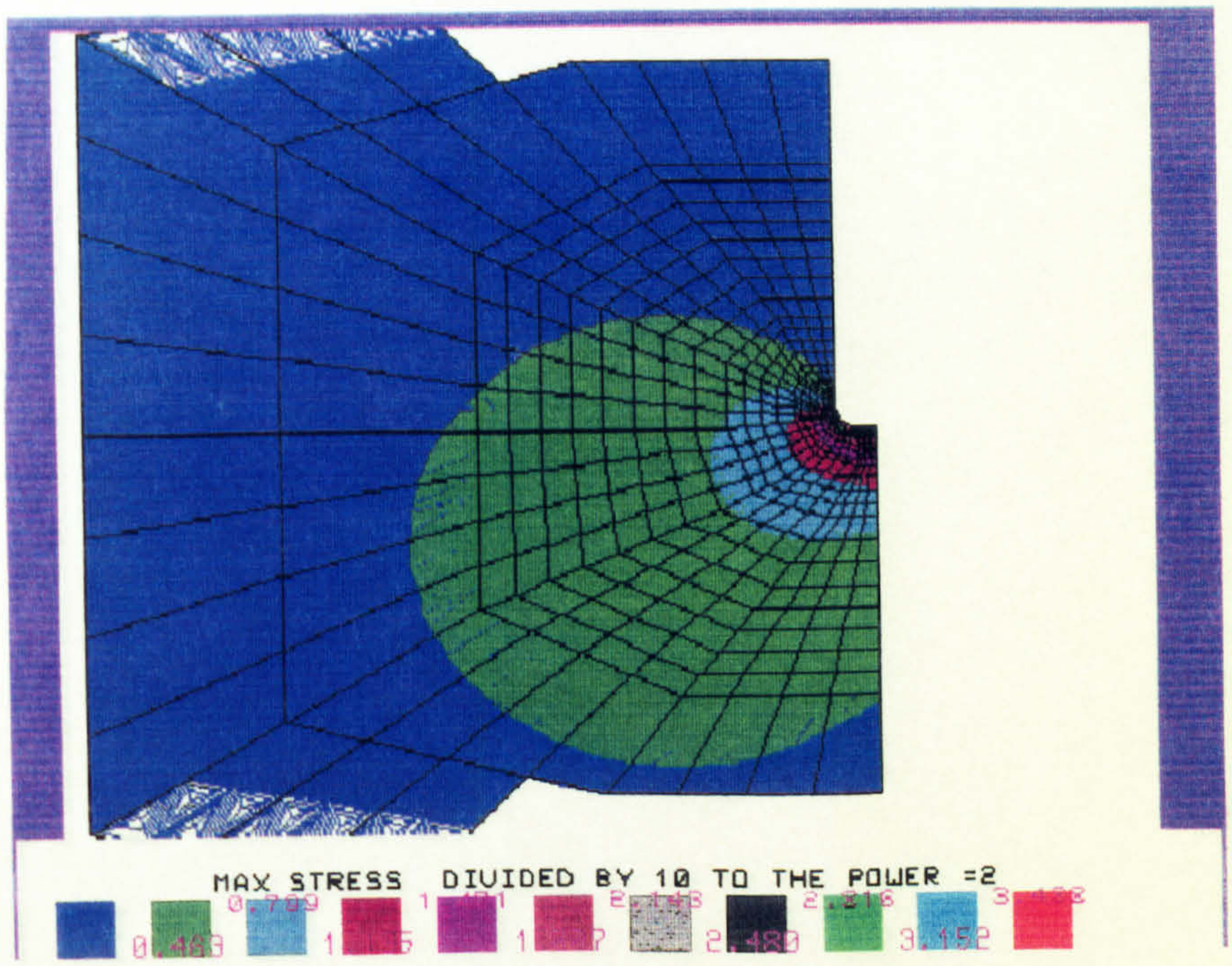

(3) $s/W = 7.35 \times 10^{-4}$ *and* $s/\rho = 2$.

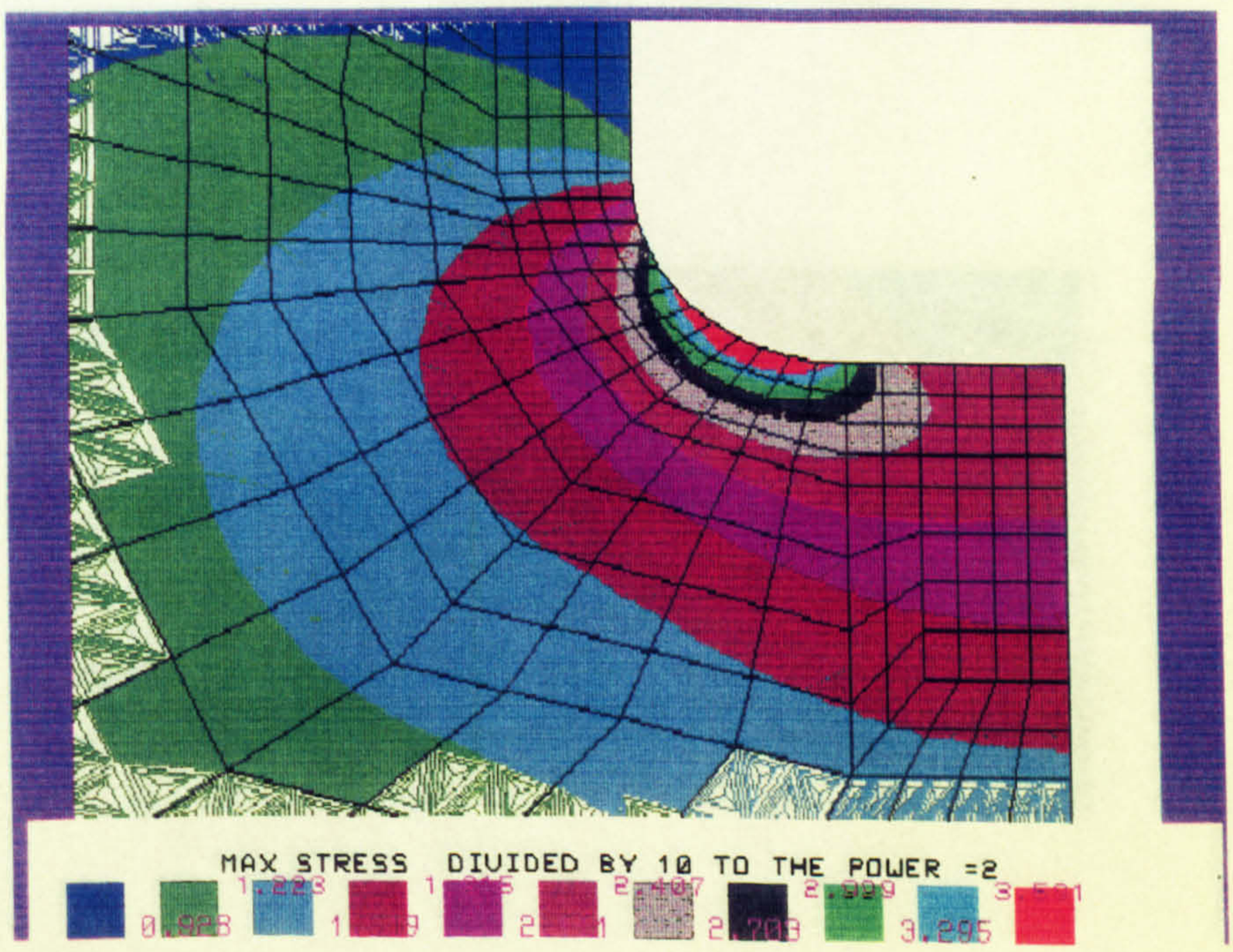

(4) $s/W = 7.35 \times 10^{-4}$ *and* $s/\rho = 2$.

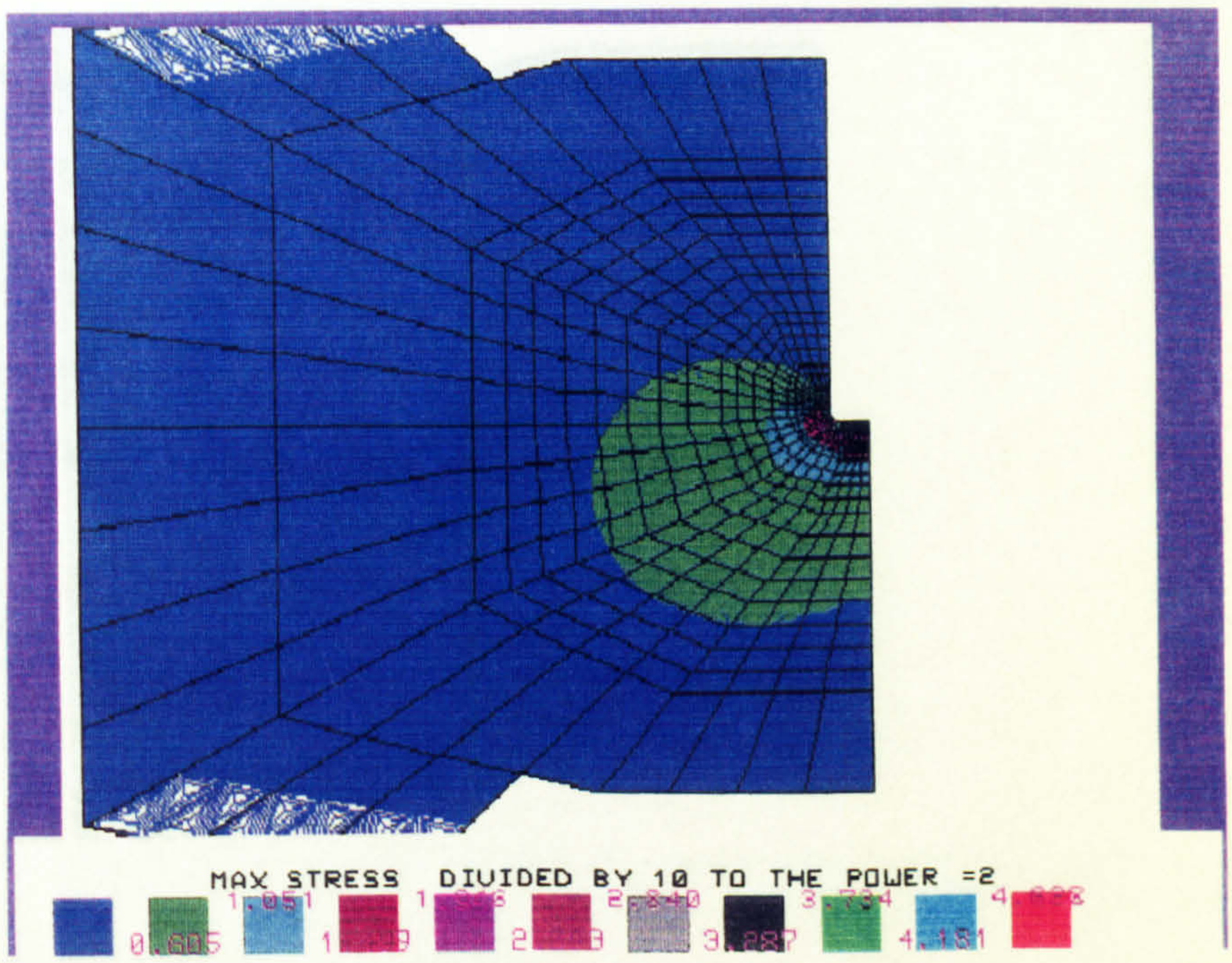

(5) $s/W = 7.35 \times 10^{-4}$ *and* $s/\rho = 4$.

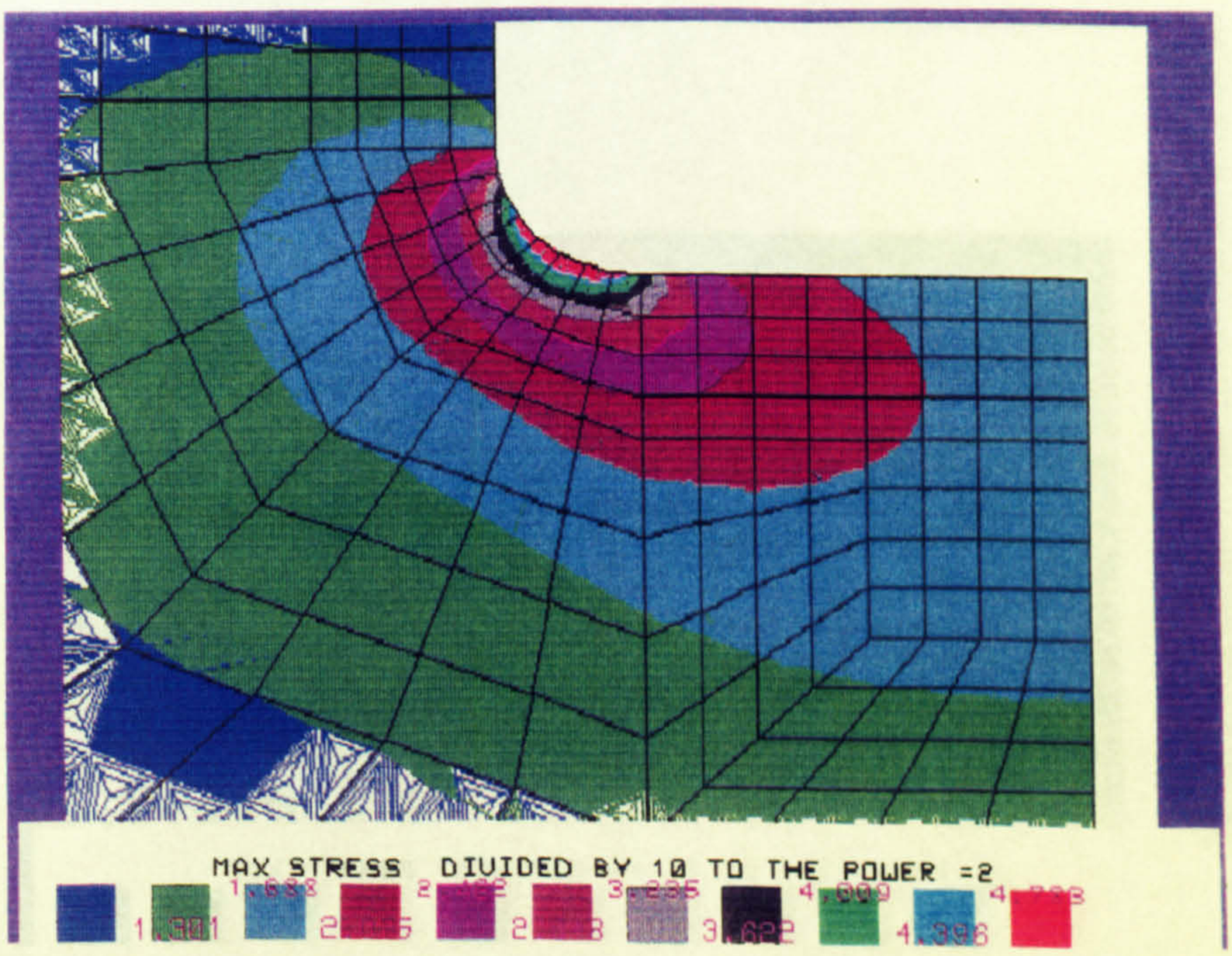

(6) $s/W = 7.35 \times 10^{-4}$ *and* $s/\rho = 4$.

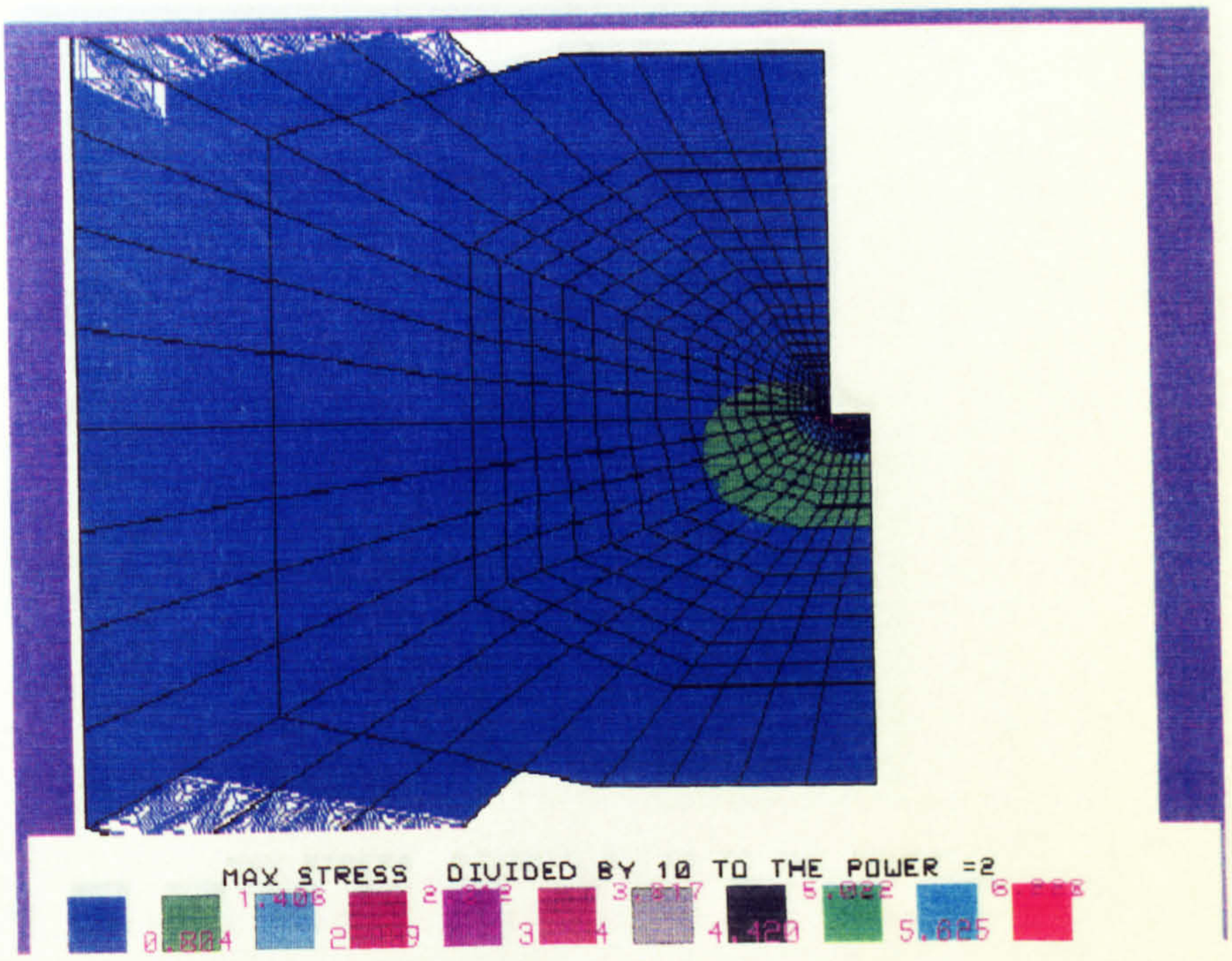

(7) $s/W = 7.35 \times 10^{-4}$ *and* $s/\rho = 8$.

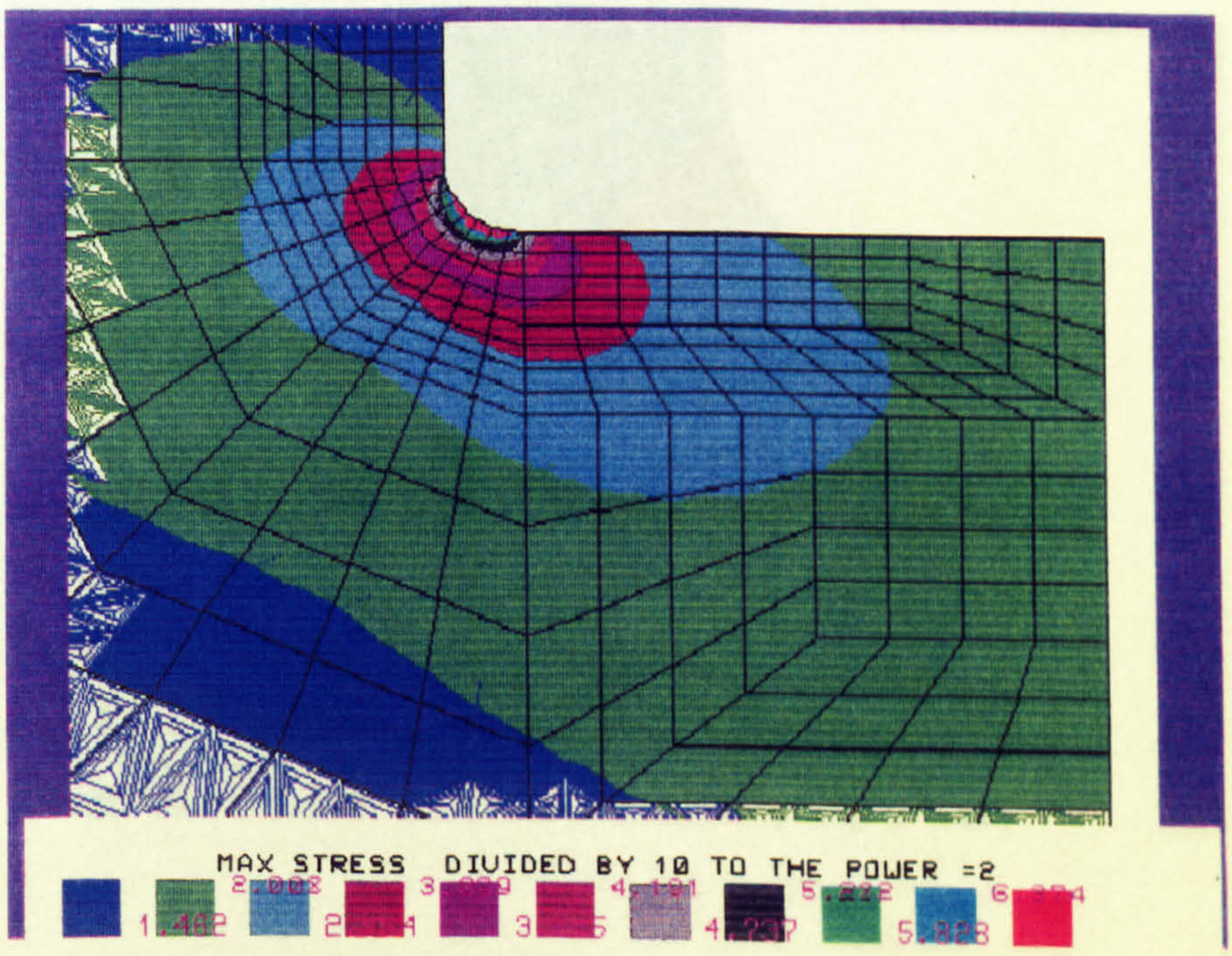

(8) $s/W = 7.35 \times 10^{-4}$ *and* $s/\rho = 8$.

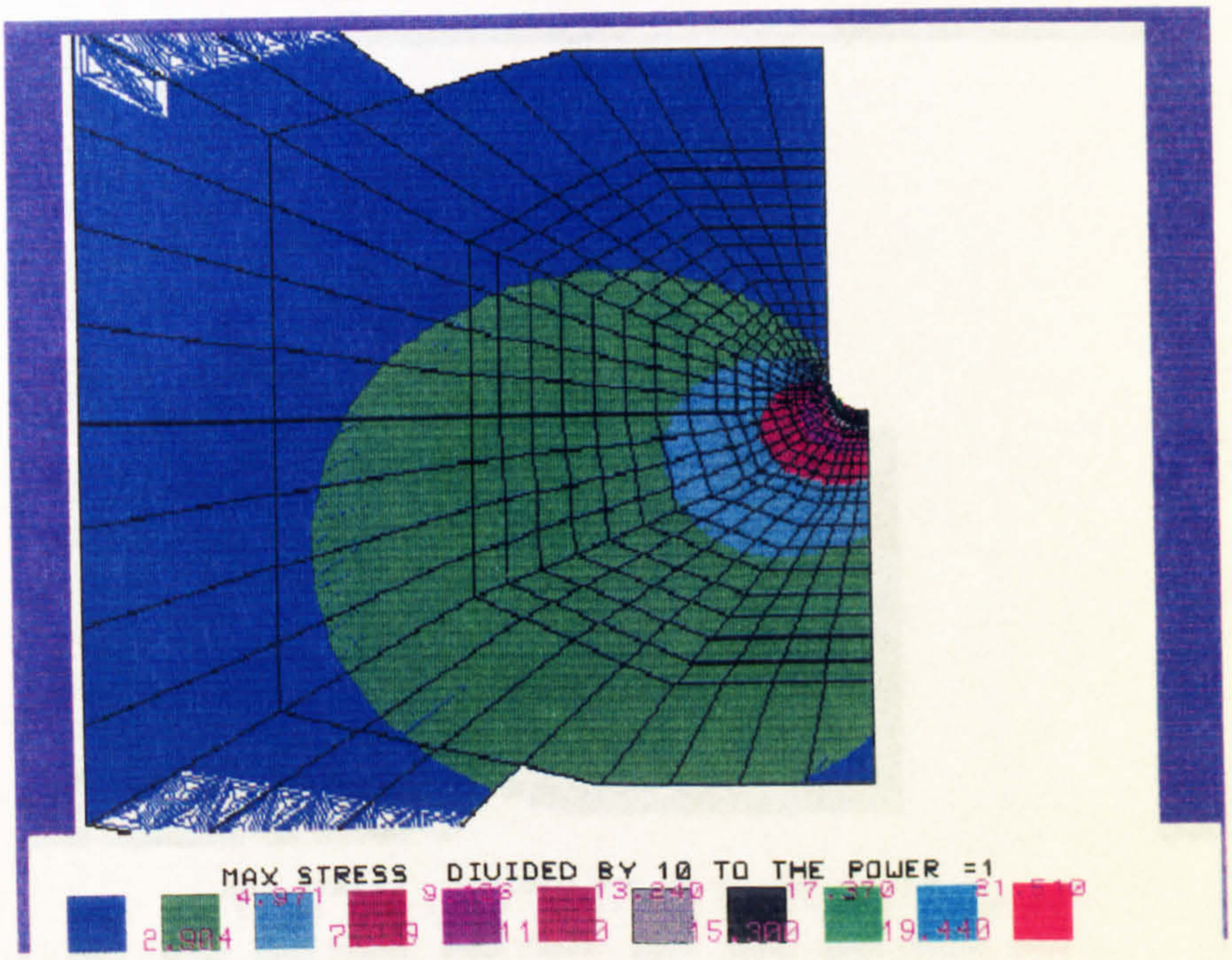

(9) $s/W = 1.47 \times 10^{-3}$ *and* $s/\rho = 1$.

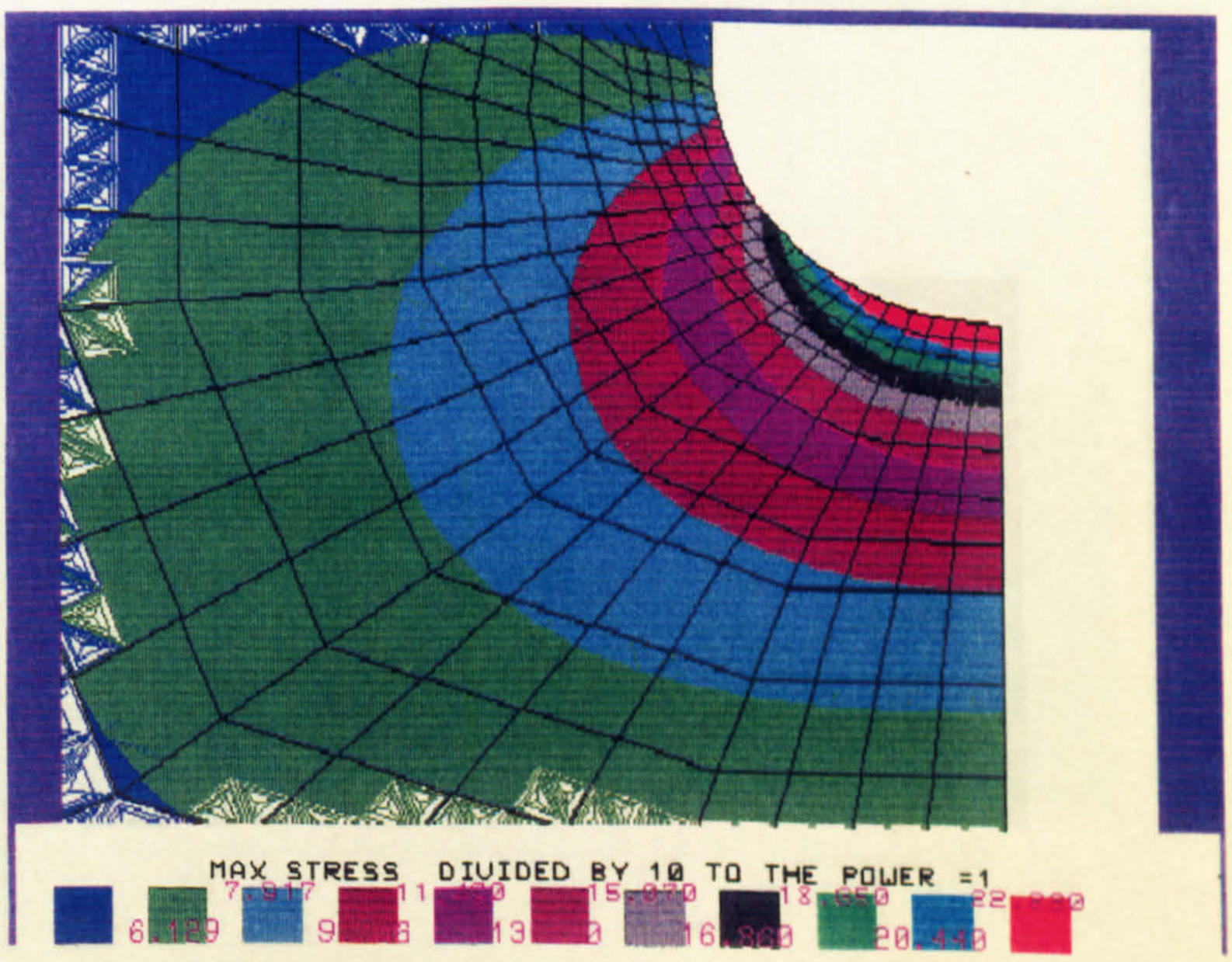

(10) $s/W = 1.47 \times 10^{-3}$ *and* $s/\rho = 1$.

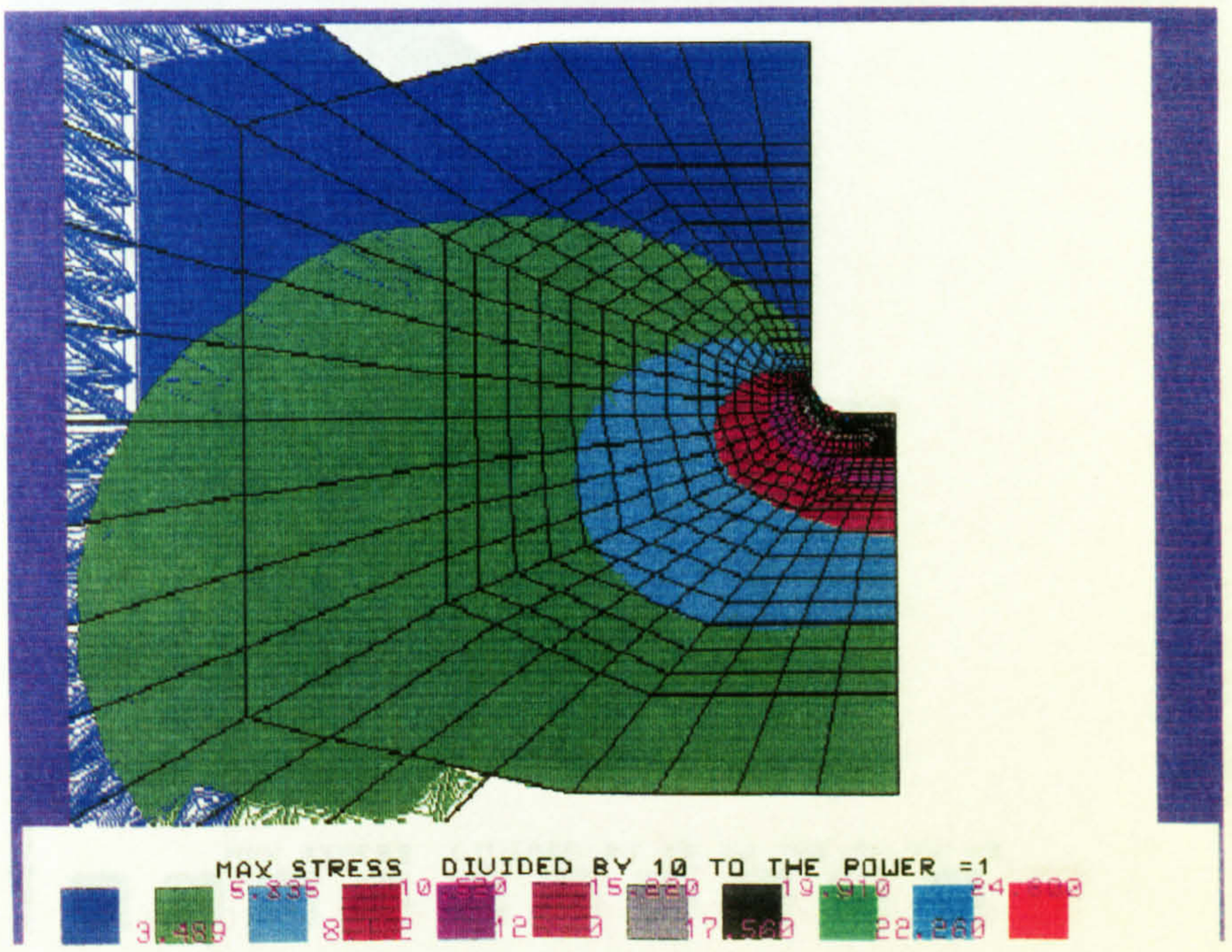

(11) $s/W = 1.47 \times 10^{-3}$ *and* $s/\rho = 2$.

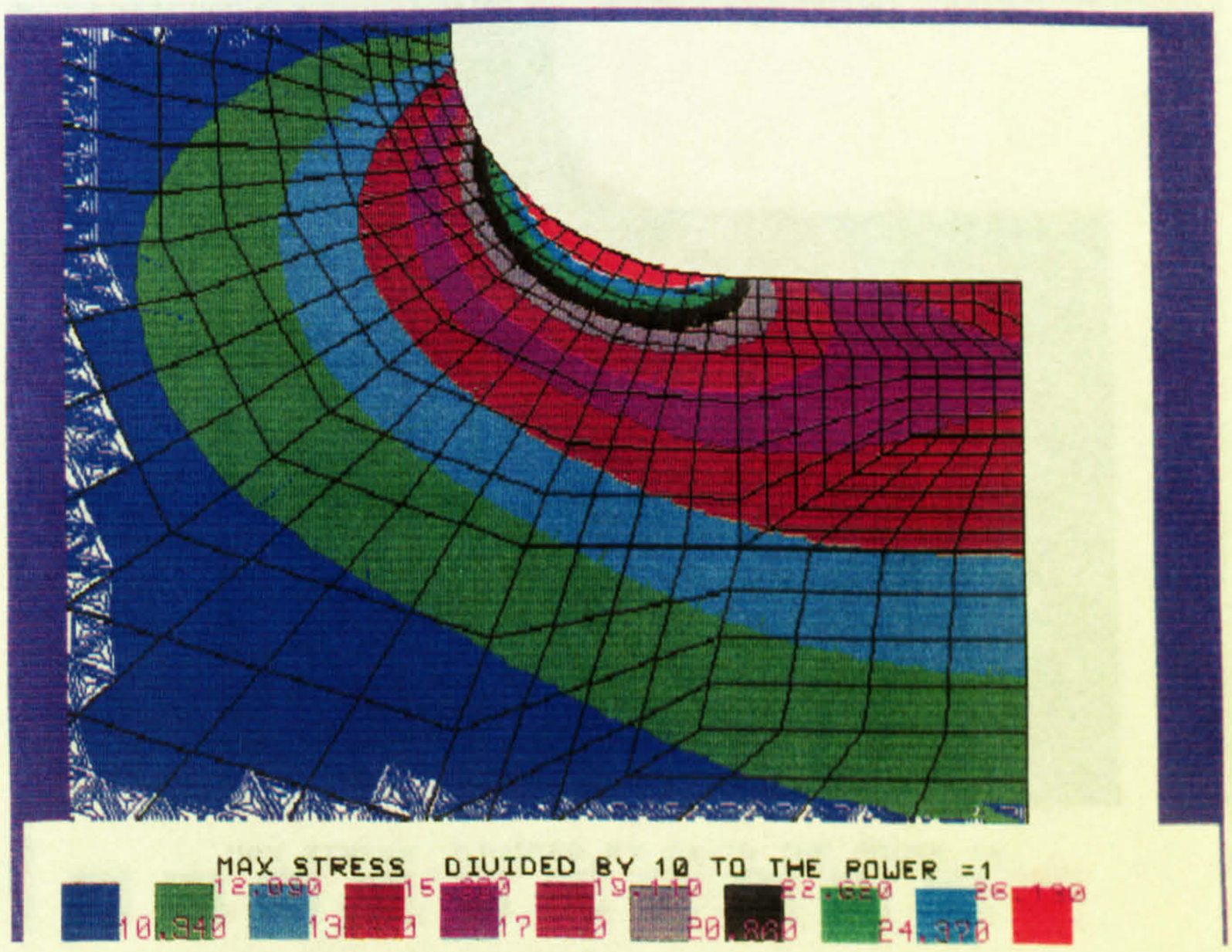

(12) $s/W = 1.47 \times 10^{-3}$ *and* $s/\rho = 2$.

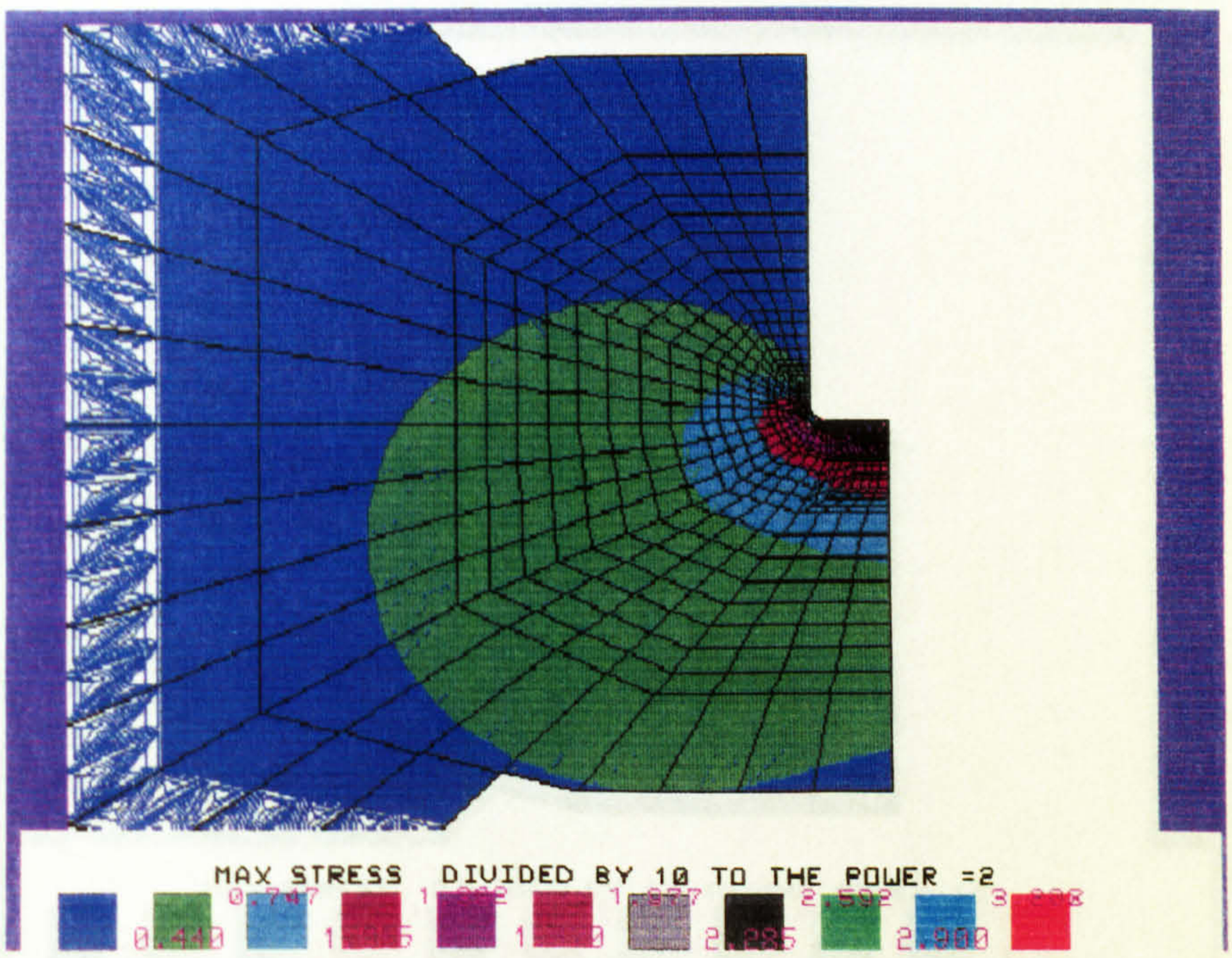

(13) $s/W = 1.47 \times 10^{-3}$ *and* $s/\rho = 4$.

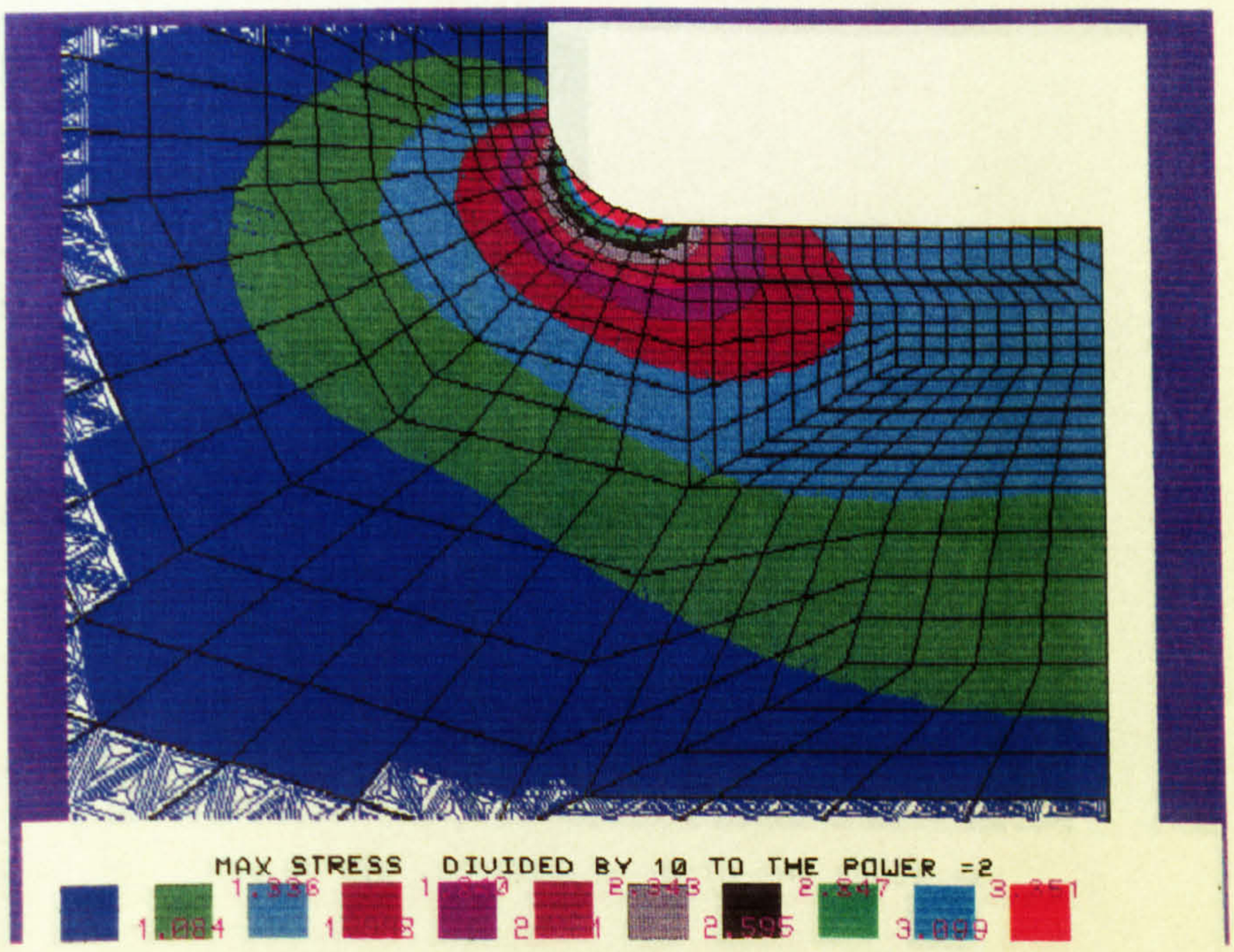

(14) $s/W = 1.47 \times 10^{-3}$ *and* $s/\rho = 4$.

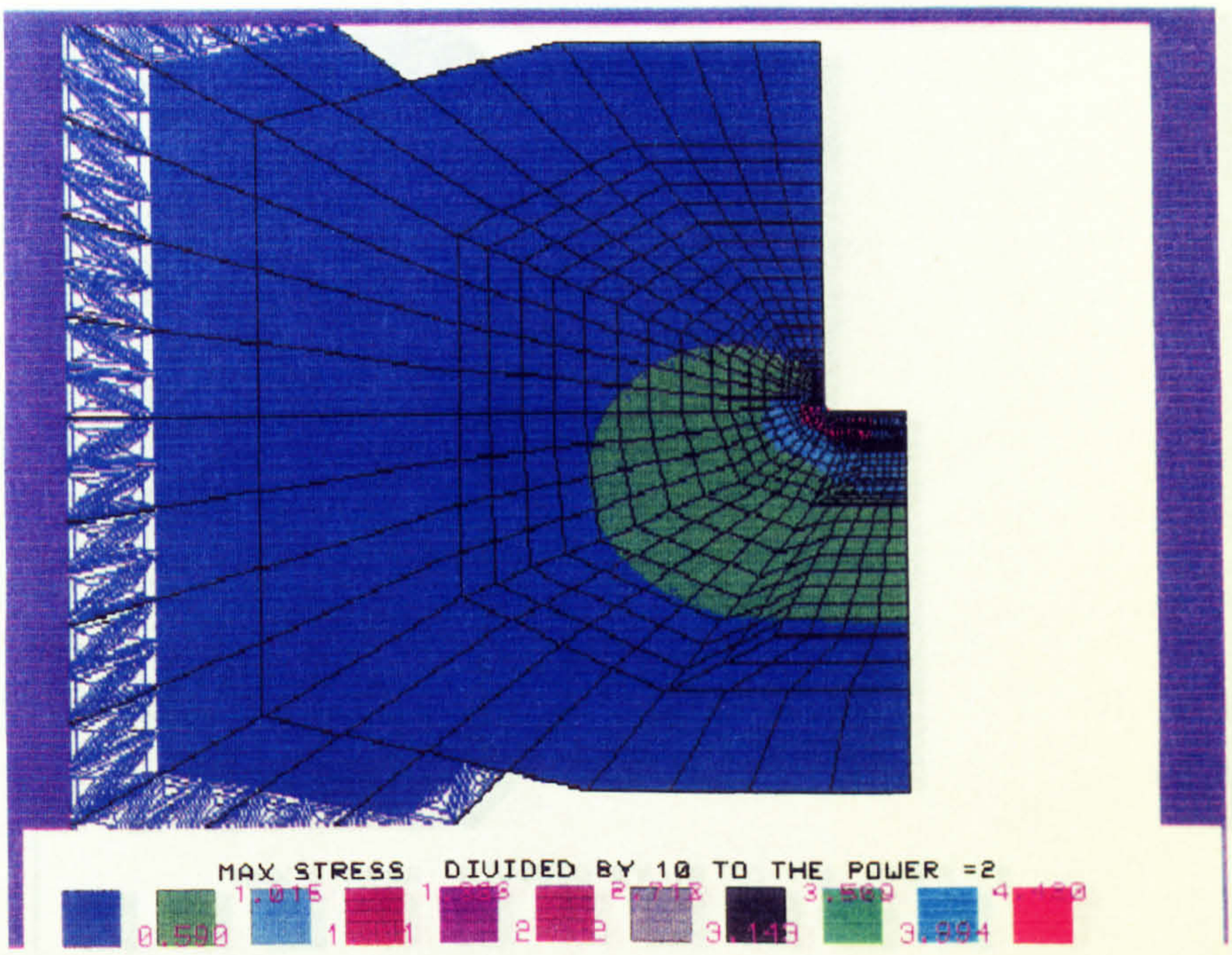

(15) $s/W = 1.47 \times 10^{-3}$ *and* $s/\rho = 8$.

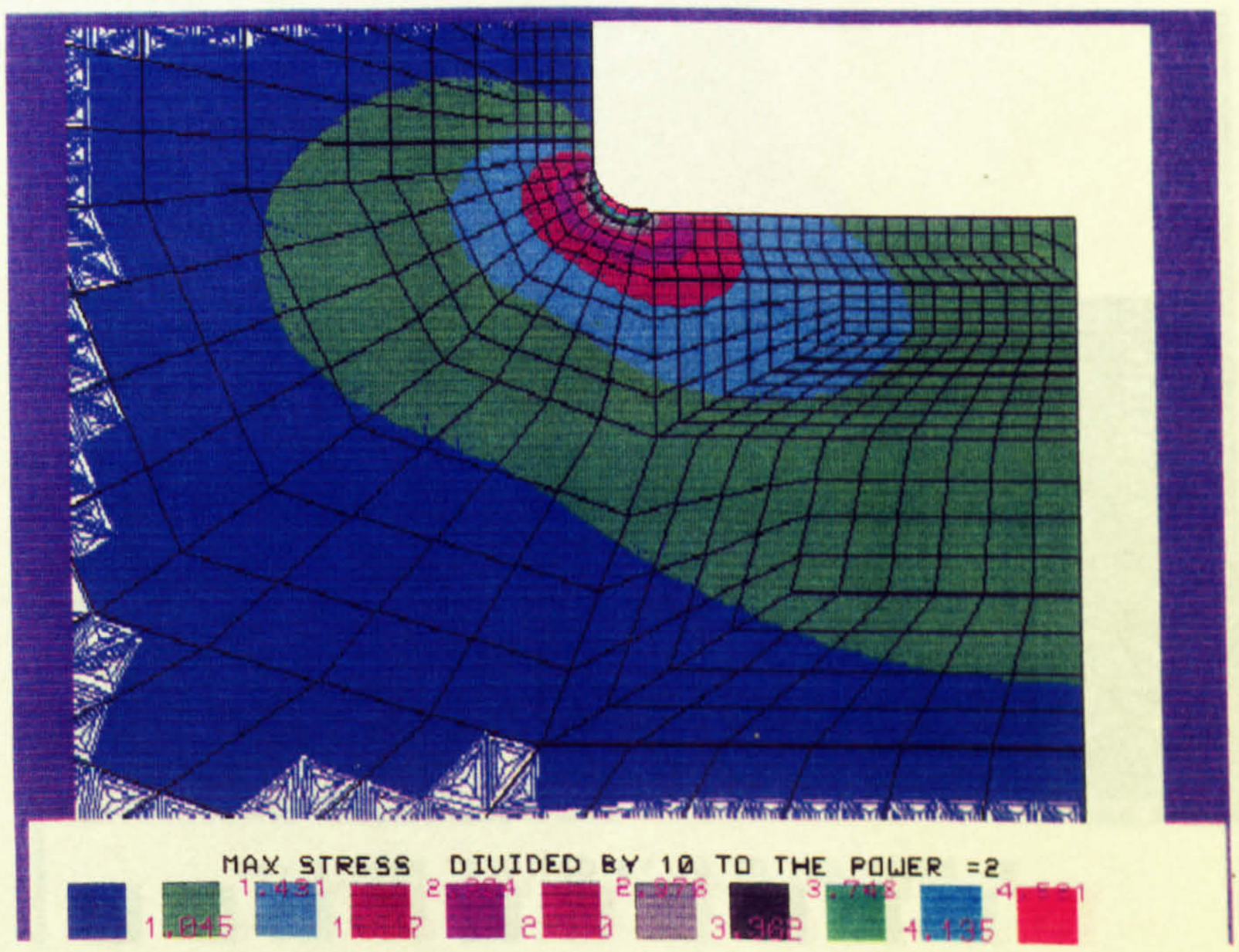

(16) $s/W = 1.47 \times 10^{-3}$ *and* $s/\rho = 8$.

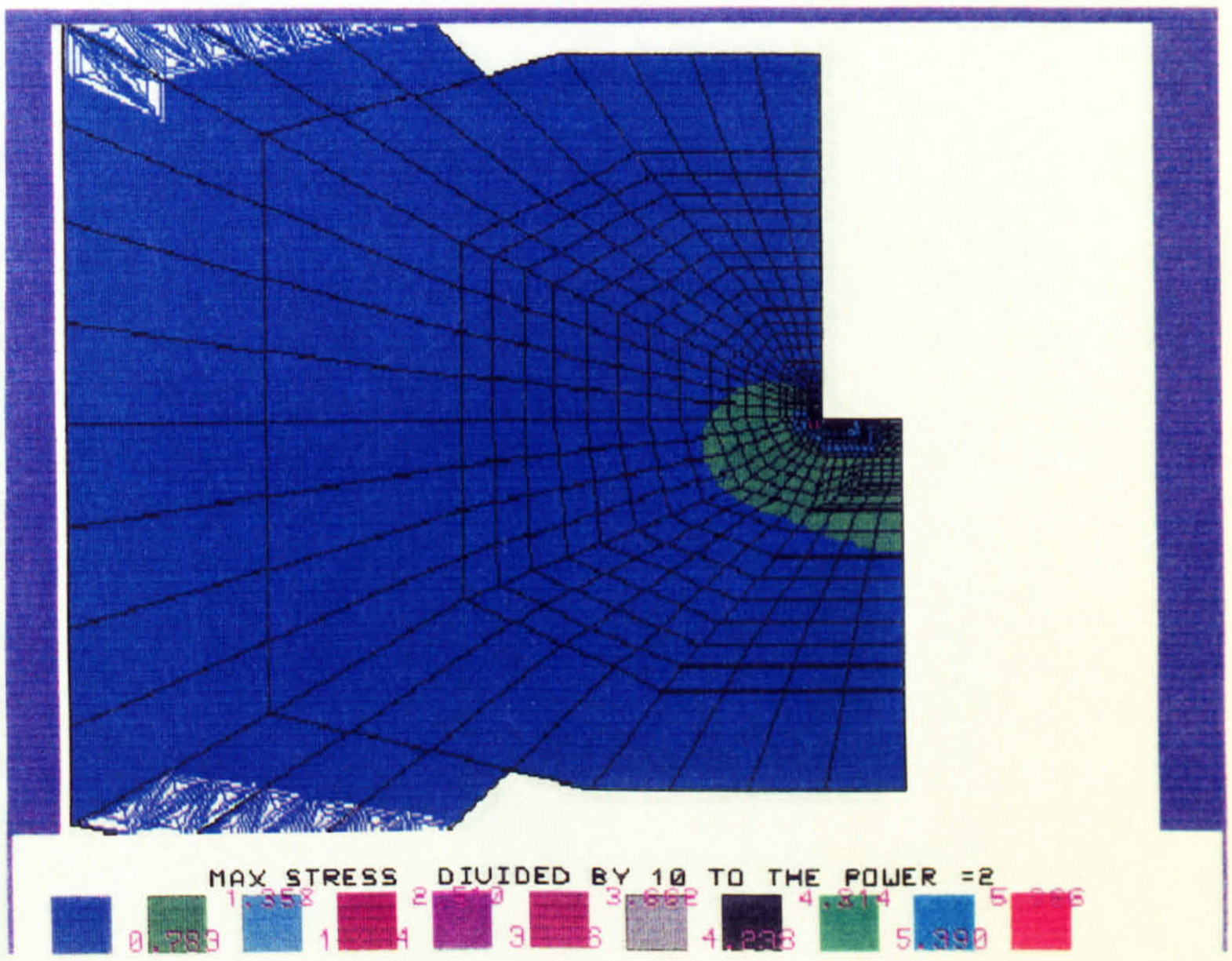

(17) $s/W = 1.47 \times 10^{-3}$ *and* $s/\rho = 16$.

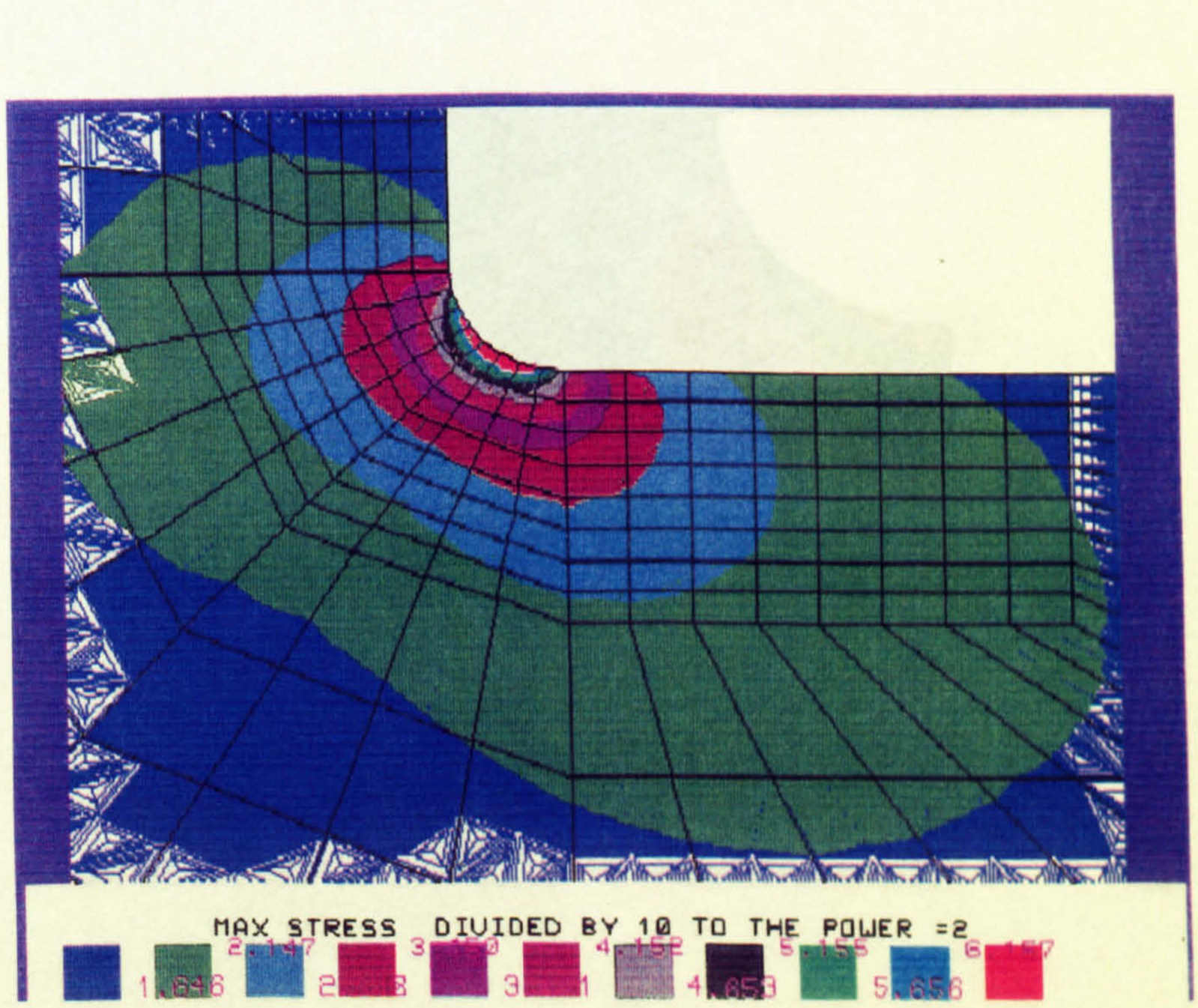

(18) $s/W = 1.47 \times 10^{-3}$ *and* $s/\rho = 16$.

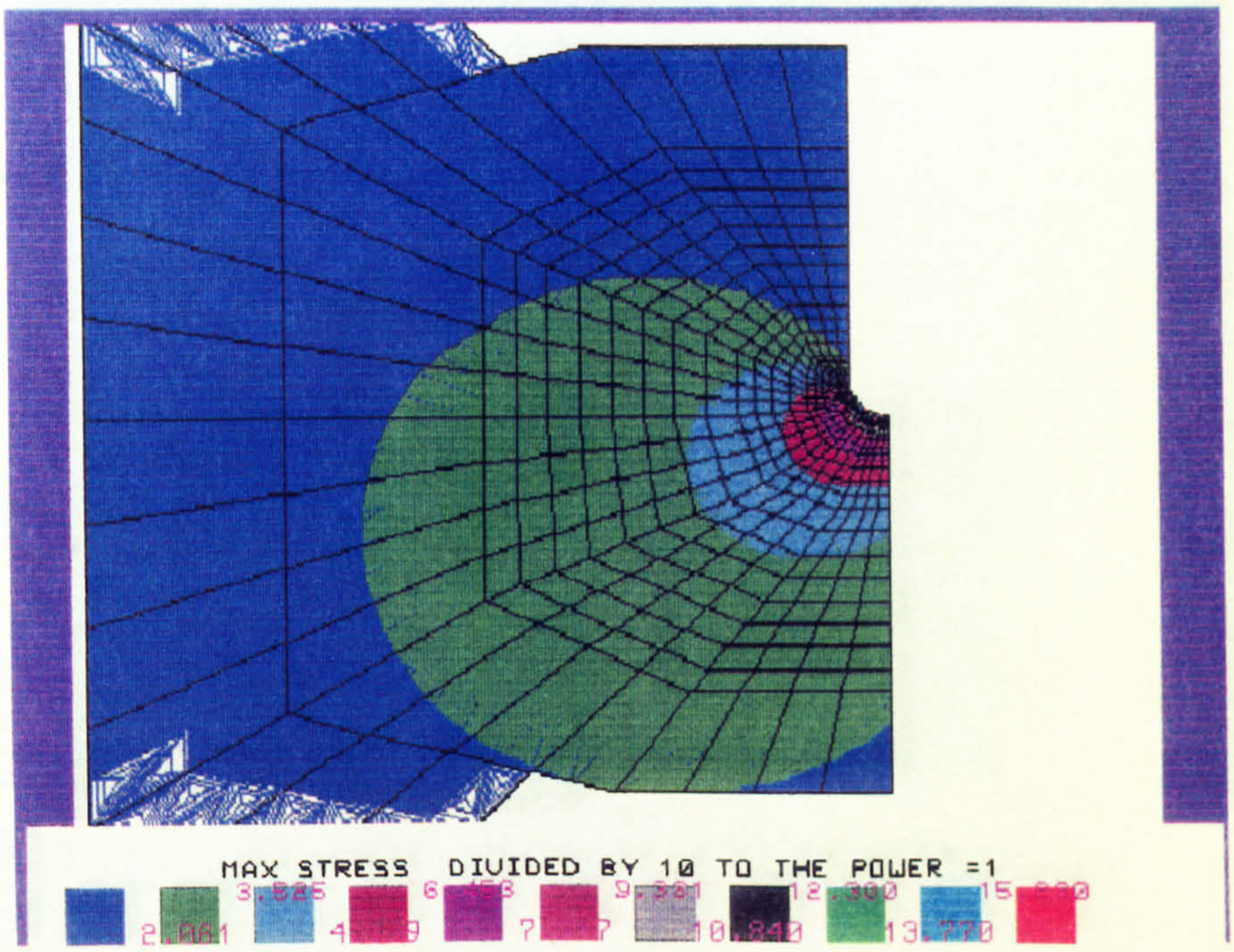

(19) $s/W = 2.94 \times 10^{-3}$ *and* $s/\rho = 1$.

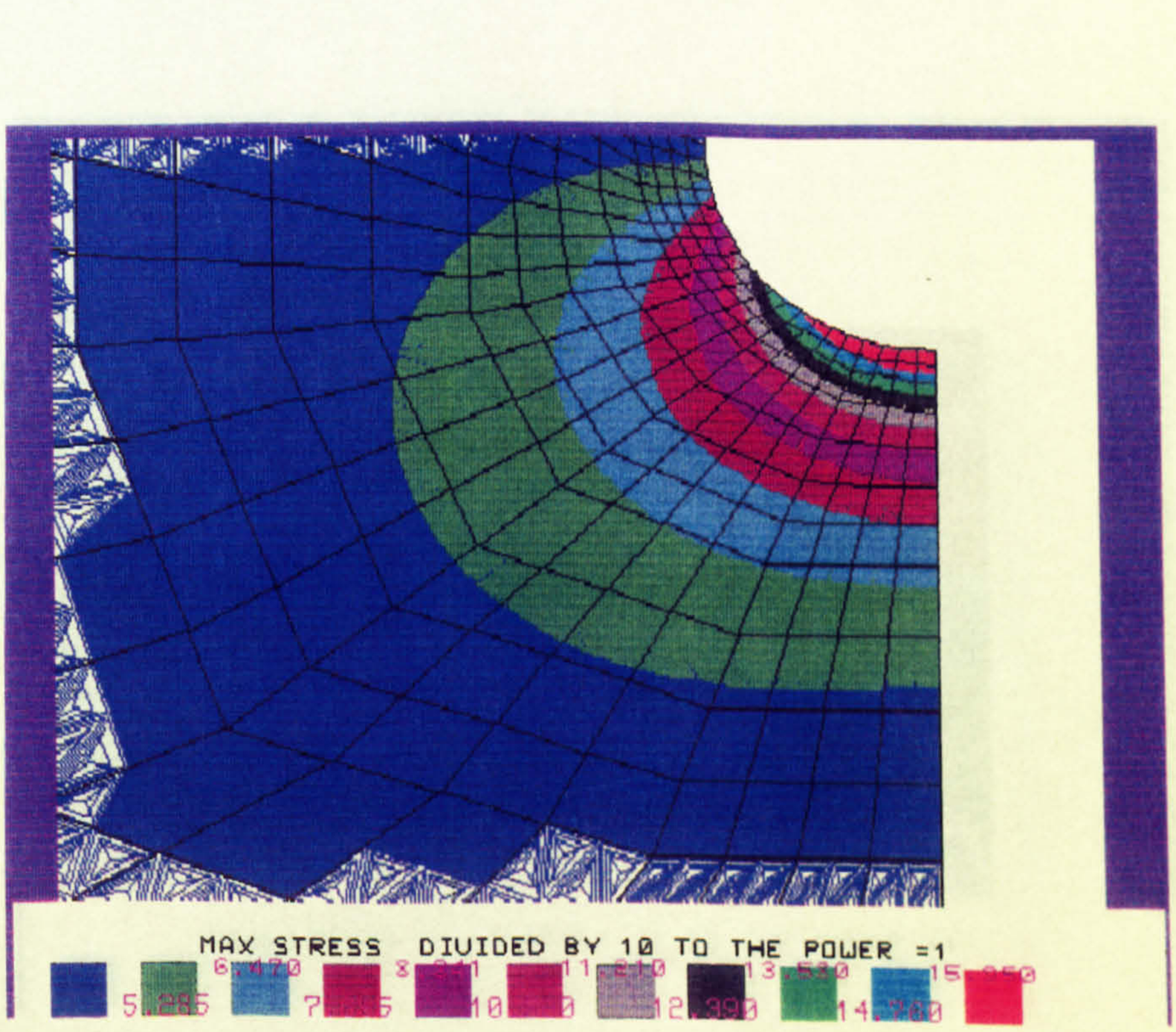

(20) $s/W = 2.94 \times 10^{-3}$ *and* $s/\rho = 1$.

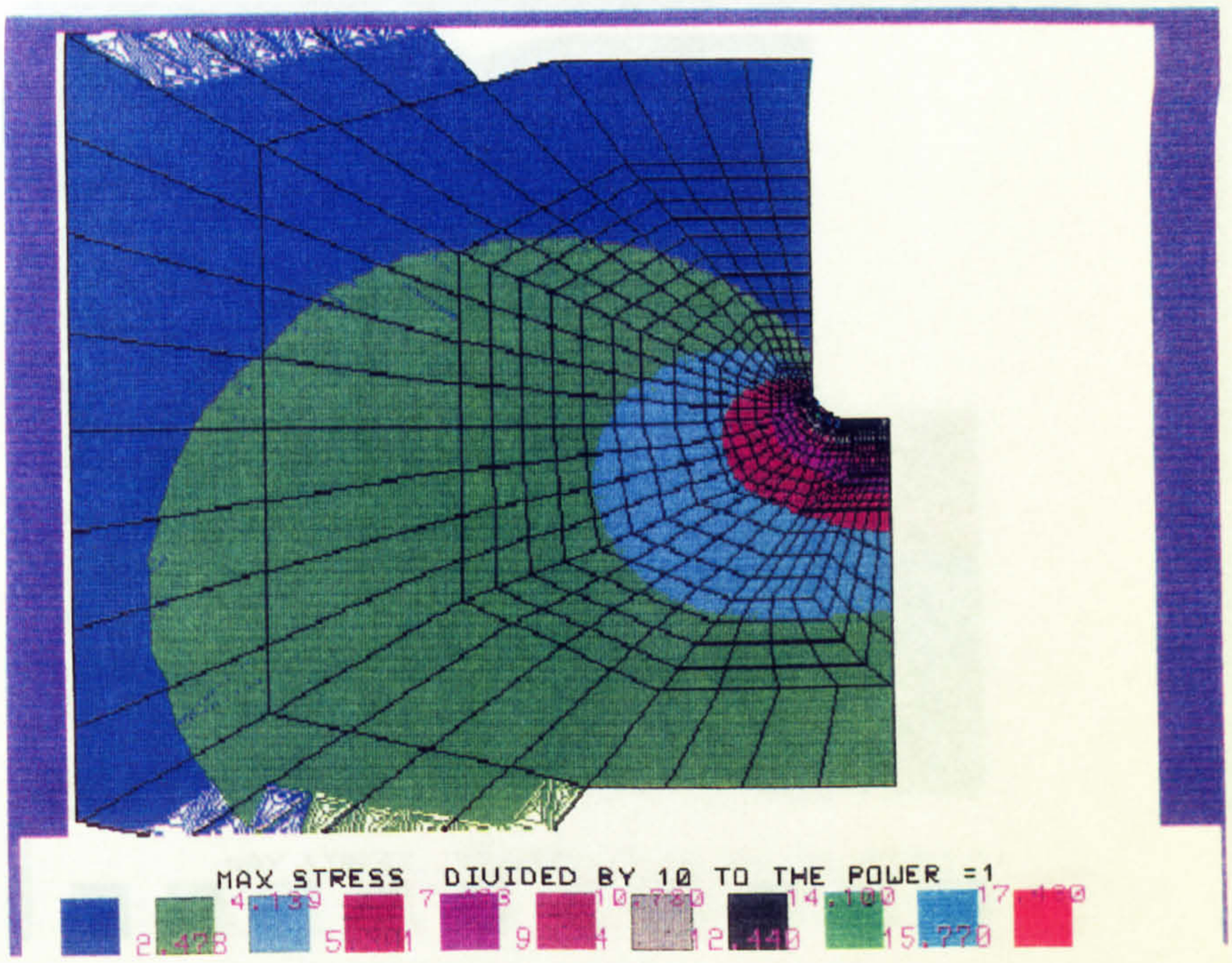

(21) $s/W = 2.94 \times 10^{-3}$ *and* $s/\rho = 2$.

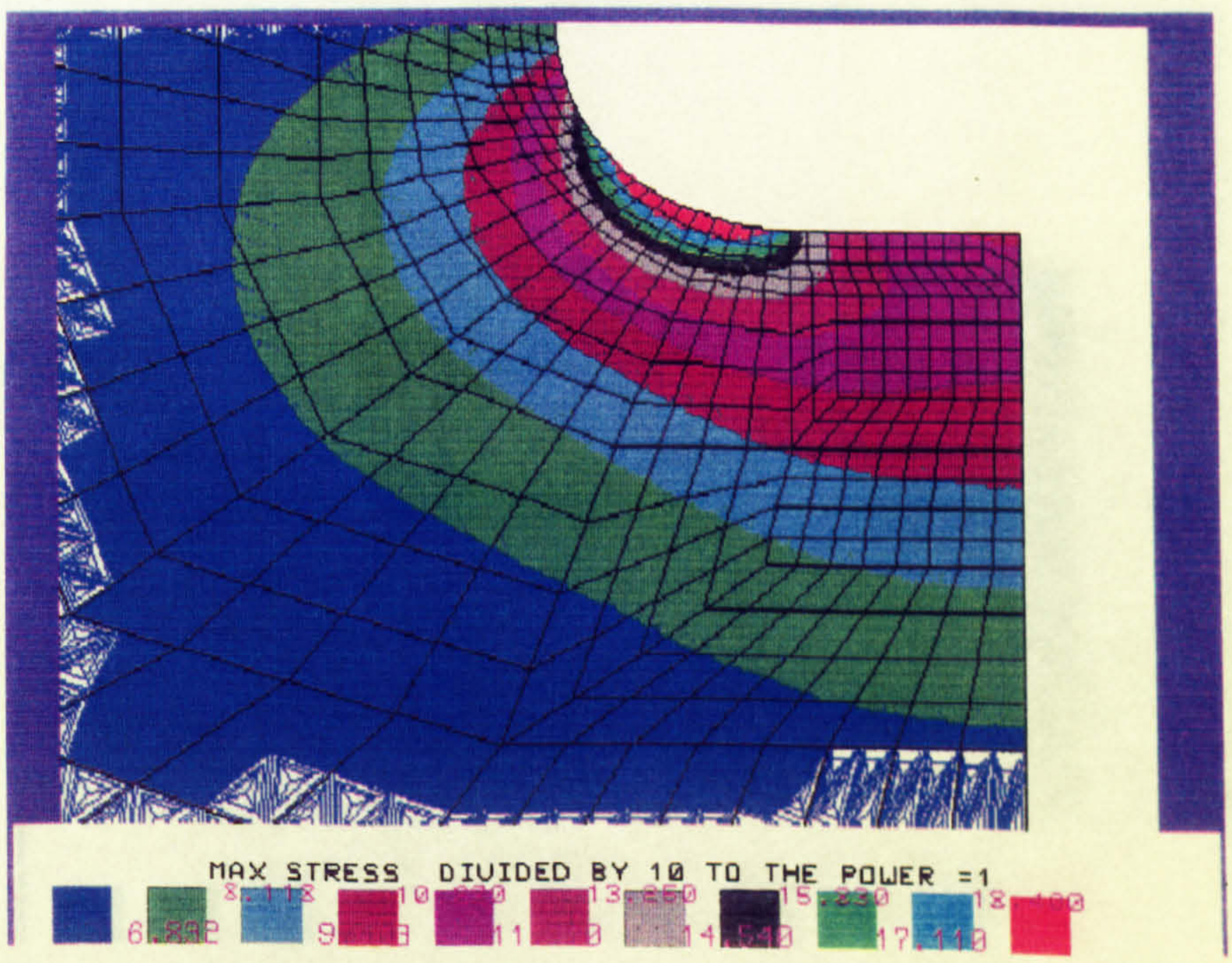

(22) $s/W = 2.94 \times 10^{-3}$ *and* $s/\rho = 2$.

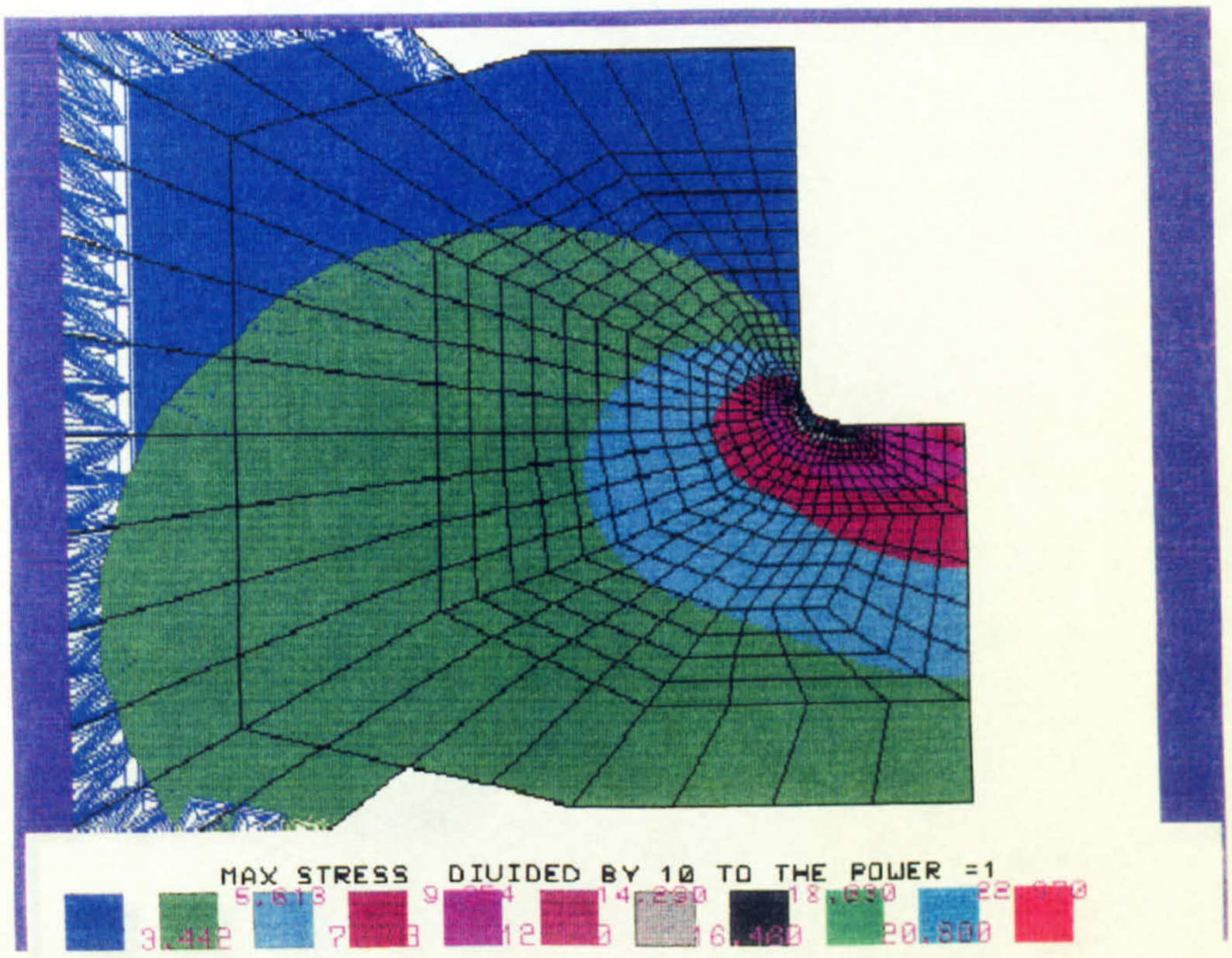

(23) $s/W = 2.94 \times 10^{-3}$ *and* $s/\rho = 4$.

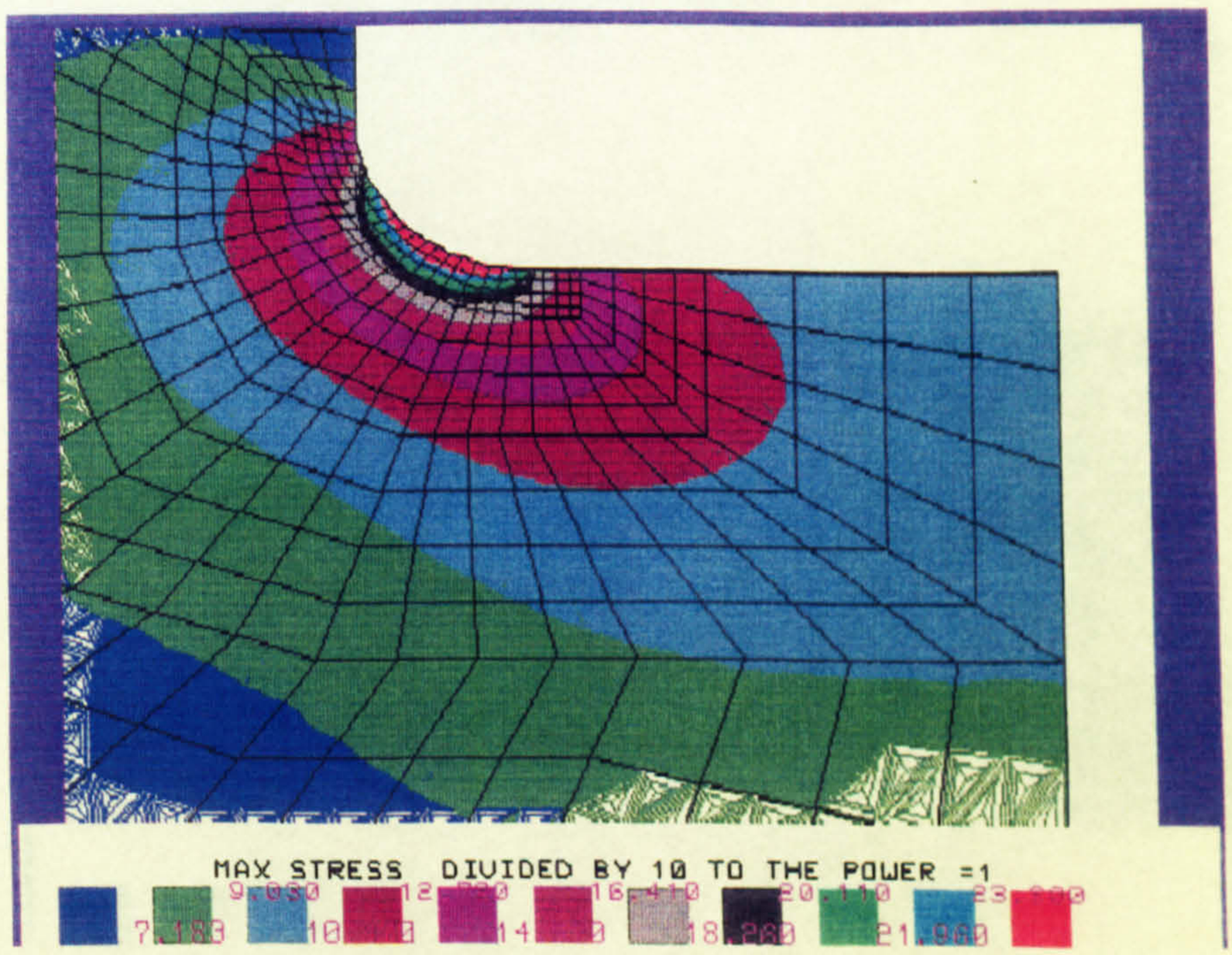

(24) $s/W = 2.94 \times 10^{-3}$ *and* $s/\rho = 4$.

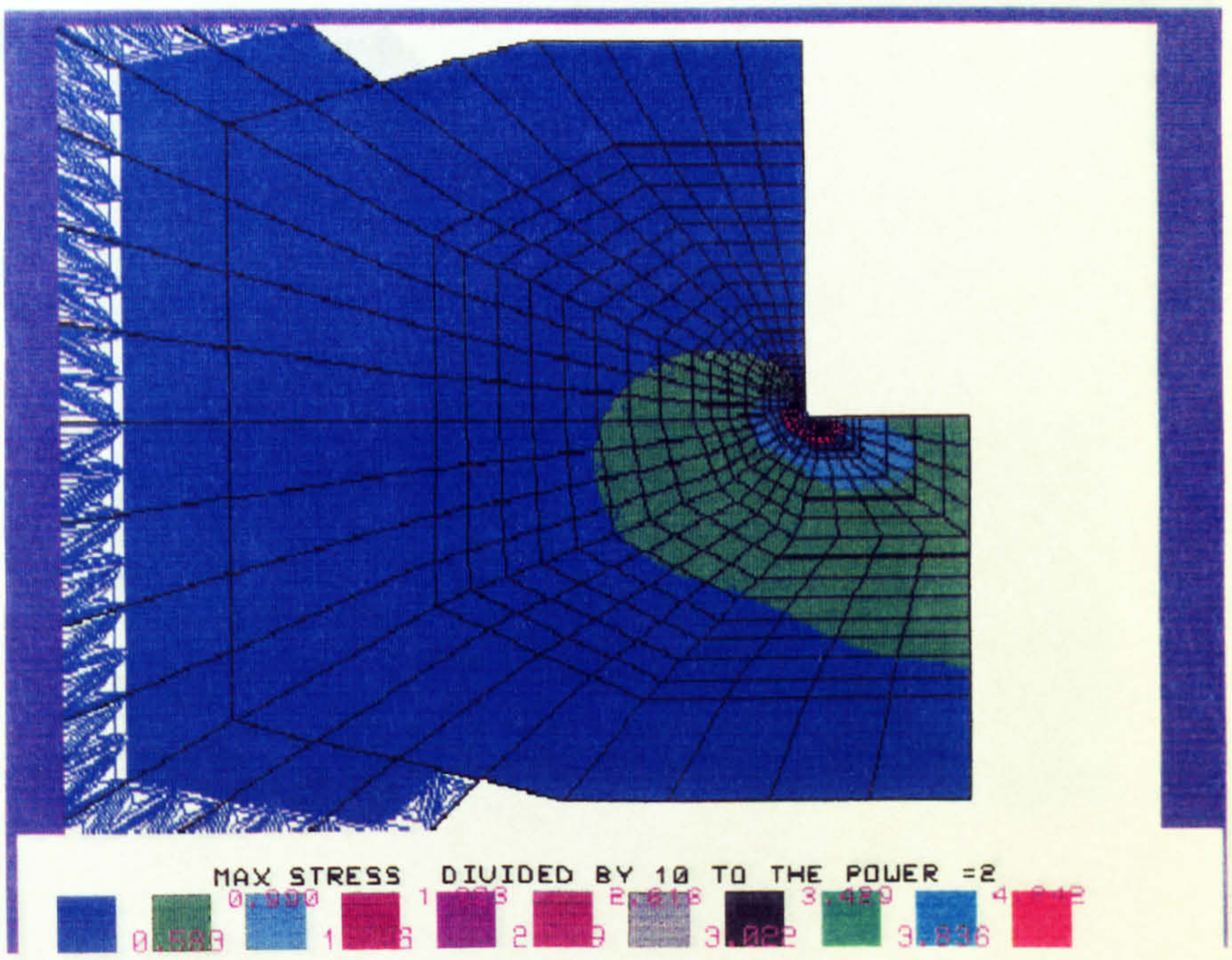

(27) $s/W = 2.94 \times 10^{-3}$ *and* $s/\rho = 16$.

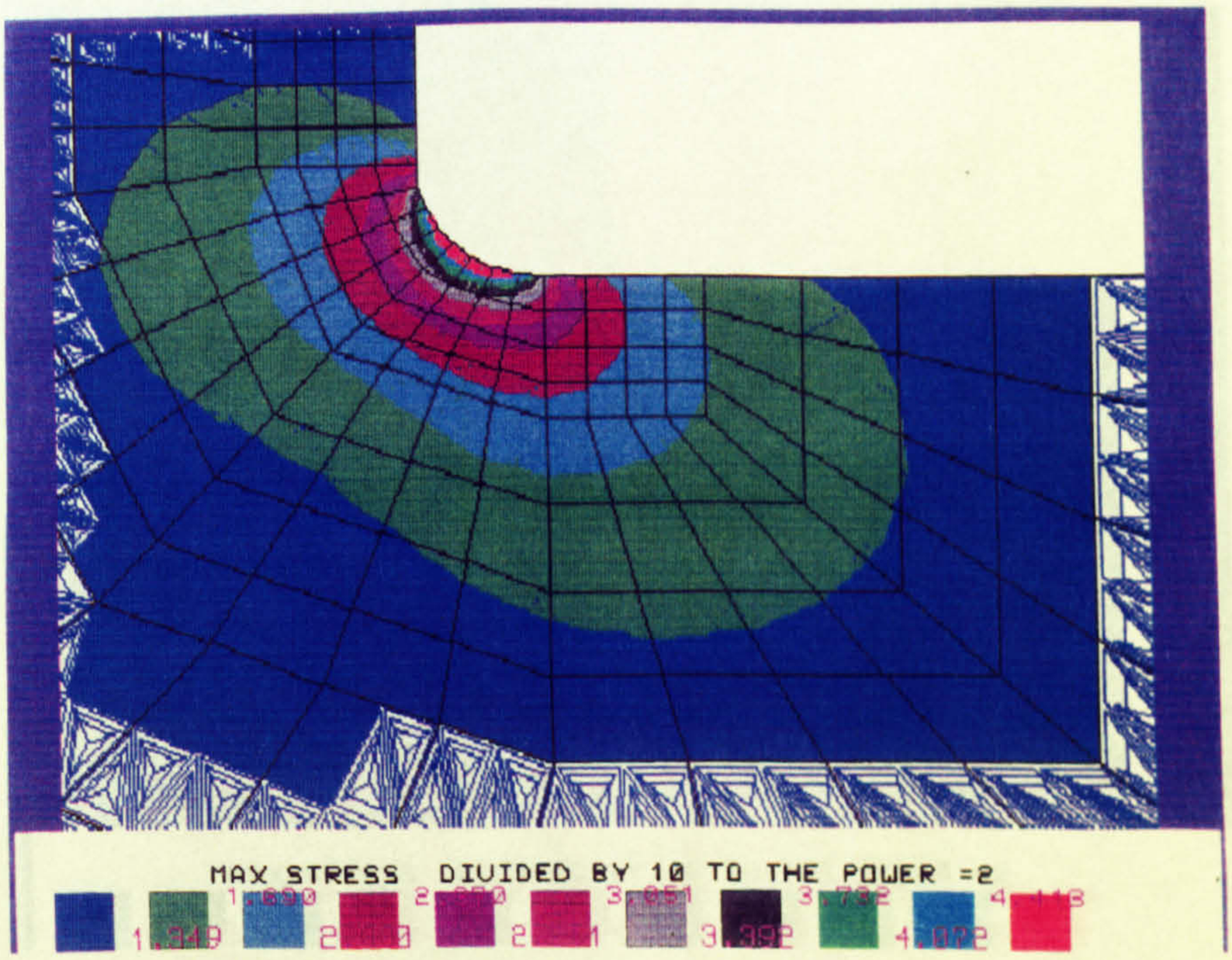

(28) $s/W = 2.94 \times 10^{-3}$ *and* $s/\rho = 16$.

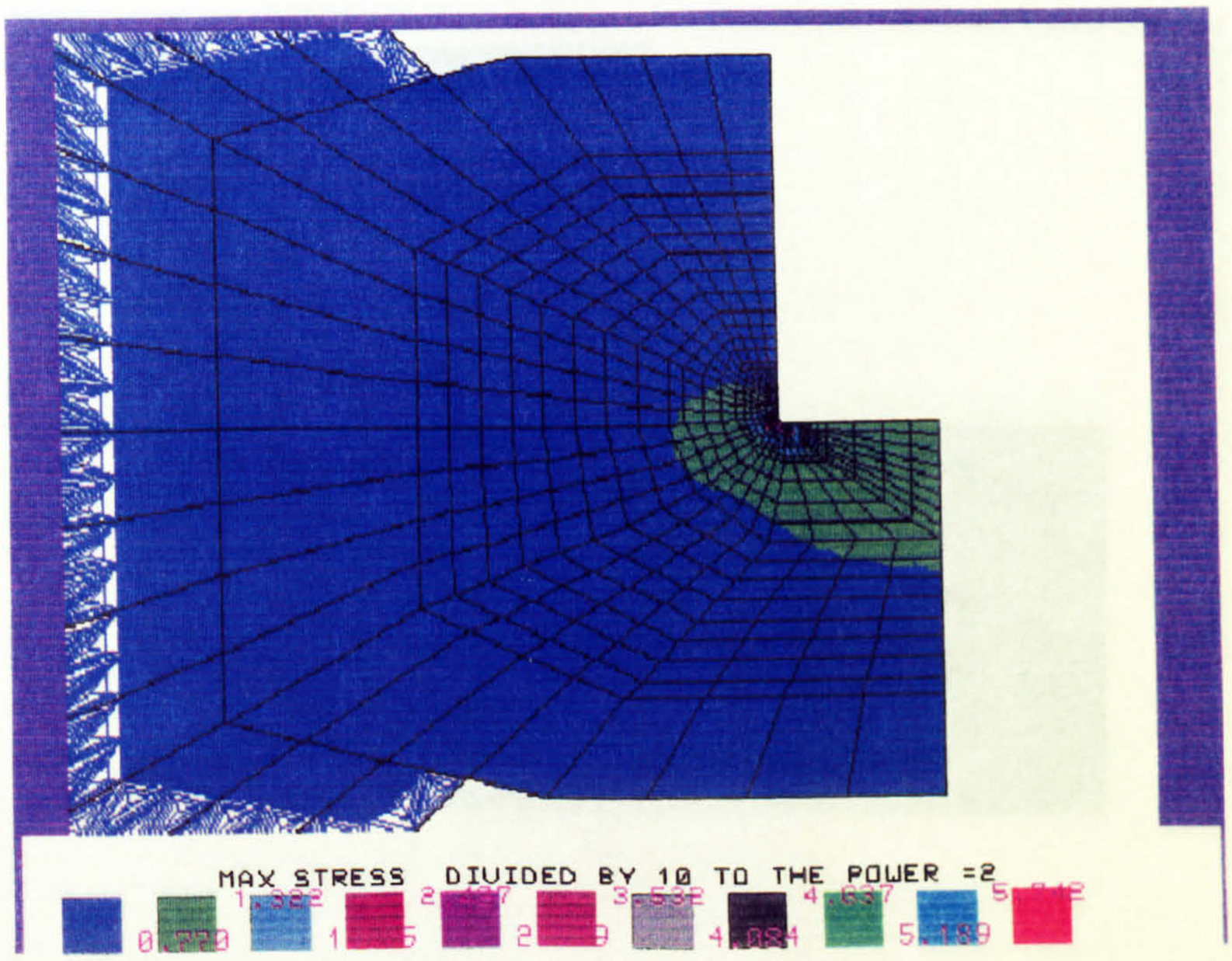

(29) $s/W = 2.94 \times 10^{-3}$ *and* $s/\rho = 32$.

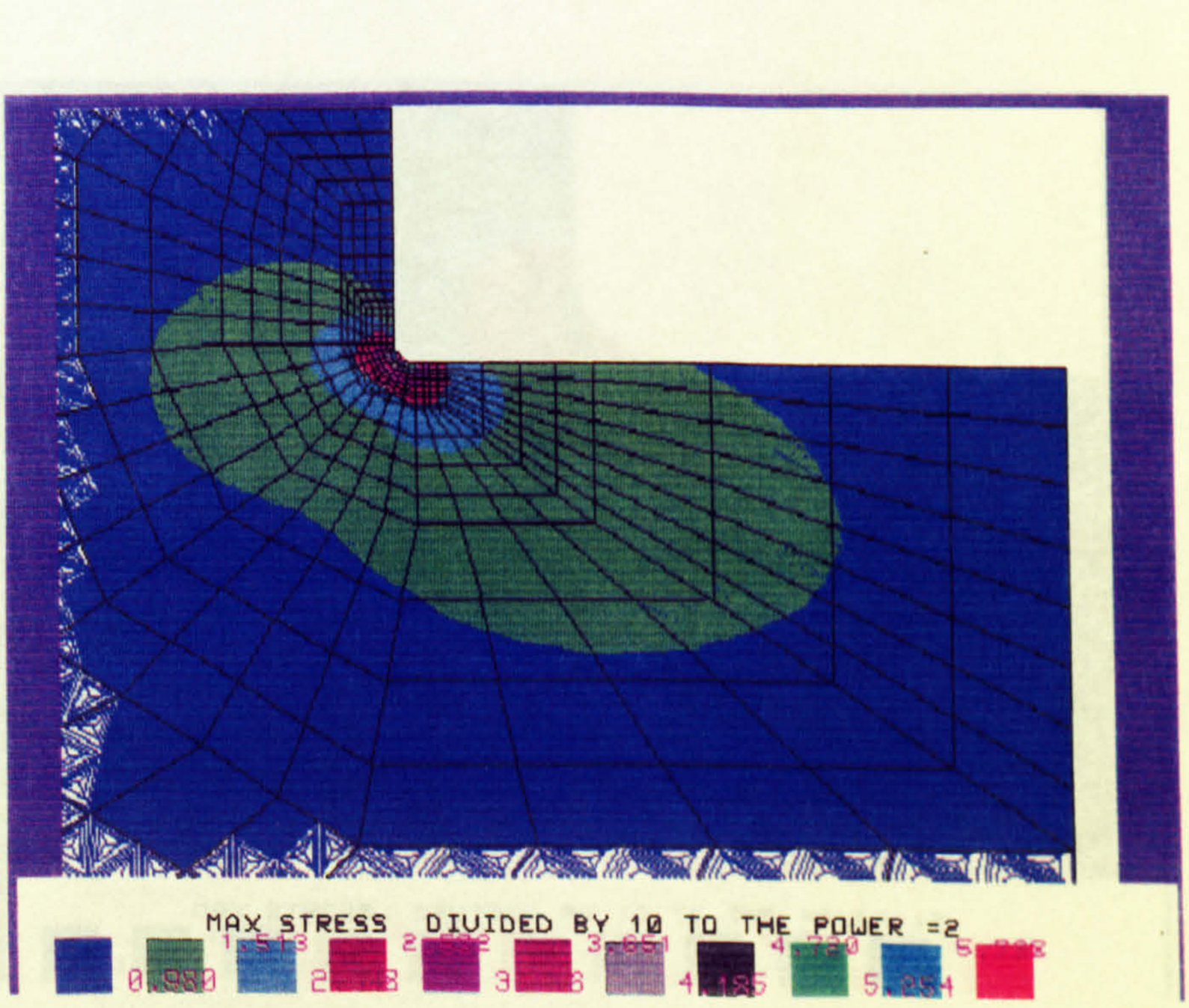

(30) $s/W = 2.94 \times 10^{-3}$ *and* $s/\rho = 32$.

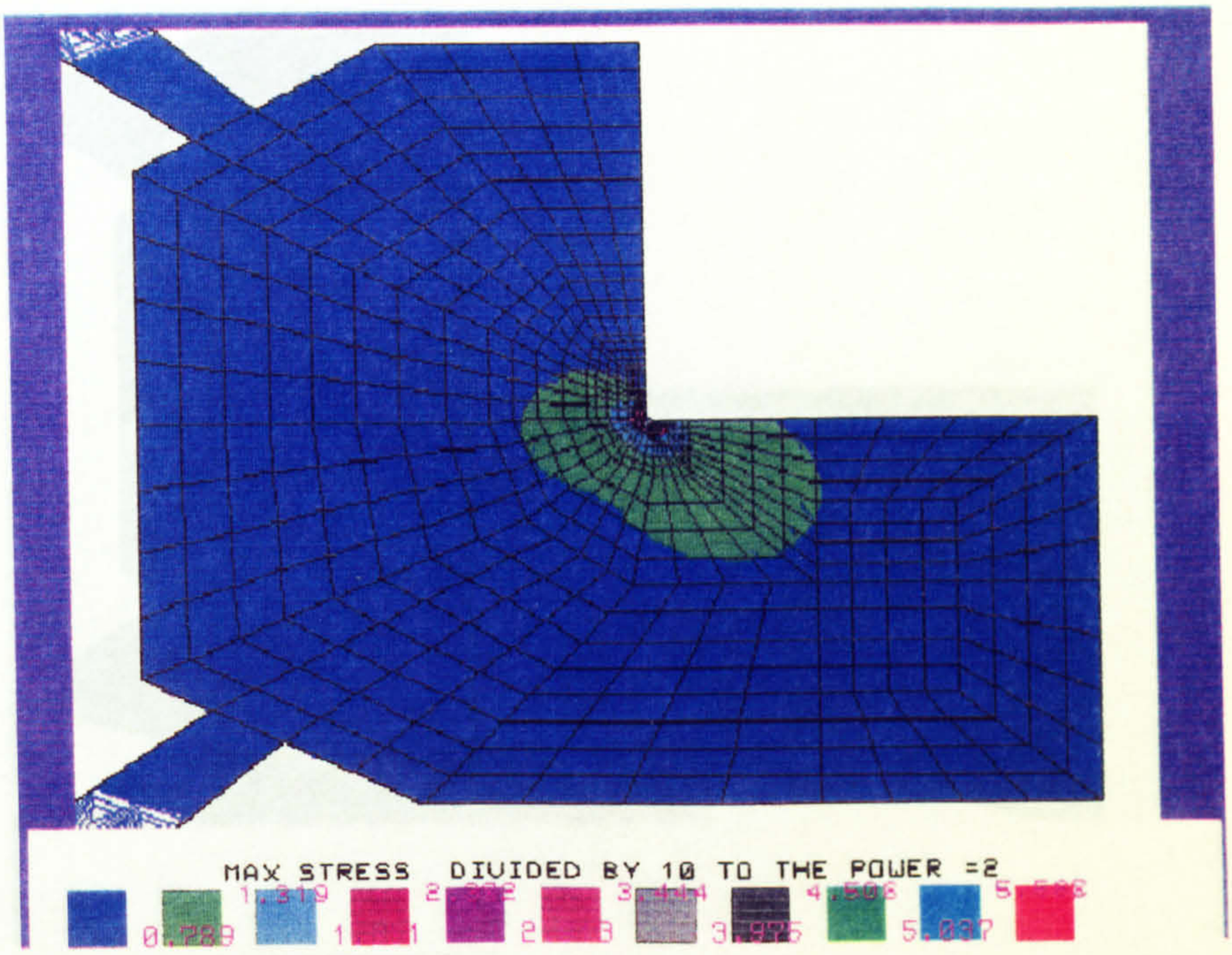

(31) $s/W = 5.88 \times 10^{-3}$ *and* $s/\rho = 64$.

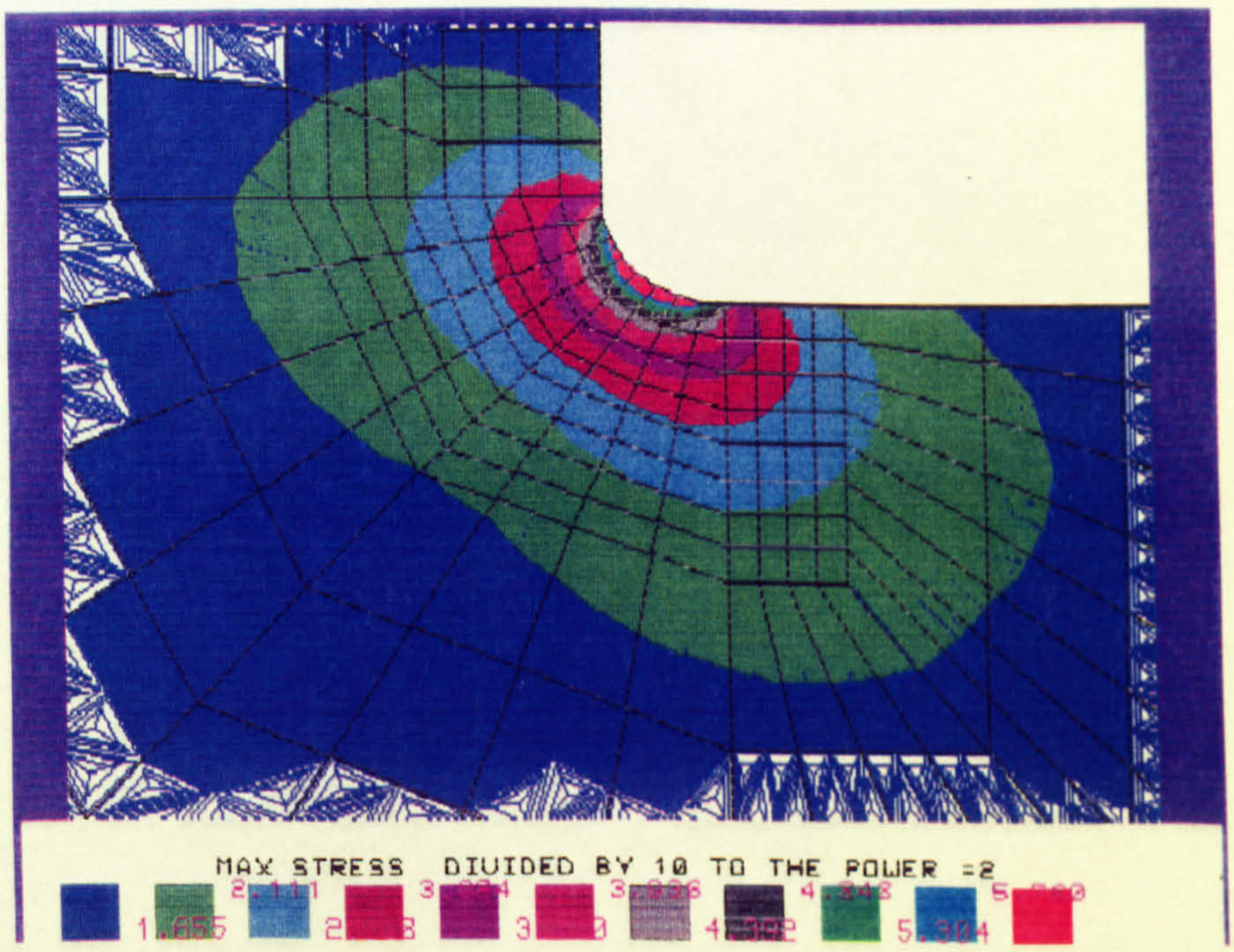

(32) $s/W = 5.88 \times 10^{-3}$ *and* $s/\rho = 64$.

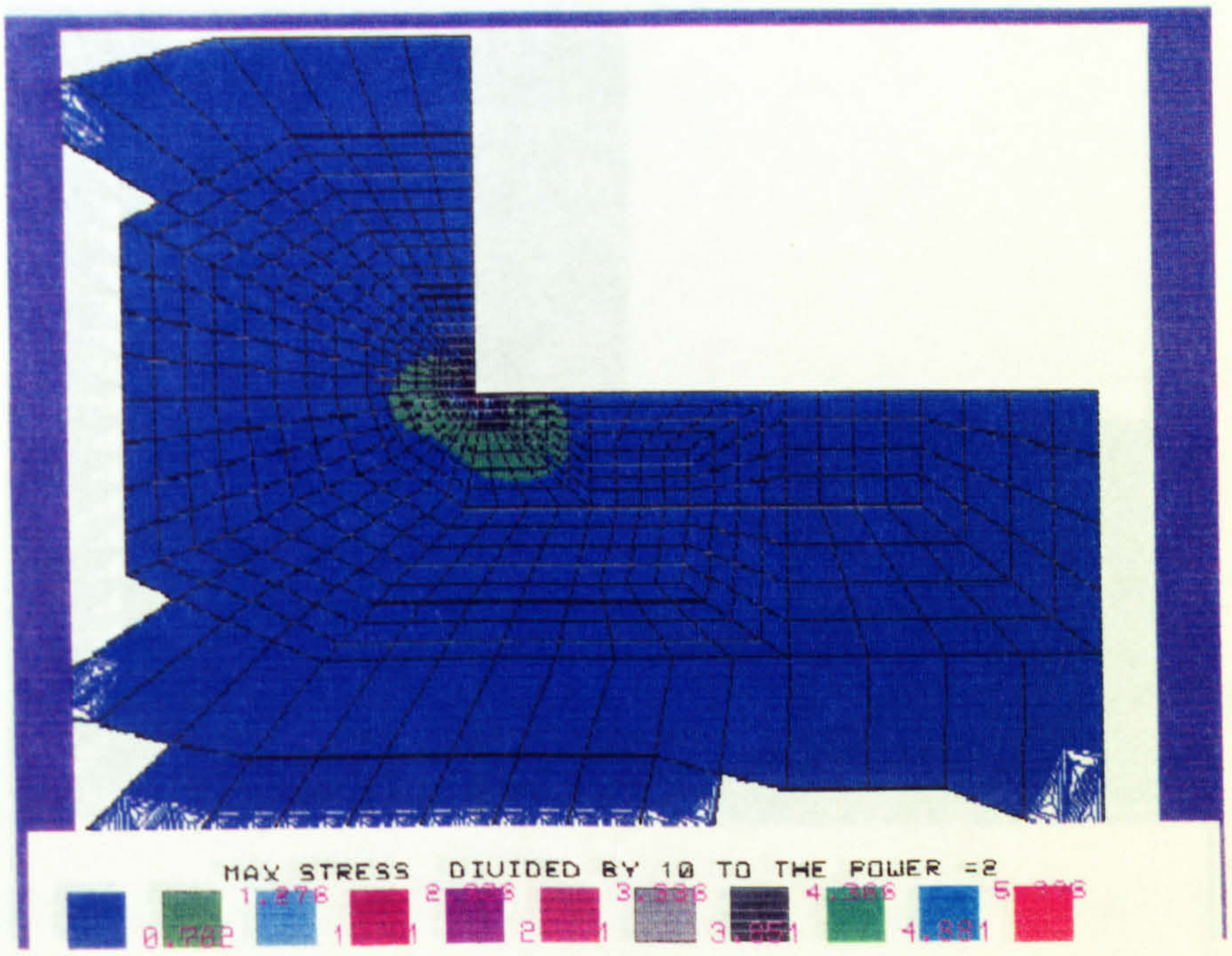

(33) $s/W = 1.18 \times 10^{-2}$ *and* $s/\rho = 128$.

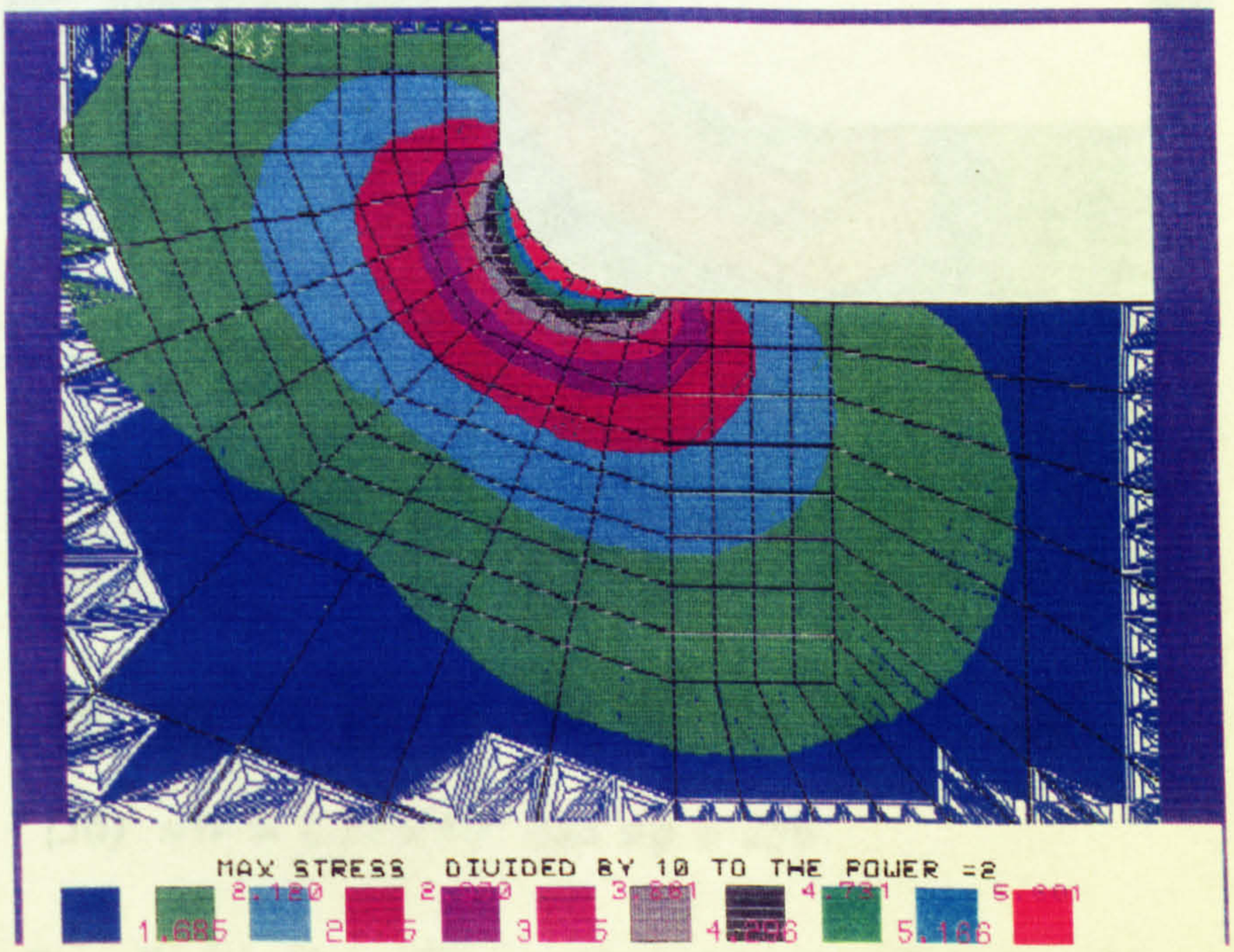

(34) $s/W = 1.18 \times 10^{-2}$ *and* $s/\rho = 128$.

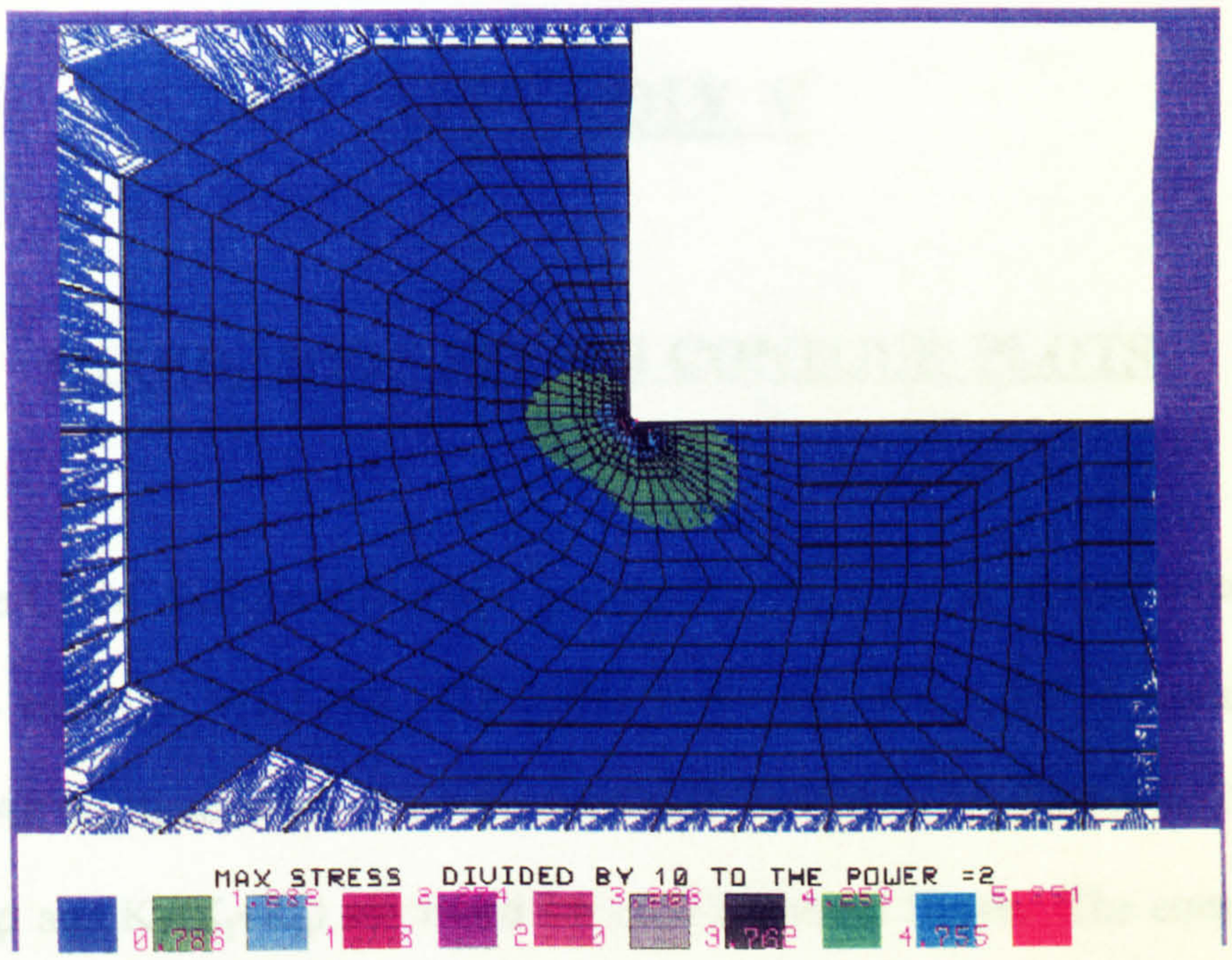

(35) $s/W = 2.35 \times 10^{-2}$ *and* $s/\rho = 256$.

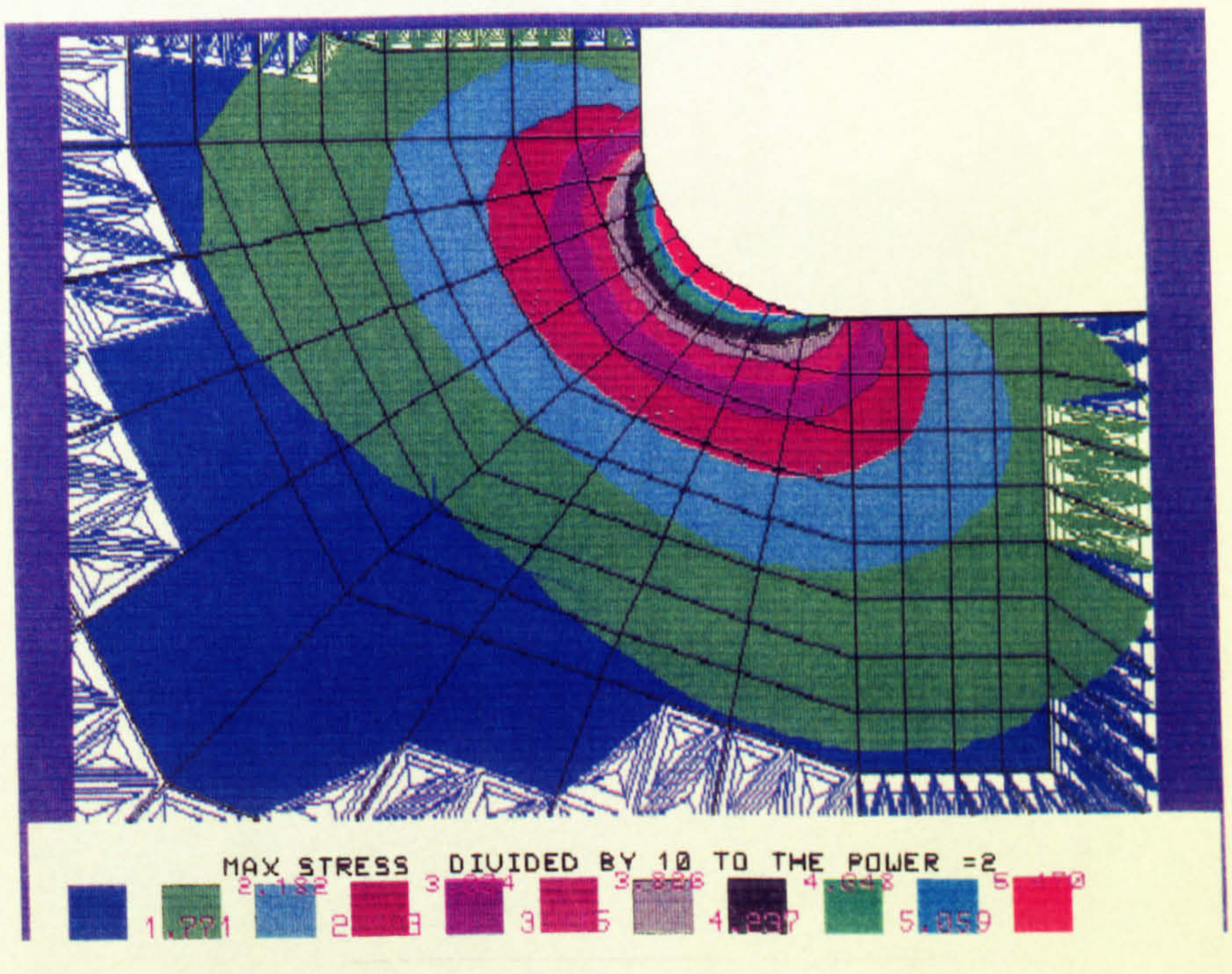

(36) $s/W = 2.35 \times 10^{-2}$ *and* $s/\rho = 256$.

Figs. IV.1(1-36). The iso-stress contours of the σ_{max} (N/mm^2) *at the notch tips of the 3PB specimens.*

APPENDIX V

MIXED-MODE STRESS CONTOUR PLOTS

The CMM specimen iso-stress contours at the notch tip are presented in this appendix - see Figs. V.1(1-26). The force, P, has the value 1000 N throughout the analysis. All the dimensions and definitions have been given in chapter 8. The values of s/W, s/ρ and $K_I/(K_I+K_{II})$ are stated for each iso-stress figure. The contours have been produced by PIGS. The maximum stresses are all given in N/mm^2.

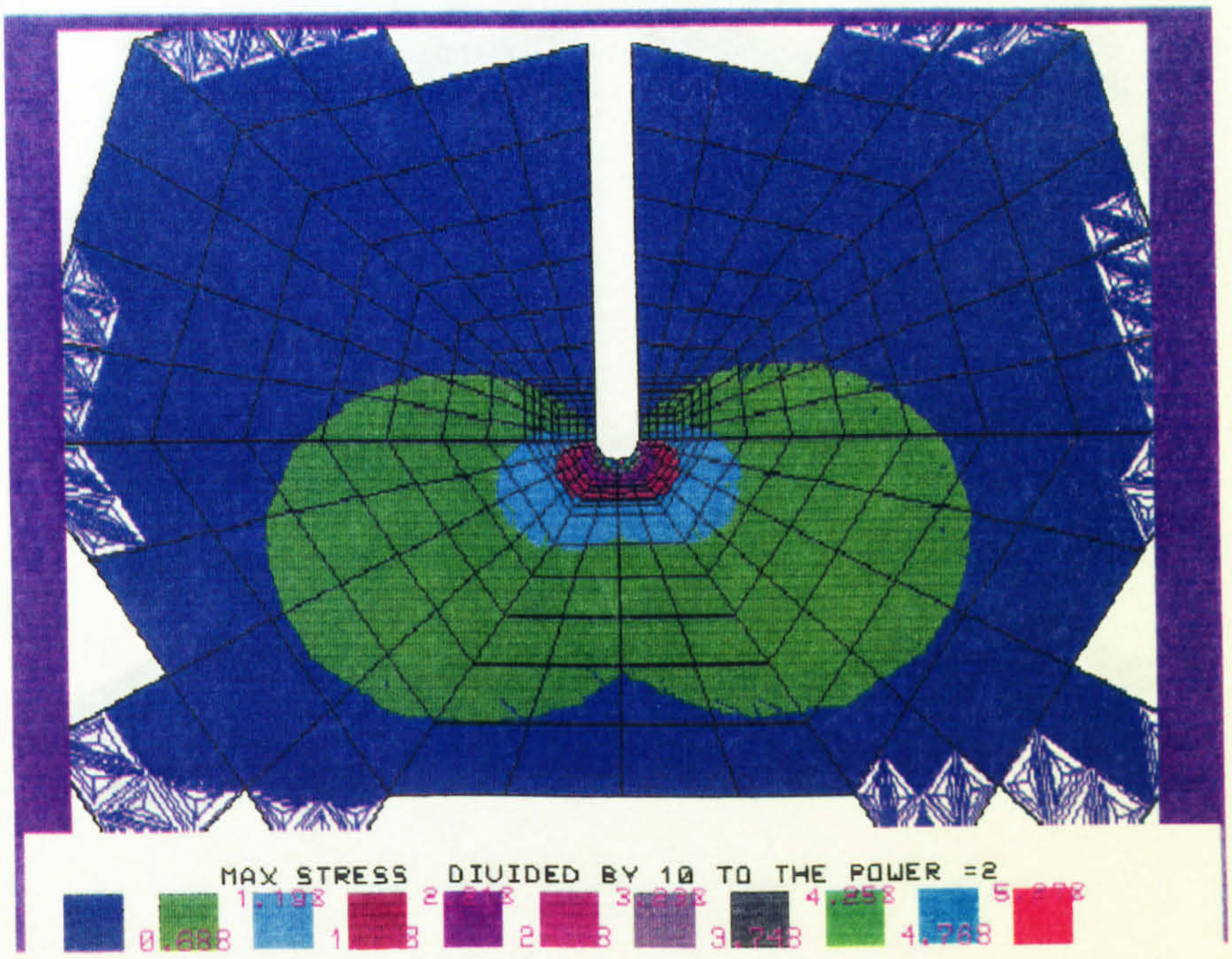

(1) $s/W = 7.35 \times 10^{-4}$, $s/\rho = 1$ *and* $K_I/(K_I + K_{II}) = 1.016$.

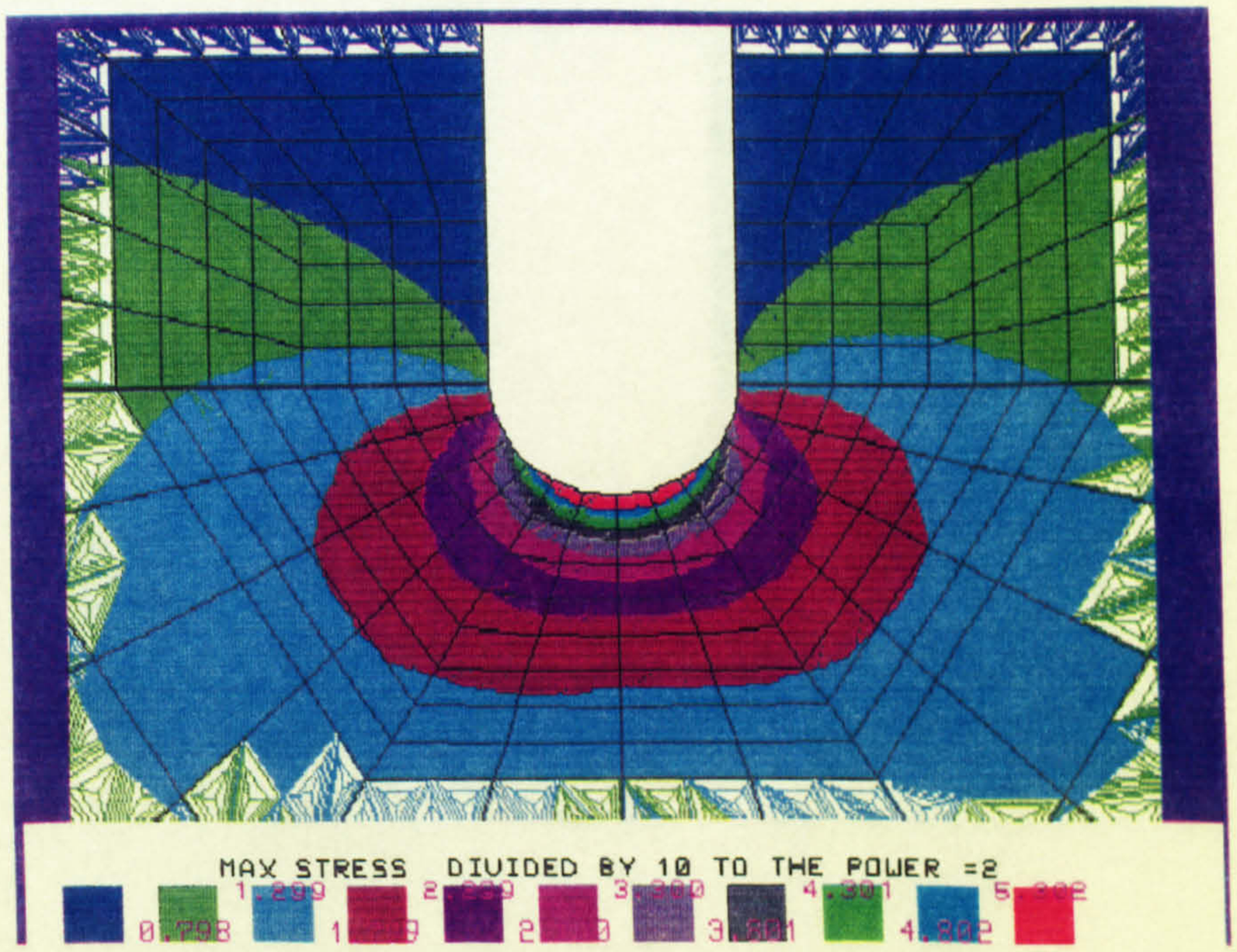

(2) $s/W = 7.35 \times 10^{-4}$, $s/\rho = 1$ *and* $K_I/(K_I + K_{II}) = 1.016$.

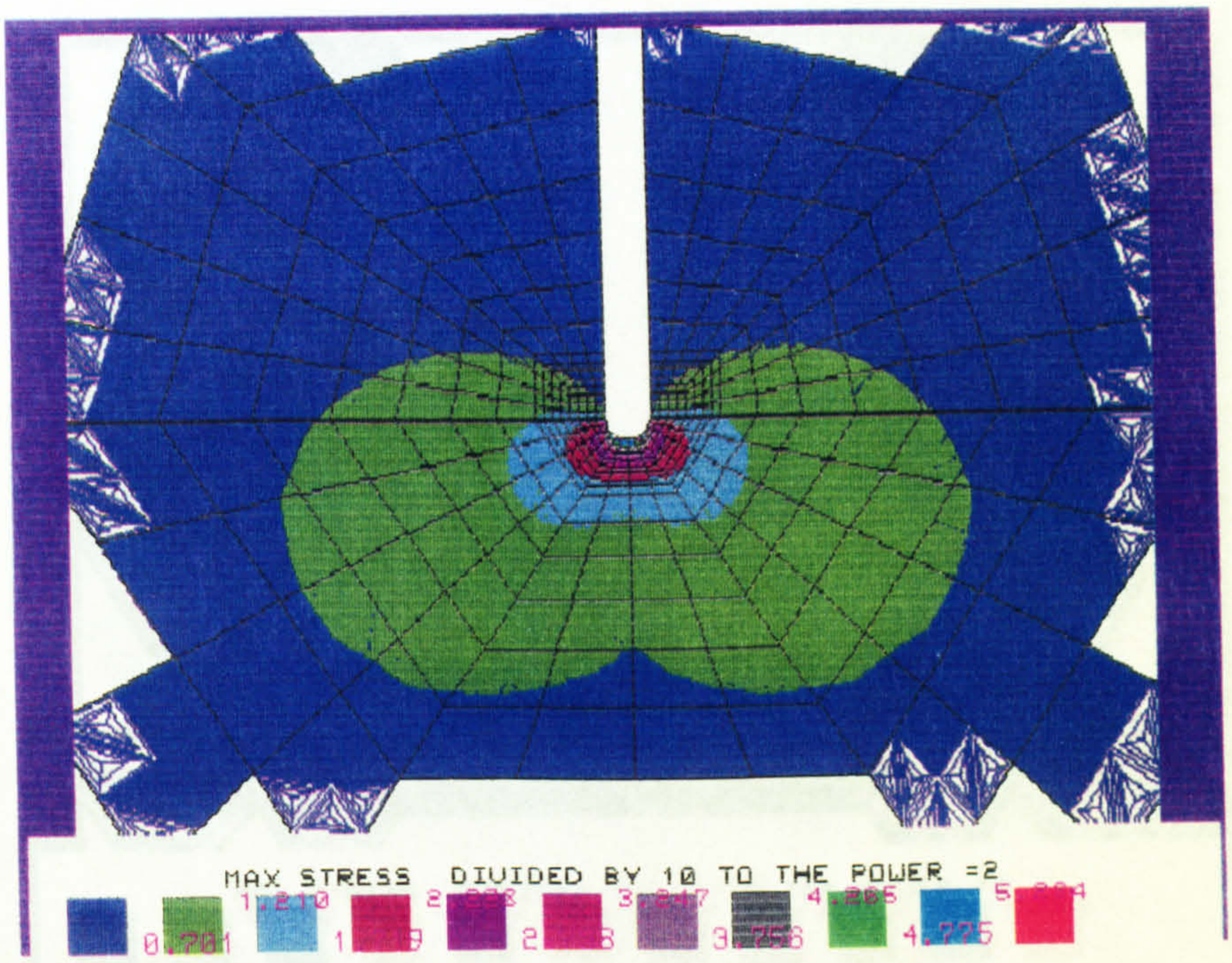

(3) $s/W = 7.35 \times 10^{-4}$, $s/\rho = 1$ *and* $K_I/(K_I + K_{II}) = 1.001$.

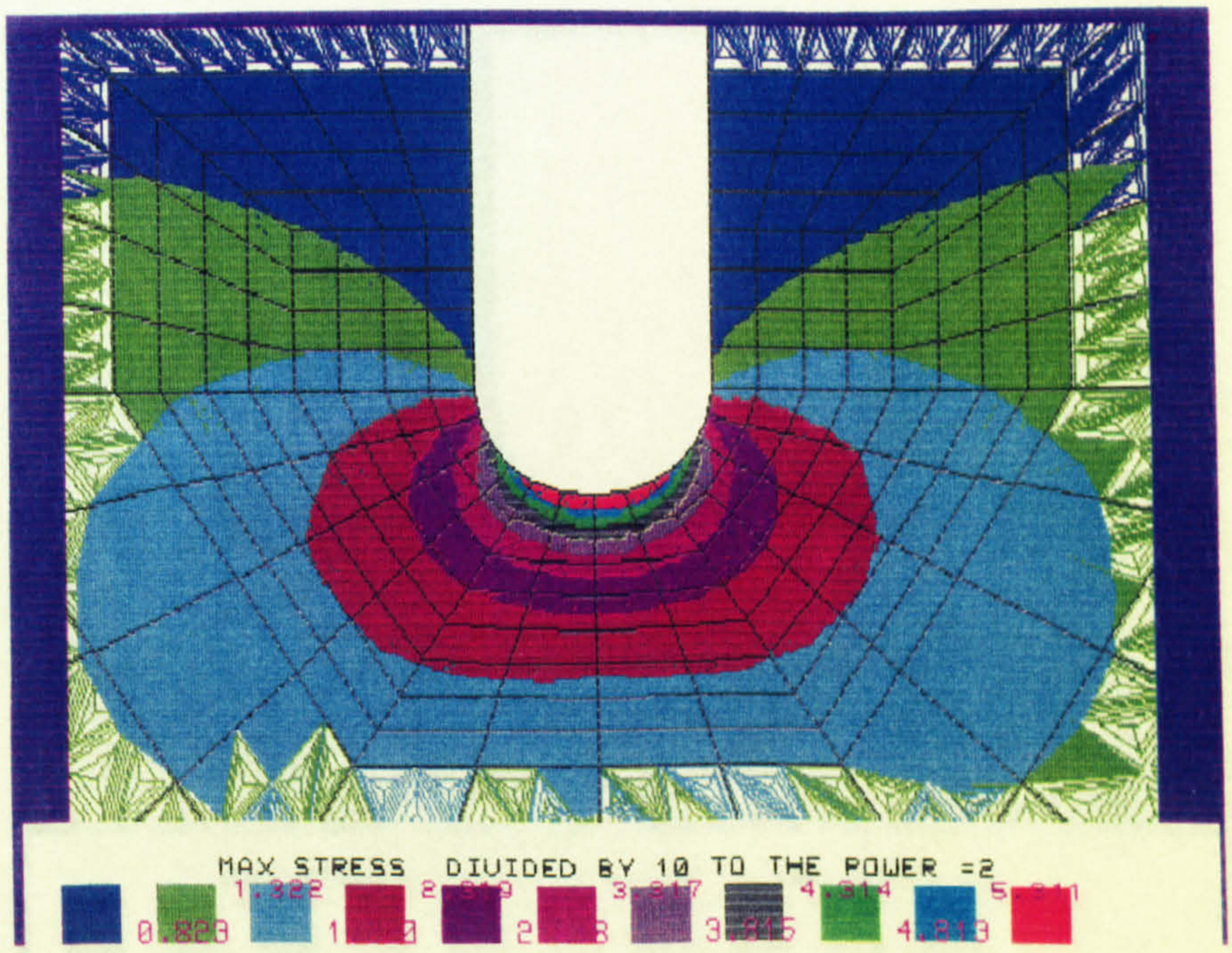

(4) $s/W = 7.35 \times 10^{-4}$, $s/\rho = 1$ *and* $K_I/(K_I + K_{II}) = 1.001$.

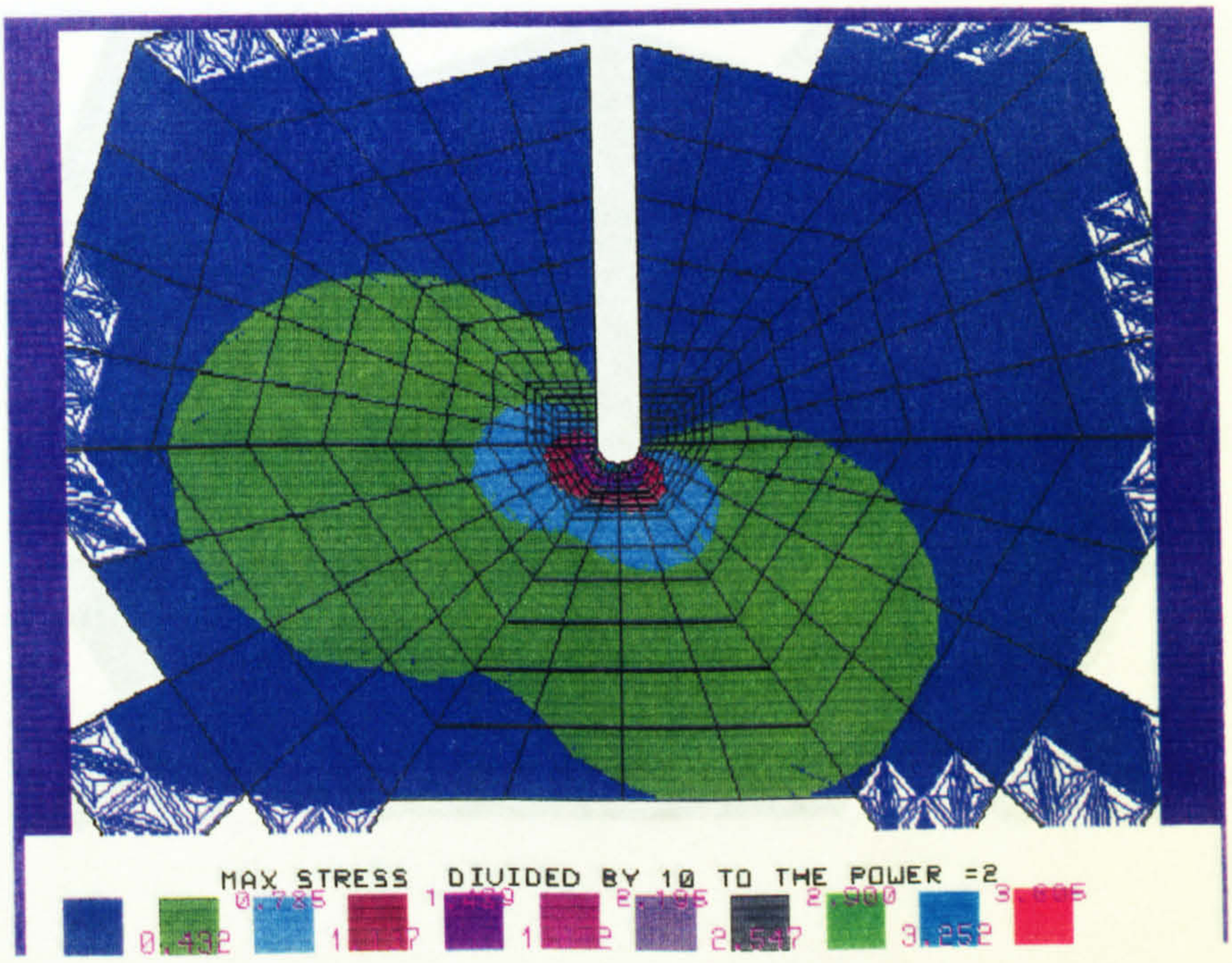

(5) $s/W = 7.35 \times 10^{-4}$, $s/\rho = 1$ *and* $K_I/(K_I + K_{II}) = 0.790$.

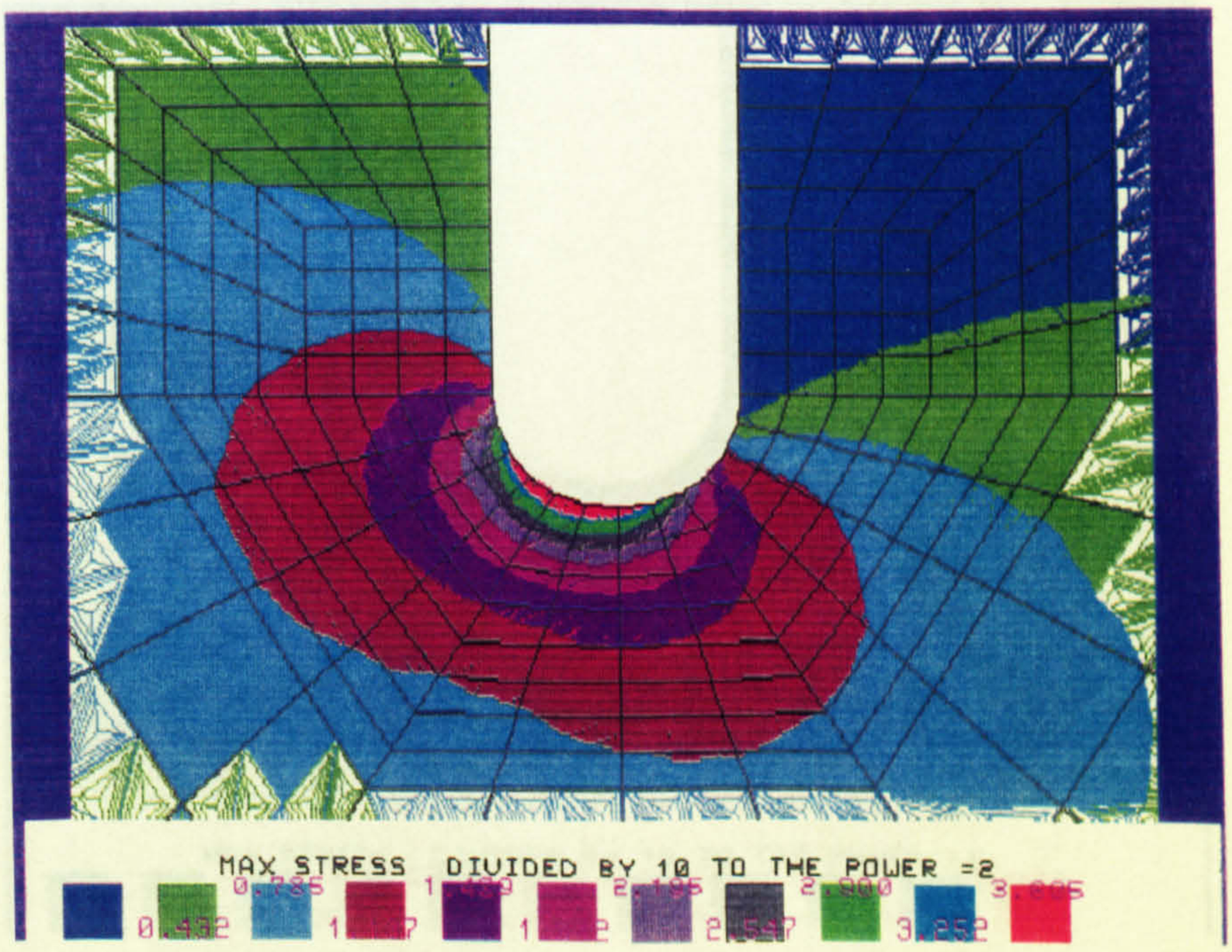

(6) $s/W = 7.35 \times 10^{-4}$, $s/\rho = 1$ *and* $K_I/(K_I + K_{II}) = 0.790$.

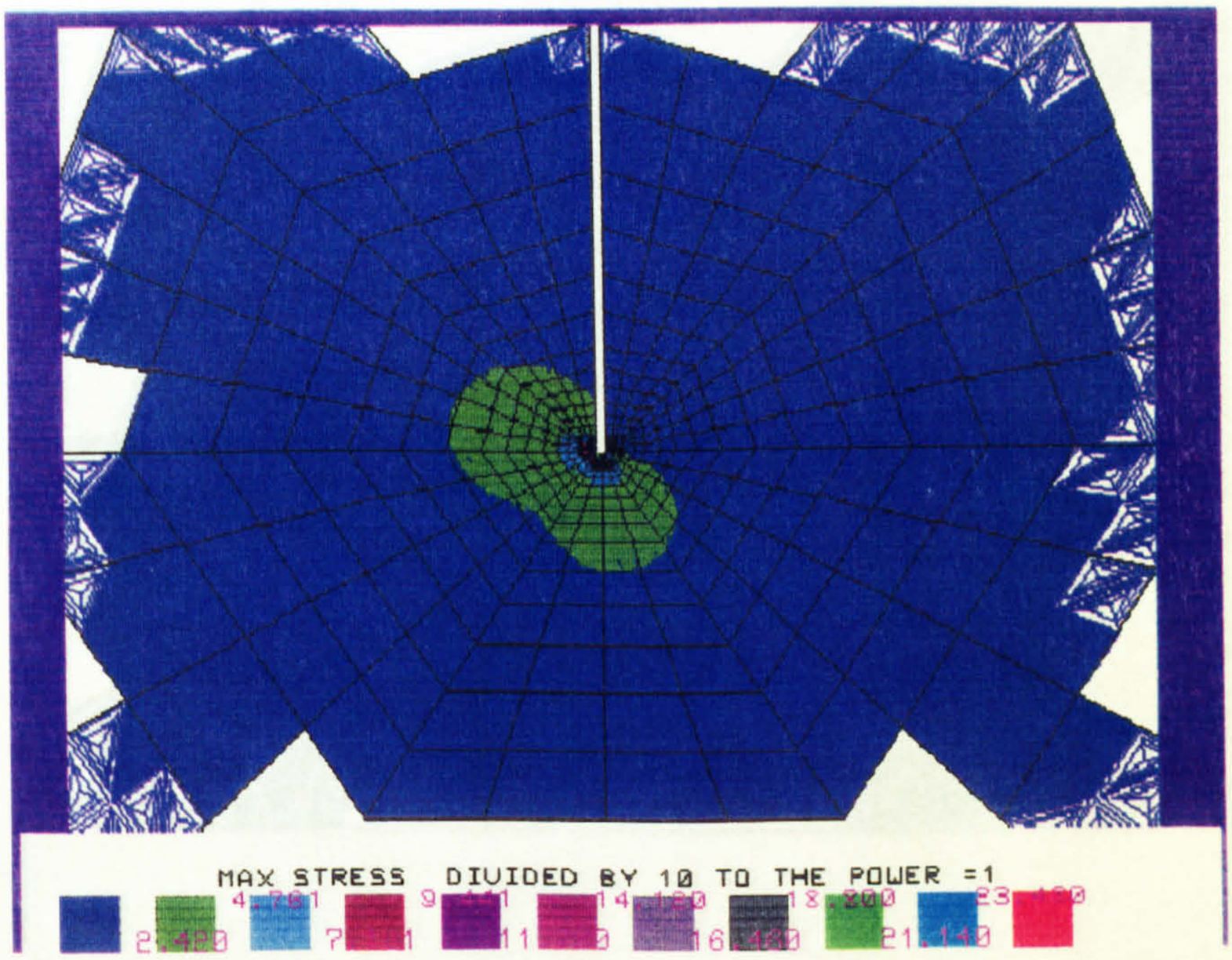

(7) $s/W = 7.35 \times 10^{-4}$, $s/\rho = 1$ and $K_I/(K_I + K_{II}) = 0.610$.

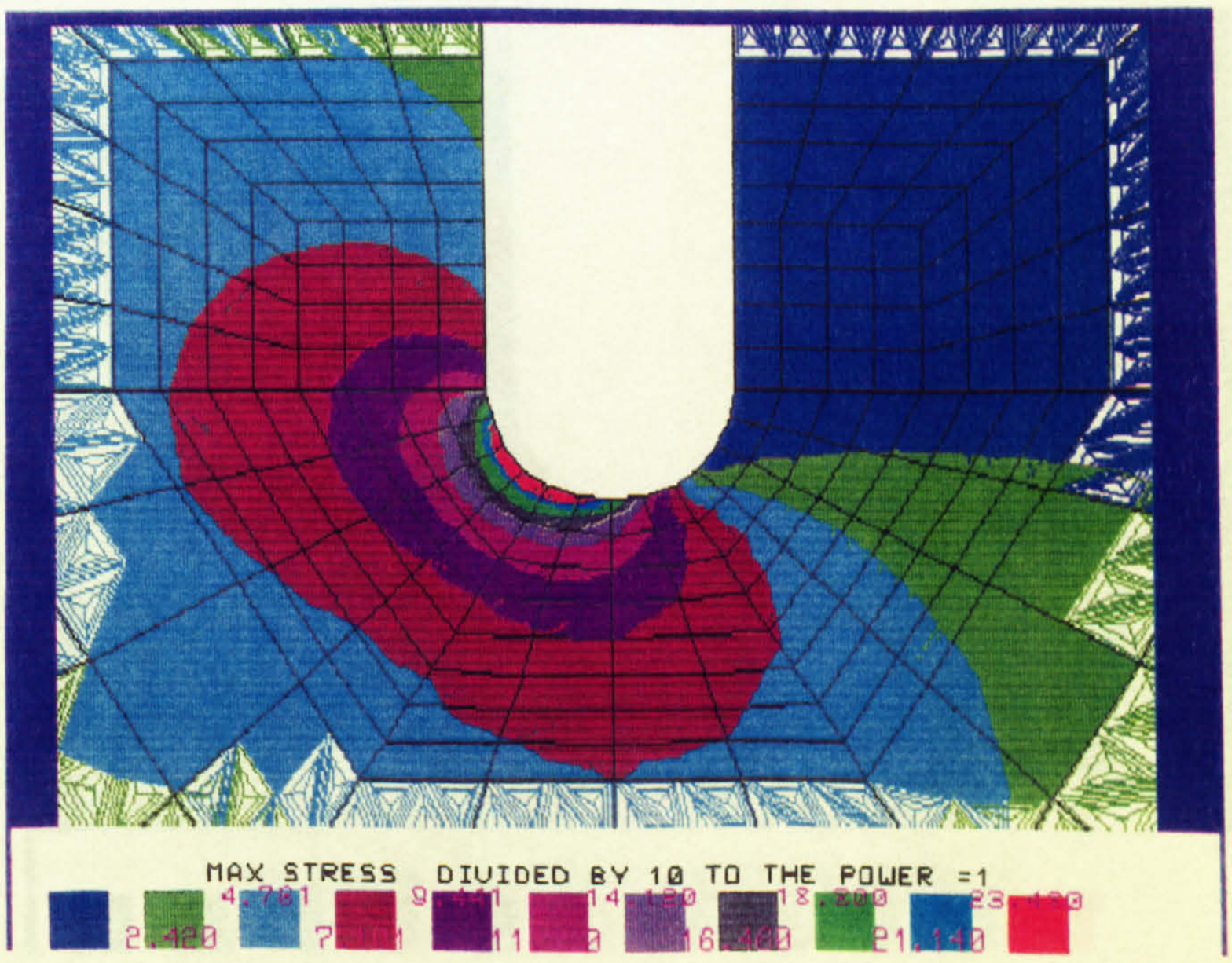

(8) $s/W = 7.35 \times 10^{-4}$, $s/\rho = 1$ and $K_I/(K_I + K_{II}) = 0.610$.

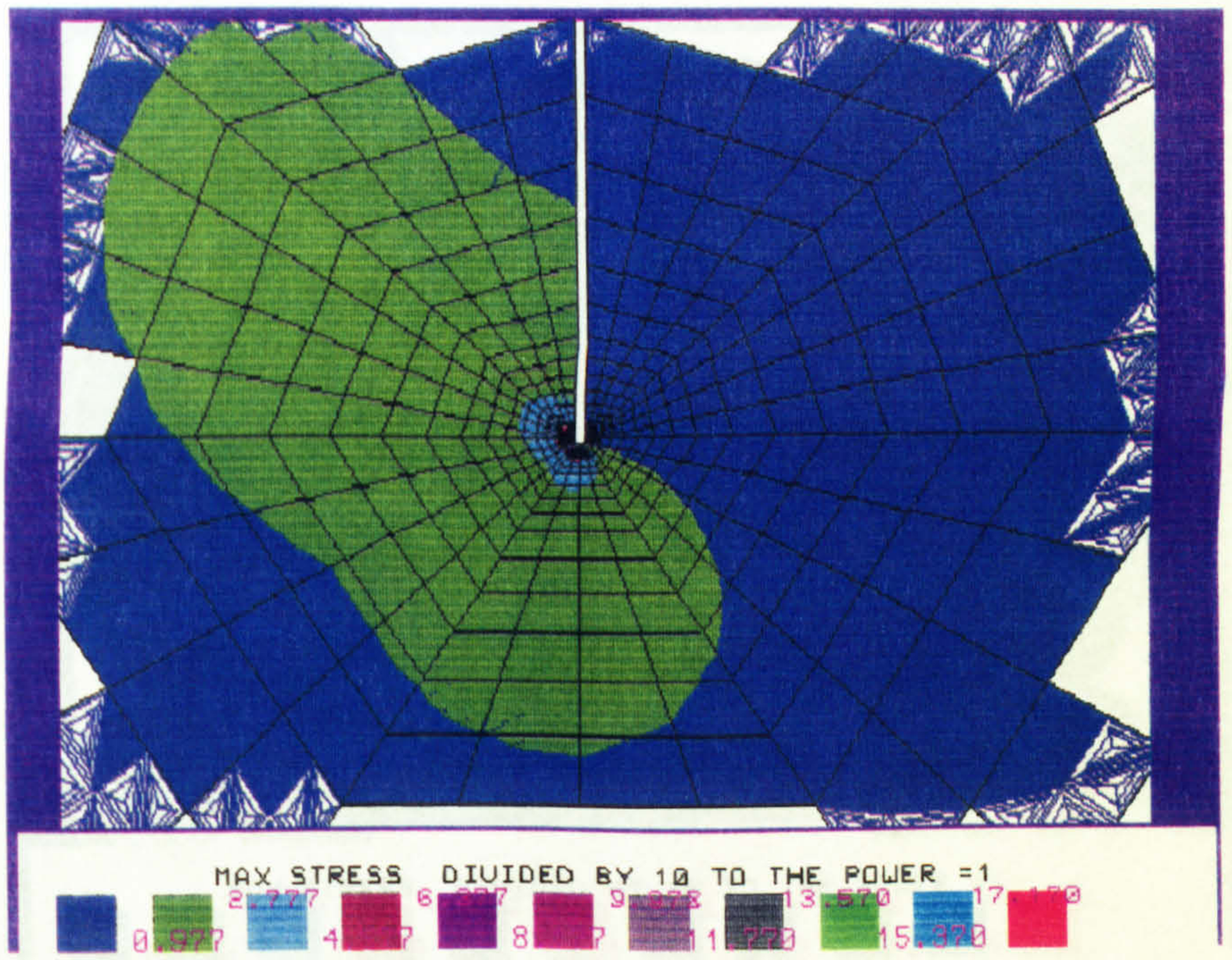

(9) $s/W = 7.35 \times 10^{-4}$, $s/\rho = 1$ *and* $K_I/(K_I + K_{II}) = 0.411$.

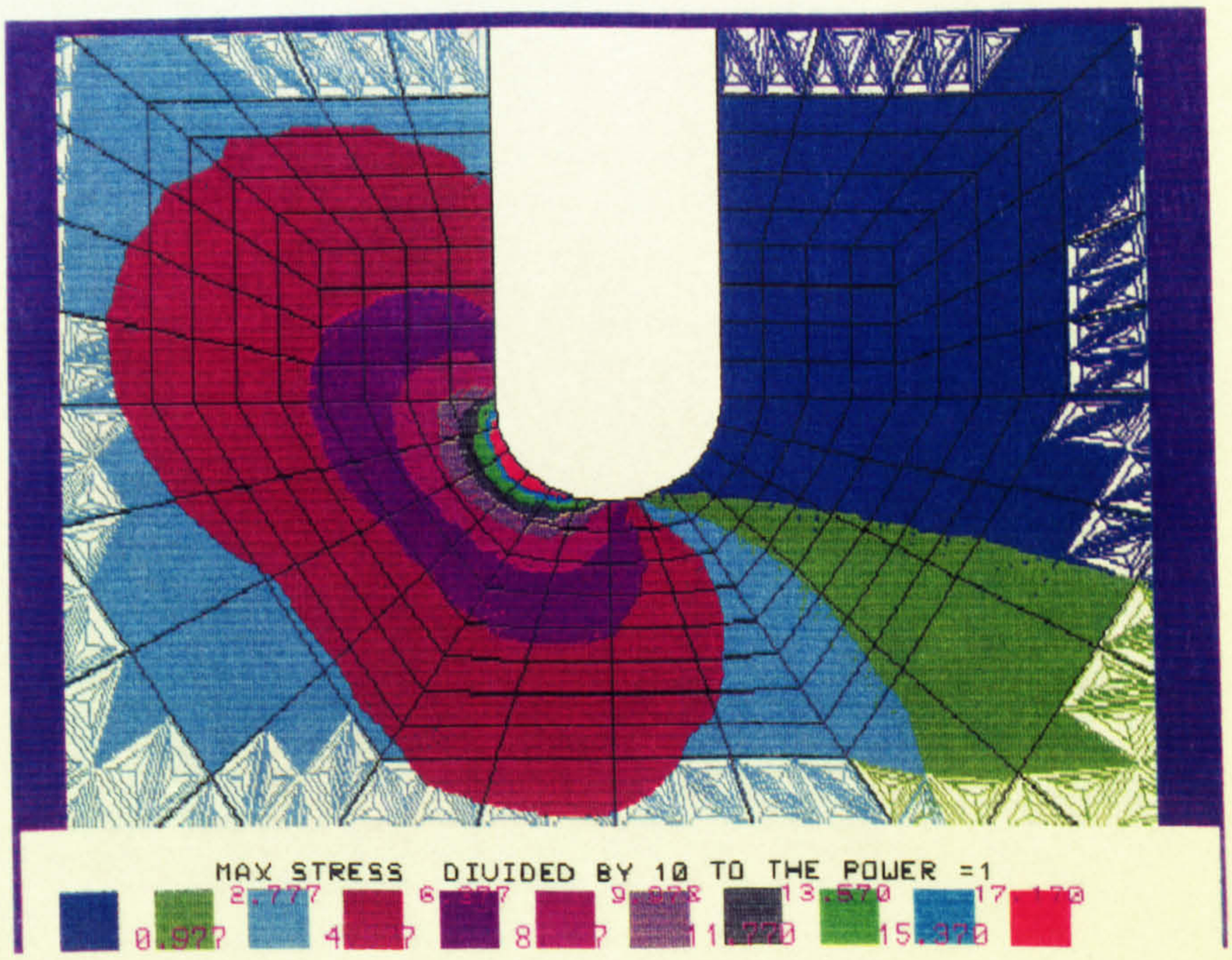

(10) $s/W = 7.35 \times 10^{-4}$, $s/\rho = 1$ *and* $K_I/(K_I + K_{II}) = 0.411$.

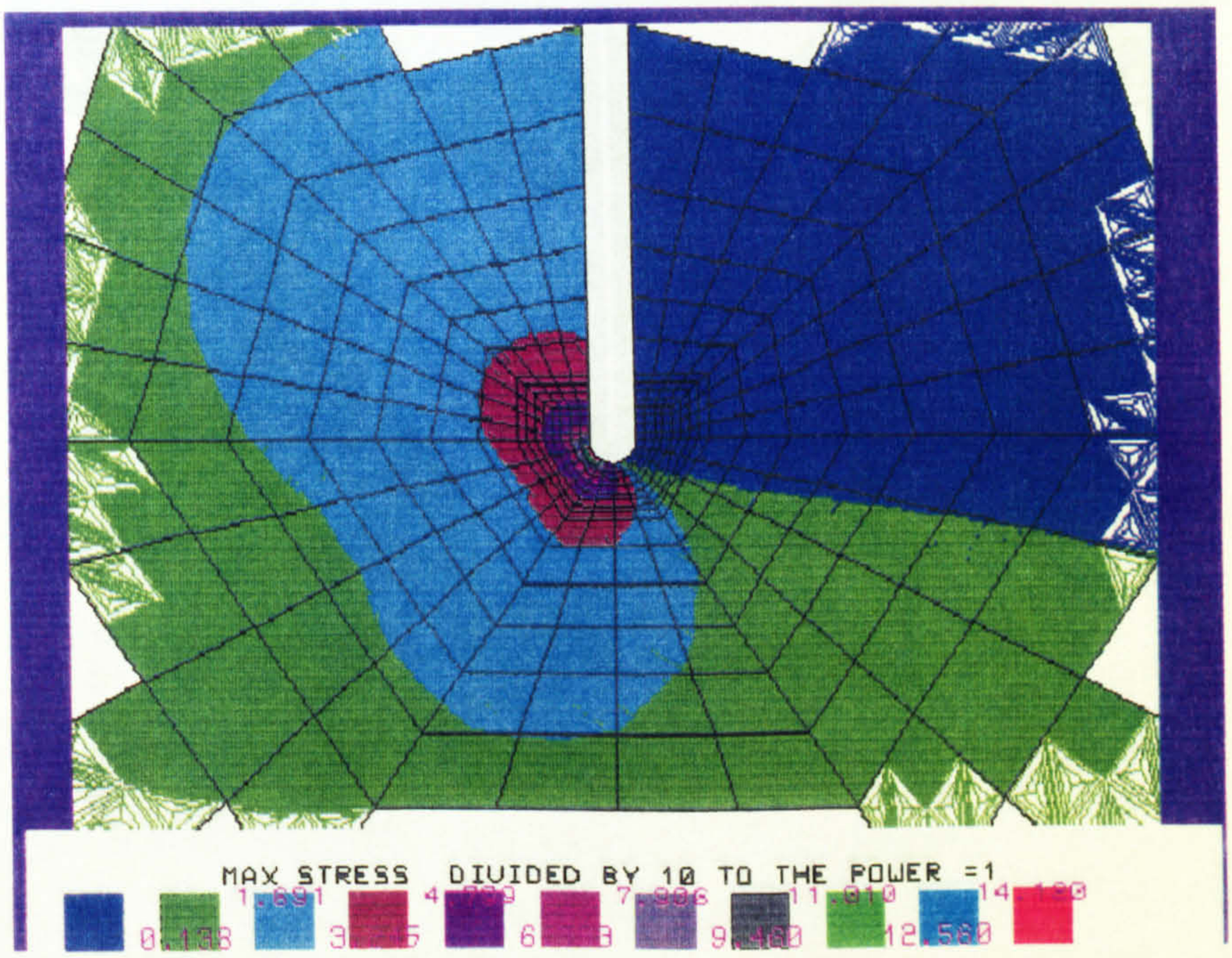

(11) $s/W = 7.35 \times 10^{-4}$, $s/\rho = 1$ *and* $K_I/(K_I + K_{II}) = 0.225$.

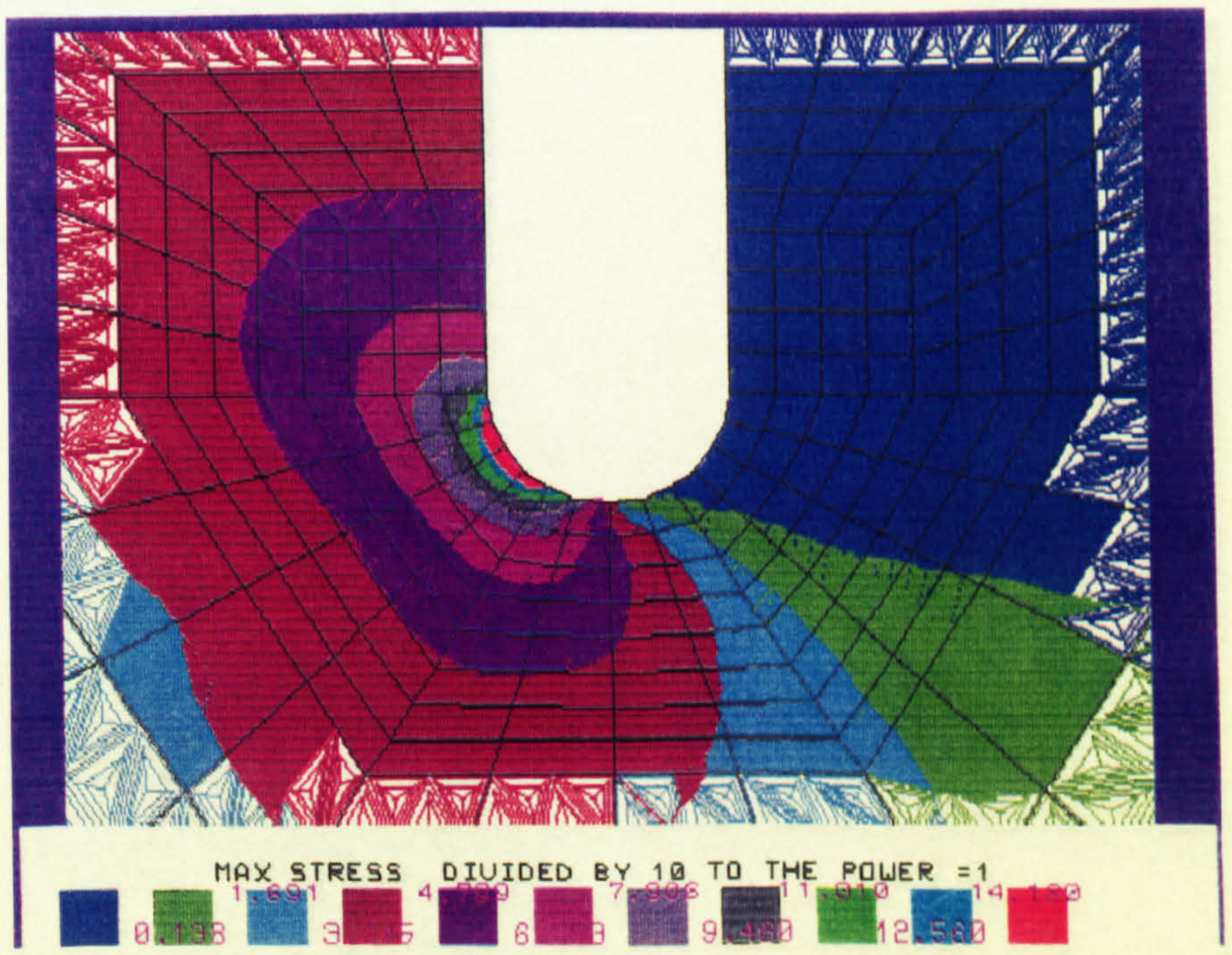

(12) $s/W = 7.35 \times 10^{-4}$, $s/\rho = 1$ *and* $K_I/(K_I + K_{II}) = 0.225$.

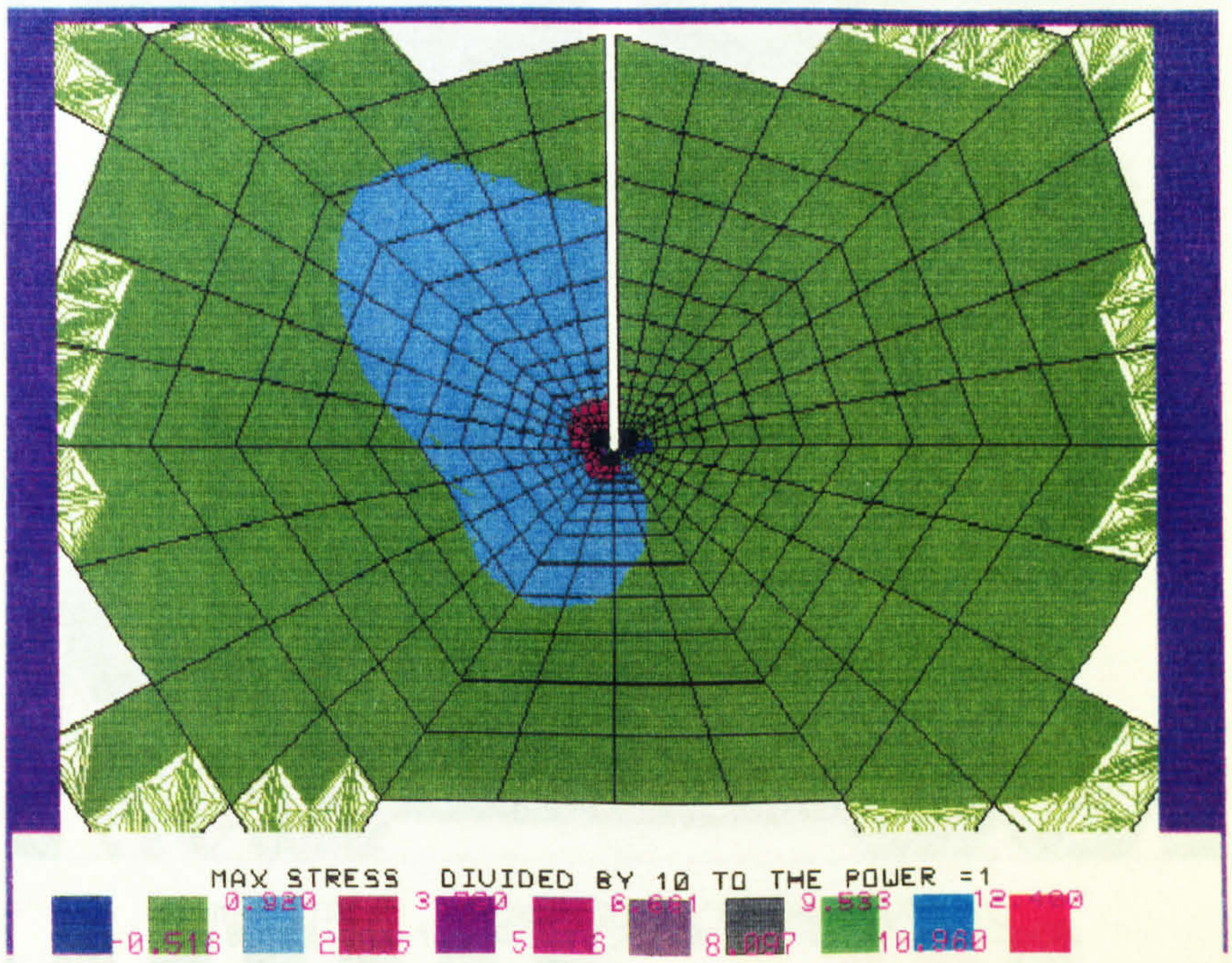

(13) $s/W = 7.35 \times 10^{-4}$, $s/\rho = 1$ *and* $K_I/(K_I + K_{II}) = 0.047$.

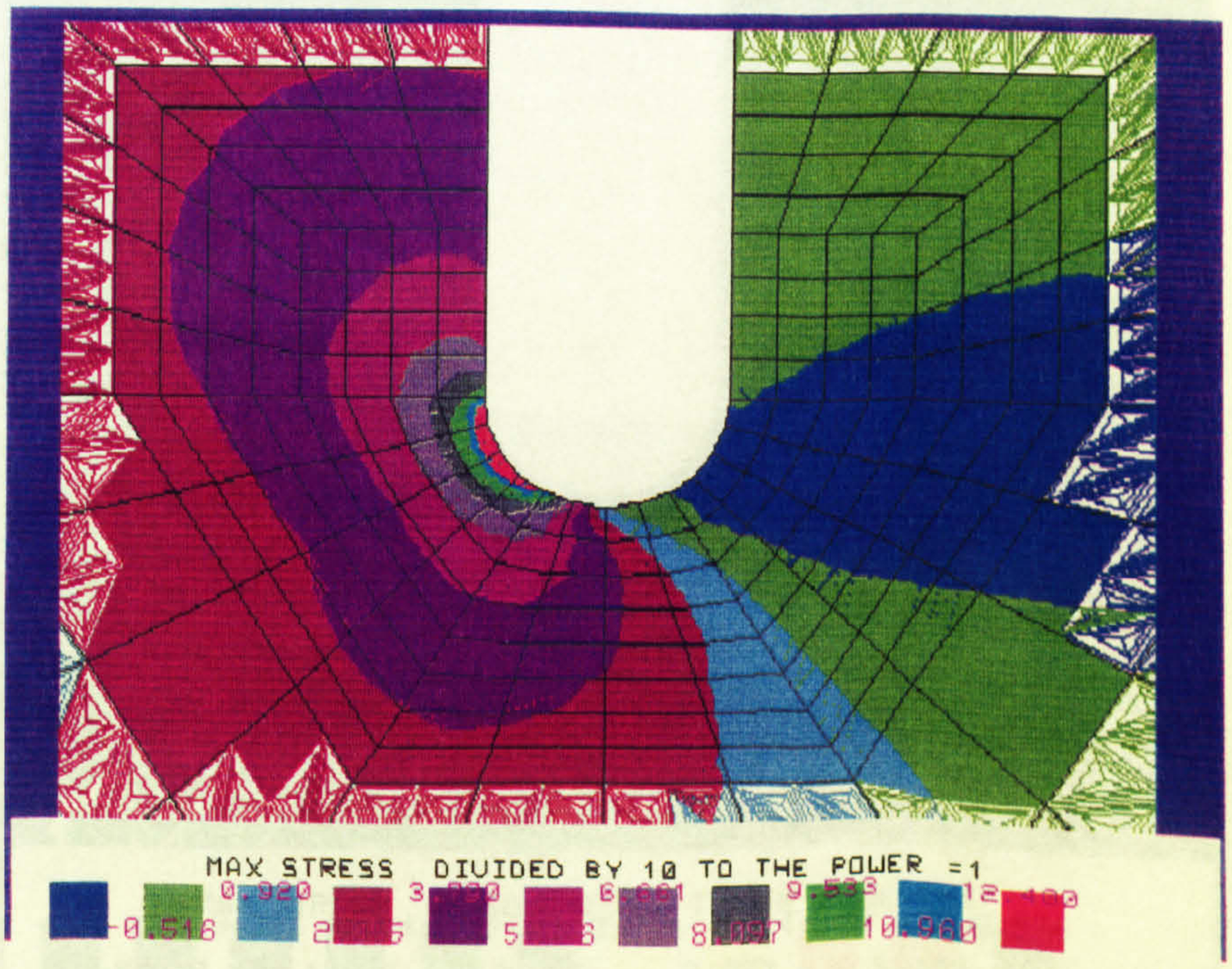

(14) $s/W = 7.35 \times 10^{-4}$, $s/\rho = 1$ *and* $K_I/(K_I + K_{II}) = 0.047$.

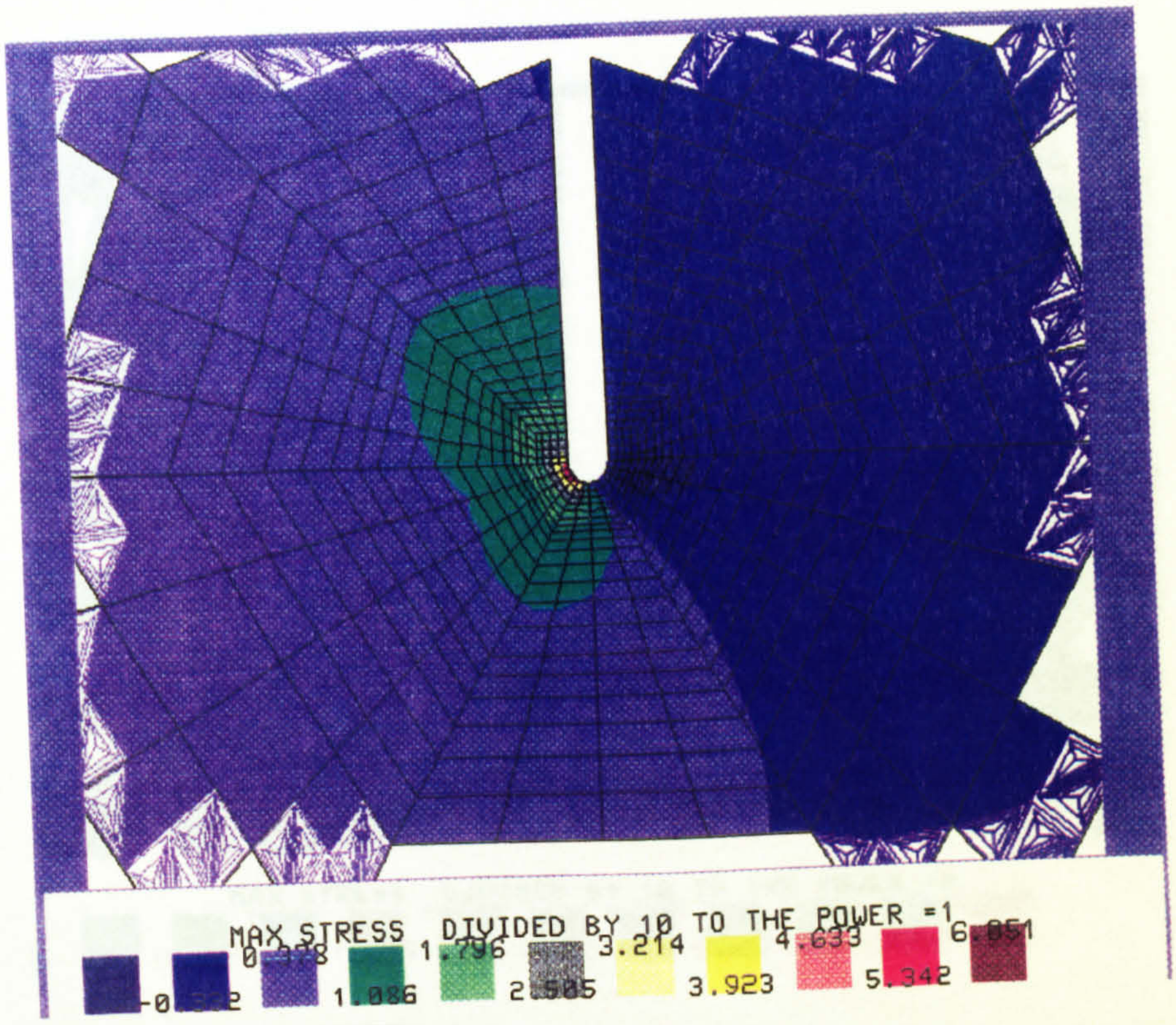

(15) $s/W = 2.94 \times 10^{-3}$, $s/\rho = 1$ *and* $K_I/(K_I + K_{II}) = 0.001$.

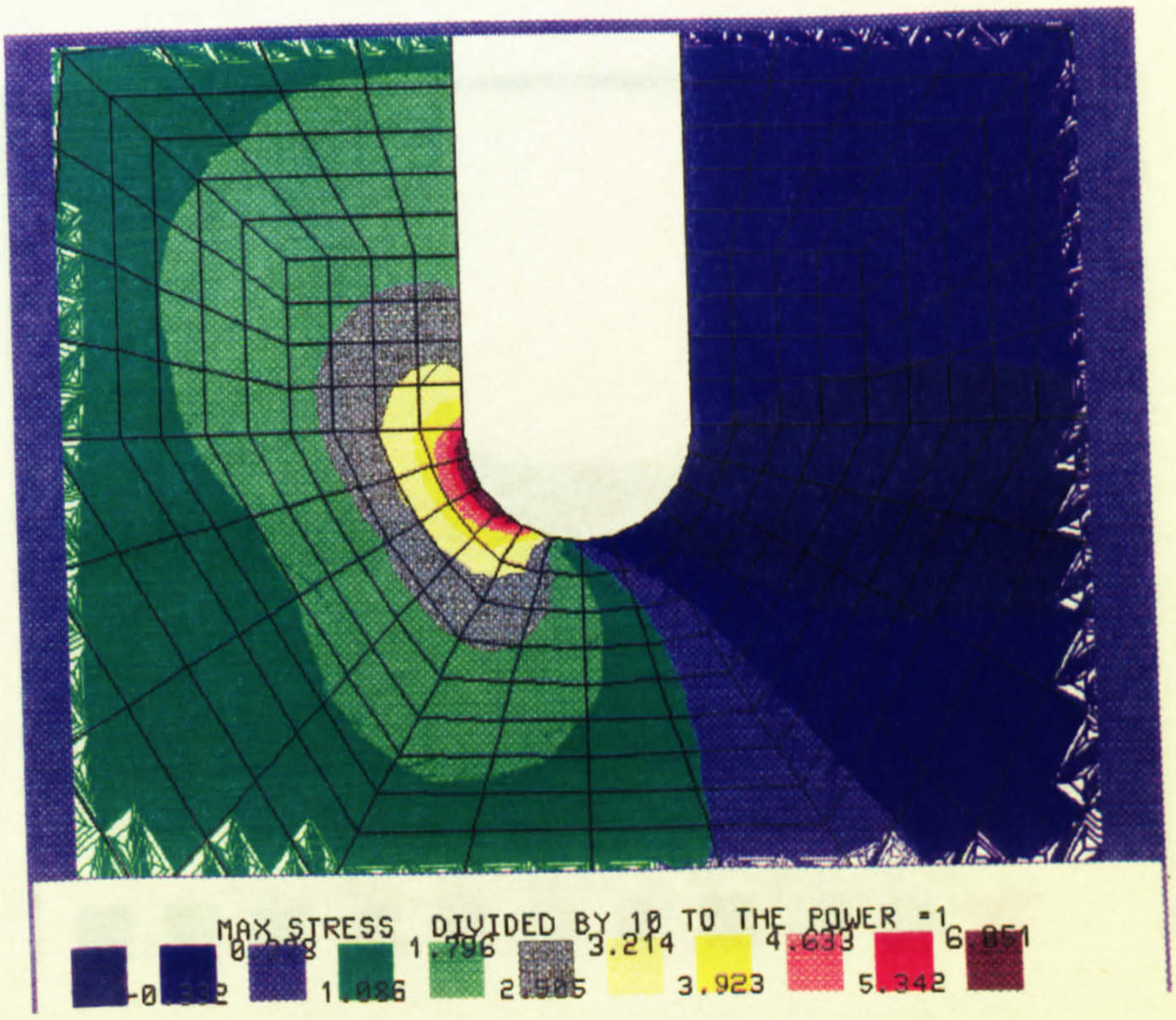

(16) $s/W = 2.94 \times 10^{-3}$, $s/\rho = 1$ *and* $K_I/(K_I + K_{II}) = 0.001$.

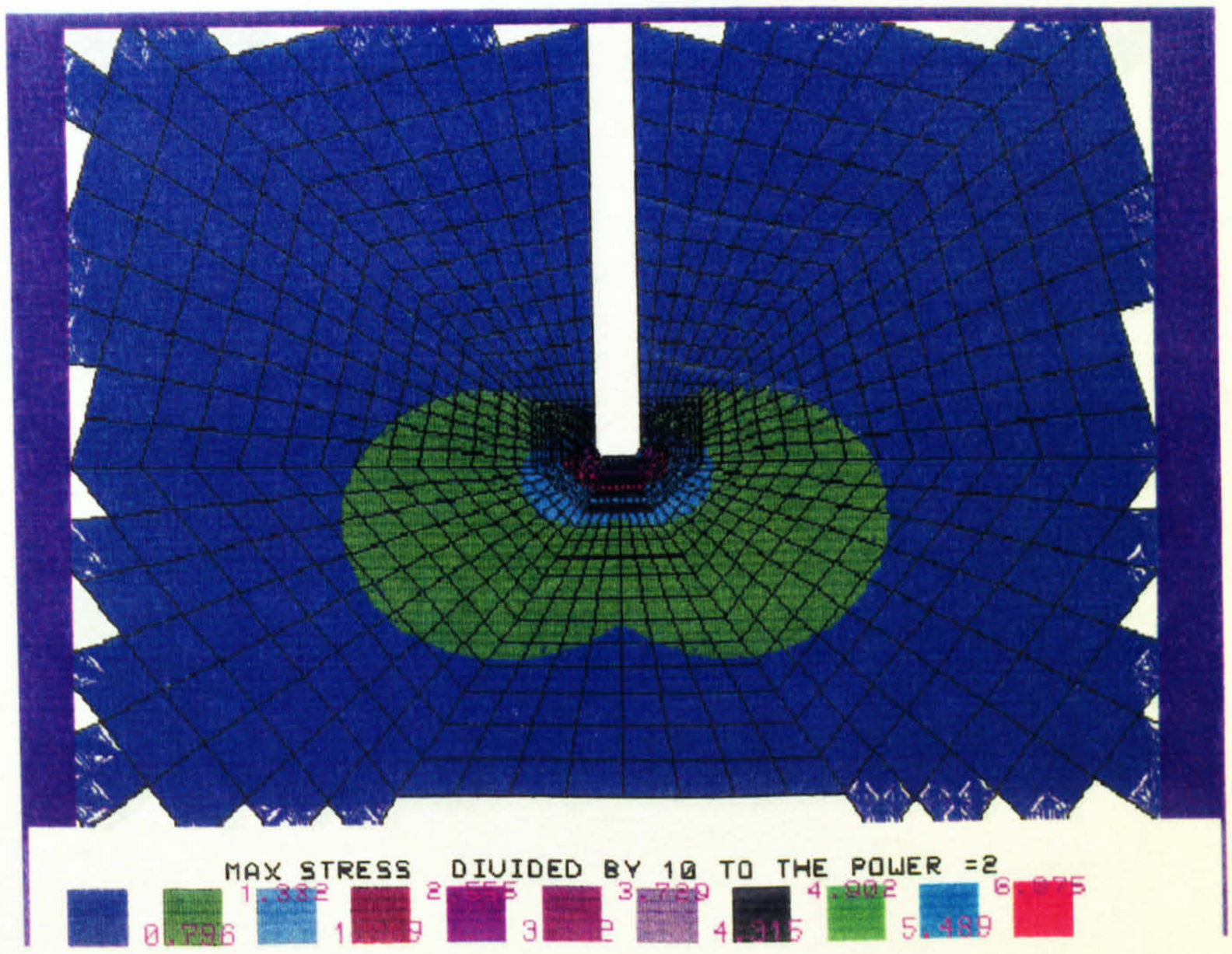

(17) $s/W = 7.35 \times 10^{-4}$, $s/\rho = 2$ *and* $K_I/(K_I + K_{II}) = 1.001$.

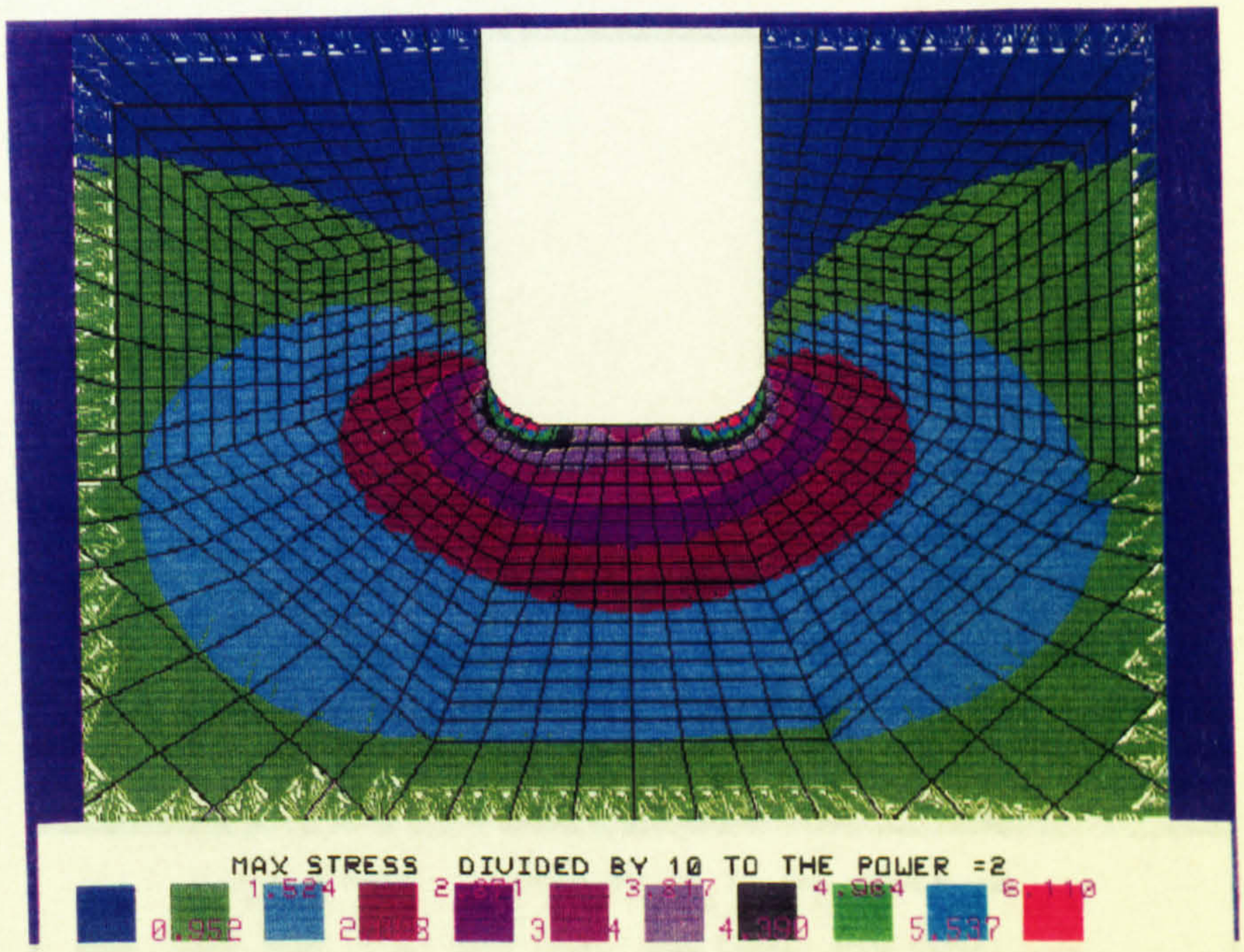

(18) $s/W = 7.35 \times 10^{-4}$, $s/\rho = 2$ *and* $K_I/(K_I + K_{II}) = 1.001$.

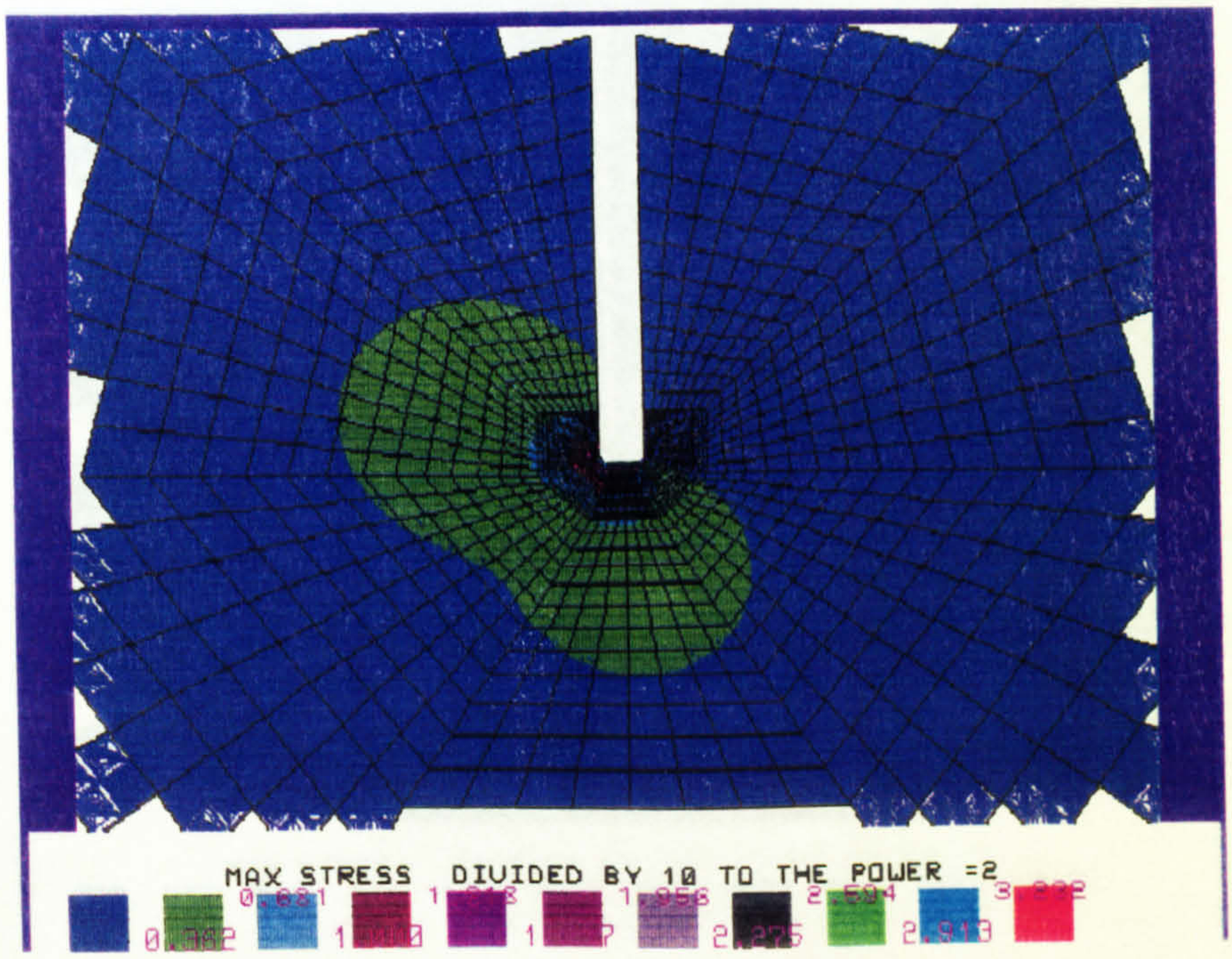

(19) $s/W = 7.35 \times 10^{-4}$, $s/\rho = 2$ *and* $K_I/(K_I + K_{II}) = 0.610$.

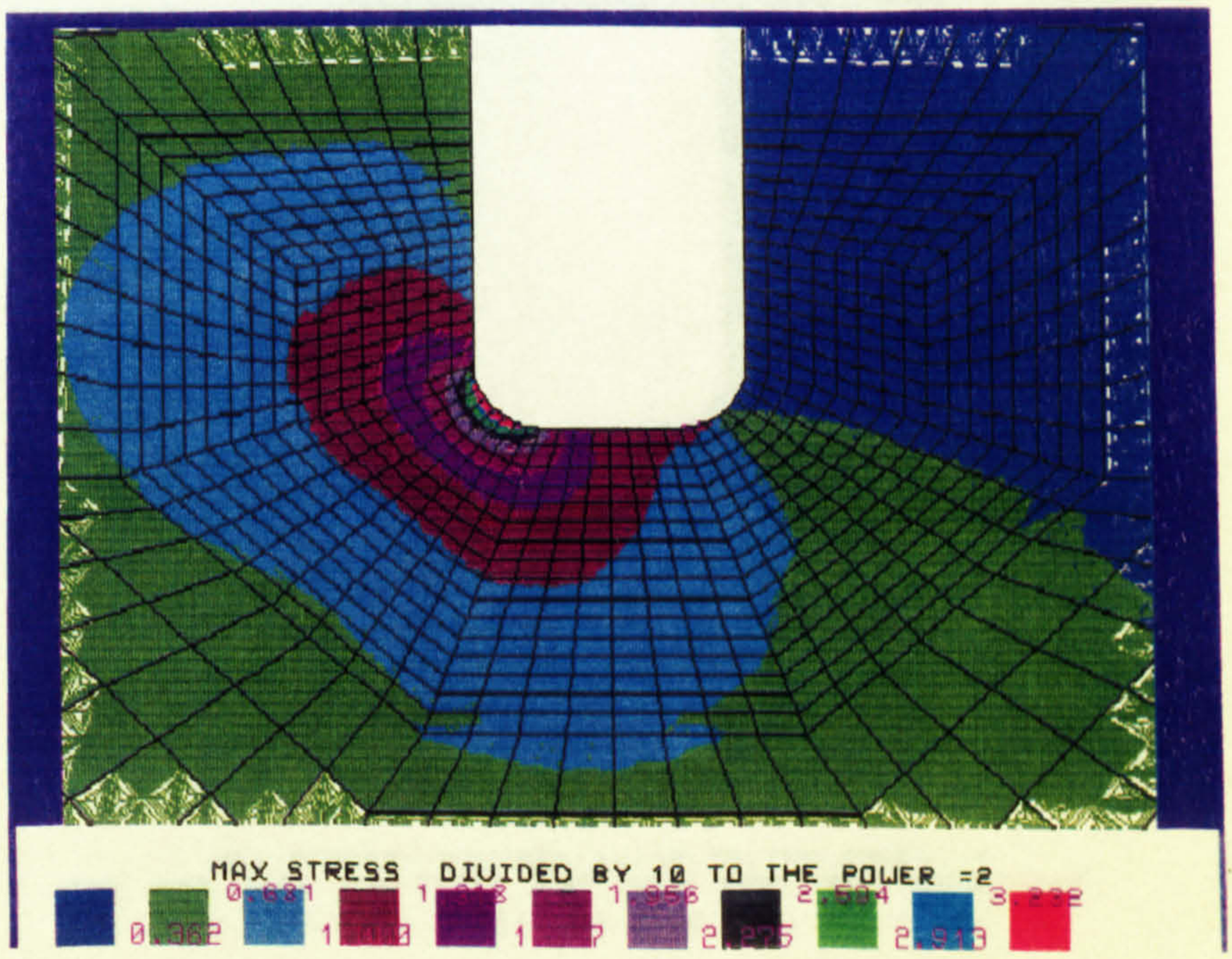

(20) $s/W = 7.35 \times 10^{-4}$, $s/\rho = 2$ *and* $K_I/(K_I + K_{II}) = 0.610$.

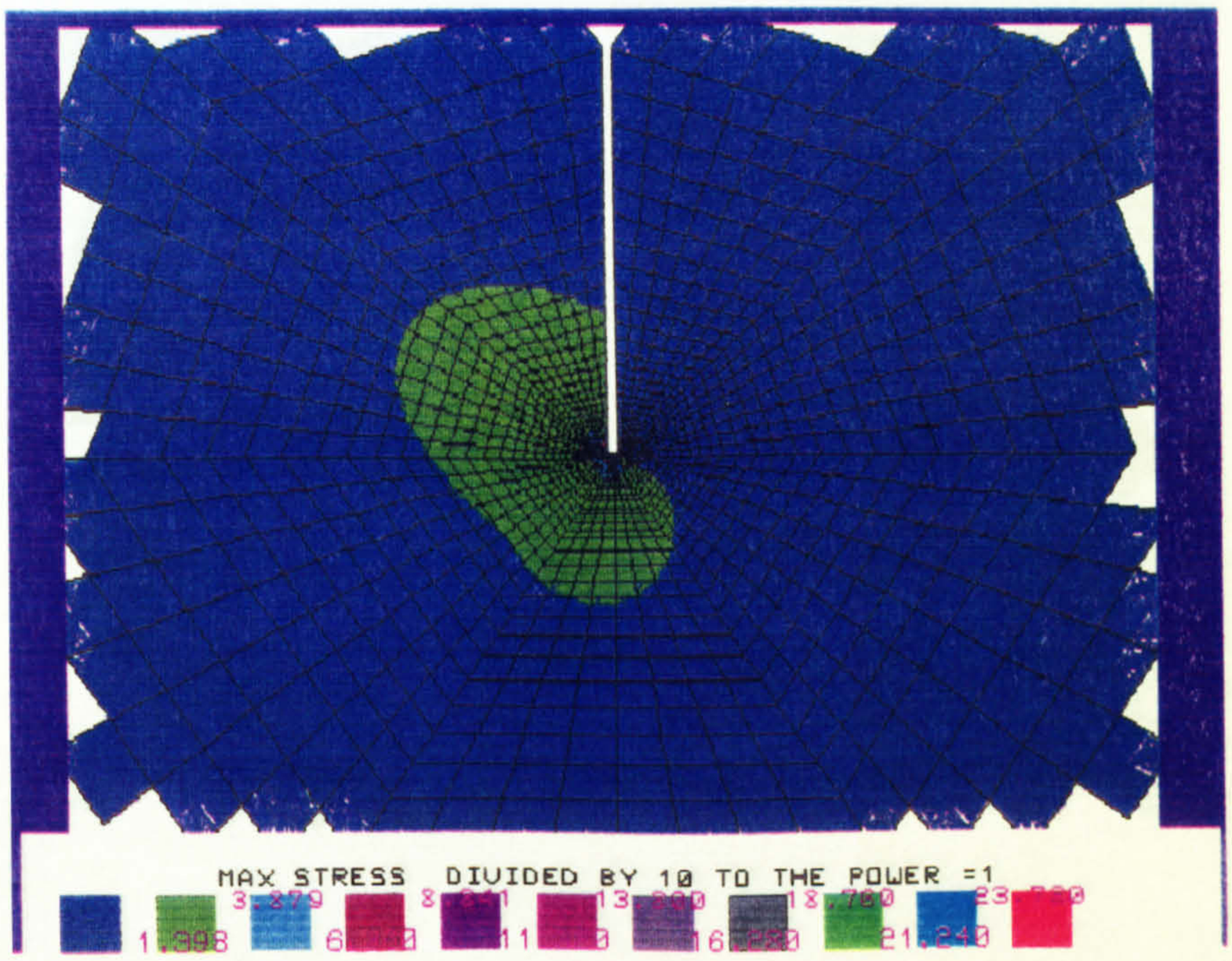

(21) $s/W = 7.35 \times 10^{-4}$, $s/\rho = 2$ *and* $K_I/(K_I + K_{II}) = 0.411$.

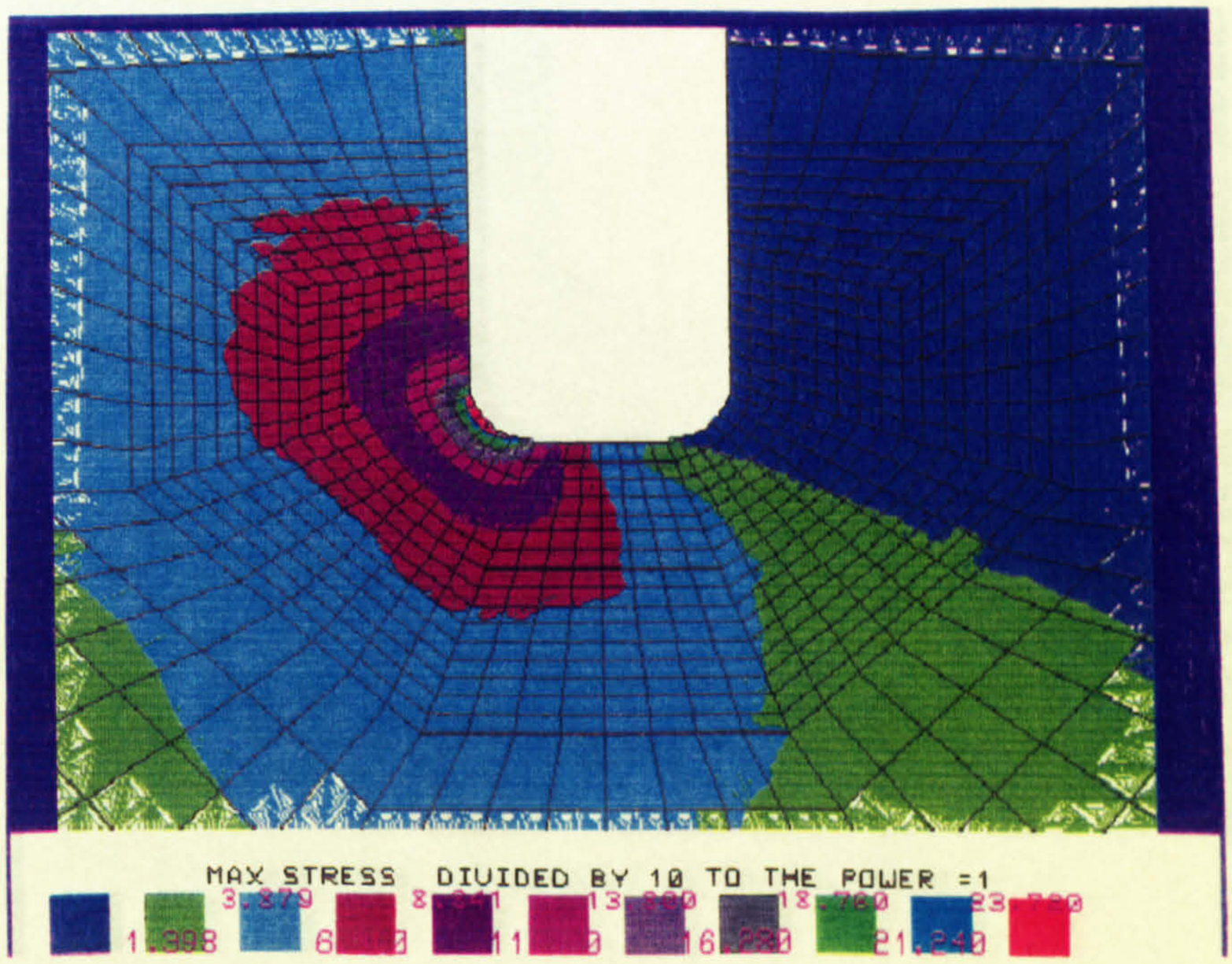

(22) $s/W = 7.35 \times 10^{-4}$, $s/\rho = 2$ *and* $K_I/(K_I + K_{II}) = 0.411$.

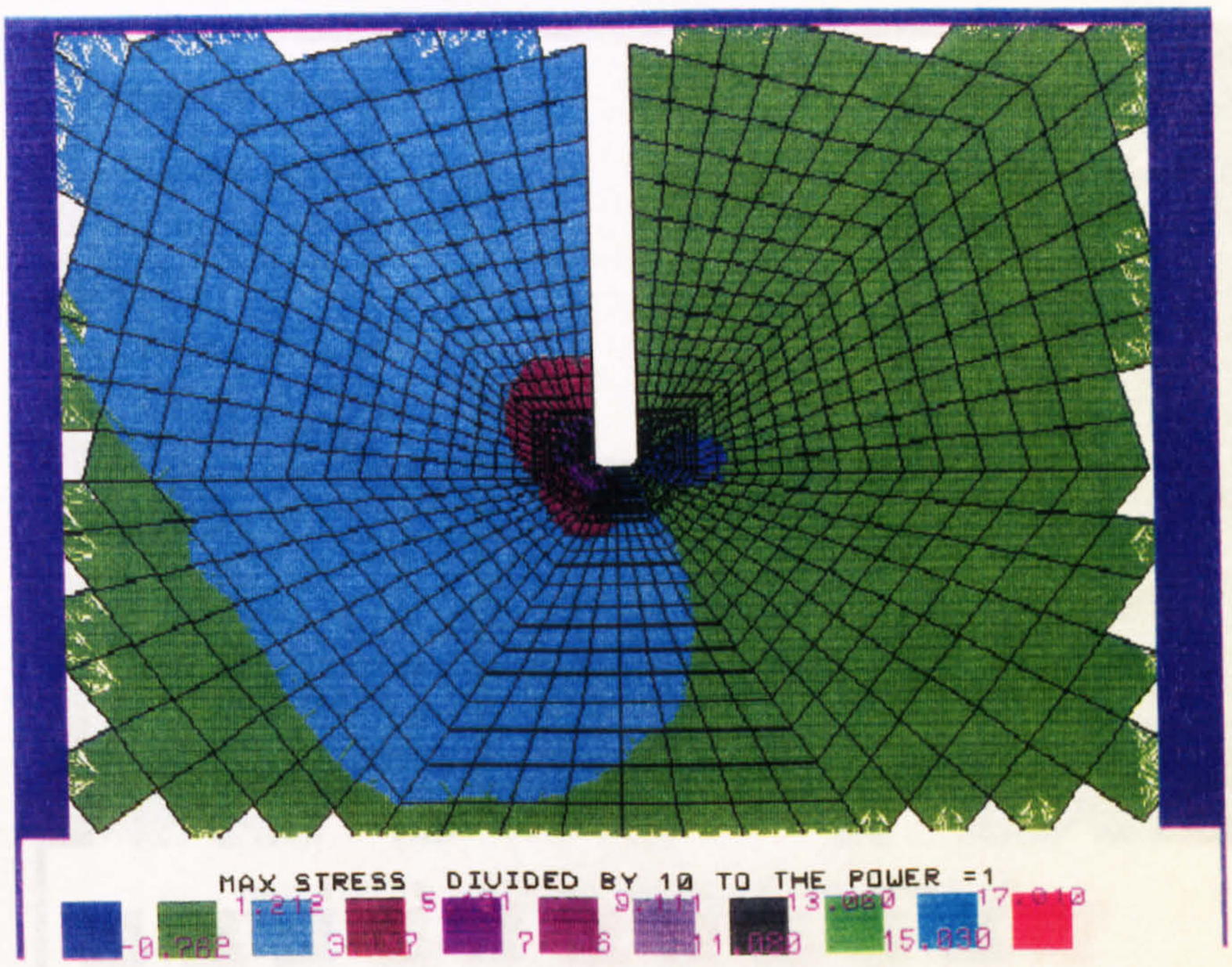

(23) $s/W = 7.35 \times 10^{-4}$, $s/\rho = 2$ *and* $K_I/(K_I + K_{II}) = 0.047$.

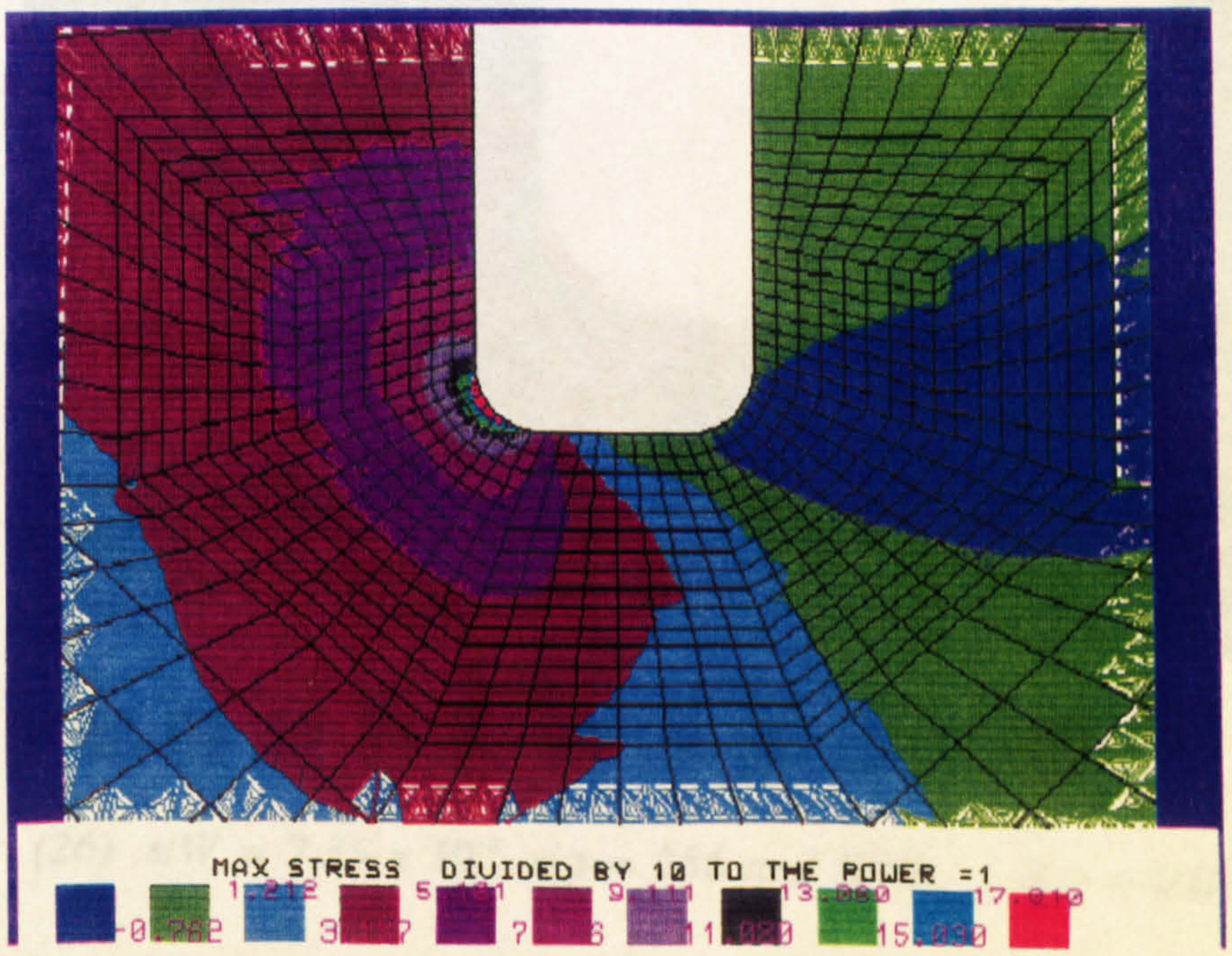

(24) $s/W = 7.35 \times 10^{-4}$, $s/\rho = 2$ *and* $K_I/(K_I + K_{II}) = 0.047$.

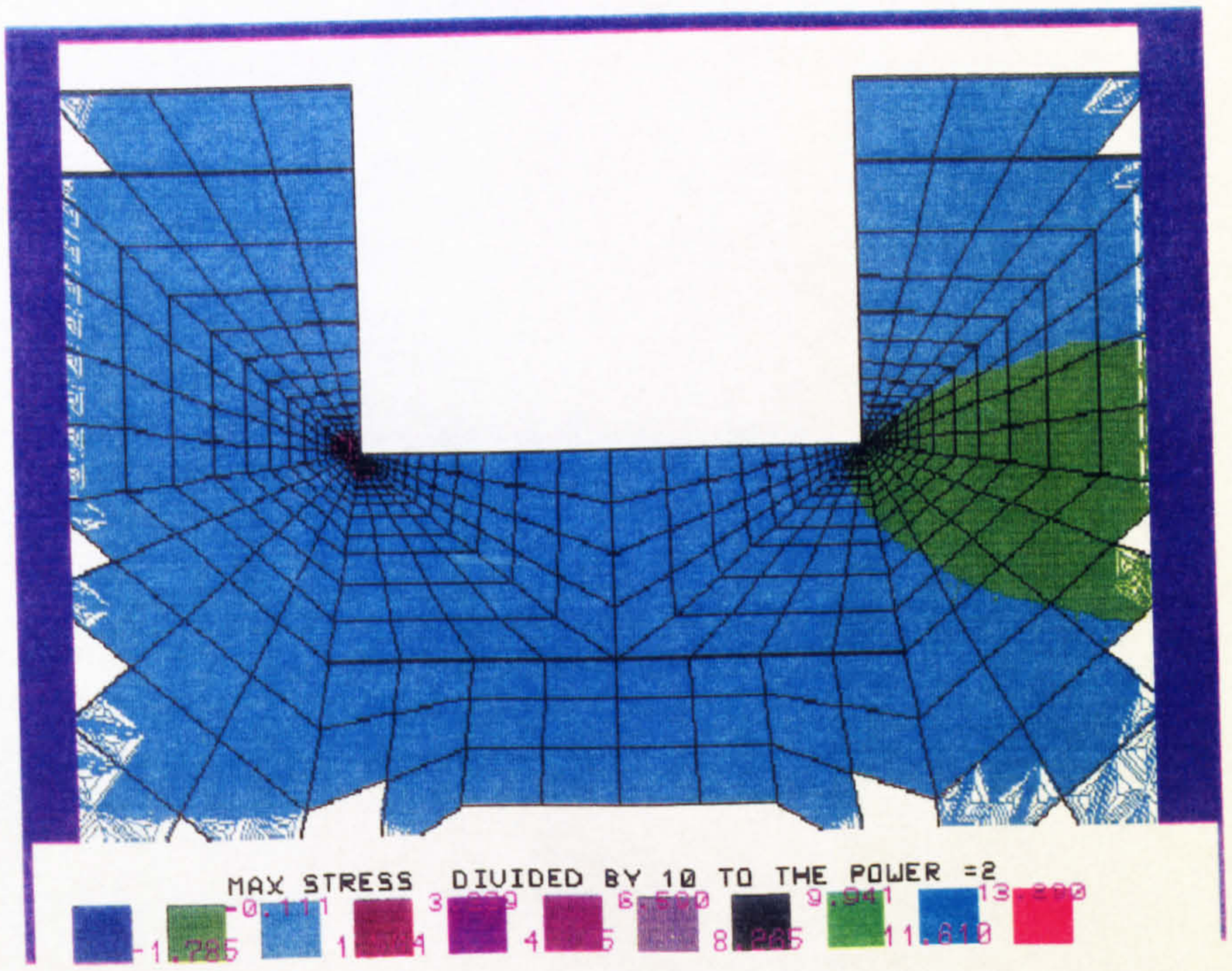

(25) $s/W = 7.35 \times 10^{-4}$, $s/\rho = 256$ *and* $K_I/(K_I + K_{II}) = 0.047$.

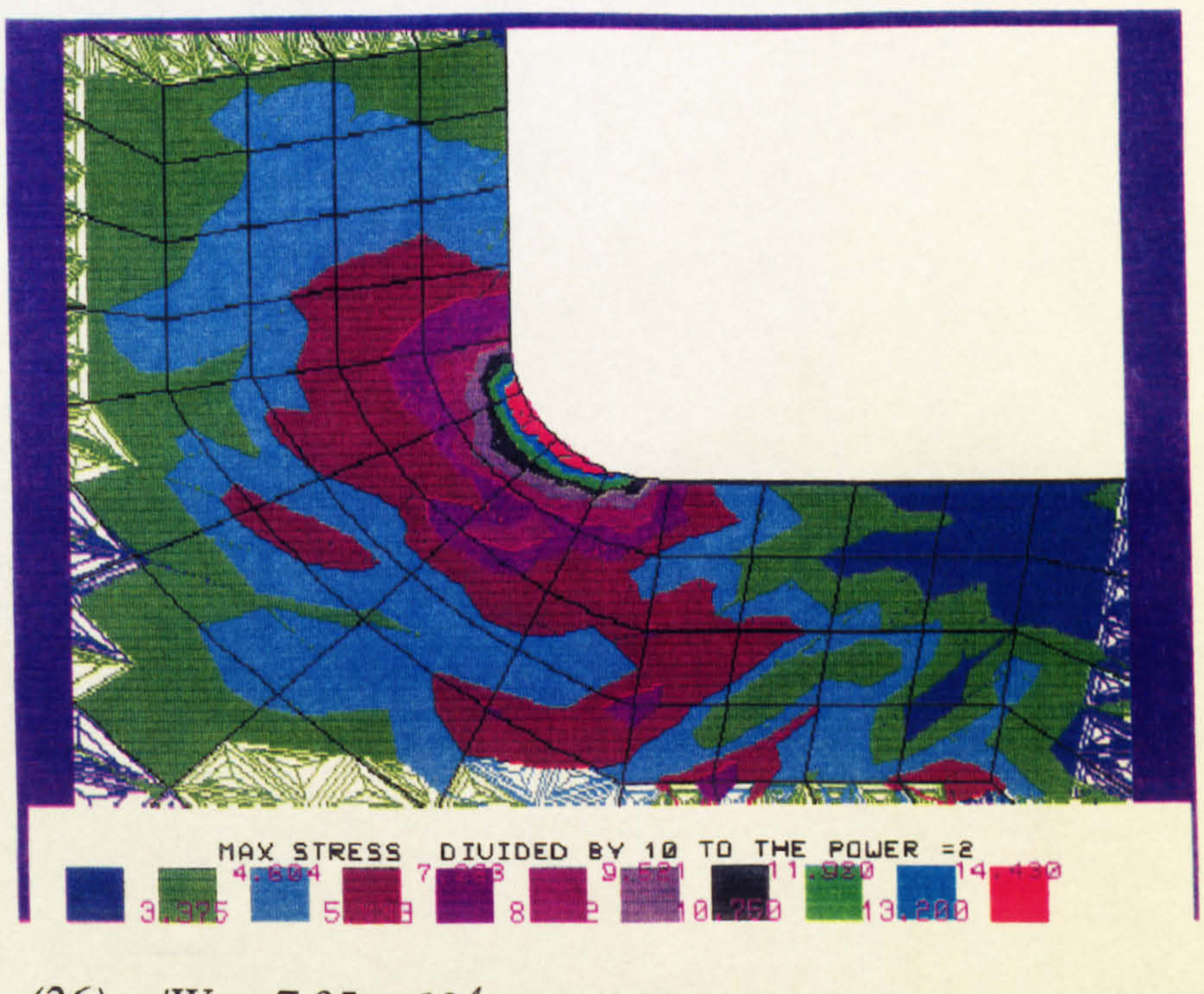

(26) $s/W = 7.35 \times 10^{-4}$, $s/\rho = 256$ *and* $K_I/(K_I + K_{II}) = 0.047$.

Figs. V.1(1-26). *The iso-stress contours of the* σ_{max} (N/mm^2) *at the notch tips of the CMM specimens.*